# Measurement of the inclusive and differential cross sections of the associated production of a top-quark pair and a $W$ boson, and search for leptoquarks in multilepton final states with the ATLAS detector

**Ph.D. dissertation**

by

**Stergios Kazakos**

Institut de Física d'Altes Energies
Universitat Autònoma de Barcelona
Departament de Física
Facultat de Ciències
Edifici Cn E-08193 Bellaterra (Barcelona)

*Thesis director*
**Aurelio Juste Rozas**
ICREA / Institut de Física d'Altes Energies
Universitat Autònoma de Barcelona

*Thesis tutor*
**Rafel Escribano Carrascosa**
Institut de Física d'Altes Energies
Universitat Autònoma de Barcelona

December 2022

CERN-THESIS-2022-384
26/01/2023






The project that gave rise to this thesis received the support of the INPhINIT fellowship from "la Caixa" Foundation (ID 100010434). The fellowship code is LCF/BQ/IN18/11660049.

This project has received funding from the European Union's Horizon 2020 research and innovation programme under the Marie Sklodowska-Curie grant agreement No. 713673.

Submitted on December 9th, 2022.

The defense took place on January 26th, 2023.

Copyright © 2022 by Stergios Kazakos. All rights reserved.

Committee members:

1. Dr. Lluïsa-Maria Mir i Martínez (Institut de Física d'Altes Energies - IFAE)
2. Dr. Francisco Javier Cuevas Maestro (Universidad de Oviedo)
3. Dr. Flavia de Almeida Dias (University of Amsterdam)

# Declaration of Authorship

I, **Stergios Kazakos**, declare that this thesis entitled:

"*Measurement of the inclusive and differential cross sections of the associated production of a top-quark pair and a W boson, and search for leptoquarks in multilepton final states with the ATLAS detector*"

and the work presented in it are my own. I confirm that:

- This work was done wholly while in candidature for a doctoral research degree at the Autonomous University of Barcelona (UAB).
- Where any part of this thesis has previously been submitted for a degree or any other qualification at this University or any other institution, this has been clearly stated.
- Where I have consulted the published work of others, this is always clearly attributed.
- Where I have quoted from the work of others, the source is always given. With the exception of such quotations and information needed for clarity and understanding of the reader, this thesis is entirely my own work.
- I have acknowledged all main sources of help.
- Where the thesis is based on work done by myself jointly with others, I have made clear exactly what was done by others and what I have contributed myself.

Signed: **S. K.**

Date: 09.12.2022

# Abstract

This dissertation presents a broad spectrum of physics analyses containing multiple leptons and $b$-tagged jets in their final state using data from proton-proton collisions at a center-of-mass energy of $\sqrt{s} = 13$ TeV recorded by the ATLAS detector at the Large Hadron Collider (LHC). The full Run-2 dataset is used, which corresponds to an integrated luminosity of 139 fb$^{-1}$. The dissertation is structured along two main axes. The first axis is centred around the measurement of the inclusive and differential cross section of the associated production of a top-quark pair and a $W$ boson ($t\bar{t}W$). This measurement is greatly motivated due to $t\bar{t}W$-like tensions in data reported by the ATLAS and CMS experiments. The theoretical modelling of this process is quite challenging due to non-negligible higher-order corrections, resulting into a great effort to achieve an accurate simulation of this contribution. The measurement is performed both inclusively and differentially, where several observables are unfolded at particle level. The $t\bar{t}W$ prediction is measured to be consistently higher than the SM expectation with an inclusive signal strength of $\mu_{t\bar{t}W}$=$1.44^{+0.14}_{-0.13}$. The second axis focuses on searches for physics beyond the SM (BSM) and, particularly, on searches for leptoquarks. Leptoquarks are one of the most favoured BSM scenarios to describe the intriguing deviations reported in $B$-meson decays by the LHCb experiment and the $B$ factories. This thesis is targeting pair-produced leptoquarks with a mass in the TeV scale each coupling simultaneously into a top quark and a lepton ($e$, $\mu$, $\tau$-lepton). This effort is divided in two dedicated searches targeting $t\ell t\ell$ and $t\tau t\tau$ signatures, respectively. No significant excess is found in both searches, and the most restrictive to date upper limits are set on the signal cross section and the branching ratio as a function of the leptoquark mass for several scalar and vector leptoquark models. In the $t\ell t\ell$ search, a scalar leptoquark with a mass about 1.6 TeV is excluded at the 95% confidence level, assuming it decays exclusively into $te$ or $t\mu$. The most stringent exclusion for a vector leptoquark reaches 2.0 TeV. In the $t\tau t\tau$ search, the corresponding exclusions for the same types of scalar and vector leptoquarks are about 1.4 TeV and 1.8 TeV, respectively. These searches are also combined with other leptoquark searches in ATLAS, significantly improving the sensitivity.

# Resumen

Esta disertación presenta un amplio espectro de análisis físicos que contienen múltiples leptones y jets etiquetados como $b$-jets en el estado final, usando los datos de colisiones protón-protón a una energía del centro de masas de $\sqrt{s} = 13$ TeV registrados por el detector ATLAS del Gran Colisionador de Hadrones (LHC, por sus siglas en inglés). Se utiliza el conjunto de datos del Run 2 completo, que corresponde a una luminosidad integrada de 139 fb$^{-1}$. La disertación se estructura a lo largo de dos ejes principales. El primer eje se centra en la medición de la sección eficaz inclusiva y diferencial de la producción asociada de un par de quarks top y un bosón $W$ ($t\bar{t}W$). Esta medida está muy motivada debido a las tensiones observadas en el análisis de los datos por parte de los experimentos ATLAS y CMS. El modelado teórico de este proceso representa un gran desafío debido a correcciones de orden superior importantes, lo cual requiere un gran esfuerzo para lograr una simulación precisa de esta contribución. La medición se realiza tanto de manera inclusiva como diferencial, donde se corrigen por efectos experimentales varios observables. La sección eficaz de $t\bar{t}W$ se mide consistentemente más alta que la predicción del Modelo Estándar (SM, por sus siglas en inglés) por un factor de $\mu_{t\bar{t}W}$=$1.44^{+0.14}_{-0.13}$. El segundo eje se centra en la búsqueda de física más allá del SM (BSM, por sus siglas en inglés) y, en particular, en la búsqueda de leptoquarks. Los leptoquarks son uno de los escenarios BSM más favorecidos para describir las intrigantes desviaciones reportadas en las desintegraciones de mesones $B$ por parte de el experimento LHCb y las fábricas de $B$. Esta tesis tiene como objetivo la producción de leptoquarks en pares con una masa en la escala del TeV, cada uno de los cuales se acopla simultáneamente con un quark top y un leptón ($e$, $\mu$, $\tau$-leptón). Este esfuerzo se divide en dos búsquedas dedicadas dirigidas a los estados finales $t\ell t\ell$ y $t\tau t\tau$, respectivamente. No se encuentra un exceso significativo en ambas búsquedas, y se establecen los límites superiores más restrictivos hasta la fecha en la sección eficaz de la señal, así como en la fracción de desintegración, en función de la masa del leptoquark para varios modelos de leptoquarks escalares y vectoriales. En la búsqueda de $t\ell t\ell$, se excluye un leptoquark escalar con una masa de aproximadamente 1.6 TeV con un nivel de confianza del 95 %, asumiendo que decae exclusivamente en $te$ o $t\mu$. La exclusión más estricta para un leptoquark vector alcanza los 2.0 TeV. En la búsqueda $t\tau t\tau$, las exclusiones correspondientes para los mismos tipos de leptoquarks escalares y vectoriales son de aproximadamente 1.4 TeV y 1.8 TeV, respectivamente. Estas búsquedas también se combinan con otras búsquedas de leptoquarks en ATLAS, mejorando significativamente la sensibilidad.

# Acknowledgements

This section is devoted to all the inspiring people that I had the chance to interact with and made this dissertation not only possible, but also turned the whole PhD period into a very educative and enjoyable journey.
I would like to express my warmest gratitude to my thesis supervisor Aurelio Juste for his guidance and patience throughout these years. Our endless discussions were really inspiring and helped me shape my own interests in the field of experimental particle physics. His physics questions made me think and question my current understanding in different physics aspects, which is all a physicist could ask for. I thank him for getting me involved in this world of multilepton and multiple $b$-jets signatures with really exciting future prospects, and for believing that I could succeed in it. He stood up for me as a spiritual father and a friend making physics fun and always pushing me to achieve great things.

On the leptoquark side, I would like to sincerely thank Tamara and Mahsana for standing up to me as second supervisors and guided me though my first steps and during the whole PhD. I learned a huge amount of things from them, and they were always available for fruitful discussions and happy to assist when needed. I owe much to them, and I thank them for the perfect collaboration we had within these years. I would also like to thank separately Yoshihiro for our nice collaboration, his valuable explanations about leptoquark phenomenology and for the cool tricks he shared with me regarding the use of terminal and the C++ programming language.

On the $t\bar{t}W$ side, I would like to thank the whole $t\bar{t}W$ to multilepton ATLAS group for the nice collaboration and discussions. There are probably no words to describe the tremendous amount of work from Brendon in this effort, and I would like to thank him for his dedication and for the very informative communication between us. Unfortunately I cannot mention everyone by name of course, but I cannot leave out the crucial contributions and commitment of Peter, Rohin, Needa-Alexandra, Nihal, Chenliang, Meng-Yu and Marcel. I thank them for their important work and for our excellent collaboration in this effort.

On the Tile calorimeter side, I would like Ilya Korolkov for being my co-supervisor and introduced me to the Tile calorimeter. He was more than willing and patient to explain me the calorimeter structure and function in detail, for which I'm grateful. I would also like to thank the members of the Tile group and especially the ones

from test-beam analysis subgroup. I would like to thank Sanya and Oleg for the useful inputs and guidance for completing the electron analysis, as well as Claudio for his support and for accepting to be the technical supervisor during my qualification task. A very warm thank you to Tigran, Tamar, Fernando and Sergi for guiding me through the test-beam setup and for the nice moments we had during meetings, shifts, and beyond.

The quality of this thesis wouldn't be the same without a healthy and prosperous working environment something that was achieved by the very friendly approach of the seniors of the IFAE ATLAS group Aurelio, Martine and Imma and the rest of the group in general. A special mention is required for Nazlim and Shalini. Apart from being fun working with them in several analyses, they contributed in their way to the results presented in this thesis, and I would like to deeply thank them for that. I would also like to thank Anil, Carlos, Tal and César, as well as the more senior IFAE and ex-IFAE people Nicola, Trisha, Javier, Danijela and Judita for the various discussions and funny moments we shared during the PhD. I would like to thank separately Adrian and Sergio as my partners in "crime" with whom I shared a flat, endless discussions about every possible subject and happy moments over beer at the famous R1 at CERN, and beyond. Their friendship and help on technical issues were greatly appreciated.

I would also like to thank people from the ATLAS PATHelp, DAST, AnalysisTop, TRExFitter and IFAE ATLAS support groups or concerned individuals for always being happy to help and answer to my emails really trying to help. There are people among them to whom I feel I own at least a beer even though I haven't personally met many of them. Therefore, just to name a few I would like to thank Tomas, Alex, Oliver, Tadej, Volker, Andreu, Rodney and Asoka for the time they spent looking into several of my issues and always being able to suggest effective solutions.

On a more formal note, I would like to thank Flavia de Almeida Dias, Javier Cuevas and LLuïsa-Maria Mir for accepting to be the members of my thesis committee as well as Rafél Escribano for accepting to be my thesis tutor (and for the dope lectures on SM!).

I am also very thankful for the generous support of the "la Caixa" Foundation, under the INPhINIT programme, which has made my PhD at IFAE possible and

gave me the opportunity to meet such amazing people through the trainings that were organised.

I would also like to thank an important fraction of people who made my stay at CERN unforgettable (in a good way!). I would like to thank my friends and lunch buddies from the Aristotle University of Thessaloniki, with whom we shared deep discussions and funny moments, and motivated each other to thrive in our own sectors of expertise. I would also like to thank the members of "greek mafia" with whom we organised several gatherings and helped in their own way to blow-off some steam from the stressful moments of the PhD. I would like to thank all the friends from the la Caixa programme with whom I came close during my stay in Barcelona for the joyful and emotional moments we shared. I would like to thank my pals from Physics department for cool reunions we had during the PhD period and for the mutual appreciation and friendship. A big thank you is reserved for my friends in Greece. In addition, I would also like to thank a smaller core of friends I made in the CERN area and apart from lunch buddies are great companions to a large fraction of activities. I'll mention a few names of these groups to make you happy in the unlikely scenario of ever reading this page, but please forgive me if I forget some. For this reason, I would like to thank Kostas, Despina, Giannis ($\times$ 3), Natalia, Christina, Aris, Rafaella, Vasilis, Grigoris, Stathis, Andreas, Myrsini, Loïc, Michalis, Vagelis, Ivan ($\times$ 2), Christoph, Arantxa, Silvia, Poonam, Yasmin, Ifaenyi, Kostas, Vasilis, Nickos, Vaggelis, Elias, Sophia, Giota, Manos, Tirsi, Maggie, Olga, and Thenia (ok I'm done!). A special thank you goes to Christos, the prodigy who keeps CERN safe from cyber attacks, and also happened to be my flatmate and a close friend for most of my time at CERN. His willingness in helping me with debugging and his great manners in general during our cohabitation period were greatly appreciated.

I am also very grateful to the families, wives and children of Christos, Odisseas, Giorgos and Vaggelis for bearing with my very close friends, and they in return are bearing up with me in my very good and bad times. I would like to really thank these guys for being "around", and I hope we keep this friendship alive for many years to come.

The warmest thank you is reserved for my partner Vasia, who really supported me during the most stressful times and she was the first one to call to share the rewarding and devastating moments of this PhD. I thank you for believing in me and feeling proud of my achievements even if we had to stay apart from each other

for large periods of time. I promise that there will be better times for us in the future.

Ultimately, I would like to thank my brother Giannis for his support in this journey and of course my parents Savvas and Maria. For this part you will allow me to switch to my mother tongue. Σας ευχαριστώ που με στηρίζετε σε κάθε μου βήμα και επιλογή, παρόλο που μας χωρίζουν χιλιάδες χιλιόμετρα. Σας ευχαριστώ που με μεγαλώσατε με τις σωστές αρχές και με μάθατε να έχω εμπιστοσύνη στον εαυτό μου. Ελπίζω να μπορέσω να σας το ανταποδώσω κάποια μέρα.

# Contents

**Declaration of Authorship** i

**Abstract** ii

**Acknowledgements** iv

**Abbreviations** xiii

**1 Introduction** 1

**2 The Standard Model** 5
2.1 Fundamental particles . . . . . 5
2.2 Lagrangian of the Standard Model . . . . . 9
2.3 The Higgs mechanism . . . . . 16
2.4 Higgs boson and top-quark properties . . . . . 23
2.5 Top-quark pair production in association with a $W$ boson . . . . . 28

**3 Beyond the Standard Model** 33
3.1 Shortcomings of the Standard Model . . . . . 33
3.2 Leptoquarks . . . . . 38
3.2.1 Motivation . . . . . 39
3.2.1.1 Appearance of leptoquarks in BSM theories . . . . 39
3.2.1.2 Flavour anomalies and muon magnetic moment . . 41
3.2.2 Leptoquark phenomenology . . . . . 47
3.2.3 Leptoquark production and decay modes . . . . . 52

**4 The LHC complex and the ATLAS detector** 59
4.1 The LHC complex . . . . . 60
4.1.1 Luminosity and pileup . . . . . 62
4.2 The ATLAS detector . . . . . 64
4.2.1 ATLAS coordinate system . . . . . 65
4.2.2 Inner detector . . . . . 67
4.2.2.1 Pixel detector . . . . . 69
4.2.2.2 Semiconductor tracker . . . . . 70
4.2.2.3 Transition radiation tracker . . . . . 71

4.2.3 ATLAS calorimeters . . . 72
4.2.3.1 Electromagnetic calorimeter . . . 72
4.2.3.2 Hadronic calorimeters . . . 74
4.2.4 Muon spectrometer . . . 76
4.2.5 Trigger system and data acquisition . . . 78
4.2.6 Data quality . . . 79
4.2.7 Luminosity measurement . . . 80

**5 Electron studies on the ATLAS Tile calorimeter towards the Phase-II upgrade 82**
5.1 ATLAS Tile calorimeter layout and the Phase-II upgrade . . . 83
5.2 TileCal test-beam setup . . . 88
5.3 Electron identification . . . 91
5.4 Electron response determination . . . 93
5.5 Estimation of systematic uncertainties . . . 96
5.6 Energy modulations . . . 97
5.7 Test-beam results . . . 98
5.7.1 Electron identification and response . . . 99
5.7.2 Setting of the electromagnetic scale . . . 104

**6 Event simulation 106**
6.1 Simulation of proton-proton collisions . . . 106
6.1.1 Factorisation theorem and parton distribution functions . . . 108
6.1.2 Matrix element . . . 109
6.1.3 Parton shower . . . 110
6.1.4 Hadronisation . . . 112
6.1.5 Underlying event and pileup . . . 113
6.2 Monte Carlo generators . . . 114
6.3 Detector simulation . . . 116

**7 Object reconstruction 119**
7.1 Tracks and vertices . . . 120
7.2 Electrons . . . 122
7.2.1 Electron reconstruction . . . 123
7.2.2 Electron identification . . . 124
7.2.3 Electron isolation . . . 125
7.2.4 Electron calibration . . . 126
7.3 Muons . . . 127
7.3.1 Muon reconstruction . . . 127
7.3.2 Muon identification . . . 129
7.3.3 Muon isolation . . . 131
7.3.4 Muon calibration . . . 131
7.4 Jets . . . 132
7.4.1 Jet reconstruction . . . 132
7.4.2 Jet calibration . . . 135

7.4.3 Jet vertex tagger and jet cleaning . . . 139
7.4.4 Jet flavour tagging . . . 141
7.5 Hadronically decaying tau-leptons . . . 147
7.5.1 Hadronic tau reconstruction . . . 147
7.5.2 Hadronic tau identification . . . 148
7.5.3 Hadronic tau calibration . . . 150
7.6 Missing transverse energy . . . 152

**8 Common aspects in signatures with multiple leptons and *b*-jets 154**
8.1 Data and simulated samples . . . 154
8.2 Background modelling . . . 157
8.2.1 $t\bar{t}W$ production . . . 157
8.2.2 $t\bar{t}Z/\gamma^*$ production . . . 158
8.2.3 $t\bar{t}H$ production . . . 160
8.2.4 $t\bar{t}$ production . . . 160
8.2.5 Diboson production . . . 161
8.2.6 $V$+jets production . . . 161
8.3 Object reconstruction and selection . . . 162
8.3.1 Framework and derivations . . . 162
8.3.2 Object and event preselection . . . 162
8.3.3 Object selection . . . 165
8.4 Analysis strategy principles . . . 168
8.4.1 Event categorisation . . . 168
8.4.2 Signal-to-background discrimination . . . 169
8.4.3 Blinding strategy . . . 169
8.5 Systematic uncertainties . . . 170
8.5.1 Instrumental uncertainties . . . 171
8.5.2 Theoretical modelling systematics . . . 173
8.6 Statistical formalism . . . 174
8.6.1 The Likelihood function . . . 175
8.6.2 Parameter estimation and the maximum likelihood method . 177
8.6.3 Hypothesis testing . . . 178
8.6.4 Limit setting and the $\mathrm{CL}_s$ method . . . 180

**9 Inclusive and differential cross-section measurements of $t\bar{t}W$ production 182**
9.1 Introduction . . . 182
9.2 Object selection . . . 183
9.3 Event categorisation and region definitions . . . 184
9.3.1 Fiducial-volume definition . . . 187
9.4 Background estimation and suppression . . . 188
9.4.1 Estimation of events with charge-misassigned leptons . . . 188
9.4.2 Data-driven corrections . . . 191
9.4.2.1 Diboson $N_{\mathrm{jets}}$-dependent correction . . . 191

9.4.2.2 $t\bar{t}$ + heavy-flavour correction . . . 193
9.4.2.3 Non-prompt lepton $N_{b-\text{jets}}$ correction . . . 194
9.4.3 Improved (non-) prompt lepton veto . . . 194
9.4.4 Template Fit method . . . 196
9.5 Systematic uncertainties . . . 207
9.5.1 Systematic uncertainties on fake-lepton background modelling and data-driven corrections . . . 208
9.6 Inclusive $t\bar{t}W$ production cross-section measurement . . . 210
9.7 Differential $t\bar{t}W$ production cross-section measurement . . . 215
9.7.1 Introduction to unfolding . . . 215
9.7.2 Profile likelihood unfolding . . . 216
9.7.3 Tikhonov regularisation . . . 221
9.7.4 Unfolded observables in the signal region . . . 223
9.7.5 Unfolding results and relative charge-asymmetry measurement 227

**10 Search for leptoquark pair production in multilepton final states 244**
10.1 Search for leptoquark pair production in $t\tau t\tau$ final states . . . 245
10.1.1 Introduction . . . 245
10.1.2 Object definition . . . 246
10.1.3 Event categorisation and discriminating variable . . . 246
10.1.4 Analysis region definitions . . . 248
10.1.5 Main background contributions . . . 253
10.1.6 Signal and background modelling . . . 256
10.1.6.1 Signal modelling . . . 256
10.1.6.2 Background modelling . . . 258
10.1.7 Analysis model and background validation . . . 263
10.1.8 Distributions with partial signal-region selections . . . 265
10.1.9 Systematic uncertainties . . . 267
10.1.10 Results . . . 268
10.1.10.1 Template Fit to data . . . 268
10.1.10.2 Expected and observed upper limits . . . 276
10.2 Search for leptoquark pair production in $t\ell t\ell$ final states ($\ell = e, \mu$) . 279
10.2.1 Introduction . . . 279
10.2.2 Event categorisation and discriminating variables . . . 280
10.2.3 Analysis region definitions . . . 281
10.2.4 Main background contributions . . . 284
10.2.5 Signal and background modelling . . . 286
10.2.5.1 Signal modelling . . . 286
10.2.5.2 Background modelling . . . 289
10.2.6 Analysis model and background validation . . . 289
10.2.7 Systematic uncertainties . . . 290
10.2.8 Results . . . 292
10.2.8.1 Template Fit to data . . . 292
10.2.8.2 Expected and observed upper limits . . . 299

10.2.8.3 Event display of a leptoquark candidate event . . . 302
10.3 Combination of leptoquark searches . . . . . 304

**11 Conclusions** **309**

**A Test-beam results of electron analysis on Tile calorimeter** **315**

**B Unfolding optimisations and setup** **321**
B.1 Parametrisation setups . . . . . 321
B.2 Binning optimisation . . . . . 323
B.3 Regularisation optimisation . . . . . 327
B.4 Sensitivity, closure and stress tests . . . . . 335

**C Limit comparison between the asymptotic approximation and the toy MC method** **342**

**Bibliography** **344**

# Abbreviations

| | |
|---|---|
| **AD** | **A**ntimatter **D**ecelerator |
| **AF** | **A**TLAS **F**ast |
| **AFP** | **A**TLAS **F**orward **P**roton |
| **ALFA** | **A**bsolute **L**uminosity **F**or **A**TLAS |
| **ATLAS** | **A** **T**orroidal **L**HC **A**pparatu**S** |
| **BCM** | **B**eam **C**onditions **M**onitor |
| **BDT** | **B**oosted **D**ecision **T**ree |
| **BNV** | **B**aryon **N**umber **V**iolation |
| **BR** | **B**ranching **R**atio |
| **BRT** | **B**oosted **R**egression **T**ree |
| **BRW** | **B**uchmüller **R**ückl **W**yler |
| **BSM** | **B**eyond the **S**tandard **M**odel |
| **CDF** | **C**umulative **D**istribution **F**unction |
| **CERN** | **C**onseil **E**uropéen pour la **R**echerche **N**ucléaire |
| **CI** | **C**onfidence **I**ntegral |
| **CIS** | **C**harge **I**njection **S**ystem |
| **CL** | **C**onfidence **L**evel |
| **CMB** | **C**osmic **M**icrowave **B**ackground |
| **CP** | **C**harge **P**arity |
| **CR** | **C**ontrol **R**egion |
| **CSC** | **C**athode **S**trip **C**hamber |
| **CTP** | **C**entral **T**rigger **P**rocessor |
| **DLT** | **D**i-**L**epton **T**rigger |
| **DM** | **D**ark **M**atter |
| **DNN** | **D**eep **N**eural **N**etwork |
| **DQ** | **D**ata **Q**uality |
| **EB** | **E**xtended **B**arrel |
| **ECal** | **E**lectromagnetic **Cal**orimeter |
| **ECIDS** | **E**lectron **C**harge **ID**entification **S**elector |
| **EM** | **E**lectro**M**agnetic |
| **ETC** | **E**xtended **T**echni**C**olour |
| **EWSB** | **E**lectro**W**eak **S**ymmetry **B**reaking |

| | |
|---|---|
| **FBU** | **F**ully **B**ayesian **U**nfolding |
| **FCal** | **F**orward **Cal**orimeter |
| **FCNC** | **F**lavour **C**hanging **N**eutral **C**urrent |
| **FNAL** | **F**ermi **N**ational **A**ccelerator **L**aboratory |
| **FS** | **F**ull**S**im |
| **FSR** | **F**inal **S**tate **R**adiation |
| **GFW1/2** | **G**roup**F**rame**W**ork **1/2** |
| **GRL** | **G**ood **R**un **L**ist |
| **GSC** | **G**lobal **S**equential **C**alibration |
| **GSF** | **G**aussian **S**um **F**ilter |
| **GUT** | **G**rand **U**nified **T**heory |
| **HCal** | **H**adronic **Cal**orimeter |
| **HEC** | **H**adronic **E**nd-Cap **C**alorimeter |
| **HF** | **H**eavy **F**lavour |
| **HGTD** | **H**igh-**G**ranularity **T**iming **D**etector |
| **HL-LHC** | **H**igh-**L**uminosity-**LHC** |
| **HLT** | **H**igh-**L**evel **T**rigger |
| **HV** | **H**igh **V**oltage |
| **IBL** | **I**nsertable **B**-**L**ayer |
| **IBU** | **I**terative **B**ayesian **U**nfolding |
| **ID** | **I**nner **D**etector |
| **IP** | **I**mpact **P**arameter & **I**nteraction **P**oint |
| **IRC** | **I**nfra**R**ed and **C**ollinear |
| **ISR** | **I**nitial **S**tate **R**adiation |
| **ITk** | **I**nner **Tk** |
| **JES** | **J**et **E**nergy **S**cale |
| **JVT** | **J**et **V**ertex **T**agger |
| **L0/1** | **L**evel-**0/1** |
| **L1Calo** | **L1 Calo**rimeter |
| **L1Topo** | **L1 Topo**logical |
| **LAr** | **L**iquid **Ar**gon |
| **LB** | **L**ong **B**arrel |
| **LC** | **L**ocal **C**alibration |
| **LEP** | **L**arge **E**lectron **P**ositron |
| **LF** | **L**ight **F**lavour |
| **LFU** | **L**epton **F**lavour **U**niversality |
| **LH** | **L**ikeli**H**ood |
| **LHC** | **L**arge **H**adron **C**ollider |
| **LNV** | **L**epton **N**umber **V**iolation |
| **LO** | **L**eading **O**rder |
| **LQ** | **L**epto**Q**uark |

| | |
|---|---|
| **LS2** | **L**ong **S**hutdown 2 |
| **LSP** | **L**ightest **S**upersymmetric **P**article |
| **LUCID2** | **LU**minosity measurement using **C**herenkov **I**ntegrating **D**etector **2** |
| **LVPS** | **L**ow **V**oltage **P**ower **S**upply |
| **MAPMT** | **M**ulti-**A**node **P**hoto**M**ultiplier **T**ube |
| **mBRW** | **m**inimal **B**uchmüller **R**ückl **W**yler |
| **MBTS** | **M**inimum **B**ias **T**rigger **S**cintillator |
| **MC** | **M**onte **C**arlo |
| **MDT** | **M**onitored **D**rift **T**ube |
| **ME** | **M**atrix **E**lement |
| **ML** | **M**aximum **L**ikelihood |
| **MPX** | **M**edi**P**i**X** |
| **MS** | **M**uon **S**pectrometer |
| **MVA** | **M**ulti-**V**ariate **A**nalysis |
| **NF** | **N**ormalisation **F**actor |
| **NLO** | **N**ext-to-**L**eading **O**rder |
| **NNLL** | **N**ext-to-**N**ext-to-**L**eading **L**ogarithmic |
| **NNLO** | **N**ext-to-**N**ext-to-**L**eading **O**rder |
| **NP** | **N**uisance **P**arameter |
| **OP** | **O**perating **P**oint |
| **OR** | **O**verlap **R**emoval |
| **OS** | **O**pposite charge (**S**ign) |
| **OSSF** | **O**pposite charge (**S**ign) **S**ame **F**lavour |
| **PDF** | **P**arton **D**istribution **F**unction |
| **pdf** | **P**robability **D**ensity **F**unction |
| **PFlow** | **P**article **Flow** |
| **PLIV** | **P**rompt **L**epton **I**mproved **V**eto |
| **PLU** | **P**rofile **L**ikelihood **U**nfolding |
| **PLV** | **P**rompt**L**epton**V**eto |
| **PMT** | **P**hoto**M**ultiplier **T**ube |
| **PS** | **P**arton **S**hower |
| **PS** | **P**roton **S**ynchrotron |
| **PSB** | **P**roton **S**ynchrotron **B**ooster |
| **PU** | **P**ile**U**p |
| **PV** | **P**rimary **V**ertex |
| **QCD** | **Q**uantum **C**hromo**D**ynamics |
| **QED** | **Q**uantum **E**lectro**D**ynamics |
| **QFT** | **Q**uantum **F**ield **T**heory |
| **RC** | **R**e**C**lustered |
| **RDO** | **R**aw **D**ata **O**bject |

| | |
|---|---|
| **RF** | **R**adio **F**requency |
| **ROC** | **R**eceiver **O**perating **C**haracteristic |
| **ROD** | **R**ead **O**ut **D**river |
| **RoI** | **R**egion **o**f **I**nterest |
| **RPC** | **R**esistive **P**late **C**hamber |
| **RPV** | **R**ight **P**arity **V**iolation |
| **SCT** | **S**emi-**C**onductor **T**racker |
| **SD** | **S**uper **D**rawer |
| **SF** | **S**cale **F**actor |
| **SLT** | **S**ingle-**L**epton **T**rigger |
| **SM** | **S**tandard **M**odel |
| **SPS** | **S**uper **P**roton **S**ynchrotron |
| **SR** | **S**ignal **R**egion |
| **SS** | **S**ame charge (**S**ign) |
| **SSB** | **S**pontaneous **S**ymmetry **B**reaking |
| **SUSY** | **SU**per**SY**mmetry |
| **SVD** | **S**ingular **V**alue **D**ecomposition |
| **TDAQ** | **T**rigger and **D**ata **A**c**Q**uisition |
| **TEEC** | **T**ransverse **E**nergy-**E**nergy **C**orrelation |
| **TES** | **T**au **E**nergy **S**cale |
| **TGC** | **T**hin **G**ap **C**hamber |
| **TileCal** | **Tile Cal**orimeter |
| **TPF** | **T**au **P**article **F**low |
| **TRT** | **T**ransition **R**adiation **T**racker |
| **UE** | **U**nderlying **E**vent |
| **varRC** | **var**iable-size radius **R**e**C**lustered |
| **VBF** | **V**ector **B**oson **F**usion |
| **vdM** | **v**an **d**er **M**eer |
| **VEV** | **V**acuum **E**xpectation **V**alue |
| **VR** | **V**alidation **R**egion |
| **WIMP** | **W**eakly **I**nteracting **M**assive **P**article |
| **WLS** | **W**ave**L**ength-**S**hifting |
| **YM** | **Y**ang-**M**ills |
| **ZDC** | **Z**ero-**D**egree **C**alorimeter |

*To my family for their endless*
*love and support ...*

# Chapter 1

# Introduction

Many attempts have been made over the centuries to understand the interactions between the most fundamental blocks of matter in the universe and be able to describe them in a concrete mathematical framework. Our current knowledge is compiled into a relatively complete theory known as the Standard Model (SM) of particle physics. The SM has been tested with remarkable precision since its formulation, providing a detailed description of the fundamental particles as well as the interactions between them. The missing piece needed to complement this theory has been discovered in 2012 and it was the so-called Higgs boson. This discovery has been considered a milestone in high energy physics, and since then the general interest was focused on trying to measure its properties with ever-increasing precision.

The precision measurements related to the Higgs boson are more than interesting, but they can also be centred around other processes like the associated production of a top-quark pair and a Higgs or a $W$ boson ($t\bar{t}H$ or $t\bar{t}W$). The measurement of the production cross section of the former process is a way to access the top Yukawa coupling, the only coupling to the Higgs boson that can be accessed directly. This cross-section measurement has been currently delayed due to potential mismodelling by the state-of-art theoretical predictions of the $t\bar{t}W$ process, one of the SM processes that constitutes a non-negligible background contribution in the $t\bar{t}H$ measurement. The modelling of the $t\bar{t}W$ process has been extremely challenging to theorists due to the need to include higher-order corrections. Therefore, a detailed measurement of this process is needed to compare to the theoretical predictions and understand how to improve them. Alternatively, deviations from the

theoretical predictions may reveal potential effects from processes beyond the SM. The inclusive and differential $t\bar{t}W$ production cross sections are measured for the first time in ATLAS and the results are discussed in this thesis.

Several physical distributions needed to be unfolded for this purpose for the differential measurement including $t\bar{t}W$ relative charge asymmetry among others, a key variable to study the dependence of charge on the cross section and understand if the $t\bar{t}W$ process is even more asymmetric than expected.

Despite its success, the SM cannot be interpreted as a complete theory of the physical universe since it does not take into account gravity, one of its fundamental forces. Apart from this fact there are additional reasons to speculate that SM is the simplification of a more general theory, yet to be determined. One of these reasons is that it only accounts for the ordinary matter (and antimatter), which only constitutes a small fraction of the known universe. The remaining part that includes the *dark matter* and *dark energy* is currently overlooked.

Furthermore, recent findings of the $B$-physics experiments are pointing to intriguing deviations from the SM expectation values that manifest themselves through deviations in the measurements of $R_{D/D^*}$ and $R_{K/K^*}$ ratios in charged and neutral current processes respectively. All of the above have led to the development of numerous extensions to the SM, which address some of these observations. Among the most popular extensions are the models involving the existence of leptoquarks (LQs), hypothesised particles expected to decay promptly into a quark and a lepton. The increasing popularity of these models lies on the fact that they could explain the $B$-physics anomalies that seem to consolidate themselves throughout the years.

The ATLAS program of LQ searches is traced back to Run 1 and it has been severely enriched since then. Some of the most promising final states are the ones involving third generation quarks (bottom or top) and leptons of all generations. Especially, final states involving $\tau$-leptons were often overlooked in the past due to their complexity and poor $\tau$ identification. For all these reasons, dedicated searches had been launched targeting leptoquarks produced in pairs with final states with top-quarks and leptons ($\ell = e, \mu, \tau$). These searches and the results obtained are discussed as part of this thesis.

The content of this dissertation is organised as follows. Chapter 2 briefly describes the theoretical overview, including the physics of the SM and its formulation. It

provides a summary of the Higgs boson and top-quark properties and it focuses on the modelling, as well as on the production and decay modes of the $t\bar{t}W$ process motivating the measurement of its production cross section. Chapter 3 describes the scenarios Beyond the Standard Model (BSM) that are relative to the content of the thesis, and focuses on the motivation for the existence of leptoquarks analysing their phenomenology, as well as their production and decay modes. In Chapter 4, the Large Hadron Collider (LHC) and ATLAS detector are introduced and the main components of the ATLAS detector and their functions are detailed. Chapter 5 describes the electron analysis on the hadronic Tile calorimeter related to the Phase-II upgrade studies for the ATLAS detector. Chapter 6 presents in detail the simulation of proton-proton interaction. Chapter 7 lists the physics objects used in the analysis, explaining the object selection and reconstruction. Chapter 8 focuses on the common aspects in analyses with multiple leptons and $b$-tagged jets. In Chapter 9, the results of the inclusive and differential measurement of the $t\bar{t}W$ production cross section are presented. Chapter 10 contains the results of the search for scalar LQ pair production in the $t\tau t\tau$ final state followed by the search for scalar LQ pair production in the $t\ell t\ell$ final state, where $\ell = e, \mu$. The conclusions and future prospects are given in the Chapter 11.

The analyses reported in this thesis are focused on final states containing multiple leptons and multiple $b$-tagged jets, a signature extremely powerful at a hadron collider, since this allows to dramatically reduce backgrounds from multijet production.

The work conducted in the context of this dissertation has led to the following publications and conference notes by the ATLAS Collaboration:

- ATLAS Collaboration, *"Measurement of the total and differential cross-sections of $t\bar{t}W$ production in pp collisions at 13 TeV with the ATLAS detector"*, ATLAS-CONF-2023-019.
- ATLAS Collaboration, *"Search for leptoquark pair production decaying into $t\ell^{-}\bar{t}\ell^{+}$ in multilepton final states in pp collisions at 13 TeV with the ATLAS detector"*, ATLAS-CONF-2022-052.
- ATLAS Collaboration, *"Search for heavy Higgs bosons from a g2HDM in multilepton plus b-jets final states in pp collisions at 13 TeV with the ATLAS detector"*, ATLAS-CONF-2022-039.

- ATLAS Collaboration, *"Search for pair production of third-generation scalar leptoquarks decaying into a top quark and a $\tau$-lepton in pp collisions at $\sqrt{s}$ = 13 TeV with the ATLAS detector"*, JHEP 06 (2021) 179.

- ATLAS Collaboration, *"Study of energy response and resolution of the ATLAS Tile Calorimeter to hadrons of energies from 16 to 30 GeV"*, Eur. Phys. J. C 81 (2021) 549.

- ATLAS Collaboration, *"Analysis of $t\bar{t}H$ and $t\bar{t}W$ production in multilepton final states with the ATLAS detector"*, ATLAS-CONF-2019-045.

(A selection of analyses had to be made to be included in this thesis and for this reason the results of the flavour-violating g2HDM search are not discussed here.)

The author has also made major contributions to the results of the following analysis that are still not public and are summarised in the following paper draft:

- ATLAS Collaboration, *"Combination of searches for pair-produced leptoquarks at $\sqrt{s}$ = 13 TeV with the ATLAS detector"*, ANA-EXOT-2020-27.

Finally, the author has also followed closely and contributed to the internal ATLAS review of the following analyses:

- ATLAS Collaboration, *"Search for new phenomena in three- or four-lepton events in pp collisions at $\sqrt{s}$ = 13 TeV with the ATLAS detector"*, Phys. Lett. B 824 (2022) 136832.

- ATLAS Collaboration, *"Search for a new scalar decaying to two beyond-the-Standard-Model light bosons and then on to a four-lepton final state with 140 $fb^{-1}$ at $\sqrt{s}$ = 13 TeV"*, ANA-HDBS-2021-13.

- ATLAS Collaboration, *"Search for non-resonant di-Higgs production with multiple lepton final states using 139 $fb^{-1}$ proton-proton collision data at $\sqrt{s} = 13$ TeV recorded by the ATLAS detector"*, ANA-HDBS-2019-04.

# Chapter 2

# The Standard Model

This chapter serves as a main introduction to the Standard Model (SM) of particle physics, the theory that provides the most accurate description of the fundamental particles and their interactions up-to-date, being able to incorporate three of the four known fundamental forces in nature. Starting from a brief description of the SM and its particle content, and then going deeper into the mathematical formulation of the SM as a quantum field theory, this chapter will try to set the theoretical basis of the necessary pieces needed to understand this prevalent theory.

The use of natural units will be adopted throughout this chapter (and the rest of this dissertation) such that the speed of light (c) and the Planck constant ($\hbar$) are both set to unity ($c = \hbar = 1$).

## 2.1 Fundamental particles

The formulation of the Standard Model (SM) [1–3] was developed in the early 1970s summarising our current understanding of how the universe works. Since then the SM had been tested with remarkable precision and it quickly became the dominant theory to explain the fundamental particles and the interactions between them. Its core structure includes the quarks and leptons that fall under a larger group of fundamental particles called fermions. It suggests that all forces are mediated by force carrying gauge bosons, and that the interaction with the

Higgs boson is the reason behind how massive fundamental particles acquire their mass.

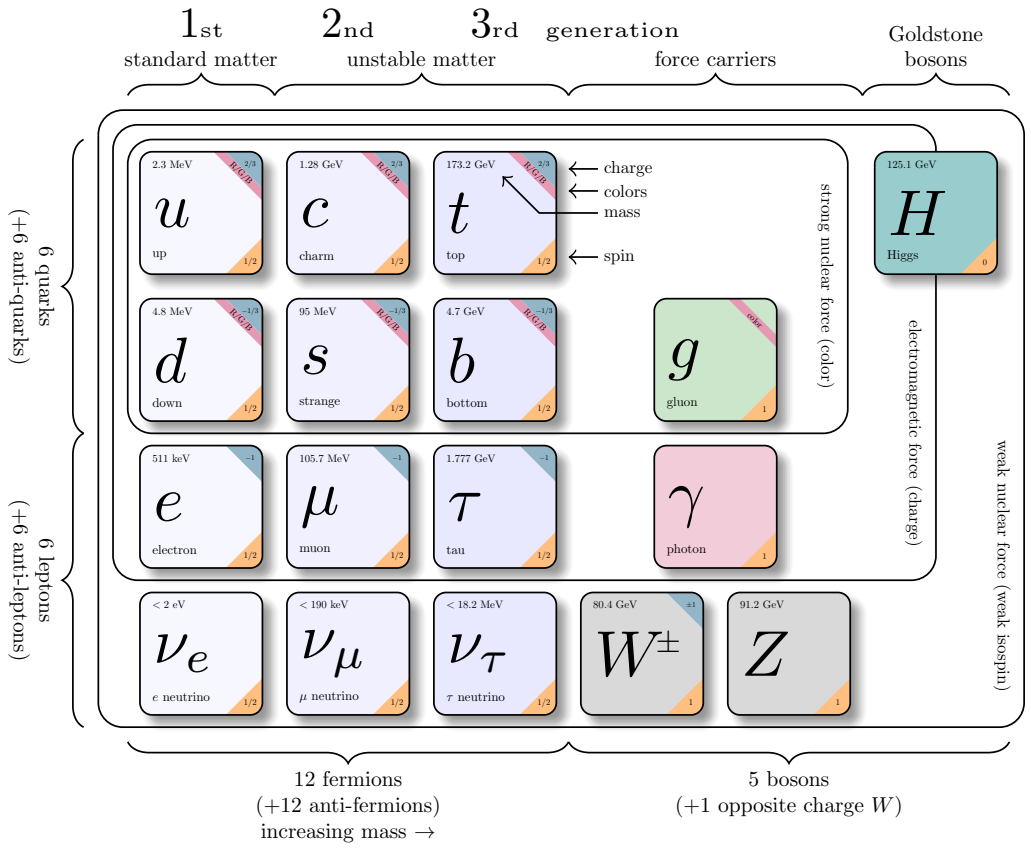



FIGURE 2.1: Illustration of the elementary particles predicted by the Standard Model. Figure adapted from Ref. [4].

Fermions have half integer spin and comply to Fermi-Dirac statistics (or Pauli's exclusion principle). Bosons have integer spin and obey Bose-Einstein statistics. Spin stands for an intrinsic property of the particles which could be interpreted as a different form of angular momentum.

### Fermions

Fermions constitute the buildings blocks of matter and can be classified in two main categories; *quarks* and *leptons*. Each of these groups consists of six particles, which are in turn divided into three subgroups (the three generations) according to their properties as shown in Figure 2.1. A free fermion state is generally described

by the Lagrangian of the Dirac equation given by

$$\mathcal{L} = \bar{\psi}(i\gamma^{\mu}\partial_{\mu} - m)\psi, \tag{2.1}$$

where $\psi$ stands for the fermion state (called *spinor*).

Despite the profound similarities between quarks and leptons as elementary particles, there are some striking differences worth spotting.

Starting the discussion with the quarks, the **up ($u$)** and **down ($d$)** quarks complete the first generation, the **charm ($c$)** and **strange ($s$)** quarks complete the second generation and the **top ($t$)** and **bottom ($b$)** quarks come to complement the third generation. Each generation corresponds to the order in which they were discovered, and the grouping is a result of the increasing mass from one generation to another.[1] Quarks carry a fractional electric charge. The upper part of each quark generation has an electric charge $Q = +2/3$ and is known as an up-type quark. The lower part of each generation has an electric charge of $Q = -1/3$ and is referred to as a down-type quark. Quarks also carry a colour charge in addition to the electric one. Every quark exists in one of the three colour states called *red*, *green* and *blue*. The colour is associated with the way they interact with each other through strong interaction. Due to colour confinement quarks cannot in principle exist freely in nature, and are always bound in colourless composite particles called hadrons. The most common hadron in particle physics is called proton ($p$), which is widely used in collision experiments at the LHC at CERN and inherits its positive electric charge through the combination of two up and one down quarks ($uud$). Additionally to the six quark flavours there are six more quarks of the same mass, but carrying the opposite electric and colour charges. These are their anti-matter partners that are called *anti-quarks* and their symbols are denoted with a bar on top of each letter.

Similar to quarks, leptons are also met in three generations of increasing mass with the **electron ($e$)** and the corresponding **electron neutrino ($\nu_e$)** in the first generation, the **muon ($\mu$)** and **muon neutrino ($\nu_\mu$)** in the second generation, and the **tau ($\tau$)** and **tau neutrino ($\nu_\tau$)** in the third generation. Leptons can exist freely in nature and the electron is the most common of them orbiting the nucleus of an ordinary atom. Muons ($\sim$200 times heavier than electrons) are mostly found in cosmic ray radiation and can be described as highly penetrating particles. These

1 The same also applies to lepton generations.

heavier versions of the electron have a finite lifetime decaying to electrons, which are stable. Although muons are not stable, they are still considered elementary particles due to the lack of inner structure. Neutrinos have a small, finite, non-zero mass, and their oscillations were currently observed by different experiments during their propagation through space. Electron, muon and tau have integer negative electric charge ($Q = -1$) and the corresponding neutrinos have zero electric charge. Additionally, leptons interact with all forces except for the strong force and, in contrast with quarks, they do not carry colour charge. Leptons have also their anti-matter partners with equal properties, but opposite electric charge and lepton number ($L$). Since neutrino does not carry electric charge the only difference with its anti-particle is the lepton number ($L = -1$ for ordinary matter and $L = 1$ for anti-matter).

### Bosons

The gauge bosons complement the rest of the SM particle content by mediating three of the fundamental forces of nature: weak, strong and electromagnetic. The gauge bosons are exchanged between particles that interact via a certain type of force. Their difference with fermions is that compared to them they have integer spin. The mediators of the weak force are $W^{\pm}$ and $Z^0$ bosons (massive spin-1 bosons), which can be also interpreted as resonances with a finite lifetime. The $W$ boson is electrically charged and changes the flavour of the quarks and leptons that interacts with, while the $Z$ boson has no electric charge and leaves their flavour unchanged. The mediators of the strong force are the eight gluons ($g$) (massless), which have no electric charge, but instead they have a "colour charge" that explains the strong interaction between colour charged particles, or quarks. The interactions of gluons are described by the theory of Quantum Chromodynamics (QCD). The mediator of the electromagnetic interaction is the photon (massless spin-1 boson). The photon ($\gamma$) is a stable particle with no electric charge. The behaviour of the photon is properly described by the theory of Quantum Electrodynamics (QED) with remarkable precision. Finally, the discovery of the Higgs boson [5, 6] (massive spin-0 boson) validated the existence of the Higgs field, which explains the mechanism by which elementary particles acquire their mass through a process that is called the Higgs mechanism [7–9]. The natural physics intuition suggests that another boson should exist that would be responsible for mediating the gravitational force. Although not yet found, a spin-2 boson, the graviton, would be the perfect candidate for a quantum description of gravity.

The Lagrangian of a free non-interacting scalar field (given from Equation 2.2) can be used to describe the behaviour of spin-0 bosons

$$\mathcal{L} = \frac{1}{2}(\partial_\mu \phi)(\partial^\mu \phi) - \frac{1}{2}m^2\phi^2, \tag{2.2}$$

where $\phi$ is a spin-0 field.

If Equation 2.2 is substituted into the Euler-Lagrange equation then it results to the Klein-Gordon equation for a free scalar field $\phi$

$$\partial_\mu \partial^\mu \phi + m^2 \phi = 0. \tag{2.3}$$

A massive spin-1 particle (like $W$ and $Z$) is described by the Proca Lagrangian

$$\mathcal{L} = -\frac{1}{4}F_{\mu\nu}F^{\mu\nu} + \frac{1}{2}m^2 A_\mu A^\mu, \tag{2.4}$$

where $F_{\mu\nu} = \partial_\mu A_\nu - \partial_\nu A_\mu$ is the field-strength tensor[2] and $A_\mu = (\phi, \vec{A})$ is the electromagnetic vector field.

For a massless spin-1 particle (like the photon) Equation 2.4 is modified to the simplest form

$$\mathcal{L} = -\frac{1}{4}F_{\mu\nu}F^{\mu\nu}. \tag{2.5}$$

## 2.2 Lagrangian of the Standard Model

The SM is a renormalisable quantum field theory (QFT) and therefore its mathematical expression is provided in the Lagrangian formalism. Particularly, the SM Lagrangian is kept invariant under the local gauge group

$$SU(3)_C \otimes SU(2)_L \otimes U(1)_Y, \tag{2.6}$$

2 An algebraic construct analogous to but more general than a vector, represented by an array of components that are functions of the coordinates of a space.

where $SU(3)_C$ is the symmetry group for colour, $SU(2)_L$ is the group for weak isospin (denoted by $L$ to show that the symmetry applies to left-handed chiral[3] fields), and $U(1)_Y$ is the group for hypercharge ($Y = 2(Q - T_3)$). The first group corresponds to the strong interaction and the rest together to the electroweak (EW) interaction. The Lagrangian invariance under these transformations results in the conservation of the three associated quantum numbers (colour - $C$, weak isospin - $L$ and hypercharge - $Y$). Here it is worth mentioning that following the spontaneous symmetry breaking (see Section 2.3) as a result of the Higgs mechanism, the tensor product of $SU(2)_L \otimes U(1)_Y$ is reduced to only $U(1)_Y$, which is the symmetry group of electromagnetism.

A simplified version of the SM Lagrangian is given by

$$\begin{aligned} \mathcal{L}_{\text{SM}} &= \mathcal{L}_{\text{gauge}} + \mathcal{L}_{\text{fermion}} + \mathcal{L}_{\text{Higgs}} + \mathcal{L}_{\text{Yukawa}} \\ \mathcal{L}_{\text{SM}} &= -\frac{1}{4}\sum_{\text{gauge}} F^{i}_{\mu\nu} F^{i,\mu\nu} + \sum_{f=q,l} \bar{f}\gamma^{\mu} D_{\mu} f + (D_{\mu}\phi)^{\dagger}(D^{\mu}\phi) \\ &\quad - \mu^2\phi^{\dagger}\phi - \lambda(\phi^{\dagger}\phi)^2 - \sum_{f=q,l} y_f \left(\bar{f}_L \phi f_R + \text{h.c.}\right). \end{aligned} \tag{2.7}$$

The first term of Equation 2.7 contains the mathematical encoding to explain the propagation of all the gauge bosons apart from the Higgs boson. The second term stands for the kinetic energies of the fermion fields and their interactions with the gauge fields. The third term stands for the kinetic energy and potential of the Higgs field (for $\mu^2 < 0$, $\lambda > 0$) and the last term stands for the Yukawa interaction. Both $\mathcal{L}_{\text{Higgs}}$ and $\mathcal{L}_{\text{Yukawa}}$ terms are further discussed in Chapter 2.3. More terms could be included in this formula about ghost fields and gauge fixing terms, but these terms are considered as technical details and are often omitted.

The SM Lagrangian can be written in an even more compact way as

$$\mathcal{L}_{\text{SM}} = \mathcal{L}_{\text{EW}} + \mathcal{L}_{\text{QCD}}, \tag{2.8}$$

where $\mathcal{L}_{\text{EW}}$ is the EW Lagrangian that governs electromagnetic and weak interactions and $\mathcal{L}_{\text{QCD}}$ is the QCD Lagrangian that describes the strong interaction.

The formulation of each component of Equation 2.8 is discussed in detail below.

3 Particle fields with negative eigenvalues or antiparticle fields with positive eigenvalues under a $\gamma^5$-matrix [10] transformation.

## Electroweak theory

The property of the variational principle used to derive classical equations is essential in the quantisation of physics models. Past experience has also showed that a powerful guidance in designing successful theories is the *gauge invariance*, defined as the property of a model to be invariant under different gauge transformations. Starting from the Dirac Lagrangian (Equation 2.1) for a massless fermion field ($\psi$) of charge $Q$ after performing a local $U(1)$ transformation the fermion field becomes

$$\psi \to \psi' = e^{-iQ\theta(x)}\psi, \tag{2.9}$$

and similarly

$$\bar{\psi} \to \bar{\psi}' = \bar{\psi}e^{iQ\theta(x)}, \tag{2.10}$$

where $\theta(x)$ is the arbitrary angle of the rotation and can be a function of space and time. Inserting these transformed fields into Equation 2.1 we get

$$\mathcal{L} \to \mathcal{L}' = \bar{\psi}i\gamma^\mu\partial_\mu\psi + Q\partial_\mu\theta(x)\bar{\psi}\gamma^\mu\psi, \tag{2.11}$$

noticing that the Lagrangian is not invariant under this transformation.

The only way to make it invariant would be to substitute the partial derivative $\partial_\mu$ with the covariant derivative $D_\mu$

$$\partial_\mu \to D_\mu = \partial_\mu - iQA_\mu(x), \tag{2.12}$$

implying that there is a generic vector field $A_\mu(x)$ that could be transformed as

$$A_\mu(x)' = A_\mu(x) - \partial_\mu\theta(x). \tag{2.13}$$

So after this substitution the Dirac Lagrangian is transformed as

$$\begin{aligned}\mathcal{L} \to \mathcal{L}' &= \bar{\psi}i\gamma^\mu D_\mu\psi \\ &= \bar{\psi}i\gamma^\mu\partial_\mu\psi + \cancel{Q\partial_\mu\theta(x)\bar{\psi}\gamma^\mu\psi} - \cancel{Q\partial_\mu\theta(x)\bar{\psi}\gamma^\mu\psi} + Q\bar{\psi}\gamma^\mu\psi A_\mu(x) \\ &= \bar{\psi}i\gamma^\mu\partial_\mu\psi + \boxed{Q\bar{\psi}\gamma^\mu\psi A_\mu(x)},\end{aligned} \tag{2.14}$$

where the last term corresponds to the fermion interaction with the gauge field $A_\mu(x)$.

This corresponds actually to the photon field that emerges from *"nothing"* and the above Lagrangian combined with the one from Equation 2.5 results in the Lagrangian of QED for a massless fermion field

$$\mathcal{L}_{\text{QED}} = \bar{\psi} i\gamma^{\mu}\partial_{\mu}\psi - e\,\bar{\psi}\gamma^{\mu}\psi A_{\mu}(x) - \frac{1}{4}F_{\mu\nu}F^{\mu\nu}, \tag{2.15}$$

where the fermion could be an electron with electric charge $Q = -e$.[4]

A similar procedure could be followed to prove that the Dirac Lagrangian is invariant under the $SU(2)$ transformation. Here since the number of generators for $SU(2)$ symmetry is $N^2 - 1 = 3$ it is assumed that the product of $\partial_{\mu}\gamma^{\mu}$ of the Lagrangian acts on a $\mathbb{I}_{3x3}$ matrix and mass $m$ is multiplied by the same matrix. So instead of the previous transformation for the fermion field the following one is used

$$\psi \rightarrow \psi' = e^{-i\,\vec{T}\;\vec{\theta}(x)}\psi, \tag{2.16}$$

where $\vec{T} = \begin{pmatrix} T^1 \\ T^2 \\ T^3 \end{pmatrix}$ is a column- and $\vec{\theta}(x) = (\theta_1,\, \theta_2,\, \theta_3)$ is a row-matrix.

The parameters $T^i\,(i = 1, 2, 3)$ correspond to the generators of $SU(2)$ which can also be expressed in terms of the three Pauli-matrices as $T^i = \frac{1}{2}\sigma^i$, where $\sigma^i$ are the Pauli-matrices

$$\sigma^1 = \begin{pmatrix} 0 & 1 \\ 1 & 0 \end{pmatrix}, \qquad \sigma^2 = \begin{pmatrix} 0 & -i \\ i & 0 \end{pmatrix}, \qquad \sigma^3 = \begin{pmatrix} 1 & 0 \\ 0 & -1 \end{pmatrix}, \tag{2.17}$$

and the parameters $\theta_i(x)(i = 1, 2, 3)$ correspond to the rotation due to the transformation.

Now after the same transformation the Dirac Lagrangian for a massless fermion field becomes

$$\mathcal{L} \rightarrow \mathcal{L}' = \bar{\psi} i\gamma^{\mu}\partial_{\mu}\psi + \bar{\psi}\, e^{i\,\vec{T}\,\vec{\theta}(x)}\,\gamma^{\mu}\,\vec{T}\,\partial_{\mu}\,\vec{\theta}(x)\, e^{-i\,\vec{T}\,\vec{\theta}(x)}\psi, \tag{2.18}$$

where because of the last term the Lagrangian is again not invariant.

4 Of course it is known already at this point that electrons are in fact massive particles.

Invariance under the local transformation of $SU(2)$ is achieved if we substitute the partial derivative $\partial_\mu$ with the covariant derivative $D_\mu$ written this time as

$$\partial_\mu \rightarrow D_\mu = \partial_\mu - ig\,\vec{T}\vec{A}_\mu(x). \tag{2.19}$$

Following similar logic the way to make the Dirac Lagrangian invariant under the local transformations of the product $SU(2)\otimes U(1)$ would be to write the covariant derivative as

$$\partial_\mu \rightarrow D_\mu = \partial_\mu - ig\,\vec{T}\,\vec{W}_\mu - ig'\frac{Y}{2}B_\mu, \tag{2.20}$$

where $g,\ g'$ are the coupling constants of the gauge groups $SU(2)$ and $U(1)$, respectively, and $\vec{W}_\mu$, $B_\mu$ are the gauge fields of the respective symmetry groups defined as

$$\begin{aligned} W^{\,i}_{\mu\nu} &= \partial_\mu W^{\,i}_\nu - \partial_\nu W^{\,i}_\mu + g\,\epsilon^{ijk}\,W^{\,j}_\mu\,W^{\,k}_\nu, \\ B_{\mu\nu} &= \partial_\mu B_\nu - \partial_\nu B_\mu. \end{aligned} \tag{2.21}$$

In the first formula $\epsilon^{ijk}$ represents the Levi-Civita tensor which gives +1 for even permutations and -1 for odd permutations of the indices $i,\ j,\ k$, and 0 in the case of a repeated index.

Making use of Equation 2.20 the Dirac Lagrangian is modified to the Lagrangian of the electroweak interaction for massless fermion and gauge-boson fields

$$\mathcal{L}_{\text{EW}} = \sum_{f=q,l} \bar{f} i\gamma^\mu D_\mu f - \frac{1}{4}W^{\,i}_{\mu\nu}W^{\,i,\,\mu\nu} - \frac{1}{4}B_{\mu\nu}B^{\,\mu\nu}, \tag{2.22}$$

where the fermion field $f$ could be either a left-handed doublet or a right-handed singlet from the options below

$$\begin{array}{lccccccc} \textit{doublets}: & \begin{pmatrix}\nu_e\\ e\end{pmatrix}_L & \begin{pmatrix}\nu_\mu\\ \mu\end{pmatrix}_L & \begin{pmatrix}\nu_\tau\\ \tau\end{pmatrix}_L & & \begin{pmatrix}u\\ d\end{pmatrix}_L & \begin{pmatrix}c\\ s\end{pmatrix}_L & \begin{pmatrix}t\\ b\end{pmatrix}_L \\ \textit{singlets}: & e_R & \mu_R & \tau_R & & u_R, d_R & c_R, s_R & t_R, b_R. \end{array} \tag{2.23}$$

## Quantum chromodynamics

The theory that describes the strong interaction between quarks and gluons in the SM is known as Quantum Chromodynamics (QCD). The name originates from the colour charge, the quantum number associated to them based on which they

can end up in different colour states. QCD could be considered as a more complex version of QED, where there are eight gluons replacing the single photon, only that in QCD the gluons are also the charge carriers of the interaction. Another complexity arises from the fact that the gluons, unlike photons which are electrically neutral, can interact among themselves since they both carry colour charge. The underlying symmetry of the strong interaction is represented by the $SU(3)$ symmetry group. In order to prove that the Lagrangian of a quark field is invariant under unitary colour transformations the global gauge symmetry needs to be promoted to a local one. Like in QED this is achieved by substituting the partial derivative with a covariant derivative of the type

$$\partial_\mu \rightarrow D_\mu = \partial_\mu - ig_s T^a G^a_\mu, \tag{2.24}$$

where $g_S$ stands for the coupling of the strong interaction (actually $\alpha_S = g_S^2/4\pi$), $T^a$ denotes the generators of the $SU(3)$ symmetry group (with $a = 1, ..., 8$) and $G^a_\mu$ represents the gluon fields. The minus term introduced in the covariant derivative encapsulates the interactions between quarks and gluons. The number of generators of the $SU(3)$ symmetry is $N^2 - 1 = 8$ following the aforementioned rule and in correspondence to QED they can be expressed using the Gell-Mann matrices $T^a = \frac{1}{2}\lambda^a$, where $\lambda^a$ can be one of the matrices

$$\begin{aligned}
\lambda^1 &= \begin{pmatrix} 0 & 1 & 0 \\ 1 & 0 & 0 \\ 0 & 0 & 0 \end{pmatrix}, \quad \lambda^2 = \begin{pmatrix} 0 & -i & 0 \\ i & 0 & 0 \\ 0 & 0 & 0 \end{pmatrix}, \quad \lambda^3 = \begin{pmatrix} 1 & 0 & 0 \\ 0 & -1 & 0 \\ 0 & 0 & 0 \end{pmatrix}, \\
\lambda^4 &= \begin{pmatrix} 0 & 0 & 1 \\ 0 & 0 & 0 \\ 1 & 0 & 0 \end{pmatrix}, \quad \lambda^5 = \begin{pmatrix} 0 & 0 & -i \\ 0 & 0 & 0 \\ i & 0 & 0 \end{pmatrix}, \quad \lambda^6 = \begin{pmatrix} 0 & 0 & 0 \\ 0 & 0 & 1 \\ 0 & 1 & 0 \end{pmatrix}, \\
\lambda^7 &= \begin{pmatrix} 0 & 0 & 0 \\ 0 & 0 & -i \\ 0 & i & 0 \end{pmatrix}, \quad \lambda^8 = \frac{1}{\sqrt{3}} \begin{pmatrix} 1 & 0 & 0 \\ 0 & 1 & 0 \\ 0 & 0 & -2 \end{pmatrix}.
\end{aligned} \tag{2.25}$$

After proceeding to the above transformation of the derivative the Dirac Lagrangian is transformed to the QCD Lagrangian, which can be written for massless fermion fields as

$$\mathcal{L}_{\text{QCD}} = \sum_{f=q} \bar{f} i\gamma^\mu D_\mu f - \frac{1}{4} G^a_{\mu\nu} G^{a,\,\mu\nu}, \tag{2.26}$$

where $\gamma^\mu$ are the Dirac $\gamma$-matrices, $f$ is the quark field written as a vector with three components in the colour space (can be represented as a column-matrix) and $G^a_{\mu\nu}$ is the quark field tensor given by

$$G^a_{\mu\nu} = \partial_\mu G^a_\nu - \partial_\nu G^a_\mu + g_s f^{abc} G^b_\mu G^c_\nu. \tag{2.27}$$

In this form, since $SU(3)$ is a non-Abelian symmetry group, the $f^{abc}$ term in the above equation is non-zero and the tensor of the third term is the one describing the gluon self-interaction. The notation of $f^{abc}$ in the third term is used to describe the structure constants of $SU(3)$ that are analogous to the Levi-Civita symbol $\epsilon^{ijk}$ of $SU(2)$ and are used for the commutation relationships of the $SU(3)$ generators as $[T^a, T^b] = i f^{abc} T^c$.

The gluon-gluon self interaction is believed to be responsible for the colour confinement and the asymptotic freedom, two of the main underlying concepts of QCD. The colour confinement suggests that quarks (or non-zero colour charge objects in general) cannot exist in isolation, but only form colourless compound objects (like the hadrons). This is supported by the fact that quarks that propagate as free particles have not been observed by the experiment. On the other hand, the asymptotic freedom is the phenomenon that at smaller distances or at higher energies the strong force becomes asymptotically weaker to the point that two partons behave freely, as they hardly interact with each other.
These two concepts are closely associated to the **running of the strong coupling constant**. As it has been shown already by multiple experiments the strong coupling constant ($\alpha_S$) is not constant, but it could be expressed as a function of the energy scale of the interaction. These experimental results are summarised in Figure 2.2 and the evolution of $\alpha_S$ as a function of $Q^2$ is expressed at a leading order approximation as

$$\alpha_S(Q^2) = \frac{\alpha_S(\Lambda^2_{\mathrm{QCD}})}{1 + B\,\alpha_S(\Lambda^2_{\mathrm{QCD}}) \ln\left(\dfrac{Q^2}{\Lambda^2_{\mathrm{QCD}}}\right)} \approx \frac{12\pi}{(33 - 2N_f) \ln\left(\dfrac{Q^2}{\Lambda^2_{\mathrm{QCD}}}\right)}, \tag{2.28}$$

where

$$B = \frac{11N_C - 2N_f}{12\pi}, \tag{2.29}$$

$N_C = 3$ is the number of possible colours, $N_f \leq 6$ is the number of the "active flavour" quarks, and $\Lambda^2_{\text{QCD}}$ is an infrared cut-off scale after which the perturbative approximation does not hold.

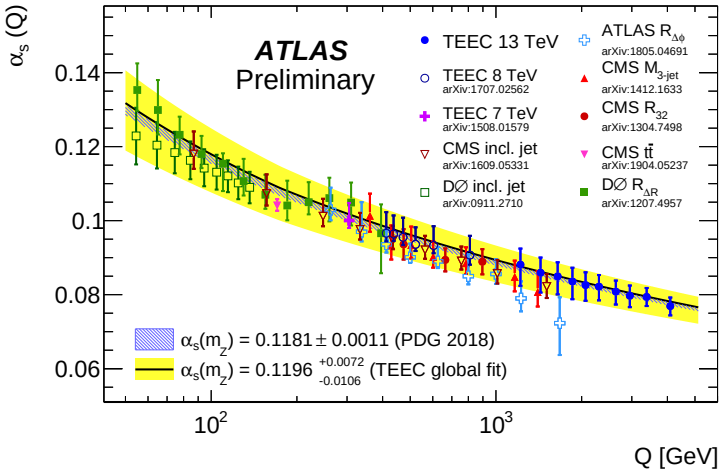



FIGURE 2.2: Summary plot of the evolution of the strong coupling constant $\alpha_S(Q)$ as a function of the energy scale $Q$ provided by the ATLAS experiment [11]. The results are obtained from fits to the transverse energy-energy correlation (TEEC) functions for 13 TeV (solid blue markers), compared to the QCD prediction of the world's average (blue dashed band), and to the resulting global fit (solid yellow band). The world average of $\alpha_S(Q)$ is measured at the energy scale equal to the $Z$-boson mass. Previous results from other experiments like CMS and D0 are also included.

From the Equation 2.28 it can be inferred that at very high energies (large $Q^2$) $\alpha_S(Q^2)$ tends to zero resulting to quarks that propagate as free particles (asymptotic freedom), while at very low energies $\alpha_S$ starts to increase up to the point where quarks and gluons are strongly bounded together (colour confinement).

## 2.3 The Higgs mechanism

The subtlety behind the discussion in Section 2.2 (apart from Equation 2.7) is hidden in the fact that the gauge fields that seem to emerge from the Lagrangians and the fermion fields themselves appear to be massless. This is something that contradicts the observation from the experiment after the discovery of $W^{\pm}$ and $Z^0$ bosons with masses 80.3 GeV and 91.2 GeV, respectively. To make things more complicated, the introduction of a mass term in the Lagrangian to account for it

would result to the breaking of the local $SU(2)$ gauge invariance, thus making it non-renormalisable.

The solution to these inconsistencies is provided by the Brout-Englert-Higgs (BEH) mechanism. The mechanism describes how particles acquire their mass through their interaction with the Higgs field. With this mechanism it could be shown how mass terms can emerge for a scalar field from a broken symmetry. This could be shown as a simple example where the mass of a gauge boson can arise from a broken $U(1)$ local gauge symmetry or in a more complex example which corresponds to the full Higgs mechanism [7–9] through the breaking of the $SU(2) \otimes U(1)$ local gauge symmetry of the EW sector. This is often called as Spontaneous Symmetry Breaking (SSB) or Electroweak Symmetry Breaking (EWSB).

## Spontaneous Symmetry Breaking: Real scalar field

In order to give some perspective the simple case of a real scalar field is being studied. In this case the Lagrangian that describes it is given by the formula

$$\mathcal{L} = T - V = \underbrace{\frac{1}{2}(\partial_\mu \phi)(\partial^\mu \phi)}_{\text{kinetic}} \underbrace{-\frac{1}{2}\mu^2\phi^2}_{\text{mass}} \underbrace{-\frac{\lambda}{4}\phi^4}_{\text{interaction}} . \tag{2.30}$$

Here it is worth noticing that in order to have invariance under the simplest transformation $\phi \to \phi' = -\phi$, only even powers of the field $\phi$ are accepted. The interaction term of the potential could be associated to a four-point interaction vertex with coupling $\lambda/4$.

If no prior knowledge on the terms $\mu^2$ and $\lambda$ was available there would be four possible cases where

$$\text{i) } \mu^2, \lambda > 0, \text{ ii) } \mu^2, \lambda < 0, \text{ iii) } \lambda > 0 \ \& \ \mu^2 < 0 \text{ and iv) } \lambda < 0 \ \& \ \mu^2 > 0.$$

Of course case ii) is dismissed since there is no state of minimum energy there and both cases ii) and iv) are rejected since the potentials are unbounded from below.

Taking the first derivative of the potential equal to zero

$$\frac{dV(\phi)}{d\phi} = \mu^2\phi + \lambda\phi^3 = \phi(\mu^2 + \lambda\phi^2) = 0, \tag{2.31}$$

it is found that the potential would either have a minimum at $\phi = 0$ or two minima at the values $\phi = \pm v = \pm\sqrt{\frac{-\mu^2}{\lambda}}$. These solutions correspond to the cases i) and iii) from above. The point of reference of lowest energy represented by these solutions is often called *vacuum expectation value* (VEV) or simply *vacuum*. It is clear that in case i) the lowest energy state occurs at $\phi = 0$ and the field has a zero vacuum expectation value $v$, while in case iii) there are two degenerate non-zero vacuum states possible. The actual vacuum state of the field will be either of these two resulting in a choice that breaks the symmetry of the Lagrangian.

Supposing that the vacuum state is chosen at $\phi = +v$ the excitations of the field could be described as perturbations around the VEV and the field is written in the form

$$\phi = v + \eta(x). \tag{2.32}$$

The potential after substituting the above definition is expressed as

$$\begin{aligned} V(\eta) &= \frac{\mu^2}{2}(v+\eta)^2 + \frac{\lambda}{4}(v+\eta)^4 \\ &= \frac{\mu^2}{2}(v^2+\eta^2+2v\eta) + \frac{\lambda}{4}(v^4+\eta^4+4v^3\eta+4v\eta^3+6v^2\eta^2) \\ &= \frac{\mu^2 v^2}{2} + \frac{\mu^2\eta^2}{2} + \mu^2 v\eta + \frac{\lambda v^4}{4} + \frac{\lambda\eta^4}{4} + \lambda v^3\eta + \lambda v\eta^3 + \frac{3}{2}\lambda v^2\eta^2 \\ &= -\frac{\lambda v^4}{2} - \frac{1}{2}\lambda v^2\eta^2 - \cancel{\lambda v^3\eta} + \frac{\lambda v^4}{4} + \frac{\lambda\eta^4}{4} + \cancel{\lambda v^3\eta} + \lambda v\eta^3 + \frac{3}{2}\lambda v^2\eta^2 \\ &= \lambda v^2\eta^2 + \lambda v\eta^3 + \frac{\lambda\eta^4}{4} + c(v), \end{aligned} \tag{2.33}$$

where the term $c(v)$ is being considered constant.

The term proportional to $\eta^2$ is a well-defined mass term and could be compared to the one of the initial Lagrangian (Equation 2.30). From this comparison it is deduced that

$$m_\eta = \lambda v^2 = \sqrt{-2\mu^2}\ (> 0), \tag{2.34}$$

and from the comparison of the final form of the Lagrangian to the initial one it is shown that the potential for the new $\eta$ field (defined at the VEV of the field $\phi$) is

$$V(\eta) = \lambda v^2\eta^2 + \lambda v\eta^3 + \frac{\lambda}{4}\eta^4. \tag{2.35}$$

## Spontaneous Symmetry Breaking: Complex scalar field

In the SM an additional level of complexity is required such that instead of a real scalar field a weak isospin doublet of complex scalar fields has to be used. This is known as the Higgs field and it is introduced as

$$\phi = \begin{pmatrix} \phi^+ \\ \phi^0 \end{pmatrix} = \frac{1}{\sqrt{2}} \begin{pmatrix} \phi_1 + i\phi_2 \\ \phi_3 + i\phi_4 \end{pmatrix}. \tag{2.36}$$

Since the masses of the three gauge bosons should be generated by the interaction with the Higgs field and the photon should be massless, one of the scalar components should be neutral to account for $Z^0/\gamma$ (which is written here as $\phi^0$) and the other should be charged to account for the longitudinal degrees of freedom of $W^\pm$ (written here as $\phi^+$).

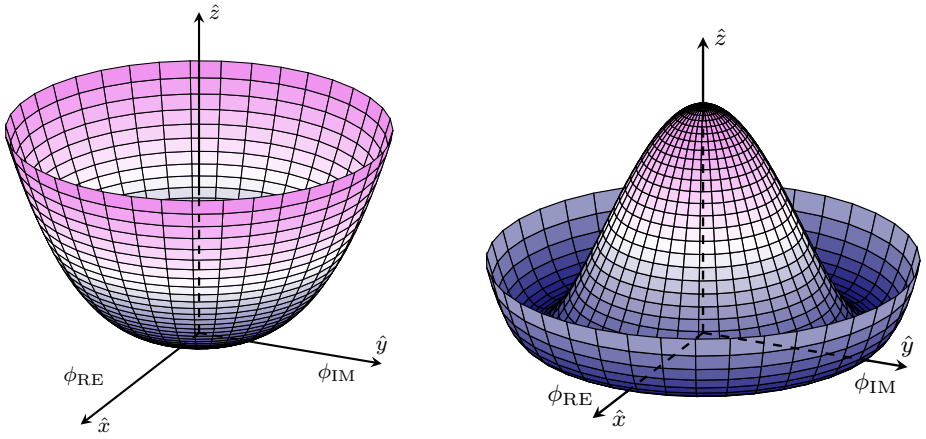



FIGURE 2.3: Shape of the Higgs-Englert-Brout potential in the case that (a) $\lambda > 0$ and $\mu^2 > 0$, and (b) $\lambda > 0$ and $\mu^2 < 0$.

The potential of complex scalar fields can be visualised in the 3D plane as shown in Figure 2.3 where $\hat{x}$ and $\hat{y}$ axes represent the real and the imaginary axes of the complex plane respectively, and the $\hat{z}$ axis points towards the direction of the potential.

The associated Higgs potential is now written as

$$V(\phi) = \mu^2 \phi^\dagger \phi + \lambda (\phi^\dagger \phi)^2, \tag{2.37}$$

and therefore the Lagrangian can be written as

$$\begin{aligned}\mathcal{L} &= (\partial_\mu \phi)^\dagger (\partial^\mu \phi) - V(\phi) \\ &= (\partial_\mu \phi)^\dagger (\partial^\mu \phi) - \mu^2 \phi^\dagger \phi - \lambda (\phi^\dagger \phi)^2,\end{aligned} \tag{2.38}$$

where the factor $\frac{1}{2}$ of the kinetic term has been absorbed into the field definition and $\phi^\dagger$ is a row doublet leading to the calculation

$$\begin{aligned}\phi^\dagger \phi &= \begin{pmatrix} \phi^{+*} & \phi^{0*} \end{pmatrix} \begin{pmatrix} \phi^+ \\ \phi^0 \end{pmatrix} \\ &= \frac{(\phi_1^2 + \phi_2^2 + \phi_3^2 + \phi_4^2)}{2}.\end{aligned} \tag{2.39}$$

Similarly to the previous example the minimum of the Higgs field is found by the points where the first derivative is equal to zero, namely

$$\begin{aligned}\frac{dV(\phi^\dagger \phi)}{d(\phi^\dagger \phi)} &= \mu^2 + 2\lambda(\phi^\dagger \phi) = 0 \\ (\phi^\dagger \phi) &= -\frac{\mu^2}{2\lambda} = \frac{v^2}{2} \\ \phi_1^2 + \phi_2^2 + \phi_3^2 + \phi_4^2 &= v^2.\end{aligned} \tag{2.40}$$

At this point a choice of VEV needs to be made and a fitting candidate for that would be to set $\phi_3 = v$, $\phi_1 = \phi_2 = \phi_4 = 0$. This choice although may seem a bit arbitrary is motivated from the fact that photon should remain massless after the symmetry breaking, and as a result the neutral scalar field $\phi_0$ should have a non-zero VEV. After this choice $\phi_0$ is written as

$$\phi_0 = \langle 0 | \phi | 0 \rangle = \frac{1}{\sqrt{2}} \begin{pmatrix} 0 \\ v \end{pmatrix}. \tag{2.41}$$

Expanding around the minimum of the potential using a perturbation term to represent the fluctuations around the vacuum state $\phi_0$ becomes

$$\phi(x) = \frac{1}{\sqrt{2}} \begin{pmatrix} 0 \\ v + \eta(x) \end{pmatrix}. \tag{2.42}$$

Substituting this form of $\phi_0$ into Equation 2.37 and making use of Equation 2.40 the Higgs potential can be written exactly as in Equation 2.35 and similarly the Higgs mass is

$$m_H = \sqrt{2\lambda}\, v. \tag{2.43}$$

In order the full Lagrangian to be invariant the partial derivative $\partial_\mu$ in the kinetic term should be replaced by the covariant derivative $D_\mu$ given in Equation 2.20, which for hypercharge $Y = 1$ takes the form

$$\partial_\mu \rightarrow D_\mu = \partial_\mu - \frac{1}{2}\left(ig\,\vec{\sigma}\,\vec{W}_\mu - ig' B_\mu\right). \tag{2.44}$$

After substituting $\phi_0$ the term $D_\mu\phi$ can be written in matrix form as

$$\begin{aligned} D_\mu\phi &= \frac{1}{2\sqrt{2}} \begin{pmatrix} 2\partial_\mu + igW_\mu^3 + ig'B_\mu & ig(W_\mu^1 - iW_\mu^2) \\ ig(W_\mu^1 + iW_\mu^2) & 2\partial_\mu - igW_\mu^3 + ig'B_\mu \end{pmatrix} \begin{pmatrix} 0 \\ v + \eta(x) \end{pmatrix} \\ &= \frac{1}{2\sqrt{2}} \begin{pmatrix} ig(W_\mu^1 - iW_\mu^2)[v + \eta(x)] \\ (2\partial_\mu - igW_\mu^3 + ig'B_\mu)[v + \eta(x)] \end{pmatrix}. \end{aligned} \tag{2.45}$$

Thus, taking the hermitian conjugate of the above quantity and substituting both terms in Equation 2.38 the kinetic term of the Lagrangian can be written as

$$\begin{aligned} (D_\mu\phi)^\dagger(D^\mu\phi) =& \frac{1}{8}\left(-ig(W_\mu^1 + iW_\mu^2) \quad (2\partial_\mu + igW_\mu^3 - ig'B_\mu)\right) \\ & \begin{pmatrix} ig(W^{1,\mu} - iW^{2,\mu}) \\ (2\partial^\mu - igW^{3,\mu} + ig'B^\mu) \end{pmatrix} [v + \eta(x)]^2 \\ =& \frac{1}{2}\,(\partial_\mu\eta)(\partial^\mu\eta) + \frac{1}{8}\,g^2\left(W_\mu^1\,W^{1,\mu} + W_\mu^2\,W^{2,\mu}\right)[v + \eta(x)]^2 \\ & + \frac{1}{8}\left(gW_\mu^3 - g'B_\mu\right)\left(gW^{3,\mu} - g'B^\mu\right)[v + \eta(x)]^2. \end{aligned} \tag{2.46}$$

The constant terms (proportional to $v^2$) obtained by the second term can be interpreted as mass terms of the $W^1$ and $W^2$ fields in the general form

$$\frac{1}{2}\,m^2\,W_\mu^1\,W^{1,\mu}, \quad \frac{1}{2}\,m^2\,W_\mu^2\,W^{2,\mu},$$

which means that by comparison the mass of the $W$ boson is given by

$$m_W = \frac{1}{2}\,v\,g. \tag{2.47}$$

The third term of Equation 2.46 also gives constant terms proportional to $v^2$, which if isolated can be written in matrix form as

$$\begin{gathered}\frac{v^2}{8}\left(gW_\mu^3 - g'B_\mu\right)\left(gW^{3,\mu} - g'B^\mu\right) = \\ \frac{v^2}{8}\begin{pmatrix} W_\mu^3 & B_\mu \end{pmatrix} \underbrace{\begin{pmatrix} g^2 & -gg' \\ -gg' & g'^2 \end{pmatrix}}_{\text{M-matrix}} \begin{pmatrix} W^{3,\mu} \\ B^\mu \end{pmatrix},\end{gathered} \tag{2.48}$$

where the non-diagonal terms of the M-matrix allow $W^3$ and $B$ fields to mix.

Diagonalising the M-matrix by requiring $det(M - \alpha\mathbb{I}) = 0$ gives the solutions

$$\begin{gathered}\begin{pmatrix} g^2 & -gg' \\ -gg' & g'^2 \end{pmatrix} - \begin{pmatrix} \alpha & 0 \\ 0 & \alpha \end{pmatrix} = 0 \\ (g^2 - \alpha)(g'^2 - \alpha) - g^2 g'^2 = 0 \\ \boxed{\alpha = 0} \quad \text{or} \quad \boxed{\alpha = g^2 + g'^2}.\end{gathered} \tag{2.49}$$

This result means that Equation 2.48 can be written in a diagonal basis as

$$\frac{v^2}{8}\begin{pmatrix} A_\mu & Z_\mu \end{pmatrix}\begin{pmatrix} 0 & 0 \\ 0 & g^2 + g'^2 \end{pmatrix}\begin{pmatrix} A^\mu \\ Z^\mu \end{pmatrix}, \tag{2.50}$$

where $A_\mu$ and $Z_\mu$ are the normalised eigenvectors of the M-matrix defined as

$$A_\mu = \frac{g'W_\mu^3 + gB_\mu}{\sqrt{g^2 + g'^2}}, \quad Z_\mu = \frac{gW_\mu^3 - g'B_\mu}{\sqrt{g^2 + g'^2}}. \tag{2.51}$$

The letters $A$ and $Z$ were used for the eigenvectors deliberately since they correspond to the massless photon and massive $Z$ fields respectively. This can be understood by looking into the diagonalised M-matrix where the diagonal values (together with the multiplicative factor proportional to $v^2$) correspond to the mass of the fields in quadrature.

By comparison to the standard mass term, the mass of the $A_\mu$ and $Z_\mu$ fields is found to be

$$m_A = 0 \quad \text{and} \quad m_Z = \frac{1}{2}v\sqrt{g^2 + g'^2}. \tag{2.52}$$

The conclusion at this stage is that the mass terms of the $W$ and $Z$ bosons emerge from the kinetic term of the initial Lagrangian and they depend on the interaction

of the boson field through the coupling constant of the $SU(2)$ or/and $U(1)$ gauge groups with the VEV of the Higgs field, while the photon field is found to be massless.

Going a bit further, it can be shown that fermions acquire their mass in a similar way in the SM through the interaction of the Higgs field with the fermion fields. This is known as *Yukawa* interaction and it is described by the corresponding Yukawa Lagrangian

$$\mathcal{L}_{\text{Yukawa}} = -y_d \bar{Q_L} \phi d_R - y_u \bar{Q_L} \bar{\phi} u_R - y_l \bar{L_L} \phi \ell_R + h.c., \tag{2.53}$$

where $\phi$ is the Higgs field given in the complex doublet form of Equation 2.36, $Q_L$, $L_L$ and $d_R$, $u_R$, $\ell_R$ are the quark/lepton doublets and singlets respectively from Equation 2.23 for all generations, and ($y_d$) $y_u$ and $y_l$ are the Yukawa couplings for (down-) up-type quarks and charged leptons of these doublets, respectively.

This interaction term for the fermions can be added to the previous Lagrangian and if the Higgs field is written in the extended form by introducing a perturbation term around the VEV (Equation 2.42) mass terms for fermions emerge in a similar form as before

$$m_f = \frac{1}{\sqrt{2}} v\, y_f, \tag{2.54}$$

where instead of the gauge group couplings $g/g'$ the yukawa couplings $y_f$ are used.

At this point it should be made clear that the Yukawa couplings $y_f$ are free parameters in the SM. As a result there cannot be a theoretical prediction of the values of the fermion masses and these values had to be determined from experiment. After the measurements of the fermion masses the yukawa couplings $y_f$ were computed for each fermion, which were all different between them.

## 2.4 Higgs boson and top-quark properties

### Higgs boson

From Equation 2.43 it can be inferred that the Higgs mass depends on the parameter $\lambda$ and the Higgs VEV ($v$). The latter can be obtained by comparing

Equation 2.47 to the formula that relates the weak coupling strength $g$ to the Fermi constant

$$\frac{G_F}{\sqrt{2}} = \frac{g_W^2}{8m_W^2}. \tag{2.55}$$

The Fermi constant could be defined in an independent way through measurements of the muon lifetime, where the Fermi theory can be used (since $m_\mu << m_W$) by making use of the formula

$$\Gamma(\mu^- \to e^- \nu_\mu \bar{\nu}_e) = \frac{1}{\tau_\mu} = \frac{G_F^2 \, m_\mu^5}{192\pi^3}, \tag{2.56}$$

where $m_\mu \sim 105.65$ MeV is the measured muon mass and $\tau_\mu \sim 2.2 \times 10^{-6}$ s the measured muon lifetime. Thus, the Fermi constant is determined quite precisely to

$$G_F = 1.16638 \times 10^{-5} \text{ GeV}^{-2}. \tag{2.57}$$

The above comparison results to the calculation of $v$ as

$$\begin{aligned} \frac{g_W^2}{8m_W^2} = \frac{G_F}{\sqrt{2}} &= \frac{1}{2v^2} \\ v = \sqrt{\frac{\sqrt{2}}{2G_F}} &\approx 246 \text{ GeV}. \end{aligned} \tag{2.58}$$

However, the coupling $\lambda$ is not known *a priori* and therefore it was not possible to have a hint about the scale of the Higgs boson mass. This was the case until its discovery on July 4$^{\text{th}}$ in 2012 by both ATLAS and CMS experiments at CERN with a mass

$$m_H = 125.25 \pm 0.17 \text{ GeV}, \tag{2.59}$$

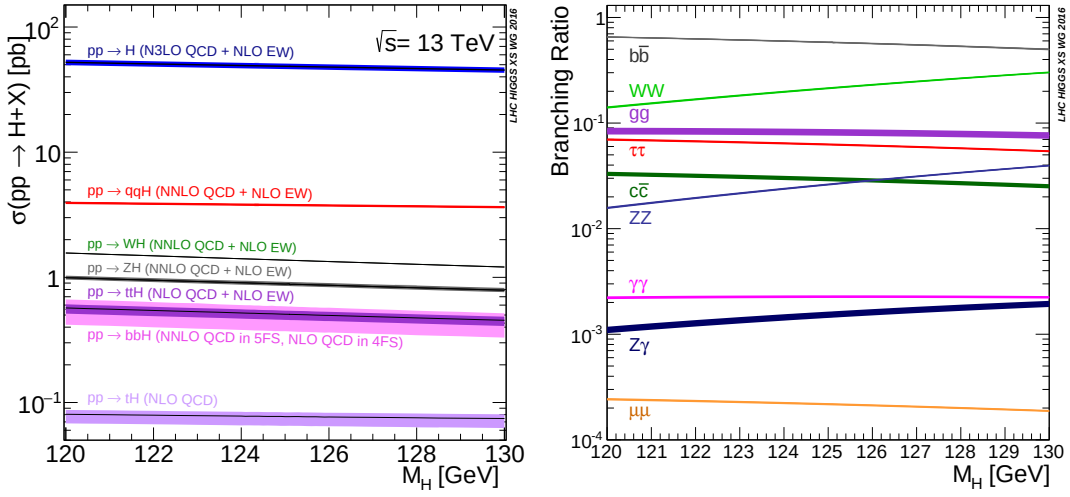
based on the latest PDG report [12].

It was first observed in $H \to ZZ^* \to 4\ell$ and $H \to \gamma\gamma$ decays, and later in $H \to WW^*$, $H \to \tau^+\tau^-$ and $H \to b\bar{b}$ decays. The production cross sections and decay branching ratios (BRs) of the Higgs boson to each channel are given in Figures 2.4a and 2.4b, respectively, based on the value of the Higgs mass.

The Higgs boson is a scalar boson associated to the existence of the Higgs field and it was the missing piece for the establishment of the SM as the nominal theory. After precise measurements it was proved that it was indeed a neutral CP[5]-even

5 Stands for the charge-parity (CP) symmetry.

(spin-0) boson as predicted by the theory. The main production modes of the Higgs boson are through gluon-gluon fusion, vector boson fusion (VBF) and associated production with a vector boson ($VH$) or with a heavy quark-antiquark pair ($t\bar{t}H$, $b\bar{b}H$).




(a) (b)

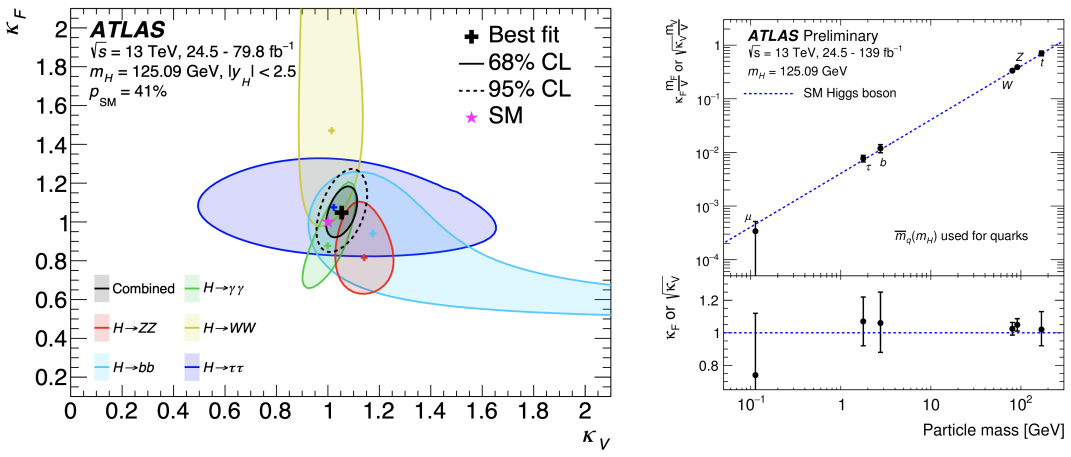
FIGURE 2.4: Predicted production cross sections (a) and decay branching ratios (b) of Higgs boson for a 10 GeV window around the measured Higgs mass ($m_H = 125$ GeV). Figures taken from Ref. [13].

The Higgs coupling-strength modifiers $\kappa$ are certain parameters introduced in order to study how potential BSM physics scenarios could modify the Higgs boson couplings. They are introduced at tree-level within the $\kappa$-framework [13] such that the Higgs production and decay can be studied by factorising them as $\kappa_j^2 = \sigma_j/\sigma_j^{\mathrm{SM}}$, where $\sigma_j$ stands for the cross section of the corresponding decay and in the SM scenario it should be $\kappa_j = 1$. There are certain models trying to measure these coupling modifiers collectively for fermions and bosons considering that $\kappa_F = \kappa_t = \kappa_b = \kappa_\tau = \kappa_\mu$ and $\kappa_V = \kappa_W = \kappa_Z$. As it is shown in Figure 2.5a the measured $(\kappa_V, \kappa_F)$ values $\kappa_V = 1.05 \pm 0.04$ and $\kappa_F = 1.05 \pm 0.09$ were found to agree within $1\sigma$ with the SM expectation value. In other measurements an independent treatment of the coupling-strength modifiers to $\mu, \tau, b, t, W$ and $Z$ is demonstrated. One can obtain the reduced coupling modifiers by using the relationships

$$y_V = \sqrt{\kappa_V \frac{g_V}{2v}} = \sqrt{\kappa_V}\,\frac{m_V}{v}, \qquad y_F = \kappa_F \frac{g_F}{\sqrt{2}} = \kappa_F \frac{m_F}{v}, \tag{2.60}$$

where $g_V, g_F$ are the absolute Higgs couplings to bosons and fermions, respectively, and $v$ is the Higgs VEV.

As shown in Figure 2.5b the reduced coupling modifiers are in line with the SM expectation (indicated by a blue dashed line), while the $\kappa_\mu$ is still not as constrained as the rest of the coupling modifiers. The precision measurement of these coupling modifiers is of outmost importance and a slight deviation from the expected SM values could point to new physics.




(a) (b)

FIGURE 2.5: (a) Measurement of $\kappa_V$ and $\kappa_F$ in the ($\kappa_V$, $\kappa_F$) plane from the ATLAS experiment. The negative log-likelihood 68% (95%) CL contours of the combined fit are given with the full (dashed) black lines, while results from individual Higgs decay modes are also overlaid. The best-fit values are shown with a cross while the SM expectation value is shown with a star. Any contributions from invisible or undetected Higgs boson decays are not considered.
(b) Measurement of the reduced coupling-strength modifiers $y_V$ and $y_F$ for weak gauge bosons ($V = W, Z$) and fermions ($F = \mu, \tau, b, t$). The black (light grey) error bars are used to represent the 68% (95%) CL intervals for the measured parameters. Any contributions from invisible or undetected Higgs boson decays are not considered. Both figures were taken from Ref. [14].

## Top quark

A special mention is attributed to the heaviest quark that has been discovered so far, the top quark, which is also the heaviest particle in the SM. It belongs to the third generation of quarks and it was first discovered in 1995 by the CDF and D0 experiments at Fermilab [15, 16]. Since then, the measurement of its properties to ever-increasing precision has been one of the priorities at the Tevatron and the LHC. The top-quark mass is measured to be $172.69 \pm 0.3$ GeV, which constitutes the world average of all the measurements conducted [12]. The fact that it weights

more than the Higgs boson itself and about 173 times the mass of the proton makes it difficult to grasp that it is actually a fundamental particle. Due to its very short lifetime ($5.0 \times 10^{-25}$ s) there is not enough time for the hadronisation procedure to take place and the top quark decays almost immediately to other particles. This offers the opportunity to directly use its decay products in order to get the information about its spin undiluted by non-perturbative effects.
Because of its very high mass the top-Higgs Yukawa coupling ends up being very close to unity since

$$y_t = \sqrt{2}\,\frac{m_t}{v} \approx 1. \tag{2.61}$$

This result might be a coincidence, but it seems unnatural that the fermion Yukawa couplings are of a different order of magnitude (something that boils down to the mass difference between them). Especially the tiny neutrino masses lead to Yukawa couplings smaller than $10^{-12}$, something that might suggest that they could be produced with a different mechanism (e.g. seesaw mechanism [17, 18]).

The top quark can be produced either through gluon-gluon fusion or quark-antiquark annihilation, with the former mode to be the dominant one at the LHC. It decays almost exclusively into a bottom quark and a $W$ boson, where the bottom quark hadronises and the $W$ boson decays either hadronically ($q\bar{q}$) or leptonically ($\ell\nu_\ell$). Subsequently, since the top quarks are mainly produced in pairs the most common $t\bar{t}$ final state could end up in three channels: *fully hadronic* (BR: ∼46%), *dilepton* (BR: ∼9%) and *single-lepton* (BR: ∼45%).

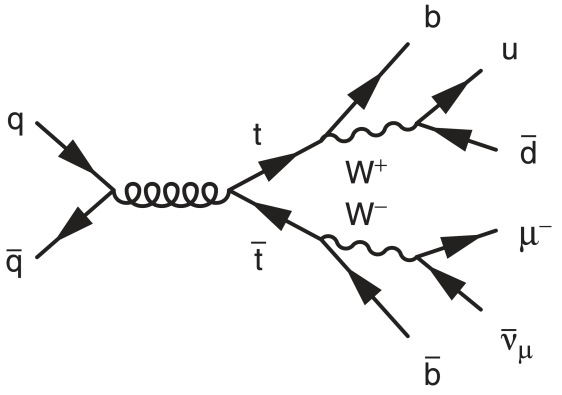
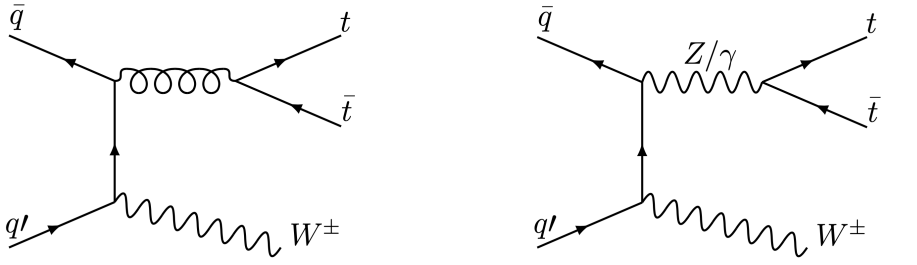



FIGURE 2.6: Illustrative Feynman diagram depicting the decay of a top-quark pair into a bottom quark and a $W$ boson, where the positively-charged $W$ boson is decaying hadronically and the negatively-charged $W$ boson is decaying leptonically. Figure taken from Ref. [10].

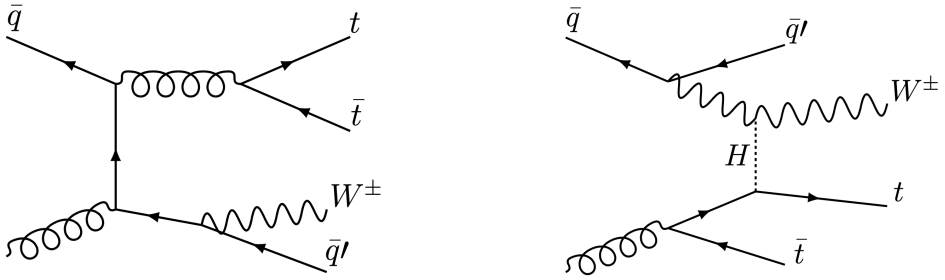
## 2.5 Top-quark pair production in association with a $W$ boson

One of the main parts of this thesis is devoted to the cross-section measurement of a top-quark pair production in association with a $W$ boson ($t\bar{t}W$). Therefore, it is important to introduce its production and decay mechanisms and try to understand the challenges that lie in the modelling of such complex process. The LHC as a $pp$ collider provides a large number of events containing a pair of top quarks. This large production of top-quark pairs allows studies of rarer processes such as $t\bar{t}W$.

### Production modes




(a) Illustrative $t\bar{t}W$ LO diagrams.




(b) Illustrative $t\bar{t}W$ NLO diagrams. The interaction of diagram on the right side can also happen with the exchange of a photon or a $Z$ boson instead of a Higgs boson.

FIGURE 2.7: Illustrative $t\bar{t}W$ LO and NLO diagrams. The diagrams were taken from Ref. [19].

A $W$ boson can be produced in association with a top-quark pair at leading order (LO) through Initial State Radiation (ISR) process, where it is radiated from one of the initial state quarks. The Feynman diagrams that describe this process are shown in Figure 2.7a, where the mediator of the interaction for the top-quark pair

production can be either a gluon through QCD contribution (left) or a photon/$Z$ boson through EW contribution (right).

At next-to-leading order (NLO) the quark-gluon initiated diagrams open up to non-negligible contributions from $t\bar{t}W+j$ final states with or without an additional boson in the interaction, as shown in Figure 2.7b.

The $t\bar{t}W$ Feynman diagrams shown in Figure 2.7 are different examples of contributions in Figure 2.8. The complexity of the $t\bar{t}W$ modelling originates from the additional terms that emerge in the $t\bar{t}W$ EW production diagrams at LO and NLO proportional to $\alpha^3$ and $\alpha_S\alpha^3$, respectively, as shown in Figure 2.8. In particular, the NLO EW term is non-negligible with respect to the NLO QCD term with an additional negative effect of ∼6% [19].

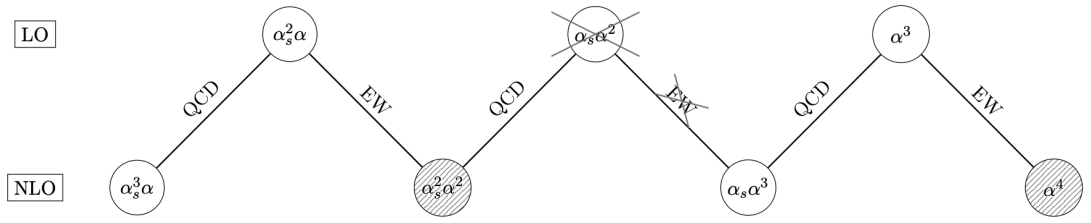



FIGURE 2.8: The possible coupling combinations contributing to the LO and NLO $t\bar{t}W^{\pm}$ cross section. The links indicate how a given NLO originates from a corresponding LO via QCD or EW corrections. The terms crossed out vanish by colour structure. In this study the orders corresponding to the shaded bubbles are neglected. The figure was taken from Ref. [20].

In a proton-antiproton collider the production cross section of $t\bar{t}W^+$ and $t\bar{t}W^-$ would be the same. The preference in the production of positively charged $W$ bosons at the LHC is attributed to the proton structure itself, since proton contains two valence $u$ quarks and one valence $d$ quark. A positively charged $W$ boson is produced in the initial state when an up-type quark changes into a down-type quark (or a down-type antiquark changes into an up-type antiquark) and the opposite happens for a negatively charged $W$ boson. Since the parton distribution function (PDF) of the $u$ quark is higher than the one of the $d$ quark, and the PDFs of the $\bar{u}$ and $\bar{d}$ antiquarks are almost the same at high energies a $W^+$ boson production is more probable.

The inclusive cross-section calculations at NLO for QCD+EW [21] that were used by the ATLAS experiment for the production of the nominal $t\bar{t}W$ sample used in

this thesis are

$$\begin{aligned}
\sigma_{t\bar{t}W^+} &= 397.6\,^{+12.7\%}_{-11.4\%}\,(\text{scale})\,^{+2\%}_{-2\%}\,(\text{PDF})\,^{+2.6\%}_{-2.6\%}\,(\alpha_S)\ \text{fb}, \\
\sigma_{t\bar{t}W^-} &= 203.2\,^{+13.3\%}_{-11.7\%}\,(\text{scale})\,^{+2.1\%}_{-2.1\%}\,(\text{PDF})\,^{+2.9\%}_{-2.9\%}\,(\alpha_S)\ \text{fb}, \\
\sigma_{t\bar{t}W} &= 600.8\,^{+12.9\%}_{-11.5\%}\,(\text{scale})\,^{+2\%}_{-2\%}\,(\text{PDF})\,^{+2.7\%}_{-2.7\%}\,(\alpha_S)\ \text{fb}.
\end{aligned} \tag{2.62}$$

These calculations are done for the charge-inclusive $t\bar{t}W$ process, and also individually for for $t\bar{t}W^+$ and $t\bar{t}W^-$ at $\sqrt{s} = 13$ TeV using a fixed renormalisation and factorisation scale choice of $\mu_0 = H_{\mathrm{T}}/2$, where $H_{\mathrm{T}}$ is defined as the scalar sum of the transverse masses $\sqrt{m^2 + p_{\mathrm{T}}^2}$ of all particles in the final state.

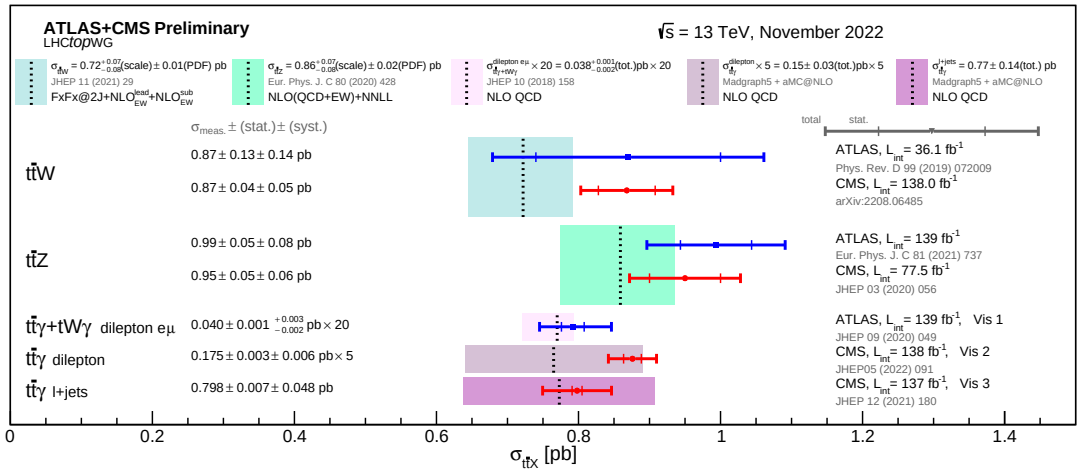
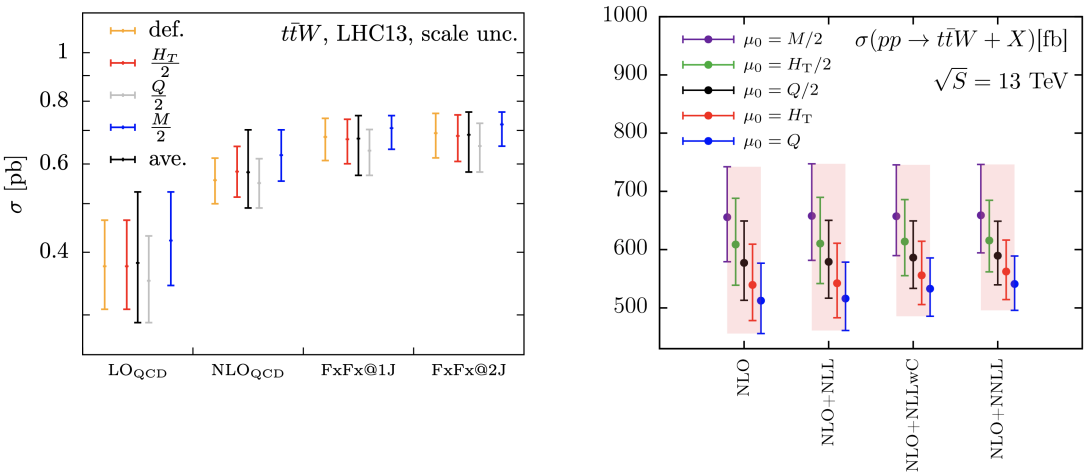



FIGURE 2.9: Measured cross sections for the associated production of a top-quark pair and a boson ($Z/\gamma, W$) from ATLAS and CMS experiments. Figure taken from Ref. [22].

Both ATLAS and CMS experiments were measuring higher $t\bar{t}W$ expectation values than the SM ones, as shown in Figure 2.9, and a closer look was required from both theorists and experimentalists. The modelling of $t\bar{t}W$ process was proved to be very challenging to the theorists mainly because of the higher-order corrections and large uncertainties in the estimations. As shown in Figure 2.10a, the NLO corrections at the QCD level provide a more accurate result with larger expected cross section compared to the LO calculation, while in both Figures 2.10a and 2.10b outline the importance of the scale choice, which could result in different outcomes for the cross section.

A more complete calculation of the $t\bar{t}W$ cross section was made available later using the FxFx@2J result of Figure 2.10a at the default scale (orange, $H_T'/2$) and




(a) (b)

FIGURE 2.10: $t\bar{t}W$ inclusive cross sections (QCD) with calculations using different scale choices at LO and higher orders. Figures taken from Refs. [23] and [24], respectively.

including the leading and subleading EW corrections at NLO [23]. This calculation resulted to a value of

$$\sigma_{t\bar{t}W} = 722.4\,^{+9.7\%}_{-10.8\%}\,(\text{scale})\,^{+1\%}_{-1\%}\,(\text{PDF})\ \text{fb}, \tag{2.63}$$

which became the common reference value for the LHC experiments at the time of the writing.

Once the NNLO QCD calculations became available the theoretical value of the $t\bar{t}W$ cross section was updated to

$$\sigma_{t\bar{t}W} = 745.3\,^{+6.7\%}_{-6.7\%}\,(\text{scale})\,^{+1.8\%}_{-1.8\%}\,(\text{PDF})\ \text{fb}, \tag{2.64}$$

as shown in [25], still being lower than the one measured in the experiment.

## Decay modes

The decay modes of the top-quark pair produced in association with a $W$ boson can vary depending on the decay of the $W$ boson. Each top quark of the top-quark pair decays into a bottom quark and a $W$ boson. This means that there are three $W$ bosons at some point in the event (two of them have always the same charge between them), which could either decay hadronically into a quark-antiquark pair or leptonically into a lepton and the associated neutrino. Depending on the $W$

boson decays final states with multiple leptons and $b$-jets could exist, making this process a non-negligible background in many SM and BSM signatures.

The main focus in this dissertation is the final states containing a pair of two light leptons of the same electric charge ($2\ell$SS) or three light leptons ($3\ell$), where $\ell = e, \mu$. In the former case one of the $W$ bosons from a top quark decays hadronically and the rest two $W$ bosons of the event decay leptonically. This decay mode is illustrated in Figure 2.11 and it could be written as

$$t\bar{t}W^{\pm} \rightarrow \left(t \rightarrow b\ell^{\pm}\nu_{\ell}\right)\left(t \rightarrow bq\bar{q}'\right)\left(W^{\pm} \rightarrow \ell^{\pm}\nu_{\ell}\right),$$

and the other decay mode as

$$t\bar{t}W^{\pm} \rightarrow \left(t \rightarrow b\ell^{+}\nu_{\ell}\right)\left(\bar{t} \rightarrow \bar{b}\ell^{-}\bar{\nu_{\ell}}\right)\left(W^{\pm} \rightarrow \ell^{\pm}\nu_{\ell}\right),$$

with branching ratios

$$\begin{aligned} &\mathcal{B}(t\bar{t}W \rightarrow \ell^{\pm}\ell^{\pm} + X) = (3.18 \pm 0.04)\%, \\ &\mathcal{B}(t\bar{t}W \rightarrow \ell^{\pm}\ell^{\mp}\ell^{\pm} + X) = (1.025 \pm 0.015)\%. \end{aligned} \tag{2.65}$$

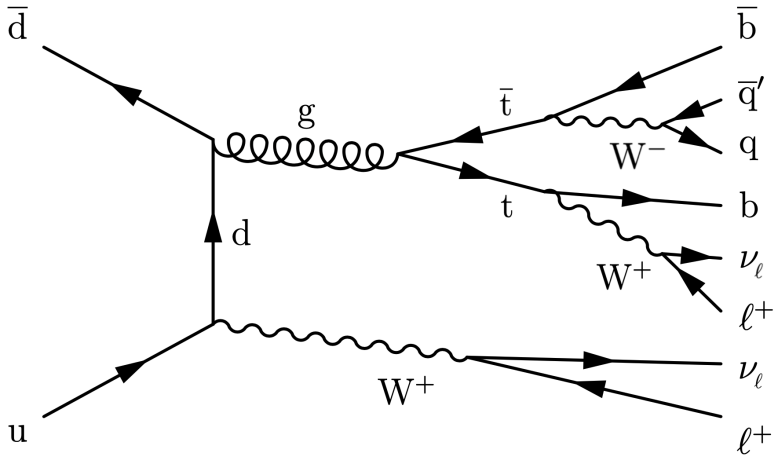



FIGURE 2.11: Illustrative Feynman diagram of $t\bar{t}W^{+}$ production at leading order with two same-sign leptons in the final state. Each of the top quarks decays into a $W$ boson and a $b$-quark. One of the $W$ bosons from the top quark decays hadronically and the other two $W$ bosons of the event decay leptonically.

Despite the fact of the low branching ratios these decay modes are particularly interesting since there are not many other background processes that contribute in these experimental signatures and a specific selection based on the number of light leptons and $b$-jets could target these $t\bar{t}W$ decays.

# Chapter 3

# Beyond the Standard Model

Since the theoretical foundations of the SM have been detailed in Chapter 2, this chapter will discuss some of the most promising theories beyond the SM (BSM) that address some of its major shortcomings, which are summarised in Chapter 3.1. For example, quarks and leptons although they share many physics properties (charge, spin, etc.) and they both come in three generations in the SM, they seem to be decoupled from each other. These similarities may hint at a connection between quarks and leptons through an underlying symmetry, which could introduce transitions between them through a new quark-lepton coupling. The mediator of this interaction could be a new particle called leptoquark, a boson that could couple simultaneously to a quark and a lepton. The presence of leptoquarks is predicted in many Grand Unified Theories (GUT) and compositeness models. Leptoquarks could provide answers in the current flavour physics puzzle, helping also in the explanation of tensions in $B$-meson decays and the anomalous magnetic moment of the muon. The phenomenology of leptoquark models and the motivation for them are being discussed in more detail in Chapter 3.2.

## 3.1 Shortcomings of the Standard Model

### Grand Unified Theories (GUTs) and gravity

Despite its great success, the SM fails to incorporate the gravitational force in its renormalisable quantum field theory. Instead, gravity can be described individually in macroscopic systems by the theory of general relativity. The unification of

the electromagnetic force in a single theory and the further unification of electromagnetic and weak forces at higher energies lays the foundation for even greater unification. In physics a force is described in terms of particle exchange, and in order to achieve a unified theory of all the fundamental forces their coupling constants should converge eventually at the same point. As shown in Chapter 2.2 the value of the coupling constants is dependent on the energy scale (running coupling constants). The strength of gravitational force and its coupling constant (assuming the graviton as the mediator) are both very far from electromagnetic force by many orders of magnitude, making such unification scenarios highly unlikely.

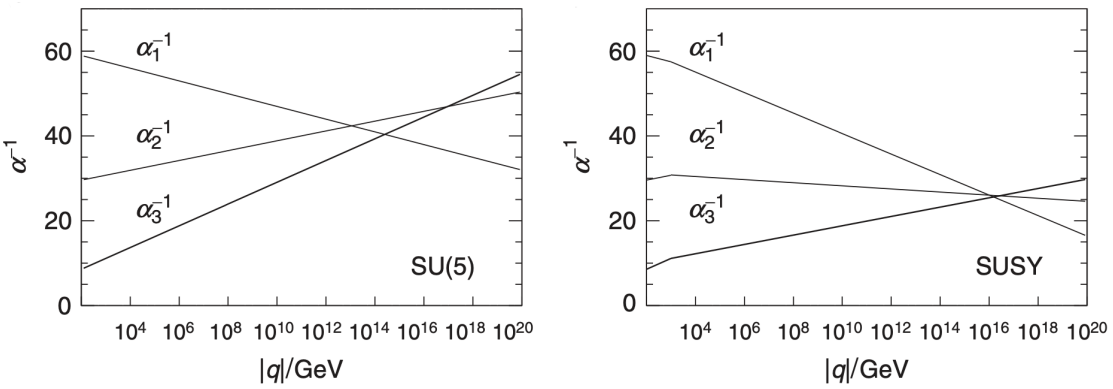



FIGURE 3.1: Schematic representation of the running coupling constants in the scenarios of the $SU(5)$ GUT (left) and the $SU(5)$ GUT with new supersymmetric particles with a mass of 1 TeV (right). Figures taken from Ref. [10].

Even for the other three fundamental forces though, it is concluded that such point cannot exist in SM even though they have similar strengths. To overcome this issue a Grand Unified Theory (GUT) was proposed in mid 1970s by Georgi and Glashow [26] suggesting that a larger $SU(5)$ symmetry group could accommodate the observed SM gauge theories. At this theory the three coupling constants were found to become very close at an energy scale of about $10^{15}$ GeV as shown in Figure 3.1, but in the end it was proven that $SU(5)$ is not the correct gauge group choice for a GUT.[1] Another fitting candidate for this unification would be Supersymmetry (SUSY) [27, 28] since with the further addition of supersymmetric particles at a scale of $\Lambda_{\text{SUSY}} = 1$ TeV the evolution of the $U(1)$, $SU(2)$ and $SU(3)$ couplings would be modified within the $SU(5)$ group resulting to the convergence of the couplings at a single value at an energy scale of $10^{16}$ GeV. Unfortunately, no such particles have been observed so far.

1 This is because the predicted and measured value for $\sin^2\theta_W$ do not agree.

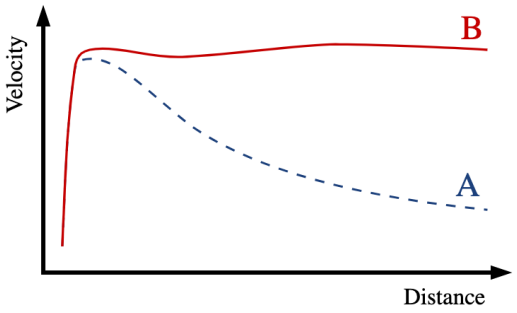
## Dark matter and dark energy

The amount of particles contained in the SM used to create the ordinary matter sums up only to approximately 5% of the total energy content of the universe. Around 27% is attributed to *dark matter* (DM), an unknown kind of matter that does not interact with the electromagnetic force. The rest, ∼68%, is believed to belong to *dark energy*.

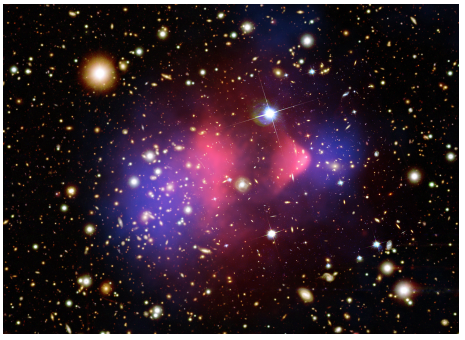
The hypothesis of dark energy is used to explain the accelerated expansion of the universe that was first observed in 1998 by cosmologists using type Ia supernovae to measure this expansion [29]. Dark energy is hypothesised to exert a repulsive negative pressure opposing gravity and driving this expansion in this period of the universe. In cosmology, this accelerated expansion is explained with a positive value of the cosmological constant $\Lambda$ within the framework of general relativity.

On the other side, the existence of DM is strongly supported by cosmological observations. To mention a few examples, the most direct evidence comes from galaxy rotation curves [30] as their stars orbit the galactic centre. According to Kepler's laws the rotation velocity of stars and gas clouds should decrease as a function of the distance to the center of the galaxy, similar to the Solar System. However, in several galaxies their rotation velocities were found to be almost flat at larger radius from the center, as shown in Figure 3.2a. That would mean that the content of visible matter in their outer radius is not sufficient to explain this phenomenon, leading to the hypothesis of DM being a form of non-luminous matter.
Another compelling example is through gravitational lensing [31], a phenomenon explained by the theory of general relativity. According to it, massive objects (like galaxy clusters) should act like lenses if they are found between an observer and a very distant source of light (like a quasar) by bending the light from this source. The amplitude of the gravitational lensing effect depends on the mass of the intermediate object, and the amount of luminous matter in them is not enough to describe the observed effect.
A more illustrative observation related to DM is known as the *bullet cluster* [32]. If visible matter were the only kind of matter in a galaxy cluster its centre of mass should be the same as the baryonic centre of mass. As shown in Figure 3.2b, after the collision of two galaxy clusters the previous assumption is inconsistent with observation, where clearly the centres of mass differ.
Other indications for the existence of DM involve arguments based on cosmic

microwave background (CMB) radiation [33], early formation of the galaxy structures, redshift-space distortions, etc.




(a) Figure of galaxy rotation velocities versus distance from the centre.



(b) Figure of the *bullet cluster* effect.

FIGURE 3.2: Figures from cosmological observations supporting the existence of dark matter. Figures taken from Refs. [34] and [35].

## Matter-antimatter asymmetry

In the very early stages of the universe it is hypothesised that the matter and antimatter particles were present on equal amounts. At some point matter dominated over antimatter ending up in the formation of material structures in the universe. This asymmetry cannot be explained by the SM. The CP violation observed in the quark sector is not able to explain the magnitude of this asymmetry. There were various attempts to explain this phenomenon involving suggestions that a possible CP violation in the lepton sector during the early stages of the universe might be responsible or that there could be yet undiscovered CP violating BSM processes, but there is not yet a clear answer to this question.

## Neutrino masses

The current description of neutrinos in the SM as massless particles is disputed since the observation of neutrino oscillations [36]. Neutrino oscillations are possible among the three generations if there is a difference in their mass. Neutrino mass terms could exist in the current SM formulation with the addition of a right-handed heavy neutrino field. The right-handed chiral neutrino states ($\nu_R$) of the SM are not interacting with any of the known bosons, and currently there is no direct proof of their existence. One of the other scenarios is that neutrinos could be their own antiparticles by being *Majorana* particles, but such scenario is also not confirmed experimentally.

## Hierarchy problem

In a quantum field theory elementary scalars like the Higgs boson are susceptible to large radiative corrections to their mass, since they are not protected by any chiral or gauge symmetries like fermions and gauge bosons. As a consequence, the presence of new particles coupling to the Higgs boson at higher energy scales such as that of a GUT ($\Lambda_{GUT} \sim 10^{16}$ GeV) or the Planck scale ($\Lambda_P \sim 10^{18}$ GeV) would raise the Higgs boson mass and equivalently its vacuum expectation value (VEV). That would mean that the masses of $W$ and $Z$ bosons, as well as the masses of all quark and charged leptons should be raised as well [37]. For example, one may consider a new Dirac fermion with mass $m_f$ interacting with the Higgs field through a Yukawa term. The mass of the Higgs boson after the virtual quantum corrections would be

$$m_H^2 = m_{H,0}^2 - \frac{|y_f|^2}{16\pi^2}\left[2\Lambda^2 + \mathcal{O}\left(m_f^2 \ln\left(\frac{\Lambda}{m_f}\right)\right)\right], \tag{3.1}$$

where $m_{H,0}$ is the bare Higgs mass, $y_f$ the fermion Yukawa coupling and $\Lambda$ the cut-off value of the introduced scale.
The second term of Equation 3.1 describes the quantum corrections introduced by a fermion quantum loop. Similar corrections can arise from other quantum loops in the Higgs boson propagator contributing to the Higgs mass including contributions from a general new massive particle X (as shown in Figure 3.3).

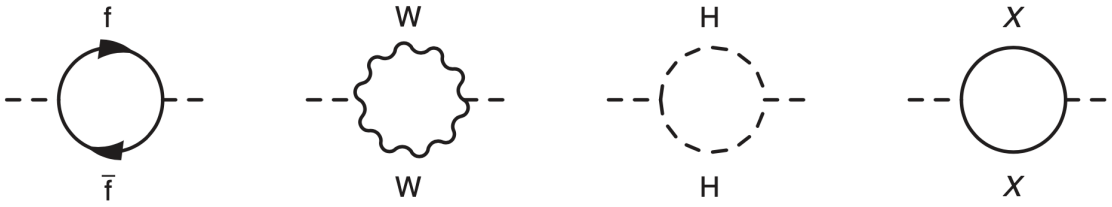



FIGURE 3.3: Loop quantum corrections to the Higgs boson self-energy.

At large energy scales it is difficult to have the Higgs mass at the electroweak scale ($\Lambda_{EW} \sim 10^2$ GeV) since the virtual corrections are quadratic in $\Lambda$. This is known as the *Hierarchy problem*. It is worth mentioning that the Hierarchy problem, which is already present in the SM, gets worse if additional BSM particles are assumed at larger energy scales (with the exception of SUSY). In this case, the square mass of the Higgs boson could increase up to 30 times compared to the experimentally observed value. Therefore, the root of the Hierarchy problem

could be attributed in general to the large discrepancy between the EW scale and the Planck scale.
The bare Higgs mass would need to get unnaturally large values to cancel out the large quantum corrections resulting to the observed Higgs mass. This cancellation is an example of a *fine-tuning* process, which although not forbidden in principle, seems unnatural to the physics community due to the difference in the scales by many orders of magnitude. The above argument is known as the *naturalness* issue and there are many extensions proposed to keep the observed Higgs boson mass at the EW scale in a "natural way", such as SUSY and Composite Higgs models.

### Fermion mass hierarchy

Over the years the mystery of the different fermion masses was always quite intriguing. Currently the SM formulation accommodates the nine fermion masses using the corresponding Yukawa couplings, but these were always arbitrary parameters with values chosen to match the experimental observations. The difference in the masses of the fermions is not associated to a higher theoretical principle and it is difficult to explain why the masses of the fundamental particles can range from the MeV scale (or eV scale if neutrinos are considered) up to the scale of the top-quark mass ($\sim$173 GeV). This difference is another thing that looks unnatural and combined with the mixing of quarks and leptons among the three families call for an explanation via an unified theory at higher energy scales.

## 3.2 Leptoquarks

Several of the BSM extensions that have been proposed to address some of the aforementioned open questions in physics involve the existence of *leptoquarks* (LQs). LQs are hypothesised particles that decay simultaneously to a quark and a lepton and they carry non-zero baryon and lepton quantum numbers. LQs are triplets with respect to the strong interaction, and are charged under all SM gauge groups, having a fractional electric charge. Since they couple both to quarks and leptons, LQs are particularly interesting because their discovery would establish a connection between the two SM sectors as a new fundamental "force" with LQs as the mediators. The similarities between quarks and leptons are numerous (as discussed in Chapter 2.1) and the existence of LQs would prove that this fact is not a coincidence by introducing quark and lepton mixing. The LQ scenario is

realised in several BSM scenarios such as GUTs, RPV SUSY and compositeness models, which can be promising candidates for a more fundamental theory. Moreover, LQs are one of the most favoured options to explain the $B$-physics anomalies reported by several experiments, which seem to persist in the latest measurements. In addition, LQs could support the findings of the $(g-2)_\mu$ measurement [38, 39], a recent hot topic in the physics community. Finally, the existence of LQs is not opposed to any experimental constraints, which further motivates a search for such particles.

## 3.2.1 Motivation

### 3.2.1.1 Appearance of leptoquarks in BSM theories

LQs appear in many BSM theories thus being a very promising candidate with rich phenomenology. Some examples are given below.

**Grand Unified Theories (GUTs)**: One of the first GUTs including LQs is the Pati-Salam model [40], which describes the lepton quantum number ($L$) as the fourth "colour" through a $SU(4)$ symmetry. The spontaneous symmetry breaking of $SU(4)$ leads to massless gluons and massive LQs carrying both baryonic and leptonic quantum numbers that would appear in semileptonic interactions in the lowest orders of perturbation theory. LQs can also appear within the context of a $SU(5)$ theory in the Georgi-Glashow model [26]. There, the mass range of scalar LQs can be found within the sub-TeV scale (only if the coupling of a LQ to two quarks is set to zero), but the masses of vector LQs are supposed to be very large at the order of the GUT scale to avoid discrepancies with the already established experimental limits on the proton decay. Thus, in this model vector LQs are not accessible by accelerators. Additional GUTs involving leptoquarks are based on the $SU(15)$ symmetry [41] or superstring inspired $E_6$ models [42, 43], which although more complex allow the addition of $U(1)$ symmetries in the proposed symmetry groups.

**Supersymmetry (SUSY) with RPV**: Supersymmetry (SUSY) [27, 28] is one of the most elegant BSM extensions introducing a transformation through the supercharge operator $Q$, which transforms a fermion field into a boson field, and vice versa

$$Q\,|\text{fermion}\rangle = |\text{boson}\rangle\,, \qquad Q\,|\text{boson}\rangle = |\text{fermion}\rangle\,. \tag{3.2}$$

This theory suggests that each particle field should have a *supersymmetric* partner (*sparticle*) with a difference of 1/2 in their spin. Provided that the SM and SUSY particles are not too far apart in mass the fine-tuning needed in the hierarchy problem can be alleviated through SUSY, since for each SM particle contributing to the Higgs mass with loop quantum corrections there would be a supersymmetric particle contributing with an opposite correction (thus cancelling it out). In the supersymmetric models, the concept of $R$-parity is introduced. $R$-parity is defined as

$$R_p = (-1)^{3(B-L)+2S}, \tag{3.3}$$

where $B$, $L$ and $S$ stand for the baryon, lepton and spin quantum numbers, respectively. Due to this notation each SM particle has positive $R$-parity ($R_p$ = +1) and each sparticle has negative $R$-parity ($R_p$ = -1). Since the SUSY particles should be produced in pairs, the $R$-parity conservation suggests that the lightest supersymmetric particle (LSP) produced cannot decay further. This stable LSP can be a good dark matter candidate, which is expected to have a mass of up to 1 TeV and interact only through weak interactions and gravitational interactions (*weakly interacting massive particle* or WIMP).

However, there are dedicated right-parity-violation (RPV) SUSY models [44, 45] in which $R$-parity violation is allowed, where Yukawa-like couplings could enable two-body decays of a supersymmetric fermion (*sfermion*) into SM fermions via baryon (BNV) and/or lepton (LNV) number violation. The subsequent violation of both quantum numbers is constrained by the limits on the lifetime of the proton such that sizeable RPV contributions could be met in either BNV or LNV interactions. In the case of significant LNV interactions supersymmetric quarks (*squarks*) could couple to a quark-lepton pair with identical interactions to those of scalar LQs, with an expected mass at the sub-TeV or TeV scale.

**Compositeness**: The similarities between quarks and leptons have led to compositeness models suggesting that the SM fermions (together with the SM gauge and Higgs bosons in some models) have a common substructure and are composite particles made of more fundamental ones that are usually referred to as *preons*. Preons are described by a new quantum number called *hypercolour* with same properties as the SM colour such that it can ensure their confinement inside the SM fermions at the Fermi scale ($\Lambda_F \sim 250$ GeV) [46–48]. Within these models LQs are predicted with a mass range of few hundred GeVs that couple preferentially to third-generation quarks and leptons.

**Technicolour**: Technicolour models [49] propose a new QCD-like interaction as an alternative version of the SM electroweak symmetry breaking instead of the Higgs mechanism. This theory predicts that bound states from technicharged fermion-antifermion pairs should act as a composite Higgs-like states through which SM gauge bosons acquire their mass. The so-called *technifermions* could be either doublets or singlets, which are in a more general way multiplets of a non-abelian gauge interaction referred to as *technicolour*. In this context a fundamental scalar Higgs is not longer needed and the masses of the $W$ and $Z$ bosons arise from the breaking of the corresponding global symmetry. In order to account for the production of the fermion masses extended technicolour (ETC) models have to be used. In these models LQs appear as *leptoquark technimesons* that are created by a techniquark and an anti-technilepton. The coupling of a technimeson leptoquark to a SM quark-lepton pair takes place when the leptoquark's technifermion constituents exchange an ETC gauge boson turning it into an ordinary quark and lepton.
A more recent example of a technicolour model is the 4321 model [50] that is based on a variant of the Pati-Salam one and is structured on the gauge group $SU(4)\times SU(3)\times SU(2)_L\times U(1)_X$. LQs are predicted together with other BSM particles as part of this larger model. In particular, the model predicts a massive $U_1$ vector LQ coupling preferably to the third generation, which is a possible solution to the $B$-meson anomalies.

#### 3.2.1.2 Flavour anomalies and muon magnetic moment

### Flavour anomalies

The decays of $W$ and $Z$ gauge bosons and the decays of SM mesons involving leptons in the final state suggest that electrons, muons and tau-leptons should be produced at equal rates (except for mass effects) since in the SM gauge interactions do not depend on the lepton flavour, a feature known as Lepton Flavour Universality (LFU). Over the past several years there are intriguing indications of LFU violation reported by different experiments in charged and neutral-currents $B$-meson decays (shown in Figures 3.4 and 3.6). These indications manifest themselves through deviations from the SM expectation value in the ratios of $B$-meson decays to the leptons of the three families and are referred to as $B$-physics or flavour anomalies. The flavour sector was always very interesting and following

the aforementioned results the corresponding theoretical studies to explain these anomalies are more timely than ever.

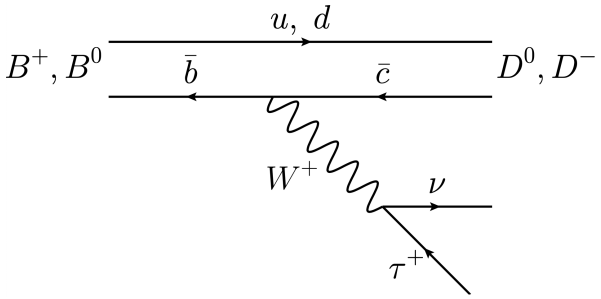



FIGURE 3.4: Illustrative Feynman diagrams of semileptonic $B$-meson decays into $D$-mesons.

Such measurements [51–56] were reported by Belle, BaBar and LHCb experiments and they were related to the $R_{D^{(*)}}$ ratio

$$R_{D^{(*)}} = \frac{\mathcal{B}(B \to D^{(*)}\,\tau\,\bar{\nu})}{\mathcal{B}(B \to D^{(*)}\,\ell\,\bar{\nu})}, \tag{3.4}$$

where $\ell = e, \mu$. An excess of about $3.2\sigma$ was found with respect to the SM expectation value due to an excess in the $B \to D^{(*)}\tau\bar{\nu}$ decays with the averaged measured values from the different experiments to be

$$\begin{aligned} R_D &= 0.358 \pm 0.025\,(\text{stat.}) \pm 0.012\,(\text{syst.}), \\ R_{D^*} &= 0.285 \pm 0.010\,(\text{stat.}) \pm 0.008\,(\text{syst.}), \end{aligned} \tag{3.5}$$

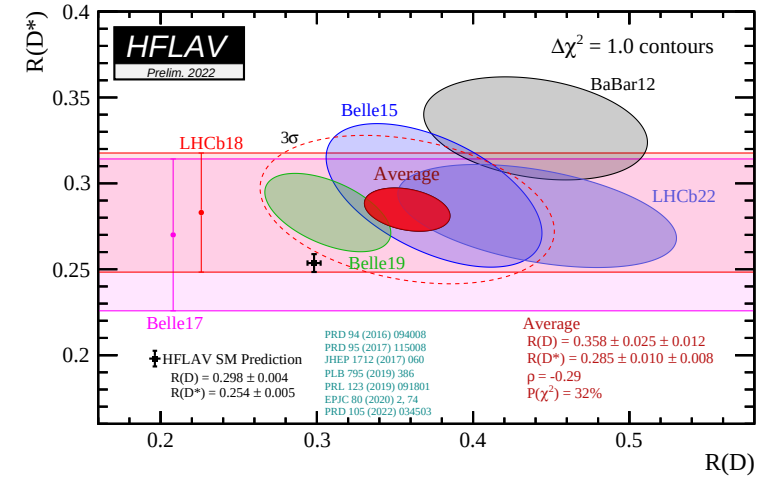
compared to the SM prediction of $R_D^{\text{SM}} = 0.298 \pm 0.004$ and $R_{D^*}^{\text{SM}} = 0.254 \pm 0.005$. A similar excess [57] of about $2\sigma$ was found by the LHCb experiment when measuring the ratio

$$R_{D^{(*)}} = \frac{\mathcal{B}(B_c \to J/\psi\,\tau\,\bar{\nu})}{\mathcal{B}(B_c \to J/\,\ell\,\bar{\nu})} = 0.71 \pm 0.248, \tag{3.6}$$

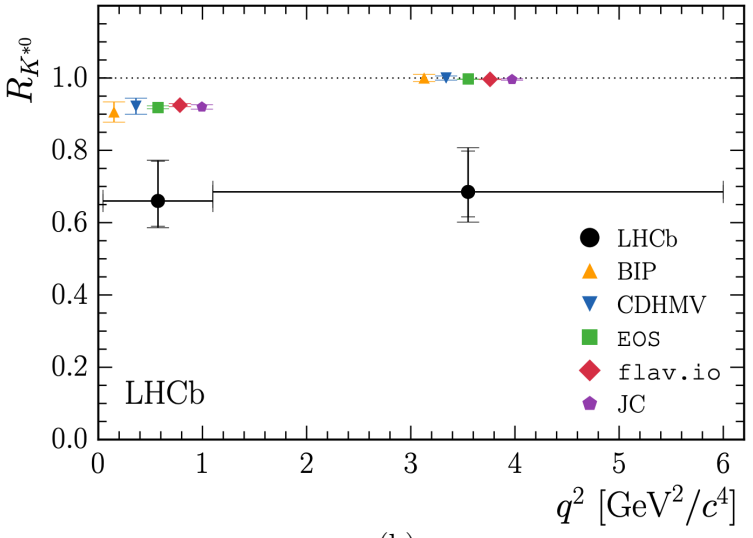
compared to the SM prediction of $0.283 \pm 0.048$.

Another set of LHCb results [58, 59] related to the flavour anomalies involved the measurement of the $R_{K^{(*)}}$ ratio in $b \to s\ell^+\ell^-$ neutral currents. This ratio is given by the formula

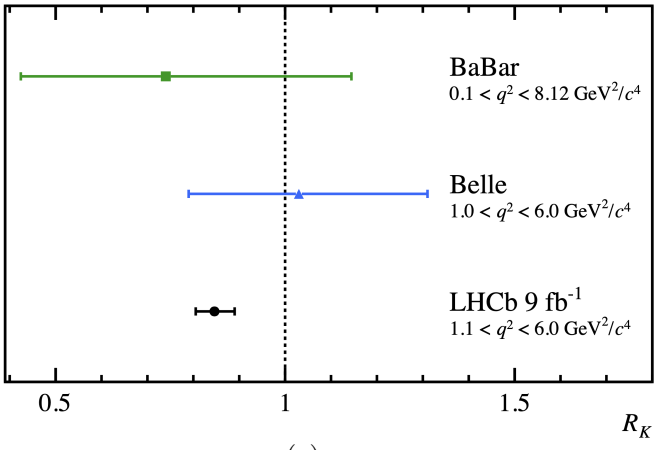
$$R_{K^{(*)}} = \frac{\mathcal{B}'(B \to K^{(*)}\,\mu^+\,\mu^-)}{\mathcal{B}'(B \to K^{(*)}\,e^+\,e^-)}, \tag{3.7}$$




(a)




(b)




(c)

FIGURE 3.5: Summary combination plots of recent measurements of $R_{D^{(*)}}$ (top) as computed by the Heavy Flavour Averaging Group in 2022 [60], $R_{K^{*0}}$ ratio (middle) [61], and $R_K$ ratio (bottom) [62].

where $\mathcal{B}'$ stands for the partial branching fraction. The $R_{K^{(*)}}$ ratios showed a deviation up to $2.5\sigma$ compared to the predicted SM values, due to a deficit in the $B \to K^{(*)}\mu^+\mu^-$ decays. The measured values for the $R_K$ and $R_{K^{*0}}$ ratios were found to be

$$\begin{aligned} R_K &= 0.7^{+0.18}_{-0.13}\,(\text{stat.})\,^{+0.03}_{-0.04}\,(\text{syst.}) \quad \text{for } 0.045 < q^2 < 6 \text{ GeV}, \\ R_{K^{*0}} &= \begin{cases} 0.66^{+0.11}_{-0.07}(\text{stat.}) \pm 0.03(\text{syst.}) & \text{for } 0.045 < q^2 < 1.1 \text{ GeV}, \\ 0.69^{+0.11}_{-0.07}(\text{stat.}) \pm 0.05(\text{syst.}) & \text{for } 1.1 < q^2 < 6 \text{ GeV}. \end{cases} \end{aligned} \tag{3.8}$$

In the SM this ratio is expected to be $R_K \sim 1$ due to LFU, but there was strong evidence [62] that this ratio was $3.1\sigma$ lower than the SM prediction with a value of $R_K = 0.846^{+0.044}_{-0.041}$, as shown in Figure 3.5c.

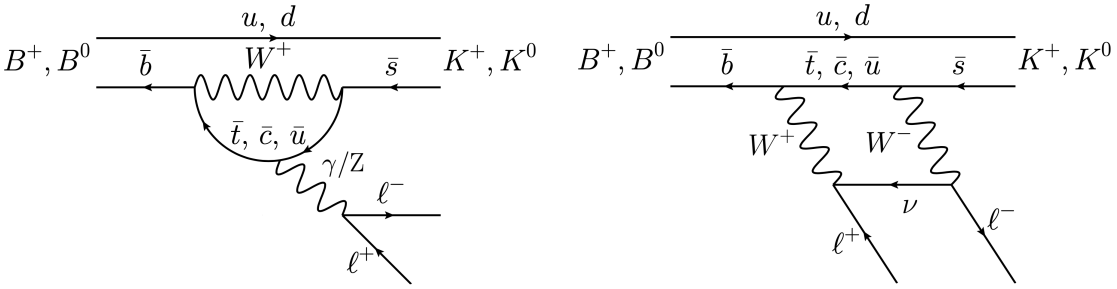



FIGURE 3.6: Illustrative Feynman diagrams of $B$-meson decays into kaons demonstrating the $b \to s\ell^+\ell^-$ decays.

A more recent study revealed that the $R_{K^{(*)}}$ tension was in fact an artifact of an electron background contribution that was not subtracted properly leading to increased electron yields in the denominator, as shown in Figure 3.7. Even if the $R_{K^{(*)}}$ variable was proved to be eventually SM-like there are many other variables with long-standing deviations.

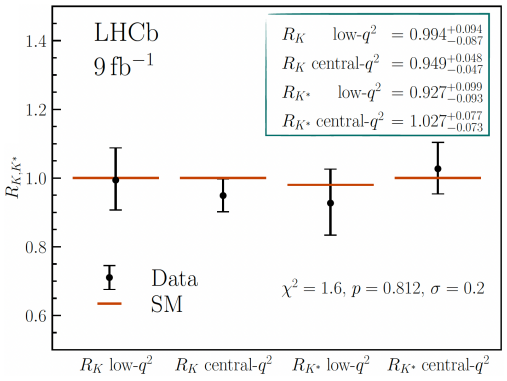



FIGURE 3.7: Measurement of the $R_{K^{*0}}$ ratios in different $q^2$ regions. Figure taken from Ref. [63].

Other measurements that point towards LFU violation involve the branching fraction of the rare $B_S^0 \to \phi\mu^+\mu^-$ decays (Figure 3.8) and in other kinematic variables of $B^0 \to K^{0*}\mu^+\mu^-$ decays (e.g. in $P_5'$ angular observable shown in Figure 3.9).

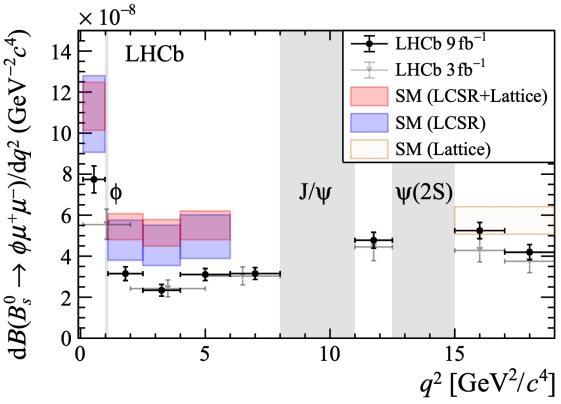



FIGURE 3.8: Differential branching fraction $dB/dq^2$ overlaid with SM predictions from the LHCb experiment [64] for integrated luminosities of 3 fb$^{-1}$ (gray) and 9 fb$^{-1}$ (black).

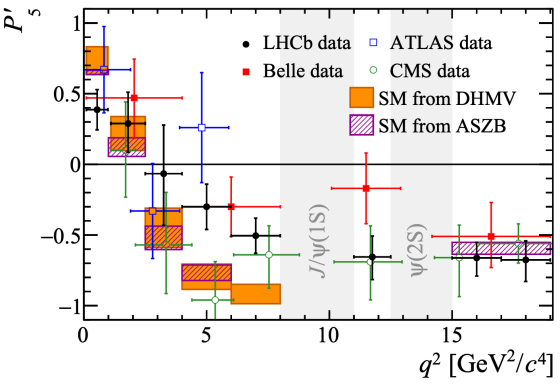



FIGURE 3.9: The $P_5'$ angular observable measured by the LHCb [65], CMS, Belle and ATLAS experiments, superimposed to the SM predictions.

One way to explain some of these anomalies is with the exchange of a leptoquark at leading order as shown in Figure 3.10.

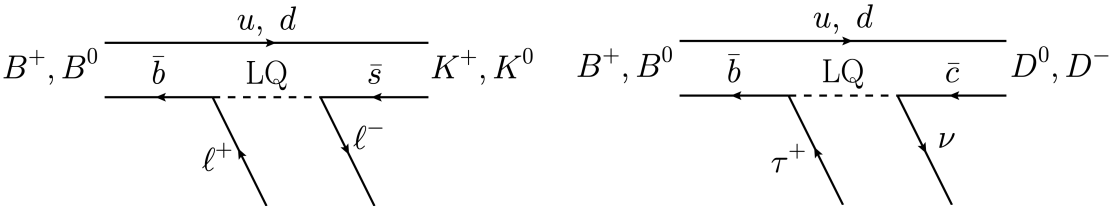



FIGURE 3.10: Illustrative Feynman diagrams of $B$-meson decays into kaons (left) and $D$-mesons (right) through a leptoquark.

## Anomalous muon magnetic moment

The magnetic moment of electrons and muons is an intrinsic property related to their spin and electric charge. It is defined by the formula

$$\vec{\mu_\ell} = g_\ell \frac{q_e}{2m_\ell}\vec{s}, \tag{3.9}$$

where $\ell = e$, $\mu$, $m_\ell$ stands for their mass, $q_e$ for the electric charge, and $g_\ell$ for the gyromagnetic ratio (also known as *g-factor*), a quantity defined as $g_\ell = 2(1 + a_\mu)$ in units of the Bohr magneton.

Their spins tend to twist in order to align with an existing magnetic field, an effect that becomes quite macroscopic in the case of electron spins that are precessed in a ferromagnet. In the microscopic scale their tiny magnetic moment interacts with the external magnetic field through the absorption of photons from which the field is comprised.

According to the Dirac equation the magnetic moment of fermions is predicted to be precisely $e/2m_\ell$, meaning that the $g$-factor should be equal to two in units of the Bohr magneton (since the amplitude of the spin vector is 1/2 for fermions). Quantum corrections increase this value by an additional 0.1% that is being accommodated in the $g$-factor definition as the "anomalous" contribution of the magnetic moment denoted as $a_\mu$.

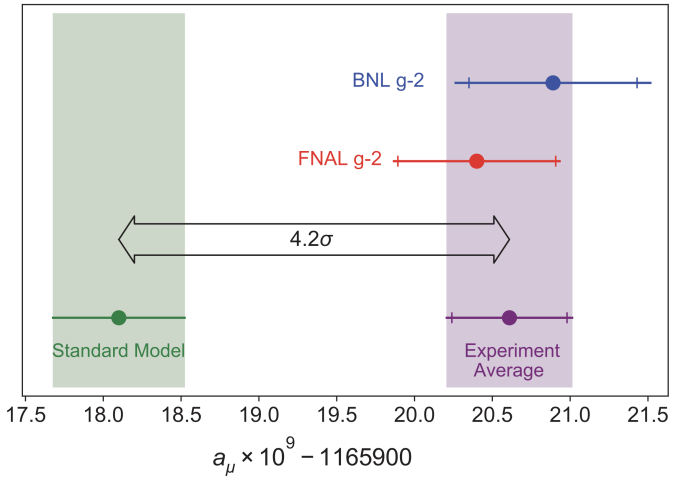



FIGURE 3.11: Measurements of the anomalous muon magnetic moment from BNL E821 experiment (top), FNAL $g-2$ experiment (middle), and their combined average (bottom). The inner tick marks are used to indicate the statistical contribution to the total uncertainties. The SM value of the $g-2$ theory expectation is also shown for comparison. Figure taken from Ref. [39].

The magnetic moment of the electron is one of the most precisely calculated quantities in physics and is found to agree with the SM expectation value at the order of $\mathcal{O}(10)$ of quantum electrodynamics (QED). However, the magnetic moment of the muon shows a tension with respect to the SM prediction, although calculated at a similar level of precision. This is known as the anomalous muon magnetic moment puzzle that has been consolidated over the years. It was first measured by

the E821 experiment at Brookhaven National Laboratory [38], and a confirmation followed quite recently by the Fermilab Muon $g-2$ experiment [39]. The first results from Fermilab (FNAL) report a value of $a_\mu(\text{FNAL}) = 116592040(54)\times10^{-11}$, which corresponds to a deviation of $3.3\sigma$ with respect to the SM. This deviation reaches $4.2\sigma$ if combined with the previous Brookhaven result reaching to a combined value of $a_\mu(\text{Exp}) = 116592061(41)\times10^{-11}$, as shown in Figure 3.11. At this point it is worth mentioning that the theory prediction is under discussion, since the latest calculation from lattice QCD shows a significantly reduced tension with the experimental result.

A LQ model with LQs decaying exclusively into quarks and muons could potentially explain the anomalous muon magnetic moment via the contributions from the additional diagrams shown in Figure 3.12.

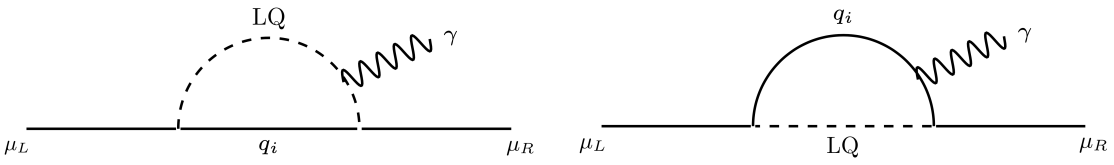



FIGURE 3.12: Illustrative Feynman diagrams demonstrating the dominant contribution to the muon magnetic moment from scalar LQs.

### 3.2.2 Leptoquark phenomenology

The Buchmüller-Rückl-Wyler (BRW) model [66] constitutes the benchmark model for the LQ interpretation offering a general model-independent approach. It relies on an effective Lagrangian, which is required to be renormalisable and invariant under the $SU(3)_C \times SU(2)_L \times U(1)_Y$ transformations. A slightly modified variation of this model has dominated over the years in the physics analyses known as minimal Buchmüller-Rückl-Wyler (mBRW) model [67], which is established as the standard BRW model.

The mBRW model relies on an effective Lagrangian $\mathcal{L}_{\mathrm{LQ}} = \mathcal{L}^f_{|F|=0} + \mathcal{L}^f_{|F|=2}$, where

$$\begin{aligned}
\mathcal{L}^f_{|F|=0} &= \Big(h_{2,L}\,\bar{u}_R\,\ell_L + h_{2,R}\,\bar{q}_L\,i\,\tau_2\,e_R\Big)\,R_2 + \tilde{h}_{2,L}\,\bar{d}_R\;\ell_L\,\tilde{R}_2 \\
&+ \Big(h_{1,L}\,\bar{q}_L\,\gamma^\mu\,\ell_L + h_{1,R}\,\bar{d}_R\,\gamma^\mu\,e_R\Big)\,U_{1,\mu} \\
&+ \tilde{h}_{1,R}\,\bar{u}_R\,\gamma^\mu\,e_R\,\tilde{U}_{1,\mu} + h_{3,L}\,\bar{q}_L\,\vec{\tau}\,\gamma^\mu\,\ell_L\,\vec{U}_{3,\mu} + h.c., \\
\mathcal{L}^f_{|F|=2} &= \Big(g_{1,L}\,\bar{q}^c_L\,i\,\tau_2\;\ell_L + g_{1,R}\,\bar{u}^c_R\,e_R\Big)\,S_1 \\
&+ \tilde{g}_{1,R}\,\bar{d}^c_R\,e_R\,\tilde{S}_1 + g_{3,L}\,\bar{q}^c_L\,i\,\tau_2\,\vec{\tau}\,\ell_L\,\vec{S}_3 \\
&+ \Big(g_{2,L}\,\bar{d}^c_R\,\gamma^\mu\,\ell_L + g_{2,R}\,\bar{q}^c_L\,\gamma^\mu\,e_R\Big)\,V_{2,\mu} \\
&+ \tilde{g}_{2,L}\,\bar{u}^c_R\,\gamma^\mu\,\ell_L\,\tilde{V}_{2,\mu} + h.c..
\end{aligned} \tag{3.10}$$

In Equation 3.10 $F = 3B + L$ stands for the fermion quantum number (where $B$ and $L$ are the baryon and lepton quantum numbers respectively), $q_L$ and $\ell_L$ denote the left-handed SU(2) quark and lepton doublets respectively, while $u_R$, $d_R$ and $e_R$ denote the corresponding right-handed singlets. The relationship $f^c = C\bar{f}^T$ is applied to obtain the charge conjugated fields shown, and the $\tau_i$ quantities correspond to the Pauli matrices. The $h_i$ and $g_i$ quantities represent the leptoquark couplings of leptoquarks with $|F| = 0$ and $|F| = 2$ respectively to the different fields, while their indices are matched to the possible LQ-types of the model corresponding to the dimension of their representation under the $SU(2)$ symmetry group and their chirality.

In general, the model includes both scalar (spin-0) and vector (spin-1) LQs. The scalar LQs can be of type $S$ or $R$ and the vector LQs can be of type $V$ or $U$ depending on their fermion number $F$, while the tilde (~) symbol is used for the right-handed LQs in contrast to the left-handed LQs without it. Among other differences the LQ transverse momentum ($p_{\mathrm{T}}^{\mathrm{LQ}}$) is known in general to be "softer" for scalar LQs and "harder" for vector LQs. These possible LQ types carry fractional electric charge of $\pm\frac{1}{3}$, $\pm\frac{2}{3}$, $\pm\frac{4}{3}$ or $\pm\frac{5}{3}$ and they are summarised in Table 3.1.

The LQ types that emerge from the mBRW model have become rather popular due to the recent $B$-physics anomalies and the $(g-2)_\mu$ results. Of course it is not straightforward for a specific LQ type to accommodate all the anomalies without

| LQ type | $S$ | $F$ | $SU(3)_C$ | $SU(2)_L$ | $U(1)_Y$ | Allowed coupling |
|---|---|---|---|---|---|---|
| $S_1$ | 0 | -2 | $\bar{3}$ | 1 | 1/3 | $\bar{q}_L^c \ell_L$ or $\bar{u}_R^c e_R$ |
| $\tilde{S}_1$ | 0 | -2 | $\bar{3}$ | 1 | 4/3 | $\bar{d}_R^c e_R$ |
| $\vec{S}_3$ | 0 | -2 | $\bar{3}$ | 3 | 1/3 | $\bar{q}_L^c \ell_L$ |
| $V_2$ | 1 | -2 | $\bar{3}$ | 2 | 5/6 | $\bar{q}_L^c \gamma^\mu e_R$ or $\bar{d}_R^c \gamma^\mu \ell_L$ |
| $\tilde{V}_2$ | 1 | -2 | $\bar{3}$ | 2 | -1/6 | $\bar{u}_R^c \gamma^\mu \ell_L$ |
| $R_2$ | 0 | 0 | 3 | 2 | 7/6 | $\bar{q}_L e_R$ or $\bar{u}_R \ell_L$ |
| $\tilde{R}_2$ | 0 | 0 | 3 | 2 | 1/6 | $\bar{d}_R \ell_L$ |
| $U_1$ | 1 | 0 | 3 | 1 | 2/3 | $\bar{q}_L \gamma^\mu \ell_L$ or $\bar{d}_R \gamma^\mu e_R$ |
| $\tilde{U}_1$ | 1 | 0 | 3 | 1 | 5/3 | $\bar{u}_R \gamma^\mu e_R$ |
| $\vec{U}_3$ | 1 | 0 | 3 | 3 | 2/3 | $\bar{q}_L \gamma^\mu \ell_L$ |

TABLE 3.1: Possible LQ types of the mBRW model [67]. The number S denotes the LQ spin and the number F the fermion quantum number defined as $F = 3B+L$, where $B$ and $L$ are the baryon and lepton quantum numbers respectively. The numbers in the fourth and fifth column give the dimension of the LQ representation under the given symmetry group. The LQ electric charge $Q$ can be derived from the numbers of the sixth column using the formula of the hypercharge (Chapter 2.2). $q_L$ and $\ell_L$ denote the left-handed quark and lepton doublets respectively, while $u_R$, $d_R$ and $e_R$ denote the corresponding right-handed singlets. The charge conjugate fields satisfy the relationship $f^c = C\bar{f}^T$. Table adapted from Ref. [12].

inducing other phenomenological problems. The most prominent LQ candidates to explain (or alleviate) these anomalies are given in Table 3.2. A single LQ explanation for both $B$-physics anomalies is provided by the $U_1$ model, which has become quite popular due to its simplicity. However, it cannot explain the tension reported by the muon $g-2$ experiment. If two scalar LQs are considered, $S_1$ and $\vec{S}_3$, both $B$-physics anomalies can be explained, and even the muon $g-2$ result, if right-handed couplings are allowed for $S_1$ [68].

The mBRW model imposes some additional constraints with respect to its predecessor, namely that the LQs should belong to three generations and they should only couple to fermions of a single generation, so that the flavour changing neutral currents (FCNC) are forbidden at tree level. The couplings imposed by the mBRW model respect chirality, and they had very low energy constraints by the time of the construction of the model suggesting that LQs could be found at masses of $\mathcal{O}(100$ GeV).

Going a step further, the interactions of LQs with the photon and the $Z$ boson can also be inserted to the general Lagrangian (as shown in Ref. [71]), which would

| LQ type | $R_{K^{(*)}}$ | $R_{D^{(*)}}$ | $(g-2)_\ell$ at 1L |
|---|---|---|---|
| $S_1$ | ✗* | ✓ | ✓ |
| $\tilde{S}_1$ | (✗) | (✗) | ✗ |
| $\vec{S}_3$ | ✓ | ✗ | ✗ |
| $R_2$ | ✗* | ✓ | ✓ |
| $\tilde{R}_2$ | ✗ | ✗ | ✗ |
| $U_1$ | ✓ | ✓ | ✗ |
| $\tilde{U}_1$ | ✓ | ✗ | (✗) |
| $\vec{U}_3$ | ✓ | ✗ | (✗) |

TABLE 3.2: Summary of the LQ types which can accommodate $R_{K^{(*)}}$ (first column), $R_{D^{(*)}}$ (second column), and $(g-2)_\ell$ results (third column) without inducing other phenomenological problems. In particular, the third column indicates whether the LQ type is able to generate one-loop (1L) corrections to the muon and electron magnetic moments with opposite sign - i.e. the LQ has mixed-chiral couplings. The symbol ✗* means that the discrepancy can be alleviated, but not fully accommodated. The symbol (✗) means that the current entry for the corresponding LQ type does not appear at all in the original table of the publication. The results in the first two columns were obtained by Ref. [69] and the ones in the last column by Ref. [70].

take the form $\mathcal{L}_{\rm LQ} = \mathcal{L}^f_{|F|=0} + \mathcal{L}^f_{|F|=2} + \mathcal{L}^{\gamma,Z}$. This formulation would be more useful for an electron-positron collider, since it would offer the possibility of probing LQ pair production from $e^+e^-$ annihilation with a $\gamma/Z$ mediator.

At the LHC the relevant interactions are the ones of a LQ with gluons or fermions resulting in an effective Lagrangian of the form $\mathcal{L}_{\rm LQ} = \mathcal{L}^f_{|F|=0} + \mathcal{L}^f_{|F|=2} + \mathcal{L}^g_S + \mathcal{L}^g_V$ [72], where $\mathcal{L}^g_S, \mathcal{L}^g_V$ are the terms that correspond to the LQ-gluon interactions. They are given by the relationships

$$\begin{aligned}
\mathcal{L}^g_S &= \sum_{\text{scalar}} \left[ \left(D_\mu \varphi\right)^\dagger \left(D^\mu \varphi\right) - M_S^2\, \varphi^\dagger \varphi \right], \\
\mathcal{L}^g_V &= \sum_{\text{vector}} \Bigg\{ -\frac{1}{2} V^\dagger_{\mu\nu} V^{\mu\nu} + M_V^2\, \varphi^\dagger_\mu \varphi^\mu \\
&\quad - i g_S \left[ (1-\kappa_G)\, \varphi^\dagger_\mu\, T^a\, \varphi_\nu\, G^{a,\mu\nu} + \frac{\lambda_G}{M_V^2} V^\dagger_{\sigma\mu}\, T^a\, V^\mu_\nu\, G^{a,\nu\sigma} \right] \Bigg\},
\end{aligned} \tag{3.11}$$

where the pairs of $M_S, \varphi$ and $M_V, \varphi_\mu$ correspond to the mass and the field of a scalar or vector LQ, respectively, $g_S$ stands for the strong coupling constant and $T^a$ are the generators of the $SU(3)$ symmetry group. The covariant derivative $D_\mu$

and the LQ field tensor $V_{\mu\nu}$ are defined as

$$\begin{aligned} D_\mu &= \partial_\mu - i g_S T^a A^a_\mu, \\ V_{\mu\nu} &= D_\mu \varphi_\nu - D_\nu \varphi_\mu, \end{aligned} \tag{3.12}$$

while the gluon field tensor $G_{\mu\nu}$ is the one defined in Equation 2.27.

In Equation 3.11 the parameters $\kappa_G, \lambda_G$ are related to the anomalous "magnetic" moment $\mu_V$ and the "electric" quadrupole moment $q_V$ of the vector LQ field. They are assumed to be real numbers given by the relationships

$$\begin{aligned} \mu_{V,G} &= \frac{g_S}{2M_V}(2 - \kappa_G + \lambda_G), \\ q_{V,G} &= -\frac{g_S}{M_V^2}(1 - \kappa_G - \lambda_G). \end{aligned} \tag{3.13}$$

The "Boston" model [73] is used in the context of this thesis for the vector LQ interpretation and the generation of $\tilde{U}_1$-type vector LQ signal events by turning on their couplings to a heavy gluon $g'$, a new massive coloured gauge boson that is introduced. The couplings $\kappa_t$ and $\kappa_s$ are introduced in this model, which correspond to the couplings of a $g$ to a $\tilde{U}_1$ and of a $g'$ to a $\tilde{U}_1$, respectively. The $\kappa_t = \kappa_s = -1$ configuration is used to produce $\tilde{U}_1$ events for the minimal coupling scenario (min. coup., $\tilde{U}_1^{\text{min}}$), while the $\kappa_t = \kappa_s = 0$ configuration is used for the Yang-Mills coupling scenario (YM, $\tilde{U}_1^{\text{YM}}$).

For the scalar LQ signal simulation an alternative parametrisation is being used from a similar model [74], which is also adopted for the results of this thesis. In this parametrisation the Lagrangians of up-type ($Q = 2/3$) and down-type ($Q = -1/3$) scalar LQs are

$$\begin{aligned} \mathcal{L}_{\text{LQ}^u_S} &= \lambda\sqrt{\beta}\,\bar{d}_R\,\ell_L^-\,\varphi^u + \lambda\sqrt{1-\beta}\,\bar{u}_R\,\nu_L\,\varphi^u + h.c., \\ \mathcal{L}_{\text{LQ}^d_S} &= \lambda\sqrt{\beta}\,\bar{u}_R\,\ell_L^+\,\varphi^d + \lambda\sqrt{1-\beta}\,\bar{d}_R\,\tilde{\nu}_L\,\varphi^d + h.c., \end{aligned} \tag{3.14}$$

where $\lambda$ is the quark-lepton-LQ coupling and $\beta$ is a model parameter. As a result, the coupling to the charged lepton is given by $\sqrt{\beta}\lambda$, while the coupling to the neutrino is given by $\sqrt{1-\beta}\lambda$. In this equation it is chosen that only left-handed leptons will be involved such that the values of $\eta_L = 1, \eta_R = 1 - \eta_L = 0$ are assumed for the charged lepton chirality fractions. The hypothesised LQ production

at the LHC is expected to be insensitive to this parameter. However, this parameter might be accessible through the top-quark spin, when a third generation LQ couples to a top-quark.

It is worth mentioning that this model is not very much in line with the mBRW one, with the core difference that the $SU(2)_L \otimes U(1)_Y$ symmetry is not preserved.

### 3.2.3 Leptoquark production and decay modes

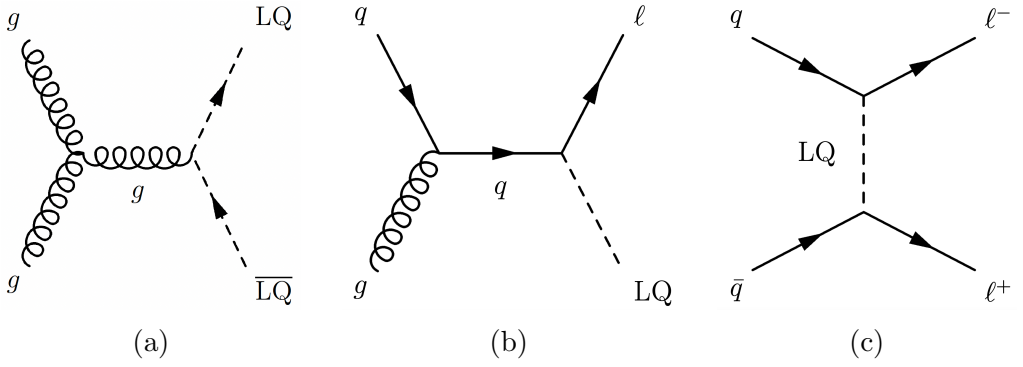



FIGURE 3.13: Illustrative Feynman diagrams representing the three possible LQ production modes at the LHC. From left to the right these are: (a) pair production, (b) single production and (c) non-resonant production.

The main LQ production modes in *pp* collisions at the LHC (shown in Figure 3.13) are through:

1) **pair production**: the cross section is dominated by QCD and it is mostly dependent on the LQ mass (doubly-resonant production),

2) **single production**: the cross section is proportional to $\lambda^2$,

3) **non-resonant production**: the cross section is proportional to $\lambda^4$,

where $\lambda$ generically refers to the $q$-$\ell$-LQ coupling strength.

In the context of this thesis the studies were focused on the pair production mode. This is the universal production mode, independent of $\lambda$, but with the disadvantage that the cross section drops faster as a function of LQ mass because two heavy particles are produced. The single and non-resonant production modes are dependent on $\lambda$, but offer a reach to higher masses because they are less kinematically suppressed. These production modes are all important and complementary, and they are being explored at the LHC.

There are two main subcategories of LQ pair production either through gluon-gluon ($gg$) fusion or through quark-antiquark ($q\bar{q}$) annihilation. At lower LQ masses at the sub-TeV scale the dominant pair production mode is through $gg$ fusion. However, at larger masses LQ production through $q\bar{q}$ annihilation becomes also important. The leading order Feynman diagrams for LQ pair production are summarised in Figure 3.14.

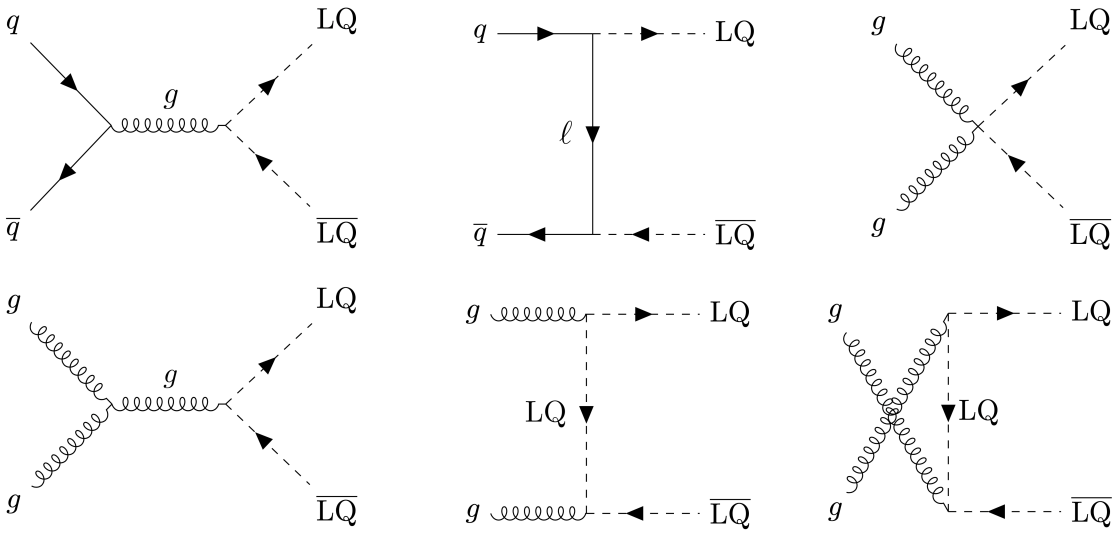



FIGURE 3.14: Illustrative Feynman diagrams for LQ pair production at leading order. LQ production through $gg$ fusion is the dominant production mode at the LHC, while at higher LQ masses the production through $q\bar{q}$ annihilation becomes also relevant.

The contribution of some of the above diagrams such as the $qq \rightarrow$LQLQ through t-channel (top middle) is small at the LHC in the case of 3$^{\text{rd}}$-generation LQs due to the small parton density of the proton. Moreover, since it also depends on $\lambda^2$, it is further suppressed if the $\lambda$ parameter is small.

The scalar LQ production cross sections at LO through $q\bar{q}$ annihilation and $gg$ fusion are given by the equations

$$\hat{\sigma}_{\text{LO}}^{q\bar{q}\rightarrow \text{LQ}_S\overline{\text{LQ}}_S} = \frac{2\alpha_S^2\pi}{27\hat{s}}\xi^3, \tag{3.15}$$

$$\hat{\sigma}_{\text{LO}}^{gg\rightarrow \text{LQ}_S\overline{\text{LQ}}_S} = \frac{\alpha_S^2\pi}{96\hat{s}}\left[(-31\xi^2+41)\xi + (-\xi^4+18\xi^2-17)\log\frac{1+\xi}{1-\xi}\right], \tag{3.16}$$

where $\alpha_S$ the strong interaction coupling constant, $\xi = \sqrt{1 - \frac{4m_{\mathrm{LQ}}^2}{\hat{s}}}$ is the LQ velocity depending on $\hat{s}$ and the mass of the LQ ($m_{\mathrm{LQ}}$), and $\hat{s}$ represents the square of the centre-of-mass energy of the partonic process.

Due to the presence of the anomalous couplings $\kappa_G$ and $\lambda_G$ in the Lagrangian of vector LQs, the vector LQ production cross sections through the same processes are more complicated and they are given be the formulas

$$\hat{\sigma}_{\mathrm{LO}}^{q\bar{q}\to \mathrm{LQ}_V\overline{\mathrm{LQ}}_V} = \frac{4\alpha_S^2\pi}{9\, m_V} \sum_{i=0}^{5} \chi_i^q(\kappa_G, \lambda_G)\, \tilde{G}_i(\hat{s}, \xi), \tag{3.17}$$

$$\hat{\sigma}_{\mathrm{LO}}^{gg\to \mathrm{LQ}_V\overline{\mathrm{LQ}}_V} = \frac{\alpha_S^2\pi}{96\, m_V} \sum_{i=0}^{14} \chi_i^g(\kappa_G, \lambda_G)\, \tilde{F}_i(\hat{s}, \xi), \tag{3.18}$$

where the functions $\chi_i^{q,g}$, $\tilde{G}_i$ and $\tilde{F}_i$ are defined in Ref. [75].

While not very obvious from the previous relationships, in general the cross section of vector LQ models is higher than the one of scalar LQ models and this is also illustrated in Figure 3.15.

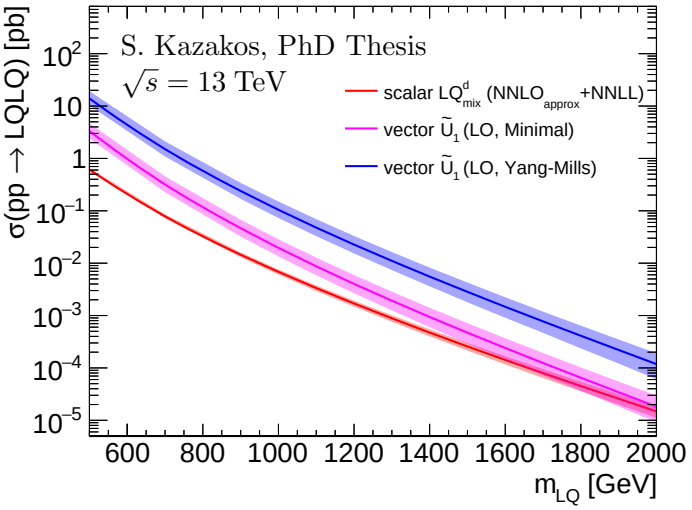



FIGURE 3.15: Leptoquark pair-production cross section as a function of LQ mass for the scalar ($\mathrm{LQ}^{\mathrm{d}}_{\mathrm{mix}}$) and vector ($\tilde{U}_1$) models. The uncertainty bands include the theory uncertainties arising from the renormalisation ($\mu_R$) and factorisation ($\mu_F$) scales, $\alpha_S$ variations and parton distributions functions (PDFs).

Higher-order perturbative corrections up to next-to-leading order (NLO) in QCD are usually required for studies with reliable precision. These corrections increase the LQ production cross section and they were included in the signal MC

production for scalar LQs in the context of this thesis, since they are already known. Nowadays, next-to-next-to-leading order (NNLO) QCD calculations with soft gluon resummation of Ref. [76] at next-to-next-to-leading logarithmic (NNLL) accuracy are available, making it possible to have even more precise predictions for the total cross section. Although the simulated MC samples are not available at NNLO in QCD, their cross section is normalised to the most precise calculation [77–79]. The values of the $\sigma_{\text{NLO}}$, $\sigma_{\text{NNLO+NNLL}}$ cross sections as well as of the $K$-factors that were used for the scaling are given in Table 3.3.

| $\text{LQ}^{\text{d}}$ mass [GeV] | $\sigma_{\text{NLO}}$ [pb] | $\sigma_{\text{NNLO+NNLL}}$ [pb] | $\delta\sigma_{\text{NNLO+NNLL}}$ % | $K$-factor |
|---|---|---|---|---|
| 500 | $4.19{\cdot}10^{-1}$ | $6.09{\cdot}10^{-1}$ | 7.53 | 1.24 |
| 600 | $1.66{\cdot}10^{-1}$ | $2.05{\cdot}10^{-1}$ | 8.12 | 1.23 |
| 700 | $6.33{\cdot}10^{-1}$ | $7.83{\cdot}10^{-2}$ | 8.80 | 1.24 |
| 800 | $2.63{\cdot}10^{-2}$ | $3.26{\cdot}10^{-2}$ | 9.53 | 1.24 |
| 850 | $1.74{\cdot}10^{-2}$ | $2.16{\cdot}10^{-2}$ | 9.93 | 1.24 |
| 900 | $1.16{\cdot}10^{-2}$ | $1.45{\cdot}10^{-2}$ | 10.33 | 1.25 |
| 950 | $7.96{\cdot}10^{-3}$ | $9.91{\cdot}10^{-3}$ | 10.76 | 1.24 |
| 1000 | $5.46{\cdot}10^{-3}$ | $6.83{\cdot}10^{-3}$ | 11.20 | 1.25 |
| 1050 | $3.79{\cdot}10^{-3}$ | $4.76{\cdot}10^{-3}$ | 11.65 | 1.26 |
| 1100 | $2.66{\cdot}10^{-3}$ | $3.35{\cdot}10^{-3}$ | 12.12 | 1.26 |
| 1150 | $1.88{\cdot}10^{-3}$ | $2.38{\cdot}10^{-3}$ | 12.62 | 1.27 |
| 1200 | $1.35{\cdot}10^{-3}$ | $1.70{\cdot}10^{-3}$ | 13.13 | 1.26 |
| 1250 | $9.67{\cdot}10^{-4}$ | $1.22{\cdot}10^{-3}$ | 13.66 | 1.26 |
| 1300 | $6.99{\cdot}10^{-4}$ | $8.87{\cdot}10^{-4}$ | 14.21 | 1.27 |
| 1350 | $5.06{\cdot}10^{-4}$ | $6.46{\cdot}10^{-4}$ | 14.78 | 1.28 |
| 1400 | $3.69{\cdot}10^{-4}$ | $4.73{\cdot}10^{-4}$ | 15.37 | 1.28 |
| 1450 | $2.70{\cdot}10^{-4}$ | $3.48{\cdot}10^{-4}$ | 15.99 | 1.29 |
| 1500 | $2.01{\cdot}10^{-4}$ | $2.57{\cdot}10^{-4}$ | 16.63 | 1.28 |
| 1550 | $1.47{\cdot}10^{-4}$ | $1.91{\cdot}10^{-4}$ | 17.28 | 1.30 |
| 1600 | $1.10{\cdot}10^{-4}$ | $1.42{\cdot}10^{-4}$ | 17.96 | 1.29 |
| 1700 | $6.13{\cdot}10^{-5}$ | $7.96{\cdot}10^{-5}$ | 19.4 | 1.29 |
| 1800 | $3.41{\cdot}10^{-5}$ | $4.51{\cdot}10^{-5}$ | 20.94 | 1.32 |
| 1900 | $1.94{\cdot}10^{-5}$ | $2.58{\cdot}10^{-5}$ | 22.6 | 1.33 |

TABLE 3.3: The signal cross sections at NLO in QCD computed with MADGRAPH5_aMC@NLO using the NNPDF 3.0 NLO PDF set, the higher-order calculations at NNLO+NNLL and their uncertainties due to QCD scale variations, $\alpha_S$ and PDFs. The cross-section values at NNLO+NNLL are taken from Ref. [77–79].

On the other hand, vector LQ are LO processes and the cross sections $\sigma_{\text{LO}}^{\text{MC}}$ and $\sigma_{\text{LO}}^{\text{YM}}$ that were used in this thesis for the minimal coupling and Yang-Mills coupling scenarios, respectively, are summarised in Table 3.4.

| $\tilde{U}_1$ mass [GeV] | $\sigma_{\text{LO}}^{\text{MC}}$ [pb] | $\delta\sigma_{\text{LO}}^{\text{MC}}$ % | $\sigma_{\text{LO}}^{\text{YM}}$ [pb] | $\delta\sigma_{\text{LO}}^{\text{YM}}$ % |
|---|---|---|---|---|
| 500 | 3.340 | 40.7 | 13.95 | 38.6 |
| 700 | $3.192 \cdot 10^{-1}$ | 42.5 | 1.5034 | 40.7 |
| 900 | $4.654 \cdot 10^{-2}$ | 44.5 | $2.389 \cdot 10^{-1}$ | 42.8 |
| 1000 | $1.966 \cdot 10^{-2}$ | 45.3 | $1.045 \cdot 10^{-1}$ | 43.9 |
| 1100 | $0.872 \cdot 10^{-2}$ | 46.5 | $4.777 \cdot 10^{-2}$ | 45.1 |
| 1200 | $4.025 \cdot 10^{-3}$ | 47.7 | $2.266 \cdot 10^{-2}$ | 46.0 |
| 1300 | $1.920 \cdot 10^{-3}$ | 48.8 | $1.107 \cdot 10^{-2}$ | 47.5 |
| 1400 | $0.939 \cdot 10^{-3}$ | 50.0 | $5.544 \cdot 10^{-3}$ | 48.7 |
| 1500 | $4.709 \cdot 10^{-4}$ | 51.9 | $2.834 \cdot 10^{-3}$ | 50.7 |
| 1600 | $2.399 \cdot 10^{-4}$ | 53.3 | $1.470 \cdot 10^{-3}$ | 52.1 |
| 1700 | $1.242 \cdot 10^{-4}$ | 55.4 | $7.732 \cdot 10^{-4}$ | 53.6 |
| 1800 | $6.493 \cdot 10^{-5}$ | 56.9 | $4.107 \cdot 10^{-4}$ | 56.1 |
| 1900 | $3.432 \cdot 10^{-5}$ | 59.7 | $2.203 \cdot 10^{-4}$ | 58.5 |
| 2000 | $1.820 \cdot 10^{-5}$ | 62.3 | $1.184 \cdot 10^{-4}$ | 61.3 |
| 2100 | $9.710 \cdot 10^{-6}$ | 65.2 | $6.380 \cdot 10^{-5}$ | 63.7 |
| 2200 | $5.186 \cdot 10^{-6}$ | 68.4 | $3.445 \cdot 10^{-5}$ | 67.5 |
| 2300 | $2.775 \cdot 10^{-6}$ | 73.5 | $1.858 \cdot 10^{-5}$ | 73.8 |
| 2400 | $1.477 \cdot 10^{-6}$ | 78.0 | $9.977 \cdot 10^{-6}$ | 76.3 |
| 2500 | $7.859 \cdot 10^{-7}$ | 84.0 | $5.342 \cdot 10^{-6}$ | 82.6 |

TABLE 3.4: The vector $\tilde{U}_1$ signal cross sections predicted by MADGRAPH5_aMC@LO using the NNPDF 2.3 LO PDF set, and their uncertainties due to QCD scale variations, $\alpha_S$ and PDFs.

Both Table 3.3 and Table 3.4 contain also the uncertainties in the NNLO+NNLL and LO calculations due to QCD scale variations, $\alpha_S$ and PDFs. In the case of the vector LQs the LO prediction for the cross section has large scale uncertainties even at low LQ mass, and significant PDF uncertainties at high LQ mass. These uncertainties are taken into account in the overall systematic errors of the LQ analyses as normalisation uncertainties on the theory cross section (see Chapter 10).

Once a LQ is produced it is expected to decay into a quark and a lepton. The branching ratio of the decay is controlled by the $\lambda$ parameter, which corresponds to the quark-lepton-LQ coupling. The coupling parameter $\lambda$ is set to 0.3 in the LQ models of this thesis resulting to a LQ width of 0.2% of its mass, satisfying the narrow-width approximation. The general formulas for the decay width of a

scalar or a vector LQ are

$$\begin{aligned}\Gamma(\mathrm{LQ}_S \to q\ell) =& \lambda^2\beta \frac{\sqrt{m_{\mathrm{LQ}}^4 + m_q^4 + m_\ell^4 - 2\left(m_{\mathrm{LQ}}^2 m_q^2 + m_{\mathrm{LQ}}^2 m_\ell^2 + m_q^2 m_\ell^2\right)}}{16\pi\, m_{\mathrm{LQ}}^3} \\ & \times (m_{\mathrm{LQ}}^2 - m_q^2 - m_\ell^2),\end{aligned} \tag{3.19}$$

$$\begin{aligned}\Gamma(\mathrm{LQ}_V \to q\ell) =& \lambda^2\beta \frac{\sqrt{m_{\mathrm{LQ}}^4 + m_q^4 + m_\ell^4 - 2\left(m_{\mathrm{LQ}}^2 m_q^2 + m_{\mathrm{LQ}}^2 m_\ell^2 + m_q^2 m_\ell^2\right)}}{48\pi\, m_{\mathrm{LQ}}^3} \\ & \times \frac{2m_{\mathrm{LQ}}^4 - m_q^4 - m_\ell^4 - m_{\mathrm{LQ}}^2 m_q^2 - m_{\mathrm{LQ}}^2 m_\ell^2 + 2m_q^2 m_\ell^2}{m_{\mathrm{LQ}}^2},\end{aligned} \tag{3.20}$$

where $q$ and $\ell$ are the quark and lepton produced by the LQ decay and $\lambda$ is the coupling of the interaction.

Among the LQ searches presented in Chapter 9 there is a dedicated search in $t\tau t\tau$ final states, which mainly includes third-generation down-type scalar LQs ($\mathrm{LQ}_3^{\mathrm{d}}$). The search was found to be sensitive to $t\tau b\nu$ final states as well, where the result is given in terms of $\sigma_{\mathrm{LQ}_3^{\mathrm{d}}\mathrm{LQ}_3^{\mathrm{d}}} \times \mathcal{B}$, where $\mathcal{B}$ stands for the partial branching ratio to this final state. One might expect the parameters $\beta$ and $\mathcal{B}$ to be identical, something that would be correct at large LQ masses. Since $\mathcal{B}$ depends on the LQ mass through the formula $\mathcal{B} = \Gamma_i/\Gamma$ the corresponding partial branching ratios $\mathcal{B}(\mathrm{LQ}_3^{\mathrm{d}} \to t\tau)$ and $\mathcal{B}(\mathrm{LQ}_3^{\mathrm{d}} \to b\nu)$ are

$$\begin{aligned}\mathcal{B}(\mathrm{LQ}_3^{\mathrm{d}} \to t\tau) &= \frac{\Gamma(\mathrm{LQ}_3^{\mathrm{d}} \to t\tau)}{\Gamma(\mathrm{LQ}_3^{\mathrm{d}} \to t\tau) + \Gamma(\mathrm{LQ}_3^{\mathrm{d}} \to b\nu)}, \\ \mathcal{B}(\mathrm{LQ}_3^{\mathrm{d}} \to b\nu) &= \frac{\Gamma(\mathrm{LQ}_3^{\mathrm{d}} \to b\nu)}{\Gamma(\mathrm{LQ}_3^{\mathrm{d}} \to b\nu) + \Gamma(\mathrm{LQ}_3^{\mathrm{d}} \to b\nu)}.\end{aligned} \tag{3.21}$$

Equation 3.19 can be written into a more compact form if the mass of the lepton $m_\ell$ is considered negligible. Substituting the short form into the above relationship, and using the values of $\lambda = 0.3$, $\beta = 0.5$, $m_t = 173$ GeV and $m_b = 4.7$ GeV, the above branching ratios can be calculated as a function of LQ mass, as shown in Figure 3.16.

It should be noted that while this discussion explains the calculation of $\mathcal{B}$ in the $\mathrm{LQLQ} \to t\tau t\tau$ search, it also applies to the general case of $\mathrm{LQ} \to t\ell$, where $\ell = e,\, \mu,\, \tau$.

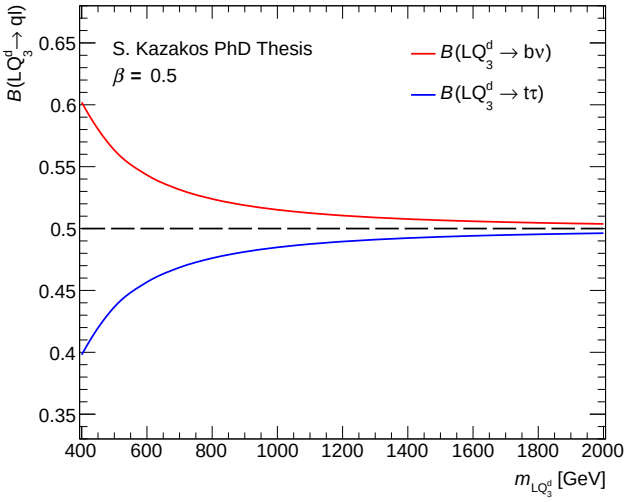



FIGURE 3.16: Branching ratios of a scalar $\mathrm{LQ}_3^{\mathrm{d}}$ decaying either to $t\tau$ (blue line) or to $b\nu$ (red line) versus $\mathrm{LQ}_3^{\mathrm{d}}$ mass for a model with $\beta = 0.5$.

# Chapter 4

# The LHC complex and the ATLAS detector

This chapter provides an overview of the Large Hadron Collider (LHC) complex and focuses on the ATLAS detector, the detector used by the ATLAS experiment to record and analyse the proton-proton collision data used for the work of this dissertation. The LHC is located at CERN (Geneva, Switzerland) and currently is the only circular accelerator worldwide designed to accelerate protons up to a centre-of-mass energy of about 14 TeV. After reaching the desired energy the two proton beams are colliding at certain points of the LHC ring, where a detector has been placed to study the collision products. The four main experiments of the LHC ring are ATLAS, CMS, LHCb and ALICE, while at the same time there are many other interesting experiments present (AD/ELENA, ISOLDE, AWAKE, n_TOF, etc.). The proton beams start from a linear accelerator (LINAC2 for Run 2) at the ground level as hydrogen atoms having "stripped off" their electron and they start accelerating first in the proton BOOSTER, then in the Proton Synchrotron (PS), afterwards in the Super Proton Synchrotron (SPS) and finally at the main LHC ring. In order to create the proper collision conditions a complex magnet system is unfolded in the LHC and a reliable cooling system has been designed along the magnets in order to maintain these conditions. Prior to the circulation of the beams the air is removed from the beam pipes in order to create void-like conditions to avoid the unwanted collisions of the accelerated protons with air molecules.

## 4.1 The LHC complex

The LHC is a circular particle accelerator of about 27 km in circumference that is installed in an underground tunnel around 100 m below the surface. It is located at CERN (European Organisation for Nuclear Research[1]) in Geneva, Switzerland, in the border between Switzerland and France. It is built to produce proton-proton ($pp$), proton-lead ($p$-Pb) and lead-lead (Pb-Pb) collisions in comparison with its predecessor LEP (Large Electron Positron) collider that was installed in the same tunnel in order to produce electron-positron collisions. The LEP collider was decommissioned in 2000, after a successful run performing collisions at centre-of-mass energy up to $\sqrt{s} = 209$ GeV. The LHC started its operations in 2008 reaching a centre-of-mass energy of $\sqrt{s} = 8$ TeV at the end of Run 1 that was later increased to $\sqrt{s} = 13$ TeV towards the end of the Run 2. After the discovery of the Higgs boson in 2012 and the analysis of the full Run-2 dataset, a very rich physics program is ongoing towards Run 3, a new period of operation that started in 2022 at $\sqrt{s} = 13.6$ TeV with the aim of reaching $\sqrt{s} = 14$ TeV by the end of the run.

The largest experiments in the LHC ring are ATLAS, CMS, LHCb and ALICE, each represented by a corresponding detector at an interaction point. While ATLAS and CMS experiments are designed to fulfil multiple purposes studying a broad range of physics processes from SM precision measurements to BSM searches, LHCb is more focused on $B$-physics processes and ALICE on heavy ion collisions. Of course, there are many other interesting physics experiments at the LHC complex using colliding beams like TOTEM, MoEDAL, FASER and LHCf, fixed-target experiments like COMPASS and NA61-64, and antimatter-related experiments like ALPHA, AEGIS, GBAR, etc., which are being performed at the Antimatter Decelerator (AD) and ELENA facilities.

In Run 2 the proton acceleration chain starts from obtaining the protons by hydrogen atoms ($H_2$) that have been stripped off their electrons during their acceleration in LINAC2 up to an energy of about 50 MeV. The protons are then inserted in the Proton Synchrotron Booster (PSB), a circular accelerator of 157 m in circumference, where they reach an energy of about 1.4 GeV. Afterwards, they enter a larger circular accelerator of 628 m in circumference, the Proton Synchrotron (PS), where they reach an energy of 25 GeV, followed by an even larger ring with a

1 Conseil Européen pour la Recherche Nucléaire.

circumference of 6.9 km that hosts the Super Proton Synchrotron (SPS) designed to bring the protons to an energy of about 450 GeV. Apart from accelerating the protons, the SPS is also providing beam for scheduled test beams and experiments conducted in the North area area or other experiments such as AWAKE, etc. Up to this point the protons are circulating in the same direction, something that changes after being injected to the Large Hadron Collider (LHC), where they start circulating in opposite directions (clockwise and anticlockwise). At the LHC protons accelerate up to an energy of 6.5 TeV, preparing for the collisions to take place. Until a full proton fill is completed at the LHC the protons circulate at the injection energy, and they start accelerating only afterwards reaching the desired energy in about 15 minutes. The collisions start taking place only if the beams are found to be stable and they are interrupted when roughly 50% of the beam luminosity is lost impacting the data collection rate. The beam is then dumped and a new proton fill takes place. The proton beam is not continuous and it is divided in 2808 bunches with a 25 ns bunch spacing, each containing about $10^{11}$ protons. This bunch spacing corresponds to $pp$ collisions at a rate of 40 MHz.

In Run 3 there are further improvements in the accelerator complex that took place during the Long Shutdown 2 (LS2), boosting the manufacturing specifications. Some of the most important improvements are that LINAC2 has been replaced by LINAC4 (able to accelerate protons up to 160 MeV), PSB is capable of accelerating them to 2 GeV (instead of 1.4 GeV) and the final beam energy at the LHC is about 6.8 TeV.

The LHC consists of 9593 magnets in total that belong in different categories depending on the task they are designed to perform. There are 1232 superconducting dipole magnets (15 m long each) built to *bend* the proton beam and keep the protons in a circular trajectory. This is achieved by introducing a 8.3 T magnetic field perpendicular to their trajectory pointing to the sky, which creates the Lorentz force towards the centre of the LHC ring that bends the beam towards the same direction. In the magnet system there are additionally 392 quadrupole magnets placed in pairs in order to focus the beam. There are additional higher-order multipole magnets (such as sextupoles, octapoles and decapoles) designed to further focus the beam and suppress any unwanted behaviour of the beams. All the main magnets are cooled down to 1.9 K, with a superfluid helium cooling system in order to ensure their proper operation.

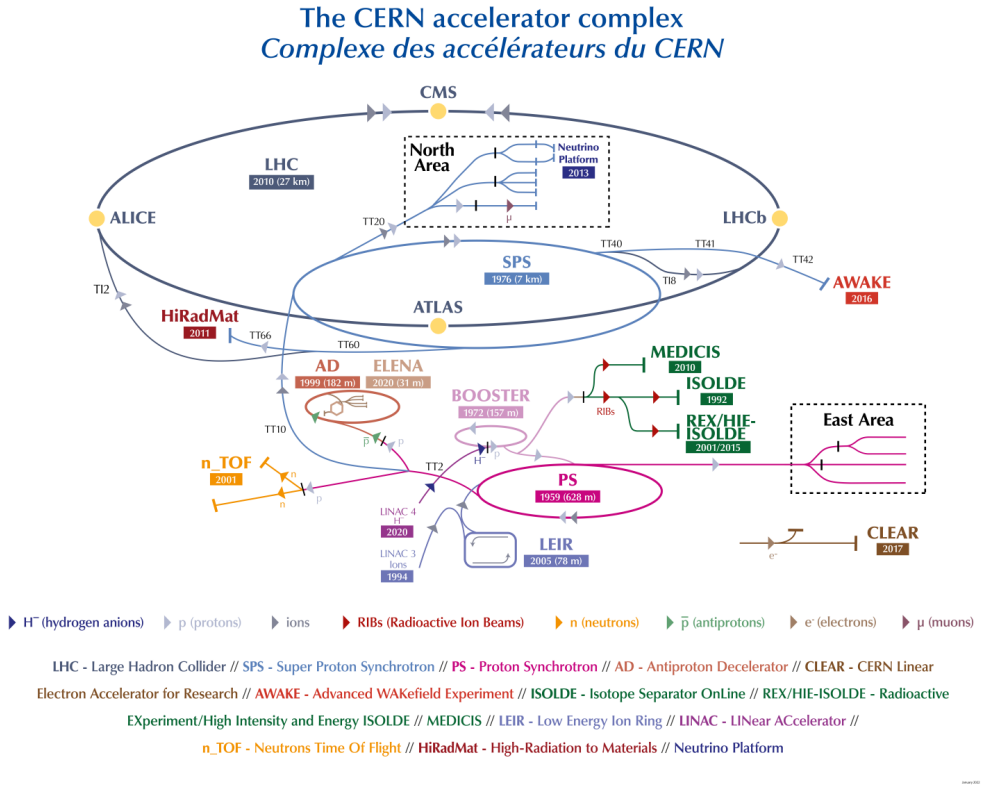



FIGURE 4.1: Schematic illustration of the Large Hadron Collider (LHC) accelerator chain at CERN. The position of the four main experiments ATLAS, CMS, LHCb and ALICE is represented by yellow dots. The light grey arrows indicate the direction of the protons that are accelerated in the LHC complex. The proton acceleration chain starts from LINAC4 and ends up with the LHC ring. Figure taken from Ref. [80].

The protons are being accelerated in the beam pipes of the LHC in *artificial-vacuum* conditions to reduce the probability of collision with the air molecules. The acceleration is accomplished by using 8 radio frequency (RF) cavities per beam direction operating at a temperature of 4.5 K. The acceleration depends on the potential difference created by the RF cavities and the proper orientation of the RF field that is either attractive or repulsive to the beam particles.

### 4.1.1 Luminosity and pileup

A useful quantity to determine the performance of a particle accelerator and its ability to produce a certain number of collisions is called *instantaneous luminosity* $\mathcal{L}$ and it is defined as

$$\mathcal{L} = \frac{1}{\sigma_i}\frac{dN_i}{dt}, \tag{4.1}$$

where $\sigma_i$ is the cross section and $dN_i/dt$ is the event rate of a given physics process $i$ (such as $pp \to X$). Luminosity $L$ is therefore defined as the integral of the instantaneous luminosity delivered within a certain time window as $L = \int \mathcal{L}\, dt$. It is measured in units of [length]$^{-2}$[time]$^{-1}$, usually cm$^{-2}$s$^{-1}$.

In an accelerator where two beams collide by crossing each other at a finite crossing angle the instantaneous luminosity is expressed as

$$\mathcal{L} = f\, \frac{N_b N_1 N_2}{4\pi\sigma_x\sigma_y}\, S, \tag{4.2}$$

where $f$ is the revolution frequency of the beam, $N_b$ the number of bunches per beam, $N_1$ and $N_2$ are the number of protons in each bunch, $\sigma_x$ and $\sigma_y$ are the horizontal and vertical widths of the colliding beams respectively assuming a Gaussian beam profile and same widths for both beams, and $S$ is the luminosity reduction factor due to crossing beams

$$S = \frac{1}{\sqrt{1 + \left(\frac{\sigma_x}{\sigma_s}\tan\frac{\phi}{2}\right)^2}} \approx \frac{1}{\sqrt{1 + \left(\frac{\sigma_x}{\sigma_s}\frac{\phi}{2}\right)^2}}, \tag{4.3}$$

where $\sigma_s$ is the bunch length and $\phi$ the crossing angle as indicated in [81]. In the case of introduced beam offsets Equation 4.2 is transformed to

$$\mathcal{L}' = \mathcal{L} \cdot W \cdot e^{\frac{B^2}{A}}, \tag{4.4}$$

where

$$W = e^{-\frac{(d_2-d_1)^2}{4\sigma_x^2}}, \qquad A = \frac{\sin^2\frac{\phi}{2}}{\sigma_x^2} + \frac{\cos^2\frac{\phi}{2}}{\sigma_s^2}, \qquad B = \frac{(d_2-d_1)\sin\frac{\phi}{2}}{2\sigma_x^2}, \tag{4.5}$$

and $d_1, d_2$ are the induced beam offsets. The parameter $W$ is a luminosity reduction factor due to the beam offsets. while the factor $e^{\frac{B^2}{A}}$ appears only when both beam offsets and a non-zero crossing angle are present.

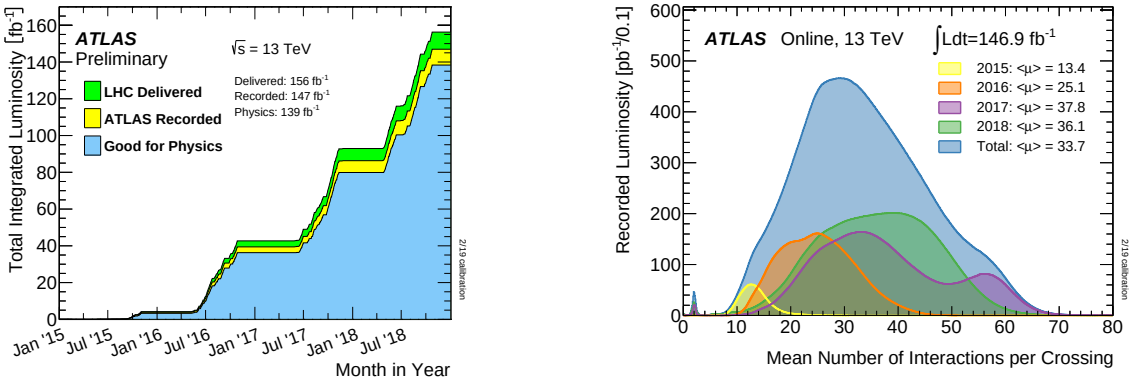
The integrated luminosity during Run 2 in ATLAS is shown as a function of time for stable beams at $\sqrt{s} = 13$ TeV in Figure 4.2a.

Another interesting accelerator-related quantity is called *pileup* and it represents the amount of additional $pp$ interactions per bunch crossing. There is a constant effort of keeping pileup levels as low as possible, a task that gets more difficult

| | Run 1 | | Run 2 | | | | Run 3 |
|---|---|---|---|---|---|---|---|
| Parameter / Year | 2011 | 2012 | 2015 | 2016 | 2017 | 2018 | 2022 |
| Centre-of-mass energy $\sqrt{s}$ [TeV] | 7 | 8 | 13 | 13 | 13 | 13 | 13.6 |
| Bunch spacing [ns] | 50 | 50 | 25 | 25 | 25 | 25 | 25 |
| Peak instantaneous luminosity $\mathcal{L}$ [$10^{34}$ cm$^{-2}$s$^{-1}$] | 0.36 | 0.77 | 0.5 | 1.38 | 2.09 | 2.1 | 2.2 |
| Integrated luminosity $L$ [fb$^{-1}$] | 5.5 | 23.1 | 4.2 | 38.5 | 50.2 | 63.4 | 35.4 |
| Average interactions per bunch crossing $<\mu>$ | 9.1 | 20.7 | 13.4 | 25.1 | 37.8 | 36.1 | 53.0 |

TABLE 4.1: Overview of the operation parameters of the LHC during Run 1 and Run 2 [82, 83]. An estimation of these parameters is given for the first year of Run 3 (2022) based on the corresponding operation report [84].

at higher luminosity when the number of interactions is increased. High pileup levels could lead the performance of the physics detectors to deteriorate, severely impacting the proper identification of physics objects matched to the hard-scatter vertex and being a continuous challenge for the proper function of trigger. The mean number of interactions per bunch crossing (pileup) in ATLAS during Run 2 was $<\mu>= 33.7$, as shown in Figure 4.2b.




(a) (b)

FIGURE 4.2: (a) Integrated luminosity as a function of time during stable beams at $\sqrt{s} = 13$ TeV. The ATLAS experiment recorded a great portion (yellow) of the total luminosity delivered by the LHC (green), while large part of it was useful for physics studies (blue). (b) Distribution of the observed mean number of interactions per bunch crossing $<\mu>$ during Run 2 (separate periods are also shown) for $pp$ collisions at $\sqrt{s} = 13$ TeV. Figures taken from Ref. [85].

## 4.2 The ATLAS detector

The ATLAS (A Toroidal LHC ApparatuS) detector is a general-purpose detector that is used in the ATLAS experiment. It serves as a solid probe for new physics checking the validity of the SM at the same time through precision tests at the

TeV scale. The detector's length reaches the 44 m, while its diameter is estimated to 25 m. It is designed to cover a solid angle of nearly $4\pi$ steradians around the interaction point (IP) and its weigh is estimated to 7000 tonnes.

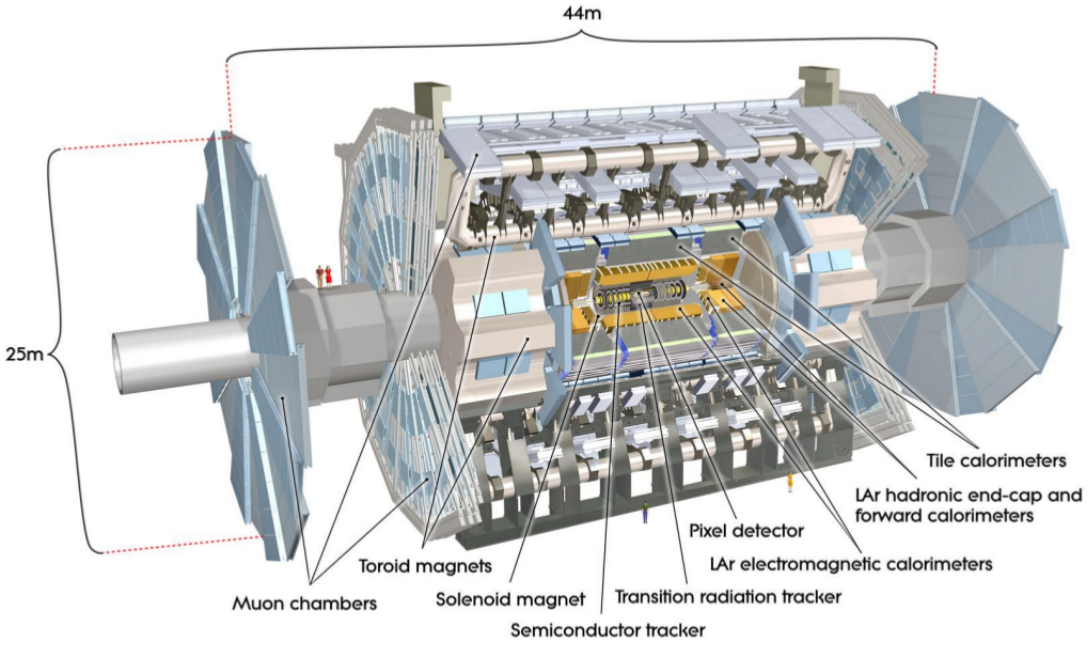



FIGURE 4.3: Side-view of the ATLAS detector and its subsystems. Figure taken from Ref. [86].

The subsystems of the detector are labelled in Figure 4.3. The ATLAS detector is a cylindrical structure and consists of an outer solenoid magnet that surrounds the inner detector. A set of different calorimeters surrounds the inner detector and three large superconducting toroids (one barrel-shaped and two end-caps) are located around them.

### 4.2.1 ATLAS coordinate system

The ATLAS experiment uses a right-handed cartesian coordinate system with respect to the interaction point in the centre of the detector. The x and y axes define the transverse plane and the z-axis follows the direction of the beam. The positive x-axis points to the center of the accelerator ring and the y-axis points upwards. The positive z-axis points to the side A of the detector, while the side C lies in the opposite direction. ATLAS also uses frequently a polar system based on the angles $\theta$ and $\phi$. The *azimuthal angle* $\phi$ is measured in the transverse plane from the positive x-axis to the positive y-axis ranging from -$\pi$ to $\pi$. On experimental

basis it is computed as

$$\phi = \arctan \frac{p_y}{p_x}, \tag{4.6}$$

where $p_x$, $p_y$ are the particle momentum projection on the x- and y-axis, respectively. The *polar angle* $\theta$ is an angle measured from the positive z-axis to the transverse plane with running values from 0 to $\pi$. It is commonly used to calculate the transverse plane projections of the fragment trajectories and momentum after collision. Some of these projected quantities like transverse momentum ($p_{\mathrm{T}}$) and transverse energy are defined as

$$p_{\mathrm{T}} = p \cdot \sin\theta = \sqrt{p_x^2 + p_y^2}, \tag{4.7}$$

$$E_{\mathrm{T}} = E \cdot \sin\theta = \sqrt{m^2 + p_{\mathrm{T}}^2}, \tag{4.8}$$

and are preferred in particle physics experiments exploiting their invariance under longitudinal boosts, something useful since the total momentum along the z-axis varies event by event.

The ATLAS cartesian and polar coordinate systems are illustrated in Figure 4.4a. Another useful quantity that transforms simply under longitudinal boosts is the *rapidity* $y$, which is defined as

$$y = \frac{1}{2} \ln \frac{E + p_z}{E - p_z}. \tag{4.9}$$

In a hadronic collider it is often more convenient to use the rapidity instead of the polar angle. The advantage of rapidity is that differences in rapidity are invariant under lorentz boosts. In the relativistic limit, where the particle mass can be neglected ($E \approx p$), Equation 4.9 simplifies to

$$\eta = \frac{1}{2} \ln \frac{|\boldsymbol{p}| + p_z}{|\boldsymbol{p}| - p_z} = -\ln \left[ \tan \left( \frac{\theta}{2} \right) \right]. \tag{4.10}$$

The quantity $\eta$ is called *pseudorapidity* and is just a special case of rapidity. It could be expressed in terms of $p$ and $p_z$ as

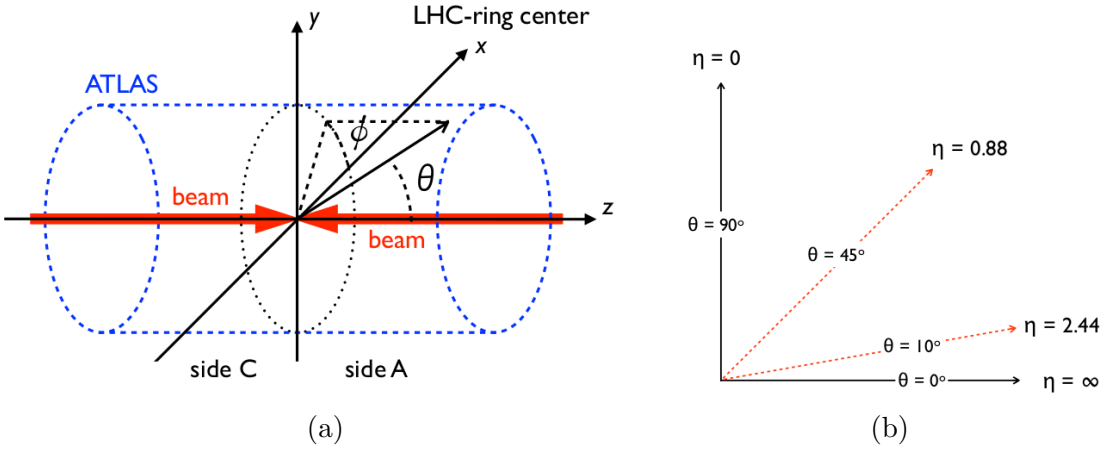
$$\eta = -\operatorname{arctanh} \frac{p_z}{p}, \tag{4.11}$$

and any shift in pseudorapidity is also invariant under Lorentz boosts along the z-axis. The correspondence between pseudorapidity $\eta$ and polar angle $\theta$ is illustrated in Figure 4.4b.

The "forward" regions of the detector that are close to the beam axis are often described in terms of $\eta$ as high $\eta$ regions, while $\eta$ drops down to 0 going closer to the transverse plane.

The angular separation between two particles in the detector region is described by the variable $\Delta R$ defined as

$$\Delta R = \sqrt{(\Delta\phi)^2 + (\Delta\eta)^2}. \tag{4.12}$$




(a) (b)

FIGURE 4.4: (a) Schematic representation of the ATLAS cartesian and polar coordinate systems. (b) Correspondence between pseudorapidity $\eta$ and polar angle $\theta$.

### 4.2.2 Inner detector

The Inner Detector (ID) [87] is the innermost subsystem of the detector that is closest to the interaction point. The central solenoid surrounding the ID generates a uniform axial magnetic field of 2 T, which bends the trajectories of the charged particles. Due to the existence of the Lorentz force $\vec{v} \times \vec{B}$, the trajectory of the charged particle is a helix with a pitch angle $\lambda$ and a radius of curvature $R$ (shown in Figure 4.5). Hence, for a charged particle in the detector region ($|q| = e$) these quantities are related to its momentum by the formula

$$p \cos\lambda = 0.3\, B\, R, \tag{4.13}$$

where $p$ is the momentum of the particle and $B$ is the magnetic flux density. By determining the parameters of the helical trajectory in the tracking detectors, $R$ and $\lambda$ can be obtained leading to the reconstruction of the particle's momentum.

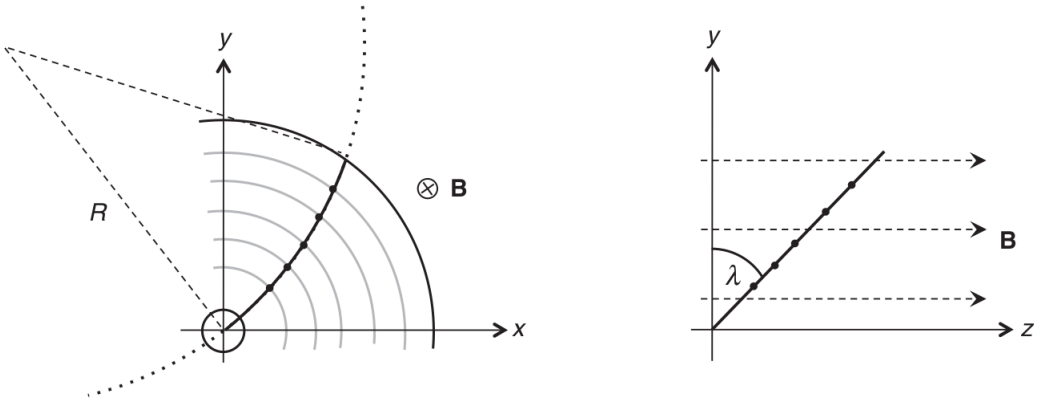



FIGURE 4.5: Principles of tracking reconstruction using a silicon tracking detector. The curvature in the xy-plane determines the transverse momentum.

The range of cover in pseudorapidity ($|\eta| < 2.5$) in addition to the high granularity and the strong bending power offers high precision tracking and excellent momentum resolution.

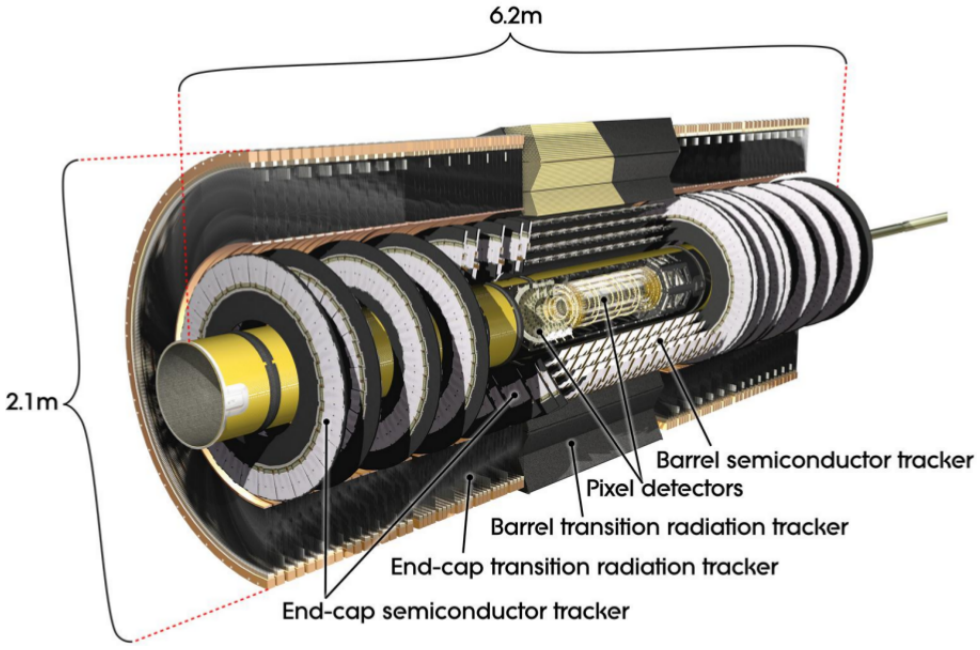



FIGURE 4.6: Layout of the ATLAS Inner Detector [87].

The precision tracking detectors are arranged in a formation of concentric cylinders around the beam axis in the barrel region. In the end-cap regions they appear as disks perpendicular to the direction of the beam axis (Figure 4.5).

The Inner Detector contains three main complementary subdetectors: the silicon Pixel Detector, the SemiConductor Tracker and the Transition Radiation Tracker.

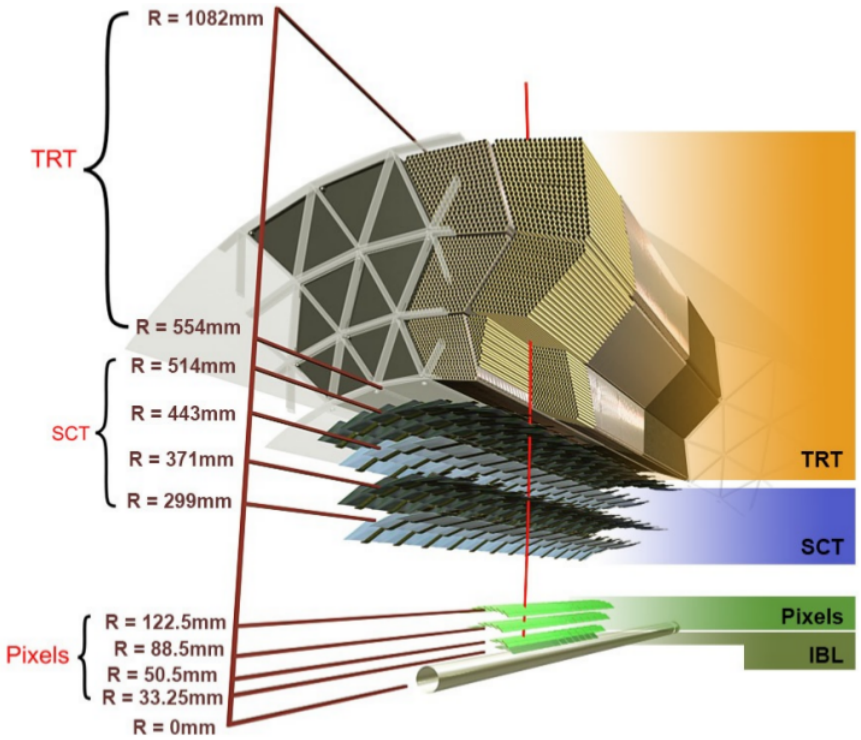



FIGURE 4.7: Overview of the Inner Detector subsystems (barrel region) [88].

#### 4.2.2.1 Pixel detector

The Pixel subdetector [89] is the "heart" of the ID, as it is the closest part to the IP. It consists of four layers, with the innermost layer known as the Insertable B-Layer (IBL) [90] that was placed at a distance of 33.3 mm from the beam pipe for the first time during the shutdown period before Run 2. It has a length of ∼72 cm, covering a region of $|\eta| < 3.0$ and having the highest granularity among the rest of the ID layers (with a pixel size of $\Delta\phi \times \Delta z = 50 \times 250$ $\mu$m). It uses a hybrid combination of planar Si and 3D pixel sensors (more than 12 million), and its close proximity to the IP is useful in the secondary-vertex reconstruction, which is essential to the identification of $B$-hadrons.

The next three barrel layers are located at a distance of 50.5 mm, 88.5 mm and 122.5 mm from the beam pipe, respectively, while there are three disks in the end-cap region located at a distance of 459 mm, 580 mm and 650 mm. The pixel size in these layers is $\Delta\phi \times \Delta z = 50 \times 400$ $\mu$m, achieving an excellent resolution of $14\mu\text{m} \times 115\mu\text{m}$. The Pixel subdetector contains more than 80 million channels in total, covering an area of about 1.7 $\text{m}^2$.

The function of the Pixel subdetector is based on semiconductor technology using silicon pixels and strips. When a charged particle traverses an appropriately doped silicon wafer and ionises it, electron-hole pairs are created, as shown in Figure 4.8. The potential difference is applied across the silicon and the holes will drift in the direction of the electric field, where they can be collected by *p*-*n* junctions. Each time the amount of charge accumulated by the sensors surpasses a threshold a "hit" is registered.

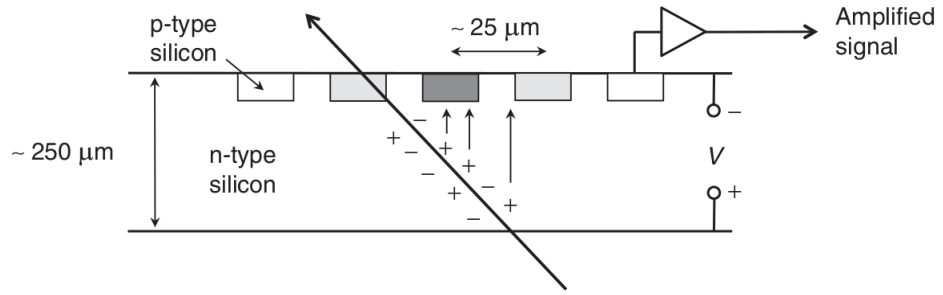



FIGURE 4.8: Illustration of the production of current in a silicon tracking sensor [10].

The sensors are arranged in silicon strips, normally separated by $\mathcal{O}(25\ \mu\text{m})$, or in silicon pixels defining a precise 2D space point. The determination of the exact hit position is done through charge interpolation over adjacent pixels. This provides the required granularity for charged particles trajectories. The produced signals in a typical silicon wafer after the crossing of a charged particle are not small and with the appropriate amplification, the output is a clear signal associated with the strip/pixel on which the charge was collected. The most urgent issue that is associated with the Pixel Detector is the damage due to overheating and radiation. To avoid such incidents the detector is operated at very low temperatures ($\sim$ -5 $^o$C to -10 $^o$C). Due to the radiation damage, the bias voltage applied to the pixel sensors needs to be increased (up to 600 V from an initial value of 150 V in a 10-year period) in order to maintain high charge-collection efficiency.

#### 4.2.2.2 Semiconductor tracker

The complementary detector around the Pixel Detector is called SemiConductor Tracker (SCT). It is also a silicon based detector, which is made of thin layers of silicon "strips" and it is mainly responsible to guarantee excellent track reconstruction. It uses strips instead of pixels providing reliable information regarding

the vertexing reconstruction, taking advantage of its structure. Each track crosses four space points located on the four cylindrical double sensor layers (eight strips) of the SCT. In this way, there is access to the two-dimensional information taken from the grid that is created. The silicon strip detector attains a resolution of 17 $\mu$m in the transverse plane and 580 $\mu$m along the direction of the z-axis. The SCT suffers from the same weaknesses as the pixel and as a result they should operate at the same conditions, since they share the same thermal enclosure.

#### 4.2.2.3 Transition radiation tracker

The outer part of the Inner Detector is called Transition Radiation Tracker (TRT). It is comprised of drift tubes, which are located both in the barrel region and the end-cap regions. In the former the tubes are tangent to each other and parallel to the direction of the beam, while in the latter the tubes are arranged radially on the caps and vertically to the beam axis. The tubes contain a certain mixture of gasses composed of 70% Xe, 27% $CO_2$ and 3% $O_2$. The length of the tubes in the end-cap regions reaches the 37 cm, while in the barrel region the tubes are almost 4 times longer measuring 4 mm in diameter. The angular cover of TRT is restricted to $|\eta| < 2.0$ with a resolution of 130 $\mu$m in the transverse ($R$-$\phi$) plane. Nevertheless, the notably large number of hits (36 hits on average per track) compensates for its low accuracy providing an optimal performance given its low price (compared to the rest of the silicon subsystems). The straw-like structure of the TRT favours the discrimination between electrons and pions since the detection of transition-radiation photons contributes to the electron identification. The TRT is designed to measure the transition radiation, which is produced when a charged particle passes through the straws. The gas inside the straws is ionised and the ions drift to the tube's wall. The electrons are driven to a central wire in the centre of the tube and the generated current is measured. The amount of radiation is higher for lighter particles and in this way electrons are distinguished over heavier hadrons such as pions. In addition, the TRT cross-checks and complements the Electromagnetic calorimeter in an energy window below 25 GeV, while contributing to the reconstruction of track segments from photon conversions.

### 4.2.3 ATLAS calorimeters

The purpose of the calorimeter system is to deliver precise measurements of the particle energies while interrupting their course as they are passing through the detector. The ATLAS calorimeters are located around the ID and they are arranged in a similar formation of two regions: the barrel region and the end-cap one.

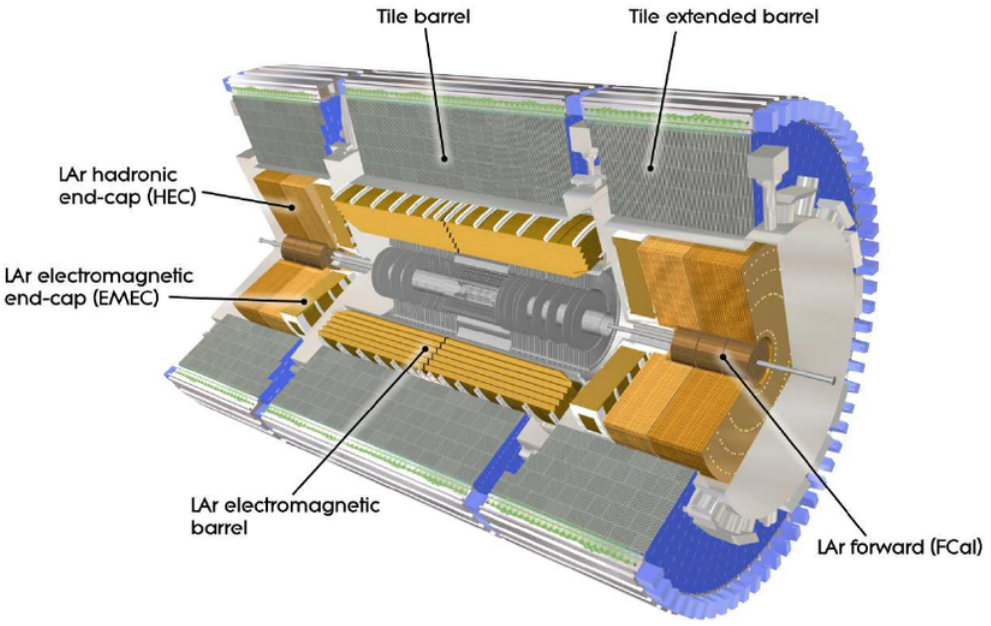



FIGURE 4.9: Inner structure of the ATLAS calorimeters [86].

#### 4.2.3.1 Electromagnetic calorimeter

The Electromagnetic calorimeter (ECal) is designed to stop particles that produce electromagnetic (EM) showers such as electrons, positrons and photons, and to provide information about some of their properties. It has an angular coverage of $|\eta| < 1.475$ in the barrel part and a coverage of $1.375 < |\eta| < 3.2$ in the two end-cap parts. The detection medium of the ECal is Liquid Argon (LAr) while there are also absorbing plates made of lead over its whole range. LAr shows remarkable radiation tolerance and it also provides a good linear response.

The incident particles pass through the lead plates and create EM showers producing secondary particles of lower energies. Therefore, the depth and the material thickness of the EM calorimeter should be carefully considered in order to prevent

shower particles from leaking into the hadronic calorimeter ("punch-through"), which has a poorer resolution. The depth of the shower is given in terms of the critical energy $E_c$ and the radiation length $\mathrm{X}_0$ as

$$X = X_0 \ln\left(\frac{E_0}{E_c} - 2\right). \tag{4.14}$$

The incoming particles interact with the traversing medium lowering their initial energy by a factor of $1/e$ for each radiation length. The material thickness of lead in the calorimeter is $\sim$22 $X_0$ in the barrel part and $\sim$24 $X_0$ in the end-caps. With this depth ECal can accumulate almost all the showers initiated by particles of energies lower than 1 TeV. In fact, lead thickness is optimised as a function of pseudorapidity ($\eta$), thus it takes different values for different values of $\eta$.

The secondary low energy particles that survive from the showers, mostly electrons and positrons, ionise the liquid argon. The electrons after the ionisation are collected on electrodes made of cooper, generating a current that is measured. The energy of the initial particle is proportional to the number of particles ionising the LAr, and so is the measured charge and maximum current. The signal derived from the electron current is amplified, digitised and recorded. Owing to its accordion-like shape the ECal presents excellent azimuthal coverage over the full range of the $\phi$ angle without any gaps or cracks. Over the angular region that it has the same coverage with the ID ($|\eta| < 2.5$), the ECal is divided into three sections or layers according to their purpose. The first layer has the finest granularity ($\Delta\eta \times \Delta\phi$) and it is designed to provide precise $\eta$ measurements determining the flight direction of the particles. Its secondary role is to distinguish photons from neutral pions that decay predominantly into two photons. The second layer focuses on the absorption of the radiation from EM showers, which justifies its larger depth compared to the other layers. The third layer attempts in principle to differentiate EM from hadronic objects by measuring the remaining energy of the incident particles. The granularity in the second and third layer, as well as the granularity in the end-caps is coarser complied with the purpose of each part. The energy resolution of the ECal is

$$\frac{\sigma(E)}{E} = \frac{10\%}{\sqrt{E}} \oplus \frac{17\%}{E} \oplus 0.7\%. \tag{4.15}$$

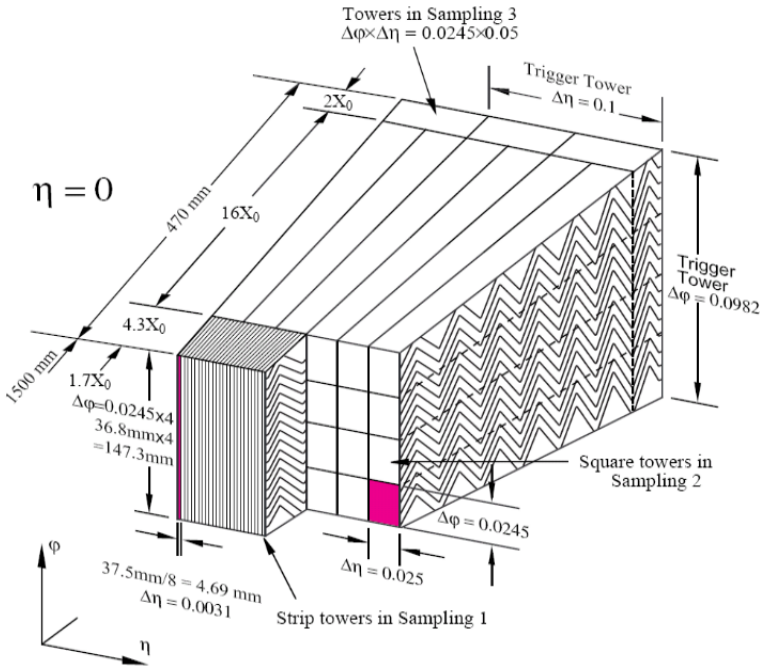



FIGURE 4.10: Detailed overview of the ECal showing its accordion-like design and the granularity for each part [86].

#### 4.2.3.2 Hadronic calorimeters

Unlike electrons and photons, hadrons traverse the ECal with no severe energy losses. The placement of the EM calorimeters prior to hadronic calorimeters is therefore justified since, in principle, hadronic showers penetrate deeper than EM showers. The Hadronic calorimeter (HCal) has an inner (outer) radius of 2.28 m (4.25 m) and it is segmented in different compartments: the Tile calorimeter, the Hadronic End-Cap calorimeter and the Forward calorimeter. Its leading objectives are jet reconstruction, energy measurements, and particle identification and determination of missing transverse energy ($E_{\mathrm{T}}^{\mathrm{miss}}$). The energy resolution of the HCal is

$$\frac{\sigma(E)}{E} = \frac{50\%}{\sqrt{E}} \oplus \frac{1\%}{E} \oplus 3\%. \tag{4.16}$$

Similarly to the electromagnetic showers, the hadrons that traverse the HCal form cascades of particles such as pions or neutrons. The nuclear interaction length $\lambda_I$ is used to parametrise the size of the cascade, and it represents the average distance travelled by a hadron before interacting with a nucleus. The HCal thickness at $|\eta| = 0$ is $9.7\lambda_I$, in order to capture all the hadronic showers, since $\lambda_I >> X_0$.

### Tile calorimeter (TileCal)

The hadronic calorimeter that surrounds the ECal is called Tile calorimeter. It is segmented in two parts: the first one can be thought of as an extension to the ECal in the barrel region with a coverage of $|\eta| < 1.0$ and the second one is located around the end-cap wheels to provide additional coverage of $0.8 < |\eta| < 1.7$. The development of the TileCal was based on scintillating tiles panelling absorbing steel plates. As the shower develops through the tiles, scintillation light is produced. The two sides of the scintillators communicate with fibres that collect and shift the wavelength of the light (from blue to green), and finally transport the signal to photomultipliers.

### LAr hadronic end-cap calorimeter (HEC)

The hadronic end-cap calorimeter resembles the ECal in the end-cap region, with the difference that it utilises parallel cooper plates as absorbers instead of lead. LAr is again the active material and flows between the two wheels from which the HEC is comprised. It covers the angular region of $1.5 < |\eta| < 3.2$ and it shares the same cryostat as the ECal in the end-caps. For an optimal performance, the HEC overlaps with the TileCal in the region $1.5 < |\eta| < 1.7$ and with the FCal in the range $3.1 < |\eta| < 3.2$. The front and back wheels are made up of copper plates that differ in number and thickness and LAr fills the gaps (8.5 mm) between the plates.

### LAr forward calorimeter (FCal)

The purpose of the forward calorimeter is to tackle the high particle flux and large energy densities in the forward region. Its coverage is restricted to the range of $3.1 < |\eta| < 4.9$ and its two hadronic components can be visualised as a follow-up to the forward part of the ECal. The existence of the two hadronic parts is crucial since the majority of the incident particles that reach the FCal are hadrons. The active material is liquid argon and the absorber plates are made of cooper for the EM part, while for the two subsequent hadronic parts the absorbers are made of tungsten. The plates are vertical to the beam direction and are held together by regularly spaced rods in a matrix formation. The gaps between the rods are filled

with LAr and the ionisation signal is measured from the rods. Overall, the depth of the FCal reaches about $10\lambda_I$ and the FCal itself still suffers from pileup issues, which are expected to be amplified in future runs.

### 4.2.4 Muon spectrometer

The outermost system of the ATLAS detector is called Muon Spectrometer (MS) [86]. It is comprised of several subsystems in order to achieve optimal coverage and performance, while each subsystem is charged with a specific task. The outlying location of the MS is aptly justified since muons are highly penetrating particles and they traverse the calorimeters without being interrupted. It is designed to measure the momentum of muons and identify their charge in the region of $|\eta| < 2.7$ and it has also triggering capabilities in the region of $|\eta| < 2.4$. The MS is imposed with the requirement of precisely determining the muon kinematics up to the TeV scale achieving a resolution of 10% at 1 TeV. The momentum measurements in the GeV scale are considered more reliable with an average resolution of 3% at approximately 200 GeV. The MS performs standalone transverse momentum measurements owing to its separate toroidal magnetic field, combining the results with the track information that utilises from the ID. In principle, the determination of the momentum is based on Equation 4.13, where $R$ is the radius of the sagitta formed by the curvature of the muon's trajectory due to the presence of the magnetic field $B$.

The subsystems of the MS (shown in Figure 4.11), and the performed tasks are briefly described below:

**Monitored drift tubes (MDTs)**: Chambers located both in the barrel and the end-cap regions. Typically, there are three to four layers of aluminium tubes filled with a gas mixture of Ar (93%) and $CO_2$ (7%). By the time a muon traverses the tubes a trail of electrons is created and drifted to a wire (anode). This constitutes the primary signal, which is then amplified and digitalised. The MDTs are responsible for muon tracking, while each chamber contains innovative sensors that monitor the temperature and the local magnetic field. The angular coverage of these chambers is extended up to $|\eta| < 2.7$.

**Cathode strip chambers (CSCs)**: Respecting the principles of energy and momentum conservation the muon flux is also expected to be larger in the kinematic

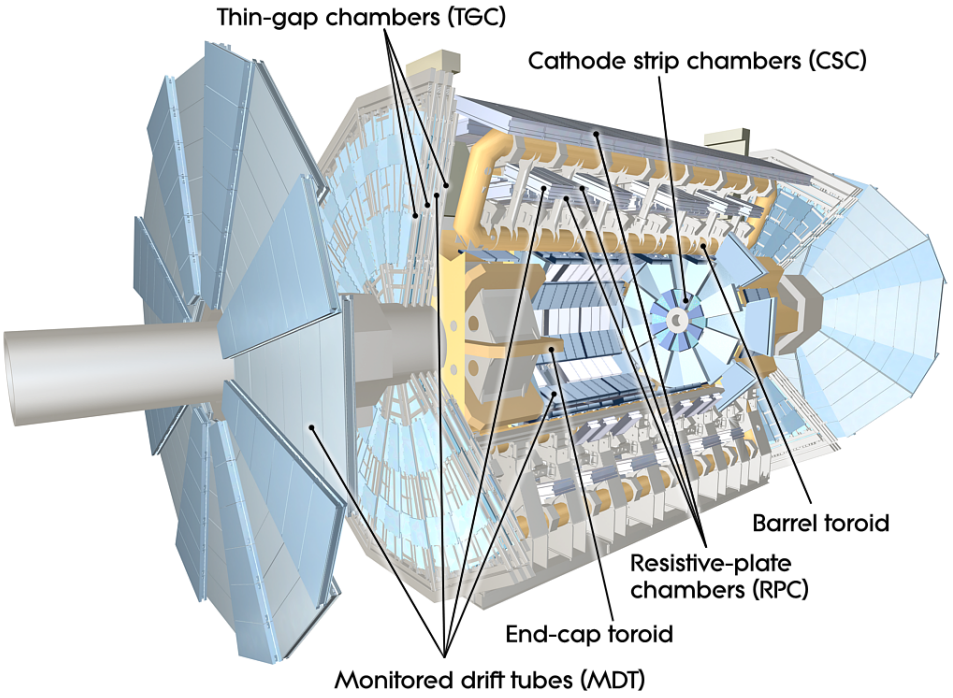



FIGURE 4.11: Cut-away 3D layout of the ATLAS Muon Spectrometer with its subsystems labelled. Figure taken from Ref. [86].

region of $2.0 < |\eta| < 2.7$. In this forward region the CSCs replaced the MTDs due to their efficient handling of large fluxes, achieving satisfactory spatial and time resolutions. CSCs are chambers made of almost orthogonal strips and filled with a combination of Ar (80%) and $CO_2$ (20%). The CSCs are designed for muon tracking and their operation is similar to the MTDs. One main advantage of these chambers is that they combine four layers of anode/cathode wires, thus providing a four-point precision and four measurements of the $\phi$ coordinate per track. This feature is missing from the MTDs, which cannot provide information about the second coordinate.

**Resistive plate chambers (RPCs)**: Resistive plate chambers are designed in the barrel region to provide complementary measurements of the second coordinate $\phi$ while being engaged in the triggering procedure. RPCs are plate detectors placed in a parallel direction to the beam axis in altering distances. The 2 mm gap created by insulating spacers between the electrodes is filled with $C_2H_2F_4$ (gas), which is ionised. The strips on the two sides of the gap are perpendicular, providing information for $\eta$ and $\phi$ coordinates with a coverage of $|\eta| < 1.05$. The spatial resolution of RPCs is $\sim$10 mm for both coordinates and the timing resolution does not surpass the threshold of 1.5 ns, allowing for precise bunch

crossing identification.

**Thin gap chambers (TGCs)**: TGCs are introduced as another solution for triggering and determination of the $\phi$ coordinate. The coverage in terms of pseudorapidity is $1.05 < |\eta| < 2.7$ (for triggering it is $1.05 < |\eta| < 2.4$) and they are placed radially on the end-caps to account for the large muon flux there. The chambers are filled with a combination of n-$C_5H_{12}$ and $CO_2$ and provide reasonable time resolution for most of the tracks, which is 4 ns on average.

### 4.2.5 Trigger system and data acquisition

The trigger and data acquisition system (TDAQ) in ATLAS is designed to perform a primary event selection on-the-fly and its development is itself a challenging task. The system is responsible for recording interesting events at a frequency of approximately 1 kHz, while the nominal bunch crossing rate is estimated to a frequency of 40 MHz. The TDAQ combined efficiency is given by the complementary operation of a **Level-1 (L1) trigger** that is implemented at hardware level, and a software-based **High-Level trigger (HLT)** [91], as shown in Figure 4.12.

The L1 is the first trigger level and it accepts or rejects an event based on the information retrieved by the trigger systems that are present in the different subdetectors. The information from the L1 calorimeter (L1Calo), L1 muon (L1Muon), and L1 topological (L1Topo) triggers reaches the Central Trigger Processor (CTP), and a decision is made about the event in less than 2.5 $\mu$s. Other trigger systems such as the Minimum Bias Trigger Scintillators (MBTS) in the TileCal, the LUCID2 Cherenkov counter, and the ZDC (Zero-Degree calorimeter), contribute in this process as well. Moreover, the ALFA (Absolute Luminosity For ATLAS) and AFP (ATLAS Forward Proton) subdetectors offer additional possible L1 trigger sources. Readout and overflow issues are suppressed by the CTP, which controls the total number of accepted events in a certain period of time, introducing some "dead-time" between them. At this level the trigger focuses on high-$p_{\mathrm{T}}$ particles and jets, as well as missing transverse energy. The L1 trigger also sets the Regions of Interest (RoIs), which are defined based on the objects that drove the trigger selection.

The RoIs defined in the L1 trigger are passed to the HLT, where a further data filtering is performed based on a fast object reconstruction. The HLT can perform

more computationally intensive tasks than the L1, and uses different trigger menus to identify which events will be saved for the full offline reconstruction. Therefore, the rate of the events saved is reduced significantly from 100 kHz to 1 kHz, ensuring the optimal use of the available disk space.

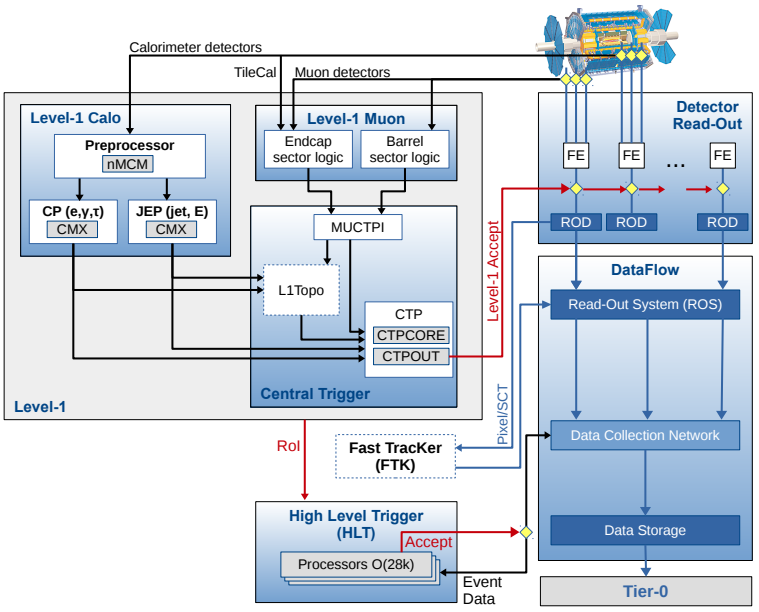



FIGURE 4.12: Schematic overview of the ATLAS TDAQ system used in Run 2 summarising the flowchart of data in the L1 and HLT trigger systems. Figure taken from Ref. [91].

### 4.2.6 Data quality

Following the local storage of the events that pass the trigger selection, a series of offline checks has been designed to ensure their good quality. The saved data are scrutinised for potential hardware or software related problems that may render them unusable for physics analyses. Some of these checks are performed during the data taking, where the fast identification of the issues can ensure quick response from the experts, preventing further data corruption. The online data quality (DQ) checks are based on the monitoring of detector-level quantities and of the characteristics of reconstructed collision events.

Apart from the online DQ checks, an offline DQ system performs checks on the fully reconstructed events, validating the corresponding histograms. DQ flags are

being assigned to each event based on these checks, which can be used by each physics analysis. In the full Run-2 dataset around 94% of the recorded events is suitable for physics analysis, representing the fraction of events with good quality.

### 4.2.7 Luminosity measurement

In order to determine the cross section of an observed physics process a precise measurement of the beam luminosity is essential. For this purpose there are two dedicated subdetectors, LUCID2 (LUminosity measurement using Cherenkov Integrating Detector 2) and BCM (Beam Conditions Monitor) that can check the beam luminosity bunch-by-bunch during the physics data collection [92].

LUCID2 is a Cherenkov detector located at both sides of the ATLAS detector (side A and side C) at a distance of $z = \pm 17$ m from the IP. There are 16 photomultiplier tubes (PMTs) in the forward region of each side inducing the production of Cherenkov light. Dedicated luminosity algorithms are used in order to convert the raw PMT signal to a luminosity measurement. The raw hit counts of the PMTs are converted to a visible interaction rate per bunch crossing ($\mu_{vis}$), which is used for to determine the luminosity values through the formula

$$\mathcal{L}_b = \frac{\mu_{vis} f}{\sigma_{vis}}, \tag{4.17}$$

where $\sigma_{vis}$ is the cross section of a visible interaction and represents the absolute luminosity calibration constant, $f$ is the revolution frequency and $\mathcal{L}_b$ is the sum of luminosity over all colliding bunches.

In BCM the read-out is based on two diamond sensors that are placed symmetrically at each side of the ATLAS detector at a distance of $z = \pm 1.84$ m corresponding to $\eta = 4.2$ [93]. BCM provides a complementary luminosity measurement to LUCID2, while at the same time it monitors the stability of the LHC beam to detect incidents that could cause detector damage.

Apart from the two luminometers above, the ALFA subdetector is used in order to provide secondary luminosity measurements. The ALFA subdetector is located at a distance of $z = \pm 240$ m from the IP and it contains scintillating fibre trackers, which are used to measure the *pp* collision total cross section. In more detail, ALFA measures the elastic scattering rate at small forward angles (3 $\mu$rad) in

special runs where the beam divergence is low [94]. The elastic scattering rate is connected to the total cross section ($\sigma_{tot}$) though the optical theorem

$$\frac{dN}{dt} = \pi \mathcal{L} |A_C + A_N|^2 \approx \pi \mathcal{L} \left| -\frac{2\alpha}{|t|} + \frac{\sigma_{tot}}{4\pi} (i + \rho) e^{\frac{-b|t|}{2}} \right|^2 , \tag{4.18}$$

where $A_C$ stands for the Coulomb interaction amplitude, $A_N$ stands for the strong interaction amplitude and $\alpha$ stands for the electromagnetic coupling constant. Equation 4.18 is fitted with four free parameters that are determined from the fit. These parameters are the luminosity ($\mathcal{L}$), the total cross section ($\sigma_{tot}$), the $\rho$ parameter and the slope parameter $b$.

Complementary to these measurements there is a network of 16 Medipix-2 (MPX) silicon pixel devices designed to measure the properties of the radiation field in the ATLAS detector [95]. The MPX subdetectors are placed very close to the IP and they are in charge of performing van der Meer (vdM) high precision calibration scans. The vdM method [96] is based on a beam displacement technique, where one of the two beams is displaced independently in the vertical and the horizontal directions and the counting rate is expressed with respect to the displacement. The calibration is performed during specific luminosity scans, where the luminosity $\mathcal{L}$ is given after the displacement by the formula

$$\mathcal{L} = f N_1 N_2 \int \int \rho_1(x_2 + \Delta x, y_2 + \Delta y)\, \rho_2(x_2, y_2)\, dx_2\, dy_2, \tag{4.19}$$

where the subscripts 1, 2 refer to the displaced and stationary beam, respectively, and $\Delta x, \Delta y$ are the horizontal and vertical displacement of the beam.

The ATLAS calorimeters (TileCal, LAr, etc.) are also able to provide luminosity measurements that are not calibrated during vdM scans. TileCal luminosity measurement is instead equalised to LUCID2 or the track measurement in a specific run, determining the calibration constant, while in the LAr luminosity measurement the calibration procedure depends on the high-voltage setting.

# Chapter 5

# Electron studies on the ATLAS Tile calorimeter towards the Phase-II upgrade

This chapter provides a more detailed description of the ATLAS Tile calorimeter (TileCal) layout and discusses the main plan for the TileCal-related developments towards the Phase-II upgrade. Part of this plan is the validation of new electronics that will be used in the upgrade through dedicated test beams conducted for that purpose. The test-beam setup is described in detail in Section 5.2. The data from test beams performed in 2018 and 2021 are being analysed in the context of this thesis. The main focus lies on the analysis of electron runs for the precise measurement of the electron response. Electron showers are often created inside the hadronic ones when pions interact with the TileCal detector material. The measurement of the electron response with the new electronics will verify if the performance is as expected, while at the same time it will validate that the electromagnetic (EM) scale has been set correctly during the cesium calibration. Since hadrons are also being produced during electron runs and contaminate the electron beam, a dedicated method has been designed to separate electrons from hadrons using a topological analysis. The electron purity of the beam is calculated each time and a model of systematic uncertainties has been developed to strengthen the validity of the separation method. Other parameters of interest are also studied such as the modulations of energy in the electron signal (verifying that these are indeed electrons), the beam impact parameters, the timing, the pulse shapes and the energy deposits in the Cherenkov counters.

## 5.1 ATLAS Tile calorimeter layout and the Phase-II upgrade

The Tile calorimeter (TileCal) is one of the main ATLAS hadronic calorimeters and its layout is shown in Figure 5.3. The TileCal is designed to measure the energy of the jets running into it capturing effectively about 30% of their total energy. As secondary objectives TileCal provides useful information about jet substructure, transverse missing energy, electron isolation (in the hadronic showers), and triggering (by also exploiting muon-related information). It is segmented in four compartments, LBA and LBC in the long barrel (LB) region, and EBA and EBC in the extended barrel (EB) region with a radius $2.28 \leq r \leq 4.23$ m and lengths of 2.82 m and 2.91 m, respectively, reaching up to 1.6 in rapidity coverage.

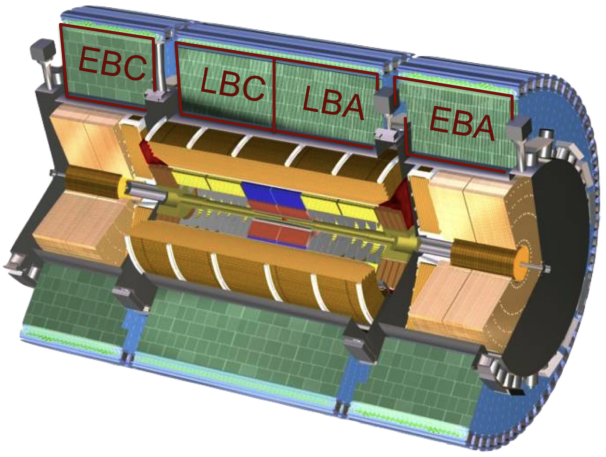



FIGURE 5.1: Side-view of the ATLAS Tile calorimeter [97]. The four read-out partitions EBC, LBC, LBA and EBA are shown in green.

Each barrel compartment contains 64 modules vertical to the beam pipe maintaining a $2\pi$ coverage in azimuthal angle. The modules are made of a succession of a 3 mm thick scintillator plate followed-up by a 14 mm thick steel plate in a 18 mm period (glue estimated to be about 1 mm), as shown in Figure 5.2. Each of these modules is segmented radially in three layers (A-, BC- and D-layer) with interaction lengths of 1.4, 3.9 and 1.8 at $\eta = 0$, respectively, and a granularity of $\Delta\eta \times \Delta\phi = 0.1 \times 0.1$ [98], as shown in Figure 5.3. The A-layer is closer to the interaction point and it contains 15 cells (A1-A10 in the LB modules, A12-A16

in the EB modules), the BC-layer is the next layer consisted of 14 cells (BC1-BC8 and B9 in the LB modules, B11-B15 in the EB modules) and the D-layer is the outer layer containing 7 cells (D0-D3 in the LB modules, D4-D6 in the EB modules). Each cell is read out by two photomultiplier tubes (PMTs), where the signal generated by the scintillators arrives, after a wavelength shift initiated by dedicated wavelength-shifting (WLS) fibres attached on each side of the PMTs. The A-, BC-, D-grouping corresponds to a trigger tower providing fast trigger.

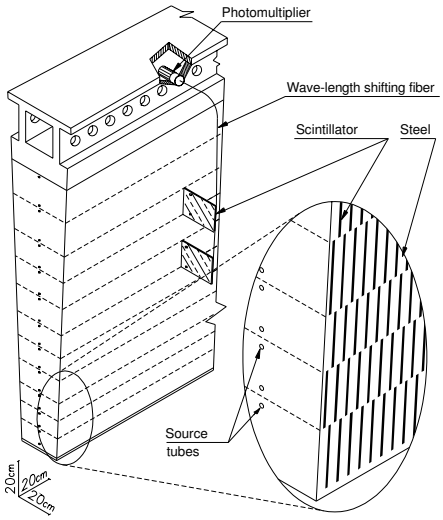



FIGURE 5.2: Tile calorimeter module inner structure [99] focusing on the pattern of scintillator and steel plates. The light signal is collected by the WLS fibres and transferred to the PMTs.

Between the LB and EB regions there are additional cells (E1-E4 known as E-cells and C10), which together with the MBTS that are placed below them are designed to provide electron identification and to monitor the luminosity values during luminosity scans [98]. The MBTS are also used to determine the minimum-bias event rates and E3 and E4 cells to contribute to the determination of the energy that is missed by the electromagnetic calorimeter, restoring the lost resolution for converted electrons and photons in the $1.2 < y < 1.6$ region.

TileCal is also equipped with a reliable front-end and back-end electronics system performing different actions. The front-end electronics part is designed to sum the signal from the PMTs, digitise it and integrate the continuous produced current to determine the event rates for calibration purposes. The data gathered is transferred to the back-end electronics system after serialisation.

In order to ensure high-precision physics measurements a calibration system is put in place providing calibrations from three different systems. One of the calibration

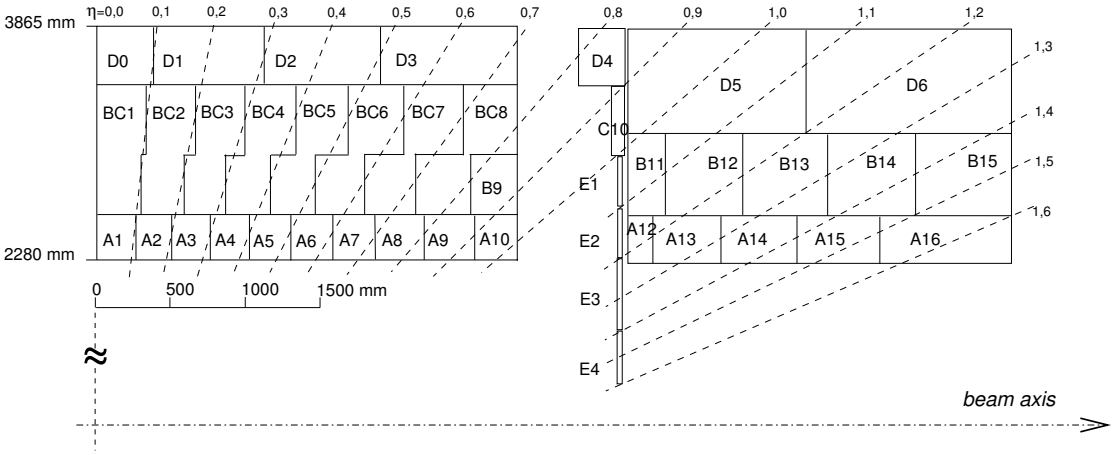



FIGURE 5.3: ATLAS Tile calorimeter cells for long and extended barrel regions in one of the detector's side (side A) [98]. The pseudorapidity values corresponding to a particle's track are shown in dash lines providing information on the cells where the energy was deposited.

constants is taken from the Charge Injection System (CIS), where charge is injected into the front-end electronics to determine the conversion factor from ADC counts to pC, a second calibration constant is taken from the Laser System using pulses and checking the PMT response, and another calibration constant is acquired by the Cesium System, where a $^{137}$Cs source passes through all the calorimeter scintillators through a tube. All these calibration constants are being used together for the offline conversion of the signal from ADC raw counts to MeV.

## Phase-II upgrade

The general plan for the ATLAS Phase-II upgrade involves a strategy to prepare the detector to handle the demanding operation conditions of High-Luminosity-LHC (HL-LHC). The delivered integrated luminosity of the HL-LHC is estimated to be ten times higher than the luminosity of Run 1 to 3 combined (3000-4000 fb$^{-1}$), as shown in Figure 5.4. This means that the average interactions per bunch crossing $<\mu>$ are expected to be around 200 requiring a peak instantaneous luminosity of about 7.5 times higher than the LHC design value. The upgrade towards HL-LHC brings forth some challenges that need to be overcome such as the proper redesign of the trigger and data acquisition systems to be able to cope with the very large trigger rates and the increased pileup. As a great compensation for these technical challenges the increased statistics are expected to offer the opportunity for numerous physics searches and measurements. The Higgs

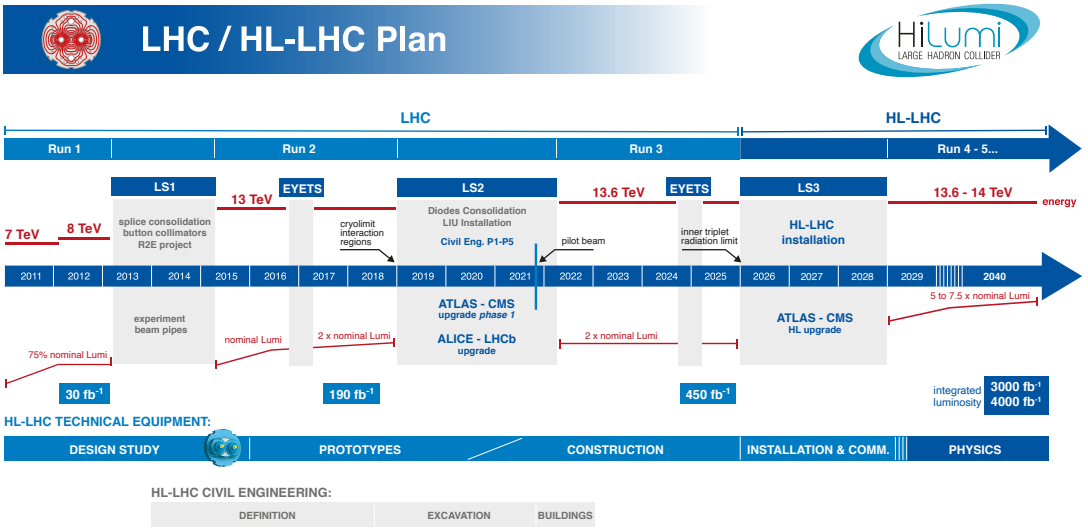



FIGURE 5.4: Timeline of the Phase-II upgrade towards the HL-LHC run [100].

boson properties will be calculated at a higher precision through the precision measurements of the Higgs couplings to fermions and vector bosons to the percent level [101]. The HL-LHC era is foreseen to provide further knowledge on the measurements of the $W$ boson and top-quark masses that constitute a central requirement for the validity and understanding of the SM, although facing the challenge of the large pileup. The increased luminosity might also open the window to low cross-section processes such as di-Higgs production, providing access to the trilinear Higgs coupling. In addition to that, the upgrade will certainly lead to a richer physics program related to searches beyond the SM, since rare physics processes will have increased discovery potential.

The Phase-II upgrade of the ATLAS detector comprises seven core projects. The most demanding one is related to the replacement of the current ID by the Inner Tracker (ITk), a fully silicon tracker extended in the forward region to profit from the physics reach of the HL-LHC. The rest of the projects are focused on the installation of a High-Granularity Timing Detector (HGTD), providing precise timing and tracking information, or in the upgrade of the muon, trigger and data acquisition systems. An ambitious program is also in the pipeline concerning the upgrade of LAr and the scintillating-tile calorimeters.

The TileCal Phase-II upgrade involves a replacement of the calorimeter on- and off-detector electronics to an improved version. The large super-drawer (SD) including

many mini-drawers, as shown in Figure 5.5, will be superseded by four independent mini-drawers, as shown in Figure 5.6, each one connected to its own high-voltage and monitoring system.

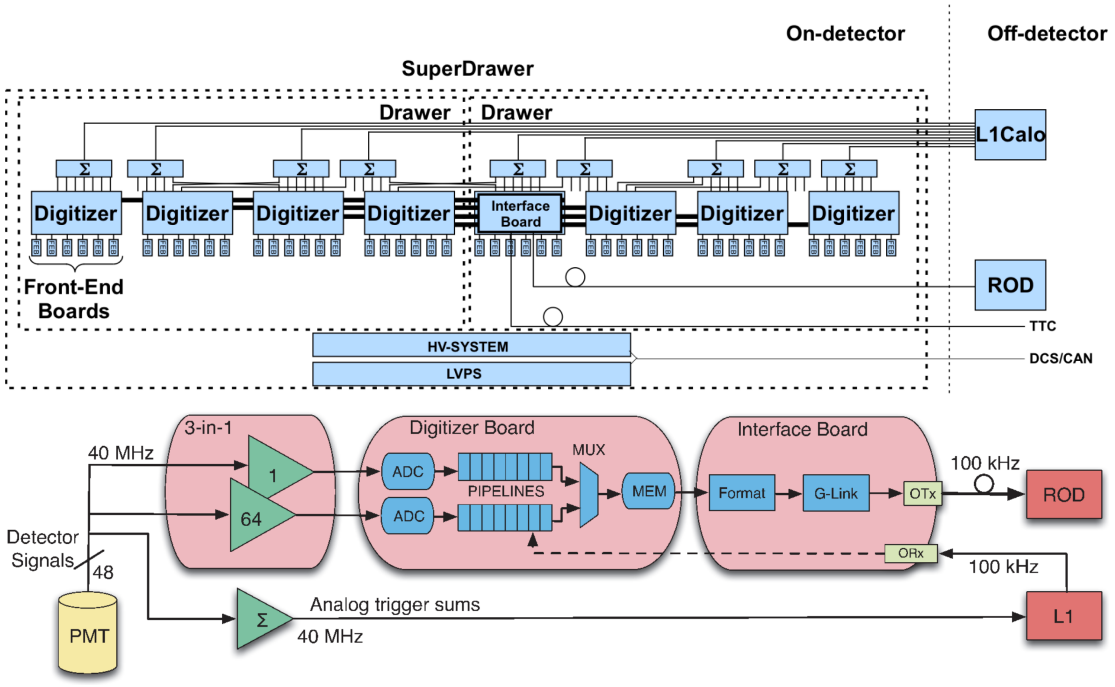



FIGURE 5.5: Illustrative sketch of the current electronics configuration used in Run 2 [98].

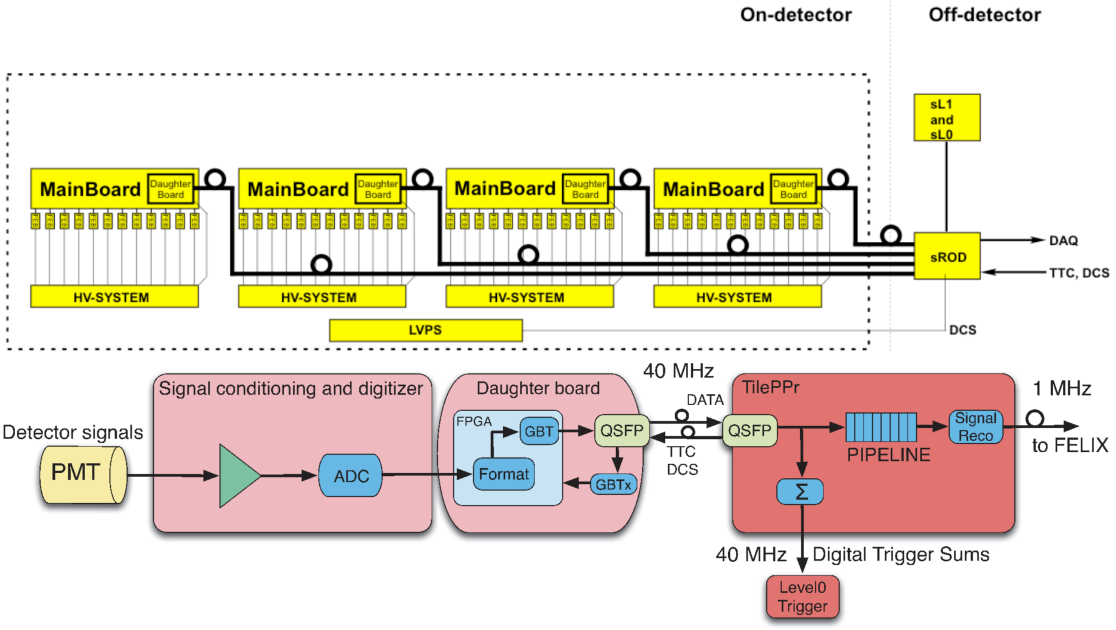



FIGURE 5.6: Illustrative sketch of the new electronics configuration that is planned for Phase-II upgrade [98].

This change is expected to reduce power distribution failures observed already in Run 1 related to the HV or the Low Voltage Power Supply (LVPS) systems. The PMT signal will reach the off-detector electronics after digitisation from the on-detector electronics. Off-detector electronics will reconstruct the digitised signal, store it and then redirect it to the Level-0 (L0) trigger with a 40 MHz rate. This roadmap is depicted in the bottom sketch of Figure 5.6. The trigger rate will be significantly increased from its former value (100 kHz), as shown in the bottom sketch of Figure 5.5, offering the possibility for the use of more sophisticated trigger algorithms.

## 5.2 TileCal test-beam setup

The updated Tile electronics designed to replace the current ones prior to the HL-LHC run should improve the quality of data collected, while maintaining a proper functionality. TileCal should be able to provide a linear response of the jet energy measurements up to several TeV. It should be also able to identify single muons depositing at least an energy of 0.4 GeV in its central cells, and provide a linear electron response, which is critical for the validation of the calibration process and the setting of the EM scale. The HV and the LVPS systems need to be tested to ensure voltage stability, and the pre-processor to ensure proper handling of the high-speed communication with the front-end electronics.

In order to test the above features dedicated test beams are organised that are accommodated in the H8 beam line in the North area of Prevessin (France) at CERN. The Super Proton Synchrotron (SPS) supplies the beam line with secondary proton beams of an energy around 400 GeV that are colliding into a primary beryllium target (T4) that is 100 mm thick. These beams are guided into secondary targets at a distance of 130 m from the T4 target, providing the beams that are incident to the scanning table. The beams are mainly composed of hadrons (pions or protons), while electrons, muons and kaons are also present. The momentum and charge of the beam particles are determined by bending dipole magnets. The energy of the beam particles ranges from 10 to 350 GeV, with the beam intensity dropping rapidly at low energies. The second target varies depending on the desired composition of the tertiary beams. For a hadron-enriched beam a 300 mm thick secondary target is used made of copper and a 6 mm thick lead absorber is being used at a later point to suppress the electrons. For an electron-enriched

beam a 400 mm thick secondary target is used made of aluminium with the same lead absorber stacked immediately after it.

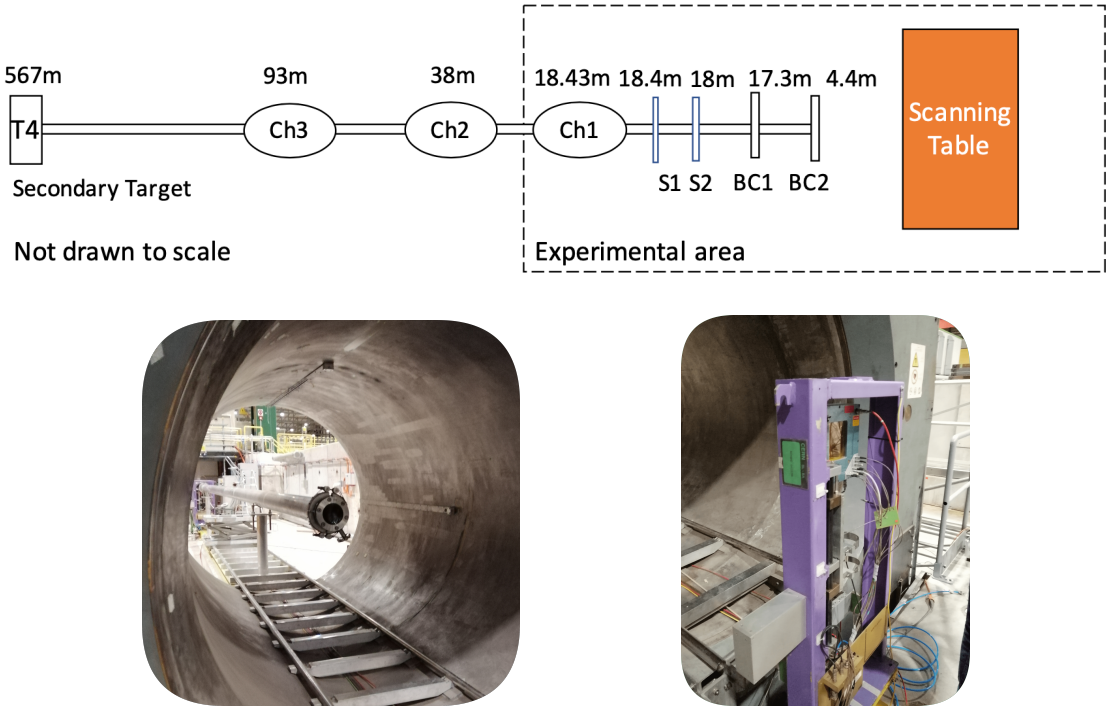



FIGURE 5.7: Beam-line setup used in Tile calorimeter test beams [98]. The beam pipe and the second beam chamber (BC2) are shown at the bottom left and bottom right pictures, respectively.

An illustrative representation of the beam-line setup is shown in Figure 5.7 (not drawn to scale). Three Cherenkov counters (Ch1, Ch2, Ch3) are placed after the secondary target allowing the identification of beam particles. Ch1 and Ch3 are particularly useful in distinguishing between electrons and hadrons, while Ch2 can be used to distinguish between kaons and protons. In the current test beams Ch1 and Ch2 were filled with carbon dioxide and Ch3 was filled with helium. The pressure of the Cherenkov counter impacts the particle separation and there are several values tested during their tuning. Two scintillating counters (S1, S2) of a $5 \times 5$ cm$^2$ active surface each are used in coincidence to fire the trigger and provide information about the trigger timing. Two wire chambers (BC1, BC2) are used to monitor the transverse beam profile.

After traversing through the beam-line elements the beam is incident on the scanning table, where spare TileCal modules are being placed for testing. There are three modules present in the setup, two from the long barrel (LBA 65, LBC 65) and one from the extended barrel (EBC 65). Two super-drawers (M0 A, M0 C) are being placed below the LBA 65 and LBC 65 modules, respectively, where M0

A is usually equipped with multi-anode photomultiplier tubes (MAPMTs). The modules are stacked together as shown in Figure 5.8. The scanning table is able to move vertically to the beam pipe and also rotate in order to achieve the desired hitting angles of the incident beam. The most common incident angle during test beams is $\theta_{\text{inc}} = \pm 20^o$, while particularly useful are the muon scans at $\theta_{\text{inc}} = 0^o$.

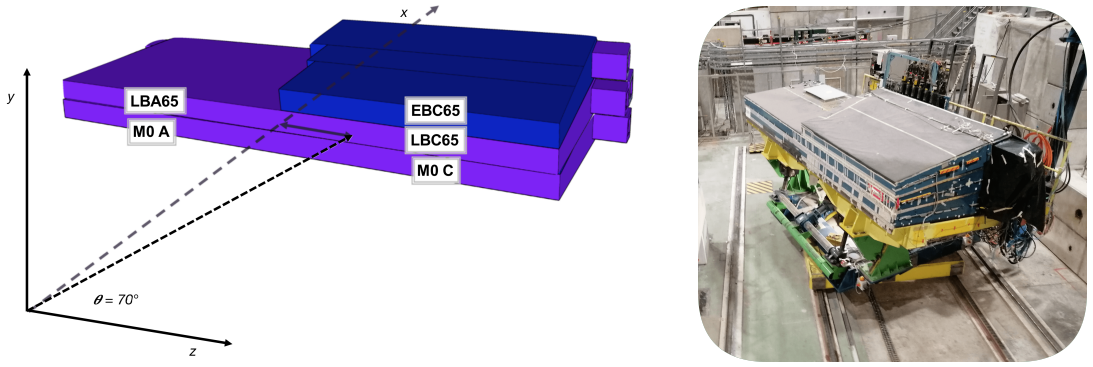
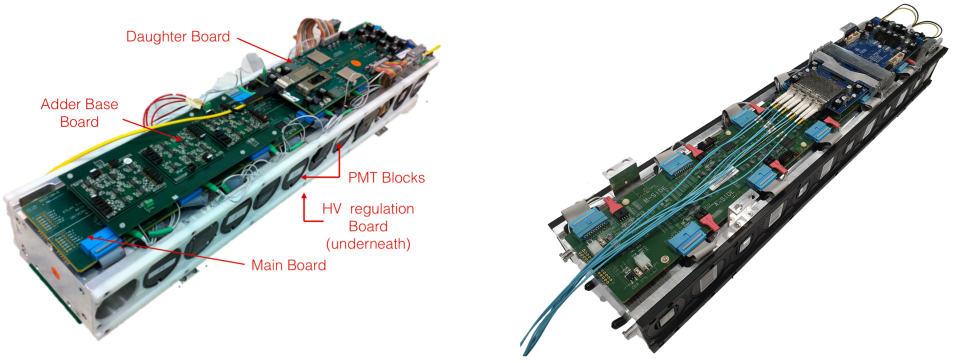



FIGURE 5.8: Configuration setup of test-beam modules (left) and view of the table at an incident angle of $\theta_{\text{inc}} = 20^o$ from the x-axis (right).

The configuration of the electronics tested in each module is not constant in every test-beam (TB) period, depending on the Phase-II upgrade plan. During the years 2015-2018 a hybrid demonstrator had been tested at the H8 SPS secondary beam tests (shown in Figure 5.9a) usually inserted inside the LBC 65 or EBC 65 modules.




(a) (b)

FIGURE 5.9: (a) Test-beam demonstrator prototype [98]. (b) Fully assembled mini-drawer after the version-6 daughterboard upgrade [102].

The demonstrator ensured backward compatibility between the new 3-in-1 [98] and the standard legacy SD systems [98], and was inserted in the ATLAS detector in 2019 [103]. In 2018 a configuration of an extended demonstrator was tested in

the EBC 65 module, where the four mini-drawers were replaced by three mini-drawers and two micro-drawers, as shown in Figure 5.10. In 2021 the version-4 daughterboard of the demonstrator was replaced by the version-6, significantly simplifying the setup as it can be placed directly on top of the mainboard without the intervention of the adder base board, as shown in Figure 5.9b.

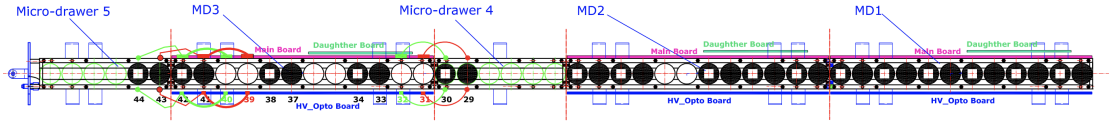



FIGURE 5.10: Configuration of mini- and micro-drawers inserted in the EBC 65 module for the 2018 test beam [104].

The signal from the daughterboard is transferred to the pre-processor, which stores the PMT data of the entire SD in pipelines until it receives a trigger decision from the trigger tower. When this happens the corresponding data get directed to the legacy read out driver (ROD). The data are then stored in raw binary files that are later reconstructed to ntuples, one for each run. The total energy deposited in a cell for each event of the run corresponds to the sum of the signal from the two PMTs that are matched to this cell.

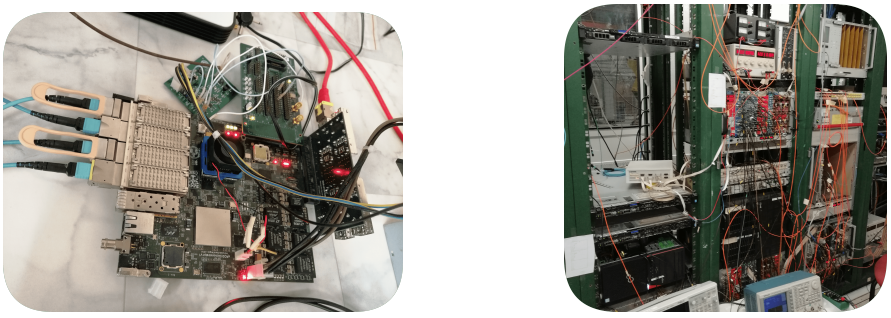


FIGURE 5.11: Off-detector electronics of the Tile test beam. The pre-processor (left) and the trigger rack (right) are shown.

## 5.3 Electron identification

Part of the work conducted in this dissertation is related to the analysis of electron data acquired during the test beam periods of 2018 and 2021. The electrons originating from the primary vertex of the event (prompt) are stopped in the electromagnetic calorimeter. Thus, the electrons appearing in the hadronic calorimeter

originate in principle from a secondary vertex (non-prompt). Electron showers are often created inside the hadronic ones as a result of pair production from photons originating from neutral pion ($\pi^0$) decays. The precise measurement of the electron response will validate if the new electronics are functioning properly, while it will be useful in the validation of the Tile calibrations through the setting of the electromagnetic scale.

The process of distinguishing between electrons and hadrons in electron runs is a challenging task, since both particle types have very similar beam profiles in the transverse plane. The electron separation at low energies up to 20 GeV can be achieved with the use of the Cherenkov counters Ch1 and Ch3. At higher energies the extraction of electron signal is achieved using a topological analysis. In principle, the hadron signal peaks at around 70% of the electron signal peak. Since a selection solely based on the energy of the particle would bias the electron response distribution, two topological variables are defined in the $C$-space known as $C_{\text{tot}}$ and $C_{\text{long}}$ [99]. These shower profile variables exploit the separation in the energy of the particles trying to reduce the correlation to the response variable.

The $C_{\text{tot}}$ variable is defined as

$$C_{\text{tot}} = \frac{1}{\sum_c (E_c^{\text{raw}})^\alpha} \sqrt{\frac{1}{N_{\text{cell}}} \sum_c \left[ (E_c^{\text{raw}})^\alpha - \frac{\sum_c (E_c^{\text{raw}})^\alpha}{N_{\text{cell}}} \right]^2}, \tag{5.1}$$

where $E_c^{\text{raw}}$ stands for the energy deposited in a cell c and the $\alpha$-exponent is a parameter optimised based on the Monte Carlo simulation in order to provide the maximum electron-hadron separation. The optimised value of the $\alpha$-exponent is found to be $\alpha = 0.6$. $N_{\text{cell}} = 9$ stands for the number of cells used in the calculation of the sum, a $3 \times 3$ cell area around the central A-cell where the beam is incident to. Since the D-cells cover a larger area than the rest of the cells there are usually only two of the D-cells close to the central A-cell, so it is effectively $N_{\text{cell}} = 8$ for each module, or $N_{\text{cell}} = 24$ for the three modules considered.

The $C_{\text{long}}$ variable is defined as

$$C_{\text{long}} = \sum_{i=1}^{2} \sum_{j=1}^{3} \frac{E_{ij}^{\text{raw}}}{E_{\text{beam}}}, \tag{5.2}$$

where $E_{\text{beam}}$ stands for the beam energy. The index $i$ represents the layers of the module and the index $j$ the number of cells in each layer close to the central cell.

$E_{ij}^{\text{raw}}$ stands for the energy deposited in each cell and the $C_{\text{long}}$ variable corresponds to the fraction of energy deposited in the first two longitudinal layers of the module (excluding the D-layer cells from the calculation).

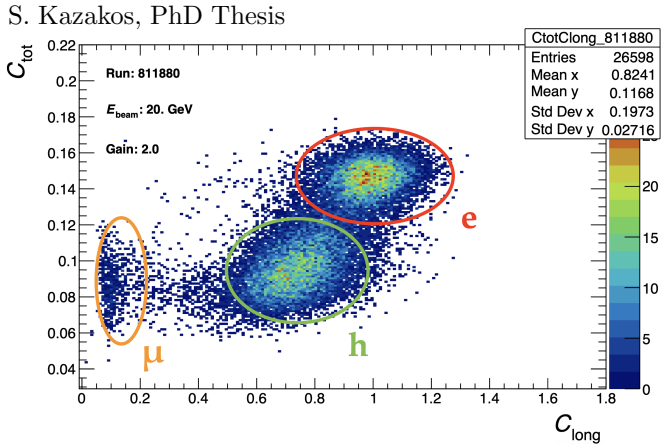



FIGURE 5.12: Scatter plot of the topological variables $C_{\text{tot}}$ versus $C_{\text{long}}$ for an $E_{\text{beam}} = 20$ GeV electron run taken during the 2018 test-beam period.

The electron-hadron separation is more effective when these two variables are used together, as shown in Figure 5.12. The use of the shower variables is recommended for all electron beam energies and it starts being weaker after 100 GeV, where the electron purity of the beam drops significantly. The muon separation is achieved with a selection on the total energy of $E^{\text{raw}} > E_{\text{beam}}/8$, cutting out effectively also the pedestal events. Additional selection cleaning cuts are applied based on the beam-chamber coordinates and timing in order to ensure that the remaining events are in well-understood regions.

## 5.4 Electron response determination

The electron signal is extracted based on the shower profile plots (similar to Figure 5.12) with simultaneous rectangular selection in the $C$-space ($C_{\text{tot}} > C_{\text{tot}}^{\text{thres}}$, $C_{\text{long}} > C_{\text{long}}^{\text{thres}}$). However, at higher energies the hadron and electron distributions are even more convoluted making the electron signal extraction challenging. A more concrete approach is developed and adopted in this thesis, where the electron signal extraction depends on an elliptical selection around the maximum of the electron distribution in the $C$-space.

The general equation of a shifted and rotated ellipse is given by the formula

$$\left[\frac{(x-x_0)\cos\theta+(y-y_0)\sin\theta}{a}\right]^2+\left[\frac{(x-x_0)\sin\theta-(y-y_0)\cos\theta}{b}\right]^2=1, \quad (5.3)$$

where $x_0, y_0$ are the shifts in the x- and y-axis, respectively, $a, b$ are the semiaxis values in the x- and y-directions, respectively, and $\theta$ is the rotation angle measured from the x-axis varying between 0 and $\pi$.

| $E_{\text{beam}}$ [GeV] | 10 | 20 | 50 | ≥100 |
|---|---|---|---|---|
| $a$ | 0.030 | 0.025 | 0.018 | 0.020 |
| $b$ | 0.40 | 0.30 | 0.18 | 0.15 |

TABLE 5.1: Nominal values of the semi-axis parameters $a$ and $b$.

The parameters $x_0, y_0$ and $\theta$ are determined by the position of the maximum, and since the $C_{\text{tot}}$ scale is changing versus beam energy, the optimised $a, b$ parameters used are given in Table 5.1.[1] The $a, b$ parameters are optimised based on the shape of the shower for each $E_{\text{beam}}$. The $\alpha$-exponent of the $C_{\text{tot}}$ definition was further optimised to $\alpha = 0.38$ for runs with beam energy higher or equal to 100 GeV, providing better separation by changing the $C_{\text{tot}}$ scale. The topological selection is also very effective at low beam energy runs, where it can be enhanced by a selection based on Cherenkov counters Ch1 and Ch3. The use of convolutional neural networks would assist further in the electron-hadron separation at higher beam energies, but such method is left for future studies.

The peak position of the electron signal distribution after the topological selection is estimated from a Gaussian fit close to the peak, as shown in Figure 5.13. The mean electron response is estimated as the mean of the electron energy distribution normalised to the beam energy

$$R^{\langle E^{\text{raw}}\rangle}=\frac{\langle E^{\text{raw}}\rangle}{E_{\text{beam}}}, \quad (5.4)$$

and the energy resolution is therefore defined as the $\sigma^{\text{raw}}$ of the electron distribution normalised to the beam energy

$$R^{\sigma^{\text{raw}}}=\frac{\sigma^{\text{raw}}}{E_{\text{beam}}}. \quad (5.5)$$

1 The parameters $a$, $b$, $x_0$, $y_0$ and $\theta$ might require further tuning according to the shower profile of each run.

The binning of the electron energy distributions is selected to match the square root of the total events of the run, since the number of events required to achieve an acceptable electron purity increases proportionally to the beam energy.

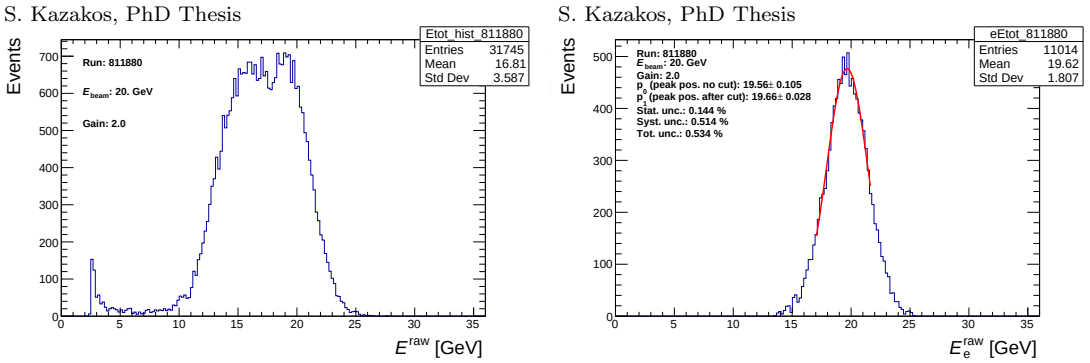



FIGURE 5.13: Electron response after the elliptical topological selection (right) of an $E_{\text{beam}} = 20$ GeV electron run taken in 2018. The total energy distribution of the run (left) is shown for comparison.

There are three different available methods used for the energy reconstruction [99]. The "*flat-filter*" method is commonly used in the online analysis, as it is considered the simplest and fastest. The "*fit*" and "*optimal-filtering*" methods are considered more sophisticated, since they exploit the pulse shape information providing better resolution in regions with non-negligible noise. The latter is considered in general more robust and it is used in the analysis of the 2018 and September 2021 TB electron data, while the former is used in the analysis of November 2021 TB electron data since the other method was not available due to a migration to a new reconstruction software version.

The reconstructed energy $E^{\text{raw}}$ in each channel is estimated using the formula

$$E^{\text{raw}} = A \cdot C_{\text{ADC}\to\text{pC}} \cdot C_{\text{pC}\to\text{GeV}} \cdot C_{\text{Cs}} \cdot C_{\text{Laser}}, \tag{5.6}$$

where $A$ is the signal amplitude measured in ADC counts and the $C$-parameters are conversion and calibration factors [105]. The factor $C_{\text{ADC}\to\text{pC}}$ is used for the conversion of ADC counts to electric charge (in pC) and it is measured for each channel using the CIS calibration system, by injecting a well-defined charge. The factor $C_{\text{pC}\to\text{GeV}}$ is used to convert the charge to energy (in GeV) and it is determined by measuring the response of electron beams of known momentum in the first radial layer (A-layer) during test-beam studies for a subset of modules. This factor is adjusted to correct for the dependence on the radial layers, and it is globally applied afterwards to all cells. The factor $C_{\text{Cs}}$ is used to correct for

residual non-uniformities following the equalisation of the high-voltage gain that is performed by the Cs radioactive source system in all channels. Finally, the factor $C_{\text{Laser}}$ is used to account for non-linearities of the PMT response, which are determined by the Laser calibration system with corrections that reach up to 1%.

## 5.5 Estimation of systematic uncertainties

The electron and hadron shower distributions are convoluted and the method of the elliptical topological selection can lead to some sort of bias by cutting away the left and right tails of the distributions in the $C$-space. A systematic uncertainty has been derived in order to take this effect into account, by comparing the peak of the electron signal distribution after the topological selection to the electron signal distribution prior to any selection. The latter is determined through a two-Gaussian fit with two Gaussian distributions corresponding to the hadron and the electron signal, respectively. The beam response is generally described by a Crystal Ball function, which can be approximated by a Gaussian function close to its peak.

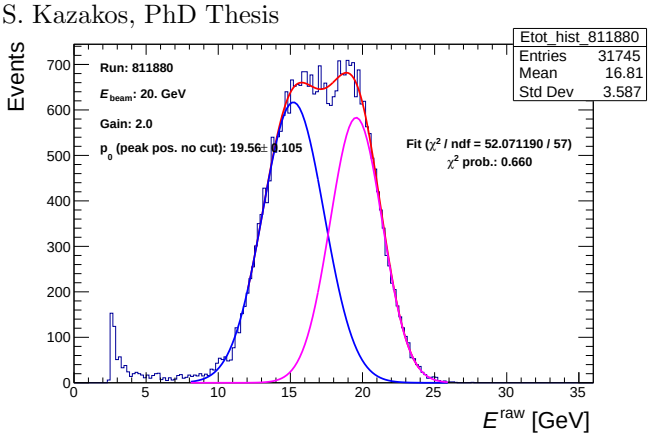



FIGURE 5.14: Two-Gaussian fit of the total energy distribution in an $E_{\text{beam}} = 20$ GeV electron run taken in 2018. The fit curves corresponding to the total fit (red), to the hadron signal distribution (blue) and to the electron signal distribution (pink) are shown.

Each Gaussian function is first fitted separately close to each peak without going too low in the distributions. The parameters from these fits are used as initial parameters to the two-Gaussian fit. The $\chi^2$/n.d.f. value is calculated to determine the goodness of the fit. In electron runs with $E_{\text{beam}} \geq 100$ GeV the electron peak

is difficult to be determined due to the low electron purity of the beam. For this reason, constrained fits are performed in this case by fixing the standard deviation of the electron Gaussian function to the values acquired from the first fit close to the electron peak. The total uncertainty on the measurement of the response is calculated as the quadrature sum of the systematic uncertainty derived from this procedure and the statistical uncertainty derived from the fit. The total uncertainty is estimated to 1-4% depending on the cell that the beam is incident to and the beam energy.

Other possible sources of systematic uncertainty have also been studied including the movement of the table during the measurement leading to a change in the incident angle. Such claims cannot be verified experimentally, since no such movement was observed and the resolution of the incident angle is restricted to $\delta\theta_{\text{inc}} = 1^o$.

## 5.6 Energy modulations

The inner structure of the modules in TileCal, containing a series of alternating scintillating tiles and steel plates perpendicular to the beam pipe, brings forward the dependence of the electron response on the $z$-axis coordinate of the impact point. This dependence results in sinusoidal modulations of the electron energy around the mean response given by the formula [99]

$$E^{\text{raw}}(z) = p_0 \left[1 + p_1 \sin\left(\frac{2\pi z}{p_2} + p_3\right)\right], \tag{5.7}$$

where $p_0$ corresponds to the mean response value, $p_1$ stands for the relative oscillation amplitude, $p_2$ represents the "thickness" period and $p_3$ is an arbitrary phase.

The parameter $p_0$ is useful to the validation of the calibration constant and it should be close to unity. The parameter $p_1$ is dependent on the beam energy and decreases at higher beam energies ($\sim 1/\sqrt{E_{\text{beam}}}$). The parameter $p_2$ is useful to check the quality of the energy modulations, since it solely depends on the TileCal period defined by the succession of the material inside the modules. For an incident angle of $\theta_{\text{inc}} = 20^o$ and a period of 18 mm the parameter $p_2$ should be

$p_2 = 18 \cdot \cos 20^o \approx 16.9$. The parameter $p_3$ should also be about the same in all the runs targeting a specific cell.

The modulations in the electron response are a useful tool to verify that the selected particles are indeed electrons as such modulations do not appear in the hadron signal. A deviation between the expected and experimental values of the parameters $p_i$ $(i = 0, \dots, 3)$ might indicate the presence of hadrons in the selected sample. The periodicity of the electron signal modulations is shown in Figure 5.15.

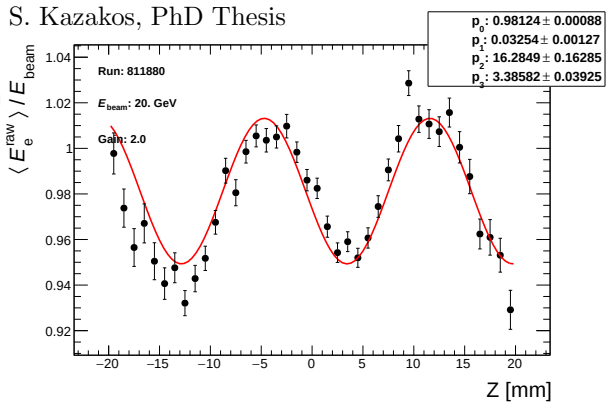



FIGURE 5.15: Modulations of electron response for $\eta = 0.35$ ($\theta_{\text{inc}} = 20^o$). The red line corresponds to the fit result of the experimental points to Equation 5.7.

## 5.7 Test-beam results

A large number of electron test-beam runs taken in 2018 and 2021 has been analysed in the context of this dissertation. In 2018, since the new electronics had been inserted in the EB, most of the runs taken at this time were with an incident beam to the EBC 65 module (A-13, A-14, A-15 and A-16 cells) at different values of $E_{\text{beam}}$ and high-voltage (HV) setting. Electron runs were taken also with an incident beam to the LBC 65 module (A-2 and A-3 cells) at $\theta_{\text{inc}} = 20^o$, since similar runs had been analysed in the past, in order to compare to the results of the EB runs.

The electron response of these runs was compared to the beam energy and a discrepancy was observed to be at the order of ∼4% for the LB runs and ∼6-10% for the EB runs. A number of studies was performed in order to check the validity of these results and to make conclusions on the dependence of the electron response

on the beam energy, on the HV setting and on the relative time between the runs, which could have impacted the stability of the high voltage. Modulations on the electron response confirmed that the hadron contamination of the electron signal was minimal. The timing of the pulses, the pulse shapes and the beam-chamber profiles were checked for potential unusual behaviour, and no deviations from the expected results were found. Therefore, since these studies did not reach a certain conclusion the above discrepancy had been attributed to potential Cesium miscalibration during the offline reconstruction.

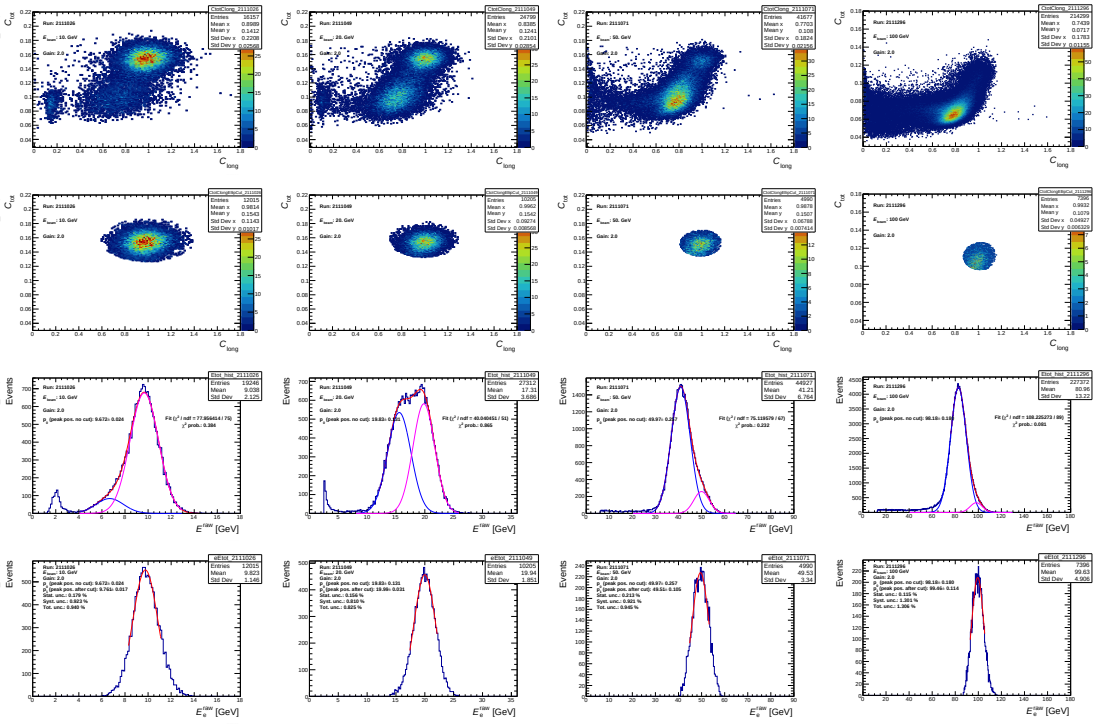
In 2021, there were two test beams conducted in September and November in order to check the validity of the new electronics (upgrade-0) inserted in the LB module. For this reason, electron runs were taken with an incident beam to the LB module (A-1 to A-10 cells) at $\theta_{\text{inc}} = \pm 20^{o}$. In both test-beam periods the averaged mean electron response $R^{\langle E^{\text{raw}} \rangle}$ was close to unity, validating the conclusion about the miscalibration in the 2018 data.

The accurate measurement of the electron response in the Tile calorimeter is useful to cross-check that the beam is correctly calibrated with a proper setting of the EM scale. The experimental value of the EM scale constant is 1.050 ± 0.003 pC/GeV with spread of 2.4 ± 0.1%, and since this value was used in the data reconstruction a deviation of $R^{\langle E^{\text{raw}} \rangle}$ from unity could mean that the EM scale needs to be updated. In that case $R^{\langle E^{\text{raw}} \rangle}$ can also be interpreted as the potential correction needed for the EM scale. Summary plots of $R^{\langle E^{\text{raw}} \rangle}$ as a function of $E_{\text{beam}}$ are given for all the runs analysed in Section 5.7.2.

### 5.7.1 Electron identification and response

The typical shower profiles, total energy distributions and electron response distributions for different values of $E_{\text{beam}}$ are shown in Figure 5.16. The electron purity is inversely proportional to the $E_{\text{beam}}$ and the electron-hadron separation becomes more difficult at higher $E_{\text{beam}}$ values. In addition, the electron response distributions are broader for low $E_{\text{beam}}$ and become narrower at high $E_{\text{beam}}$ values, as the resolution deteriorates with $E_{\text{beam}}$.

The electron response is found to be very close to the $E_{\text{beam}}$ value and the electron peak position together with the goodness of the two-Gaussian fit are shown in



(a) (b) (c) (d)

FIGURE 5.16: Test-beam results from characteristic electron runs taken during the test-beam period in September 2021. Each column corresponds to a different run with an incident beam to cell A-3 and beam energies: (a) 10, (b) 20, (c) 50 and (d) 100 GeV, respectively. The rows from top to bottom correspond to: the 2D histogram of the $C_{\text{tot}}$ as a function of $C_{\text{long}}$ before and after the elliptical selection, a two-Gaussian fit to the total energy distribution and a fit on the peak of the electron response after the elliptical selection.

these figures. Since in the results of the 2018 TB the electron response was systematically lower than unity the checks that were done to understand the reason of this behaviour are summarised below.

In Figure 5.17 the averaged mean electron response is shown as a function of the gain, which is proportional to the HV setting. The average operating voltage for the nominal ATLAS gain (gain 1) is 690 V [94], and the gains 0.5, 2 and 5 are multiples or submultiples of that value. No significant difference is observed at different values of the gain with similar dispersion of the averaged electron response. In Figure 5.18 the averaged mean electron response is shown as a function of the $E_{\text{beam}}$. The electron runs with $E_{\text{beam}} = 10$ GeV appear to have systematically lower electron response than the rest of the runs something that was observed also in the past [98]. The electron response seems to increase as a function of $E_{\text{beam}}$ for

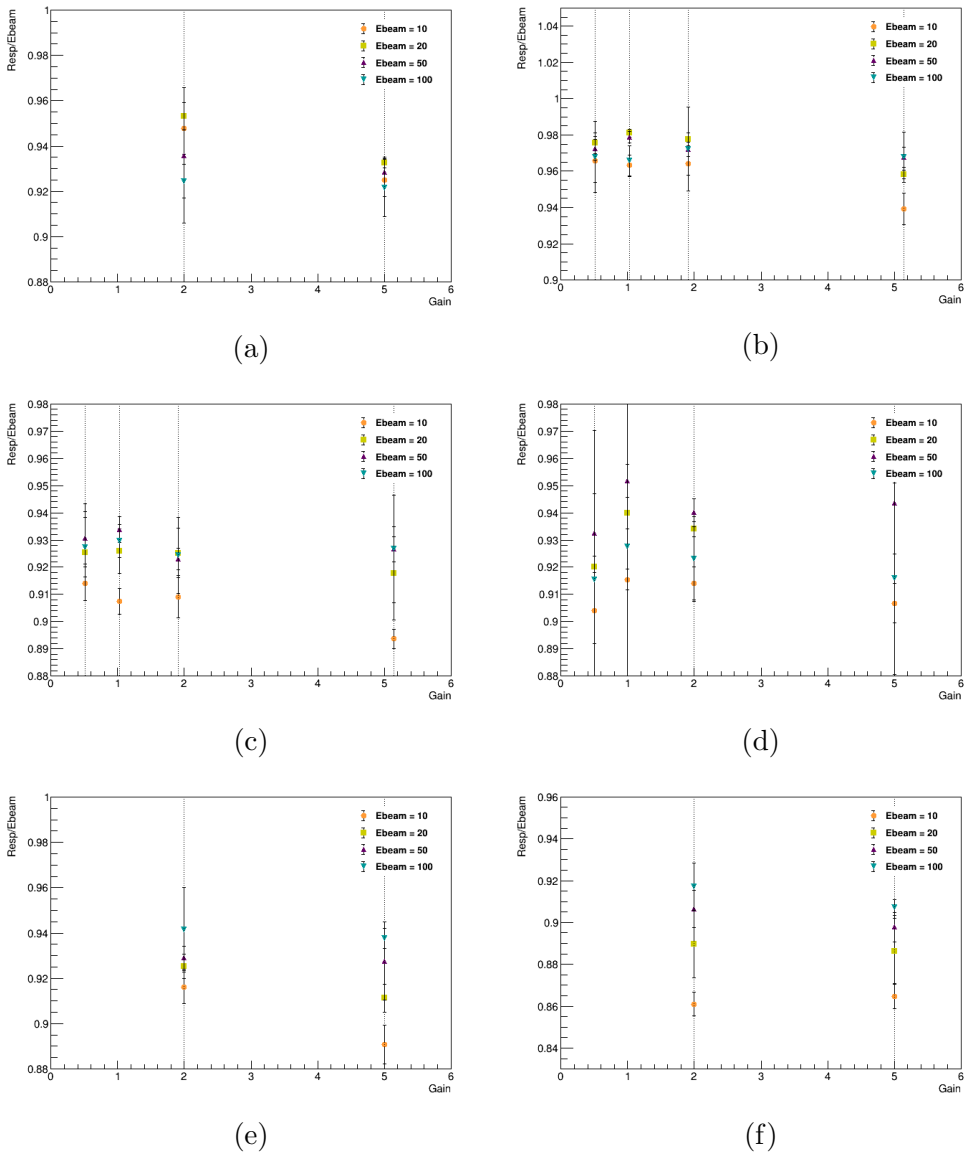



FIGURE 5.17: Averaged mean electron response as a function of the ATLAS gain, and therefore of the HV setting. The $E_{\text{beam}}$ of the runs corresponds to 10 GeV (orange circle), 20 GeV (yellow square), 50 GeV (purple triangle), 100 GeV (blue upside-down triangle). The beam is incident to the cells: (a) A-2, (b) A-3, (c) A-13, (d) A-14, (e) A-15 and (f) A-16.

the runs in some of the cells, while it stays constant (or even decreases) for other cells.

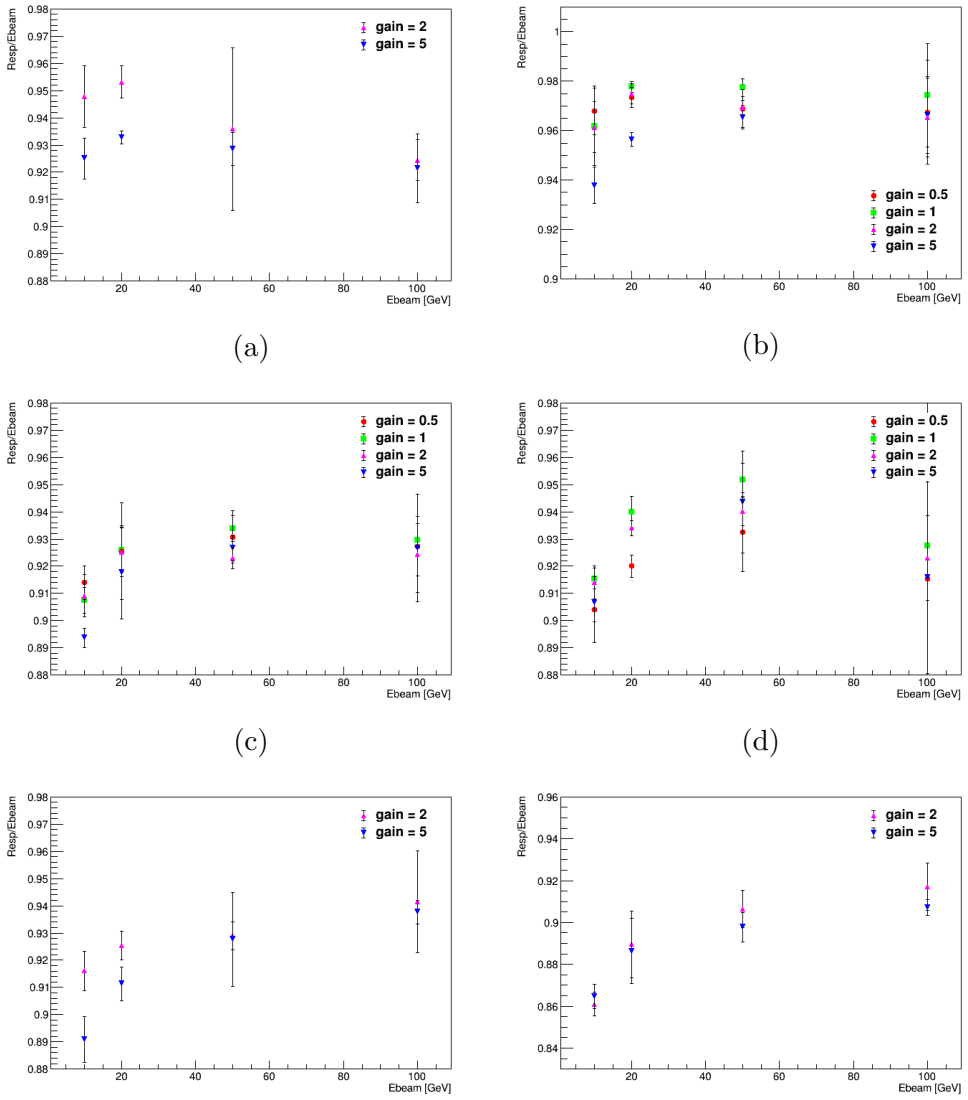



FIGURE 5.18: Averaged mean electron response as a function of $E_{\text{beam}}$. The HV gain is set to: 0.5 (red circle), 1 (green square), 2 (pink triangle), and 5 (blue upside-down triangle) times the nominal gain. The beam is incident to the cells: (a) A-2, (b) A-3, (c) A-13, (d) A-14, (e) A-15 and (f) A-16.

The above behaviour was speculated to be due to the difference in the order of changing the $E_{\text{beam}}$ and HV, while moving from one run to another. For this reason, the runs are also analysed in "chronological" order as a function of the relative time between the runs.

S. Kazakos, PhD Thesis

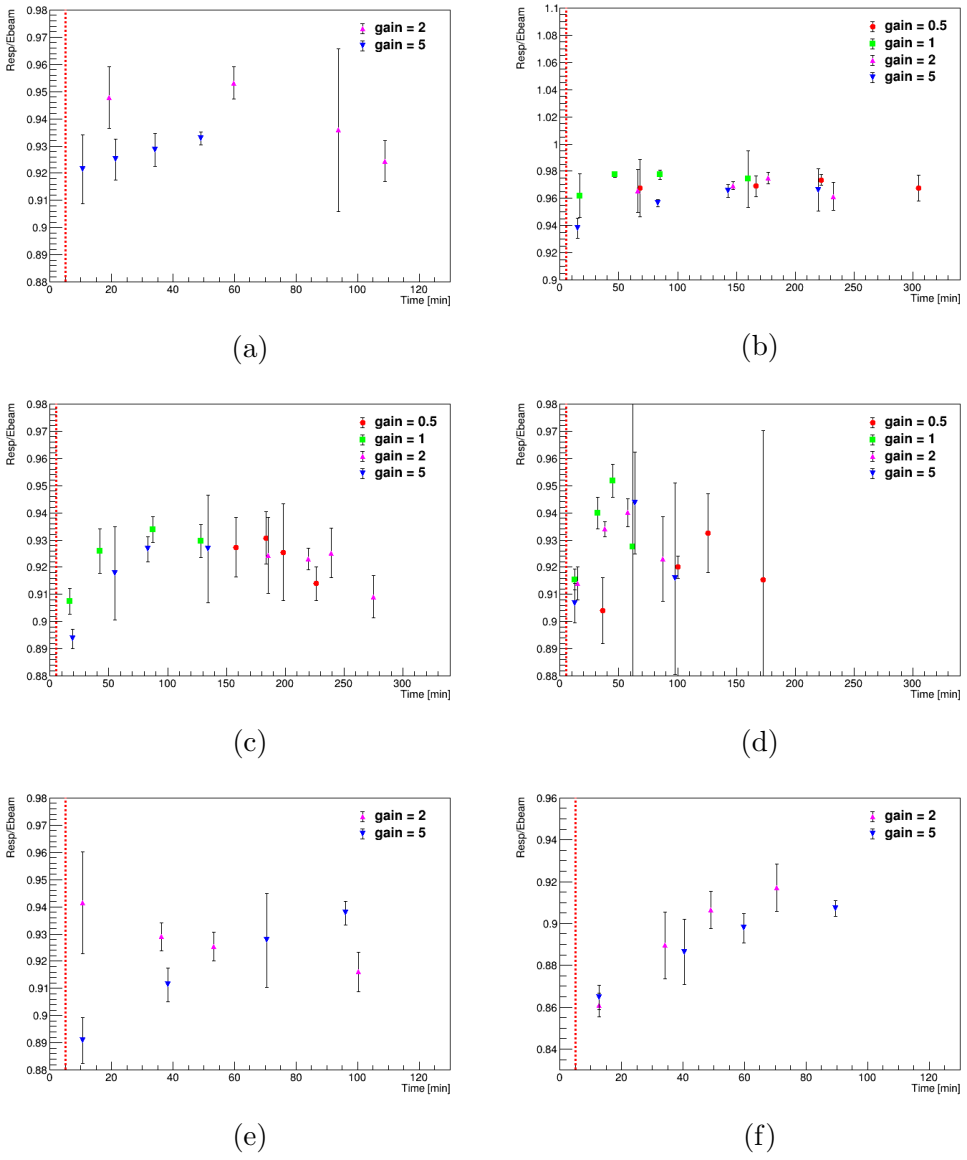



FIGURE 5.19: Averaged mean electron response as a function of the relative time of the runs. The HV gain is set to: 0.5 (red circle), 1 (green square), 2 (pink triangle), and 5 (blue upside-down triangle) times the nominal ATLAS gain. The beam is incident to the cells: (a) A-2, (b) A-3, (c) A-13, (d) A-14, (e) A-15 and (f) A-16. The time difference is calculated from the moment that the HV is assumed to stabilise (red dashed line).

In some of the cells and HV values the runs were recorded in an increasing value of $E_{\text{beam}}$ starting from 10 GeV, while in other combination of cells and HV they

were recorded in a decreasing value of $E_{\text{beam}}$ starting from 100 GeV. Particularly interesting are the Figures 5.19e and 5.19f, where the increase in the averaged electron response is found to be consistent with an increase in the $E_{\text{beam}}$ and not being dependent on the time from the HV setting.

### 5.7.2 Setting of the electromagnetic scale

The main purpose of the studies in this chapter are to validate that the EM scale had been set correctly during the Cs calibration. The results from the 2018 TB are not considered due to the potential miscalibration issue. The results from the 2021 September and November TBs are shown in the summary plots of Figure 5.20. The averaged electron response represents the correction to the EM scale, which is shown to be very close to unity for almost all runs, confirming the correct EM scale setting during the TBs.

S. Kazakos, PhD Thesis

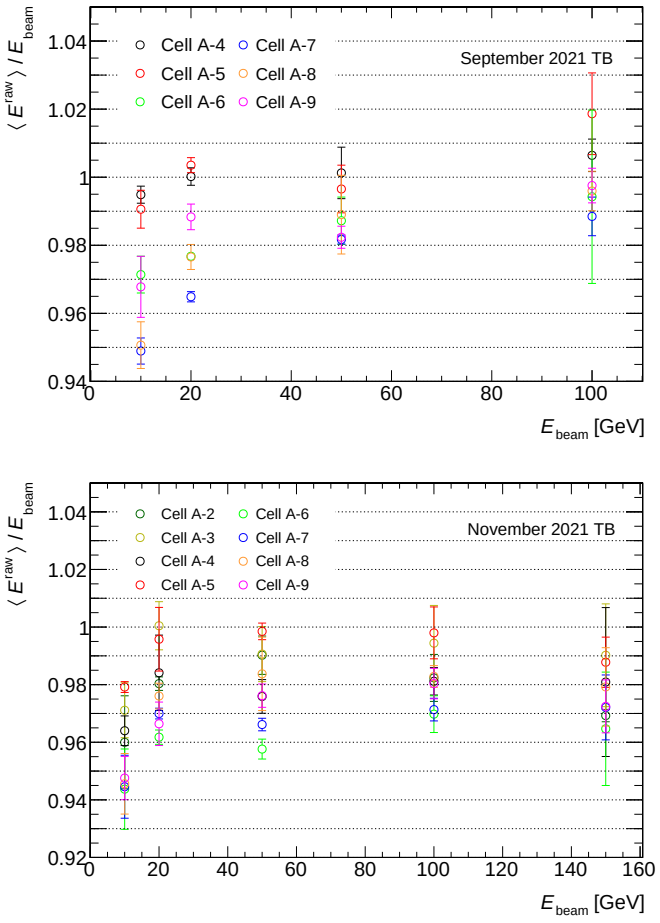



FIGURE 5.20: Correction to the EM scale obtained from the September (top) and November (bottom) test-beam runs in 2021.

In the 2021 September TB, the runs with the beam incident to the A-2 and A-3 cells were not used since the HV cables were not properly connected during the drawer installation in the BC-2 cell. In the 2021 November TB, it was possible to record electron runs at a high $E_{\text{beam}} = 150$ GeV with reasonable electron purity. The averaged electron response is found to be relative stable as a function of $E_{\text{beam}}$ even at higher values making the scenario of energy dependence less likely. Lower response is observed consistently in the $E_{\text{beam}} = 10$ GeV runs as expected from previous results.

The correct EM scale setting in the 2021 TBs suggests that the updated electronics for the Phase-II upgrade perform as expected without any significant impact in their response. The summary tables of the electron-analysis results from the test-beam periods 2017-2021 are found in Appendix A.

# Chapter 6

# Event simulation

The precision measurements and searches for new physics conducted by the ATLAS experiment depend on comparisons of Monte Carlo (MC) simulated data to the real data recorded. The accurate simulation of physics data is the key element for the reliable modelling of both signal and background processes upon which the physics analyses rely to proceed to conclusions. The event simulation encapsulates all the physics information related to the dynamics of a hard-scatter process in proton-proton ($pp$) collisions, while initiated from pseudo-random number MC generators in order to mimic the probabilistic nature of $pp$ interactions. The comparison of the MC generated events to the real data takes place after their interaction with the detector volume, where they get corrected by the reconstruction and identification efficiencies of the detector.

This chapter provides an outlook of the $pp$ collision simulation process in ATLAS, explaining the physics interactions that need to be taken into account (Section 6.1). A description of the common Monte Carlo generators used (Section 6.2) and the detector simulation in ATLAS (Section 6.3) are also included.

## 6.1 Simulation of proton-proton collisions

The products of a $pp$ collision depend on the centre-of-mass energy of the colliding protons. At low energies, where there is no significant amount of momentum transfer between the protons, the objects at the final state are the same as in the initial state with some shift in their trajectory. This process is known as *elastic*

*scattering*. At higher energies the momentum transfer increases up to a point where interactions between the inner partons inside the protons start to become possible. This process is known as *deep-inelastic scattering* (also referred to as hard scattering) and it can lead to the production of particles that were not present in the initial state. The hard-scatter process is described by perturbative QCD and its cross section can be calculated numerically at a fixed order in perturbation theory through the PDFs and the matrix element (ME) squared.

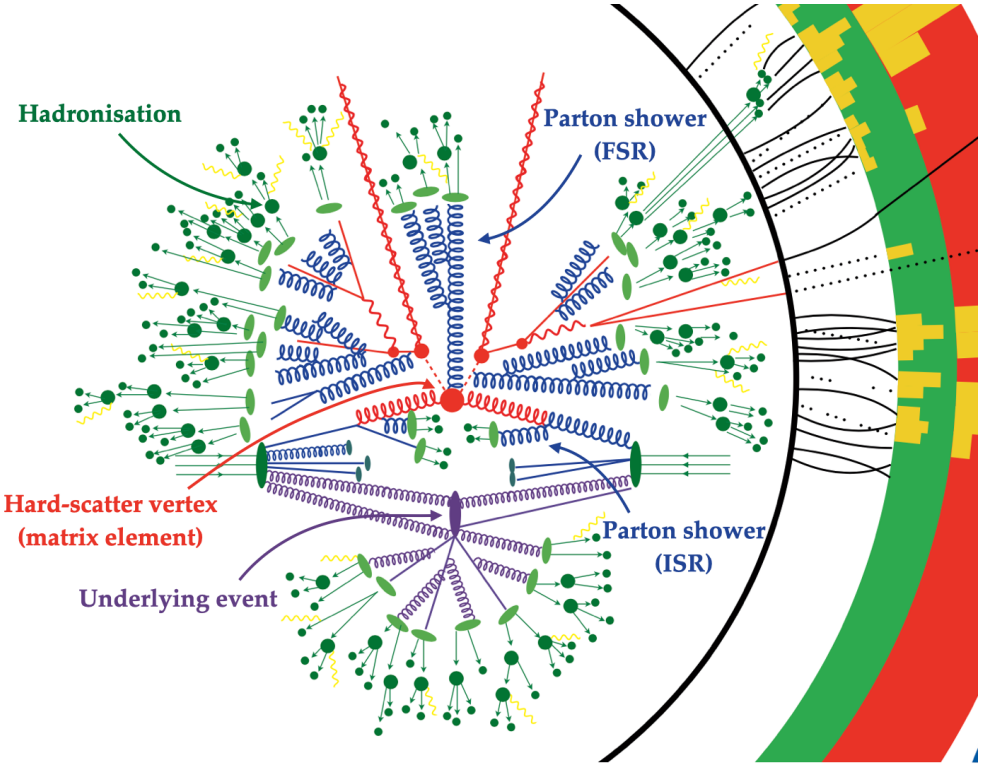



FIGURE 6.1: Illustrative diagram of the simulation of a proton-proton collision. Figure adapted from Ref. [106].

The physics objects in the final state originate from parton emission either from the partons of the initial state (*initial-state radiation*) or from the partons created from the hard-scatter vertex (*final-state radiation*). Both processes are referred to as *parton shower*. The energy of quarks and gluons in the shower decreases with time leading to their recombination into colourless hadrons, a process called *hadronisation*. The hadronisation process cannot be described using perturbative QCD, and instead is based on phenomenological models that are adjusted to experimental data. Sometimes there are more than one pairs of partons interacting during a $pp$ collision, and these interactions together with the products constitute the underlying event. In addition to this, interactions from softer QCD processes

like the ones originating from pileup should also be considered in an accurate event simulation.

### 6.1.1 Factorisation theorem and parton distribution functions

The event simulation of a $pp$ collision involves processes at different energy scales, thus amplifying its complexity. The factorisation theorem [107] offers a permanent solution to this problem by allowing the factorisation in subprocesses introducing an adhoc energy scale (factorisation scale) that separates short-distance from long-distance physics. It is introduced by the formula

$$\sigma_{pp\to X} = \sum_{i,j} \int dx_i dx_j \, f_i(x_i, \mu_F^2) f_j(x_j, \mu_F^2) \, \hat{\sigma}_{ij\to X}(x_i p_i, \, x_j p_j, \, \mu_R^2, \, \mu_F^2), \tag{6.1}$$

where the indices $i$, $j$ correspond to the parton types that participate in the process and the sum indicates that all possible parton type combinations are taken under consideration. The terms $f_i(x_i, \mu_F^2)$, $f_j(x_j, \mu_F^2)$ stand for the PDFs of each parton type $i$, $j$ and they represent the probability for the parton to carry a fraction of momentum equal to $x_i$, $x_j$ (Bjorken scaling) given a certain factorisation scale $\mu_F$. The parameter $\hat{\sigma}_{ij\to X}$ corresponds to the partonic cross section at a centre-of-mass $\sqrt{\hat{s}} = \sqrt{s}\sqrt{x_i \, x_j}$ (where $\sqrt{s}$ is the centre-of-mass energy of the $pp$ collision), and it also depends on the factorisation and renormalisation scales $\mu_F$ and $\mu_R$, respectively. The dependence on the factorisation scale choice vanishes once the calculation is performed at all orders in perturbation theory.

The PDFs depend on the factorisation scale $\mu_F$ as shown in Figure 6.2. At low energy scales ($\mu^2 = 10$ GeV$^2$) the valence quarks of the proton ($uud$) carry the largest fraction of the proton's energy. At higher energy scales ($\mu^2 = 10^4$ GeV$^2$), while the momentum fraction of the valence quarks is still significant, the energy of the proton is distributed more evenly to the "sea"[1] partons inside the proton, increasing their probability to interact. As it can be inferred from the above the centre-of-mass energy $\sqrt{\hat{s}}$ of the colliding partons during the hard-scatter process is much lower than the one referred to the total energy of the protons.

1 Gluons and $q\bar{q}$ pairs produced through gluon splitting inside the proton.

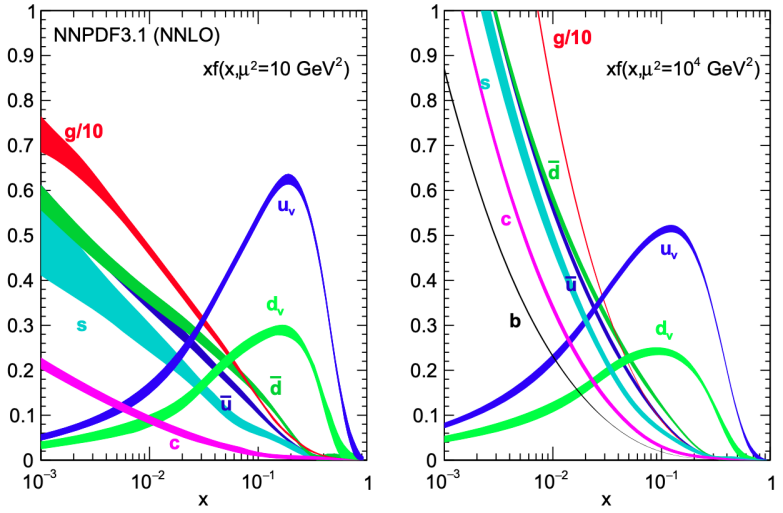



FIGURE 6.2: Parton distribution functions at an energy scale of $\mu^2 = 10$ GeV$^2$ (left) and $\mu^2 = 10^4$ GeV$^2$ (right) as a function of the Bjorken scaling x-variable [108].

The evolution of PDFs as a function of the energy scale $\mu$ is given by the Altarelli-Parisi equations (DGLAP) [109]

$$\begin{aligned} \frac{\partial q_i(x,\mu^2)}{\partial \mu^2} &= \frac{\alpha(\mu)}{2\pi}\int_x^1 \frac{dy}{y}\left[q_i(y,\mu)P_{qq}\left(\frac{x}{y}\right) + g(y,\mu)P_{qg}\left(\frac{x}{y}\right)\right], \\ \frac{\partial g(x,\mu^2)}{\partial \mu^2} &= \frac{\alpha(\mu)}{2\pi}\int_x^1 \frac{dy}{y}\left[\sum_{i=1}^{2f} q_i(y,\mu)P_{qq}\left(\frac{x}{y}\right) + g(y,\mu)P_{gg}\left(\frac{x}{y}\right)\right], \end{aligned} \tag{6.2}$$

where $q_i, g$ stand for the quark and gluon PDFs, respectively, and $x/y$ corresponds to the momentum fraction of the parton. The terms $P_{ij}$ are called *splitting* functions and are used to describe the probability of an outgoing parton $j$ to be emitted by an initial parton $i$, where $i$, $j$ can both correspond to quarks and gluons. The sum in the second equation runs over all the quark and antiquark flavours ($i = 1, ..., 2f$).

### 6.1.2 Matrix element

A key aspect in the event simulation is the calculation of the *matrix element* (or scattering amplitude) $\mathcal{M}_{X+k}$, a quantity that describes the transition from an initial to a final state in a parton interaction. The matrix element is used in the definition of the partonic production cross section of a final state $X$, which is given

by the formula

$$\hat{\sigma}_{ij\to X} = \sum_{k=0}^{\infty} \int d\Phi_{X+k} \left| \sum_{l=0}^{\infty} \mathcal{M}^{l}_{X+k}(\Phi_{X+k}) \right|^2 . \tag{6.3}$$

In this equation $\Phi_{X+k}$ stands for the available phase space of the interaction resulting in a $X + k$ final state. The sum over $k$ corresponds to the sum of the additional real emissions that can occur, and the sum over $l$ is the sum over the number of virtual correction loops. The matrix element $\mathcal{M}_{X+k}$ is computed as the sum of the Feynman diagrams resulting in a $X + k$ final state with $l$ loops.

The numbers $k, l$ are used to describe the order of the perturbative calculations needed for the determination of the partonic cross section. A configuration of $\{k = 0,\ l = 0\}$ means that the inclusive production cross section of a final state $X$ is performed at LO, a configuration of $\{k = n,\ l = 0\}$ describes the LO cross-section calculation for a final state of $X$ produced in association with n jets and a more generic configuration of $\{k + l \geq n\}$ stands for a cross-section calculation of a final state $X$ at $\mathrm{N}^n\mathrm{LO}$, where the calculations at $\mathrm{N}^{n-1}\mathrm{LO}$ for $X + 1$ jet, $\mathrm{N}^{n-2}\mathrm{LO}$ for $X + 2$ jets, ..., up to LO for $X +$ n jets are also included.

### 6.1.3 Parton shower

The analogue of the photon emission from charged particles through bremsstrahlung radiation[2] in QED, is the gluon emission that occurs by "coloured partons" in QCD. The gluon emission can take place prior to or post to the hard-scatter process and it is therefore categorised as *initial-state radiation* (ISR) and *final-state radiation* (FSR), respectively. The colour charge of the emitted gluons can lead to the further emission of colour-charged objects (quarks and leptons) creating what is known as *parton shower* (PS). In order to ensure a proper emulation of the final state these parton showers are taken into account in the MC simulations as higher-order corrections to the hard-scatter process. The simulation of the quark and gluon emissions is approximate since only the dominant contribution (in the soft and collinear regime) is considered to each order without including virtual corrections and the parton emissions are considered independent from each other.

2 Electromagnetic radiation produced due to the deceleration of a charged particle (usually an electron), also known as "braking" radiation.

The $n$+1-parton differential cross section, assuming almost-collinear splitting of a parton $(i)$ to two partons $(j, k)$ at a given energy scale $\mu$, is calculated in perturbation theory by the formula

$$d\sigma_{n+1} \approx d\sigma_n \frac{\alpha_S}{2\pi} \frac{d\mu^2}{\mu^2} \, dx \, P_{ij}(x), \tag{6.4}$$

where $\alpha_S$ is the strong coupling constant, $d\sigma_n$ represents the $n$-parton differential cross section before splitting and $P_{ij}$ stands for the splitting functions described above.

The three possible processes of QCD emission (splitting) that can occur are: $g \to gg$, $g \to q\bar{q}$ and $q \to gq$. The shower is developed by the MC simulation algorithms that generate values for the splitting angles and the momentum fraction transferred in each splitting through a sequential application of Equation 6.4.

The shower is developed based on the Sudakov form factor

$$\Delta_i(\mu_1^2, \mu_2^2) = \exp\left( - \sum_j \int_{\mu_2^2}^{\mu_1^2} \frac{\alpha_S}{2\pi} \frac{d\mu^2}{\mu^2} \int_{x_{\min}}^{x_{\max}} P_{ij}(x) \, dx \right), \tag{6.5}$$

where $\mu_1^2$, $\mu_2^2$ are the energy scales before and after each splitting, respectively. This factor represents the probability of a parton to not split at all during its transition from an energy scale $\mu_1^2$ to a lower energy scale $\mu_2^2$, enclosing in this way the virtual (quantum loop) corrections at each order that had been neglected before.

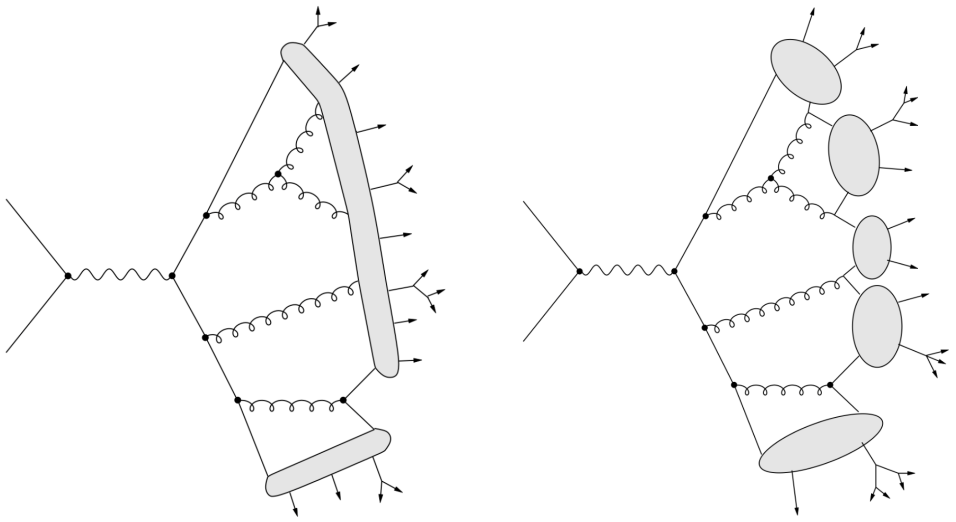
In order to determine the evolution of showers from FSR the equation $\Delta_i(\mu^2, \mu_1^2) = r_1$ is being solved numerically, where $\mu^2$ is the energy scale of the initial parton, $\mu_1^2$ the scale after the first splitting and $r_1 \in [0, 1]$ is a random number. In the case that $\mu_1^2 < \mu^2$ the parton is considered split in two partons $(j, k)$, and the equation $\Delta_p(\mu_1^2, \mu_2^2) = r_2$ (where $p \in \{j, k\}$) is evaluated for each of the partons with a lower scale (before) after splitting $(\mu_1^2)$ $\mu_2^2$ and $r_2$ is a new random number. The process is terminated when $\mu_f^2 < \mu_0^2 \sim 1$ GeV$^2$, which is also the moment that the energy scale of the last parton $\mu_f^2$ reaches the hadronisation scale and the progress of the simulation onwards is based on phenomenological models.

In the case of showers from ISR, among the radiated partons could be the ones from which the hard-scatter vertex is created. Thus the final energy scale $\mu_f^2$ of the shower is in this case the initial energy scale for the hard-scatter interaction.

This condition is incompatible with the approach used by the MC generators for the showers from FSR. For this reason, a backward evolution is being used in this case, where the shower from ISR is developed backwards by the MC generators with each of the partons before the splitting being at a higher energy scale.

### 6.1.4 Hadronisation

The evolution of a shower is terminated when the hadronisation scale is being reached by the radiated partons. In this regime the perturbative QCD calculations do not hold and phenomenological models are used to describe the hadronisation procedure. At the low parton energies at the hadronisation scale, the strong coupling constant $\alpha_S$ is increasing leading to the colour confinement briefly discussed in Section 2.2. The partons get bound together into colourless objects, the hadrons, which can further decay to other particles. In order to simulate the hadronisation process there are two main phenomenological models used in the event generators, the string model [110] and the cluster model [111, 112], both illustrated in Figure 6.3.



(a) (b)

FIGURE 6.3: Illustrative diagrams of the string (a) and cluster (b) hadronisation models [113].

#### String model

The string model is structured following a linear confinement approach, where there is a linear increase of the potential energy between two coloured partons

depending on their distance from each other. It is common to refer to it as the Lund model, since it is the name that has dominated in this category. A gluonic string is used to explain the colour force between a quark-antiquark ($q\bar{q}$) pair. As the components of the pair start to separate from each other the string is stretched leading to an increase of the potential energy. In order to reach a lower potential energy it is favourable that the string breaks and the two segments form $q\bar{q}$ pairs connected by shorter virtual strings. As the process is repeated, the initial potential energy is reduced to the level where the quarks get strongly confined into hadrons. Radiated gluons are also considered in this process carrying some fraction of the system's momentum.

#### Cluster model

The cluster model is based on the *preconfinement* property [114] of QCD, where the partons after the shower are grouped into colourless clusters of finite mass. The clusters are created by the gluons of the shower that are considered to split eventually into a $q\bar{q}$ pair. Heavy clusters are allowed to split to smaller clusters or a combination of clusters and hadrons. This process is repeated until all the initial clusters end up to final state hadrons. The mass of the initial colour-singlet clusters is independent of the energy scale of the hard-scatter process with a distribution peaking below 1 GeV and a right high-mass tail reaching up to 10 GeV.

### 6.1.5 Underlying event and pileup

Apart from the two colliding partons participating in the hard-scatter process there are other soft secondary interactions that can take place initiated by other partons in the protons. These interactions are known as the *underlying event* (UE) and need to be included in the MC simulations for the correct modelling of the different physics processes. They typically occur at lower energy scales and closer to the beam axis, not severely affecting the activity in the transverse plane. Due to their low-energy-scale nature the description of these interactions depends on phenomenological models, similar to the case of hadronisation models. These models contain free parameters that are usually tuned by making use of experimental data and they include colour-reconnection information relative to the initial partons.

Unlike the UE interactions originating from the same protons that interacted in the hard scattering, additional soft QCD interactions can take place from protons from the same or another bunch crossing. These interactions are known as *pileup* (briefly discussed in Section 4.1.1). The beam parameters need to be considered for the proper modelling of the interactions in the same bunch crossing (in-time pileup), while the modelling of interactions in other bunch crossings (out-of-time pileup) is subject to the readout electronics time response.

## 6.2 Monte Carlo generators

The event simulation of a physics process relies on Monte Carlo (MC) generators, software tools embedding dedicated algorithms for each simulation stage. MC generators are categorised based on their functionality into ***general-purpose***, ***matrix-element*** and ***special-purpose*** generators. A summary of the MC generators used in the context of this thesis and their characteristics is presented below.

### General-purpose generators

A general-purpose generator is able to perform a complete event simulation starting from the matrix element (ME) calculation up to the hadronisation process. These generators are often used primarily for the parton showering (PS) and the hadronisation parts, while they are interfaced with other generators specialised in the ME calculations. The main general-purpose generators used in the context of this thesis are summarised below:

- Pythia [115, 116] is a general-purpose MC generator that performs ME calculations for $2 \to n$ ($n \leq 3$) physics processes at LO accuracy. It is reliable during the PS simulation providing an accurate description both at high and low energy scale regimes. The PS emissions are ordered in transverse momentum ($p_{\mathrm{T}}$). Apart from the ME and PS simulation Pythia is able to perform the hadronisation step following the Lund string model, while it can also simulate the UE interactions. It is commonly used mainly for the PS step in combination with other more accurate ME generators.
- Herwig [117] is another general-purpose MC generator alternative. It performs ME calculations at LO for $2 \to 2$ physics processes. The PS emissions

are ordered with respect to their opening angle and are accurately simulated due to the full spin correlation information that is included for the emitted partons. In contrast to PYTHIA, HERWIG makes use of the cluster model in the hadronisation and UE simulations.

- SHERPA [118] is a MC generator able to perform multi-leg ME calculations at LO (for $\leq 4$ additional partons) and at NLO (for $\leq 2$ additional partons). It uses a dedicated PS algorithm following the Catani-Seymour dipole formalism [119], a ME to PS matching algorithm based on the CKKW procedure [120] and the cluster model for the hadronisation step.

## Matrix-element generators

A matrix-element (ME) generator is specialised in providing accurate ME calculations and cannot perform the rest of the simulation steps (PS, hadronisation, etc.). The most common ME generators used in this thesis are summarised below:

- POWHEG-BOX [121] is a MC event generator that performs ME calculations in perturbative QCD at NLO. It uses the POWHEG method [122] as the standard procedure for ME to PS to matching and it is usually used together with PYTHIA or HERWIG, which are responsible for the PS, hadronisation and UE simulations.

- MADGRAPH5_AMC@NLO [123, 124] is a MC event generator able to produce ME calculations at LO for $2 \to n$ ($n \leq 6$) physics processes and at NLO for specific processes. The LO calculations depend on user-defined Lagrangians, while the NLO calculations rely on the MC@NLO method [125] for the ME to PS matching.

## Special-purpose generators

Among the several MC generators there are some that are specialised in the improvement of the physics description of processes at different stages of the event simulation. These packages are used after the ME computation, prior to the PS or at the hadronisation step. Some of these special-purpose MC generators are listed below:

- EVTGEN [126] is a MC generator that is used for a more accurate description of the physics processes involving $B$- and $D$-mesons. It includes dedicated

algorithms for the modelling of heavy-flavour semileptonic decays and decays that are CP-violating. The high quality in the simulation of these processes is achieved with the use of decay amplitudes and the inclusion of spin correlations. It is often interfaced with PYTHIA and HERWIG after the PS and hadronisation, replacing their decay chains for the heavy-flavour hadrons.

- MADSPIN [127] is a package used for the modelling of heavy resonance decays after their ME has been estimated at NLO by MADGRAPH5. The tool takes into account the spin correlations among the decay products and it includes off-shell corrections, leading to a more accurate description of these processes.

## 6.3 Detector simulation

The MC generators provide a four-vector list with entries corresponding to each of the stable particles produced in the final state of the event after the hadronisation. This output is stored in HepMC format and it can used to study the kinematics of the collision from the full decay tree. This type of MC simulated data is often referred to as *particle level*. In order to compare them to the real data acquired by the ATLAS detector an additional simulation is required that simulates the interaction of the produced particles with the detector. The simulated data acquired from this procedure correspond to the *reconstruction level*, and are the ones used in comparisons with real data in the different physics analyses. An accurate simulation of the ATLAS detector is achieved with GEANT4 [128], a detector simulation software that defines the geometry and the phase space of the detector and models the interaction of particles with the detector material. The particles interacted with the detector are known as "hits" and the energy deposits to the detector are digitalised to a raw data object (RDO) format in order to emulate the detector electronics response. During this stage the L1 trigger response is simulated depending on the trigger menu used as input. The raw data are eventually reconstructed into physics objects, a procedure that is common for both simulated and real data (described in detail in Chapter 7). The path of simulated data at particle and reconstructed level from the MC generators to reconstruction is shown in Figure 6.4, compared to the course of real data from the ATLAS detector to reconstruction.

The full simulation of the ATLAS detector is known as FullSim (FS), and it is a quite CPU-intensive process requiring significant computer resources and time. A faster approach is known as ATLFAST-II (AF2) [129] providing a decent quality result by using the full GEANT4 simulation for the inner detector and muon spectrometer and parametrised simulations for others parts of the detectors such as the calorimeters. The FS-simulated samples are preferred for the modelling of main physics processes since they are more accurate than the AF2 ones. The AF2-simulated samples are often used during the optimisation process of a physics analysis or to evaluate the theory systematic uncertainties from an alternative sample corresponding to the same process. In the context of this dissertation AF2-simulated samples were used for the signal processes involved in the BSM searches conducted, while for the rest of the processes FS-simulated samples were used.

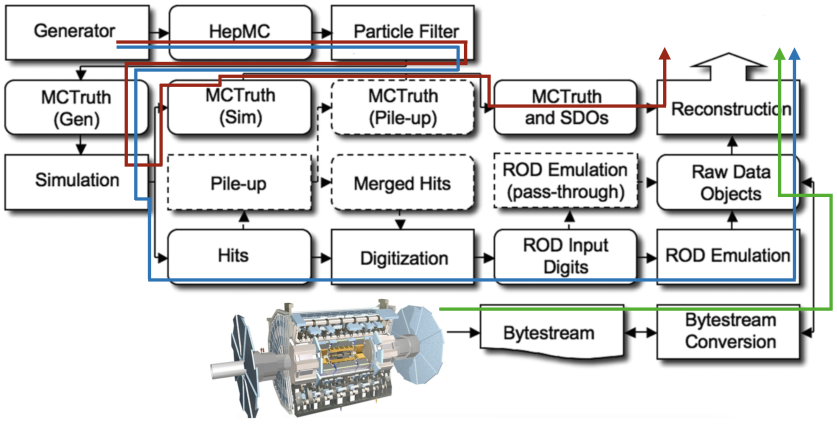



FIGURE 6.4: Schematic representation of the path from the Monte Carlo event generation to the event reconstruction during the proton-proton event simulation in ATLAS. The route of the events at particle level (red line), the route of the fully reconstructed simulated events (blue line) and the route of the real data recorded and reconstructed by ATLAS (green line) are shown. Original figure taken from Ref. [130].

The reconstruction of the simulated MC samples is often followed by certain corrections in order to scale their cross section to the highest order available. A pileup-reweighting procedure takes place, where the simulated pileup distribution is matched to the one of real data. Despite these corrections and the high simulation quality, there could be still detector effects affecting the reconstruction and identification of particles. To ensure that these effects are taken properly into account the MC samples are further corrected by applying multiplicative scale

factors (SFs) calculated as

$$\mathrm{SF} = \frac{\varepsilon_{data}}{\varepsilon_{MC}}. \tag{6.6}$$

The terms $\varepsilon_{data}$ and $\varepsilon_{MC}$ stand for the efficiencies in data and MC, respectively, and are measured in dedicated samples used for calibration. Similar corrections are also applied to the energy scale and resolution of the simulated particles to be in agreement with the ones in real data.

# Chapter 7

# Object reconstruction

The raw data produced from the MC generators and the real data recorded by the ATLAS detector are reconstructed into physics objects that are analysed by the collaboration. This chapter focuses on the algorithms and techniques used for the reconstruction, identification and calibration of the physics objects used in this thesis. These objects are categorised as electrons, muons, jets, hadronically decaying $\tau$-leptons and missing transverse energy. Although these objects are quite accurate representations of physics particles, they should always be considered as "candidates", since the reconstruction procedure is not perfect. The same also applies to heavier parent objects from which they may originate. The characteristics of their interaction with the different ATLAS subdetectors are demonstrated in Figure 7.1.

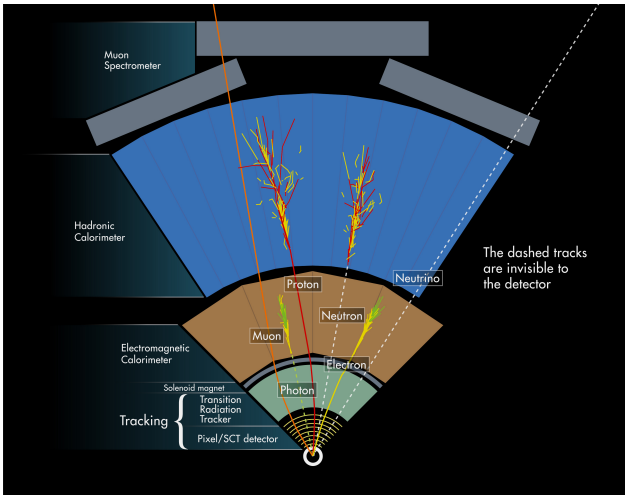



FIGURE 7.1: Transverse view of particle interactions with the different layers of the ATLAS detector. Figure taken from Ref. [131].

## 7.1 Tracks and vertices

In order to reconstruct the candidate particles in ATLAS an accurate measurement of their energy and trajectory is required. The energy deposits in the calorimeters are primarily used for the energy measurements, while the energy can also be determined through other techniques (e.g. from their curvature when entering the magnetic field of the detector in the case of a charged particle). Objects with neutral electric charge can be only identified by the energy deposits in the corresponding subdetectors, since they are not affected by the magnetic field of the detector and their trajectory cannot be measured. The trajectory of charged particle candidates is reconstructed through the "hits" in the different layers of the ID (mainly in the pixel and SCT subdetectors). The spacial coordinates of each hit determine points in the detector space that when connected they compose the **track** of the particle.

Tracks are described by a perigee approach based on the relative distance to the primary vertex expressed by a five-parameter notation

$$(d_0, z_0, \theta, \phi, q/p).$$

The parameters $d_0$, $z_0$ are the transverse and longitudinal impact parameters. The $d_0$ parameter is defined as the smallest closing perpendicular distance between the trajectory of a track and its primary vertex in the transverse plane, while a similar definition yields for the definition of the longitudinal impact parameter $z_0$ with respect to the longitudinal plane. The parameters $\theta$, $\phi$ correspond to the polar and azimuthal angles, respectively, and $q/p$ corresponds to the ratio of the charge to the momentum of the track. A schematic view of the perigee track representation is shown in Figure 7.2.

Track reconstruction becomes an extremely challenging task especially at high pileup, where there are multiple hits in the different ID layers in such dense environment. Dedicated tracking algorithms based on pattern recognition are required to solve this complex combinatorial problem aiming to make the tracking procedure as reliable as possible.

The track reconstruction in ATLAS is typically performed by an algorithm based on an *inside-out* approach, starting from track "seeds"[1] in the pixel and SCT layers

1 Three hits in the silicon detectors are considered as seed.

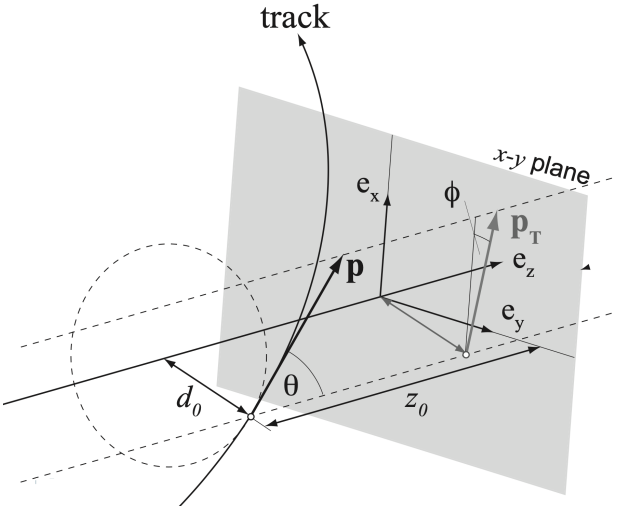



FIGURE 7.2: Illustration of the perigee representation used to describe a reconstructed track [132].

of the ID and extending them into a complete track by adding hits in the outer layers of the ID (mainly TRT) that are matched to the expected trajectory. The additional space points to the track seeds are combined using a Kalman filter [133], an algorithm that creates multiple possible alternatives per track seed trying to eliminate the contribution of "fake" tracks created by false combinations. A score is assigned to each track candidate based on the probability to describe accurately the measured hits. After this score is assigned an additional algorithm is used to resolve the ambiguity between space points that are overlapping among the tracks or are incorrectly assigned.

A complementary *outside-in* algorithm is used that considers all the hits not taken into account by the previous algorithm. This sequence begins with the reconstruction of track segments in the TRT (with seeds from regions indicated by the ECal) and extrapolates them backwards into the pixel and SCT layers. The algorithm is specialised in the reconstruction of tracks originating from secondary vertices that do not satisfy the quality selections imposed by the inside-out algorithm.

The efficiency of the reconstruction algorithms [134] is measured as a function of track $p_{\mathrm{T}}$ and $\eta$ and can be determined from MC simulated data as

$$\varepsilon_{\mathrm{trk}}(p_{\mathrm{T}}, \eta) = \frac{N_{\mathrm{reco}}^{\mathrm{matched}}(p_{\mathrm{T}}, \eta)}{N_{\mathrm{gen}}(p_{\mathrm{T}}, \eta)}. \tag{7.1}$$

The reconstruction efficiency also depends on the quality selections as shown in Figure 7.3 for *Loose* and *Tight-Primary* tracks.

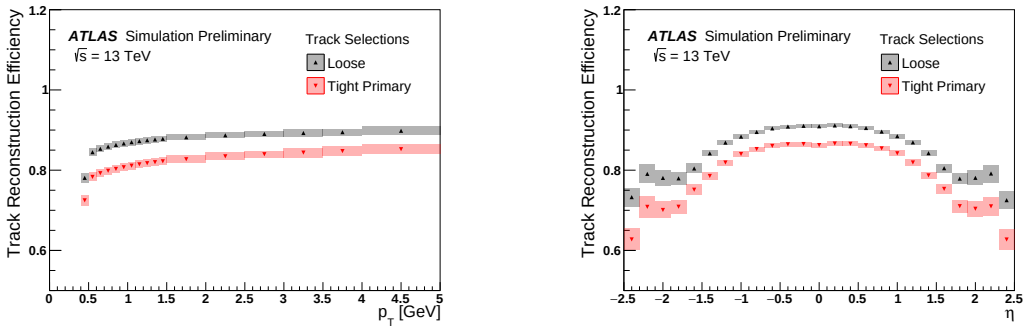



FIGURE 7.3: Track reconstruction efficiency as a function of track $p_{\mathrm{T}}$ (left) and $\eta$ (right) for "Loose" (grey) and "Tight Primary" (red) track working points. The coloured band corresponds to the total systematic uncertainty. Figure taken from Ref. [134].

The interesting tracks in a $pp$ collision are typically the ones originating from the *primary vertex* of the event. The primary vertex (PV) is defined as the vertex with the largest $\sum p_{\mathrm{T}}^2$ of the reconstructed tracks associated to it, and it is considered the hard-scatter vertex of the event. The PV reconstruction begins with a vertex-finding algorithm used to identify the PV candidates based on the reconstructed tracks pointing to them. A subsequent adaptive vertex-fitting algorithm is used to reconstruct the vertex position and estimate the corresponding uncertainties from the covariance matrix. In order to improve the resolution of the PV spatial position the tracks need to satisfy certain conditions to be considered in the reconstruction process. Some of these requirements are to have track $p_{\mathrm{T}} > 500$ MeV, and to have at least 9 (11) hits in the silicon subdetectors for $|\eta| < 1.65$ ($|\eta| > 1.65$) among which at least 1 of them should be in the first two pixel layers [135, 136].

Once the PV is defined the rest of the available vertices are attributed to pileup interactions. The vertices that are reconstructed outside the beam collision region are known as secondary (or displaced) vertices described in more detail in Section 7.4.4.

## 7.2 Electrons

Electrons are charged particles that leave a track in the ID and deposit their energy in the ECal when traversing the ATLAS detector. The electromagnetic showers that are developed are mainly restricted within the ECal without reaching

the outer layers of the detector. The electron reconstruction, identification and calibration procedures are described below.

### 7.2.1 Electron reconstruction

The reconstruction of electron candidates begins from pinpointing the energy clusters in the ECal by using a sliding-window clustering algorithm [137]. This algorithm scans the second layer of the calorimeter (largest one in length) with a $3 \times 5$ granularity in energy towers[2] in order to identify the centres of the energy clusters. The energy clusters are used as seeds and are matched to potential electron tracks reaching from the ID following loose matching criteria ($|\Delta\eta| < 0.05$ and $|\Delta\phi| < 0.05$). Loosely matched tracks are refitted using a Gaussian Sum Filter (GSF) algorithm [138] that provides more accurate results compared to the standard Kalman Filter algorithm by considering electron bremsstrahlung effects and interactions with the material of the detector. Following the cluster-track matching the energy clusters are regrouped into superclusters with a larger window of $3 \times 7$ ($5 \times 5$) towers in the barrel (end-cap) regions. The grouping into superclusters can be formed around seed energy clusters with $E_{\mathrm{T}} > 1$ GeV and it includes energy deposits from secondary showers triggered by the initial electron candidate.

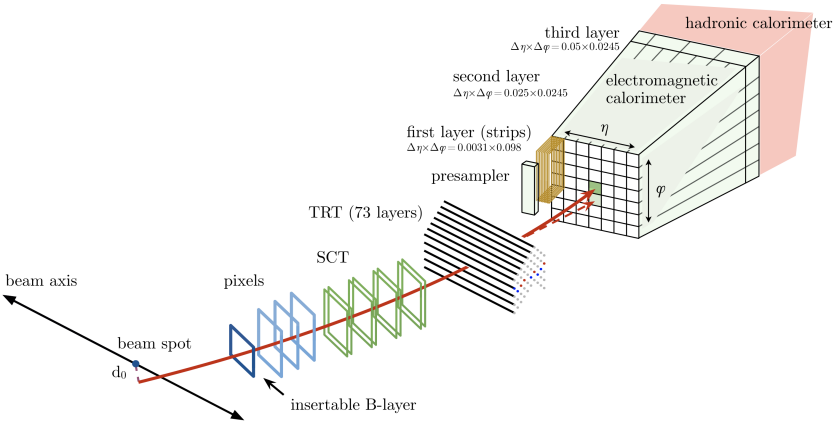



FIGURE 7.4: Illustration of an electron track candidate traversing the different layers of the ATLAS detector that are considered in the electron reconstruction and identification processes [139].

2 Each tower is defined in units of $0.025 \times 0.025$ in $\Delta\eta \times \Delta\phi$ space, as shown in Figure 7.4.

### 7.2.2 Electron identification

The electron reconstruction is followed by the electron identification process, which is performed with a likelihood (LH) based approach. A LH discriminant is been built to distinguish electrons originating directly from the PV (signal) from non-prompt[3] electron tracks (background). The LH discriminant is defined as

$$d_{\mathscr{L}} = \frac{\mathscr{L}_S}{\mathscr{L}_S + \mathscr{L}_B}, \tag{7.2}$$

where $\mathscr{L}_S, \mathscr{L}_B$ are the LH functions for signal and background samples, respectively. The log-transformed shape of the LH discriminant is showed in Figure 7.5.

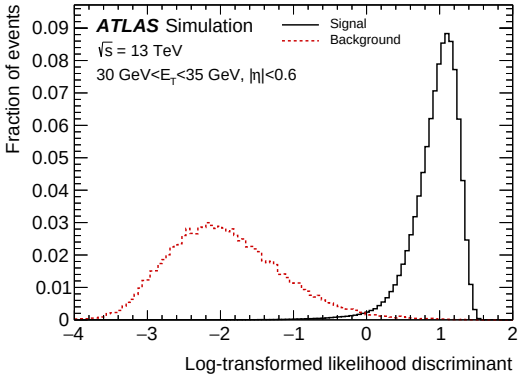



FIGURE 7.5: Log-transformed LH discriminant $d_{\mathscr{L}}{}'$ used in the electron identification for tracks with $30 < E_{\mathrm{T}} < 35$ GeV and $|\eta| < 0.6$. Figure taken from Ref. [139].

The LH is defined as

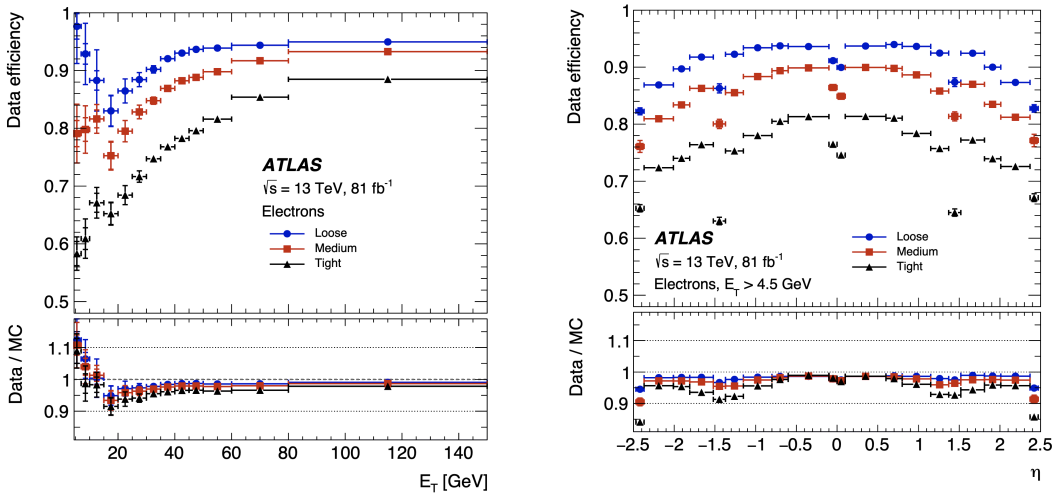
$$\mathscr{L}(\vec{x}) = \prod_{i=1}^{n} P_i(x_i), \tag{7.3}$$

where $P(x)$ stands for the signal or background PDFs and the product runs overs a set of input variables $i$ that demonstrated promising signal versus background separation, exploiting the information from the ID and ECal.

The signal PDFs are extracted from $Z \to e^+e^-$ simulated samples in the high-$E_{\mathrm{T}}$ region and $J/\psi \to e^+e^-$ simulated samples in the low-$E_{\mathrm{T}}$ region. In the same regions the background PDFs are extracted from dijet and minimum bias samples, respectively.

3 As non-prompt sources are considered electrons from photon conversions, from hadronic jets or from heavy-flavour hadron decays.

There are three operating points (OPs) that are commonly used in physics analyses and are defined based on the minimum value of the LH discriminant. These points are known as ***LooseLH***, ***MediumLH***, and ***TightLH*** and are ordered in decreasing identification efficiency with an inversely proportional increase in electron signal purity. The TightLH identification OP is used for electrons candidates in the context of this thesis. The identification efficiency of these OPs in MC samples is shown in Figure 7.6, where it is compared to the corresponding efficiencies in real data.




(a) (b)

FIGURE 7.6: Electron identification efficiencies for LooseLH (blue), MediumLH (red), and TightLH (black) operating points as a function of $E_{\mathrm{T}}$ (a) and $\eta$ (b). The bottom ratio panel shows the data-to-simulation ratio. Figure taken from Ref. [140].

### 7.2.3 Electron isolation

The prompt electrons originating from the PV of the event are in general more isolated compared to non-prompt electrons since the latter can be closer to tracks belonging to the other products of heavy-flavour hadronic decays or photon conversions. For this reason, multiple OPs are defined in ATLAS based on the calorimeter and/or track isolation quantities of an electron candidate to further suppress the non-prompt electron contamination. The calorimeter-based isolation is defined with the variable $E_{\mathrm{T}}^{\mathrm{cone20}}/p_{\mathrm{T}}$, in which the numerator represents the transverse energy sum of energy clusters within a cone of $\Delta R = 0.2$ around the track-matched electron cluster. The track-based isolation is defined with the variable

$p_{\mathrm{T}}^{\mathrm{varcone20}}/p_{\mathrm{T}}$, in which the numerator represents the scalar sum of transverse momentum of tracks within a $p_{\mathrm{T}}$-dependent size cone of $\Delta R = \min(0.2, 10\ \mathrm{GeV}/E_{\mathrm{T}})$. The isolation OP used for the event preselection of the analyses in this thesis is called ***FCLoose*** (or "Loose_VarRad") and it corresponds to $E_{\mathrm{T}}^{\mathrm{cone20}}/p_{\mathrm{T}} < 0.2$ and $p_{\mathrm{T}}^{\mathrm{varcone20}}/p_{\mathrm{T}} < 0.15$. In the main event selection of the same analyses two recently developed OPs are used based on a non-prompt electron veto discriminant trained with several variables as input. The OPs[4] are called ***PLImprovedTight*** and ***PLImprovedVeryTight***, and they offer significantly better non-prompt electron rejection compared to other isolation working points. More details about the (non-) prompt lepton improved veto (PLIV) are given in Section 9.4.3.

### 7.2.4 Electron calibration

The efficiencies of the electron reconstruction, identification and isolation are defined respectively as

$$\varepsilon_{e,\,\mathrm{reco}} = \frac{N_{\mathrm{clust}}^{\mathrm{matched}}}{N_{\mathrm{clust}}}, \quad \varepsilon_{e,\,\mathrm{id}} = \frac{N_{\mathrm{trk}}^{\mathrm{id\,OP}}}{N_{\mathrm{trk}}^{\mathrm{reco}}}, \quad \varepsilon_{e,\,\mathrm{iso}} = \frac{N_{\mathrm{trk}}^{\mathrm{iso\,OP}}}{N_{\mathrm{trk}}^{\mathrm{id}}}. \tag{7.4}$$

The electron reconstruction efficiency is defined as the fraction of the energy clusters matched to a track compared to the total number of energy clusters in the ECal. The electron identification and isolation efficiencies are defined based on the fraction of tracks satisfying an identification or isolation OP to the total number of tracks after reconstruction or identification, respectively. The total electron efficiency is defined as the product of the above efficiencies and the trigger efficiency. The efficiencies in data are estimated using the tag-and-probe method [141, 142] in $Z \to e^+e^-$ and $J/\psi \to e^+e^-$ decays. This method is a data-driven approach in which one of the decay products is "tagged" satisfying tight requirements and the other decay product is "probed" with looser requirements.

The detector simulated samples can only provide approximate results on the above efficiencies due to the complexity of the simulation process. This leads to corrections derived from real data and applied to the MC simulated samples in the form of scale factors (SFs) as mentioned in Section 6.3. The SFs are estimated to deviate only by few percent from unity and they are measured both as a function

4 These OPs were first developed and calibrated in the context of the $t\bar{t}W$ cross-section measurement, which is discussed in Section 9.4.3.

of $E_{\mathrm{T}}$ and $\eta$. The combined uncertainties on electron reconstruction are ∼1% for $E_{\mathrm{T}} < 20$ GeV and at the per-mille level for $E_{\mathrm{T}} \geq 20$ GeV. The uncertainties on electron identification can range from 3% (4%) at $E_{\mathrm{T}} = 4.5$ GeV to 0.1% (0.3%) at $E_{\mathrm{T}} \geq 40$ GeV for the LooseLH (TightLH) operating points [139].

In addition, there are further corrections applied to real and/or MC simulated data related to the electron energy scale and resolution [143]. Data-driven corrections are applied to data to account for the non-uniform effects in detector response and a calibration derived from MC simulated samples is applied to both real and simulated MC data to correct for the electron energy losses before reaching the ECal. The latter is based on a boosted-decision-tree (BDT) approach that incorporates the relative information from the calorimeter. Following these corrections an *in-situ* calibration is further applied to real data in order to account for energy scale corrections and another calibration is applied to the MC simulated data so that the energy resolution matches the one of the data.

## 7.3 Muons

Muons are charged particles that barely interact with the ATLAS calorimeters and are not stopped by some layer of the detector. Instead, they leave tracks in the ID and the MS, where their reconstruction solely relies. The muon reconstruction, identification and calibration procedures are described below.

### 7.3.1 Muon reconstruction

The muon candidate tracks are reconstructed using the combined information from independent measurements in the ID and MS. The muon track reconstruction in the ID depends on the same principles discussed in Section 7.1. In the MS (described in Section 4.2.4) muon track reconstruction begins from the MDT layer, where the combined "hits" are fitted to a straight line in order to build track segments. The segments formed in the central MS layers are then acting as seed-segments that will be extended by nearby hits in the inner and outer MS layers. Afterwards, the seed-segment search is expanded to the inner and outer MS parts. A muon candidate track will consist of the combined segments from different MS

layers, with the requirement of at least two matching segments.[5] A $\chi^2$ fit is performed to assess the probability that the hits associated to each track really correspond to it, and based on this $\chi^2$ value the track candidate is accepted or rejected. The RPC and TGC trigger layers are complementary to determine the $\phi$ coordinate of the track, while the CSC layer is helpful in the reconstruction of tracks at $|\eta| > 2.0$.

Four reconstructed muon types are defined based on the algorithms and subdetectors used to reconstruct the muon tracks, and they are described below.

**Combined muons**: The muon candidate tracks of this category are reconstructed by using the tracking information from both ID and MS subdetectors independently in a global fit. In this second fit the track quality can be improved by the addition or removal of hits in the MS. Typically an outside-in algorithm is used in this category where the track reconstruction begins in the MS and then is extrapolated to the ID.

**Segment-tagged muons**: In this category the muon candidate tracks are reconstructed by combining the ID track with a single MS segment that is the result of muons falling in lower acceptance regions of the MS or because of their low $p_{\mathrm{T}}$.

**Calorimeter-tagged muons**: The reconstructed muon candidate tracks of this category are formed by an ID track pointing to an energy deposit in the calorimeter most probably originating from a minimum-ionising particle, without any track information from the MS. The calorimeter-tagged muons are characterised by a lower purity, but can contribute to recover the acceptance lost for muons falling outside the MS coverage.

**Extrapolated muons**: The reconstruction of the muon candidate tracks in this category is performed based on a MS track satisfying loose quality compatibility criteria to the IP. The extrapolated muon candidates are useful to recover the acceptance in the region $2.5 < |\eta| < 2.7$, where there is no ID coverage.

5 A high-quality single segment can be accepted in the barrel to end-cap transition region.

### 7.3.2 Muon identification

In order to discriminate between the prompt and non-prompt[6] muon tracks several identification OPs are defined in ATLAS to match each analysis needs. The quality criteria for the identification OP definition are subject to the reconstructed muon type and to certain discriminating variables. In particular, for combined muon tracks the identification relies on:

(i) $q/p$ significance, defined as the absolute value of the difference between charge to transverse momentum ratios of the ID and MS muon tracks over quadrature sum of the associated uncertainties

$$\varsigma\,(q/p) = \frac{|(q/p)^{\mathrm{ID}} - (q/p)^{\mathrm{MS}}|}{\sqrt{\sigma(p_{\mathrm{T}}^{\mathrm{ID}})^2 + \sigma(p_{\mathrm{T}}^{\mathrm{MS}})^2}}, \tag{7.5}$$

(ii) $\rho'$ parameter, defined as the absolute value of the muon transverse momentum difference in ID and MS over the transverse momentum of the combined muon

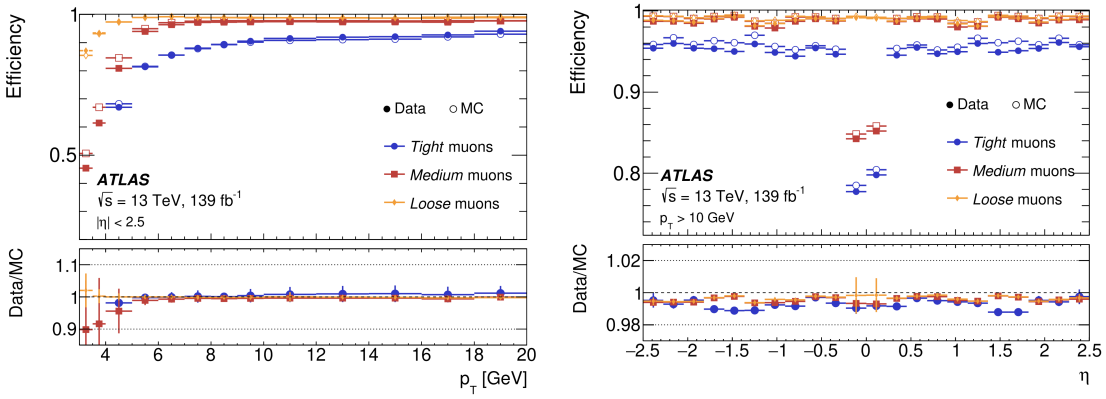
$$\rho' = \frac{|p_{\mathrm{T}}^{\mathrm{ID}} - p_{\mathrm{T}}^{\mathrm{MS}}|}{p_{\mathrm{T}}^{\mathrm{Comb}}}, \quad \text{and} \tag{7.6}$$

(iii) the normalised $\chi^2$ value of the combined track fit.

The muon identification OPs defined are known as ***Loose***, ***Medium***, ***Tight*** and ***High-$p_{\mathrm{T}}$***, increasing in prompt muon purity, but decreasing in prompt muon efficiency. The identification efficiencies of the first three OPs over the total reconstructed muon candidates are estimated as a function of track $p_{\mathrm{T}}$ and $\eta$, as shown in Figure 7.7.

The Medium identification OP is used for the majority of analyses in this thesis, while a hybrid High-$p_{\mathrm{T}}$ identification OP was required in one of them used instead of Medium OP for muons with $p_{\mathrm{T}} > 800$ GeV. In contrast to the other OPs, the purpose of the High-$p_{\mathrm{T}}$ OP is not the suppression of non-prompt muons, but the suppression of the muon $p_{\mathrm{T}}$ mismeasurement, which can be mismodelled by the simulation. In the High-$p_{\mathrm{T}}$ OP at least three hits are required in the MS in order to improve the sagitta measurement, and therefore improve resolution at high $p_{\mathrm{T}}$. Additionally, this OP rejects the muon tracks that fall into poorly aligned MS chambers according to their $\eta$ and $\phi$ coordinates, and it requires that $z(q/p) < 7$.

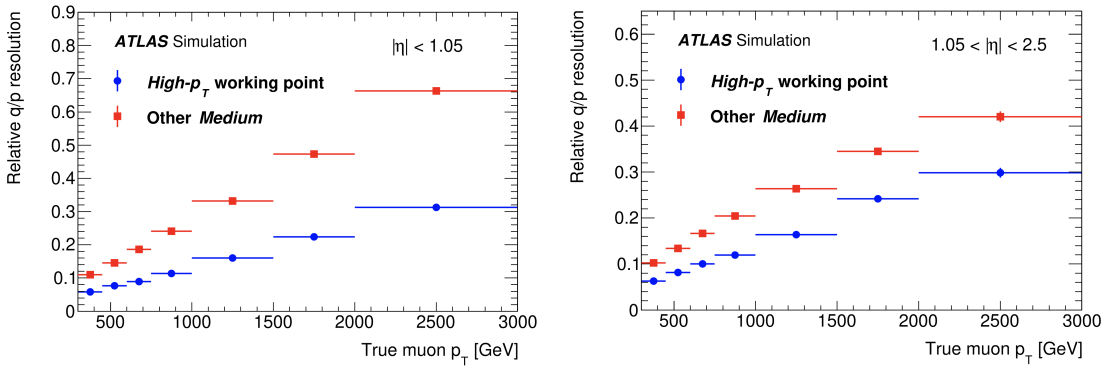
6 As non-prompt muons are considered the ones originating from semileptonic $B$-hadron decays, or in-flight pion or kaon decays.




(a) (b)

FIGURE 7.7: Muon identification efficiencies for Loose (orange), Medium (red), and Tight (blue) operating points as a function of $p_{\mathrm{T}}$ (a) and $\eta$ (b). The bottom ratio panel shows the data-to-simulation ratio. Figure taken from Ref. [144].

The $q/p$ criterion is used to reject muons in the tail of the $\sigma(p_{\mathrm{T}})/p_{\mathrm{T}}$ distributions, with a selection based on the relative uncertainty on the $q/p$ measurement. The relative $q/p$ resolution for the Medium and High-$p_{\mathrm{T}}$ OPs is shown as a function of true muon $p_{\mathrm{T}}$ in Figure 7.8, separately for barrel and end-cap muons. The resolution worsens for both OPs at high $p_{\mathrm{T}}$ followed by a decrease in the identification efficiency, with the High-$p_{\mathrm{T}}$ OP to perform better than the Medium OP in that regime.




(a) (b)

FIGURE 7.8: Muon $q/p$ resolution as a function of true muon $p_{\mathrm{T}}$ for High-$p_{\mathrm{T}}$ (blue) and Medium (red) operating points for barrel (a) and end-cap (b) muons. Figure taken from Ref. [144].

### 7.3.3 Muon isolation

Prompt muons (just like prompt electrons) are typically more isolated from other physics objects than non-prompt muons. Similar isolation quantities to those described in the electron case are adopted for the definition of isolation OPs for muons targeting at suppressing non-prompt muon candidates. The ***FCLoose*** (or "Loose_VarRad") isolation OP was used in the event preselection of the analyses in this thesis, which corresponds to $E_{\mathrm{T}}^{\mathrm{cone20}}/p_{\mathrm{T}} < 0.3$ and $p_{\mathrm{T}}^{\mathrm{varcone30}}/p_{\mathrm{T}} < 0.15$. For the main event selection of the same analyses the ***PLImprovedVeryTight*** and ***PLImprovedVeryTight*** OPs were used based on the (non-) prompt lepton improved veto (PLIV) discriminant that will be discussed more in Section 9.4.3.

### 7.3.4 Muon calibration

Similar to the case of electron candidates the muon candidate efficiencies are estimated with similar relationships to those established in Equation 7.4. The tag-and-probe method is used for efficiency measurements in data based on $Z \to \mu^+\mu^-$ and $J/\psi \to \mu^+\mu^-$ events.

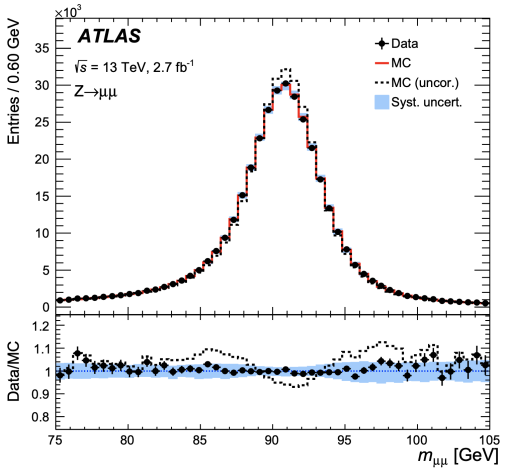



FIGURE 7.9: Dimuon invariant mass distribution before (dashed black line) and after (red line) the momentum correction in $Z \to \mu^+\mu^-$ MC samples. The light blue band corresponds to the systematic uncertainties of the correction. Figure taken from Ref. [144].

A data-driven smearing is applied to the transverse momentum distribution of the muon candidates from these events in the MC simulated samples such that the relative $p_{\mathrm{T}}$ resolution, $\sigma(p_{\mathrm{T}})/p_{\mathrm{T}}$, matches that from the data. The impact

of this smearing is depicted in the dimuon invariant mass distribution, shown in Figure 7.9. Additional correction factors are also derived for the muon scale and resolution separately from the ID and MS measurements.

## 7.4 Jets

Jets are sprays of collimated hadronic showers that are created from quarks and gluons, since because of the colour confinement they cannot exist freely in nature. Jets are in principle halted by the hadronic calorimeters in ATLAS, where they deposit their energy. The jet reconstruction, cleaning, calibration and flavour-tagging techniques are discussed below.

### 7.4.1 Jet reconstruction

Jet reconstruction relies on the formation of topological clusters (*topo-clusters*) [137, 145], three-dimensional clusters that are built based on the jet energy deposition in the calorimeters. The topo-cluster formation is controlled by the cell signal significance, $\varsigma_{\text{cell}}$, which is defined as the ratio of the absolute readout signal from the energy deposition to the total noise from electronics and pileup. A calorimeter cell with $\varsigma_{\text{cell}} \geq 4$ is used as seed and neighbouring cells in the 3D-plane are added to it if they satisfy the condition $\varsigma_{\text{cell}} \geq 2$. The topo-cluster formation ends when nearby cells with $\varsigma_{\text{cell}} > 0$ surrounding the ones with higher $\varsigma_{\text{cell}}$ are also included in the cluster. The energy of the topo-clusters is eventually calibrated based on the EM scale.

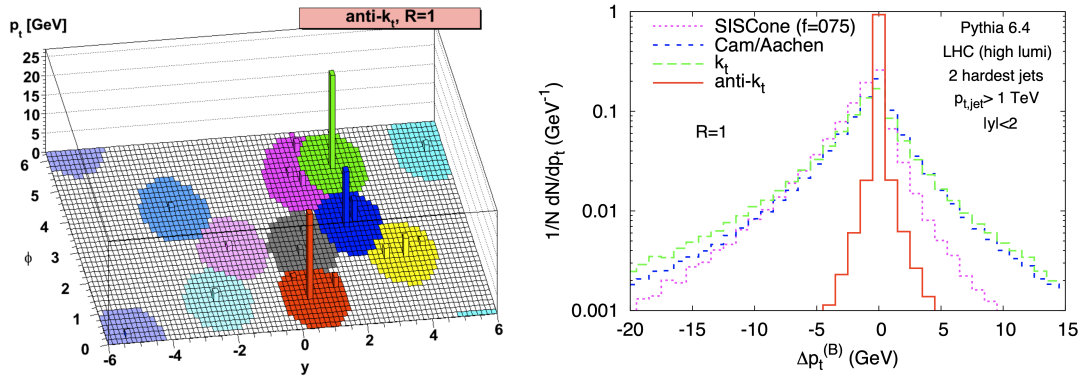
The formed topo-clusters are then associated to jets with dedicated jet-finding algorithms. There is a wide variety of jet-finding algorithms depending on the steps they follow for the topo-cluster grouping. The most common ones are: the Cambridge-Aachen algorithm [146], the $k_t$ algorithm [147], and the anti-$k_t$ algorithm [148]. The anti-$k_t$ algorithm is the one most commonly used in ATLAS and consequently the one used for the reconstruction of jets in this dissertation. It relies on the distance metrics

$$d_{ij} = \min\left(\frac{1}{k_{t,i}^2}, \frac{1}{k_{t,j}^2}\right)\frac{\Delta R_{ij}^2}{R^2}, \tag{7.7}$$

$$d_{iB} = \frac{1}{k_{t,i}^2}, \tag{7.8}$$

where $d_{ij}$ is the distance between two constituents $i, j$ (here topo-clusters) and $d_{iB}$ is the distance of a topo-cluster from the beam axis. In these formulas $k_{t,i}$, $k_{t,j}$ represent the transverse momentum of the two topo-clusters compared, $\Delta R_{ij}$ stands for their angular separation defined as $\Delta R_{ij} = (y_i - y_j)^2 + (\phi_i - \phi_j)^2$, and $R$ is the radius parameter that defines the size of the final reconstructed jet.

The parameter $d_{ij}$ is calculated iteratively for all the topo-clusters and then compared to the $d_{iB}$ parameter for each cluster. If $d_{ij} < d_{iB}$ the contents of $i$ and $j$ are merged, and the process is repeated until $d_{iB} \leq d_{ij}$, with the merged cluster to be classified as a jet and be removed by the cluster input list (together with its subcomponents). The procedure is repeated until all the energy deposits are clustered into a jet.




(a) (b)

FIGURE 7.10: (a) Example of clustering with the anti-$k_t$ algorithm. (b) Probability of back-reaction as a function of net transverse momentum change for various clustering algorithms. Figures taken from Ref. [148].

The anti-$k_t$ algorithm is preferred by the other sequential recombination algorithms for a number of reasons. Apart from being infrared and collinear (IRC) safe, meaning that the formation of the clustered jet will not change by soft emissions or additional collinear splitting of its constituents, it also creates circular cone-shaped jets as shown in Figure 7.10a. This approach offers a more homogenous shape of the hadronic showers in the detector and this approximation is closer to their expected shapes. Additionally, this algorithm is shown to be particularly insensitive to interactions originating from UE and PU an attribute known as *back-reaction*. As shown in Figure 7.10b in a high-PU event the probability of back-reaction is reduced in the case of the anti-$k_t$ algorithm not because of the

amount of the effect itself, but because of the small change in the net transverse momentum of the jet.

### EMTopo and PFlow jets

The standard approach in jet reconstruction was to rely on the energy deposits in the calorimeter for the inputs in the clustering algorithm. The calorimeter is the only part of the detector where there is information about neutral particles, since they do not leave any sign in the tracker. This category of jets is known as *EMTopo* jets and their jet energy resolution is estimated to $\sim 60\%/\sqrt{E_{\text{reco}}}$.

The jets used in the context of this thesis belong to a category known as Particle Flow (*PFlow*) jets [149]. This more recently developed type of jets offers better jet energy resolution by utilising tracking information of the charged particles from the ID in the jet reconstruction. In this way the jet energy resolution is improved to $\sim 30\%/\sqrt{E_{\text{reco}}}$ together with the accuracy of the jet reconstruction. The PFlow jets are constructed using the accurate spatial coordinates of the topo-clusters as 4-vector inputs and the high-resolution measurement of the track momentum. These PFlow objects are used as an input in the anti-$k_t$ algorithm resulting to PFlow jets of a certain $R$.

### Large-$R$ and reclustered jets

The jet radius parameter $R$ determines the size of a jet and it can affect the jet reconstruction as an input to the clustering algorithm. In the analyses of this thesis small-$R$ jets with $R = 0.4$ were used as the standard option for the jet reconstruction. It is possible, however, that the configuration of this jet collection is suboptimal in topologies with very energetic jets. In these boosted regimes the jets are usually very collimated and are better described by single jets with larger radius $R = 1.0$ known as large-$R$ jets.

A more optimal way to obtain jets with larger radius without changing jet collections and with more reasonable total reconstruction uncertainties is by using *reclustered* (RC) jets [150, 151]. In order to construct these objects the standard anti-$k_t$ $R = 0.4$ jets are fed to similar jet-finding algorithms as inputs (instead of the four-vectors that were used for the construction of standard jets). The algorithms merge the small-$R$ jets into jets with larger radius, and as a result the final RC jets are fully calibrated without any additional corrections required.

An illustration of the RC-jets construction is shown in Figure 7.11, where the RC jets are compared to large-$R$ jets of $R = 1.0$. RC jets are divided in two categories: the fixed-radius RC jets with $R = 1.0$ and the variable-size radius RC (varRC) jets. VarRC jets can be computed for any effective clustering radius $R = \rho/p_{\mathrm{T}} \approx 2m/p_{\mathrm{T}}$, offering greater flexibility in targeting the boosted decays of heavier particles like $W, Z$ and Higgs bosons or even top quarks. The value of the $\rho$ parameter depends on the mass of the heavy particle that is being probed such that it is always $R = 1.0$. VarRC jets were studied in the context of a LQ search of this thesis in order to verify whether they could be used as a "pseudo top-tagging" method ($m \geq m_t$) adding the reconstructed LQ mass to the list of observables. Since the signal-to-background separation was not as large as expected in the varRC jet variables, the reclustered jets were not used.

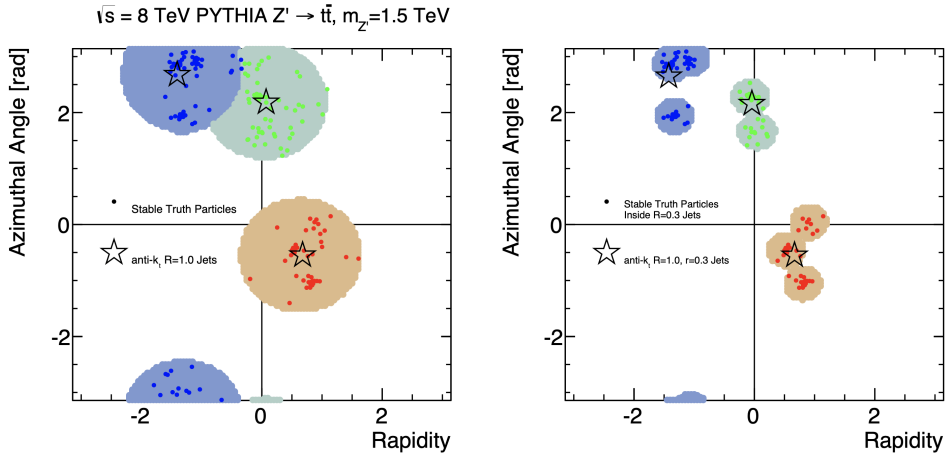



FIGURE 7.11: Example of anti-$k_t$ large-$R$ jets of $R = 1.0$ (left) and reclustered jets of $R = 1.0$ with anti-$k_t$ small-$R$ jets of $R = 0.3$ as input (right). Figure taken from Ref. [150].

### 7.4.2 Jet calibration

The reconstructed jets are being subject to several corrections and calibrations prior to, during and after the reconstruction procedure. A sequence of **jet energy scale (JES)** calibrations is applied to the four-vectors of the reconstructed jets in order to resemble in scale to the truth jets at particle level. These corrections are summarised in a comprehensive flowchart shown in Figure 7.12 and they are listed below:

- **Origin correction**: The jet four-vectors are recalculated on an event-by-event basis to point to the PV of the event, instead of the center of the detector. The correction is applied to the topo-clusters entering the clustering algorithms and the angular jet resolution is improved without a major effect on jet $p_{\mathrm{T}}$.

- **Pileup correction**: Jet reconstruction in dense environments can be affected by pileup interactions that can potentially modify the area and the energy of the reconstructed jets. In order to correct for this effect the $p_{\mathrm{T}}$ of the redundant contributions is subtracted from the reconstructed jet $p_{\mathrm{T}}$ based on the formula

$$p_{\mathrm{T}}^{\mathrm{corr}} = p_{\mathrm{T}}^{\mathrm{reco}} - \rho\, A - \alpha\,(N_{\mathrm{PV}} - 1) - \beta\,\langle\mu\rangle\,. \tag{7.9}$$

  The estimation of the corrected jet $p_{\mathrm{T}}$ relies on the number of PV candidates, on an estimate of the pileup contribution in an area $A$ expressed as $\rho\, A$ (where $\rho$ is the pileup density) and on the derivatives $\alpha = \partial p_{\mathrm{T}}/\partial N_{\mathrm{PV}}, \beta = \partial p_{\mathrm{T}}/\partial\,\langle\mu\rangle$. The jet area $A$ is estimated by introducing a number of "ghost" particles of negligible momentum in a uniform distribution prior to jet reconstruction and checking the fraction of them that get associated to the jet after the clustering. However, a residual dependence on the jet $p_{\mathrm{T}}$ remains even after the subtraction of the $\rho\, A$ term since $\rho$ calculation is not accurate enough in some calorimeter regions.[7] For this reason, the third and fourth terms of Equation 7.9 are used to correct for the dependence on the in-time and out-of-time pileup, respectively.

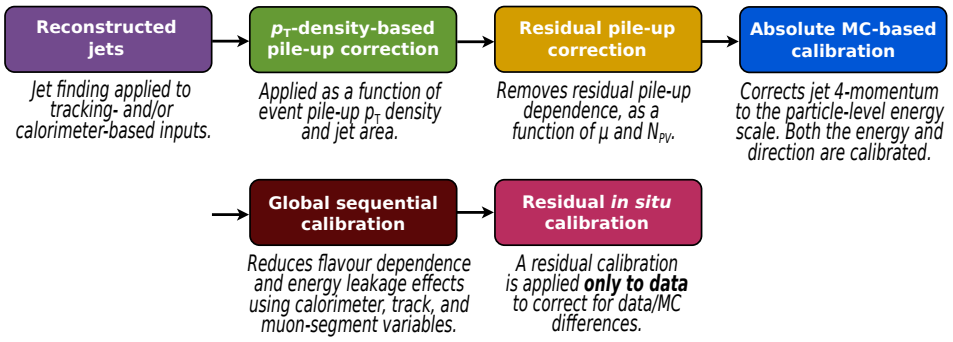



FIGURE 7.12: Flowchart of the JES calibration steps. The corrections are applied to the four-momentum of each jet. Figure taken from Ref. [152].

- **Absolute calibration**: The absolute JES and $\eta$ calibration is derived in order to correct for the difference of the reconstructed jet energy to the jet energy at particle level. The difference between the two can be a result of detector

7 Forward region of the calorimeter or regions containing large fraction of high-$p_{\mathrm{T}}$ jets.

response effects, mismodelling occurred by energy deposits in inactive detector material regions or inefficiencies in the reconstruction process due to the transition between regions of different granularity. This calibration is derived from MC simulated samples with dijet events making use of truth information by matching the reconstructed jets to jets at truth level with a cone of $\Delta R \leq 0.3$. The jet energy response is then defined as $E^{\text{reco}}/E^{\text{truth}}$ and the inverse of this quantity is applied to the reconstructed jets as a correction. Jet energy response is shown in Figure 7.13 as a function of $E^{\text{reco}}$ and $\eta_{\text{det}}$,[8] demonstrating its strong dependence on these variables. In particular, an additional correction is applied as a function of $|\eta_{\text{det}}|$ in order to account for the bias shown in Figure 7.13c.

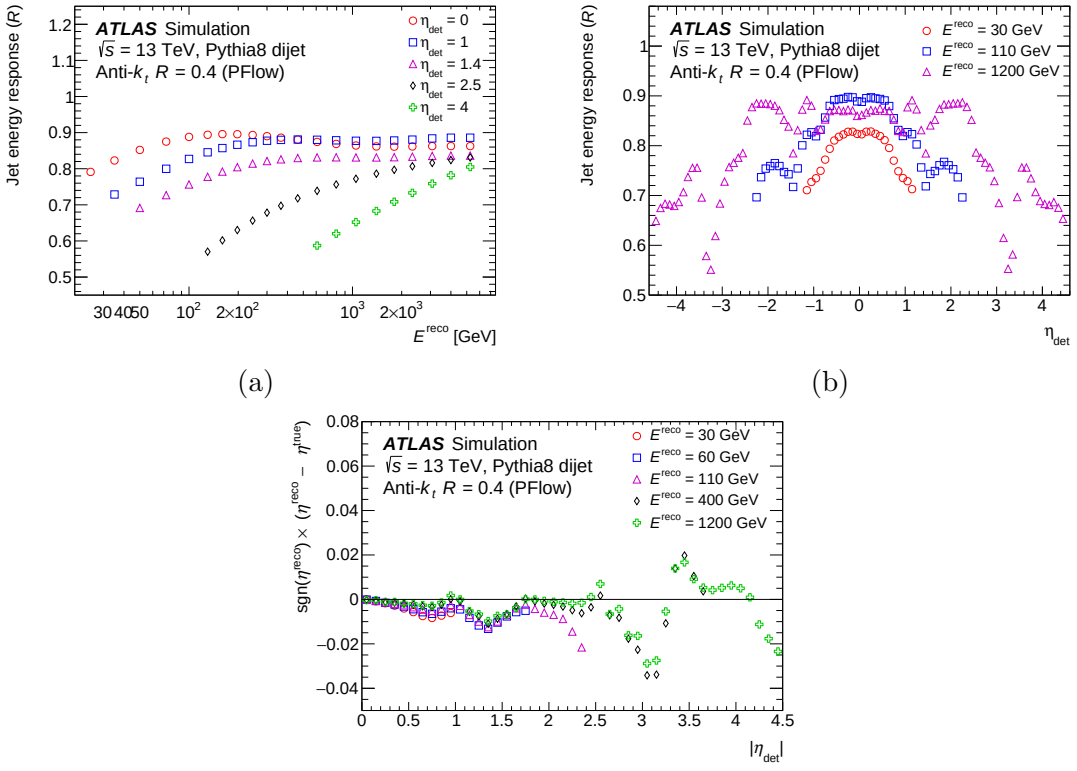


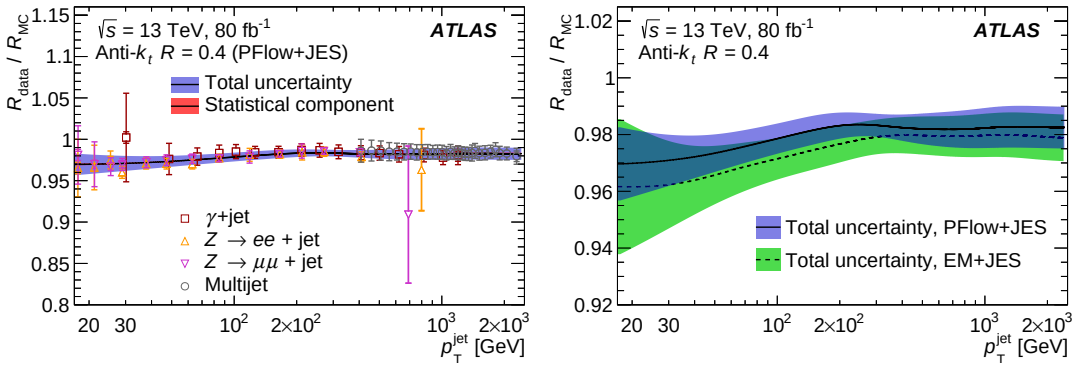

FIGURE 7.13: Jet energy response as a function of (a) $E^{\text{reco}}$ and (b) $\eta_{\text{det}}$ for reconstructed jets with $p_{\text{T}} > 20$ GeV. The signed difference between the truth and reconstructed jet $\eta$ (c) is shown as a function of $\eta_{\text{det}}$. Figures taken from Ref. [152].

- **Global sequential calibration**: The global sequential calibration (GSC) [153] is applied on top of the previous calibrations in order to correct JES for residual dependencies on various other jet variables. For example, strong dependence on

8 Defined as the pseudorapidity measured with respect to the center of the detector (and not with respect to the main PV).

JES is observed based on the origin of the jet, since quark- and gluon-initiated jets can have differences in the jet shape and particle composition. The flavour and energy distribution of the jet constituents are additional parameters that could affect the response of a jet. Therefore, a GSC is applied to the jet four-vectors with one multiplicative factor per jet observable. Jet energy resolution (JER) is also improved by this process through energy deposit information from the calorimeter and from muon chambers (in the case of very energetic jets escaping the calorimeter).

- **In-situ calibration**: A final calibration is only applied to data *in-situ* in order to correct for the differences between the MC simulated samples and the real data. In order to derive these corrections events with dijets (produced back-to-back) are used and the corrections are calculated in $\eta$ regions where the jet $p_{\mathrm{T}}$ is well-balanced ($\eta$-intercalibration). According to that, well-measured central jets ($|\eta| < 0.8$) are used to correct the JES of forward jets ($0.8 < |\eta| < 4.5$) by a multiplicative factor corresponding to the data-to-simulation ratio of the jet $p_{\mathrm{T}}$ response. On the other hand, the central jet response is calibrated using other well-measured objects used as a reference such as $Z$ bosons or photons in $Z$+jets or $\gamma$+jets events, while multi-jet events are used in the calibration of high-$p_{\mathrm{T}}$ jets. The data-to-simulation ratio of the in-situ calibration is shown in Figure 7.14a for all the processes considered, while a comparison to the EMtopo jets is shown in Figure 7.14b.



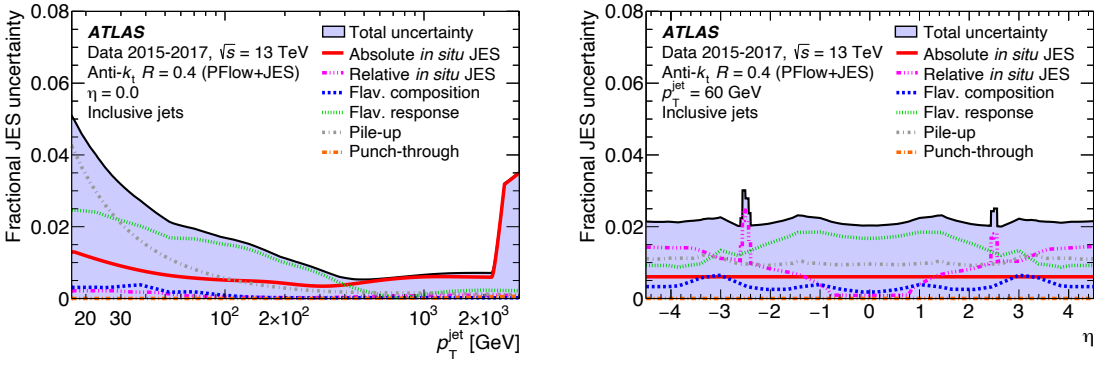

(a) (b)

FIGURE 7.14: (a) Data-to-simulation ratio of PFlow+JES jet response as a function of jet $p_{\mathrm{T}}$ for $Z$+jets, $\gamma$+jets, and multi-jet events calculated for the in-situ calibrations. (b) Comparison of the in-situ JES uncertainty between EMTopo and PFlow jets. Figures taken from Ref. [152].

The uncertainties originating from the above calibration process in Run 2 (80 fb$^{-1}$) are shown in Figure 7.15. The largest part of the uncertainties corresponds to the

in-situ final calibration step with 67 uncertainties related to physics modelling, sample statistics and calibration of other physics objects used to derive these calibrations. Additionally, there are 13 uncertainties related to pileup correction, the flavour composition and the energy distribution of the different jet constituents.

In the most recent configuration this set of systematic uncertainties is reduced to 30 nuisance parameters (NPs) that are commonly used in physics analyses. A number of 14 systematic uncertainties attributed to JER is also included in the calculations derived by variations of jet $p_{\mathrm{T}}$ with respect to the nominal prediction in MC simulated data.




(a) (b)

FIGURE 7.15: Impact of different sources of systematic uncertainty corresponding to JES calibration procedure using $R = 0.4$ anti-$k_t$ PFlow jets as a function of (a) $p_{\mathrm{T}}^{\mathrm{jet}}$ and (b) $\eta$. Figures taken from Ref. [152].

### 7.4.3 Jet vertex tagger and jet cleaning

In order to distinguish the jets originating from the main PV ($\mathrm{PV}_0$) versus the ones originating from pileup interactions a multi-variate analysis (MVA) discriminant is used called **jet vertex tagger (JVT)**. The output of the JVT algorithm (shown in Figure 7.16) corresponds to the probability of a jet originating from $\mathrm{PV}_0$ and a selection based on this quantity is commonly used in physics analyses.

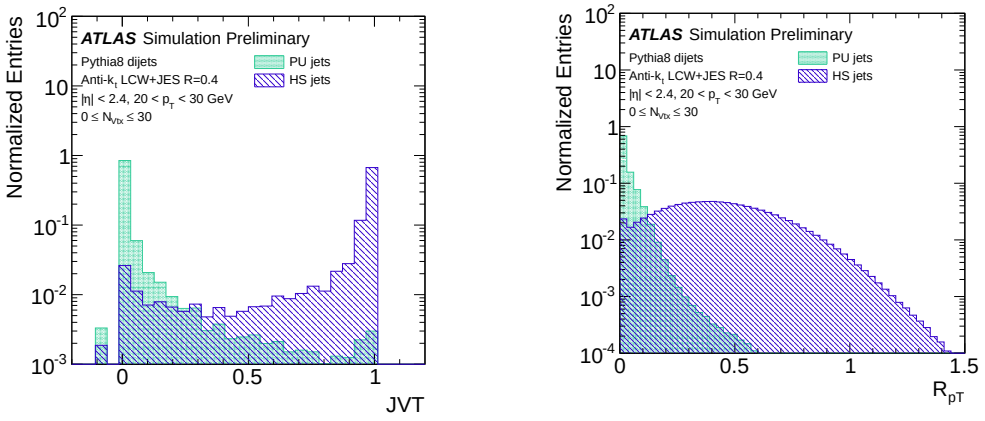
The JVT discriminant is calculated based on the k-nearest neighbour approach including as inputs the **corrJVF** and $\boldsymbol{R_{p_{\mathrm{T}}}}$ variables, which correspond to the corrected jet vertex fraction and the ratio of the $p_{\mathrm{T}}$ scalar sum of the tracks

originating from $\mathrm{PV}_0$ to the jet $p_{\mathrm{T}}$. These variables are defined as

$$\mathrm{corrJVF} = \frac{\sum_m p_{\mathrm{T},m}^{\mathrm{trk}}(\mathrm{PV}_0)}{\sum_m p_{\mathrm{T},m}^{\mathrm{trk}}(\mathrm{PV}_0) + \frac{\sum_{n\geq 1}\sum_l p_{\mathrm{T},l}^{\mathrm{trk}}(\mathrm{PV}_n)}{n_{\mathrm{trk}}^{\mathrm{PU}} \cdot k}}, \qquad R_{p_{\mathrm{T}}} = \frac{\sum_m p_{\mathrm{T},m}^{\mathrm{trk}}(\mathrm{PV}_0)}{p_{\mathrm{T}}^{\mathrm{jet}}}. \tag{7.10}$$

The corrJVF variable is a modified version of the JVF variable, which corresponds to the fraction of $p_{\mathrm{T}}$ scalar sum of the tracks associated to $\mathrm{PV}_0$ to the $p_{\mathrm{T}}$ scalar sum of all the tracks associated to a PV. The correction lies on the term $n_{\mathrm{trk}}^{\mathrm{PU}} \cdot k$ that was added in order to suppress the rapid increase of the denominator at very high pileup events ($k = 10^{-3}$).

The JVT discriminant is optimised separately for central ($|\eta| < 2.5$) and forward jets ($|\eta| > 2.5$). In the forward region a similar discriminant (fJVT) is used as described in [154]. A systematic uncertainty corresponding to the JVT selection is added in physics analyses.




(a) (b)

FIGURE 7.16: JVT discriminant score (a) and $R_{p_{\mathrm{T}}}$ distribution (b) distinguishing jets originating from the hard-scatter main PV (violet) from jets from pileup interactions (green) at the $20 < p_{\mathrm{T}}^{\mathrm{jet}} < 30$ GeV and $|\eta^{\mathrm{jet}}| < 2.4$ region. The negative JVT entries correspond to jets with no associated track. Figures taken from Ref. [155].

Apart from the JVT implementation to remove the jets that do not originate from the main PV, there is a dedicated jet cleaning procedure in order to remove fake jets not belonging to a $pp$ collision. Typical sources of fake jets are muons originating from beam losses ("beam-induced" background) or muons from cosmic radiation. These muons could leave minor energy deposits at the HCal that could

be interpreted as jets, while a similar effect can also occur from the coherent noise in the calorimeter.

The presence of fake jets is mitigated by several quality criteria based on tracking information to reconstruct variables sensitive to this background, the shape of ionisation signal in the LAr calorimeter and the energy ratios at different calorimeter layers. These criteria led to the definition of two OPs used to distinguish versus fake jets, *BadLoose* and *BadTight*. The efficiency of these OPs is 99.5% and 95% for $20 < p_{\mathrm{T}}^{\mathrm{jet}} < 100$ GeV and 99.9% and 99.5% for $p_{\mathrm{T}}^{\mathrm{jet}} > 100$ GeV, respectively. The BadLoose OP is chosen for the studies presented in this thesis.

### 7.4.4 Jet flavour tagging

The idea of jet flavour tagging relies on the ability to identify jets based on the initial parton from which they originate. Jets originated from the hadronisation of $b$-quarks are referred to as "$b$-jets", jets originated from the hadronisation of $c$-quarks are referred to as "$c$-jets", and jets originated from the hadronisation of gluons and $u$- or $d$-quarks are referred to as light-flavour jets ("light-jets"). The categorisation of a jet as $b$-jet is known as *b-tagging* and it has been of great importance in physics especially for signatures with large number of $b$-quarks in the final state. The study of the top-quark (decaying as $t \to Wb$) is strongly dependent on reliable $b$-tagging algorithms, while these algorithms could contribute to Higgs boson studies through $H \to b\bar{b}$ decays.

The algorithms used for $b$-tagging exploit the characteristic lifetime of $B$-hadrons ($\sim 1.5 \cdot 10^{-12}$ s), that corresponds to a travelled distance of $c\tau \sim 4.5$ mm inside the detector before they decay. A secondary vertex is created at their decay point with large transverse and longitudinal impact parameters $d_0$ and $z_0$, as shown in Figure 7.17. These attributes are used together with tracking information of jet associated tracks as input to low-level algorithms. The outputs of the low-level algorithms are combined in high-level algorithms designed to achieve the highest possible $b$-tagging efficiency, while maintaining low mistag rates.

The low-level algorithms are categorised based on the following attributes:

**Impact Parameter (IP)**: The algorithms in this category exploit the large transverse and longitudinal impact parameters (defined in Section 4.2.1) of $b$-jets compared jets of other flavour. Traditionally, the two algorithms in ATLAS making

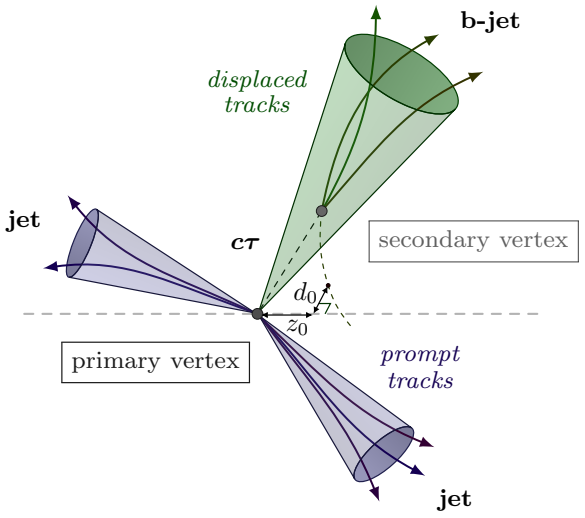



FIGURE 7.17: Topology of a $b$-jet emphasising the parameters that are exploited in $b$-tagging algorithms.

use of these parameters are called IP2D and IP3D [156]. The former is making use of the signed significance of the transverse impact parameter ($d_0/\sigma_{d_0}$), and the latter develops a two-dimensional template that additionally includes the significance of the longitudinal impact parameter ($z_0 \sin\theta/\sigma_{z_0}$). These algorithms need to assume that all tracks are independent, but a more advanced method was recently introduced to take into account track-to-track correlations using a recurrent neural network [157].

**Secondary Vertex Finding**: The algorithms in this category specialise in the identification of jets with a single secondary vertex compatible to the $B$-hadron decay. The most widely known algorithm of this type in ATLAS is called SV1 [156] and is based on a likelihood discriminant exploiting track information. A set of all two-track vertex candidates is identified and the track pairs most likely to belong to decays of long-lived particles ($K_S, \Lambda$), photon conversions or hadronic interactions with the material of the detector are removed. The rest of the tracks are used for the secondary vertex reconstruction.

**Multi-Vertex Finding**: Similarly to the previous category multi-vertex finding algorithms are used to identify jets with more than one secondary vertices. It is quite common a $B$-hadron to subsequently decay into a $D$-hadron corresponding to the decay of a $b$- into a $c$-quark. This additional secondary vertex is often very close to the first one and the low resolution does not allow the individual reconstruction of the two vertices. A dedicated algorithm called JetFitter [158] is

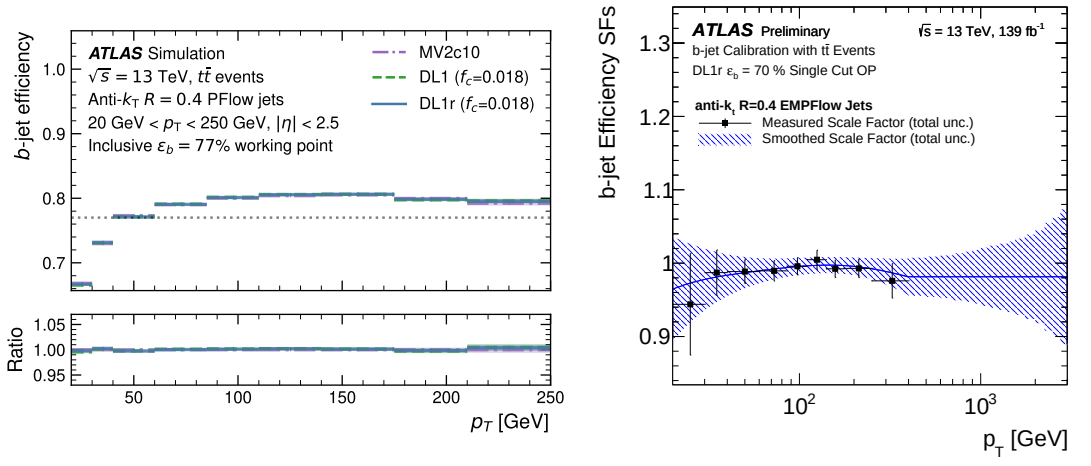
used for this reason aiming to reconstruct the full decay chain of a $B$-hadron using a modified Kalman filter and assuming that all the vertices lie on the same axis.

## High-level *b*-tagging algorithms

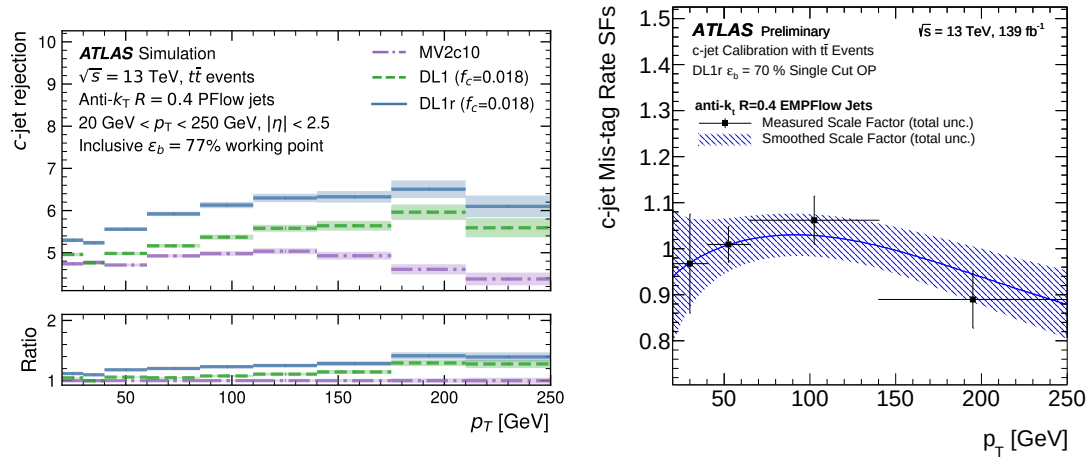
The outputs of the low-level algorithms described above are included as inputs in high-level $b$-tagging algorithms that are either using MVA techniques or deep neural networks (DNNs) to classify the probability of a jet originating from a $b$-,$c$- or light-quark. There is a constant development in the high-level algorithms used in ATLAS and the recommendations for physics analyses are evolving rapidly. The most common high-level $b$-tagging algorithms in ATLAS are described below.

**MV2c10**: The MV2c10 algorithm [159] relies on MVA techniques using BDTs for the discrimination between $b$-, $c$- and light-jets. It is trained on $t\bar{t}$ MC simulated events providing a final discriminant with a score corresponding to the probability of a jet to originate from a $b$-quark. The difference of the MV2c10 algorithm with the rest of the MV2 algorithms is the dedicated treatment of $c$-jets, with the number in the name indicating the approximate $c$-jet fraction included in the background sample used in the training (here the exact number is 7%). MV2c10 algorithm was the recommended one in ATLAS for a large part of Run 2, but it is currently mentioned only for historical reasons since most of the current analyses have already moved to $b$-tagging algorithms from the DL1 family.

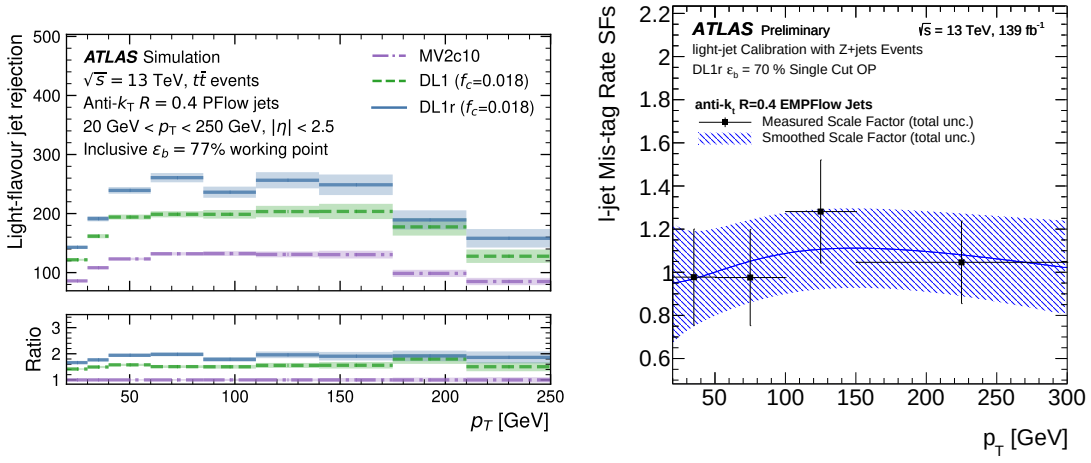
**DL1(r)**: The DL1 algorithm [161] uses a DNN approach providing a multi-dimensional discriminant as output that corresponds to the three probabilities of a jet to originate from a $b$-, $c$- or light-quark, respectively. The DL1 algorithm makes use of the low-level variables described above (IP2D, IP3D, SV1 and JetFitter outputs) as inputs. The increased performance and the great separation achieved in the case of the DL1 algorithms is demonstrated in Figure 7.19, where the DL1 discriminant is compared to the MV2 one. A more recent version of this algorithm, known as DL1r, is developed in a similar way. Its only difference is that it includes an additional input from an advanced IP estimation algorithm that uses a recurrent neural network (RNNIP) [157]. As shown in the left column of Figure 7.18 in general the DL1r algorithm provides largest $c$- and light-jet rejection compared to the DL1 and MV2 ones as a function of jet $p_{\mathrm{T}}$.




(a)



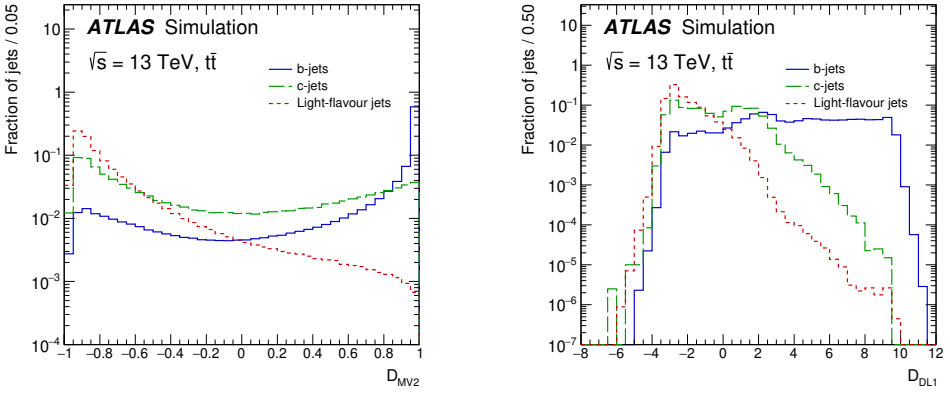

(b)




(c)

FIGURE 7.18: Identification efficiency (left) and scale factors (right) for $b$-jets (a). Rejection rate (left) and mistag rate (right) for $c$-jets (b) and light-jets (c). Figures taken from Refs. [160, 161].

The analyses presented in this thesis use one of the DL1 or DL1r algorithms, according to the recommendations at each time. OPs are defined based on these taggers targeting a specific $b$-jet acceptance efficiency that is inversely proportional to the mistag probability. These OPs correspond to 60%, 70%, 77% and 85% $b$-tagging efficiency, respectively, with the 60% being the tightest and the 85% being the loosest. A different OP is used in each of the analysis in this thesis according to sensitivity results from optimisation studies.



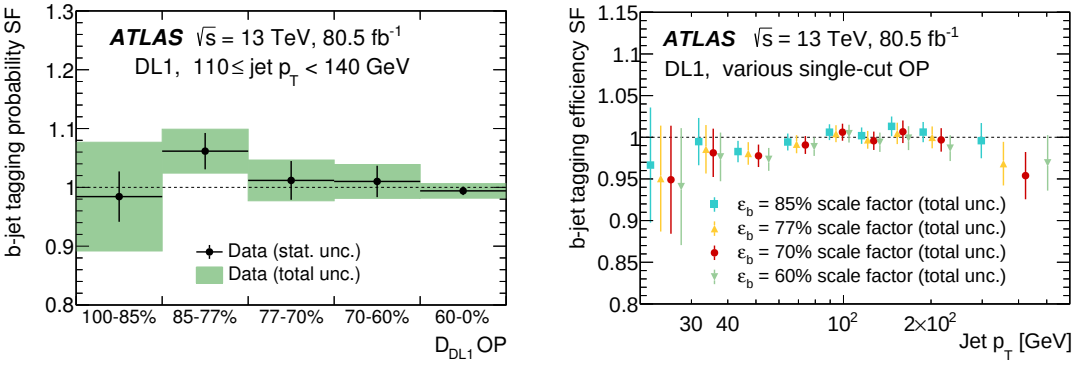

(a) (b)

FIGURE 7.19: MV2c10 (a) and DL1 (b) discriminants used for $b$-tagging computed in $t\bar{t}$ simulated events and split based on truth jet flavour to $b$- (blue), $c$- (green) and light-jets (red). Figures taken from Ref. [162].

## $b$-tagging calibration and uncertainties

In order to derive the $b$-tagging efficiencies the corresponding taggers need to be trained on MC simulated datasets in order to have access to truth information concerning the flavour of a jet. Therefore, multiplicative SFs need to be applied to the simulated data in order to address potential differences with real data. These SFs are defined as $\mathrm{SF}_{b-\mathrm{tag}} = \varepsilon_{\mathrm{data}}/\varepsilon_{\mathrm{MC}}$ and they are derived together with their corresponding uncertainties.

The calibration of **$b$-jet** events is derived in $t\bar{t}$ samples requiring two leptons of opposite charge ($2\ell$OS) in the final state, making it enriched in $b$-jets. The efficiency SFs and jet flavour composition are derived using a combinatorial likelihood approach in a range of $20 < p_{\mathrm{T}}^{\mathrm{jet}} < 600$ GeV, while an extrapolation needs to be made for jets with $p_{\mathrm{T}}^{\mathrm{jet}} > 600$ GeV. These SFs are shown for all the $b$-tagging OPs in Figure 7.20b together with their total uncertainties that range from 1% to 8% at high- and low-$p_{\mathrm{T}}^{\mathrm{jet}}$, respectively.




(a) (b)

FIGURE 7.20: (a) Scale factors (SFs) for exclusive $b$-tagging OPs and (b) efficiency SFs for various $b$-tagging operating points defined based on the DL1 discriminant [162].

In the calibration procedure it should be taken into account that the $b$-tagger algorithm could mistag $c$- or light-jets as $b$-jets. As a result a proper calibration needs to be derived for the mistag efficiencies as well. The calibration of ***c*-jet** events [163] is performed by estimating the $c$-jet mistag rate using a likelihood fit approach in semileptonic $t\bar{t}$ events to exploit the hadronic $W$ decay originating from one of the top-quarks. The derived SFs are shown for DL1r tagger at the 70% efficiency OP in Figure 7.18b (right), together with their total associated uncertainties ranging from 3% to 17% at high- and low-$p_{\mathrm{T}}^{\mathrm{jet}}$, respectively.

The calibration of **light-jet** events is performed with two methods [164]. The most established one is known as the negative-tag method and it is based on similar discriminating variables as in $b$-tagging, but with reversed signs. This method is based on the assumption that the signed IP distribution of light-jets should be more symmetrical around zero compared to the one from $b$-jets. The same tagging criteria are applied for the estimation of the mistag rate, which is defined as the negative-tag efficiency. The second method is known as the adjusted-MC method, where MC simulated events are modified to match the tracking performance in data and the mistag rate SFs are given as the ratio of the efficiency in the MC-adjusted samples to the efficiency of the initial MC samples. The mistag rates are derived from multi-jet events and they are shown for the negative-tag method at the DL1r 70% OP in Figure 7.18c (right), together with their corresponding total uncertainties. The uncertainties can range from 18% to 39% for this OP at high- and low-$p_{\mathrm{T}}^{\mathrm{jet}}$, respectively.

In the studies of this thesis there are 60 systematic uncertainties taken into account

corresponding to $b$-tagging (20), and mistag rates from $c$-jets (20) and light-jets (20).

## 7.5 Hadronically decaying tau-leptons

### 7.5.1 Hadronic tau reconstruction

Tau-leptons are charged particles that can decay either leptonically (35%) or hadronically (65%). Due to their short decay length (87 $\mu m$) they mostly decay before reaching the pixel subdetector in the ID, and they are detected by their decay products. Since the leptonic tau-lepton decays result in light leptons and have a smaller branching ratio, the interest is focused mainly on the hadronic tau-lepton decays that are discussed in this section. Among the hadronic tau-lepton decay products there are typically one (72%) or three (22%) charged pions in addition to one neutrino,[9] which can be produced together with one or more neutral pions (68% of the times). Due to this signature, the hadronic tau-leptons are identified in the detector as narrow jets with one (one-prong) or three (three-prong) tracks associated to them. The reconstruction of hadronic tau-leptons is based on the sum of all visible decay products (since the neutrinos of the decay cannot be reconstructed), and they are referred to as $\tau_{\text{had-vis}}$ or $\tau_{\text{had}}$.

The reconstruction of $\tau_{\text{had-vis}}$ candidates begins from energy deposits in the calorimeter that are used as seeds for jets. The topo-clusters associated to these energy deposits are calibrated with a local hadronic calibration and are used as inputs in the anti-$k_t$ jet algorithm to form jets with $R = 0.4$. Only central jets ($|\eta| < 2.5$) with $p_{\text{T}} > 10$ GeV are considered in this process. The barycentre of the topo-clusters involved is used to define the seed jet axis, which is matched to a track pointing to a PV in the event. In the case of $\tau_{\text{had-vis}}$ candidates with high $p_{\text{T}}$ this PV coincides with the main PV of the event ($\text{PV}_0$) with tracks of $p_{\text{T}} > 500$ MeV within a cone of $\Delta R < 0.2$ around the jet axis [165, 166].

Tracks are categorised as *core* and *isolation* with a BDT approach depending on their $p_{\text{T}}$, the number of hits in the tracking detectors and their impact parameters ($d_0$, $z_0$). Core tracks are defined as those within a cone of $\Delta R < 0.2$ around the jet axis, while the isolation tracks fall within a region of $0.2 < \Delta R < 0.4$ around

9 The fractions refer to the total of hadronic tau decays.

it. Core tracks are the only ones considered in the $\tau_{\text{had-vis}}$ reconstruction, while isolation tracks are used for the definition of variables used in the identification of $\tau_{\text{had-vis}}$ candidates. The $\tau_{\text{had-vis}}$ tracks in both categories are required to have $p_{\text{T}} > 1$ GeV, at least two associated hits in the pixel subdetector of ID, and a total of at least seven hits in the pixel and the SCT subdetectors. The tracks are also required to have $|d_0| < 1.0$ mm and $|z_0 \sin\theta| < 1.5$ mm. The reconstruction efficiency of the $\tau_{\text{had-vis}}$ $p_{\text{T}}$ remains almost constant in the high-$p_{\text{T}}$ region for 1-prong candidates and it deteriorates a bit for 3-prong candidates, as shown in Figure 7.23

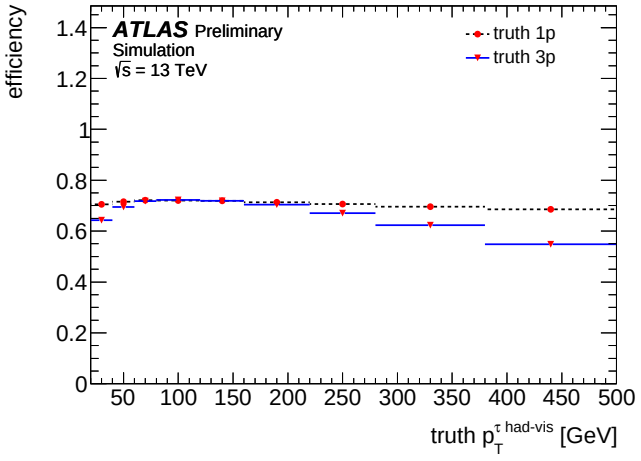



FIGURE 7.21: Reconstruction efficiency as a function of $\tau_{\text{had-vis}}$ $p_{\text{T}}$ for one- (black dashed line) and three-prong (blue solid line) candidates. Figure taken from Ref. [167].

### 7.5.2 Hadronic tau identification

A RNN approach is used in ATLAS for the identification of $\tau_{\text{had-vis}}$ candidates that replaced the previous BDT approach due to the significant gain in performance achieved with the RNN algorithm [165]. Various low-level variables related to tracks and clusters are used in the RNN training, together with high-level variables calculated from track and calorimeter quantities. In particular, the low-level variables make use of the cluster moments and transverse energy, the track momentum and impact parameters, the angular distances $\Delta\eta$ and $\Delta\phi$ and the number of track hits in the different subdetector layers. The high-level variables rely on more complex quantities such as the transverse flight path significance ($S_{\text{T}}^{\text{flight}}$), central

energy fraction ($f_{\text{cent}}$), maximum track $\Delta R$, track momentum, mass of core and isolation tracks, and so forth [165].

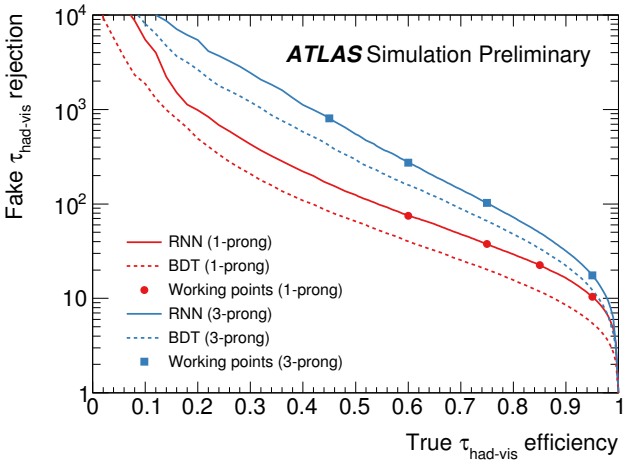
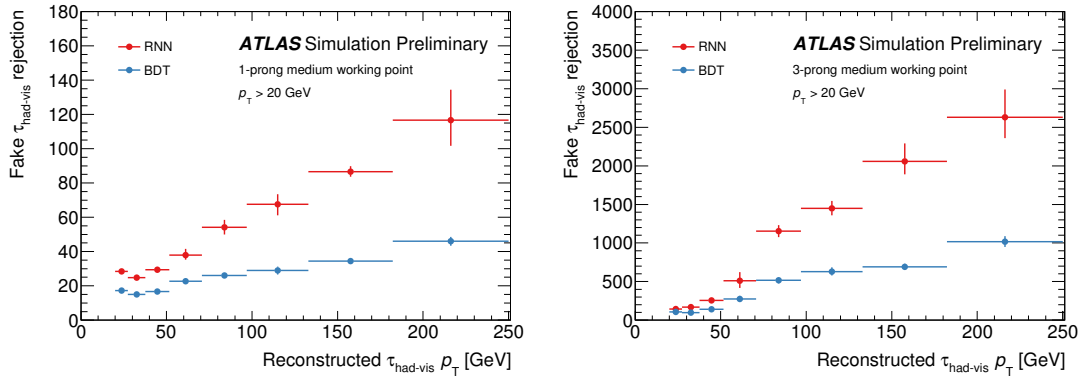



FIGURE 7.22: ROC curves comparing the fake $\tau_{\text{had-vis}}$ rejection as a function of real $\tau_{\text{had-vis}}$ efficiency obtained from the BDT- (dashed line) and RNN (solid line) approaches for one- (red) and three-prong (blue) $\tau_{\text{had-vis}}$ candidates. Figure taken from Ref. [165].

The RNN training is based on $Z/\gamma^* \to \tau\tau$ simulated events that are required to decay hadronically. The challenging purpose of the RNN $\tau_{\text{had-vis}}$ ID is to successfully identify the real $\tau_{\text{had-vis}}$ candidates by rejecting fake $\tau_{\text{had-vis}}$ candidates originating from quark- or gluon-initiated jets. There are four OPs recommended for RNN $\tau_{\text{had-vis}}$ ID labelled as ***VeryLoose***, ***Loose***, ***Medium***, and ***Tight***, based on the signal efficiency and fake $\tau_{\text{had-vis}}$ rejection. The Loose and Medium ID OPs are used in the LQLQ$\to t\tau t\tau$ analysis described in this thesis. The ROC (Receiver Operating Characteristic) curves demonstrating the higher fake $\tau_{\text{had-vis}}$ rejection at the same true $\tau_{\text{had-vis}}$ efficiency of the RNN versus the older BDT approach are shown in Figure 7.22 for these four OPs and separately for one- and three-prong $\tau_{\text{had-vis}}$ candidates. Apart from the RNN classification an additional BDT discriminant trained on $Z \to e^+e^-$ events is used specifically for the rejection against electron candidates as part of the $\tau_{\text{had-vis}}$ ID. An OP of (75) 60% real $\tau_{\text{had}}$ efficiency is used, with a rejection factor of (40) 300 for (1-) 3-prong candidates, which is dependent on $\tau_{\text{had-vis}}$ $p_{\text{T}}$ and $|\eta|$.

In the RNN approach the rejection power is improved at higher values of $\tau_{\text{had-vis}}$ $p_{\text{T}}$ as shown for the Medium OP in Figure 7.23. The RNN method improved significantly the $\tau_{\text{had-vis}}$ ID in ATLAS allowing for dedicated studies including hadronically decaying tau leptons, which were overlooked in the past.




(a) (b)

FIGURE 7.23: Comparison of fake $\tau_{\text{had-vis}}$ rejection as a function of reconstructed $\tau_{\text{had-vis}}$ $p_{\text{T}}$ for the Medium identification operating point obtained from the BDT (blue) and RNN (red) approaches for (a) one- and (b) three-prong $\tau_{\text{had-vis}}$ candidates. Figure taken from Ref. [165].

### 7.5.3 Hadronic tau calibration

Following the identification of the $\tau_{\text{had-vis}}$ candidates, their measured energy is corrected for detector effects by a dedicated calibration procedure [167]. The limited acceptance and efficiency of the detector are the main sources of the detector effects, which are reduced due to inactive detector material regions, incomplete coverage and non-uniformity of the detector. There are two calibrations available in ATLAS: the baseline calibration and the Boosted Regression Tree (BRT) calibration.

The calibration process begins with a standard local calibration (LC) [168], which is applied to all jet-like objects. The calibration is further improved by using information from the tracker for a more precise result. This process becomes complicated due to the nature of the tau decay involving neutral pions. The energy deposits of these particles with zero electric charge can overlap with the deposits of the charged pions, and it is often difficult to distinguish between the two since neutral pions do not leave any track when traversing the ID. Moreover, the calibration process takes into account that there could be tracks associated to the tau decay that are found outside of the core region, resulting in an underestimation of the $\tau_{\text{had-vis}}$ energy. In addition to this, tracks from pileup (PU) interactions or from the UE can also interfere in the measurement, as shown in Figure 7.24.

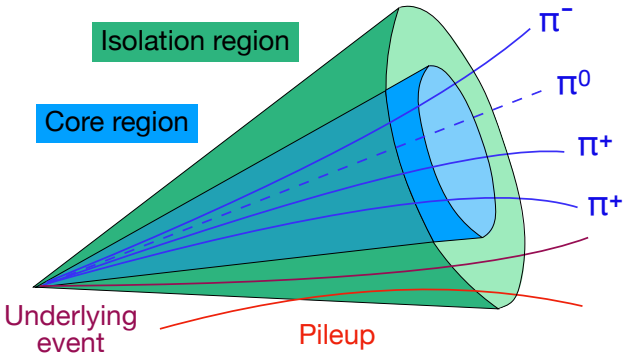



FIGURE 7.24: Illustration of a hadronic tau-lepton decay, where the core and isolation regions are highlighted. Potential tracks from pileup interactions and the underlying event are also overlaid.

Therefore, the correction on the $\tau_{\text{had-vis}}$ energy is estimated using the formula

$$E_{\text{calib.}} = \frac{E_{\text{LC}} - E_{\text{PU}}}{\mathcal{R}(E_{\text{LC}} - E_{\text{PU}},\ |\eta|,\ n_p)}, \tag{7.11}$$

where $E_{\text{LC}}$ corresponds to the sum of $\tau_{\text{had-vis}}$ energy in the core region ($\Delta R < 0.2$) after the LC, $E_{\text{PU}}$ is the sum of the energy originating from PU and UE, $n_p$ is the number of associated tracks (one or three) and $\mathcal{R}$ stands for the detector response calibration. $\mathcal{R}$ is defined as the Gaussian mean of the $(E_{\text{LC}} - E_{\text{PU}})/E^{\text{vis}}_{\text{true}}$ distribution, where $E^{\text{vis}}_{\text{true}}$ corresponds to energy of the generated $\tau_{\text{had-vis}}$. $E_{\text{PU}}$ is expressed as a function of the number of primary vertices ($N_{\text{PV}}$), $|\eta|$ and $n_p$, exhibiting a linear increase proportional to the increase in $N_{\text{PV}}$. $E_{\text{PU}}$ is therefore estimated by the formula

$$E_{\text{PU}}(N_{\text{PV}},\ |\eta|,\ n_p) = A(|\eta|,\ n_p) \cdot (N_{\text{PV}} - \langle N_{\text{PV}} \rangle), \tag{7.12}$$

where $A$ is a linear coefficient extracted from a fit to simulated data.

The baseline calibration is sufficient for $\tau_{\text{had-vis}}$ candidates with high $p_{\text{T}}$, while the resolution begins to degrade at low $p_{\text{T}}$. Therefore, in analyses with less energetic $\tau_{\text{had-vis}}$ candidates the BRT calibration is selected. The BRT multivariate method is an improved version of the baseline calibration that additionally includes Tau Particle Flow (TPF) [169] information, together with calorimeter and tracking information. The precise tracking information on the measurement of charged pions significantly improves the resolution of $\tau_{\text{had-vis}}$ candidates at low $p_{\text{T}}$, as shown in Figure 7.25.

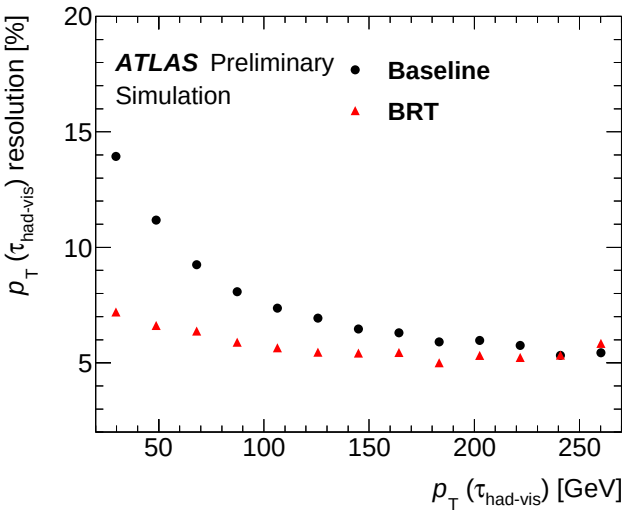



FIGURE 7.25: Comparison of the $\tau_{\text{had}-\text{vis}}$ energy resolution between the baseline and BRT calibration as a function of $p_{\text{T}}(\tau_{\text{had}-\text{vis}})$. Figure taken from Ref. [170].

Further corrections are applied based on the difference of real and simulated data by an in-situ measurement of the Tau Energy Scale (TES) using $Z \to \tau\tau$ events. The energy of the $\tau_{\text{had}-\text{vis}}$ candidates is recalculated as $E_{\text{T}} \to (1+\alpha)E_{\text{T}}$, where $\alpha$ is a correction factor estimated by a $\chi^2$ minimisation. The uncertainty on the TES correction factor is estimated to be (2%) 3% for (one-) three-prong $\tau_{\text{had}-\text{vis}}$ candidates. The tag-and-probe method is used to evaluate the performance of the energy calibrations and the efficiency of the identification algorithms. The efficiency SFs are close to unity with an uncertainty of about (5%) 6% for (one-) three-prong $\tau_{\text{had}-\text{vis}}$ candidates [167, 170].

Finally, there are additional corrections applied related to the tau trigger identification efficiency and the misidentification probability of an electron as a decay product of a hadronic tau-lepton. The former is measured with an uncertainty of 3-8% for $p_{\text{T}}(\tau_{\text{had}-\text{vis}}) < 100$ GeV and 8-14% for $100 < p_{\text{T}}(\tau_{\text{had}-\text{vis}}) < 300$ GeV, and the latter with an uncertainty of 3-14%, with a dependence on the $|\eta|$ of the $\tau_{\text{had}-\text{vis}}$.

## 7.6 Missing transverse energy

Some of the particles produced in a $pp$ collision are very weakly interacting with matter and as a result they do not leave any tracks or energy deposits in the detector. Since the reconstruction of these particles is not possible their presence is

indirectly detected through the energy imbalance that occurs in the corresponding events. This imbalance is observed at the transverse plane, where due to momentum conservation the vector sum of the transverse momentum of all particles in the event should be equal to zero. It is expressed as a variable called *missing transverse energy*, $E_{\mathrm{T}}^{\mathrm{miss}}$, calculated by the formula

$$\vec{E}_{\mathrm{T}}^{\,\mathrm{miss}} = -\sum \vec{p}_{\mathrm{T}}^{\,e} - \sum \vec{p}_{\mathrm{T}}^{\,\mu} - \sum \vec{p}_{\mathrm{T}}^{\,\tau} - \sum \vec{p}_{\mathrm{T}}^{\,\mathrm{jets}} - \sum \vec{p}_{\mathrm{T}}^{\,\gamma} - \sum \vec{p}_{\mathrm{T}}^{\,\mathrm{soft-terms}}. \quad (7.13)$$

$E_{\mathrm{T}}^{\mathrm{miss}}$ is defined as the negative vector sum of the $p_{\mathrm{T}}$ of all physics objects such as electrons, muons, jets, photons and hadronically decaying tau-leptons (*hard term*) together with the negative sum of all the tracks not used in the reconstruction of a physics object but associated to the PV (*soft term*). It is commonly attributed to the transverse momentum of a neutrino in the event, but it can also serve as a probe for BSM physics that can manifest as weakly interacting particles not predicted by the SM.

# Chapter 8

# Common aspects in signatures with multiple leptons and $b$-jets

This chapter provides an overview of the commonalities in the datasets, region categorisation, background modelling, object and event selection, and template fit method that are used in the analyses of this thesis involving multiple leptons and $b$-jets in their final states. It focuses on the techniques used for the background suppression and estimation, while there is an extensive discussion about the systematic uncertainties used in the corresponding studies. Moreover, the statistical formalism is introduced explaining the methods used for the interpretation of the physics results. The analyses that are studied involve LQ searches in $t\ell t\ell$ ($\ell = e, \mu$) and $t\tau t\tau$ final states and the cross-section measurement of the $t\bar{t}W$ process. Despite their common characteristics there are subtle differences among them, which will be stressed below if needed.

## 8.1 Data and simulated samples

### Collision dataset

In the studies of this thesis the full Run-2 dataset is used, corresponding to 139 fb$^{-1}$ of $pp$ collision data at $\sqrt{s} = 13$ TeV, collected by the ATLAS experiment during the period 2015-2018 with a bunch crossing of 25 ns. The data considered

correspond only to the periods when all detector subsystems were operational and there were stable beam conditions during data taking.

From the total amount of data collected, only a portion of it is suitable for physics analysis. These events are specified in the Good Run List (GRL) that corresponds to each period of data taking. The GRL files considered are listed below:

- **2015**: data15_13TeV.periodAllYear_DetStatus-v89-pro21-02_Unknown_PHYS_StandardGRL_All_Good_25ns.xml,
- **2016**: data16_13TeV.periodAllYear_DetStatus-v89-pro21-01_DQDefects-00-02-04_PHYS_StandardGRL_All_Good_25ns.xml,
- **2017**: data17_13TeV.periodAllYear_DetStatus-v99-pro22-01_Unknown_PHYS_StandardGRL_All_Good_25ns_Triggerno17e33prim.xml,
- **2018**: data18_13TeV.periodAllYear_DetStatus-v102-pro22-04_Unknown_PHYS_StandardGRL_All_Good_25ns_Triggerno17e33prim.xml.

After the GRL selection, there are additional event quality requirements that need to be satisfied. The problematic events are removed by using predefined flags, avoiding in this way to discard the whole luminosity block.

## Simulated MC samples

The estimation of most of the background processes is performed using simulated MC samples. Most of them are produced in full simulation going through the complete ATLAS detector simulation based on GEANT4, and only a small fraction of them is produced in fast simulation (AF2), namely the samples corresponding to $tWH$, $tHqb$ and rare top-quark decay processes. The signal samples used in the LQ analyses are also produced in AF2. A comparison between the FS and AF2 simulated samples showed that the difference in the targeted observables is minor. The in- and out-of-time pileup effects are modelled with minimum-bias interactions generated with PYTHIA-8 [171] using the A3 set of tuned parameters [172] (often referred to as the "tune"), and overlaid onto the simulated hard-scatter events according to the luminosity profile of the recorded data. The pileup distribution acquired by this procedure is reweighed to reflect the average number of pileup interactions in data. The produced simulated events have been corrected in order to match the object reconstruction and identification efficiencies, energy scales

and energy resolutions from real data, as explained in Chapter 7. An overview of the background processes used in the analyses of this thesis is shown in Table 8.1, corresponding to the most up-to-date versions used ($t\bar{t}W$ analysis). Due to the earliest time scale of the LQLQ$\rightarrow t\tau t\tau$ analysis, older generator versions might have been used for some processes. Note that in the $t\bar{t}W$ measurement the $t\bar{t}W$ process in this table is treated as signal.

| Process | Generator (alternative) | Parton Shower (alternative) | PDF | Tune |
|---|---|---|---|---|
| $LQ_3^d\overline{LQ_3^d}$ | MadGraph5_aMC@NLO | Pythia-8 | NNPDF 3.0 NLO | A14 |
| $LQ_{mix}^d\ \overline{LQ}_{mix}^d$ | MadGraph5_aMC@NLO | Pythia-8.230 | NNPDF 3.0 NLO | A14 |
| $\tilde{U}_1\ \tilde{\bar{U}}_1$ | MadGraph5_aMC@NLO | Pythia-8.244 | NNPDF 2.3 LO | A14 |
| $t\bar{t}W$ | Sherpa-2.2.10 (MadGraph5_aMC@NLO) | Sherpa-2.2.10 (Pythia-8) | NNPDF 3.0 NNLO | Sherpa default |
| $t\bar{t}H$ | Powheg-Box (Powheg-Box) (MadGraph5_aMC@NLO) | Pythia-8 (Herwig-7) (Pythia-8) | NNPDF 3.0 NLO (NNPDF 3.0 NLO) (NNPDF 3.0 NLO) | A14 (H7-UE-MMHT [117]) (A14) |
| $t\bar{t}t\bar{t}$ | MadGraph5_aMC@NLO | Pythia-8 | NNPDF 3.0 NNLO | A14 |
| $t\bar{t}Z$ | MadGraph5_aMC@NLO (Sherpa-2.2.10) | Pythia-8 (Sherpa-2.2.10) | NNPDF 3.0 NNLO NNPDF 3.0 NNLO | A14 Sherpa default |
| $t\bar{t}\gamma$ | MadGraph5_aMC@NLO | Pythia-8 | NNPDF 2.3 LO | A14 |
| Rare top | MadGraph5_aMC@NLO | Pythia-8 | NNPDF 2.3 LO | A14 |
| $t\bar{t}$ | Powheg-Box (Powheg-Box) (MadGraph5_aMC@NLO) (aMC@NLO) | Pythia-8 (Herwig-7.1) (Pythia-8) (Herwig-7.1) | NNPDF 2.3 LO | A14 |
| Single-top ($s$-/$t$-channels) | Powheg-Box | Pythia-8 | NNPDF 2.3 LO | A14 |
| $tW$ | Powheg-Box | Pythia-8 | NNPDF 2.3 LO | A14 |
| $t\bar{t}WW$ | MadGraph5_aMC@NLO | Pythia-8 | NNPDF 2.3 LO | A14 |
| $tZq$ | MadGraph5_aMC@NLO | Pythia-8 | NNPDF 3.0 NLO | A14 |
| $tWZ$ | MadGraph5_aMC@NLO | Pythia-8 | NNPDF 2.3 LO | A14 |
| $tWH$ | MadGraph5_aMC@NLO | Pythia-8 | NNPDF 2.3 LO | A14 |
| $tHqb$ | MadGraph5_aMC@NLO | Pythia-8 | NNPDF 2.3 LO | A14 |
| $ttt$ | MadGraph5_aMC@NLO | Pythia-8 | NNPDF 2.3 LO | A14 |
| $VV$ | Sherpa-2.2.2 | Sherpa-2.2.2 | NNPDF 3.0 NNLO | Sherpa default |
| $VVV$ | Sherpa-2.2.2 | Sherpa-2.2.2 | NNPDF 3.0 NNLO | Sherpa default |
| $ggVV$ | Sherpa-2.2.2 | Sherpa-2.2.2 | NNPDF 3.0 NNLO | Sherpa default |
| $V$ + jets | Sherpa-2.2.1 | Sherpa-2.2.1 | NNPDF 3.0 NNLO | Sherpa default |
| $VH$ | Pythia-8 | Pythia-8 | NNPDF 2.3 LO | A14 |
| $V\gamma$ | Sherpa-2.2.8 | Sherpa-2.2.8 | NNPDF 3.0 NNLO | Sherpa default |

Table 8.1: Overview of MC samples used to simulate the different signal and background processes. The alternative samples used for the derivation of the systematic uncertainties are shown in the same entries. Information on the generator and parton shower is also included.

Apart from differences in the generator version it is worth mentioning that in the LQ analyses the nominal $t\bar{t}Z$ sample was the one produced from Sherpa due to its better kinematic modelling, while in the $t\bar{t}W$ analysis the MadGraph $t\bar{t}Z$ sample was selected as the nominal due to its better supported model for systematic uncertainties incorporated from the $t\bar{t}Z$ measurement [173]. An older

MadGraph version was used for the simulation of the nominal $t\bar{t}W$ sample in the LQLQ $\to t\tau t\tau$ analysis, while also some minor background contributions such as $tWH$, $tHqb$ and $V\gamma$ were not included.

## 8.2 Background modelling

In this section the modelling of the major background samples is discussed. There is no specific order in the discussion of the samples since the main background process are analysis and channel dependent.

### 8.2.1 $t\bar{t}W$ production

The theoretical modelling of the $t\bar{t}W$ process is very challenging due to higher-order effects in the strong QCD coupling ($\alpha_S$) and the electroweak coupling ($\alpha$) becoming critical for this process, as discussed in Section 2.5. The modelling of this process has been studied through its production by different MC generators. These samples are generated in general in two components (for QCD and electroweak contributions respectively) and are detailed below:

- A Sherpa-2.2.10 sample (QCD), which includes additional weights accounting for the subleading electroweak (EW) interference effects.
- A standalone LO Sherpa-2.2.10 sample (EW).
- MadGraph5_aMC@NLO sample (QCD) with FxFx merging scheme.
- MadGraph5_aMC@NLO sample (QCD) with improved FxFx merging scheme.
- Inclusive NLO MadGraph5_aMC@NLO sample (QCD) without including any information about subleading EW interference effects.
- A LO MadGraph5_aMC@NLO sample (EW).
- Powheg-Box + Pythia-8 samples (QCD) and subleading EW corrections.
- Powheg-Box + Herwig-7 samples (QCD) and subleading EW corrections.

The Sherpa sample was decided to be the nominal sample due to its better modelling, and some of the rest were used for the derivation of the modelling

systematic uncertainties. In particular, **shower**-related systematics are derived through a comparison of the PYTHIA versus HERWIG POWHEG-BOX samples. The **generator**-related systematics are derived through a comparison of the nominal SHERPA sample versus the main alternative from MADGRAPH5_AMC@NLO with the improved FxFx merging scheme. Both comparisons are performed once the cross sections of the alternative samples have been normalised to that of the nominal sample.

The reference cross section for $t\bar{t}W$ QCD production is 597 fb before the application of the EW related weights. After these EW internal weights are applied in order to account for normalisation and shape effects, the reference cross section is reduced by ∼4% to 573.68 fb. A reference cross section of 42.1 fb is used for the $t\bar{t}W$ EW component. All $t\bar{t}W$ alternative samples are normalised to these cross sections according to their component (QCD or EW).

The renormalisation and factorisation scales $(\mu_R, \mu_F)$ of the nominal SHERPA sample are set to $\mu_R = \mu_F = H_T/2$, where the $H_T$ variable is defined as

$$H_T = \sum_i m_{\mathrm{T},i} = \sum_i \sqrt{m_i^2 + p_{\mathrm{T},i}^2}\,, \tag{8.1}$$

with the sum running over all outgoing partons $i$ in the matrix element calculation.

The sample is generated at NLO ME accuracy for up to 1j and at LO accuracy for up to 2j. The additional partons are matched and merged with the SHERPA parton shower based on Catani-Seymour dipole factorisation using the MEPS@NLO prescription with CKKW [174, 175] merging scale of 30 GeV. The virtual QCD correction for matrix elements at NLO accuracy is provided by the OPENLOOPS2 [176] library, which is combined with the Comix [177] package. The samples are generated using the NNPDF 3.0 NNLO PDF set.

The alternative $t\bar{t}W$ FxFx samples have the same precision as the nominal SHERPA sample ensuring a fair comparison for the derivation of the corresponding uncertainty.

### 8.2.2 $t\bar{t}Z/\gamma^*$ production

In the $t\bar{t}W$ measurement the $t\bar{t}Z$ background process is modelled with simulated samples using the MADGRAPH5_AMC@NLO generator at NLO accuracy with

the NNPDF 3.0 NLO PDF set. The top-quark mass is set to 172.5 GeV and top-quark decays are generated at LO using MadSpin [127] to preserve spin correlations. Pythia-8 generator is being used for the PS and the hadronisation procedure using the NNPDF 2.3 LO PDF set and the A14 tune. Hadronic decays into $b$- and $c$-quarks are simulated using the EvtGen [126] package. The $t\bar{t}Z/\gamma^*$ sample is normalised to the cross section $\sigma(t\bar{t}Z/\gamma^*) = 839$ fb calculated at NLO accuracy for both QCD and EW components using MadGraph5_aMC@NLO as reported in [21] and scaled by an off-shell correction estimated at one-loop level in $\alpha_S$.

The modelling systematic uncertainties of the $t\bar{t}Z$ process include the production of $t\bar{t}Z$ alternative samples interfaced with Herwig instead of Pythia in order to account for the difference in the PS, hadronisation and UE modelling. There are also alternative samples available still interfaced with Pythia, but with different A14 tune variations in order to account for this effect. Finally, the scales $\mu_R$ and $\mu_F$ are varied similarly to the $t\bar{t}W$ process to account for the ISR- and FSR-related uncertainties.

In the LQ analyses the nominal $t\bar{t}Z$ sample is generated with Sherpa both for the ME and the PS calculations, using the NNPDF 3.0 NNLO PDF set and the default Sherpa tune. This sample is generated at higher precision compared to the MadGraph one, and it also demonstrates better modelling at a large number of kinematic variables ($m_{\text{eff}}$, $H_{\text{T, lep}}$, etc.). In these analyses, the MadGraph sample is used as the alternative sample to account for the differences due to generator choice, and the varRF systematics are included as already discussed.

The nominal $t\bar{t}Z$ samples are produced for $m_{\ell^+\ell^-} > 5$ GeV, where $m_{\ell^+\ell^-}$ corresponds to the dilepton $Z$-boson mass. Dedicated samples are generated to model the rare top-quark radiative decays $t \to Wb\gamma^*(\to \ell^+\ell^-)$ and $t\bar{t} \to W^+bW^-\bar{b}\ell^+\ell^-$, using a ME calculation at LO accuracy and requiring $m_{\ell^+\ell^-} > 1$ GeV. The LO cross section from the $t\bar{t} \to W^+bW^-\bar{b}\ell^+\ell^-$ sample is scaled by a factor of 1.54, based on comparisons between the NNLO+NLL and LO cross sections for $t\bar{t}$ production [178–182]. These samples are "stitched" together during the physics analysis, so that the rare top-quark decays only cover the phase space of $1 < m_{\ell^+\ell^-} < 5$ GeV. The combined contribution of the above processes is often denoted in the next chapters as $t\bar{t}Z/\gamma^*$ or $t\bar{t}Z/\gamma^*$ (high-mass).

The additional contribution from internal photon conversions ($\gamma^* \to \ell^+\ell^-$) is modelled in an inclusive POWHEG-BOX + PYTHIA-8 $t\bar{t}$ sample representing the QED multiphoton radiation via PS for $m_{\ell^+\ell^-} < 1$ GeV, which is denoted as $t\bar{t}\gamma^*$ (low mass or LM). Dedicated $Z$+jets samples enriched in electrons from material photon conversion ($\gamma^* \to e^+e^-$) or internal photon conversion are generated with POWHEG-BOX + PYTHIA-8 for the modelling of the material and internal conversion contributions in the dedicated conversion-enriched control regions (in the $3\ell$ channel), as explained in Chapter 9.

### 8.2.3 $t\bar{t}H$ production

The samples simulating the $t\bar{t}H$ background process are generated with the POWHEG-BOX generator at NLO accuracy and with the NNPDF 3.0 NLO PDF set. The $h_{damp}$[1] parameter for this sample is set to $3/4\ (m_t + m_{\bar{t}} + m_H) = 325$ GeV. The generated events are interfaced to PYTHIA-8 with the A14 tune, and using HDECAY [21, 183] to calculate the Higgs decay branching ratios. The $t\bar{t}H$ sample is normalised to 507 fb, which is computed at NLO in QCD with NLO electroweak corrections [21, 124, 184–190].

The systematic uncertainties due to the initial- and final-state radiation (ISR and FSR) are estimated using weights in the ME and in the PS. The scales $\mu_R$ and $\mu_F$ are varied by a factor of 0.5 (2.0) to simulate higher (lower) parton radiation, using the var3c up (down) variation of the A14 tune (*varRF* systematics). The systematic uncertainties concerning the ME and PS modelling are estimated through comparisons with the corresponding alternative samples.

### 8.2.4 $t\bar{t}$ and single-top production

The $t\bar{t}$ process is modelled by simulated samples generated using the POWHEG-BOX generator with a NLO ME calculation, and interfaced with PYTHIA-8 for the PS (A14 tune). The NNPDF 3.0 NLO PDF and NNPDF 2.3 LO PDF sets are used for the ME and PS, respectively. The $h_{damp}$ parameter is set to $1.5\,m_t$.

1 This parameter controls the transverse momentum ($p_T$) of the first additional emission beyond the LO Feynman diagram in the PS and therefore regulates the high-$p_T$ emission against which the $t\bar{t}$ system recoils.

Alternative $t\bar{t}$ MC samples are generated to account for uncertainties related to the modelling of non-prompt leptons. The POWHEG-BOX + HERWIG-7.1.3 and SHERPA-2.2.10 samples are used for this comparison. Further details about the systematics model based on these contributions are given in Section 8.5.

The contribution of the single top-quark process is modelled in the s- and t-channels using the same generators as in $t\bar{t}$ production (POWHEG-BOX + PYTHIA-8). The $tW$ process is modelled separately with the same generator configuration. The diagram removal scheme [191] is used to avoid overlaps between $t\bar{t}$ and $tW$ final states.

### 8.2.5 Diboson production

Diboson production is modelled with simulated samples generated with SHERPA-2.2.2 with a ME calculation at NLO accuracy in QCD for up to one additional parton and at LO accuracy for up to three additional partons, using the Comix and OpenLoops libraries. The PS matching with SHERPA is performed using the MEPS@NLO prescription. The NNPDF 3.0 NNLO PDF set is used including the set of tuned PS parameters proposed by the SHERPA authors. The samples are normalised to the reference cross section of $\sigma(VV) = 104$ pb, and include contributions from $ZZ$, $WZ$ and $WW$ production resulting in different final states. The varRF systematics are derived in a similar way as in the other processes by varying up and down the $\mu_R$ and $\mu_F$ scales.

### 8.2.6 $V$+jets production

The $V$+jets processes are modelled with simulated samples from SHERPA-2.2.1 generator using NLO calculations in the ME for up to two partons, and LO calculations for up to four partons using the Comix and OpenLoops libraries. The PS matching with SHERPA is performed using the MEPS@NLO prescription including the set of tuned parameters proposed by the SHERPA authors. The NNPDF 3.0 NNLO PDF set is used and the samples are normalised to the NNLO prediction. There are separate samples produced for $Z$+jets and $W$+jets accounting also for their different final states.

## 8.3 Object reconstruction and selection

### 8.3.1 Framework and derivations

The event preselection and object reconstruction, cleaning and calibration are performed using "GroupFramework 1" (GFW1) [192], a derivation framework based on AnalysisTop and its standard object containers. This framework is used to produce common root files for each physics process from different derivations. TOPQ1 derivations are used in the LQLQ $\rightarrow t\tau t\tau$ analysis processed with AnalysisTop version 21.2.96, while HIGG8D1 derivations are used in the rest of the analyses included in this thesis, which were processed with AnalysisBase version 21.2.196 (no need to setup AnalysisTop separately any more). The GFW1 output is processed by "GroupFramework 2" (GFW2) [193], where an event-level selection is performed and further useful analysis variables are defined.

The statistical analysis is performed based on the GFW2 output using the TRExFitter framework [194, 195].

### 8.3.2 Object and event preselection

#### Event preselection

The event preselection starts from the primary vertex finding based on the highest $\sum p_{\mathrm{T}}^2$ of the associated tracks, where the sum runs over all the associated tracks with transverse momentum $p_{\mathrm{T}} > 0.5$ GeV, as described in Section 7.1. Events with significant noise in the calorimeters or data corruption are removed by using the corresponding flags about LAr or Tile errors.

#### Trigger selection

Trigger selection information is saved at the preselection level for all single-lepton and dilepton triggers (SLT and DLT) making the combination of them easier at the late stages of the analysis chain if needed. Dilepton triggers are used in the $t\bar{t}W$ measurement, a choice supported by relevant sensitivity studies, while a logical

OR of single-lepton and dilepton triggers is used in the LQ analyses in order to increase the signal acceptance.

Electron and muon triggers [196–198] are combined for the selection of the events. Each trigger satisfies certain identification criteria and has a predefined $p_{\mathrm{T}}$ threshold, which varies depending on the year of operation and the lepton type. The $p_{\mathrm{T}}$ thresholds of the single-electron triggers are 24 (26) GeV, 60 (60) GeV and 120 (140) GeV for data taken in 2015 (2016-2018). The $p_{\mathrm{T}}$ thresholds of the single-muon triggers are 20 (26) GeV and 50 (50) GeV for data taken in 2015 (2016-2018). The identification criteria are relaxed in the single-electron triggers with the higher $p_{\mathrm{T}}$ thresholds, while the low-$p_{\mathrm{T}}$ threshold single-lepton triggers with various lepton isolation requirements are combined with the high-$p_{\mathrm{T}}$ threshold triggers with looser or no isolation requirements in a logical OR way.

The $p_{\mathrm{T}}$ thresholds of the dielectron trigger are 12 GeV, 17 GeV and 24 GeV for the data taken in 2015, 2016 and 2017-2018, respectively, while both electrons should satisfy the loose identification criteria. The $p_{\mathrm{T}}$ thresholds of the dimuon trigger are 8 (8) GeV and 18 (22) GeV for data taken in 2015 (2016-2018). The $p_{\mathrm{T}}$ thresholds of the electron+muon trigger are 17 (14) GeV for the electron (muon) candidate for data taken in 2015-2018, while the electron candidate is required to also satisfy the loose identification criteria.

In the DLT case the events are required to satisfy the lowest-$p_{\mathrm{T}}$ threshold unprescaled trigger chains for $ee$, $e\mu$ and $\mu\mu$ events, as shown in Table 8.2.

In the SLT OR DLT case the events are required to either satisfy the lowest-$p_{\mathrm{T}}$ threshold unprescaled dilepton triggers defined above or satisfy the corresponding single-lepton triggers shown in Table 8.3.

## Object preselection

The loosest set of physics objects stored in the GFW2 output root files ("ntuples") is often known as preselection.
The electron candidates kept at preselection level are reconstructed from ECal energy clusters associated with tracks of charged particles reconstructed in the ID. The preselected electron candidates are required to have $p_{\mathrm{T}} > 10$ GeV and $|\eta_{\mathrm{cluster}}| < 2.47$, while candidates in the transition calorimeter region, $1.37 <$

| | | |
|---|---|---|
| Dilepton triggers (2015) | | |
| $\mu\mu$ | HLT_mu18_mu8noL1 | $p_{\mathrm{T,HLT}} \geq 18$ and 8 GeV |
| $ee$ | HLT_2e12_lhloose_L12EM10VH | $p_{\mathrm{T,HLT}} \geq 12$ GeV (both) |
| $e\mu, \mu e$ | HLT_e17_lhloose_mu14 | $p_{\mathrm{T,HLT}} \geq 17$ ($e$) and 14 ($\mu$) GeV |
| Dilepton triggers (2016) | | |
| $\mu\mu$ | HLT_mu22_mu8noL1 | $p_{\mathrm{T,HLT}} \geq 22$ and 8 GeV |
| $ee$ | HLT_2e17_lhvloose_nod0 | $p_{\mathrm{T,HLT}} \geq 17$ GeV (both) |
| $e\mu, \mu e$ | HLT_e17_lhloose_nod0_mu14 | $p_{\mathrm{T,HLT}} \geq 17$ ($e$) and 14 ($\mu$) GeV |
| Dilepton triggers (2017 and 2018) | | |
| $\mu\mu$ | HLT_mu22_mu8noL1 | $p_{\mathrm{T,HLT}} \geq 22$ and 8 GeV |
| $ee$ | HLT_2e24_lhvloose_nod0 | $p_{\mathrm{T,HLT}} \geq 17$ GeV (both) |
| $e\mu, \mu e$ | HLT_e17_lhloose_nod0_mu14 | $p_{\mathrm{T,HLT}} \geq 17$ ($e$) and 14 ($\mu$) GeV |

TABLE 8.2: List of lowest $p_{\mathrm{T}}$-threshold, unprescaled dilepton triggers used in the different Run-2 data taking periods.

| | |
|---|---|
| Single-lepton triggers (2015) | |
| $\mu$ | HLT_mu20_iloose_L1MU15, HLT_mu50 |
| $e$ | HLT_e24_lhmedium_L1EM20VH, HLT_e60_lhmedium, HLT_e120_lhloose |
| Single-lepton triggers (2016) | |
| $\mu$ | HLT_mu26_ivarmedium, HLT_mu50 |
| $e$ | HLT_e26_lhtight_nod0_ivarloose, HLT_e60_lhmedium_nod0, HLT_e140_lhloose_nod0 |
| Single-lepton triggers (2017 and 2018) | |
| $\mu$ | HLT_mu26_ivarmedium, HLT_mu50 |
| $e$ | HLT_e26_lhtight_nod0_ivarloose, HLT_e60_lhmedium_nod0, HLT_e140_lhloose_nod0 |

TABLE 8.3: List of lowest $p_{\mathrm{T}}$-threshold, unprescaled single-lepton triggers used in the different Run-2 data taking periods.

$|\eta_{\mathrm{cluster}}| < 1.52$, are rejected. The **LooseLH** ID OP and the **FCLoose** isolation OP are used. The electron candidate tracks are required to originate from the PV, while the standard impact parameter selections $|d_0|/\sigma_{d_0} < 5$ and $|\Delta z_0 \sin\theta_\ell| < 0.5$ mm are required.

The muon candidates kept at preselection level are reconstructed by combining tracks ID with track segments or full tracks in the MS. The candidates in the $|\eta| < 0.1$ region are reconstructed from ID tracks matched to energy deposits in the calorimeters corresponding to a minimum-ionising particle due to the low coverage of the MS there. The preselected muon candidates are required to have $p_{\mathrm{T}} > 10$ GeV and $|\eta| < 2.5$. The **Loose** ID OP and the **FCLoose** isolation OP are used. The muon candidate tracks are also required to satisfy the standard impact parameter selections $|d_0|/\sigma_{d_0} < 3$ and $|\Delta z_0 \sin\theta_\ell| < 0.5$ mm.

### 8.3.3 Object selection

#### Electrons and muons

On top of the preselection criteria a tighter set of electron candidates is used in certain analysis regions in order to reduce the fake and non-prompt lepton contributions. They are required to satisfy the **TightLH** ID OP combined with the electron/photon ambiguity bit set to 0 ensuring the tightest ambiguity selection. The electron candidates should also pass the vetoes used to reject candidates from photon conversion and charge misassignment. The candidates failing the conversion vetoes are used to define the conversion control regions in the analyses. These vetoes are based either on reconstructed variables or on BDT discriminants, and are further discussed in Section 9.4.

A similar approach is followed for muon candidates to reduce the fake and non-prompt lepton contributions. They are required to satisfy the **Medium** ID OP, except in the LQ analyses, where a hybrid **High-$p_{\mathrm{T}}$** ID OP is used (Medium ID OP for $p_{\mathrm{T}}^{\mu} < 800$ GeV, High-$p_{\mathrm{T}}$ ID OP for $p_{\mathrm{T}}^{\mu} \geq 800$ GeV).

#### Jets

The `AntiKt4EMPFlowJets` jet collection is used for the studies in this thesis. In this set the jets are formed from particle-flow jet constituents and are reconstructed using the anti-$k_{\mathrm{T}}$ algorithm for $R = 0.4$. The jets are required to satisfy the selections $p_{\mathrm{T}} > 25$ GeV and $|\eta| < 2.5$, while forward jets ($2.5 < |\eta| < 4.5$) are not considered. The jets satisfying the above requirements are the ones entering the overlap removal procedure (discussed later in this section). The final jets are required to pass the **Medium** JVT OP (default), which corresponds to a selection of JVT $> 0.59$.

#### *b*-tagged jets

Jets originating from $B$-hadrons ($b$-tagged or $b$-jets) are flagged using different MVA discriminants of the DL1 family (according to the analysis) combining the

impact parameter information of displaced tracks associated with secondary vertices. In the LQLQ $\to t\tau t\tau$ analysis the DL1 discriminant was used with an OP corresponding to 77% efficiency. In the LQLQ $\to t\ell t\ell$ analysis the DL1r discriminant was used instead, with OPs corresponding to 85% efficiency. In the $t\bar{t}W$ measurement the DL1r discriminant was also used, but combining different OPs with most of the regions using either the 77% efficiency OP or a hybrid $b$-tagging OP corresponding to a logical OR of the 60% OP for events with exactly one $b$-jet and the 77% OP for events with at least two $b$-jets.

## Missing transverse energy

The missing transverse energy ($E_{\mathrm{T}}^{\mathrm{miss}}$) is primarily used to define certain additional selections for the validation of background modelling in the control regions, while it is also included in the definition of the main discriminating variable used in the LQ analyses. The missing transverse energy is reconstructed as described in Section 7.6 with the default settings of AnalysisTop. The $E_{\mathrm{T}}^{\mathrm{miss}}$ calculation includes $\tau$-leptons in the case of the LQLQ $\to t\tau t\tau$ analysis, while it is agnostic to them in the other two analyses covered in this thesis.

## Overlap removal

| Reject | Against | Criteria |
|---|---|---|
| Muon (calorimeter-tagged) | Electron | $\Delta R < 0.1$ |
| Electron | Muon (not calorimeter-tagged) | $\Delta R < 0.1$ |
| Jet (if not $b$-tagged) | Electron | $\Delta R < 0.2$ |
| Jet (if not $b$-tagged, $N_{\mathrm{trk}} < 3$) | Muon ("ghost-matched") | $\Delta R < 0.4$ |
| Electron / Muon | Jet | $0.04 + 10\ \mathrm{GeV}/p_{\mathrm{T},\ell} < \Delta R < 0.4$ |

TABLE 8.4: Summary of the overlap removal procedure between electrons, muons, and jets used in the $t\bar{t}W$ and LQLQ $\to t\ell t\ell$ analyses.

The procedure of overlap removal (OR) is critical in a physics analysis, as the objects that overlap during reconstruction are evaluated based on certain criteria ensuring that only one of them is kept according to the analysis needs. In this way a potential double counting of physics objects is avoided. A $b$-jet aware OR is used in the LQLQ $\to t\ell t\ell$ and $t\bar{t}W$ analyses, same as the one commonly used in SUSY analyses [199]. The OR is performed using the loosest set of physics objects in

each category. The steps and the order in which the $b$-jet aware OR is performed are summarised in Table 8.4.

In the LQLQ $\rightarrow t\tau t\tau$ analysis a different OR procedure than the above is used that takes into account hadronically decaying tau-leptons ($\tau_{\text{had}}$). Loose RNN ID $\tau_{\text{had}}$ candidates are used in the OR, which is summarised in Table 8.5.

| Reject | Against | Criteria |
|---|---|---|
| Electron | Muon | $\Delta R < 0.1$ |
| Jet | Electron | $\Delta R < 0.2$ |
| Jet | Muon | $\Delta R < 0.2$ |
| Tau | Electron | $\Delta R < 0.2$ |
| Tau | Muon | $\Delta R < 0.2$ |
| Jet | Tau | $\Delta R < 0.2$ |

TABLE 8.5: Summary of the overlap removal procedure between electrons, muons, hadronically decaying tau-leptons, and jets used in the LQLQ $\rightarrow t\tau t\tau$ analysis.

## Hadronically decaying tau-leptons

This section is specific to the LQLQ $\rightarrow t\tau t\tau$ search, since it is the only one including hadronically decaying $\tau$-lepton candidates ($\tau_{\text{had}}$). These physics objects are reconstructed from energy clusters in the calorimeters and associated tracks from the ID. The candidates are required to have either one or three associated tracks with a total charge of $\pm 1$, categorised as one- and three-prong, respectively. The candidates are required to have $p_{\text{T}} > 25$ GeV and $|\eta| < 2.5$, while candidates in the transition ECal region (crack region) are not considered. A RNN discriminant is used based on calorimeter- and tracking-related variables in order to identify the $\tau_{\text{had}}$ candidates and reject other jet backgrounds. There are two identification OPs used in this analysis. The **Loose** ID OP with efficiency of (85%) 75% for (one-) three-prong decays is used to define a loose set of $\tau_{\text{had}}$ candidates, which is used in the OR and in the definition of control and validation regions (analysis regions introduced in Section 8.4.1). The **Medium** ID OP, corresponding to efficiencies of (75%) 60% for (one-) three-prong $\tau_{\text{had}}$ decays is used in the signal regions and some of the control regions. Each $\tau_{\text{had}}$ candidate is required to originate from the main PV of the event in order to reduce the contribution of pileup jets. The ambiguity with other physics objects is resolved with the OR procedure discussed before,

in which muons are rejected within a cone of $\Delta R < 0.2$ if they are calorimeter-tagged and have $p_{\mathrm{T}} > 2$ GeV. A BDT approach is used to suppress the electron candidates, as explained in Section 7.5.

## 8.4 Analysis strategy principles

### 8.4.1 Event categorisation

The definition of the various regions used in physics analyses is driven by the need to check the modelling of the different backgrounds that mimic the signature of the signal, and the necessity to find the region of phase space where the signal of interest is significant. These regions are defined in general by applying certain selection criteria on different kinematic variables or objects of the event.

The first category of the analysis regions defined is known as **signal regions (SRs)**, which are designed to be enriched in the targeted signal. These are the regions where the BSM signal is expected to "live" in a BSM search and they basically determine the sensitivity of a search. In a measurement they are used as the regions where a SM signal is unfolded aiming to the measurement of its differential cross section versus a set of kinematic variables. Increasing the number of bins in a SR distribution is expected to increase the sensitivity in general or reduce the total uncertainty in a cross-section measurement, but the final decision is usually driven by a number of considerations, like the actual shape of the signal compared to the background, the limited MC statistics, etc.

The second category of analysis regions are known as **control regions (CRs)**, which are signal-depleted regions enriched with events from targeted background processes. The aim of these regions is to ensure that the modelling of the main backgrounds is reasonable, and in the results of this thesis they are also used for the estimation of these backgrounds, e.g. through the so-called "template fit method" (discussed in Section 9.4.4).

Both SRs and CRs are entering the final fit of real to simulated data. Apart from these two categories, there is an additional one in which a set of **validation regions (VRs)** is defined. These regions are not used in the fit, but are useful to validate the background modelling in regions close to SRs. This is achieved

by inverting one or more of the SR selections or by looking into the data/MC agreement in other variables than the one used in the fit. Of course in the case that these regions are not totally signal depleted a blinding strategy needs to be put in place that will determine which of the bins are safe to look into. All the above regions are usually orthogonal to each other, something especially important for the regions used in the fit in order to avoid duplicate events.

### 8.4.2 Signal-to-background discrimination

This section is mostly relevant to the BSM searches covered in this thesis, and it refers to the main variables/observables used in the analysis in order to discriminate a BSM signal from the SM background. The definition of these variables relies on the signal kinematics and the one demonstrating the largest separation between signal and background is chosen to be included in the fit. After performing the relevant studies in the LQ analyses the most sensitive variable was found to be the effective mass, $m_{\text{eff}}$, defined as the sum of transverse momentum of all physics objects added to the missing transverse energy, $E_{\text{T}}^{\text{miss}}$, of the event. Hadronically decaying $\tau$-leptons are included in the $m_{\text{eff}}$ definition in the LQLQ $\rightarrow t\tau t\tau$ analysis, but are excluded in the LQLQ $\rightarrow t\ell t\ell$ one. Thus, the $m_{\text{eff}}$ definition for these analyses is

$$m_{\text{eff}} = \sum_{e,\,\mu,\,j,\,\tau_{\text{had}}} p_{\text{T}} + E_{\text{T}}^{\text{miss}} \quad \text{and} \quad m_{\text{eff}} = \sum_{e,\,\mu,\,j} p_{\text{T}} + E_{\text{T}}^{\text{miss}}, \tag{8.2}$$

respectively. The $m_{\text{eff}}$ distribution for LQ signal events is known to peak at around two times the LQ mass, providing a very strong signal-to-background separation. Additionally, it is also known as a mass-sensitive variable, an attribute very useful in a search especially when the invariant mass of the LQ cannot be reconstructed (e.g. in $t\tau t\tau$ final states).

### 8.4.3 Blinding strategy

Prior to looking into real data in the SRs, a blinding strategy needs to be defined ensuring that the physics analysis strategy is constructed without being subject to any bias from the analysers. The blinding strategy in the two LQ analyses is defined based on the S/B ratio of the $m_{\text{eff}}$ variable. In the LQLQ $\rightarrow t\tau t\tau$ analysis

the $m_{\text{eff}}$ bins were allowed to be unblinded if this ratio was S/B $< 10\%$ of the benchmark LQ signal at $m_{\text{LQ}} = 900$ GeV, a decision motivated by previous upper limits in this final state from the CMS experiment [200]. In the LQLQ $\rightarrow t\ell t\ell$ analysis the $m_{\text{eff}}$ bins were allowed to be unblinded if this ratio was S/B $< 5\%$ of the benchmark LQ signal at $m_{\text{LQ}} = 1500$ GeV, also motivated by previous limits (such as in [201]). The blinding strategy in the $t\bar{t}W$ measurement was initially to not look into real data at all, and then as an intermediate step before the unblinding to look into data versus MC comparisons, but without looking at the fitted normalisation factor for $t\bar{t}W$. All analyses included in this thesis have been unblinded, at the time of the thesis writing.

## 8.5 Systematic uncertainties

A summary of systematic uncertainties is given in this section covering theoretical and instrumental systematics, including those related to background modelling. The default smoothing algorithm is used for all theoretical and instrumental systematics in order to mitigate the impact of low statistics on the systematics, while the use of the smoothing algorithm affects the shape of distributions. This algorithm follows the *MaxVariation* approach, which is based on the rebinning of the distribution until the relative MC statistical uncertainty gets below a predefined threshold of tolerance. A two-sided symmetrisation is used for all instrumental uncertainties, while an one-sided symmetrisation is used for most of the theoretical uncertainties. A pruning procedure is applied to the systematic uncertainties based on their shape and normalisation effects, which should be at least 1% for each uncertainty to be included in the fit. All these uncertainties are used in the fit as separate nuisance parameters.

The signal modelling uncertainties are discussed separately for each analysis at the corresponding chapters, since they are analysis specific. The same applies to the uncertainties related to hadronic $\tau$-leptons, which are discussed in Chapter 9. Most of the systematic uncertainties related to data-driven corrections, the template fit method and the physics objects themselves are discussed in Chapters 9 and 10, but are also being listed here for consistency.

### 8.5.1 Instrumental uncertainties

| **Instrumental systematics on leptons** | | | |
|---|---|---|---|
| Type | Description | Systematics name | Application |
| | | **Trigger** | |
| Scale Factors | Ele./Muon Trigger Eff | custTrigSF_TightElMediumMuID_ FCLooseIso_DLT | Event weight |
| | | **Muons** | |
| Efficiencies | Reconstruction and identification | MU_SF_ID_[STAT,SYST] | Event weight |
| | Reconstruction and Identification (low $p_{\mathrm{T}}$) | MU_SF_ID_[STAT,SYST]_LOWPT | Event weight |
| | Isolation | MU_SF_Isol_[STAT,SYST] | Event weight |
| | Track-to-vertex association | MU_SF_TTVA_[STAT,SYST] | Event weight |
| $p_{\mathrm{T}}$ Scale | $p_{\mathrm{T}}$ Scale | MUONS_SCALE | $p_{\mathrm{T}}$ correction |
| Resolution | ID Momentum Resol. | MUONS_ID_[STAT,SYST] | $p_{\mathrm{T}}$ correction |
| | MS Momentum Resol. | MUONS_MS | $p_{\mathrm{T}}$ correction |
| | Sagitta corr. (charge dep.) | MUONS_SAGITTA_[RHO,RESBIAS] (RHO part deprecated; removed in new analyses) | $p_{\mathrm{T}}$ correction |
| | | **Electrons** | |
| Efficiencies | Reconstruction | EL_SF_Reco | Event weight |
| | Identification | EL_SF_ID | Event weight |
| | Isolation | EL_SF_Isol | Event weight |
| Scale Factor | Energy Scale | EG_SCALE_ALL | Energy correction |
| Resolution | Energy Resol. | EG_RESOLUTION_ALL | Energy correction |

TABLE 8.6: Overview of instrumental systematics used in multi-lepton analyses related to muon and electron candidates.

The instrumental systematic uncertainties considered in the analyses presented in this thesis are related to the trigger efficiency, lepton reconstruction and identification, jet calibration, $b$-tagging, and the global event activity. The recommendations for these uncertainties are provided by ATLAS performance groups, which suggest a proper treatment for each uncertainty. Instrumental uncertainties are applied as event weights or as a rescaling factor in the energy and momentum of a physics object.

The "CategoryReduction" scheme is used for the implementation of the JES uncertainties, while the "FullJER" scheme is selected for the JER uncertainties. To reduce the JES flavour composition and response uncertainties, dedicated gluon composition maps were derived.

| **Instrumental systematics on jets and MET** | | | |
|---|---|---|---|
| Type | Origin | Systematics name | Application |
| | | **Jets** | |
| Jet Vertex Tagger | | JVT | Event weight |
| Energy Scale | Calibration Method | JET_EffectiveNP_Detector1 | $p_{\mathrm{T}}$ correction |
| | | JET_EffectiveNP_Mixed[1,3] | $p_{\mathrm{T}}$ correction |
| | | JET_EffectiveNP_Modelling[1,4] | $p_{\mathrm{T}}$ correction |
| | | JET_EffectiveNP_Statistical[1,6] | $p_{\mathrm{T}}$ correction |
| | $\eta$ inter-calibration | JET_EtaIntercalibration_Modelling | $p_{\mathrm{T}}$ correction |
| | | JET_EtaIntercalibration_NonClosure ($\times$4) | $p_{\mathrm{T}}$ correction |
| | | JET_EtaIntercalibration_TotalStat | $p_{\mathrm{T}}$ correction |
| | High-$p_{\mathrm{T}}$ jets | JET_SingleParticle_HighPt | $p_{\mathrm{T}}$ correction |
| | Pileup | JET_Pileup_OffsetNPV | $p_{\mathrm{T}}$ correction |
| | | JET_Pileup_OffsetMu | $p_{\mathrm{T}}$ correction |
| | | JET_Pileup_PtTerm | $p_{\mathrm{T}}$ correction |
| | | JET_Pileup_RhoTopology | $p_{\mathrm{T}}$ correction |
| | Non Closure | JET_PunchThrough_MC16 | $p_{\mathrm{T}}$ correction |
| | Flavour | JET_Flavor_Response | $p_{\mathrm{T}}$ correction |
| | | JET_BJES_Response | $p_{\mathrm{T}}$ correction |
| | | JET_Flavor_Composition | $p_{\mathrm{T}}$ correction |
| Resolution | | JET_JER | $p_{\mathrm{T}}$ correction |
| | | **MET** | |
| Soft Tracks Terms | Resolution | MET_SoftTrk_ResoPerp | $p_{\mathrm{T}}$ correction |
| | Resolution | MET_SoftTrk_ResoPara | $p_{\mathrm{T}}$ correction |
| | Scale | MET_SoftTrk_Scale | $p_{\mathrm{T}}$ correction |

TABLE 8.7: Overview of instrumental systematics considered in multi-lepton analyses related to jets and missing transverse energy. The jet systematics take into account the effects of the jet calibration method (*e.g.* in situ), $\eta$ inter-calibration, high-$p_{\mathrm{T}}$ jets, pileup, non closure and flavour response. They are all diagonalised into effective parameters.

The lists of the different types of instrumental uncertainties are summarised in Tables 8.6, 8.7 and 8.8. The uncertainty on the luminosity measurement corresponding to the full ATLAS Run-2 dataset is estimated to 1.7% and it is also defined as a separate nuisance parameter in the fit.

| **Instrumental systematics on *b*-jets** | | |
|---|---|---|
| Type | Origin | Systematics name |
| | | *b*-tagging |
| Scale Factors | DL1/DL1r *b*-tagger eff. on *b*-originated jets | weight_bTagSF_DL1r_Continuous_FT_EFF_Eigen_B[0-19] |
| | | DL1_FixedCutBEff_77_EventWeight_B[0-8] |
| | DL1/DL1r *b*-tagger eff. on *c*-originated jets | weight_bTagSF_DL1r_Continuous_FT_EFF_Eigen_C[0-19] |
| | | DL1_FixedCutBEff_77_EventWeight_C[0-4] |
| | DL1/DL1r *b*-tagger eff. on light-flavoured jets | weight_bTagSF_DL1r_Continuous_FT_EFF_Eigen_Light[0-19] |
| | | DL1_FixedCutBEff_77_EventWeight_Light[0-5] |
| | DL1 *b*-tagger extr. eff. | DL1_FixedCutBEff_77_EventWeight_extrapolation<br>DL1_FixedCutBEff_77_EventWeight_extrapolation_from_charm |
| **Pileup reweighting** | | |
| Pileup rew. | | weight_pileup |

TABLE 8.8: Overview of instrumental systematics related to the DL1(r) *b*-tagging algorithms, used in multi-lepton analyses. The entries in gray correspond to the related uncertainties used in the LQLQ $\rightarrow t\tau t\tau$ analysis.

### 8.5.2 Theoretical modelling systematics

Concerning the theoretical modelling systematics used in the covered analyses, the list starts with systematic uncertainties related to the cross section of different processes. These uncertainties are motivated by recent physics results and ATLAS recommendations, and are only applied to processes whose normalisation is not free-floated in the template fit. Systematic uncertainties concerning the renormalisation and factorisation scale choices are introduced in most of the irreducible background processes by corresponding variations (called "varRF"). The $t\bar{t}W$ and $t\bar{t}Z$ + heavy flavour (HF) cross-section uncertainties are only used in the cases where these contributions are not left free-floated.

The thorough systematics model of the $t\bar{t}W$ and $t\bar{t}Z$ processes including various generator comparisons and PDF uncertainties for $t\bar{t}W$ is only used in the $t\bar{t}W$ measurement, while a simpler version is preferred in the LQ analyses. The uncertainties on the $t\bar{t}W$ PDF modelling include different sets varying the nominal $\alpha_s = 0.118$ to $\alpha_s = 0.117$ and $\alpha_s = 0.119$ (PDF $\alpha_s$), while a two-sided uncertainty is assigned to the PDF set itself (PDF alternate).

An overview of the theoretical modelling systematics is shown in Table 8.9.

| Process (default) | Cross-section uncertainty | Theoretical systematic uncertainty type |
|---|---|---|
| $t\bar{t}W$ (QCD, EW) | (± 50% / ± 13%, ± 20%) | ME (gen. comp. with MadGraph5_aMC@NLO +Pythia-8 FxFx sample)<br>PS (gen. comp. between Powheg-Box + Pythia-8 and Powheg-Box + Herwig-7.1.3; effect propagated to nominal)<br>EW fraction (difference of EW fraction in Sherpa & MadGraph)<br>PDF $\alpha_S$, PDF alternate, varRF |
| $t\bar{t}Z + \{l, c/b\}$ | −, (± 50%) | PS (gen. comp. with MadGraph5_aMC@NLO +Herwig-7)<br>var3c (varying Pythia A14 tune)<br>varRF |
| $t\bar{t}H$ | ± 11% | ME (gen. comp. with MadGraph5_aMC@NLO + Pythia-8),<br>PS (gen. comp. with Powheg-Box + Herwig-7.1.3),<br>varRF |
| $t\bar{t}$ | − | PS (gen. comp. with Powheg-Box + Herwig-7.1.3)×$(e, \mu)$ |
| $VV + \{l, c/b\}$ | (± 2%), − | varRF |
| $VVV$ | ± 30% / ± 50% | − |
| $VH$ | ± 50% | − |
| $ttt$ | ± 50% | − |
| $t\bar{t}t\bar{t}$ | ± 30% | − |
| $t\bar{t}WW$ | ± 50% | − |
| $tZ$ | ± 5% / ± 15% | − |
| $tWZ$ | ± 50% | − |

Table 8.9: Overview of theoretical uncertainties considered for the MC expectation value of different processes. The parentheses in the second column denote that the uncertainties are used if the contribution is not free-floated in the fit. The entries in grey correspond to the choice made in the LQLQ $\rightarrow t\tau t\tau$ analysis (if it is different).

## 8.6 Statistical formalism

Due to the probabilistic nature of quantum field theory the outcome of a $pp$ collision is not deterministic. This is exploited already by the MC generators in the event generation, and it is evident that a proper statistical treatment is needed for the interpretation of the results in order to conclude on quantitative statements about the observed data. The purpose of this section is not to elaborate on the definitions used in statistics, but to provide some basic understanding to the reader concerning the statistical methods used in this thesis for parameter estimation, hypothesis testing and limit setting.

There are two well-established and equivalent approaches for the definition of probability in statistics: the **bayesian** approach and the **frequentist** approach. According to the **bayesian** approach, probability represents the degree of belief on a certain hypothesis and it is defined by the Bayes theorem, which can be written in a particle physics notation as

$$P(\text{model} \,|\, \text{data}) = \frac{P(\text{data} \,|\, \text{model}) \cdot P(\text{model})}{P(\text{data})}. \tag{8.3}$$

In this formula the probability of a given model to describe the observed data, $P(\text{model}\,|\,\text{data})$, depends on the probability of a predicted number of data to be observed under a certain model, $P(\text{data}\,|\,\text{model})$, the probability to observe a number of data regardless of the assumed model, $P(\text{data})$, and the probability that the model correctly describes the data *prior* to the measurement, $P(\text{model})$ (often referred to as prior probability). While there are many use-cases where Bayes theorem can be used in particle physics, the natural argument against it is that the prior probability of the model cannot be known until the experiment is performed.

In the **frequentist** approach, which is more commonly used in particle physics experiments, the probability $P_{\text{model}}$ is defined as the fraction of favourable outcomes of a repeatable experiment assuming that it is repeated infinite number of times or that the number of repetitions tends to infinity such that

$$P_{\text{model}} = \lim_{N_{\text{tot}} \to \infty} \frac{N_{\text{model}}}{N_{\text{tot}}}. \tag{8.4}$$

### 8.6.1 The Likelihood function

A simple example of the frequentist approach in particle physics is the Poisson model, describing the outcome of a counting experiment, where

$$P(k\,|\,\lambda) = \frac{\lambda^k \cdot e^{-\lambda}}{k!} \tag{8.5}$$

is the probability to observe $k$ events when $\lambda$ events are expected on average. Poisson distributions describe a large number of physics processes such as the radioactive decays and can be used for any counting experiment in particle physics. Therefore, the Poisson distribution is used for the construction of *likelihood* models, where likelihood $\mathscr{L}$ corresponds to the Poisson probability defined as

$$\mathscr{L} = P(N_{\text{obs}}\,|\,N_{\text{exp}}) = \frac{N_{\text{exp}}^{N_{\text{obs}}} \cdot e^{-N_{\text{exp}}}}{N_{\text{obs}}!}. \tag{8.6}$$

In this formula $N_{\text{obs}}$ corresponds to the number of observed events in the experiment and $N_{\text{exp}}$ corresponds to the number of expected events that relies on the assumed physics model. In a physics analysis $N_{\text{exp}}$ is equal to the sum of the number of the expected signal ($\mu s$) and background ($b$) events, $N_{\text{exp}} = \mu s + b$.

The parameter $\mu$ is known as *signal strength* and it is a multiplicative factor to the cross section of the corresponding process. Since the probability density functions (pdfs) of the signal and background are not always known a priori, a binned likelihood approach is used where the combined likelihood takes the form

$$\mathscr{L}(\mu) = \prod_{i=1}^{n} \frac{(\mu s_i + b_i)^{N_{\text{obs},\,i}}}{N_{\text{obs},\,i}\,!}\, e^{-(\mu s_i + b_i)}, \tag{8.7}$$

with index $i$ running over the total number of bins and $s_i$, $b_i$ the signal and background yield in each bin, respectively.

The above likelihood model does not include the statistical and systematic uncertainties that can affect the number of expected events in a measurement. These uncertainties can be modelled as a set of NPs, $\vec{\theta} = (\theta_1, \ldots, \theta_j)$, which enter the likelihood as additional multiplicative terms $\rho(\vec{\theta})$ often referred to as penalty terms on $\theta$. The consideration of the NP terms affects the signal and background pdfs such that their expectation values become a function of the NPs, $s(\vec{\theta}_s)$ and $b(\vec{\theta}_b)$, where $\vec{\theta}_s$ and $\vec{\theta}_b$ are two subsets of the total NP set.

Each $\rho(\theta)$ term represents the pdf of a single NP and it is determined beforehand in subsidiary measurements aiming to constrain it. Since these subsidiary measurements could happen in an independent sample of events compared to the one used in the analysis from a constructed histogram with $m$ bins, Equation 8.7 takes the form

$$\mathscr{L}(\mu, \vec{\theta}) = \prod_{i=1}^{n} \frac{\left[\mu s_i(\vec{\theta}_s) + b_i(\vec{\theta}_b)\right]^{N_{\text{obs},\,i}}}{N_{\text{obs},\,i}\,!}\, e^{-\left[\mu s_i(\vec{\theta}_s) + b_i(\vec{\theta}_b)\right]} \prod_{k=1}^{l} \rho_k(\vec{\theta}). \tag{8.8}$$

The $\rho(\theta)$ terms in the above formula are described by one of the following distributions for the parameter $\theta$.

**Poisson**: Also referred to as "gamma" constraint since the posterior of a Poisson-distributed parameter is a Gamma function. It is usually used to describe the MC statistical uncertainties in the fit, with the determination of the multiplicative $\gamma$ terms for each bin with nominal value set to 1.

**Log-normal**: Used mostly to describe the uncertainties originating from normalisation factors, exploiting its property that the result is bound to positive values.

It is defined as

$$\rho(\theta) = \frac{1}{\sqrt{2\pi}\ln\sigma} \exp\left[-\frac{\ln^2(\theta/\hat{\theta})}{2\ln^2\sigma}\right]\frac{1}{\theta}. \tag{8.9}$$

**Gaussian**: Normally used for the rest of the systematic uncertainties and it is defined as

$$\rho(\theta) = \frac{1}{\sqrt{2\pi}\sigma} \exp\left[-\frac{(\theta-\hat{\theta})^2}{2\sigma^2}\right], \tag{8.10}$$

resulting to Gaussian terms centred around 0 and with a standard deviation equal to 1.

### 8.6.2 Parameter estimation and the maximum likelihood method

The formalisation of the likelihood function offers a powerful tool to the estimation of the signal strength value that is more probable by the observed data. This is achieved with a method of maximum likelihood (ML). According to it, the $\mu$ value is estimated at the point where the likelihood function is maximised. For complex likelihood expressions like the ones in Equation 8.8 it is often more straightforward to minimise the quantity $-\ln\mathscr{L}$ instead, since each product in the equation is turned into a sum. Therefore, in the absence of any NPs the estimation of $\mu$ is given by the formula

$$-\frac{\partial \ln \mathscr{L}(\mu)}{\partial \mu}\bigg|_{\mu=\hat{\mu}} = 0. \tag{8.11}$$

The $\hat{\mu}$ notation is being used to declare that this is just an estimation of the parameter $\mu$ that might not coincide with its true value. If $\hat{\mu} = 1$ (or close) the conclusion is that the observed data favour the existence of signal, while if $\hat{\mu} = 0$ (or close) it means that the background-only scenario is favoured.

The ML method is preferred for the minimisation (e.g. compared to the $\chi^2$ method), since ML estimators are invariant and mostly unbiased, and the method itself has faster convergence, increased accuracy and it is efficient and consistent even for low number of observed events. In the more realistic case that there is a set of NPs present in the likelihood model the $-\ln\lambda(\mu)$ quantity is minimised

instead, where $\lambda(\mu)$ is known as ***profile likelihood ratio*** defined as

$$\lambda(\mu) = \frac{\mathscr{L}(\mu, \hat{\hat{\vec{\theta}}})}{\mathscr{L}(\hat{\mu}, \hat{\vec{\theta}})}. \tag{8.12}$$

Since the minimisation of $-\ln\lambda(\mu)$ is performed in a multidimensional space the notation of Equation 8.12 is explained as follows. The denominator represents the global maximum of the likelihood for specific $\hat{\mu}$ and $\hat{\vec{\theta}}$ estimators, while the numerator (thus the $\hat{\hat{\vec{\theta}}}$ notation) represents the local maxima of the likelihood, where $\vec{\theta}$ is the value that maximises it for a specific value of $\mu$.

### 8.6.3 Hypothesis testing

In particle physics a statistical test is required in order to exclude a new physics model or claim the discovery of new particles suggested by it. The statistical test relies on two hypotheses, one based on the established physics processes, and one including new physics in addition to them. In particular, in a physics search the two competing hypotheses are often defined as:

- **Null hypothesis ($H_0$)**: representing the SM hypothesis ($\mu = 0$). It is usually referred to as the background-only (B-only) hypothesis.
- **Alternative (or test) hypothesis ($H_1$)**: representing the BSM hypothesis with the inclusion of a BSM signal ($\mu > 0$). It is often referred to as the signal-plus-background (S+B) hypothesis.

The two hypotheses are tested versus each other and their compatibility with the observed data is quantified with a test statistic $t$. A test statistic defined based on a likelihood ratio is proved to demonstrate the highest statistical power. For this reason, the profile likelihood ratio defined in Equation 8.12 is used to define a test statistic as

$$t_\mu = -2\ln\lambda(\mu). \tag{8.13}$$

A *p-value* is defined based on this test statistic that corresponds to the probability of getting a higher value for the observed $t$, $t_{\text{obs}}$, compared to the current one if

the experiment is repeated. It is defined as

$$p_\mu = \int_{t_{\mu,\text{obs}}}^{\infty} f(t_\mu \,|\, \mu)\, dt. \tag{8.14}$$

If the $p$-value computed for the test hypothesis is lower than a predefined threshold, the test hypothesis is excluded up to a certain confidence level (CL). In particle physics this threshold is set to 0.05, which corresponds to 95% CL exclusion.

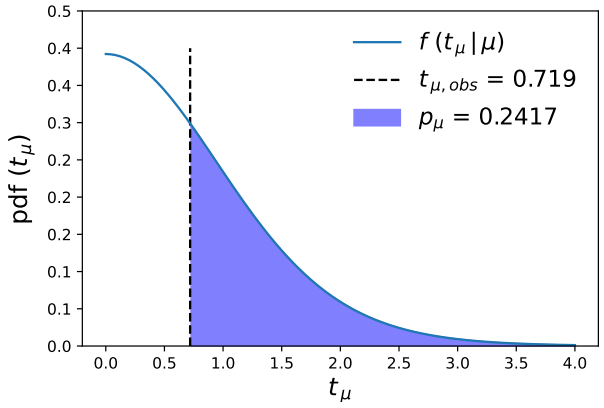



FIGURE 8.1: Visual representation of the $p$-value computed in a $t$-test.

The test statistic that is used for discovery provides the estimation of the probability to reject the BSM hypothesis ($H_1$) if it is correct. This is often known as $p_0$ and very low values of this quantity indicate the existence of new physics. The figure of merit to exclude or not the $H_0$ hypothesis is called ***significance*** and it is defined as

$$Z = \Phi^{-1}(1 - p_0), \tag{8.15}$$

where $\Phi^{-1}$ corresponds to the inverse of the cumulative distribution function (CDF) of the standard normal distribution.

The significance corresponding to $p_0 = 0.05$ is $Z = 1.68$ (or $1.68\sigma$), which is in general a not so tight requirement. Therefore, by convention the threshold in significance to exclude the $H_0$ hypothesis and declare a discovery is set to $5\sigma$, which corresponds to a $p$-value of $p_0 = 2.9 \cdot 10^{-7}$. A precursor of the discovery is usually a computed significance around $3\sigma$ that indicates evidence for new physics.

### 8.6.4 Limit setting and the CL$_s$ method

In the case of no significant excess over the SM expectation value after the fit, an one-sided profile-likelihood test statistic $q_\mu$ is defined as

$$q_\mu = \begin{cases} -2\ln\lambda(\mu) & \hat{\mu} \leq \mu, \\ 0 & \hat{\mu} > \mu, \end{cases} \tag{8.16}$$

which is the most common test statistic used for limit setting.

In order to set upper limits on the signal strength, $\mu$, the above definition for the test statistic is being used in the CL$_s$ method [202]. The figure of merit in this method is defined as

$$\mathrm{CL}_s = \frac{\mathrm{CL}_{s+b}}{\mathrm{CL}_b} = \frac{p_{s+b}}{1-p_b}, \tag{8.17}$$

where

$$\begin{aligned} p_{s+b} &= P(q_\mu \geq q_{\mu,\mathrm{obs}}|H_1) = \int_{q_{\mu,\mathrm{obs}}}^{\infty} f(q_\mu|H_1)\, dq_\mu, \\ p_b &= P(q_\mu \leq q_{\mu,\mathrm{obs}}|H_0) = \int_{0}^{q_{\mu,\mathrm{obs}}} f(q_\mu|H_0)\, dq_\mu, \end{aligned} \tag{8.18}$$

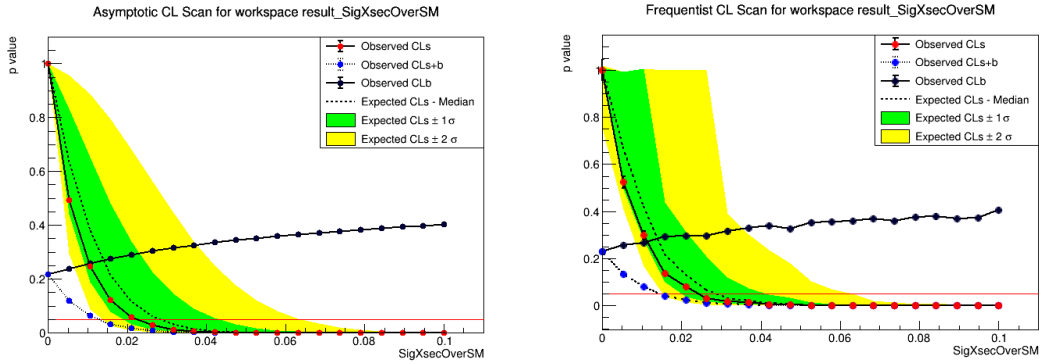
with $q_{\mu,\mathrm{obs}}$ being common between the two hypotheses.

The CL$_s$ method solves a long standing issue of excluding parameter values that are limited by low sensitivity [202] meaning that the distributions of the test statistics for the two hypotheses are very close. A $\mu$ value is excluded at 95% CL by requiring that $\mathrm{CL}_s \leq 0.05$. The highest $\mu$ value that can be excluded by this criterion is known as upper limit on $\mu$, $\mu_{\mathrm{up}}$. This upper limit is computed both for real and simulated MC data and it is known as **expected** and **observed** upper limit, respectively. In the case of simulated MC data, it is possible to calculate the associated confidence integrals (CIs) on $\mu_{\mathrm{up}}$ populated by all the potential values that $\mu_{\mathrm{up}}$ can take if the experiment is repeated, and for which the $H_0$ hypothesis cannot be rejected. The boundaries of the CIs, $\mu_{\mathrm{up}}^{\pm 1\sigma}$ and $\mu_{\mathrm{up}}^{\pm 2\sigma}$, are found at the $\pm 1\sigma$ and $\pm 2\sigma$ points of the $f(\mu_{\mathrm{up}} \,|\, H_0)$ distribution and are used to construct the $\pm 1\sigma$ and $\pm 2\sigma$ bands in the limit plots shown in Chapter 10. This procedure is repeated for all available signal mass points in a search, where an observed limit would correspond to a disagreement with the $H_0$ hypothesis.

A graphical representation of the upper limit estimation is shown in Figure 8.2a, where the upper limits were calculated using the asymptotic approximation [203].

This approximation is based on Wilk's theorem, according to which the pdf of the test statistic follows a $\chi^2$ distribution at the large sample limit. This assumption is particularly useful since the pdfs of the test statistic under both hypotheses are not known, and the asymptotic formula offers a quick and reliable computation.

S. Kazakos, PhD Thesis




(a) (b)

FIGURE 8.2: Graphical illustration of the upper limit estimation with the $CL_s$ method using the asymptotic approximation (a) and the toy MC (b) approaches at $m_{LQ} = 800$ GeV.

There are some cases though that in certain regions of phase space there is very small number of background events predicted under the $H_0$ hypothesis, and at these regions the asymptotic approximation does not hold. In such circumstances, the pdfs of the test statistic are estimated by generating a number of **pseudo-experiments**, which is referred to as the *toy MC* method. This was the standard method used for limit setting in particle physics experiments in the past, and it is known as a very computationally intensive procedure. The toy MC method is used to validate the results for the upper limits calculated for the analyses of this thesis with the asymptotic approximation, since the background expectation in some of the signal regions is rather small. In particular, in the LQLQ $\rightarrow t\ell t\ell$ search the upper limits could differ up to $\sim$30%, making the use of the toy MC method necessary for more accurate results. As shown in Figure 8.2b, in the limit estimation with toys the interval bands are less smoother and more asymmetric compared to the ones from the asymptotic approximation.

# Chapter 9

# Inclusive and differential cross-section measurements of $t\bar{t}W$ production

## 9.1 Introduction

The associated production of a top-antitop quark pair and a $W$ boson, $t\bar{t}W$, is one of the most interesting SM processes that can be measured at the LHC. It was first observed only during Run 2, due to its relative low cross section and since then there is an undiminished interest in precise measurements of such a rare process with the full Run-2 dataset.

The understanding of the $t\bar{t}W$ production mechanisms is also important since the $t\bar{t}W$ process is one of the main sources of irreducible background in several physics analyses focused on events with two leptons of same charge ($2\ell$SS) or three leptons $3\ell$. These signatures are commonly used in searches for BSM physics such as in SUSY and Exotics analyses [204–207]. The $t\bar{t}W$ background is also relevant in measurements of other rare SM processes, where a top-quark pair is produced in association with other particles such as in $t\bar{t}H$ [208] and $t\bar{t}t\bar{t}$ [209] production. In particular, the $t\bar{t}H$ process is a unique probe for the direct determination of the top-Higgs Yukawa coupling, which governs the interaction of the top quark with the Higgs boson. A precise measurement of the $t\bar{t}W$ production cross section is additionally motivated by tensions with the SM expectation value reported by the

above analyses, as well as in $t\bar{t}W$ measurements already conducted by ATLAS and CMS experiments at $\sqrt{s} = 13$ TeV [210–213].

One of the most challenging aspects in a precise $t\bar{t}W$ measurement is the accurate modelling of the process. The $t\bar{t}W$ contribution is known as a charge-asymmetric process with unusually complex higher-order QCD and EW corrections. The production and decay modes of this process are already discussed in Section 2.5, while the modelling of this process is detailed in Section 8.2.

This chapter discusses the inclusive and differential measurements of the $t\bar{t}W$ production cross section, starting with the object selection (Section 9.2) and the event categorisation including also the definitions of the analysis regions (Section 9.3). The differential cross section is measured in the fiducial volume defined in Section 9.3.1, whereas the inclusive cross section measurement is not fiducial, but extrapolated to the full phase-space region. The methods used for the background estimation and suppression in this complex analysis are described in Section 9.4, while the analysis-specific systematics are mentioned in Section 9.5. The results from the inclusive measurement are given in Section 9.6. In the case of the differential measurements, the $t\bar{t}W$ contribution is unfolded at particle level in several observables proposed by theorists, and further motivated by the experiment. The relative charge asymmetry distribution is also unfolded for all these observables, as a key variable to understand if the $t\bar{t}W$ contribution is more asymmetric than expected. The Profile Likelihood Unfolding method is used for the differential measurement, which is also explained in this chapter together with the optimisation procedure that preceded. The results from the differential measurement are given in Section 9.7.5.

## 9.2 Object selection

The selection of physics objects (electrons, muons, jets, $b$-jets) and the definition of overlap removal described in Section 8.3.3 is applied to the events of this analysis. Additionally to the tighter definitions on electrons defined in Section 8.3.3, this "tight" electron candidate set is further split according to the *PromptLeptonImprovedVeto* (PLIV) inclusive and exclusive OPs in order to be used for proper fake estimation through the template fit method (discussed in Section 9.4.4). The

tightest PLIV OP is used for the definition of the analysis signal regions. Additional information about the PLIV discriminant is given in Section 9.4.3.

Similar to electron candidates, muon candidates are further split according to the PLIV inclusive and exclusive OPs, with the tightest PLIV OP to be used for the definition of the analysis signal regions. The light-lepton candidate definitions involving the splitting according to the PLIV OPs together with the rest of the selections are shown in Table 9.1.

| | $e$ / $\mu$ | | | | |
|---|---|---|---|---|---|
| Lepton definition | [Linc] | [L] | [Minc] | [M] | [T] |
| FCLoose isolation | Yes | | | | |
| Non-prompt lepton BDT (PLIV) | No | PLIV $< 0$ and *not-Tight* | *Tight* | *Tight-not-VeryTight* | *VeryTight* |
| Identification | Loose | Tight / Medium | | | |
| Charge misassignment BDT (ECIDS) | — / NA | $> 0.7$ / NA | | | |
| Conversion vetoes | — / NA | Yes (except in conversion CRs) / NA | | | |
| Transverse impact parameter significance $\lvert d_0\rvert/\sigma_{d_0}$ | $< 5$ / $< 3$ | | | | |
| Longitudinal impact parameter $\lvert z_0 \sin\theta\rvert$ | $< 0.5$ mm | | | | |

TABLE 9.1: Loose inclusive [Linc], Loose exclusive [L], Medium inclusive [Minc], Medium exclusive [M], and Tight [T] light-lepton definitions.

## 9.3 Event categorisation and region definitions

The events of this analysis are selected by using dilepton triggers, as described in Section 8.3.2. A loose preselection is applied to the events passing the trigger selection, where the leptons of the event should be trigger-matched and at least one PV is required in each event. The events at this stage are categorised according to their lepton multiplicity and charge into events with two light leptons of same charge ($2\ell$SS) and three light leptons ($3\ell$). The categorisation at this stage into $2\ell$SS and $3\ell$ channels, where the light leptons are following the [Linc] definition

of Table 9.1, is preferred in order to minimise the migration effects from the $3\ell$ channel into the $2\ell$SS channel due to the lepton reconstruction inefficiencies.

Following the channel categorisation, CRs, VRs and SRs are defined that are orthogonal to each other. The CRs and VRs are used for background estimation and validation, respectively, while the SRs are chosen in a phase space with high purity in $t\bar{t}W$ signal events to ensure a precise measurement.

The SR definition contains events from both $2\ell$SS and $3\ell$ channels. The $2\ell$SS events in the SR are required to have two SS leptons of $p_{\mathrm{T}} > 20$ GeV ($p_{\mathrm{T}}$-ordered) following the [T] lepton definition of Table 9.1. The events are additionally required to have at least two jets and at least one $b$-jet at 60% efficiency DL1r OP or, at least two $b$-jets at 77% efficiency DL1r OP. The same $b$-tagging requirement applies to the events in the $3\ell$ channel, where at least one jet and total lepton charge of $Q = \pm 1$ are required. The OS lepton ($\ell_0$) is required to be defined as [Linc] and have $p_{\mathrm{T}} > 10$ GeV, due to its low probability of being a "fake"-lepton candidate. The leptons of the SS pair ($\ell_1$ and $\ell_2$) are required to follow the [T] definition and have $p_{\mathrm{T}} > 20$ GeV, while they are sorted based on the closest $\Delta R$ to $\ell_0$. The $3\ell$ events are additionally required to satisfy the "$Z$-vetoes" both in the dilepton ($|m^{\mathrm{OSSF}}_{\ell^+\ell^-} - m_Z| > 10$ GeV) and trilepton ($|m_{\ell\ell\ell} - m_Z| > 10$ GeV) mass. The mass of the SS dilepton pair is also required to be higher than 12 GeV to suppress quarkonia decays ($J/\psi$, $\Upsilon$, etc.). Both events in $2\ell$SS and $3\ell$ channels are split into categories with positive and negative total lepton charge.

| Signal regions | $2\ell$SS | $3\ell$ |
|---|---|---|
| Lepton definition | [TT] | [LincTT] |
| Lepton $p_{\mathrm{T}}$ [GeV] | $> 20$ | $> 10$ ($\ell_0$), $> 20$ ($\ell_1,\ \ell_2$) |
| $m^{\mathrm{OSSF}}_{\ell^+\ell^-}$ [GeV] | — | >12 |
| $\lvert m^{\mathrm{OSSF}}_{\ell^+\ell^-} - m_Z\rvert$ [GeV] | — | >10 |
| $\lvert m_{\ell\ell\ell} - m_Z\rvert$ [GeV] | — | >10 |
| $N_{\mathrm{jets}}$ | $\geq 2$ | $\geq 1$ |
| $N_{b-\mathrm{jets}}$ | $\geq 1$ (60% DL1r) OR $\geq 2$ (77% DL1r) | |
| Region split | $(\ell_0^+\ell_1^+,\ \ell_0^-\ell_1^-)$ | $(\ell_0^-\ell_1^+\ell_2^+,\ \ell_0^+\ell_1^-\ell_2^-)$ $\times$ {[0], [1], [2] OSSF lepton pairs} |

TABLE 9.2: Overview of event categorisation in $2\ell$SS and $3\ell$ signal regions. The lepton definitions are defined in Table 9.1.

In the differential measurement the $3\ell$ SRs are further split according to the number of opposite-charge same-flavour (OSSF) pairs they contain. This splitting exploits the difference between the shapes of $t\bar{t}W$ and $t\bar{t}Z$ (leading background in the $3\ell$ channel) contributions leading to a more precise measurement by reducing the total uncertainty on the signal strength. To account for event migrations, the $2\ell$SS and $3\ell$ SRs are combined into a single region by "stitching" together all the bins in a single histogram for each of the observables considered, and the $t\bar{t}W$ sample is unfolded in this region.

In the inclusive measurement these SRs are further categorised in single bins according to lepton flavour, and the multiplicity of jets and $b$-jets, where the number of events is fitted. The categorisation used in the inclusive measurement is summarised in Table 9.3, resulting in 48 (8) bins in the $2\ell$SS ($3\ell$) channel. This categorisation aims at the reduction of the total systematic uncertainty in the final $t\bar{t}W$ cross section.

| Signal regions (incl.) | $2\ell$SS | $3\ell$ |
|---|---|---|
| Lepton charge split | $(\ell_0^+\ell_1^+,\ \ell_0^-\ell_1^-)$ | $(\ell_0^-\ell_1^+\ell_2^+,\ \ell_0^+\ell_1^-\ell_2^-)$ |
| Lepton flavour split | ($\mu\mu$, $e\mu$, $\mu e$, $ee$) | — |
| Jet multiplicity split | (3, 4, $\geq 5$) | (2, $\geq 3$) |
| $b$-jet multiplicity split | (1, $\geq 2$) | (1, $\geq 2$) |
| Total number of bins | 48 | 8 |

TABLE 9.3: Overview of the additional $2\ell$SS and $3\ell$ channel categorisation used in the inclusive measurement.

The CRs of this analysis are enriched in some of the leading backgrounds in order to determine their normalisation by letting it free-float in a template fit (see Section 9.4.4). There are 6 CRs defined in the $2\ell$SS channel targeting events with non-prompt leptons from heavy-flavour (HF) decays. The leptons of the events in these CRs are required to follow different combinations of [T] and [M] lepton definitions with the exception of the [TT] selection, which is reserved for the SRs and ensures the orthogonality among the regions. These events are further split based on the subleading lepton flavour to $ee/\mu e$ (electron "fakes") and $\mu\mu/e\mu$ (muon "fakes"). An additional selection of $m_{\mathrm{T}}(\ell_0,\ E_{\mathrm{T}}^{\mathrm{miss}}) < 250$ GeV is applied in these CRs in order to reduce the $t\bar{t}W$ contamination, where $m_{\mathrm{T}}(\ell_0,\ E_{\mathrm{T}}^{\mathrm{miss}})$ is the transverse mass of the leading lepton and of the missing transverse energy defined as $m_{\mathrm{T}}(\ell_0,\ E_{\mathrm{T}}^{\mathrm{miss}}) = \sqrt{2E_{\mathrm{T}}^{\mathrm{miss}} p_{\mathrm{T},\ell_0}(1-\cos(\phi_{miss}-\phi_{\ell_0}))}$.

There are 4 CRs defined in the $3\ell$ channel. Two of them, $3\ell$IntC and $3\ell$MatC, are enriched in events with electrons from photon conversions (either internal or material) from $Z \to \mu\mu\gamma^*(\to ee)$ decays. In these regions an inverse $Z$-veto is applied on the trilepton mass to select these events, while the lepton-flavour combination in them is required to be $\mu\mu e$ (with the leading lepton in $p_{\mathrm{T}}$ being a muon). These regions are defined inclusively across the whole jet multiplicity spectrum, and are required to have exactly zero $b$-jets at 77% efficiency $b$-tagging OP. The rest of the $3\ell$ CRs, $3\ell$VV and $3\ell$ttZ, are enriched in either diboson or $t\bar{t}Z$ backgrounds defined by requiring exactly one $Z$-boson candidate with different requirements in the number of jets and $b$-jets. A summary of the CR selections is given in Table 9.4.

| Control regions | Non-prompt HF$e/\mu$ | Conversions | $VV$ | $t\bar{t}Z$ |
|---|---|---|---|---|
| Lepton requirement | $2\ell$SS | $\mu\mu e^*$ | $3\ell$ | |
| Lepton definition | {[TM], [MT], [MM]} | [LincMincMinc] | | |
| Lepton $p_{\mathrm{T}}$ [GeV] | $> 20$ | $> 10$ ($\ell_0$), $> 20$ ($\ell_1$, $\ell_2$) | | |
| $m^{\mathrm{OSSF}}_{\ell^+\ell^-}$ [GeV] | — | $> 12$ | | |
| $\lvert m^{\mathrm{OSSF}}_{\ell^+\ell^-} - m_Z\rvert$ [GeV] | — | $> 10$ | $< 10$ | |
| $\lvert m_{\ell\ell\ell} - m_Z\rvert$ [GeV] | — | $< 10$ | — | |
| $m_{\mathrm{T}}(\ell_0, E^{\mathrm{miss}}_{\mathrm{T}})$ [GeV] | $< 250$ {[TM], [MT]} | — | | |
| $N_{\mathrm{jets}}$ | $\geq 2$ | $\geq 0$ | 2 or 3 | $\geq 4$ |
| $N_{b-\mathrm{jets}}$ | 1 (77% DL1r) | 0 (77% DL1r) | 1 (60% DL1r) | $\geq 1$ (60% DL1r) OR $\geq 2$ (77% DL1r) |
| Region split | subleading $e/\mu \times$ {[TM], [MT], [MM]} | internal / material | — | — |

TABLE 9.4: Overview of event categorisation in the $2\ell$SS and $3\ell$ control regions. The lepton definitions are given in Table 9.1.

### 9.3.1 Fiducial-volume definition

Since the unfolding of the $t\bar{t}W$ signal in the differential measurement is performed at particle level, the particle-level fiducial phase space should be defined as close as possible to the reconstruction-level one in order to reduce the extrapolation uncertainties that may arise otherwise. The simulated events at particle level contain physics objects obtained from $pp$ collisions, which are selected after the hadronisation process, and prior to their interaction with the detector parts. The pileup effects are not considered in this selection. An overview of the object definition and selection, as well as the overlap removal used in the particle-level selection are shown in Table 9.5.

| Objects | |
|---|---|
| $e$ | $p_{\mathrm{T}} \geq 10$ GeV and $\lvert\eta\rvert < 2.47$ (excluding the LAr crack region at $1.37 < \lvert\eta\rvert < 1.52$) |
| $\mu$ | $p_{\mathrm{T}} \geq 10$ GeV and $\lvert\eta\rvert < 2.5$ |
| jets | anti-$k_{\mathrm{T}}$ $R = 0.4$ jets with $p_{\mathrm{T}} \geq 25$ GeV and $\lvert\eta\rvert < 4.5$ (with $N_{\mathrm{jets}}$ restricted to $\lvert\eta\rvert < 2.5$) |
| $b$-jets | tagged if jet originates from a ghost-matched $B$-hadron with $p_{\mathrm{T}} > 5$ GeV |
| $E_{\mathrm{T}}^{\mathrm{miss}}$ | vector sum of $p_{\mathrm{T}}(\nu)$ for all neutrinos in the event (apart from the ones from hadron decays) |
| **Overlap removal** | |
| $e$/jet | jet is removed if $\Delta R(e, \mathrm{jet}) < 0.2$ (applicable also for $b$-jets with $p_{\mathrm{T}} < 200$ GeV) |
| jet/$e, \mu$ | lepton is removed if $\Delta R(\ell, \mathrm{jet}) < \min(0.4, 0.04 + 10\,\mathrm{GeV}/p_{\mathrm{T},\ell})$ |
| **Selections** | |
| $2\ell$ | exactly two SS leptons<br>$p_{\mathrm{T}} \geq 20$ GeV<br>$N_{\mathrm{jets}} \geq 2$, $N_{b-\mathrm{jets}} \geq 1$ |
| $3\ell$ | exactly three leptons with total charge of $\pm 1e$<br>$p_{\mathrm{T}} \geq 20$ GeV (SS lepton pair)<br>$N_{\mathrm{jets}} \geq 1$, $N_{b-\mathrm{jets}} \geq 1$<br>$m_{\ell^+\ell^-}^{\mathrm{OSSF}} > 12$ GeV and $\lvert m_{\ell^+\ell^-}^{\mathrm{OSSF}} - m_Z\rvert > 10$ GeV<br>$\lvert m_{\ell\ell\ell} - m_Z\rvert > 10$ GeV |

TABLE 9.5: Object definitions and selections used for the fiducial phase space definition.

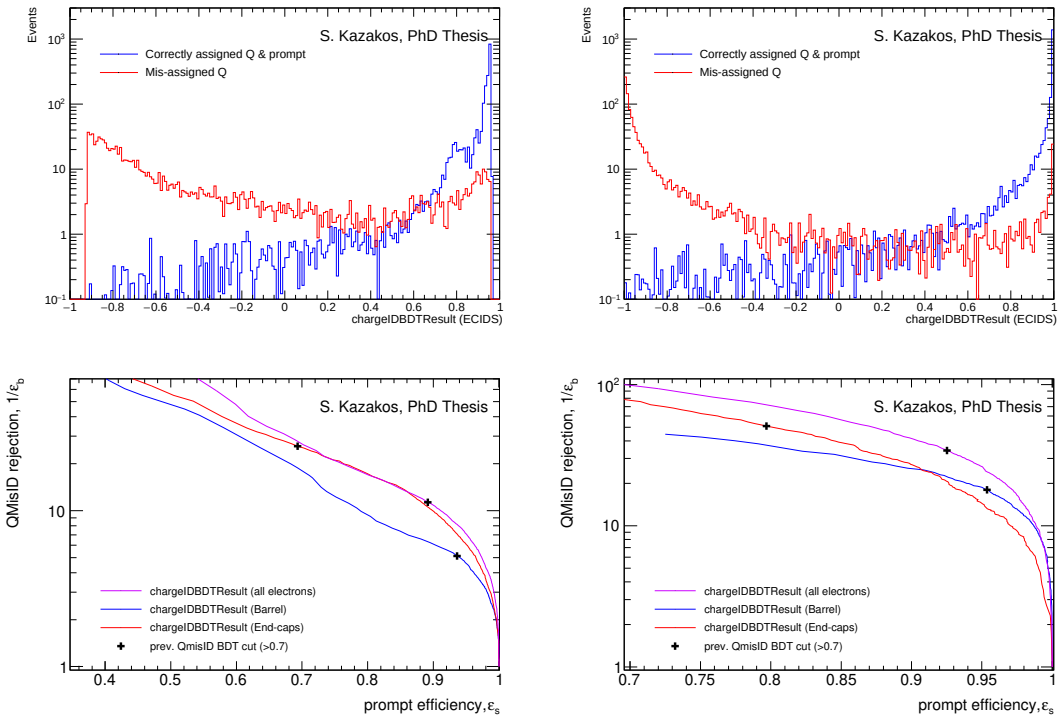
## 9.4 Background estimation and suppression

### 9.4.1 Estimation of events with charge-misassigned leptons

The estimation of the number of events containing leptons with misassigned charge is based on a data-driven approach in the $2\ell$SS channel. These charge-flipped leptons originate mainly from $t\bar{t}$ events and populate the $ee$ and $e\mu$ regions. They are the result of hard bremsstrahlung radiation and an asymmetric conversion ($e^{\pm} \to e^{\pm}\gamma^* \to e^{\pm}e^+e^-$) or the result of a wrongly measured track curvature. The fraction of events with charge-flipped muon candidates is negligible in the $p_{\mathrm{T}}$ range of the current analyses. The contribution of these events is often denoted as "QMisID" in the results discussed in Sections 9.6 and 9.7.

A dedicated Electron Charge Identification Selector (ECIDS) tool is used to suppress this background based on a BDT discriminant. The most up-to-date version of this discriminant showed worse performance than the one that had been previously used in other analyses. This effect is only observed in the region of phase space where the PLIV OP is applied, and it is more likely to originate from the

choice to train it on real instead of simulated MC data. A double-peak structure is also seen in the distribution of prompt electron in the discriminant of the recent version, amplifying the motivation to switch to the previous one. A comparison of the two versions is done using $t\bar{t}$ events, by requiring $2\ell$SS $e\mu$ events with lepton $p_{\mathrm{T}} > 20$ GeV. The distribution of the ECIDS discriminant and the corresponding ROC curves for central electrons are shown in Figure 9.1 for both versions after the `Tight` PLIV OP is applied. Based on these findings the selection of ECIDS BDT $> 0.7$ is applied as part of the tight electron definition.



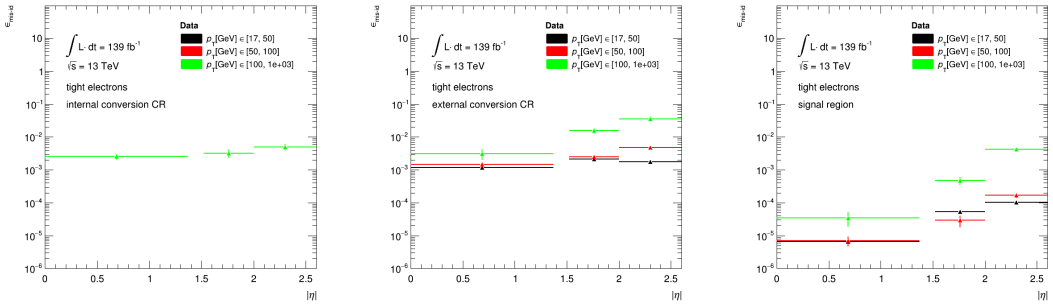

(a) (b)

FIGURE 9.1: Comparison of the ECIDS discriminants and ROC curves between the new (a) and the retrained older (b) ECIDS version. The figures correspond to $2\ell$SS $e\mu$ events with leptons of $p_{\mathrm{T}} > 20$ GeV and central electrons.

The events with charge-misassigned electrons that survive the selection criteria of the above tool are estimated using a data-driven method. The event rates are estimated from $Z \to e^+e^-$ events, using a likelihood-based method. The rates are derived as a function of electron $\eta$ and $p_{\mathrm{T}}$ (Figure 9.2) for electrons in the internal and material conversion CRs and in the SRs using the tight electron definition.

The rates are estimated using the fraction of $2\ell$OS events that are reconstructed as same SS

$$\epsilon_i(1-\epsilon_j) + \epsilon_j(1-\epsilon_i) = \epsilon_i + \epsilon_j - 2\epsilon_i\epsilon_j, \tag{9.1}$$




(a) (b) (c)

FIGURE 9.2: Electron charge-misassignment rates as a function of $|\eta|$, and parameterised in $p_{\mathrm{T}}$ for internal-conversion (a), external-conversion (b) and prompt (c) candidates. The rates are extracted from data using the likelihood method and the Tight electron definition at the VeryTight PLIV operating point.

where $\epsilon_i$ and $\epsilon_j$ are the QMisID rates for the leading and subleading electron, respectively.

The QMisID rates are used to compute the expected number of events with misidentified SS leptons $\bar{N}_{\mathrm{SS}}$ from the total number of observed OS events $N_{\mathrm{OS}}$, using the expressions

$$\bar{N}_{\mathrm{SS}} = \frac{\epsilon_i + \epsilon_j - 2\epsilon_i\epsilon_j}{1 - (\epsilon_i + \epsilon_j - 2\epsilon_i\epsilon_j)} N_{\mathrm{OS}} \quad \text{and} \quad \bar{N}_{\mathrm{SS}} = \frac{\epsilon_i}{1 - \epsilon_i} N_{\mathrm{OS}} \tag{9.2}$$

for the $ee$ and $e\mu$ channel, respectively. In the case of $e^{\pm}\mu^{\mp}$ events the respective fraction depends only on the QMisID rate, $\epsilon_i$, of the electron.

The estimation of the QMisID rates depends on data, based on the fraction of $Z \to ee$ decays that are reconstructed as SS pairs, around the reconstructed $Z$-boson peak. For a total number of electron pairs, $N^{ij}$, the expected number of events with misidentified SS leptons is

$$\bar{N}^{ij}_{\mathrm{SS}}(\epsilon_i, \epsilon_j) = N^{ij}\,(\epsilon_i + \epsilon_j - 2\epsilon_i\epsilon_j), \tag{9.3}$$

which can also be estimated as the expectation value of the Poisson distribution

$$f(N^{ij}_{\mathrm{SS}} \,|\, \bar{N}_{\mathrm{SS}}(\epsilon_i, \epsilon_j)) = \frac{[\bar{N}^{ij}_{\mathrm{SS}}]^{N^{ij}_{\mathrm{SS}}}\, e^{-\bar{N}^{ij}_{\mathrm{SS}}}}{N^{ij}_{\mathrm{SS}}!}. \tag{9.4}$$

This expression is integrated into a likelihood formalism

$$\mathscr{L}(\vec{\epsilon}\,|\,N_{\mathrm{SS}}) = \prod_{i,j} f(N_{\mathrm{SS}}^{ij}\,|\,\bar{N}_{\mathrm{SS}}(\epsilon_i,\epsilon_j)), \tag{9.5}$$

which is maximised (minimisation of $-2\ln\mathscr{L}$) to obtain the rates that best describe the data.

There are four sources of systematic uncertainty related to the estimation of QMisID rates that are combined into a single nuisance parameter defined as the quadratic sum of these contributions. These sources of uncertainty are:

- the statistical uncertainty from the likelihood maximisation depending on the sample size in the regions where the rates are extracted,
- the difference between the rates measured with the likelihood method and those obtained by truth-matching with simulated $Z \to ee$ events,
- the variation of the rates based on the $m_Z$ window, and
- the difference between the rates of electrons and positrons.

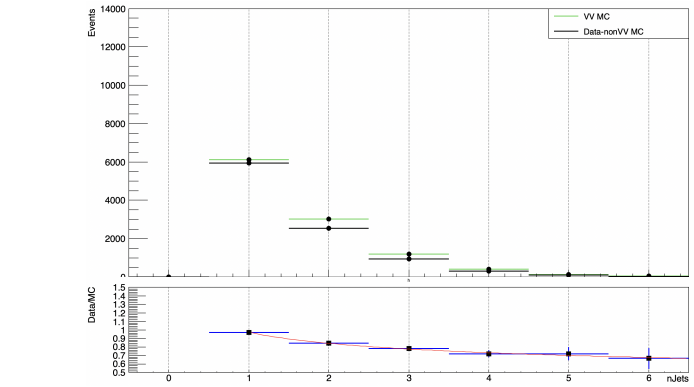
### 9.4.2 Data-driven corrections

The data-driven corrections mentioned in this section are used to correct the expectation value of various background processes known to be mismodelled.

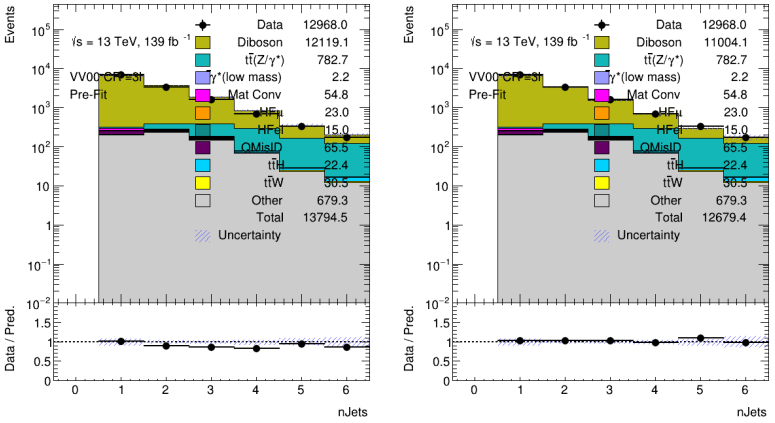
#### 9.4.2.1 Diboson $N_{\mathrm{jets}}$-dependent correction

An inclusive dedicated region enriched in diboson events is defined in order to derive a diboson correction as a function of number of jets. The so-called "$VV00$" region uses the same selections as in the definition of the diboson CR, apart from the selection on number of jets and $b$-jets, where at least one jet and exactly zero $b$-jets at 85% $b$-tagging OP are required. The selection in the number of $b$-jets serves as a way to suppress the $t\bar{t}Z$ background contribution, which is non-negligible at high number of jets.

The diboson sample is additionally split by flavour into the heavy-flavour (HF) part corresponding to diboson contributions from $b$- and $c$-quark-originated hadrons




(a)




(b) (c)

FIGURE 9.3: (a) Result of a polynomial fit to the ratio of non-diboson background subtracted data over the diboson MC expectation. The number of jets distribution in $VV00$ region is shown before (b) and after (c) the data-driven correction.

($VV$+HF), and the light-flavour part ($VV$+LF). Even though the $VV00$ region is dominated by the $VV$+LF part, the correction is assumed to be independent of the flavour of the extra jet(s). The correction is derived by fitting the ratio of the non-diboson background-subtracted data over the diboson MC contribution per number of jets. The polynomial used to fit the ratio is

$$f(x) = \frac{(2^c\, b - a)}{(2^c - 1)} + \frac{(b - a) \cdot 2^c}{(2^c - 1)x^c}, \tag{9.6}$$

which is actually a reparametrisation of the function

$$f(x) = a + \frac{b}{x^c}, \tag{9.7}$$

used to reduce correlations between the parameters $a$, $b$ and $c$.

After a $\chi^2$ fit to the polynomial above the parameters are found to be

$$a = -0.693 \pm 0.012, \quad b = -0.563 \pm 0.014, \quad \text{and} \quad c = 0.246 \pm 0.018.$$

The fit result is shown in Figure 9.3a and the number of jets distribution in the $VV00$ region is shown before and after the correction in Figures 9.3b and 9.3c, respectively. The derived correction is applied to the flavour-inclusive diboson MC contribution in the $VV$ CR.

A systematic uncertainty is derived related to this correction accounting for the different functions that could have been used, by taking into account the correlations between the three fit parameters. For this reason, the chosen fit function is studied in the eigen space, where it is characterised by three independent variations (fA, fB, fC). Each variation in the eigen space would move all three parameters up/down by different amounts. The largest $1\sigma$ effect among the three independent variations belongs to the fC variation. A conservative $3\sigma$ shape-only uncertainty based on the effect of the "fC" variation is derived, which is correlated between LF and HF contributions. A comparison of the 1, 2 and $3\sigma$ systematic variations are shown in Figure 9.4.

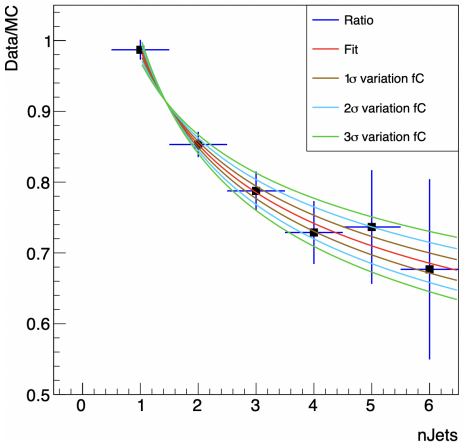



FIGURE 9.4: Comparison of 1, 2 and $3\sigma$ systematic variations related to the diboson $N_{\text{jets}}$ dependent correction.

#### 9.4.2.2 $t\bar{t}$ + heavy-flavour correction

Due to the known mismodelling of the $t\bar{t} + \geq 1b$-jets background (see $t\bar{t}H(bb)$ [208] and $t\bar{t}t\bar{t}$ $1\ell/2\ell$OS [209] analyses), the associated contribution from fakes is scaled

up by a factor of 1.3 following the measured correction in the aforementioned analyses.

#### 9.4.2.3 Non-prompt lepton $N_{b-\text{jets}}$ correction

The mismodelling in the $N_{b-\text{jets}}$ observed in the [TL] VRs (following the same selection as the one in 2$\ell$SS CRs, but with different lepton definitions and for $N_{\text{jets}} \geq 3$) is corrected with a data-driven correction derived as a function of $N_{b-\text{jets}}$ from the ratio of non-fake lepton background-subtracted data over the fake lepton MC contribution. These VRs are fitted separately together with the rest of the CRs and this ratio is obtained by the post-fit distribution after the previous $t\bar{t}$ +HF correction is applied. The post-fit distributions of the [TL] VRs, where this correction is derived, are shown in Figure 9.5 separately for the electron and muon channel. The derived correction is shown for both channels in Figure 9.6. This correction is applied to all fake-lepton contributions in MC in all analysis regions prior to the final template fit to data, resulting in an improved agreement between real and simulated MC data. The statistical uncertainty associated with this correction is added as a nuisance parameter in the final fit.

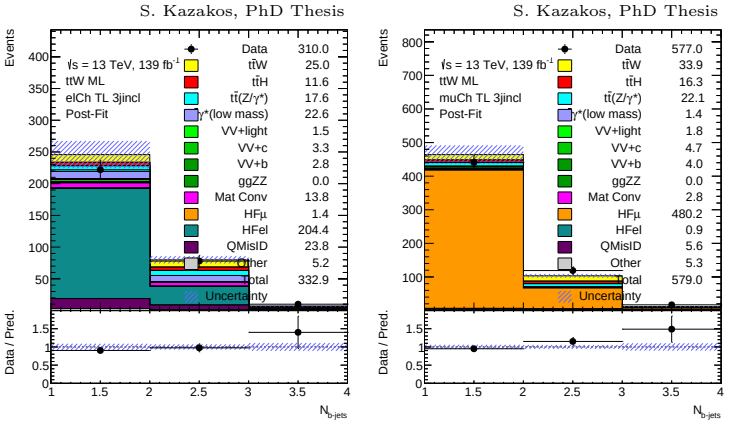



FIGURE 9.5: Post-fit data/MC agreement in the $N_{b-\text{jets}}$ distribution in [TL] VRs for the electron (left) and muon (right) channels.

### 9.4.3 Improved (non-) prompt lepton veto

The **PromptLeptonImprovedVeto (PLIV)** (introduced in [214]) is a BDT discriminant developed within ATLAS. This discriminant is a more recent version of the PromptLeptonVeto (PLV), which was first developed to be used in the

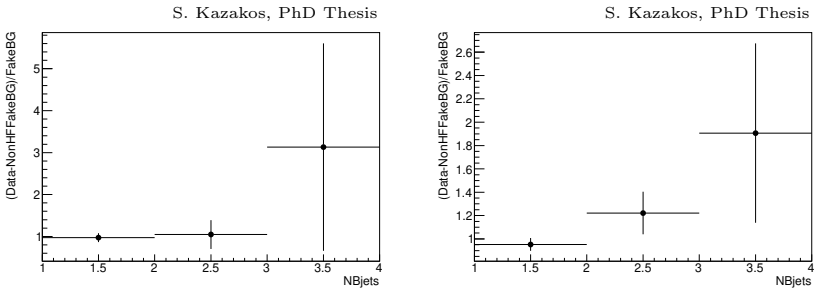



FIGURE 9.6: Data-driven correction derived for fake-lepton contributions as a function of $N_{b-\text{jets}}$ bin for the electron (left) and muon (right) [TL] VRs.

$t\bar{t}H$ [208] and $t\bar{t}t\bar{t}$ [209] cross-section measurements in the multilepton final state. The purpose of the PLIV is to discriminate between the prompt and non-prompt leptons in an event, and reject the latter, making it essentially a non-prompt lepton veto.

Non-prompt leptons originate from semileptonic decays from hadrons containing $b$- or $c$-quarks. Non-prompt leptons often fail the isolation selection criteria, but a small fraction of them can pass this selection. In the training, the prompt leptons originate from $WZ$ or $WH$ events, while the non-prompt leptons from $t\bar{t}$ events. The PLIV discriminant is trained based on jet-associated track information and the information about the secondary vertices of the jet.

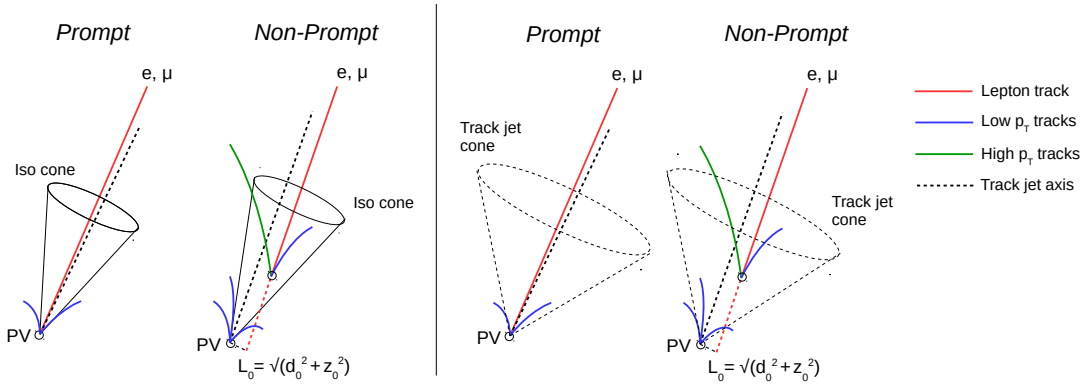
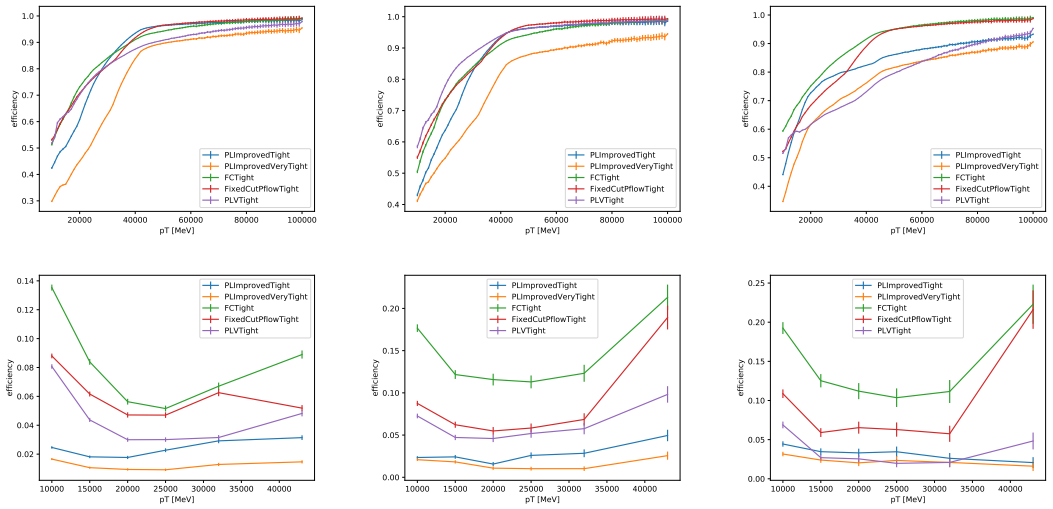



FIGURE 9.7: Schematic illustration of prompt and non-prompt lepton candidates that pass basic impact parameter ($d_0$, $z_0$) and isolation cuts. The parameter $L_0$ corresponds decay length from the primary vertex (PV) to the secondary vertex. Figure taken from Ref. [214].

The list of the PLIV input variables used in the training also contains variables related to the association of the lepton candidate to a track jet, variables related to the isolation and $p_{\text{T}}$ of the lepton candidate and variables related to the hadron lifetime. The PLIV input-variable list is given in Table 9.6.




(a) (b) (c)

FIGURE 9.8: Prompt and non-prompt lepton efficiencies for the PLIV Tight and VeryTight operating points for muon (a), central electron (b), and forward electron (c) candidates.

There are three discriminants trained separately that correspond to muon, central and forward electron candidates. The same PLIV input variables are used in the two electron cases, while a slightly modified set of variables is used in the muon case.

A $p_{\mathrm{T}}$-dependent selection approach is used in the PLIV OP definition aiming to smoothen lepton efficiencies versus lepton $p_{\mathrm{T}}$, resulting to relatively flat non-prompt lepton rejection efficiency as a function of lepton $p_{\mathrm{T}}$. The prompt and non-prompt lepton efficiencies are shown separately for $\mu$, $e$ (barrel) and $e$ (end-cap) in Figure 9.8. Two PLIV OPs are defined and calibrated based on this approach known as `Tight` and `VeryTight`.

### 9.4.4 Template Fit method

The estimation of $2\ell$SS and $3\ell$ events containing non-prompt leptons from HF semileptonic decays and leptons originating from photon conversions is achieved through the Template Fit method. This method was first developed during the $t\bar{t}H$ cross-section measurement in the multilepton final state [208], and it is a semi data-driven method. It relies on the definition of proper CRs targeting these specific backgrounds, and the splitting of MC samples in templates using truth information.

| Inputs | Description | PLIV$_\mu$ | PLIV$_e$ |
|---|---|---|---|
| PromptLeptonRNN | Used RNN track impact parameters and relationship between track jet and lepton | ✓ | ✓ |
| $l_{\text{SVtoPV}}^{\text{longitudinal}}/\sigma$ | Secondary vertex longitudinal significance using tracks with $p_{\text{T}} > 500$ MeV | ✓ | ✓ |
| $p_{\text{T}}$VarCone30/$p_{\text{T}}$ | Lepton isolation using ID tracks within a cone of $\Delta R < 0.3$ | - | ✓ |
| $p_{\text{T}}$Cone30TightTTVA500/$p_{\text{T}}$ | Similar as $p_{\text{T}}$VarCone30/$p_{\text{T}}$, additional cuts on tracks are $p_{\text{T}} > 0.5$ GeV and pass loose vertex association requirement | ✓ | - |
| $E_{\text{T}}$TopoCone30/$p_{\text{T}}$ | Lepton isolation using topological clusters within a cone of $\Delta R < 0.3$ | ✓ | ✓ |
| $E_{\text{cluster}}^{\mu}/E_{\text{expected}}$ | Relative muon calorimeter cluster energy | ✓ | - |
| $\sum_{\text{cluster}}^{\Delta R<0.15} E_{\text{T}}/p_{\text{T}}$ | Sum of cluster energy divided by lepton $p_{\text{T}}$ | - | ✓ |
| $N_{\text{track}}$ in track jet | Number of tracks clustered by the track jet | - | ✓ |
| $p_{\text{T}}^{\text{rel}}$ | Lepton $p_{\text{T}}$ along the track jet axis: $p \cdot \sin(\langle \text{lepton}, \text{track jet} \rangle)$ | - | ✓ |
| $p_{\text{T}}^{\text{lepton track}}/p_{\text{T}}^{\text{track jet}}$ | Lepton track $p_{\text{T}}$ divided by track jet $p_{\text{T}}$ | ✓ | ✓ |
| $\Delta R(\text{lepton}, \text{track jet})$ | $\Delta R$ between the lepton and the track jet axis | ✓ | ✓ |
| $p_{\text{T}}^{\text{lepton}}$ bin number | Index of the bin of lepton $p_{\text{T}}$ | ✓ | ✓ |

TABLE 9.6: A table of the variables used in the training of PromptLeptonImprovedVeto.

The main contribution to non-prompt lepton background comes from $t\bar{t}$, followed by smaller contributions from $V$+jets and single-top processes. The simulated MC samples corresponding to these processes are grouped together as "fake-lepton" samples, and are categorised in templates based on lepton truth attributes of the *MCTruthClassifier* as follows:

- **Prompt leptons**: leptons that originate directly from the top-quark decay (truth origin = 10), from Bremsstrahlung radiation (truth origin = 5, truth type = 2, and parent of the truth particle to be the same particle) or rare top decay (muon truth origin = 0).

- **Non-prompt leptons**: leptons originating from heavy-flavour (HF) hadronic decays of $b$-quark- (truth origin = 26, 29, 33) or $c$-quark- (truth origin = 25, 27, 28, 32) initiated jets. Events with leptons from other decays such as light-flavour (LF) hadronic decays are also included in this category, since their contribution is minor. This category is further split according to the light-lepton flavour to contributions from electron and muon candidates (**Non-prompt $e$** or **HF$e$**, and **Non-prompt $\mu$** or **HF$\mu$**).

- **Conversion electrons**: electrons from photon conversion (truth origin = 5, except Bremsstrahlung radiation, or truth parent type = 21 and truth parent origin = 0). This category is further split in electrons originating from external/-material conversions (**ExtCO or MatConv**), and electrons originating from internal conversions ($\gamma^* \to \ell\ell$) with $m_{\ell\ell} < 1$ GeV (**IntCO or $t\bar{t}\gamma^*$(low mass)**).

Four normalisation factors (NFs) are attributed to the above non-prompt and conversion templates, namely $\hat{\lambda}_e^{\mathrm{HF}}$, $\hat{\lambda}_\mu^{\mathrm{HF}}$, $\hat{\lambda}_e^{\mathrm{MatC}}$ and $\hat{\lambda}_e^{\mathrm{IntC}}$, which will be determined from the fit to real data affecting the MC contributions of these templates in all analysis regions. The $\mathrm{HF}_e$ and $\mathrm{HF}_\mu$ NFs are also found to be independent of the $p_{\mathrm{T}}$ of the lepton.

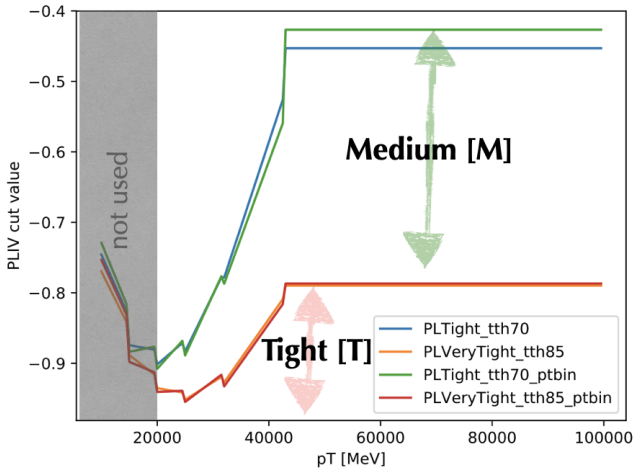
A precise estimate of the non-prompt HF lepton background is put in place being part of the so-called **extended** template fit. This is achieved by constructing fake-enriched CRs by exploiting the exclusive working points (WPs) defined by the PLIV OPs. These exclusive WPs together with the rest of selections of Table 9.1 constitute the WPs for the lepton definitions, which are labelled as:

- **Tight** [**T**]: corresponding to lepton candidates that pass the `VeryTight PLIV` isolation requirement.
- **Medium** [**M**]: corresponding to lepton candidates that fail the `VeryTight PLIV` isolation requirement, but pass the `Tight PLIV` requirement.
- (**Loose** [**L**]: corresponding to lepton candidates that fail the `Tight PLIV` isolation requirement, but satisfy the selection criteria of $\mathrm{PLIV}_{e/\mu} < 0$.)

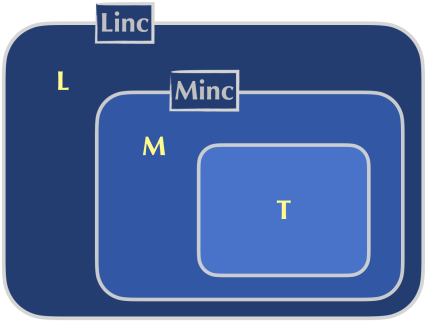
The $p_{\mathrm{T}}$-dependent nature of the PLIV is shown for the [T] and [M] WPs in Figure 9.9a, while the lepton definitions based on the PLIV WPs is demonstrated in Figure 9.9b.

The definition of the non-prompt lepton CRs is based on these WPs leading to the definition of the [TM], [MT] and [MM] CRs, in which the two letters correspond to the WP of the leading and subleading (in $p_{\mathrm{T}}$) lepton candidates, respectively.

Overall, this approach leads to a very sophisticated non-prompt lepton estimation, where the associated contributions are modelled in a "pseudo-continuous" way (à la $b$-tagging) by performing a simultaneous fit in all regions. Notice that the $\mathrm{HF}e/\mu$ non-prompt NFs are correlated between [T] and [M] lepton candidates.




(a)




(b)

FIGURE 9.9: (a) Illustrative sketch demonstrating the $p_{\mathrm{T}}$-dependent nature of exclusive PromptLeptonImprovedVeto (PLIV) operating point definitions. The red/orange curve indicates the VeryTight PLIV threshold, whereas the green/blue curve indicates the Tight PLIV threshold. (b) Sketch of the lepton definitions based on the inclusive and exclusive PLIV working points.

The [T] and [M] lepton definitions are pretty close in terms of PLIV cuts and the PLIV input variable distributions are also similar and well-described post-fit for both [T] and [M] WPs. This justifies the assumption that the calibration of the [M] non-prompt leptons derived from the fit could be applied to the [T] non-prompt lepton events contributing to the SRs. In order to further support this argument, an additional [M]-to-[T] flat extrapolation uncertainty of 20% is added to the fit to account for possible differences between the two WPs in the non-prompt lepton calibration, based on comparisons among the $t\bar{t}$ generators (POWHEG-BOX + PYTHIA-8 vs POWHEG-BOX + HERWIG-7). The input PLIV variables used in the training of the PLIV discriminant are also studied in a [TM] VR with exactly one $b$-jet, and an additional uncertainty is derived corresponding to bins that show data/MC mismodelling. [TL] VRs were also defined based on this approach to derive corrections associated to this extrapolation, such as the $N_{b-\mathrm{jets}}$ correction explained in Section 9.4.2.3.

The variable fitted in these non-prompt lepton CRs is the $p_{\mathrm{T}}$ of the subleading lepton and the corresponding distributions in each CR prior to the likelihood fit are shown in Figure 9.10.

The CRs targeting events with leptons from internal ($3\ell$IntC) and material ($3\ell$MatC)

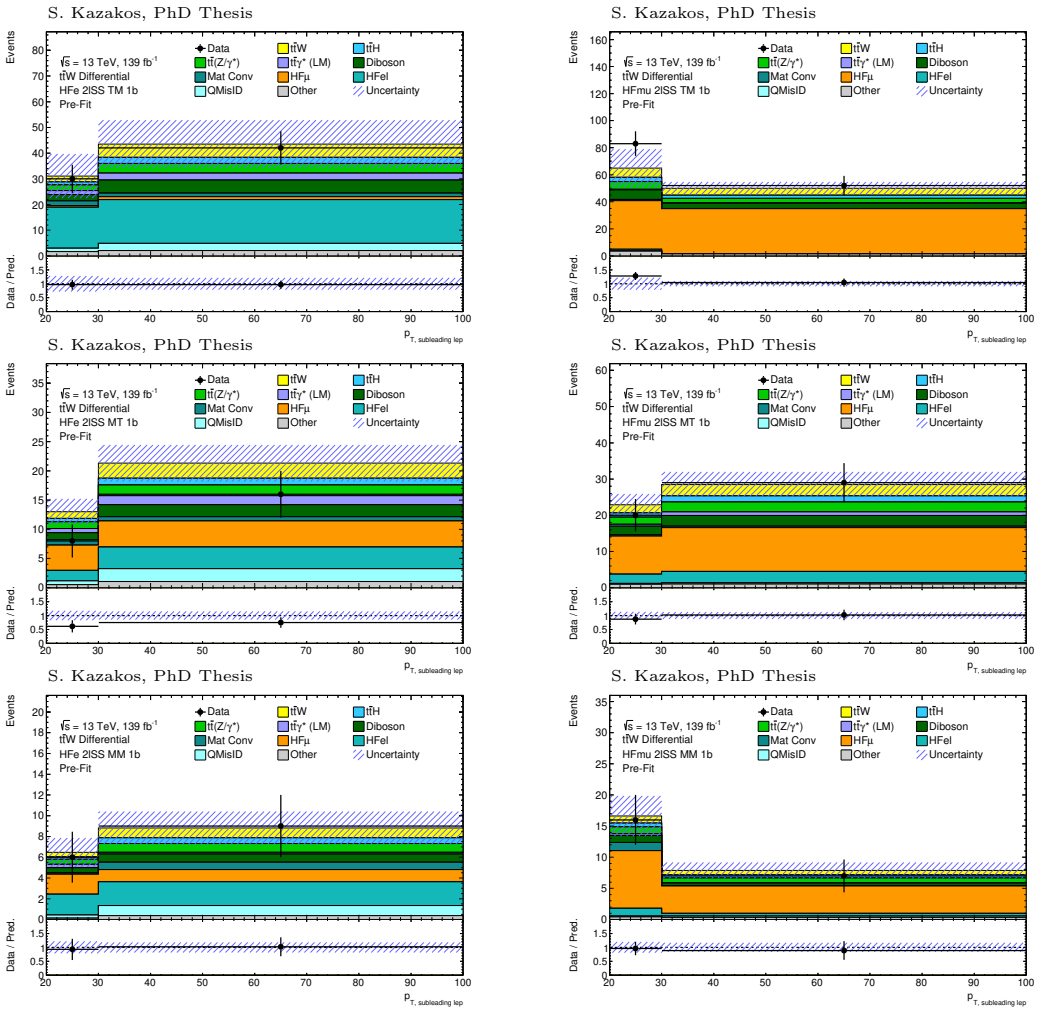



FIGURE 9.10: Data-to-simulation ratio of the variables used in the template fit (prior to the fit). The blue hatched band includes both statistical and systematic uncertainties.

conversions are defined based on three electron reconstructed variables: the conversion radius ($r_{\text{conv}}$), the invariant mass of the electron associated track and the track closest to it (assuming it is originating from a photon conversion) calculated at conversion vertex ($m_{\text{trk}-\text{trk, CV}}$), and the same invariant mass calculated at the primary vertex ($m_{\text{trk}-\text{trk, PV}}$).

The following conversion CR definitions are considered:

- **Material conversion CR ($3\ell$MatC)**: a region enriched in events where there is at least a conversion vertex (CV) within a radius of $r_{\text{conv}} > 20$ mm, and there is at least one electron candidate with invariant track mass at the CV in the range of $0 < m_{\text{trk}-\text{trk, CV}} < 100$ MeV.

- **Internal conversion CR ($3\ell$IntC)**: a region enriched in events not present in the material conversion CR that contains at least one electron with invariant track mass at the PV in the range of $0 < m_{\text{trk}-\text{trk, PV}} < 100$ MeV.

The number of events is fitted in these CRs and their data-to-simulation agreement before the likelihood fit to data is shown in Figure 9.11.

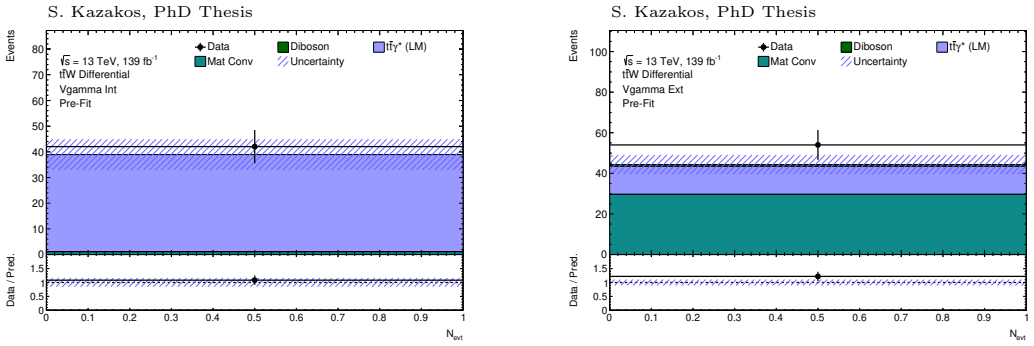



FIGURE 9.11: Data-to-simulation ratio of the variables used in the template fit (prior to the fit). The blue hatched band includes both statistical and systematic uncertainties.

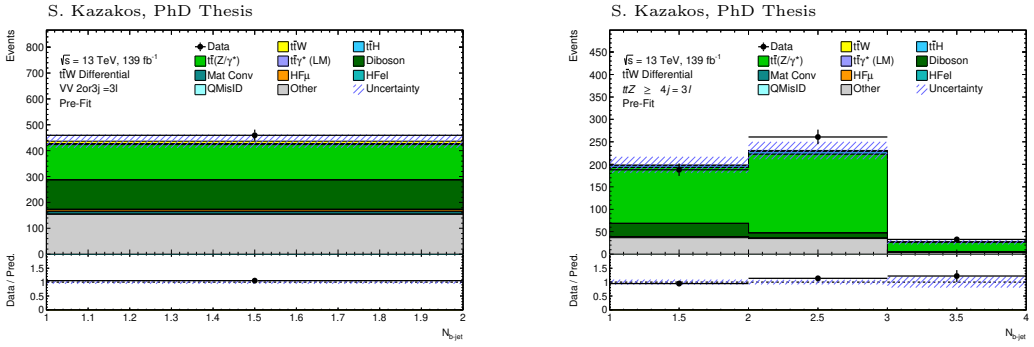



FIGURE 9.12: Data-to-simulation ratio of the variables used in the template fit (prior to the fit). The blue hatched band includes both statistical and systematic uncertainties.

Furthermore, two NFs, $\hat{\lambda}^{VV}$ and $\hat{\lambda}^{t\bar{t}Z}$, are associated to the diboson and $t\bar{t}Z$ contributions in all regions. These NFs are constrained in the final fit in principle from the $3\ell$VV and $3\ell$ttZ CRs that are enriched in the corresponding background contributions. The [Minc] lepton definition is used for these CRs, which covers lepton candidates passing [T] or [M] PLIV WPs. In these CRs the number of $b$-jets is fitted and the distributions are shown before the likelihood fit to data in Figure 9.12.

An additional NF, $\hat{\lambda}^{t\bar{t}W}$, is assigned to the $t\bar{t}W$ contribution corresponding to the signal strength of the analysis, which is mainly determined by the SRs (having high purity in $t\bar{t}W$ events). This NF can be further split in affecting separately

the events in the $2\ell$SS and $3\ell$ channels, and sometimes additionally split by total lepton charge.

The CRs defined up to this point are fitted together with the SRs of the analysis in a simultaneous **Template Fit** (TF), with the above NFs left free-floating. Similar to a BSM search, in the case of the inclusive $t\bar{t}W$ cross-section measurement the NF corresponding to the signal strength is also left free-floating in the fit. In this way the normalisation of the signal is estimated at the same time with the background estimation, after the background contributions are corrected according to their associated NFs derived from the fit. In the case of a differential cross-section measurement the TF method can be used in a similar fashion in a **Profile Likelihood Unfolding (PLU)** approach (see Section 9.7.2), where the unfolding of the signal contribution is performed at the same time with the TF, after the background contributions in the SR distributions have been corrected from the TF.

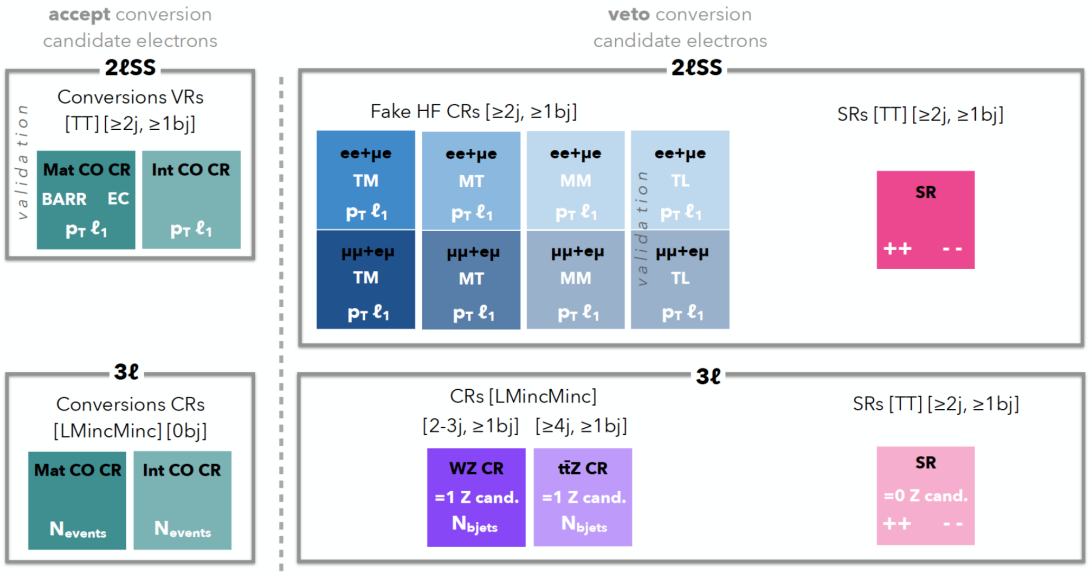



FIGURE 9.13: Illustrative sketch of all the analysis regions per channel. The discriminating variable shown per region in the CRs and SRs is the one used in the likelihood fit to data. The number of jets and $b$-jets selections as well as the lepton definitions are also shown.

A summary of all the analysis regions used in the fit together with their fitted variables is shown in Figure 9.13. In the same sketch some of the basic selections are denoted concerning number of jets and $b$-jets, while the lepton definition in

each region is also shown. The VRs of the analysis are included for completeness, though not participating in the fit.

The CRs participating in the template fit are shown in a single-bin summary plot prior to the fit together with their background compositions in Figure 9.14.

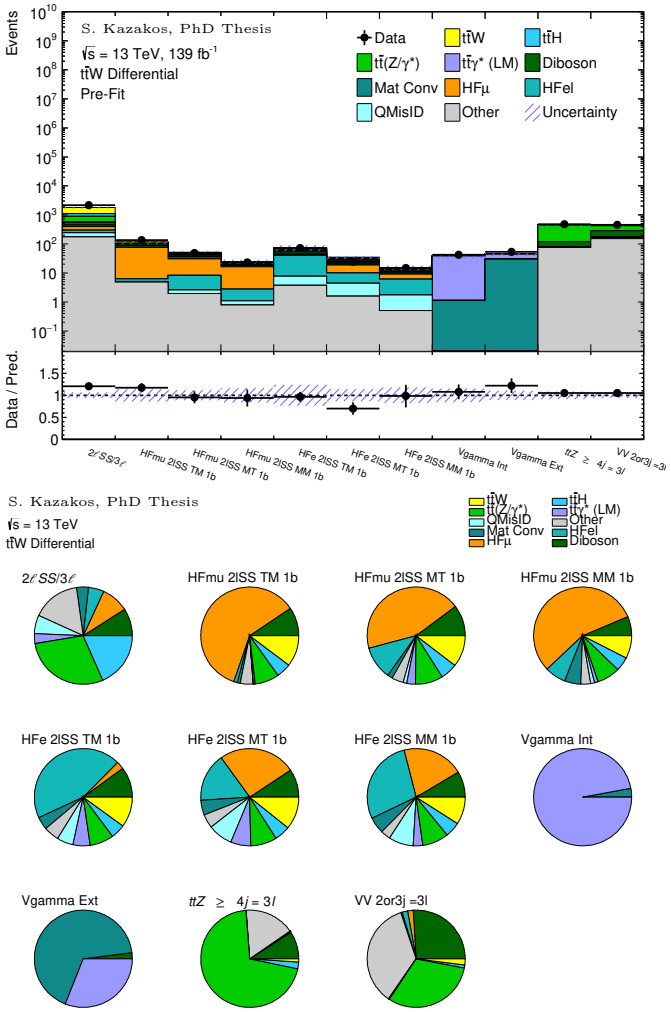



FIGURE 9.14: Data-to-simulation comparison (top) and background composition (bottom) in control regions before the template fit. The blue hatched band includes all statistical and systematic uncertainties. The $2\ell$SS/$3\ell$ signal region is also shown for consistency.

The results of a maximum likelihood template fit to data performed under the background-only hypothesis in the CRs of the analysis are summarised below. Since $\hat{\lambda}^{t\bar{t}W}$ is not left free-floating in this fit the associated cross-section uncertainties are used on the QCD and EW $t\bar{t}W$ components as Gaussian constraints. The fitted NFs together with their total uncertainties, and the correlation matrix demonstrating the correlations between the nuisance parameters (NPs) and NFs,

together with the "gamma" parameters after the fit are shown in Figure 9.15. Figures 9.16 and 9.17 show the pulls and constraints on the NPs that are included in the fit. The major pulls and constraints are observed in the $t\bar{t}Z$ variation and modelling uncertainties.

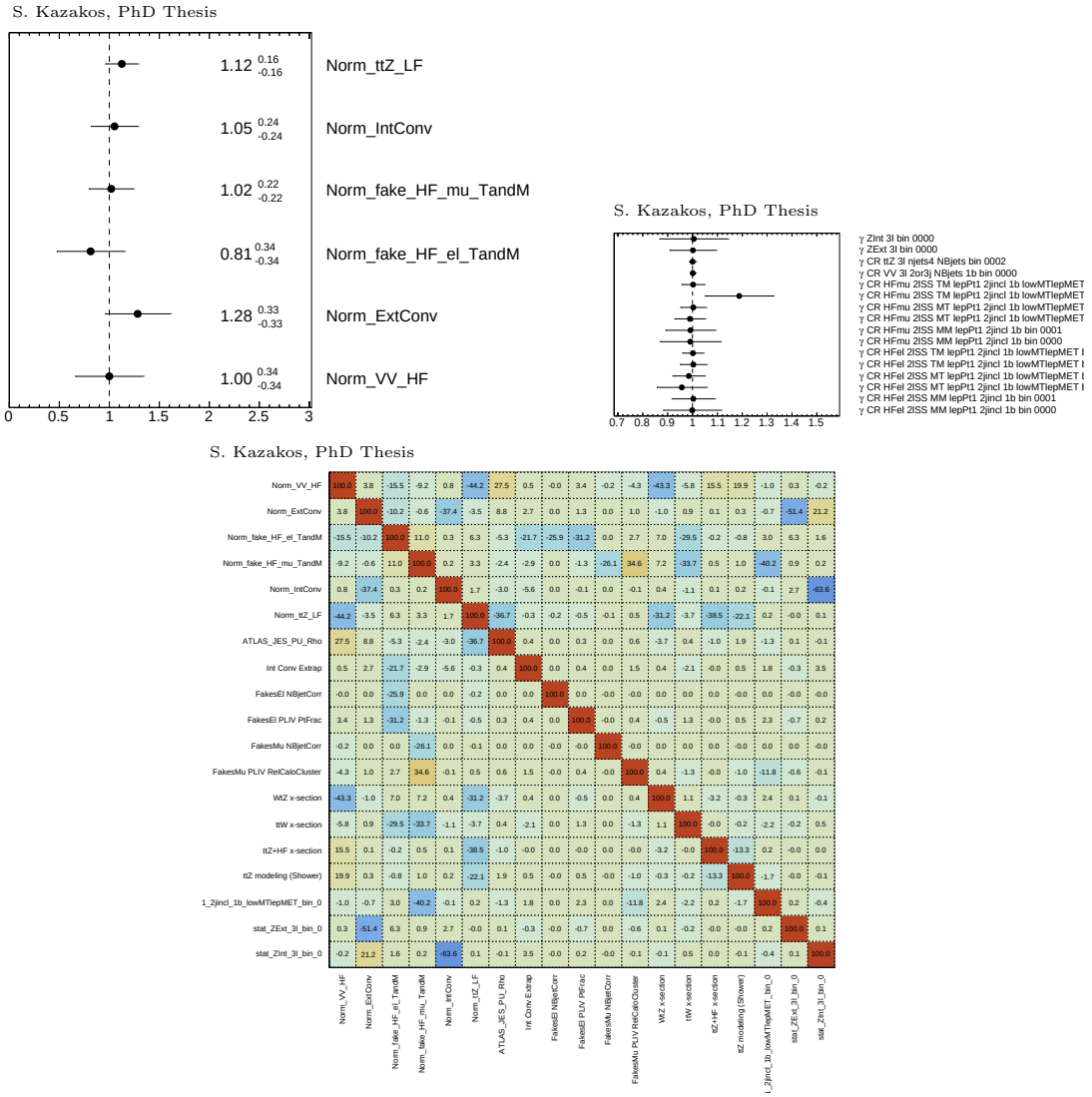



FIGURE 9.15: Fitted normalisation factors (top left), MC statistical "gamma" parameters (top right) and correlation matrix (bottom) from a template fit under background-only hypothesis in control regions. The normalisation factors for the background components of HF$e$, HF$\mu$, internal and material conversions, as well as diboson (HF) and $t\bar{t}Z$ (LF), are left free-floating.

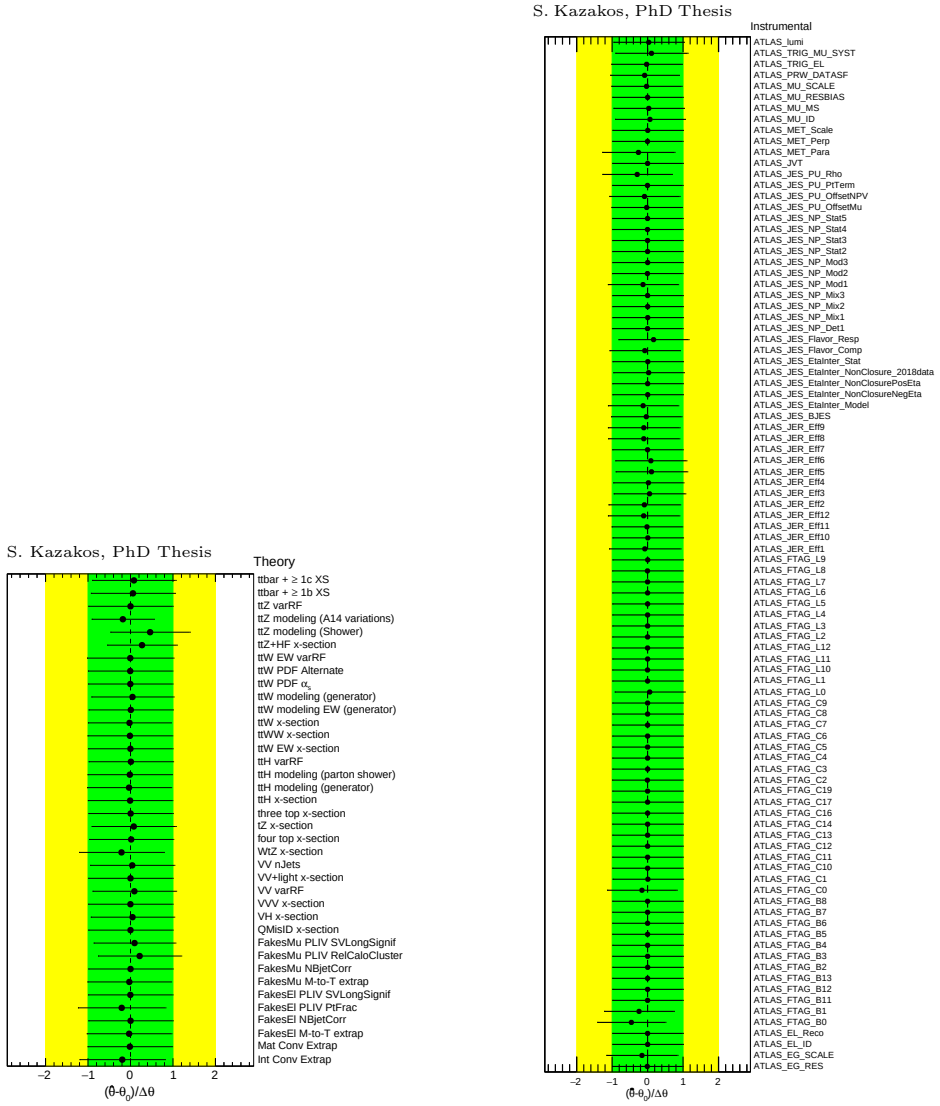



FIGURE 9.16: Pulls and constraints on the theory nuisance parameters (left) and on the instrumental nuisance parameters (right) after a template fit in control regions under the background-only hypothesis.

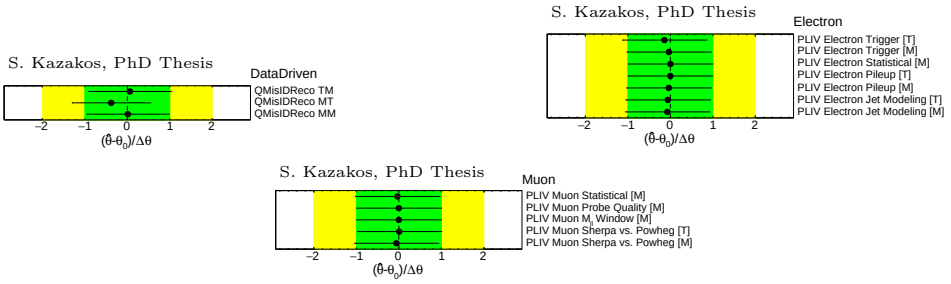



FIGURE 9.17: Pulls and constraints on the nuisance parameters of the data-driven QMisID background (upper left), electron PLIV SF uncertainties (upper right) and muon PLIV SF uncertainties (bottom) after a template fit in control regions under the background-only hypothesis.

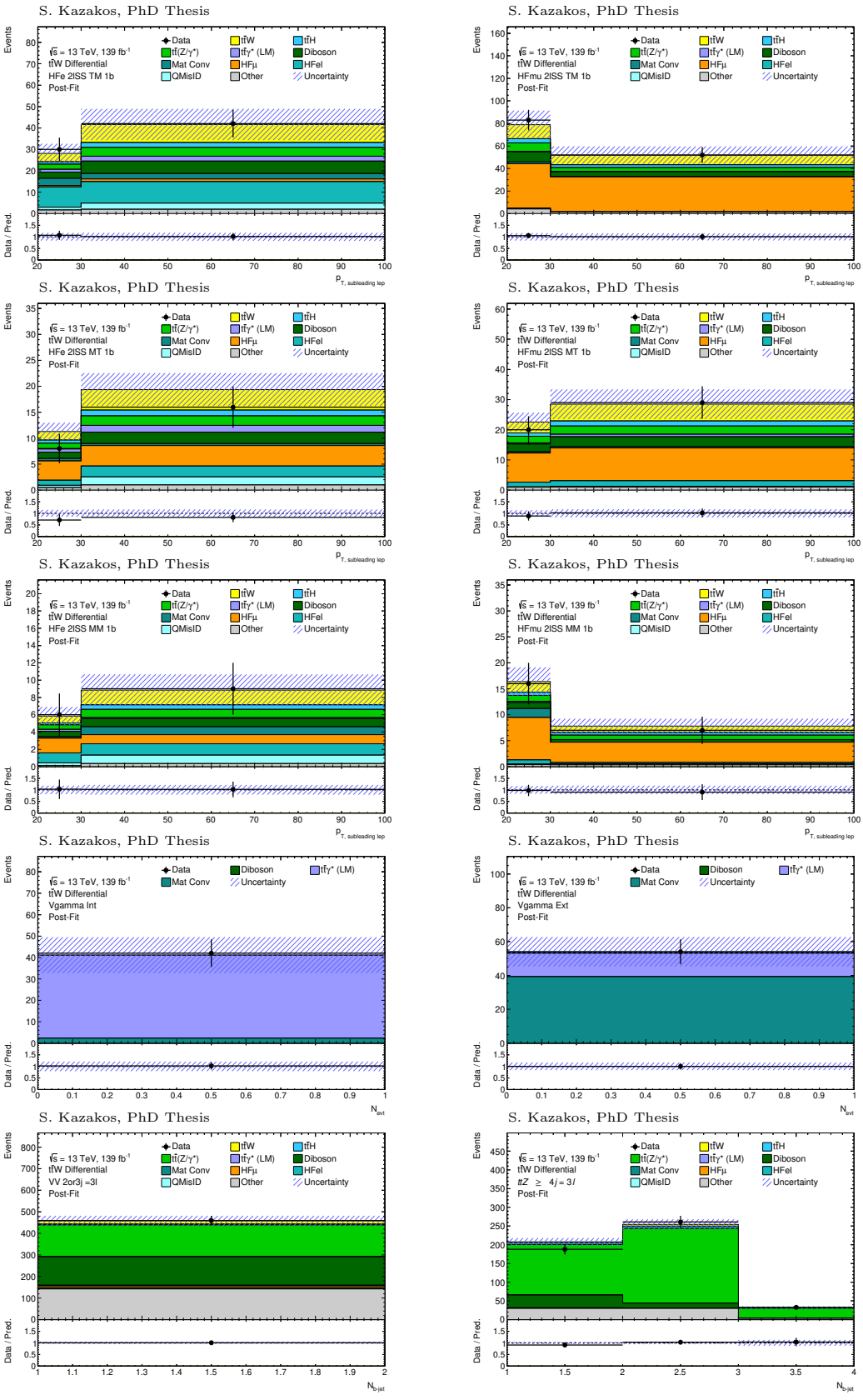



FIGURE 9.18: Data-to-simulation comparison and fitted variables in control regions after a template fit under the background-only hypothesis. The blue hatched band includes all statistical and systematic uncertainties.

The agreement of data to simulation in the variables fitted in the CRs after the template fit is shown in Figure 9.18. The CRs used in the fit are shown as single bins in a summary plot together with the background composition after the template fit in Figure 9.19.

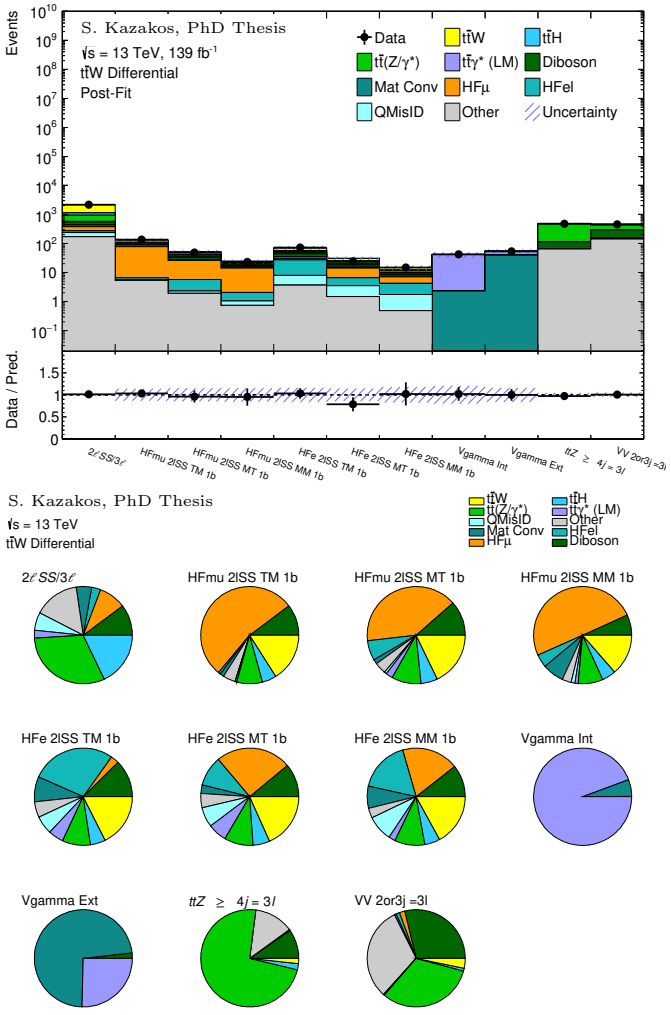



FIGURE 9.19: Data-to-simulation comparison (top) and background composition (bottom) in control regions after the template fit in CRs under the background-only hypothesis. The blue hatched band includes all statistical and systematic uncertainties. The $2\ell$SS/$3\ell$ signal region is also shown for consistency.

## 9.5 Systematic uncertainties

Apart from the systematic uncertainties defined in Section 8.5, additional uncertainties are defined in this analysis concerning the PLIV calibration, the correlation

between the lepton definitions, as well as on the fake-lepton background modelling and data-driven corrections.

Regarding the uncertainties related to the PLIV Tag & Probe calibration, the variations of the calibration procedure are included as separate nuisance parameters. In case of the electron channel, there are six uncertainties considered about: "jet modelling" (i.e. the SF difference between POWHEG-BOX + PYTHIA-8 and SHERPA $Z$ + jets simulated MC samples), pileup (i.e. the SF difference in different bins of $\langle\mu\rangle$), $m_{\ell\ell}$ window, template cut, tag-side ID and isolation OP variations. For the muon channel, there are ten uncertainties considered about: "jet modelling", $m_{\ell\ell}$ window, template shapes, probe-side ID OP, $\Delta R(\mu, jet)$, QCD fit, $\Lambda$-SC,[1] luminosity, cross sections of the relative processes, and MC statistics. Additionally in both channels the data statistics in the $Z \to \ell\ell$ CRs is considered as a systematic uncertainty on the scale factors. The uncertainties are treated as uncorrelated between the [M] and [T] lepton definitions. Additional uncertainties are derived to cover the difference between the FCLoose-isolation-only electron trigger calibration and the PLIV trigger calibration.

### 9.5.1 Systematic uncertainties on fake-lepton background modelling and data-driven corrections

Apart from the systematic uncertainties described above a dedicated systematics model is introduced concerning the estimation of processes containing HF non-prompt lepton, conversion and charge-misassigned candidates. These uncertainties were discussed at the corresponding sections, and are also summarised here in a more detailed way where needed:

- Uncertainties based on the mismodelling in the PLIV input variables in a [TM] VR with exactly one $b$-jet. They manifect themselves mainly in the variables: relative muon calorimeter cluster energy ($\boldsymbol{E_{\text{cluster}}/E_{\text{expected}}}$), the electron track $p_{\text{T}}$ divided by the jet track $p_{\text{T}}$ (**PtFrac**) and the secondary vertex longitudinal significance using tracks with $p_{\text{T}} > 500$ MeV ($\boldsymbol{l^{\text{longitudinal}}_{\text{SVtoPV}}/\sigma}$) for both electrons and muons. These uncertainties are considered as shape-only variations, based on the ratio of (data−nonFakeBG)/FakeBG as shown in Figure 9.20.

1 Related to the $\Lambda$ parameter used to approximate the energy required to produce a dimuon pair.

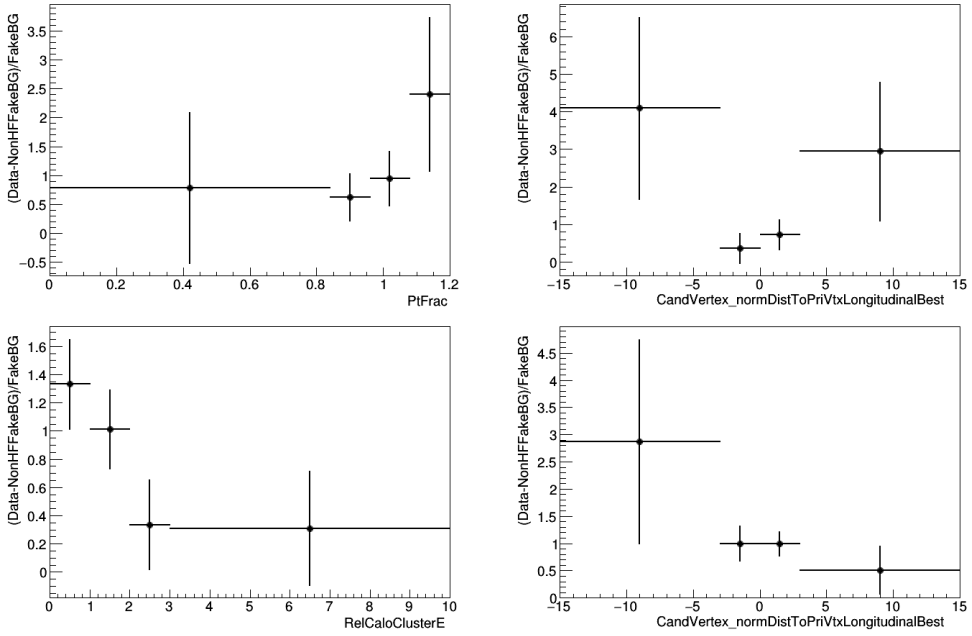



FIGURE 9.20: Residual data/MC difference in the distributions of the PLIV input variables in a [TM] region for electron (top) and muon candidates (bottom), based on which the corresponding uncertainties are derived.

- Extrapolation uncertainties for the fake-background yields between the [M] and [T] lepton definitions, which account for potential differences in the fakes rates between fake leptons passing the corresponding PLIV WPs.

  The non-prompt efficiencies are compared as a function of the fake-lepton $p_{\mathrm{T}}$ separately for electrons and muons, in a double-ratio plot including the PLIV WP and generator comparisons. Since the SHERPA prediction is known to be a bit far from the other generator options a flat 20% variation was used, based on the $t\bar{t}$ POWHEG-BOX + HERWIG-7.1.3 alternative sample as shown in Figure 9.21.

- Uncertainties on $t\bar{t}+$HF jets mismodelling for which an uncorrelated 50% uncertainty on the $t\bar{t}+b$ and $t\bar{t}+c$ background processes is assigned, to account for the uncertainty of the $t\bar{t}+$HF correction (Section 9.4.2.2).

- Internal and material conversion extrapolation uncertainties of 50% and 10%, respectively, to account for the extrapolation from $Z$-enriched to $t\bar{t}$-enriched regions. These uncertainties are derived through the residual data/MC mismodelling in the $2\ell$SS electron conversion VRs.

- QMisID uncertainties assigned uncorrelated to the corresponding QMisID contributions in the [TM], [MT] and [MM] CRs.

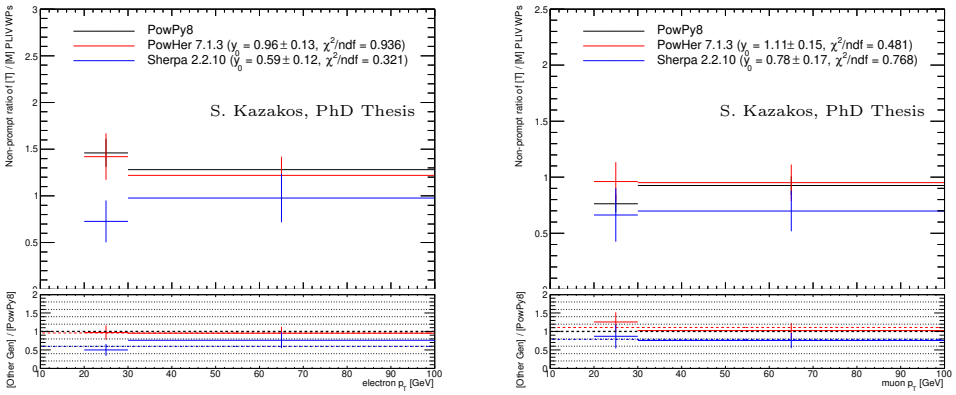
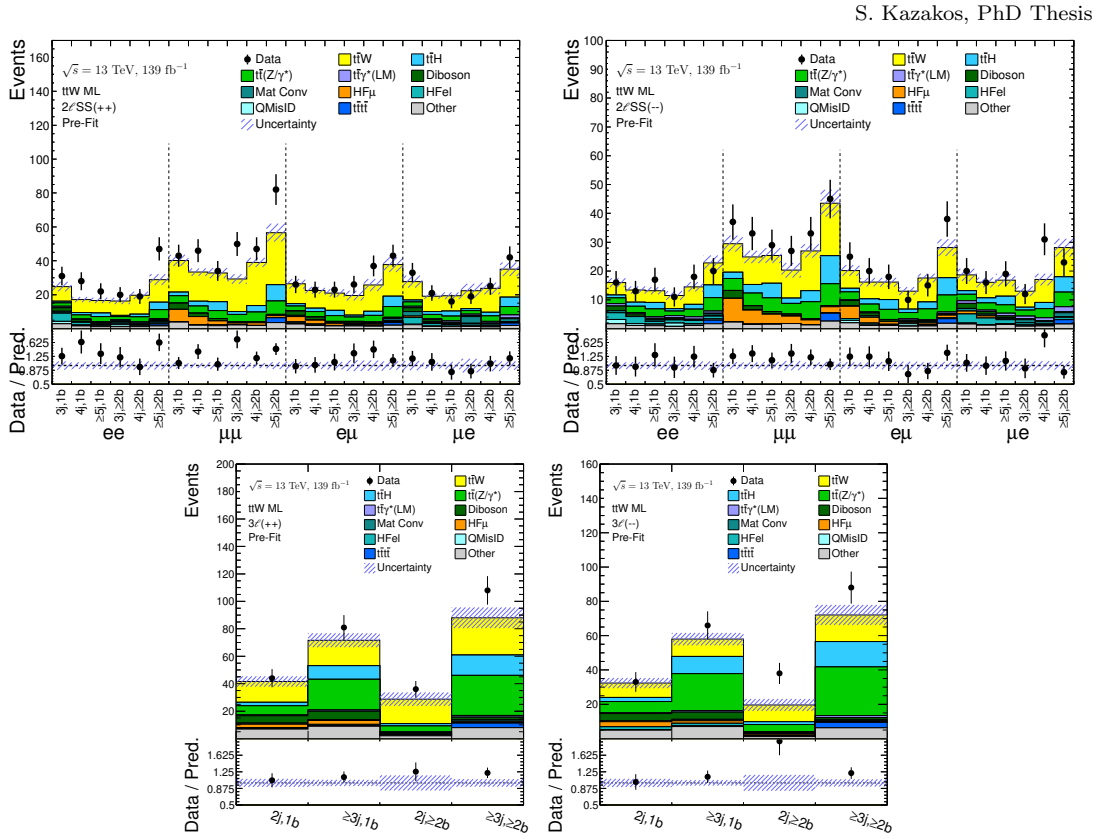



FIGURE 9.21: Comparison of non-prompt efficiency as a function of lepton $p_{\mathrm{T}}$ between Tight [T] and Medium [M] lepton definitions for different $t\bar{t}$ generators and separately for electron (right) and muon (left) candidates. In the upper pad the ratio [T]/[M] is shown for the different MC generators, while in the lower pad the ratio of each generator versus the nominal is shown.

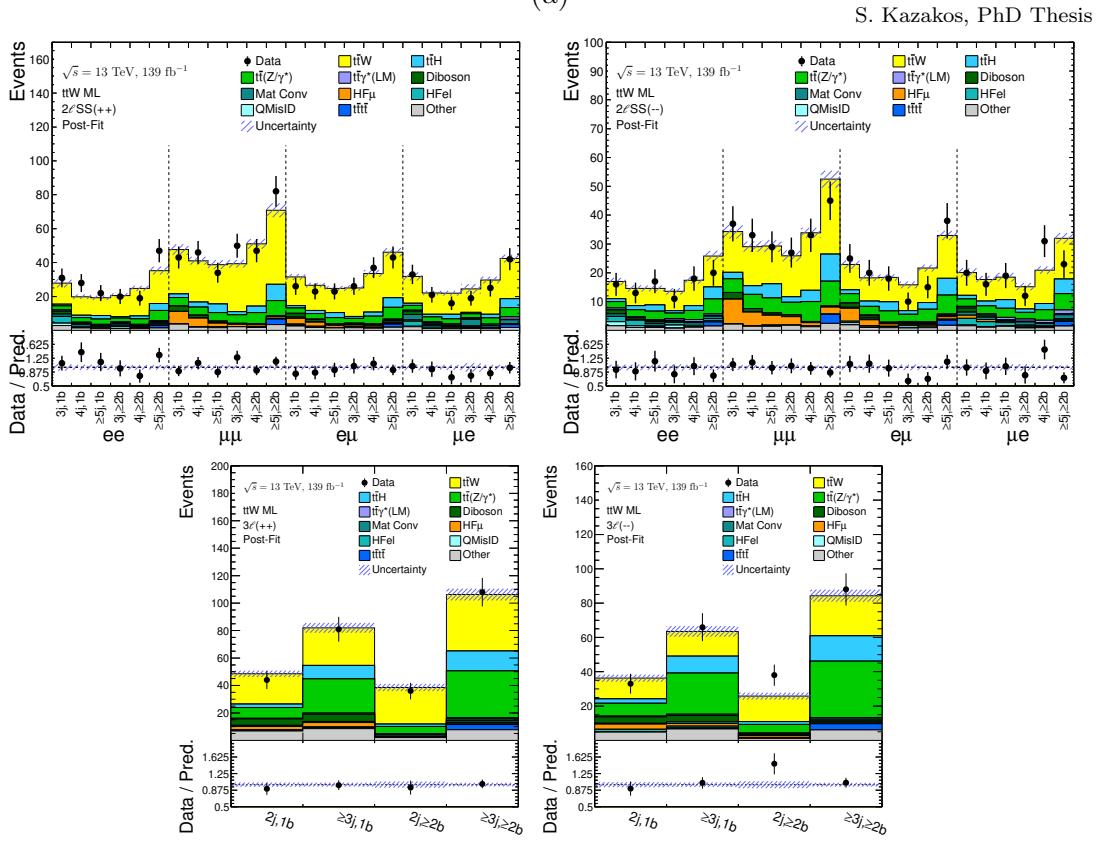
Additionally, a systematic uncertainty is assigned to diboson and $gg \to ZZ$ contributions to account for the different $N_{\mathrm{jets}}$ reweighting functions that can be used for the $N_{\mathrm{jets}}$ data-driven correction discussed in Section 9.4.2.1 (conservative $3\sigma$ variation). Finally, two nuisance parameters are introduced uncorrelated for non-prompt electron and muon contributions, which correspond to the statistical uncertainty related to the $N_{b-\mathrm{jets}}$ data-driven correction discussed in Section 9.4.2.3.

## 9.6 Inclusive $t\bar{t}W$ production cross-section measurement

The inclusive cross-section measurement is performed in an inclusive SR containing all events of the $2\ell$SS and $3\ell$ channels. The total event yields of the SR are split in single-bin templates, as shown in Table 9.3, and they are fitted together with the CRs of the analysis in a simultaneous template fit under the signal-plus-background hypothesis, where the signal strength $\mu$ is left free-floating together with the rest of the NFs. The signal strength $\mu$ in this case is defined as $\mu = \sigma_{\mathrm{meas.}}/\sigma_{\mathrm{SM}}$ and the fitted value represents the level of agreement between the measured cross section for a given process and its reference SM cross section (given in Section 2.5). A comparison of real to simulated events in the 56 bins fitted in the inclusive SR is shown before and after the likelihood fit to data under the signal-plus-background hypothesis in Figure 9.22.




(a)




(b)

FIGURE 9.22: Data-to-simulation comparison in the $2\ell$SS $++$ (top left), $2\ell$SS $--$ (top right), $3\ell$ $+$ (bottom left) and $3\ell$ $-$ (bottom right) signal region bins before (a) and after (b) a template fit in control and signal regions under the signal-plus-background hypothesis. The blue hatched band includes all statistical and systematic uncertainties.

A summary of the event yields in the inclusive SR split by channel and total lepton charge is shown after the template fit in Table 9.7.

| | $2\ell$SS $++$ | $2\ell$SS $--$ | $3\ell$ $+$ | $3\ell$ $-$ |
|---|---|---|---|---|
| Data | 803 | 546 | 269 | 225 |
| Total background | 790 ± 24 | 557 ± 16 | 273 ± 9 | 208 ± 7 |
| $t\bar{t}W$ | 472 ± 30 | 261 ± 20 | 116 ± 10 | 64 ± 6 |
| $t\bar{t}H$ | 66 ± 9 | 66 ± 9 | 28 ± 4 | 29 ± 4 |
| $t\bar{t}(Z/\gamma*)$ | 100 ± 10 | 95 ± 9 | 72 ± 8 | 69 ± 8 |
| $t\bar{t}\gamma*$ (LM) | 9 ± 5 | 9 ± 5 | 2.6 ± 1.5 | 2.6 ± 1.5 |
| Diboson | 22 ± 6 | 16 ± 5 | 12 ± 4 | 9.0 ± 2.7 |
| Mat Conv | 19 ± 5 | 11.1 ± 3.3 | 3.9 ± 1.1 | 2.5 ± 0.8 |
| HF$\mu$ | 30 ± 10 | 35 ± 11 | 6.6 ± 2.6 | 6.2 ± 2.6 |
| HF$e$ | 15 ± 6 | 14 ± 6 | 2.0 ± 0.8 | 2.9 ± 1.3 |
| QMisID | 8.2 ± 2.7 | 8.2 ± 2.7 | 0.66 ± 0.13 | 0.69 ± 0.15 |
| $t\bar{t}t\bar{t}$ | 9 ± 7 | 9 ± 7 | 4.2 ± 3.3 | 4.0 ± 3.2 |
| Other | 42 ± 6 | 32 ± 5 | 25.0 ± 3.3 | 18.6 ± 3.1 |

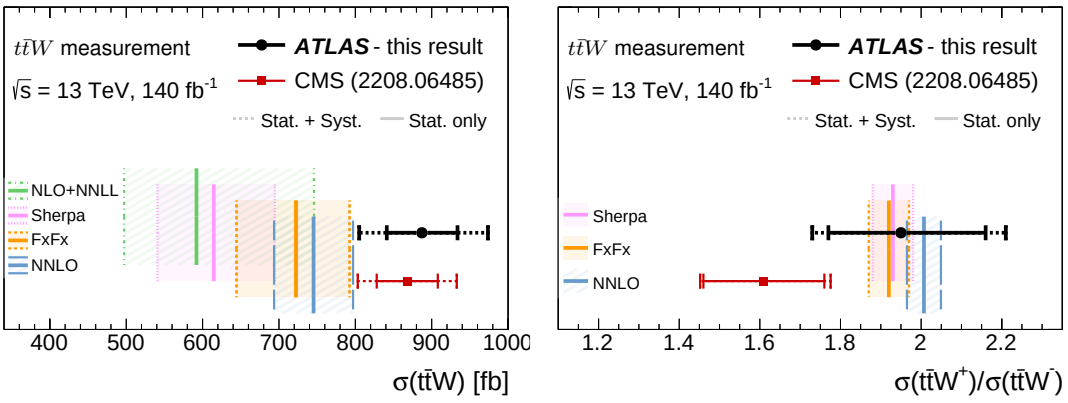
TABLE 9.7: Overview of the predicted and observed yields in the inclusive signal region after a likelihood fit to data under the signal-plus-background hypothesis. Dashes are used to denote the contributions that are either negligible or not applicable. Table taken from Ref. [215].

The fitted value of the observed $\mu_{t\bar{t}W}$ from the inclusive measurement is found to be $\mu_{t\bar{t}W} = 1.44^{+0.14}_{-0.13}$. The free-floated NFs are found to be $\hat{\lambda}_e^{\mathrm{HF}} = 0.83 \pm 0.31$, $\hat{\lambda}_\mu^{\mathrm{HF}} = 1.01 \pm 0.21$, $\hat{\lambda}_e^{\mathrm{MatC}} = 1.15 \pm 0.31$, $\hat{\lambda}_e^{\mathrm{IntC}} = 1.07 \pm 0.24$, $\hat{\lambda}^{VV\,\mathrm{HF}} = 0.87 \pm 0.33$, and $\hat{\lambda}^{t\bar{t}Z} = 1.16 \pm 0.15$. In addition to this fit, alternative setups are studied, where there are independent NFs assigned to $t\bar{t}W$ events in the $2\ell$SS and $3\ell$ channels, or to $t\bar{t}W^+$ and $t\bar{t}W^-$ events. The observed signal strength parameters from all these setups are summarised in Table 9.8, where they are also "translated" to the associated cross-section values as the product of a reference SM cross section and signal strength. The fitted NFs in these setups are very close to the ones from the inclusive $\mu_{t\bar{t}W}$ measurement, which are already reported above. The observed results show that the production cross section of the $t\bar{t}W$ process is measured to be larger than the SM reference value by about a factor of 1.44.

The cross-section ratio $R$ of $\sigma(t\bar{t}W^+)$ over $\sigma(t\bar{t}W^-)$ is extracted from another fit configuration by fitting the corresponding signal strength $\mu(R)$ resulting to a measurement of

$$R(t\bar{t}W) = 1.95\,^{+0.21}_{-0.18}\,(\mathrm{stat.})\,^{+0.16}_{-0.13}\,(\mathrm{syst.}) = 1.95\,^{+0.26}_{-0.22}\,(\mathrm{tot.}), \tag{9.8}$$

which is in very good agreement with the theoretical prediction of $R(t\bar{t}W) = 1.93 \pm 0.02\,(\text{scale}) \pm 0.04\,(\text{PDF})$ [215, 216]. The measured $t\bar{t}W$ inclusive cross section and the measured cross-section ratio, $R$, are shown in Figures 9.23a and 9.23b, respectively, where a comparison with the CMS result is also included.




(a) (b)

FIGURE 9.23: Comparison of the results of (a) the measured inclusive $t\bar{t}W$ cross section and (b) the cross-section ratio $\sigma(t\bar{t}W^+)/\sigma(t\bar{t}W^-)$ between ATLAS and CMS experiments. The theoretical predictions from SHERPA and MADGRAPH5_aMC@NLO + PYTHIA-8 (using the FxFx prescription and including EW corrections), together with the NNLO QCD + NLO EW state-of-art prediction from Ref. [25] are also overlaid. Figure adjusted from Ref. [215].

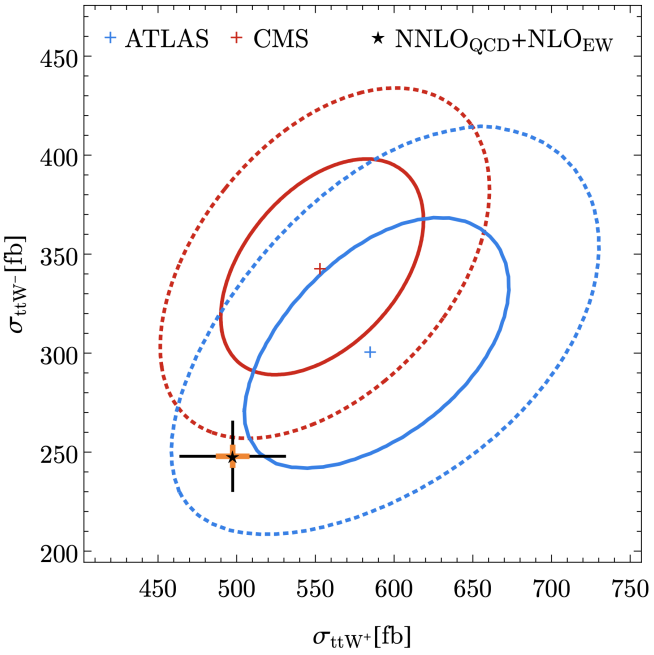



FIGURE 9.24: Comparison of the theoretical prediction corresponding to the NNLO QCD + NLO EW result to the measurements from the ATLAS (blue) and CMS (red) experiments. The 68% (solid) and 95% (dashed) confidence-level bands are also overlaid. Figure taken from Ref. [25].

Both ATLAS and CMS experiments are measuring higher inclusive $t\bar{t}W$ production cross section than expected, with their results being consistent to each other. However, in the result from ATLAS the cross-section ratio $\sigma(t\bar{t}W^+)/\sigma(t\bar{t}W^-)$ agrees well with the theoretical prediction, while the $t\bar{t}W^+$ versus $t\bar{t}W^-$ asymmetry is not as pronounced in the result of the CMS experiment.

| | Signal strength $\mu$ | Cross section $\sigma$ [fb] |
|---|---|---|
| $t\bar{t}W$ ($2\ell$SS) | $1.44\,^{+0.14}_{-0.13}\,(\text{tot.})\,\{\pm 0.08\,(\text{stat.})\,^{+0.12}_{-0.11}\,(\text{syst.})\}$ | $43.2\,^{+4.3}_{-4.0}\,(\text{tot.})\,\{\pm 2.4\,(\text{stat.})\,^{+3.5}_{-3.3}\,(\text{syst.})\}$ |
| $t\bar{t}W$ ($3\ell$) | $1.59\,^{+0.31}_{-0.26}\,(\text{tot.})\,\{\,^{+0.19}_{-0.18}\,(\text{stat.})\,^{+0.25}_{-0.19}\,(\text{syst.})\}$ | $16.3\,^{+3.2}_{-2.7}\,(\text{tot.})\,\{\pm 1.9\,(\text{stat.})\,^{+2.6}_{-2.0}\,(\text{syst.})\}$ |
| $t\bar{t}W$ | $1.44\,^{+0.14}_{-0.13}\,(\text{tot.})\,\{\,^{+0.08}_{-0.07}\,(\text{stat.})\,^{+0.12}_{-0.11}\,(\text{syst.})\}$ | $890\,\pm 80\,(\text{tot.})\,\{\pm 50\,(\text{stat.})\pm 70\,(\text{syst.})\}$ |
| $t\bar{t}W^+$ | $1.44 \pm 0.14\,(\text{tot.})\,\{\,^{+0.09}_{-0.08}\,(\text{stat.})\,^{+0.12}_{-0.11}\,(\text{syst.})\}$ | $585\,^{+58}_{-55}\,(\text{tot.})\,\{\,^{+35}_{-34}\,(\text{stat.})\,^{+47}_{-44}\,(\text{syst.})\}$ |
| $t\bar{t}W^-$ | $1.43\,^{+0.21}_{-0.20}\,(\text{tot.})\,\{\pm 0.13\,(\text{stat.})\,^{+0.17}_{-0.15}\,(\text{syst.})\}$ | $301\,^{+45}_{-41}\,(\text{tot.})\,\{\,^{+28}_{-27}\,(\text{stat.})\,^{+35}_{-31}\,(\text{syst.})\}$ |

TABLE 9.8: Summary of the fitted $t\bar{t}W$ signal strength parameters ($\mu$) and the cross-section ($\sigma$) values to which they correspond.

The relative charge asymmetry is another interesting observable that can be expressed using the measured cross sections as

$$A^R_{C,\,t\bar{t}W} = \frac{\sigma(t\bar{t}W^+) - \sigma(t\bar{t}W^-)}{\sigma(t\bar{t}W^+) + \sigma(t\bar{t}W^-)}. \tag{9.9}$$

The fitted value of this observable is measured to

$$A^R_{C,\,t\bar{t}W} = 0.32 \,\pm\, 0.05\,(\text{stat.}) \,\pm\, 0.03\,(\text{syst.}) = 0.32 \,\pm\, 0.06\,(\text{tot.}), \tag{9.10}$$

compared to the expected value of $A^R_{C,\,t\bar{t}W} = 0.322 \pm 0.003\,(\text{scale}) \pm 0.007\,(\text{PDF})$ [215, 216], the result corresponding to the SM prediction for the SHERPA sample. A fitted value close to the expected one suggests that even if the $t\bar{t}W$ production cross section is found to be larger in the inclusive $\mu_{t\bar{t}W}$ measurement, the relative charge asymmetry between $t\bar{t}W^+$ and $t\bar{t}W^-$ events is not affected. The total uncertainty is lower on this observable since some of the systematic uncertainties are cancelled out due to the $A^R_{C,\,t\bar{t}W}$ definition.

The correlations among the NPs and their pulls and constraints in the different configurations are similar to the ones shown in the CR-only fit shown in Section 9.4.4.

## 9.7 Differential $t\bar{t}W$ production cross-section measurement

### 9.7.1 Introduction to unfolding

In particle physics the typical measurements that are performed are based on counting experiments, where the observed events are classified according to their properties. The reconstructed distributions that are analysed for various observables are different from their "true" distributions due to limited detector resolution effects, as well as limited acceptance and efficiency. These factors lead to a distortion or *smearing* of the measured distributions compared to the expectation from an ideal detector. The procedure used to remove the detector effects from the observed distribution and to extract the underlying true distribution is known as *unfolding*. Unfolding is usually used to extract inclusive or differential cross sections of targeted physics processes, and it is usually performed at parton or particle level (the latter is used in this analysis). The unfolding problem always comes down to a matrix inversion problem, where the inverse of the response matrix $\mathcal{R}$ that is used to get to the reconstructed distribution from the true distribution is used to achieve the opposite result.

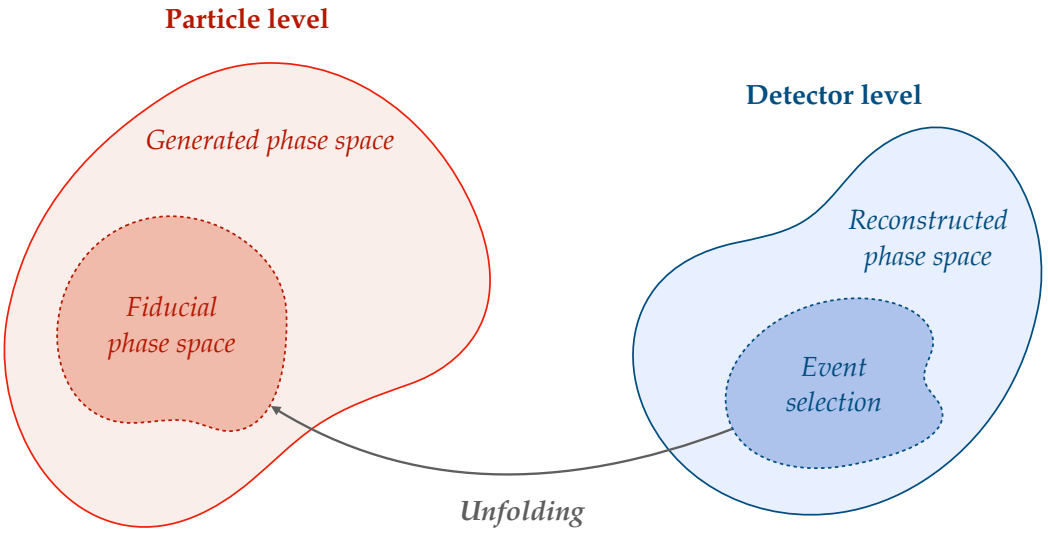



FIGURE 9.25: Illustrative sketch demonstrating the unfolding procedure from a selected region at detector level to particle level.

There are many alternative methods typically used for unfolding such as bin-by-bin correction unfolding [217], singular value decomposition (SVD) [218], Iterative Bayesian Unfolding (IBU) [219–221], Fully Bayesian Unfolding (FBU) [222], OmniFold [223] and so forth, each of which has its own advantages and disadvantages. Although IBU is the standard unfolding technique used in ATLAS the preferred method used in this analysis is known as Profile Likelihood Unfolding (PLU) and it is described in Section 9.7.2. IBU is often problematic in the case where signal and background are correlated and the use of this method is further motivated by the long-term plan of the ATLAS statistics committee for a common unfolding method. In principle, the optimal method for unfolding is mostly analysis dependent and as shown below it is always related to finding the proper balance between bias and smoothness.

### 9.7.2 Profile likelihood unfolding

A true distribution $f_{\text{true}}(x)$ of a true variable $x$ that is not often accessible is related to the measured distribution $f_{\text{meas.}}(y)$ of a measured variable $y$ for a given physics process through the relation

$$f_{\text{meas.}}(y) = \int \mathcal{R}(y,x)\, f_{\text{true}}(x)\, dx, \tag{9.11}$$

where $\mathcal{R}(y,x)$ represents the response matrix.

Since the distributions are studied in bins it makes sense to use the discretised form of this equation in a histogram formalisation where it can be transformed to the sum

$$N_i^{\text{det.}} = \sum_{j=1}^{m} \mathcal{R}_{ij}\, N_j^{\text{fid.}} = \sum_{j=1}^{m} \mathcal{R}_{ij}\, \mu_j\, s_j + b_i, \tag{9.12}$$

where $N_i^{\text{det.}}$ ($N_j^{\text{fid.}}$) corresponds to the expected number of events in the $i^{\text{th}}$ ($j^{\text{th}}$) bin of the detector-level (particle-level) histogram, with index $i$ ($j$) running over the detector-level (particle-level) bins $i = 1, \ldots, n$ ($j = 1, \ldots, m$).

Equation 9.12 is used to substitute the expected events, $N_{\text{exp},\,i}$, in Equation 8.8, which is transformed into

$$\mathscr{L}(\mu, \vec{\theta}\,) = \prod_{i=1}^{n} P\left( N_{\text{obs},\,i} \,\middle|\, \sum_{j=1}^{m} \mathcal{R}_{ij}(\vec{\theta}_s\,)\, \mu_j\, s_j(\vec{\theta}_s\,) + b_i(\vec{\theta}_b\,) \right) \prod_{k=1}^{l} \rho_k(\vec{\theta}\,). \tag{9.13}$$

In these equations $\mathcal{R}_{ij}$ takes the form of a $n \times m$ matrix defined as

$$\mathcal{R}_{ij} = \frac{1}{\alpha_i}\,\varepsilon_j\,\mathcal{M}_{ij}, \tag{9.14}$$

where $\alpha_i$ represents the acceptance, $\varepsilon_j$ represents the efficiency and $\mathcal{M}_{ij}$ is known as the *migration* matrix. This matrix is used to quantify the bin-to-bin migrations of events from particle to detector level (occurring because of resolution effects), and it is defined as

$$\mathcal{M}_{ij} = \frac{N_{ij}^{\text{det.}\cap\text{fid.}}}{N_{j}^{\text{det.}\cap\text{fid.}}}. \tag{9.15}$$

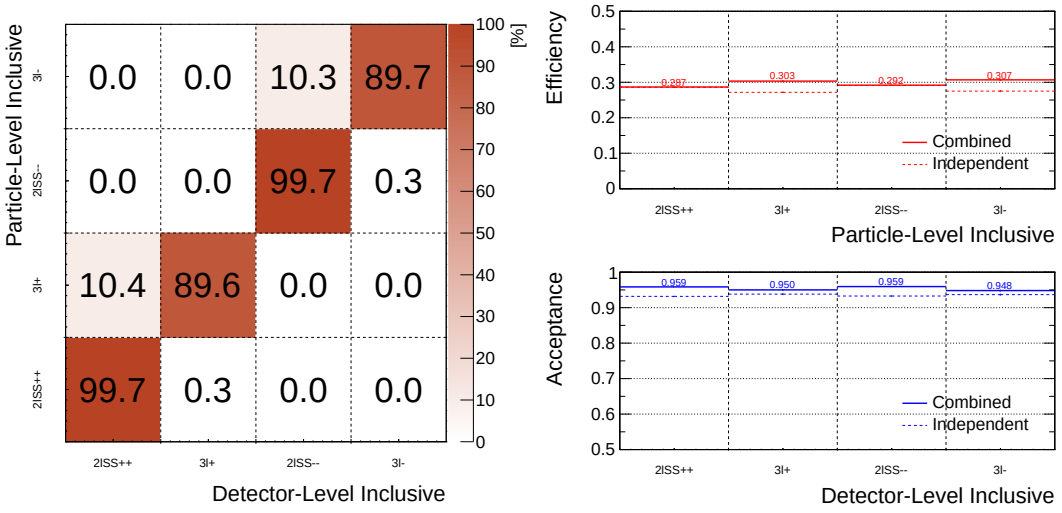
In this formula, the superscript "det. ∩ fid." refers to events that pass both the event selection at the detector level and the fiducial-space selection.

The acceptance and efficiency factors, $\alpha_i$ and $\varepsilon_j$ are used to correct the migration matrix by their corresponding effects and are defined as

$$\alpha_i = \frac{N_{i}^{\text{det.}\cap\text{fid.}}}{N_{i}^{\text{det.}}}, \qquad \varepsilon_j = \frac{N_{j}^{\text{det.}\cap\text{fid.}}}{N_{j}^{\text{fid.}}}. \tag{9.16}$$

The acceptance correction is used to account for the events that do not pass the fiducial volume selection, while satisfying the requirements of the detector-level selection. Since the occurrence of these events is not common the acceptance factor is expected to be close to unity (∼95%). The efficiency correction is used to account for the events that do not pass the detector-level selection, while passing the fiducial-space selection. The fraction of these events is relatively larger since the total events are usually reduced during the detection and reconstruction processes, resulting to efficiency correction values of ∼30%.
The validity of the above equations is preserved only in the case where the first and last bins of the particle- and detector-level histograms contain the underflow and overflow events, which is the case in this analysis.

A demonstration of the acceptance and efficiency corrections, as well as of the normalised migration matrix used in the inclusive channels ($2\ell$SS $++/--$, $3\ell$ $+/-$) and for one of the unfolded distributions ($N_{\text{jets}}$) is shown in Figures 9.26 and 9.27, respectively. It is worth noticing that in Figure 9.27 the splitting of the $3\ell$ SRs according to the number of OSSF lepton pairs is used only at the detector level resulting to a non-diagonal migration matrix, where the reconstructed events are mapped to the same fiducial phase space. The fraction of events appearing

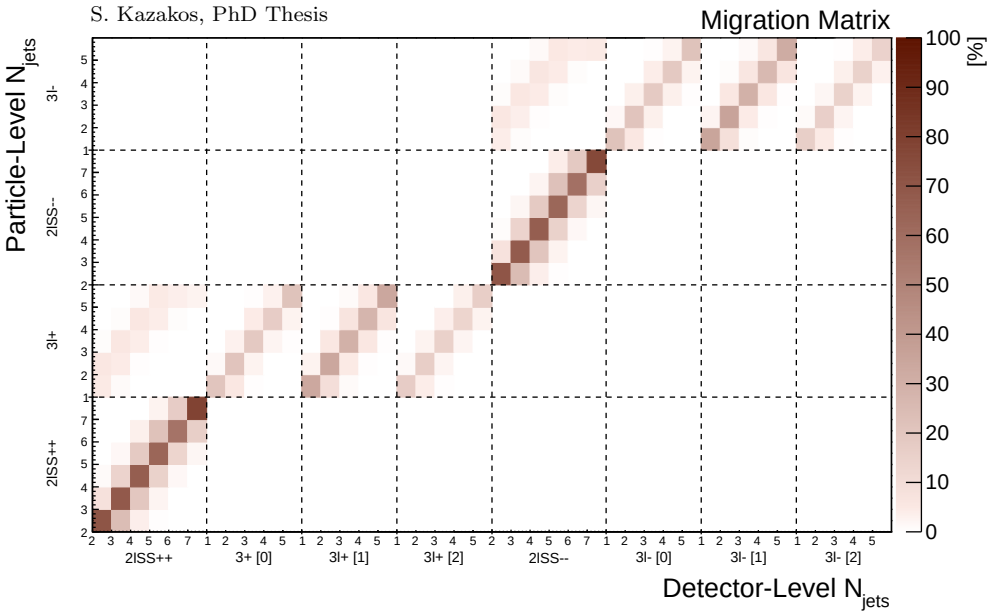



(a) (b)

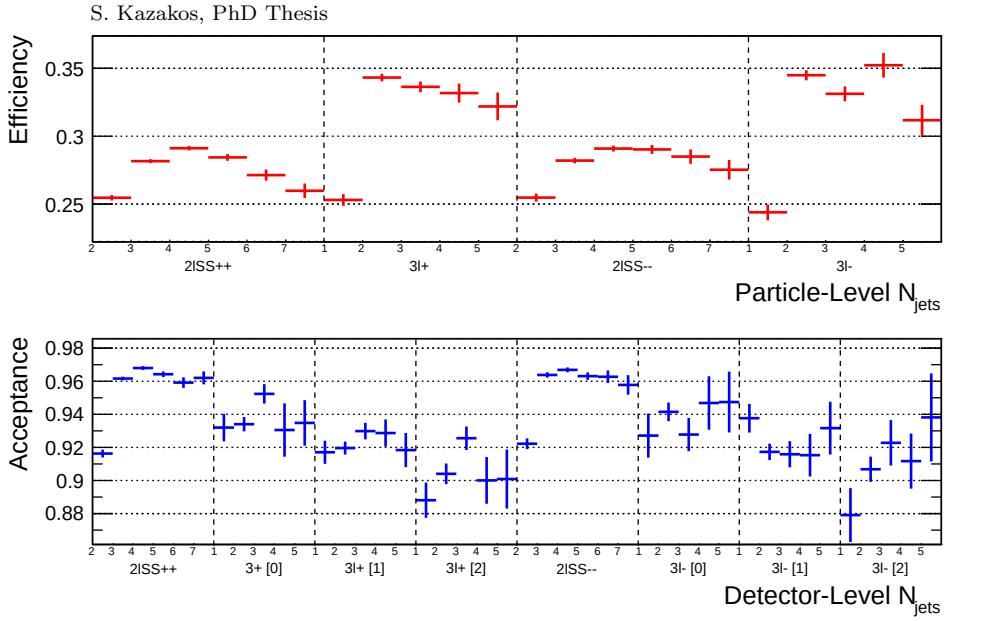
FIGURE 9.26: (a) Normalised migration matrix and (b) corrections related to efficiency and acceptance in the inclusive $2\ell$SS and $3\ell$ SRs. The "Combined" and "Independent" labels are used to distinguish the cases where there is a combined or independent treatment of the $2\ell$SS and $3\ell$ regions.

in the diagonal of the migration matrix discloses the resolution quality for each observable. In most of the observables, an acceptable diagonality is preserved in the migration matrix, while the limited $b$-tagging efficiency leads to migrations that show up in the migration matrix of the $N_{b-\text{jets}}$ distribution.

The use of Equation 9.13 introduces the Profile Likelihood Unfolding (PLU) method, which is the preferred method used for unfolding in this analysis. PLU is a binned unfolding technique based on profile likelihood and it is selected among other unfolding alternatives for a number of reasons. To start with, the unfolding takes place after the background prediction is estimated through the template fit method, inheriting the advanced methods of fake-background estimation developed within this framework. Another benefit of this method is that the inclusion of systematic uncertainties happens in a natural way as constrained NPs in the likelihood, and the inclusion of control regions helps further on the systematics profiling. The establishment of the PLU as the main unfolding method is further justified since it is accommodated in the same framework used for statistical analysis (TRExFitter), and additionally because the number of particle- and detector-level bins in the distributions do not have to match. Apart from the above, the log-likelihood minimisation and evaluation of systematic uncertainties is performed without the need for generation of pseudo-experiments, something that is required in other unfolding methods.




(a)




(b)

FIGURE 9.27: (a) Normalised migration matrix and (b) corrections related to efficiency and acceptance in the $N_{\text{jets}}$ observable.

The PLU approach succeeds in transforming the unfolding problem into a standard problem of fitting the normalisation in distributions, and then the standard profile-likelihood machinery can be used. The technical implementation of PLU can be summarised in the following steps:

- Each bin of the signal distribution at particle level is "folded" into a distribution at detector level via the response matrix, $\mathcal{R}_{ij}$.

- A normalisation factor (NF) is assigned to each "folded" truth bin (cross-section NFs).
- The cross-section NFs are correlated to the four inclusive $t\bar{t}W$ NFs assigned to the $2\ell$SS $++/--$ and $3\ell$ $+/-$ $t\bar{t}W$ events, controlling the normalisation of the corresponding $t\bar{t}W$ contributions in CRs (non-negligible $t\bar{t}W$ contribution) according to one of the four available parametrisations described in Appendix B.1, and are allowed to be free-floating in the template fit.
- The background contributions are estimated through the template fit (normalisations mostly constrained through the CRs) and the total background prediction in the SR is corrected by the fitted NFs.
- The corrected total background prediction is subtracted from data in the SR, which are fitted to the $t\bar{t}W$ reconstructed distribution, "unfolding" it to particle level.

The key concept in this method is the realisation that the normalisation of the folded distribution (cross-section NFs to signal strength) at the detector level is identical to the normalisation of the truth distribution. Thus, measuring the normalisation of each folded distribution at the detector level (in a "standard"-fit way), one directly measures the normalisation at the truth level, which is the purpose of the unfolding.

As is the case with the rest of unfolding methods there are a few subtle points related to the PLU method requiring further attention. The measured unfolded cross section could be affected by the systematic uncertainties on signal, which are evaluated at detector level and are able to modify the response matrix. For the derivation of the signal-related uncertainties a response matrix is created for each uncertainty and the difference to the nominal value is interpolated up and down in $\pm 1\sigma$ variations in the same way as the rest of the NPs in the fit.
Additional Tikhonov $\tau_j$ parameters are added to the full likelihood for the regularisation of the unfolding process. The need for regularisation and the regularisation optimisation used in the analysis are summarised in Section 9.7.3.
Moreover, since PLU is a binned method the binning of observables with continuous distributions needs to be carefully chosen. The optimised binning in the distributions of the observables unfolded is shown in Table 9.9.
A wide number of closure and stress tests is performed to validate the unfolding procedure prior to looking into real data, where a full closure is observed in fits

to an Asimov dataset, as expected. Tests of injecting normalisation changes in various regions or introducing linear slopes in the distributions at particle level, all yielded the expected results with a correct retrieval of the injected quantities. Some of these tests as well as the binning optimisation procedure are summarised in Appendices B.2 and B.4.

### 9.7.3 Tikhonov regularisation

A simple inversion of the response matrix for unfolding often leads to undesirable results, which are not wrong but they do not correspond to a physical truth distribution. This is an implication of statistical fluctuations, which cause the appearance of large anti-correlations between neighbouring bins in the inverse migration matrix $\mathcal{M}_{ij}^{-1}$, shown in Figure 9.28. In this toy example the reconstruction is not totally accurate and this manifests as sizeable non-diagonal elements in the migration matrix.

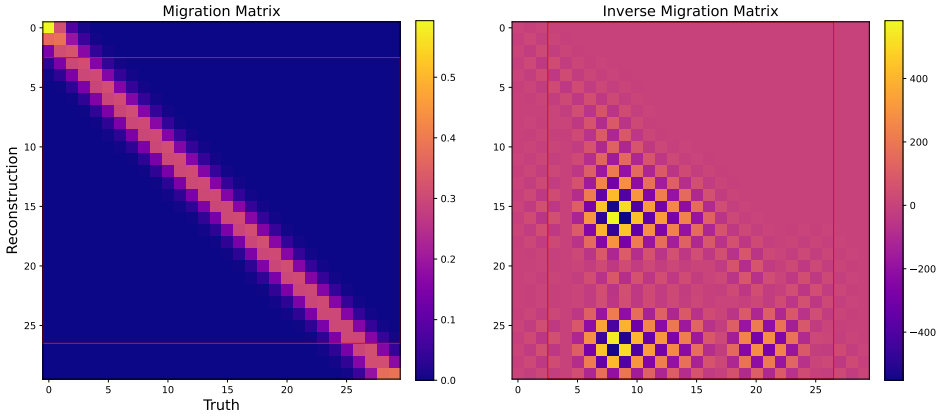



FIGURE 9.28: Normalised migration matrix (left), and inverse of the migration matrix (right) in the case of a less accurate reconstruction from a toy example. Figures created using the code from Ref. [224].

In the case of a perfect reconstruction and a measurement with zero bias the matrix inversion would return the correct values since the input data would correspond to the expectation value of the reconstructed distribution. However, the matrix inversion is applied to one instance of the data, which differs from the expectation value due to the statistical errors and the migration matrix could be itself ill-defined. As a result, in a narrative way, $\mathcal{M}_{ij}$ "assumes" that the fluctuations in the

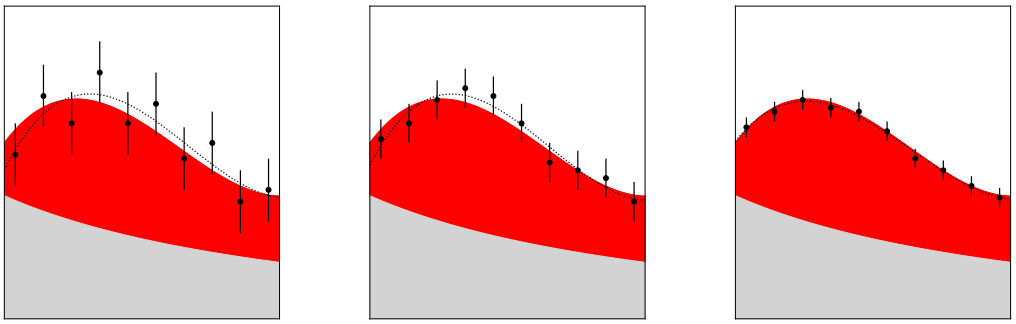
reconstructed histogram correspond to the residual effect of an original structure in the truth distribution that is diluted by detector effects. In order to deal with that, it uses the given input and the available model for migrations to calculate the corresponding $\mu_j$ values during the unfolding, bringing these fluctuations back into the result, but magnified.

The technique used to suppress this effect is known as *regularisation*. PLU uses Tikhonov regularisation and allows for different choices of the regularisation parameter $\tau$ among the unfolded bins, allowing in this way different values of regularisation to be used for each one of the four fiducial regions when unfolded simultaneously. At the same time regularisation is optimised for each of the observables that are unfolded to ensure the optimal result. Tikhonov regularisation is imposed as an additional term in the likelihood function used to constrain the discrete second derivative of the cross-section NFs close to zero, and it is described by the formula

$$\begin{aligned} \mathscr{L}'(\mu, \vec{\theta}) &= \mathscr{L}(\mu, \vec{\theta}) \times \prod_{j=2}^{m-1} G\left(\mu_{j-1} - 2\mu_j + \mu_{j+1} \,|\, 0,\, 1/\tau_j\right) \\ &\equiv \mathscr{L}(\mu, \vec{\theta}) \times \prod_{j=2}^{m-1} G\left(\Delta\mu_j - \Delta\mu_{j+1} \,|\, 0,\, 1/\tau_j\right). \end{aligned} \tag{9.17}$$

This form of regularisation ensures the smoothness of the unfolded distribution by imposing a linearity constraint on the $\mu_j$ NFs, making it the most natural choice for this analysis. In particular, the allowed difference in the slope of the $\mu_j$ NFs around the $j^{\text{th}}$ bin is constrained proportionally to an increase in $\tau_j$. Therefore, it could be characterised as an unbiased approach since it is not affected by zero and first order differences between data and the "prior" of the signal distribution (i.e. linear shape and normalisation effects).

In the limit of infinitely large $\tau$, this regularisation method is equivalent to a linear parametric unfolding and it is expected to introduce some bias because of that. At the same time, in the case of no regularisation the result is susceptible to random statistical fluctuations. Therefore, an optimal choice of regularisation parameters $\tau$ is done with a regularisation strength of medium value that results to a robust measurement against fluctuations, while being sensitive only to higher-order effects. An illustration of the extreme cases and optimal choice in the selection of $\tau$



(a) (b) (c)

FIGURE 9.29: Illustrative sketch of unfolded distributions (a) without regularisation ($\tau = 0$), (b) with an optimal regularisation choice and (c) with very large regularisation ($\tau >> 1$).

parameter is shown in Figure 9.29, demonstrating the need for a proper balance between smoothness and bias.

The regularisation optimisation used for each observable in this analysis for all $2\ell$SS and $3\ell$ regions is summarised in Appendix B.3.

### 9.7.4 Unfolded observables in the signal region

The observables that are unfolded in the SR in the differential $t\bar{t}W$ measurement are chosen based on experimental and theoretical motivation, according to if there were modelling discrepancies reported for them in the past or if they are expected to demonstrate significant shape changes originating from NLO corrections. A list of potential observables to unfold was provided by theorists and it is summarised in Tables B.1-B.3 in Appendix B with an optimised binning for each observable in the $2\ell$SS and $3\ell$ channels. A selection of variables is made from the original list resulting in the list summarised in Table 9.9 with the eight variables that are unfolded in this analysis and their corresponding binning. The first and last bins of the distributions contain the underflow and overflow events, respectively. The binning used in the PLU implementation is the same for the reconstructed and unfolded distributions in the SRs.

The angular observables $|\Delta\eta_{\ell_0^{\mathrm{SS}}\ell_1^{\mathrm{SS}}}|$ and $|\Delta\phi_{\ell_0^{\mathrm{SS}}\ell_1^{\mathrm{SS}}}|/\pi$ correspond to the absolute value $\Delta\eta$ and (normalised) $\Delta\phi$ between the first and the second lepton of the same-charge (SS) pair. The $H_{\mathrm{T,\,lep}}$ and $H_{\mathrm{T,\,jets}}$ observables correspond to the sum

of momentum of all the light-leptons and jets in each event, respectively. The observables $m_{\ell_0^{\text{SS}}\ell_1^{\text{SS}}}$ and $m_{j_0j_1}$ correspond to the invariant mass between the first and second lepton of the SS pair and the leading and subleading (in $p_{\text{T}}$) jet in each event, respectively.

During the binning optimisation for these observables at least 60% of the total number of events in a particular bin of the truth distribution should correspond to the diagonal element of the migration matrix, while low statistical uncertainty is required for the events in all of the bins of the reconstructed distribution. In particular, the statistical uncertainty is required to be less than (10) 16% on the total yield for (high-) low-statistics channels.

| Observable | Channel | Binning |
|---|---|---|
| $N_{\text{jets}}$ | $2\ell$SS | [2, 3, 4, 5, 6, 7, 8] (6 bins) |
| | $3\ell$ | [2, 3, 4, 5, 6] (4 bins) |
| $N_{b-\text{jets}}$ | $2\ell$SS | [1, 2, 3, 4] (3 bins) |
| | $3\ell$ | [1, 2, 3] (2 bins) |
| $\lvert\Delta\eta_{\ell_0^{\text{SS}}\ell_1^{\text{SS}}}\rvert$ | $2\ell$SS | [0.0, 0.2, 0.4, 0.65, 0.9, 1.2, 1.6, 2.0] (7 bins) |
| | $3\ell$ | [0.0, 0.25, 0.5, 0.8, 1.1, 1.5, 2.0] (6 bins) |
| $\lvert\Delta\phi_{\ell_0^{\text{SS}}\ell_1^{\text{SS}}}\rvert/\pi$ | $2\ell$SS | [0.0, 0.15, 0.3, 0.45, 0.6, 0.7, 0.8, 0.9, 1.0] (8 bins) |
| | $3\ell$ | [0.0, 0.2, 0.4, 0.55, 0.7, 0.85, 1.0] (6 bins) |
| $H_{\text{T, lep}}$ [GeV] | $2\ell$SS | [40, 70, 85, 100, 115, 130, 150, 180, 220] (8 bins) |
| | $3\ell$ | [40, 115, 145, 170, 200, 245, 325] (6 bins) |
| $H_{\text{T, jets}}$ [GeV] | $2\ell$SS | [50, 135, 185, 245, 305, 375, 500] (6 bins) |
| | $3\ell$ | [50, 110, 165, 225, 300, 400] (5 bins) |
| $m_{\ell_0^{\text{SS}}\ell_1^{\text{SS}}}$ [GeV] | $2\ell$SS | [0, 44, 65, 85, 105, 125, 145, 180, 220] (8 bins) |
| | $3\ell$ | [0, 50, 75, 100, 125, 160, 200] (6 bins) |
| $m_{j_0j_1}$ [GeV] | $2\ell$SS | [12, 90, 120, 165, 225, 300, 400, 600] (7 bins) |
| | $3\ell$ | [15, 80, 130, 190, 250, 380, 600] (6 bins) |

TABLE 9.9: List of observables that are unfolded together with their corresponding optimised binning.

The distributions unfolded in the SR for all the observables considered are shown before and after the profile likelihood fit to data in Figures 9.30 and 9.31. A good agreement is observed in all variables after the fit, with the exception of few bins in the $3\ell$ − [0] and [2] regions that are attributed to statistical fluctuations of the data.

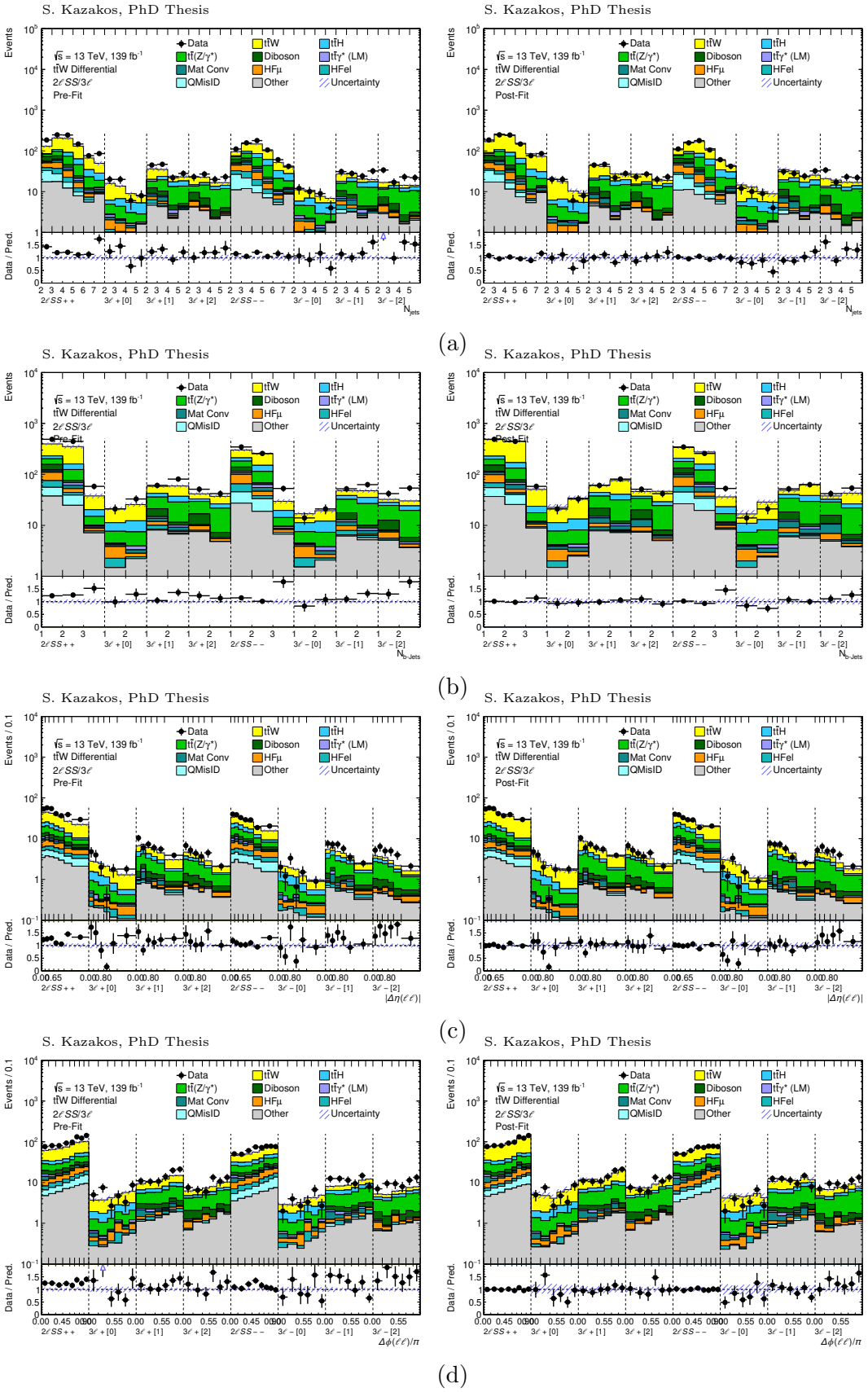



FIGURE 9.30: Data-to-simulation comparison in the $2\ell$SS $++$ / $--$ and $3\ell$ $+/-$ regions for the observables (a) $N_{\text{jets}}$, (b) $N_{b-\text{jets}}$, (c) $|\Delta\eta_{\ell_0^{\text{SS}}\ell_1^{\text{SS}}}|$, and (d) $|\Delta\phi_{\ell_0^{\text{SS}}\ell_1^{\text{SS}}}|/\pi$ before (left) and after (right) the profile likelihood unfolding. The blue hatched band includes all statistical and systematic uncertainties.

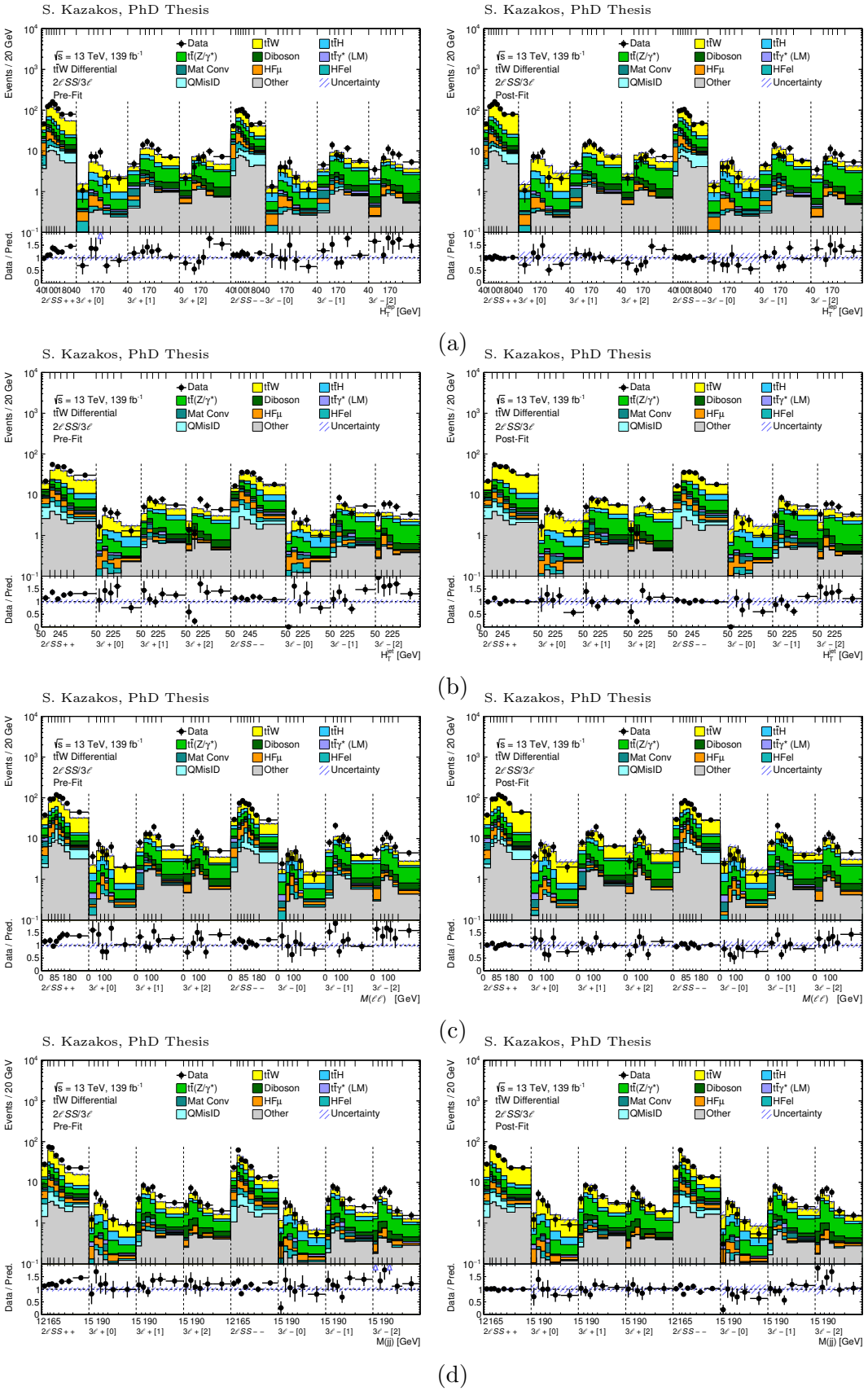



FIGURE 9.31: Data-to-simulation comparison in the $2\ell$SS $++/--$ and $3\ell$ $+/-$ regions for the observables (a) $H_{\mathrm{T,lep}}$, (b) $H_{\mathrm{T,jets}}$, (c) $m_{\ell_0^{\mathrm{SS}}\ell_1^{\mathrm{SS}}}$, and (d) $m_{j_0j_1}$ before (left) and after (right) the profile likelihood unfolding. The blue hatched band includes all statistical and systematic uncertainties.

### 9.7.5 Unfolding results and relative charge-asymmetry measurement

The fit results from the profile likelihood fit to data in the SR and CRs unfolding simultaneously the $t\bar{t}W$ contribution in the SR are shown in Figures 9.32 - 9.46. Figures 9.32 - 9.34 show the fit results for the observables $N_{\text{jets}}$, $N_{b-\text{jets}}$, $|\Delta\eta_{\ell_0^{\text{SS}}\ell_1^{\text{SS}}}|$ and $|\Delta\phi_{\ell_0^{\text{SS}}\ell_1^{\text{SS}}}|/\pi$, while the correlation matrix and MC statistical "gamma" parameters are shown only for the $N_{\text{jets}}$ observable. Figures 9.35 - 9.36 show the fit results for the observables $H_{\text{T, lep}}$, $H_{\text{T, jets}}$, $m_{\ell_0^{\text{SS}}\ell_1^{\text{SS}}}$ and $m_{j_0j_1}$. The fit results are in general similar across the unfolded observables with minor deviations in the fitted NFs and in the pulls and constraints of the NPs. These results were acquired using the differential parametrisation (see Appendix B.1).

Figures 9.37 - 9.38 show the unfolded $t\bar{t}W$ differential cross section for each of these observables together with the systematic impact on the unfolded signal strengths. The systematic uncertainties are grouped in subcategories related to background-fitted NFs, flavour tagging (FTAG), JER/JES, instrumental uncertainties (including lepton- and PLIV-related ones), MC statistics, non-prompt and prompt background modelling, and $t\bar{t}W$ modelling. The largest systematic impact originates from the ME+PS uncertainty (through the comparison between the nominal Sherpa and the alternative MG5 FxFx sample). At the differential level, the JES uncertainty becomes more important compared to the FTAG uncertainties. Off-shell $t\bar{t}W$ predictions provided by theorists are also overlaid only in the $3\ell$ channel and without parton shower (Off-Shell), and were afterwards corrected for this effect (Off-Shell Corr) by studies using a Rivet routine in the same fiducial phase space. The same differential parametrisation as before is used for these results.

Figures 9.39 - 9.46 show the unfolded $t\bar{t}W$ differential cross section inclusively in electric charge in $2\ell$SS and $3\ell$ channels, as well as the unfolded $t\bar{t}W$ differential relative charge asymmetry $A_C^R$ for each of these observables. This measurement is not assuming the $A_C^R$ as predicted by the SM, since it is measured simultaneously with the cross section. The grouped impact of systematic uncertainties on the $t\bar{t}W$ $2\ell$SS and $3\ell$ NFs and $A_C^R$ parameters is also included in these figures. Most of the systematic uncertainties on $A_C^R$ "cancel" out, and the statistical uncertainty is the dominant component in most of the bins of the different observables. These results are produced using the differential asymmetry parametrisation (see Appendix B.1), and the $t\bar{t}W$ off-shell predictions are also overlaid in the $3\ell$ channel.

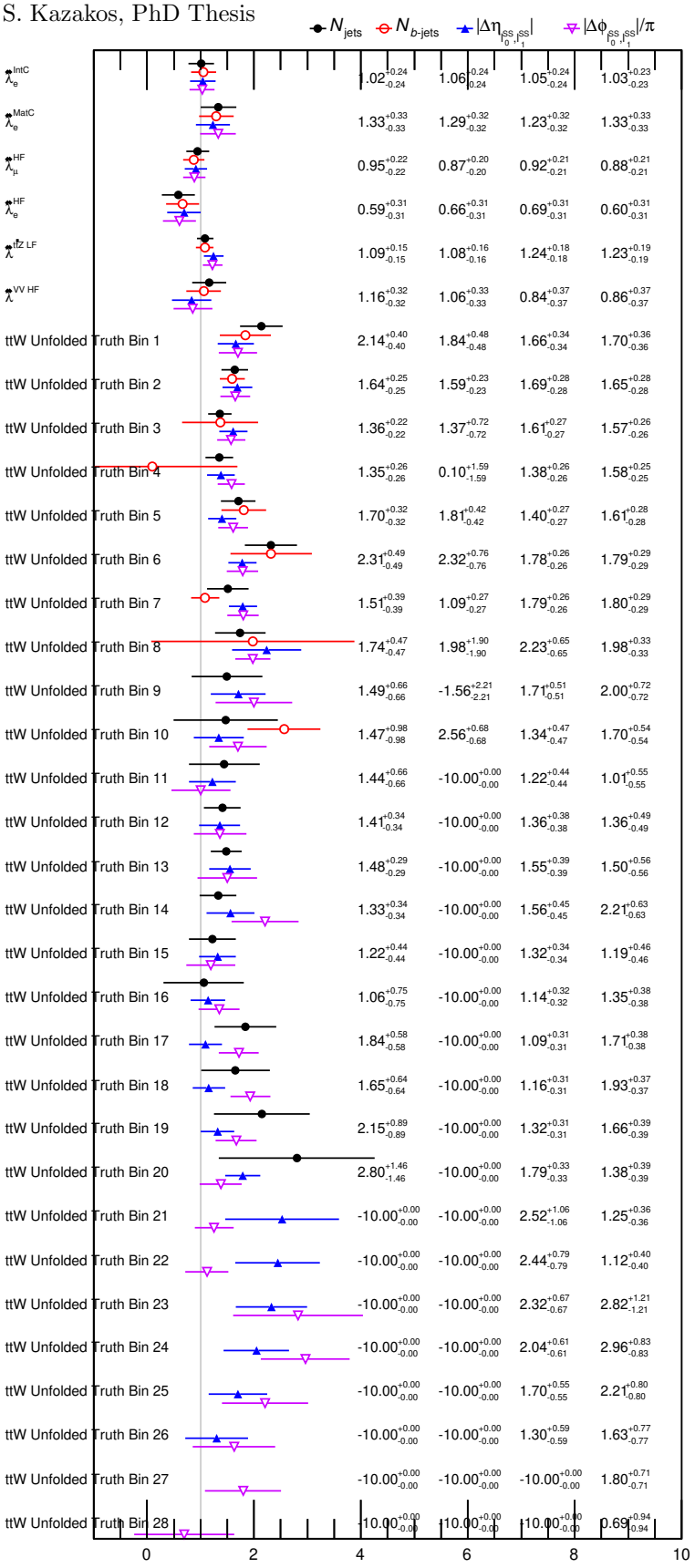



FIGURE 9.32: Overview of fitted background and unfolded ($\mu_j$) normalisation factors after a profile likelihood fit to data for the observables: $N_{\text{jets}}$, $N_{b-\text{jets}}$, $|\Delta\eta_{\ell_0^{\text{SS}}\ell_1^{\text{SS}}}|$ and $|\Delta\phi_{\ell_0^{\text{SS}}\ell_1^{\text{SS}}}|/\pi$.

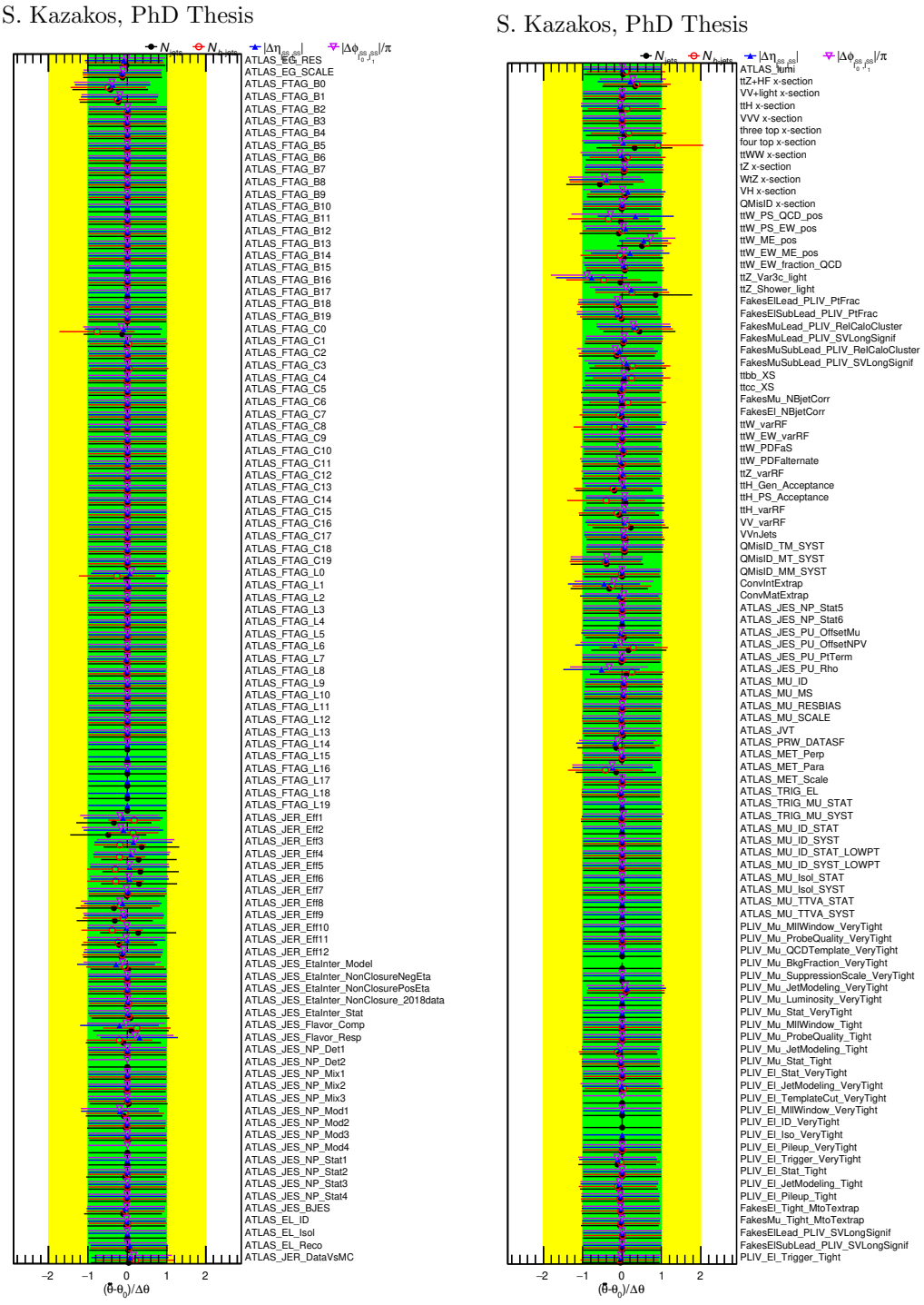
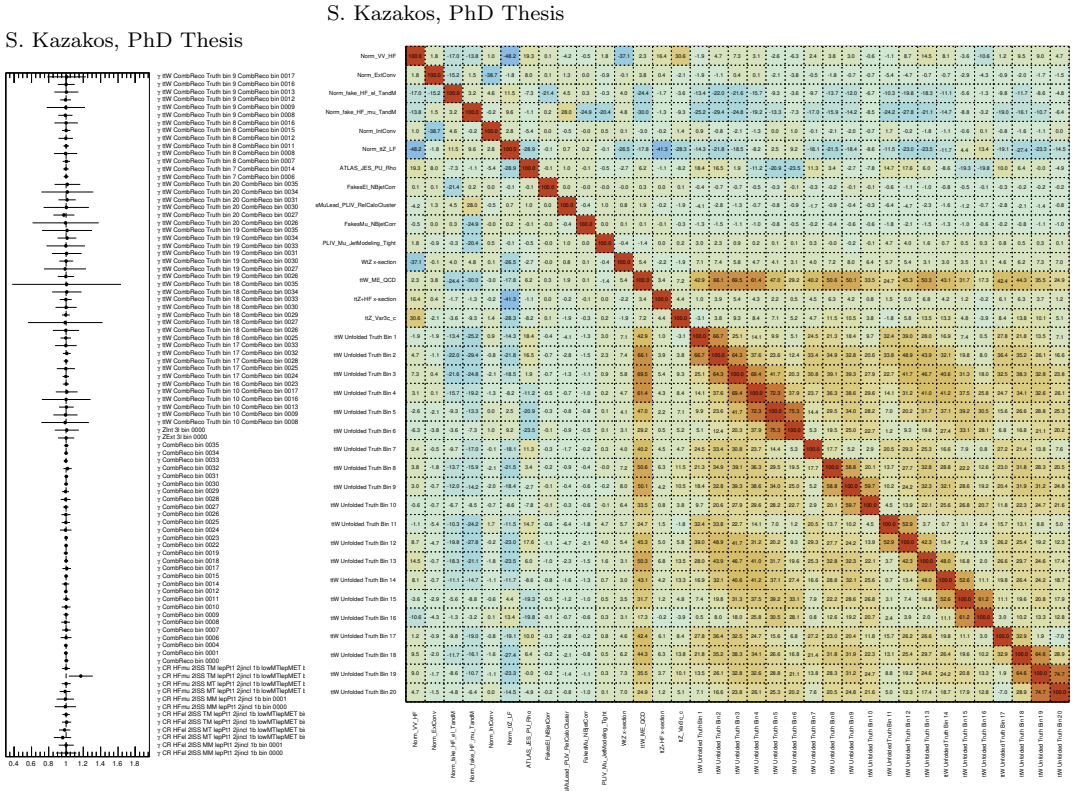



FIGURE 9.33: Nuisance parameter pulls and constraints from profile likelihood fits of the observables: $N_{\text{jets}}$, $N_{b-\text{jets}}$, $|\Delta\eta_{\ell_0^{\text{SS}}\ell_1^{\text{SS}}}|$ and $|\Delta\phi_{\ell_0^{\text{SS}}\ell_1^{\text{SS}}}|/\pi$.




(a) (b)

FIGURE 9.34: (a) MC statistical "gamma" parameters and (b) correlation matrix of the nuisance parameters from the profile likelihood unfolding in the $N_{\text{jets}}$ distribution.

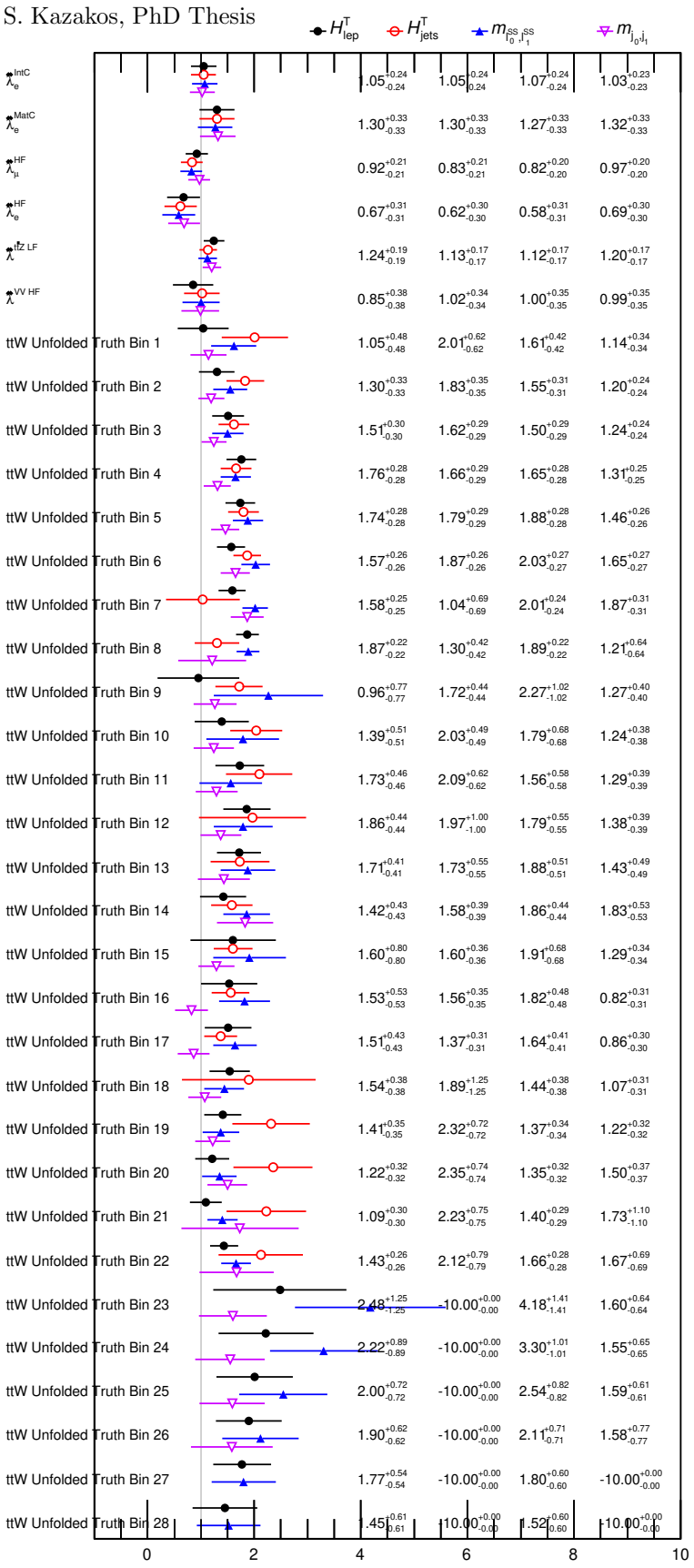



FIGURE 9.35: Overview of fitted background and unfolded ($\mu_j$) normalisation factors after a profile likelihood fit to data for the observables: $H_{\mathrm{T,\,lep}}$, $H_{\mathrm{T,\,jets}}$, $m_{\ell_0^{\mathrm{SS}}\ell_1^{\mathrm{SS}}}$, and $m_{j_0 j_1}$.

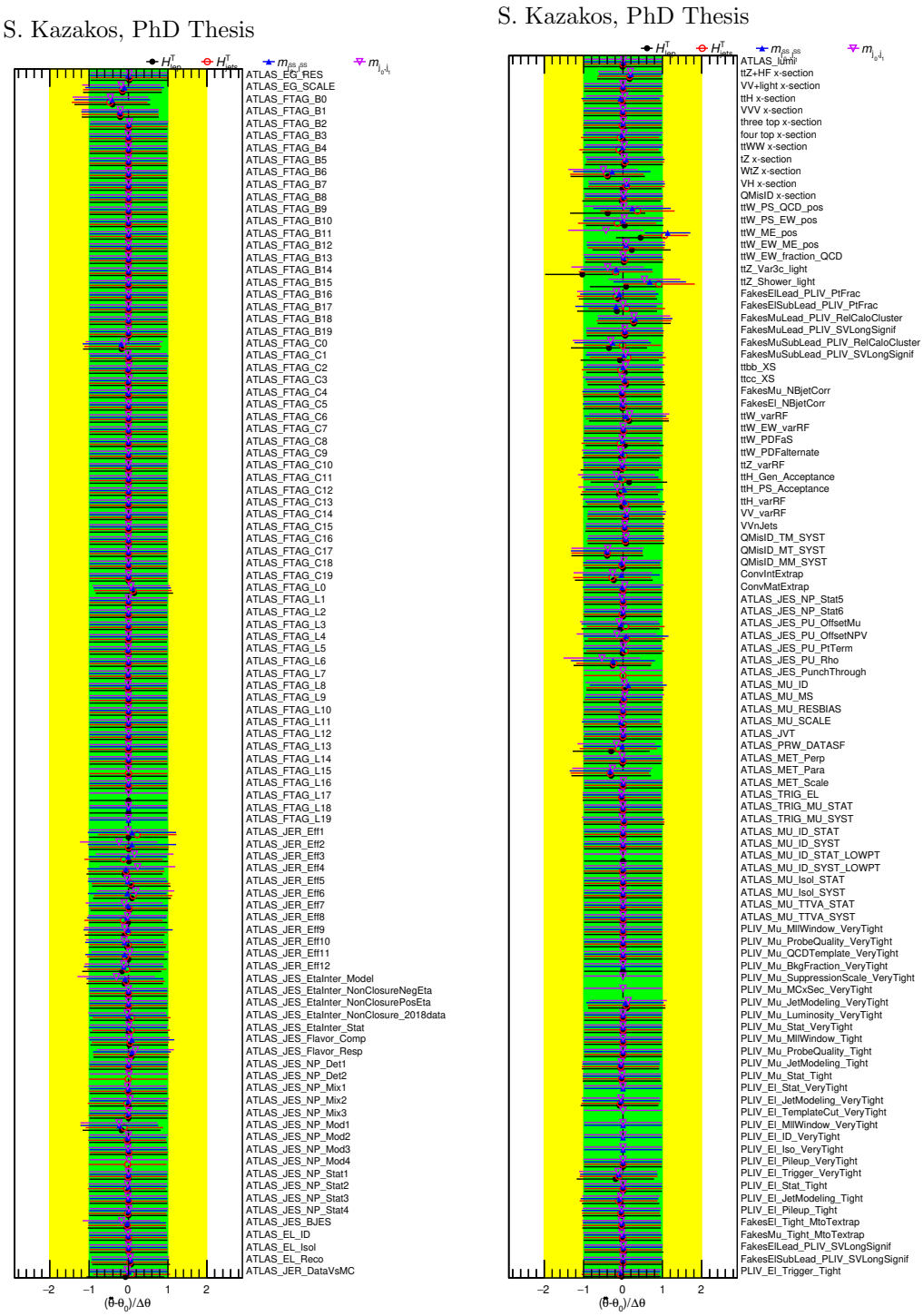



FIGURE 9.36: Nuisance parameter pulls and constraints from profile likelihood fits of the observables: $H_{\mathrm{T,\,lep}}$, $H_{\mathrm{T,\,jets}}$, $m_{\ell_0^{\mathrm{SS}}\ell_1^{\mathrm{SS}}}$, and $m_{j_0 j_1}$.

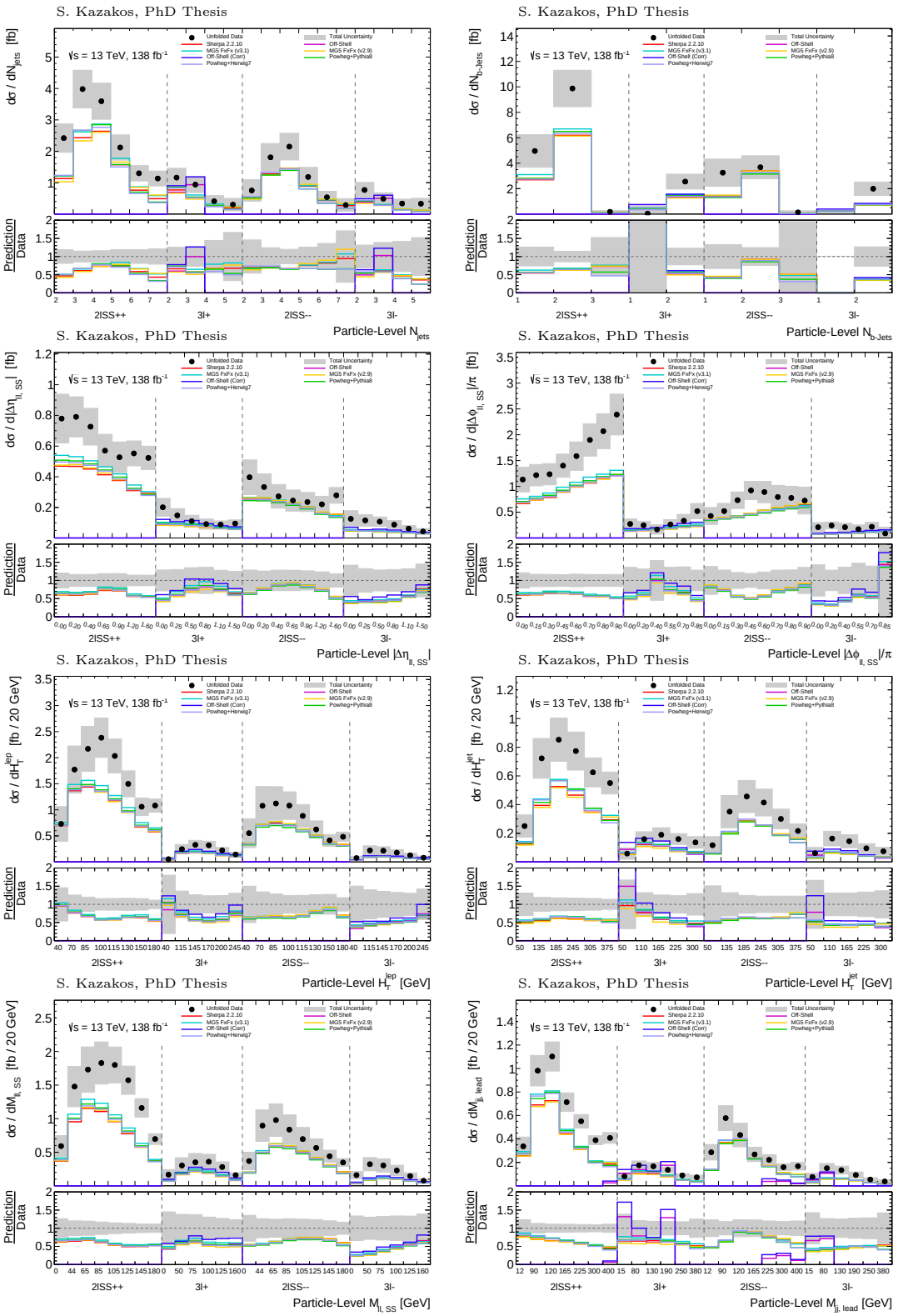



FIGURE 9.37: Unfolded differential cross section in the $2\ell$SS $++/--$ and $3\ell$ $+/-$ regions for the all observables considered. A comparison of the unfolding of several $t\bar{t}W$ samples is overlaid in additional to the nominal.

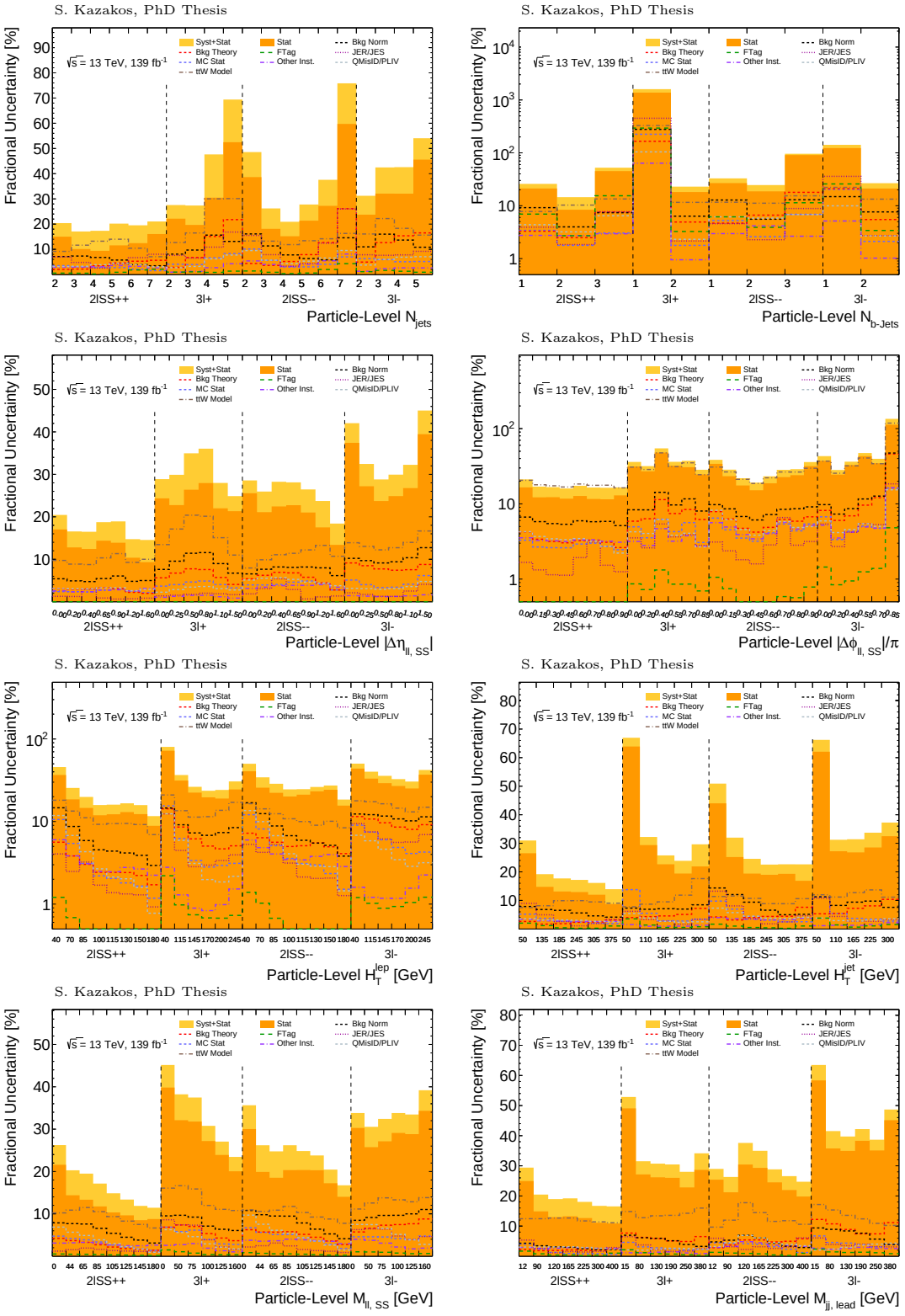



FIGURE 9.38: Grouped systematic impact on the $2\ell$SS $++/--$ and $3\ell$ $+/-$ $t\bar{t}W$ NFs for the all observables considered.

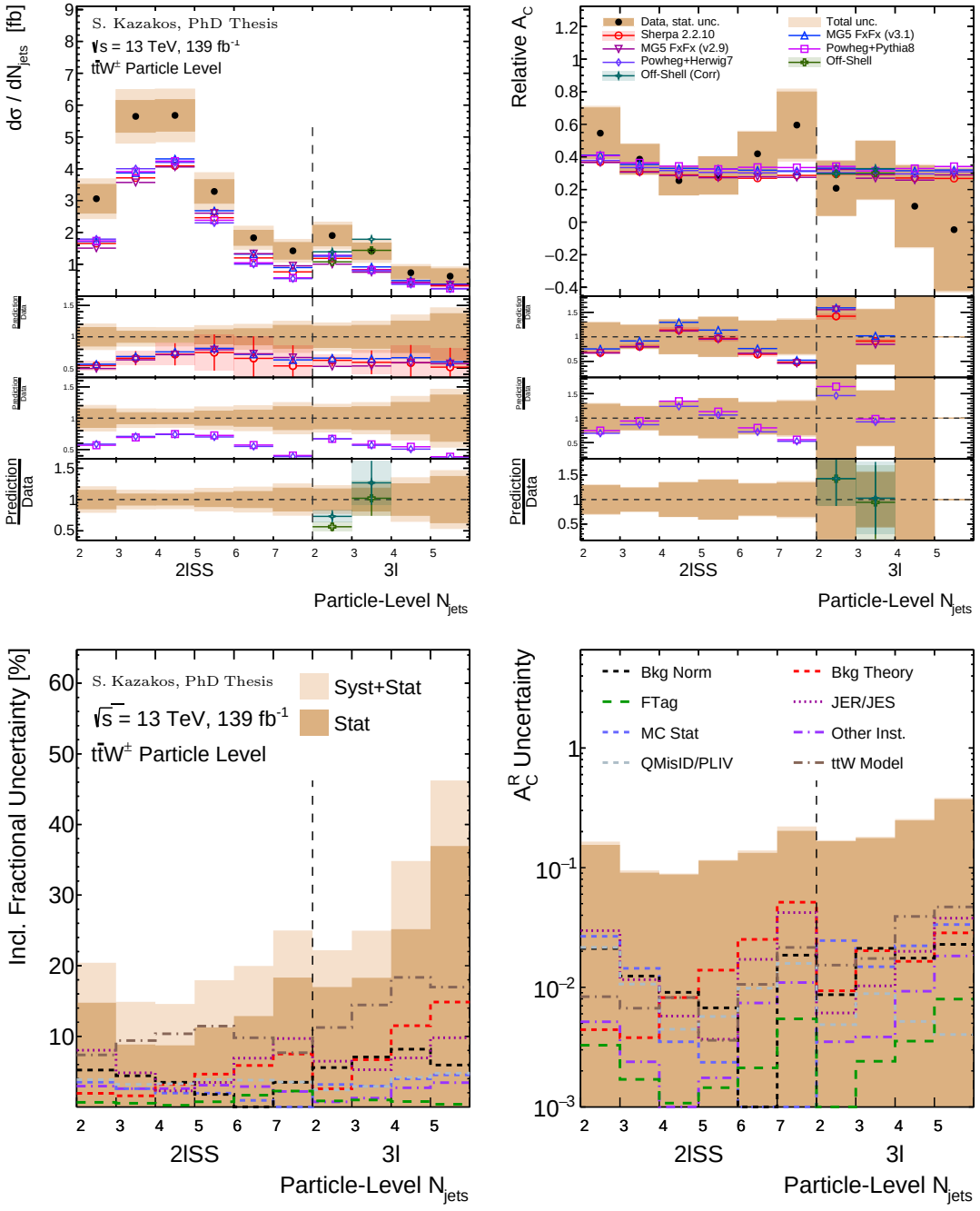



FIGURE 9.39: Unfolded differential cross section (top left) and relative charge asymmetry (top right) in $2\ell$SS and $3\ell$ regions (charge-inclusive) as a function of jet multiplicity together with the corresponding grouped impact of systematic uncertainties.

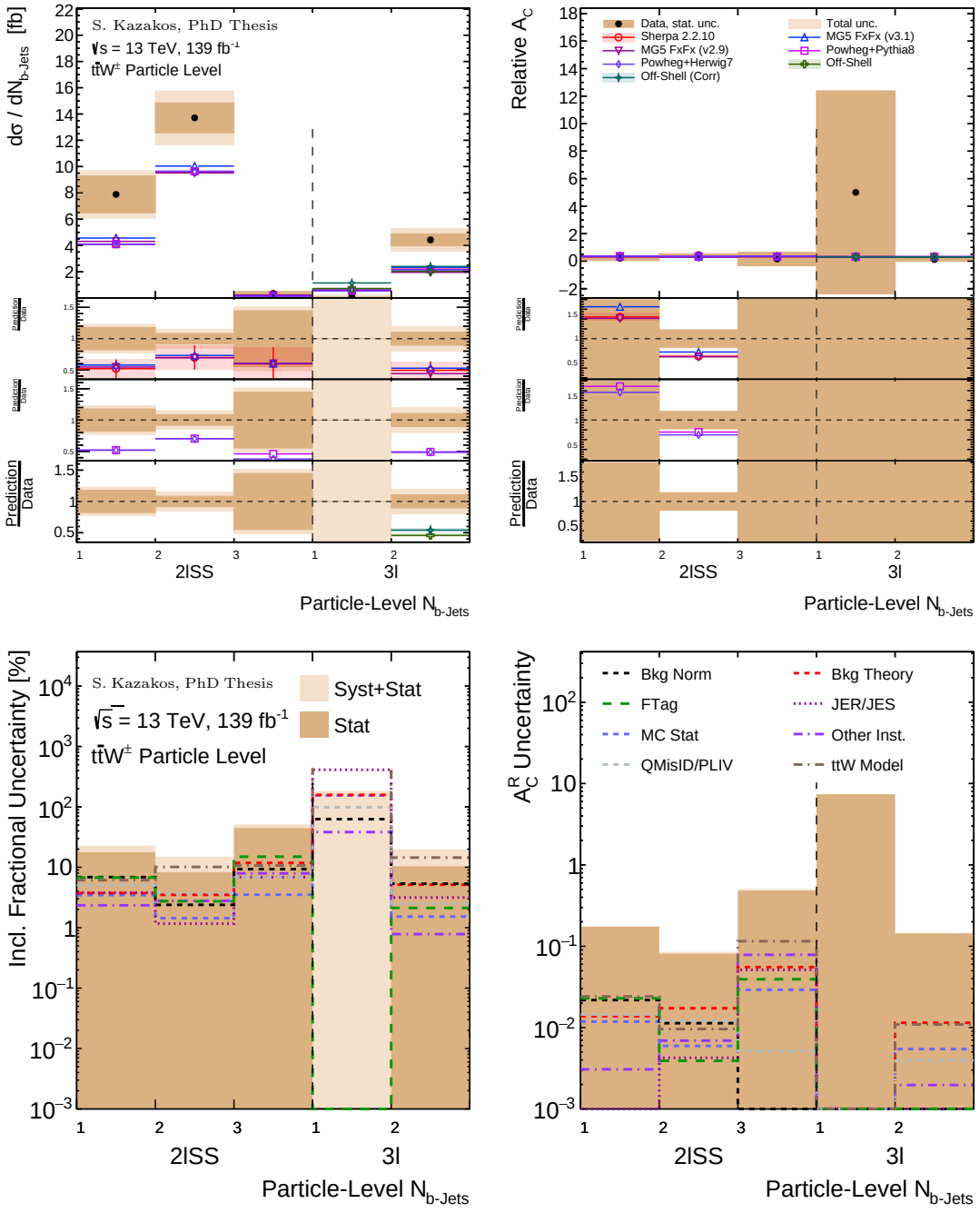



FIGURE 9.40: Unfolded differential cross section (top left) and relative charge asymmetry (top right) in $2\ell$SS and $3\ell$ regions (charge-inclusive) as a function of $b$-jet multiplicity together with the corresponding grouped impact of systematic uncertainties (bottom).

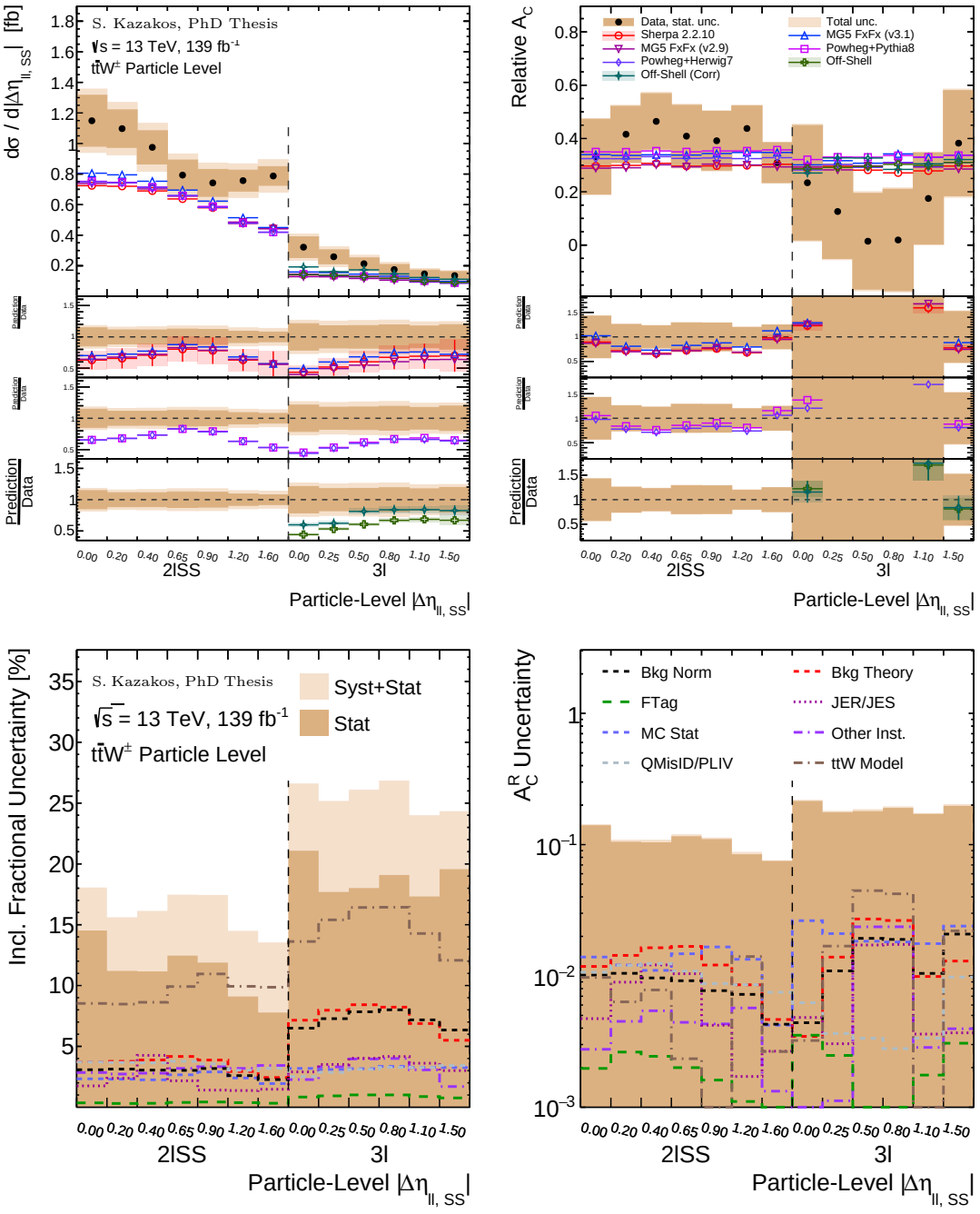



FIGURE 9.41: Unfolded differential cross section (top left) and relative charge asymmetry (top right) in 2$\ell$SS and 3$\ell$ regions (charge-inclusive) as a function of $|\Delta\eta_{\ell_0^{SS}\ell_1^{SS}}|$ together with the corresponding grouped impact of systematic uncertainties.

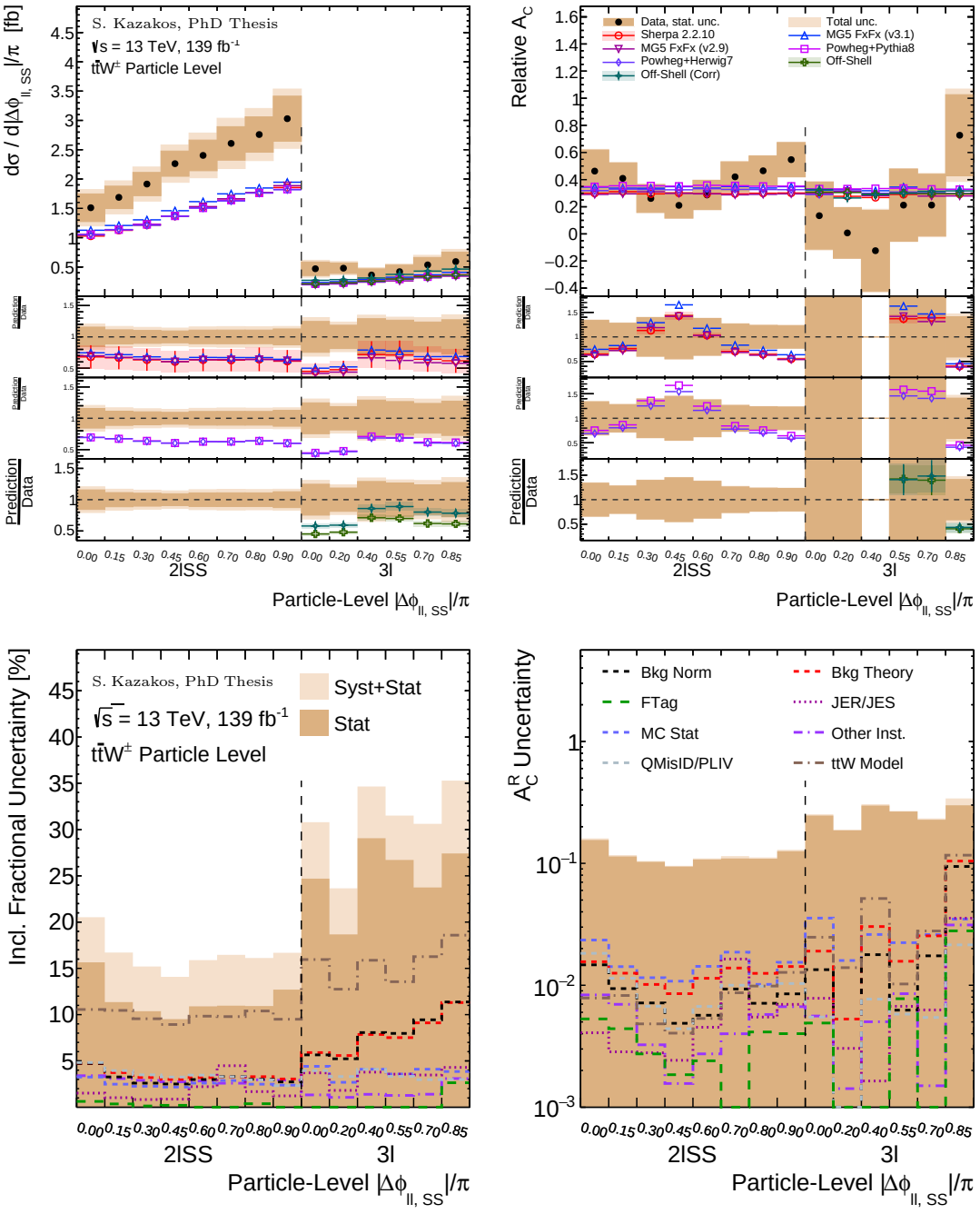



FIGURE 9.42: Unfolded differential cross section (top left) and relative charge asymmetry (top right) in 2$\ell$SS and 3$\ell$ regions (charge-inclusive) as a function of $|\Delta\phi_{\ell_0^{SS}\ell_1^{SS}}|/\pi$ together with the corresponding grouped impact of systematic uncertainties (bottom).

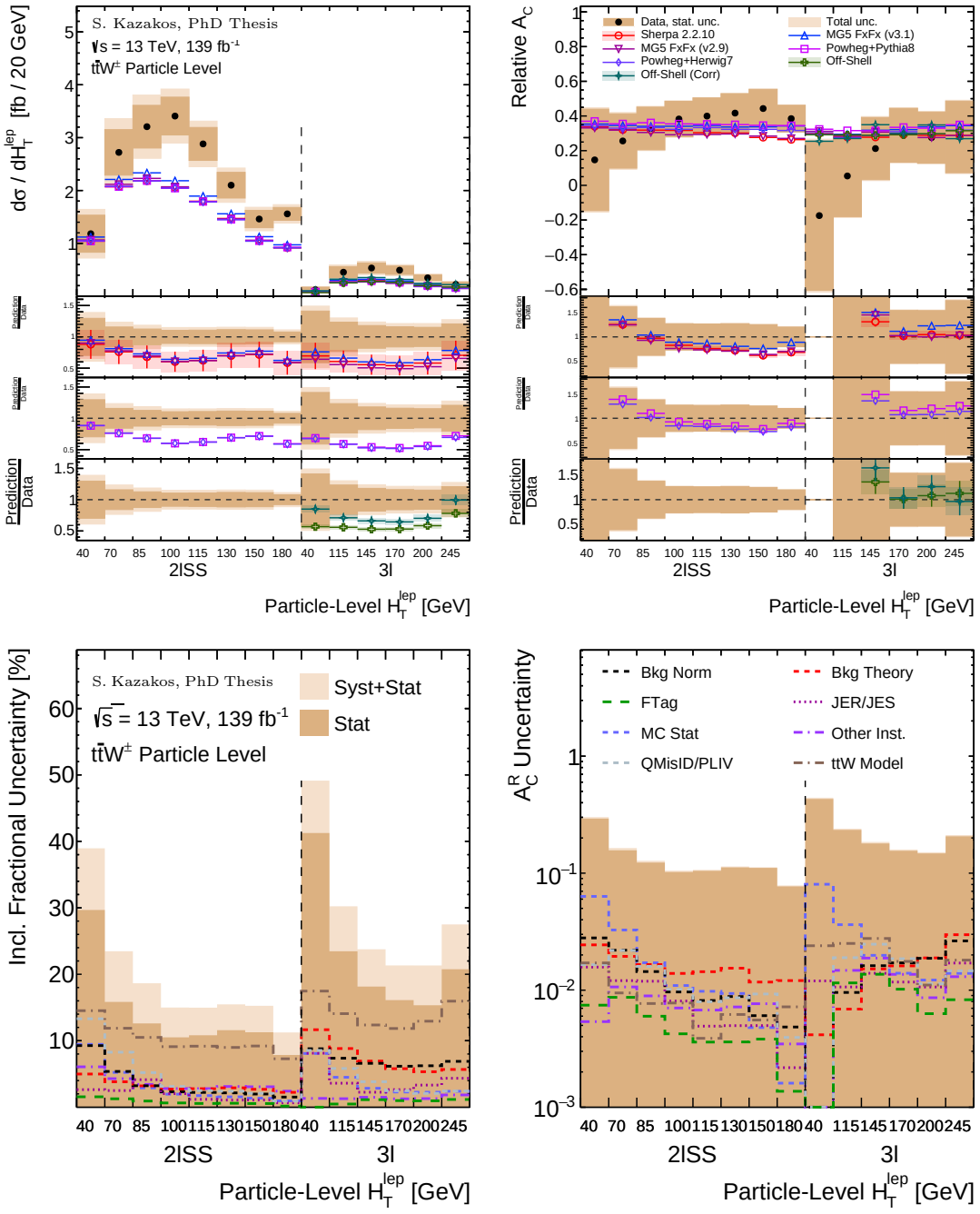



FIGURE 9.43: Unfolded differential cross section (top left) and relative charge asymmetry (top right) in 2$\ell$SS and 3$\ell$ regions (charge-inclusive) as a function of $H_{\mathrm{T,\,lep}}$ together with the corresponding grouped impact of systematic uncertainties (bottom).

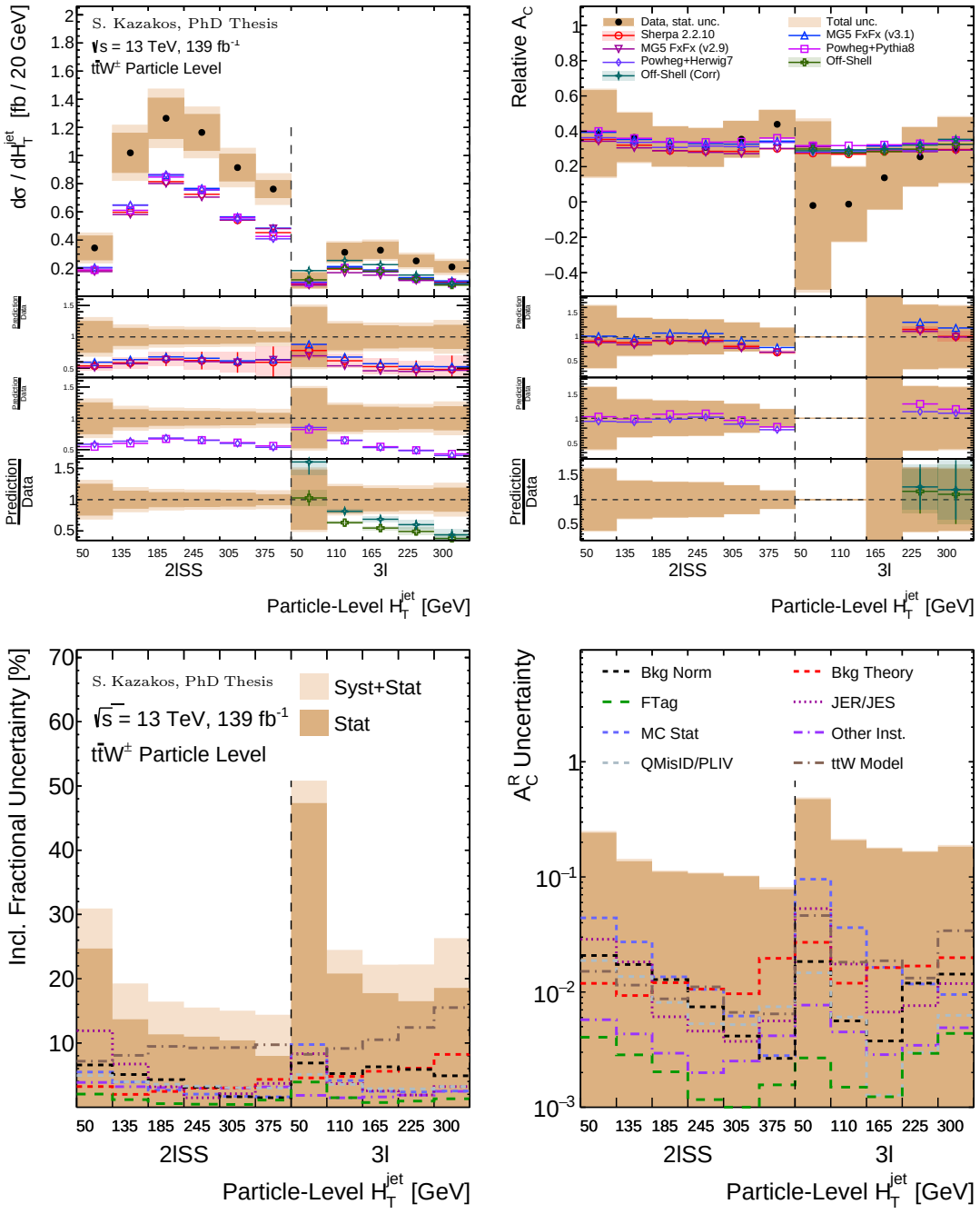



FIGURE 9.44: Unfolded differential cross section (top left) and relative charge asymmetry (top right) in 2$\ell$SS and 3$\ell$ regions (charge-inclusive) as a function of $H_{\mathrm{T,jets}}$ together with the corresponding grouped impact of systematic uncertainties (bottom).

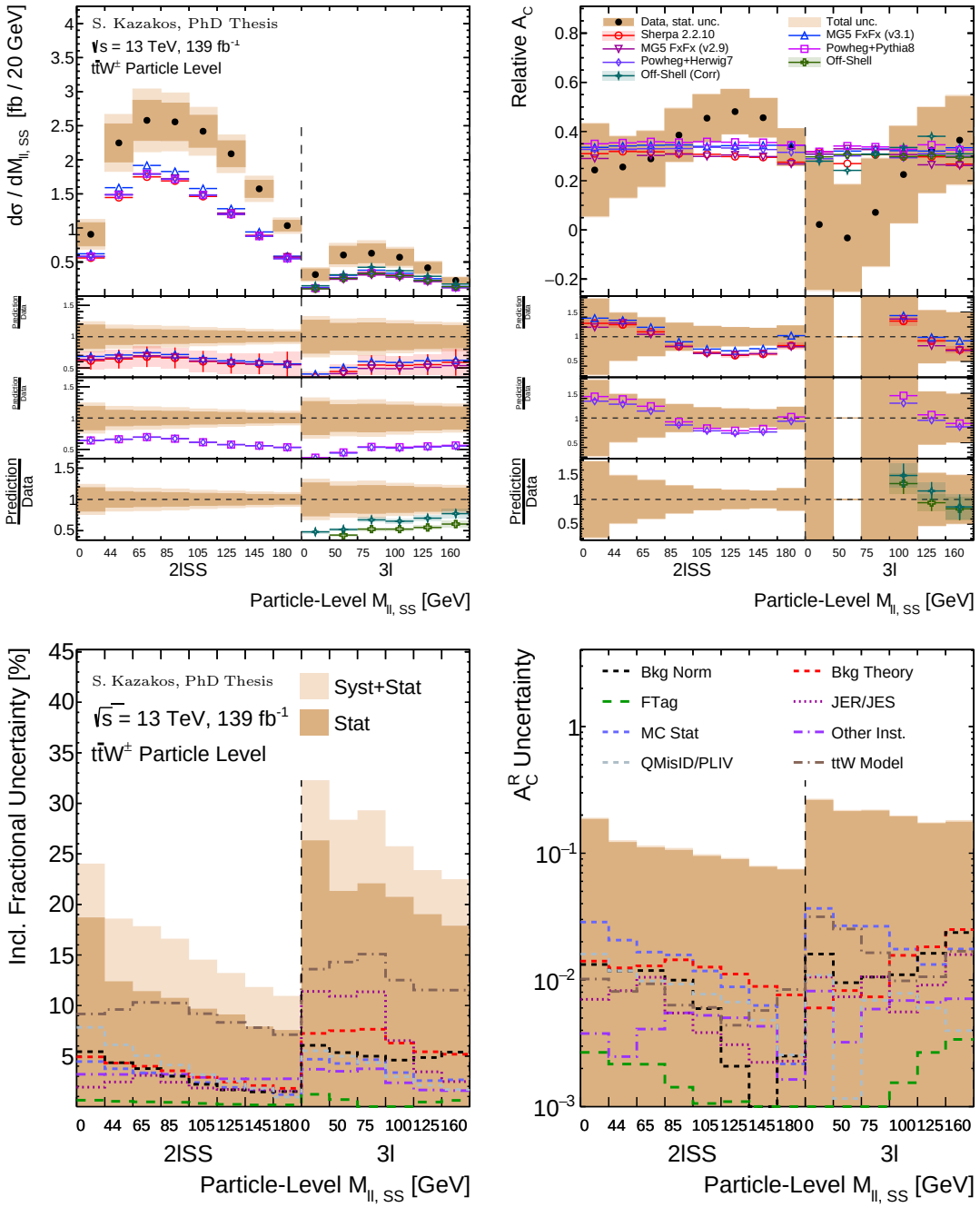



FIGURE 9.45: Unfolded differential cross section (top left) and relative charge asymmetry (top right) in 2$\ell$SS and 3$\ell$ regions (charge-inclusive) as a function of $m_{\ell_0^{\mathrm{SS}}\ell_1^{\mathrm{SS}}}$ together with the corresponding grouped impact of systematic uncertainties (bottom).

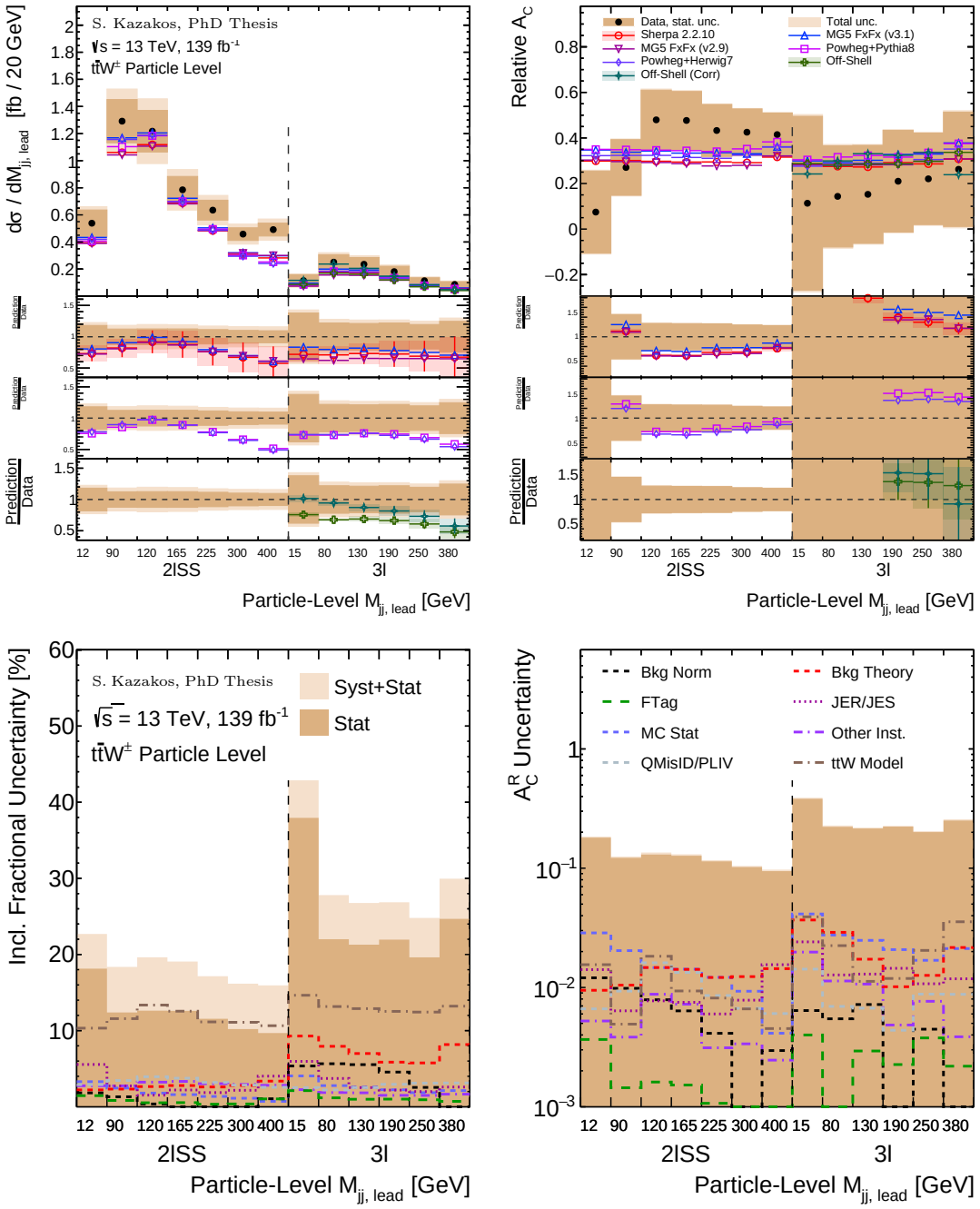



FIGURE 9.46: Unfolded differential cross section (top left) and relative charge asymmetry (top right) in $2\ell$SS and $3\ell$ regions (charge-inclusive) as a function of $m_{j_0 j_1}$ together with the corresponding grouped impact of systematic uncertainties (bottom).

In the results presented in this section the data overshoot the prediction from the simulation in most of the unfolded bins, with very few exceptions such as the events of the $3\ell$ channel with one $b$-jet. Large data-to-simulation discrepancy is observed in the $3\ell - [2]$ region resulting in very large values of cross-section NFs ($\mu_j$) for some of the observables. The discrepancy seems to originate from the $\mu\mu\mu$ signature and it is attributed to statistical fluctuations of the data. The $t\bar{t}W$ unfolded cross-section NFs are consistently larger than the SM expectation value with values consistent to the inclusive $t\bar{t}W$ measurement. The results are also in accordance with the previous findings reported by the $t\bar{t}H$ to multilepton measurement [208].

The $N_{\text{jets}}$ distribution shows a large data/MC discrepancy at low and high values, where the data show a larger deviation in the charge asymmetry. Other unfolded distributions show interesting features, such as $|\Delta\phi_{\ell_0^{\text{SS}}\ell_1^{\text{SS}}}|/\pi$ in the $2\ell$SS $++$ and $--$ channels, and $H_{\text{T, lep}}$, which is harder than the data particularly in the $2\ell$SS $++$ channel. These differential measurements across the different observables will allow to explore to what extent the SM predictions can be tuned in order to match data, not just in cross section, but also in the kinematics and the interpretation of residual discrepancies in the context of BSM scenarios.

The results of this first ever $t\bar{t}W$ differential cross-section measurement show that it is largely dominated by statistical uncertainties. This fact yields some interesting future prospects with the start of Run 3 and beyond, where a more precise measurement can be obtained, in particular regarding the $A_C^R$.

# Chapter 10

# Search for leptoquark pair production in multilepton final states

This chapter discusses two of the leptoquark (LQ) searches that were performed as the product of this thesis. The first section (Section 10.1) provides an overview of the search for LQ pair production in the $t\tau t\tau$ final state. The second section (Section 10.2) describes the search for LQ pair production in the $t\ell t\ell$ final state, where $\ell$ stands for light-lepton candidates (i.e. electrons and muons). The last section (Section 10.3) provides an overview of the combination of multiple LQ-related analyses and highlights the overall contribution of the LQ results in this thesis to this important effort.

The motivation in order to look into these LQ signatures, as well as the LQ phenomenology are explained in more detail in Section 3.2. The common aspects concerning the principles of these analyses are discussed in Chapter 8. The methods described in Chapter 9 about background estimation and suppression (including the Template Fit method) are also applied to these analyses, where the exact methods are used in the LQLQ$\rightarrow t\ell t\ell$ analysis and a less sophisticated version of the Template Fit including an older PLV discriminant version is used in the LQLQ$\rightarrow t\tau t\tau$ analysis. The aim of this chapter is to stress the specific points that make these searches special and to focus on their final results.

## 10.1 Search for leptoquark pair production in $t\tau t\tau$ final states

### 10.1.1 Introduction

The search discussed in this section targets $\mathrm{LQ}_3^{\mathrm{d}}$ pair production in the $t\tau t\tau$ final state, being particularly sensitive to high branching ratio ($\mathcal{B}$) values. In this decay mode, light-lepton candidates are produced through the semileptonic decay of a top quark (via a $W$ boson) or through the leptonic decay of a $\tau$-lepton. These light leptons are used to trigger on the events of interest by passing the requirements of single-lepton or dilepton triggers. The presence of light leptons combined with the presence of hadronically decaying $\tau$-leptons (originating from the LQ decay) is also useful for the categorisation of the events in regions and to reduce the contribution of SM backgrounds, increasing the sensitivity of the search. The final state under study usually contains two energetic $b$-jets originating from the top-quark decays and additional light-flavoured jets originating from ISR or FSR processes and from hadronic $W$-boson decays (originating from the top quarks). An illustrative Feynman diagram of this final state is shown in Figure 10.1.

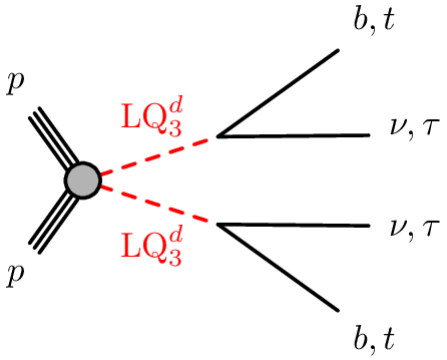



FIGURE 10.1: Illustrative LO Feynman diagram of third-generation LQ pair production with subsequent LQ decay into $b\nu$ or $t\tau$. Figure taken from Ref. [225].

The complicated signature of this final state motivates a sophisticated categorisation of events into channels, which are used to define the analysis regions. Some of these regions are used to validate the modelling of the leading background contributions, while others are used in a maximum-likelihood template fit to real data in order to constrain these backgrounds simultaneously with the signal search. The

presence of multiple neutrinos in the targeted events complicates the kinematic reconstruction of the LQ mass (depending on a proper top-quark mass reconstruction). Nevertheless, there are other discriminating variables that can be defined providing remarkable sensitivity through strong signal-versus-background separation when used in the fit. The sensitivity of the search is further improved by tightening up the object selection in the various channels by basing the selection criteria on the rest of the variables with high signal discrimination that are not used in the fit.

### 10.1.2 Object definition

The light-lepton definition in this search differs slightly from the one described in Section 8.3.3. One of the main differences is that the classification of the light-lepton WPs defined here is not based entirely on the PLIV OP, rather that it corresponds to a specific set of selections including a selection based on the PLV value. The [L] definition corresponds to the loosest definition that is selected for the light leptons of the search. The [M] definition corresponds to a tighter light-lepton ID WP, while the [T] definition corresponds to selections based on the PLV and ECIDS BDT discriminants and the additional application of conversion vetoes. The light-lepton definitions are explained in detail in Table 10.1.

| | $e$ | | | $\mu$ | | |
|---|---|---|---|---|---|---|
| | [L] | [M] | [T] | [L] | [M] | [T] |
| Identification | Loose | Tight | Tight | Loose | Medium or High-$p_{\mathrm{T}}$ | Medium or High-$p_{\mathrm{T}}$ |
| Isolation | | FCLoose | | | FCLoose | |
| Non-prompt lepton BDT (PLV) | — | — | $< -0.7$ | — | — | $< -0.5$ |
| Charge-misassignment BDT (ECIDS) | — | — | $> 0.7$ | | — | |
| Conversion vetoes | No | No | Yes | | — | |
| $\lvert d_0\rvert/\sigma_{d_0}$ | | $< 5$ | | | $< 3$ | |
| $\lvert z_0 \sin\theta\rvert$ [mm] | | $< 0.5$ | | | $< 0.5$ | |

TABLE 10.1: Definition of Loose [L], Medium [M], and Tight [T] light leptons. Table adapted from Ref. [226].

### 10.1.3 Event categorisation and discriminating variable

The events targeted in this search are categorised in channels based on the light-lepton and $\tau_{\mathrm{had}}$ multiplicities, as shown in the sketch of Figure 10.2. The categorisation is based on leptons defined at the preselection level with the loosest

definitions available. In this way, the orthogonal selection of events falling into the various channels is ensured.

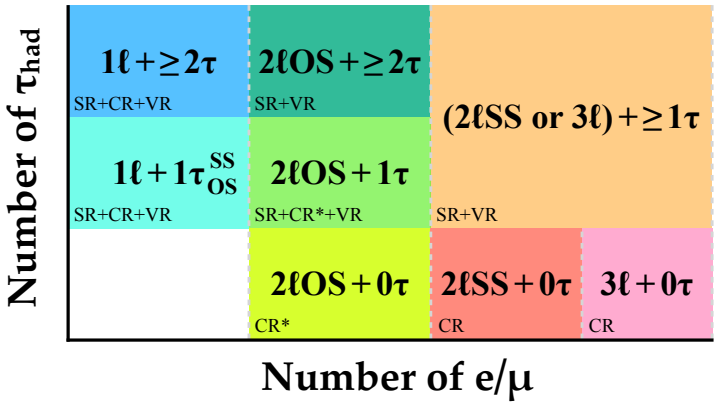



FIGURE 10.2: Overview of the channel categorisation based on light-lepton and $\tau_{had}$ multiplicities. The control regions marked with an asterisk (*) are not used in the combined fit.

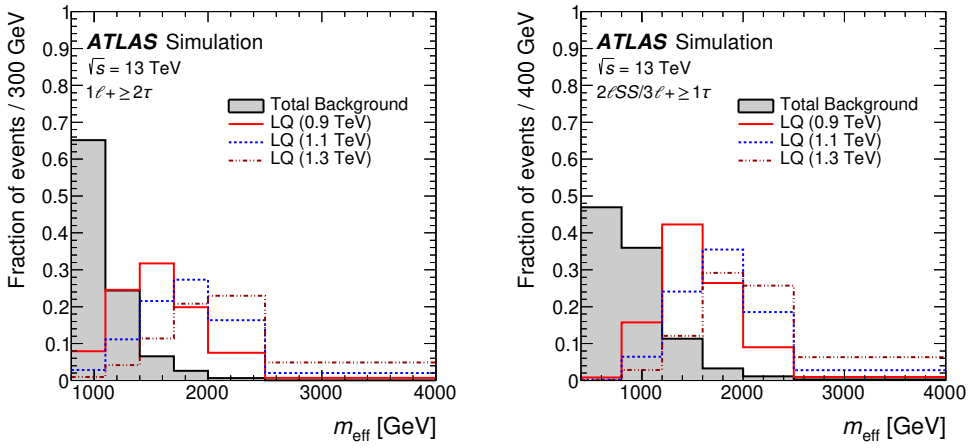
The final states (or channels) analysed are [226]:

- $1\ell+\geq 1\tau_{had}$: one light lepton and at least one $\tau_{had}$ candidate;
- $2\ell$OS$+\geq 1\tau_{had}$: two opposite-charge (denoted by OS, standing for opposite-sign) light leptons and at least one $\tau_{had}$ candidate;
- $2\ell$SS$/3\ell+\geq 1\tau_{had}$: two same-charge (denoted by SS, standing for same-sign) light leptons or three light leptons, and at least one $\tau_{had}$ candidate;
- $2\ell$OS$+0\tau_{had}$: two OS light leptons and no $\tau_{had}$ candidates;
- $2\ell$SS$+0\tau_{had}$: two SS light leptons and no $\tau_{had}$ candidates;
- $3\ell+0\tau_{had}$: three light leptons and no $\tau_{had}$ candidates.

The signal search is performed in the analysis channels with at least one $\tau_{had}$ candidate, while the channels with no $\tau_{had}$ candidates serve to the estimation of background contributions. The $2\ell$SS$+\geq 1\tau_{had}$ and $3\ell+\geq 1\tau_{had}$ channels are merged into a single one due to the low statistics at the current luminosity.

The search is performed by following a cut-based approach, where a number of selections are applied in each channel in order to suppress background, and then the distribution of the discriminating variable is exploited. This discriminating variable is called effective mass, $m_{\text{eff}}$, which is already defined in Equation 8.2, and its shape is fitted in the SRs. The discriminating power of this variable to

distinguish the LQ signal from the SM background is demonstrated in Figure 10.3 for the $1\ell{+}{\geq}2\tau_{\text{had}}$ and $2\ell\text{SS}/3\ell{+}{\geq}1\tau_{\text{had}}$ channels.




(a) (b)

FIGURE 10.3: Comparison of the $m_{\text{eff}}$ distribution in (a) the $1\ell{+}{\geq}2\tau_{\text{had}}$, and (b) the $2\ell\text{SS}/3\ell{+}{\geq}1\tau_{\text{had}}$ channel, between the LQ signal for different mass values and the SM background (shaded histogram). Figures taken from Ref. [226].

### 10.1.4 Analysis region definitions

Within each analysis channel several regions are defined optimised for signal search (SRs), background estimation (CRs), or background validation (VRs). There are 18 CRs, 6 VRs, and 7 SRs defined in this search. In the SR optimisation, apart from the use of the $m_{\text{eff}}$ variable, there are other kinematic variables useful in the signal discrimination such as the $\tau_{\text{had}}$ $p_{\text{T}}$, and different dilepton invariant mass variables (including also $\tau_{\text{had}}$ candidates in the dilepton combinations). The CR definitions are based on inverting some of the SR selections creating background-enriched samples orthogonal to the ones in the SRs. The VR definitions are also orthogonal to the ones from the CRs and SRs, while being kinematically closer to the latter. In all analysis channels events with light-lepton candidates with $p_{\text{T}} \geq 25$ GeV are required.

The events in the $1\ell{+}{\geq}1\tau_{\text{had}}$ channel are required to have one light lepton satisfying the [M] definition, and exactly one Medium ID $\tau_{\text{had}}$ candidate or two Loose ID $\tau_{\text{had}}$ candidates. In the case of one Medium ID $\tau_{\text{had}}$ candidate, events with additional $\tau_{\text{had}}$ candidates of Loose ID are vetoed. The same category is subdivided in two depending on the charge of the light-lepton and $\tau_{\text{had}}$ candidates into OS

and SS. This splitting is motivated by an improvement in sensitivity due to the different S/B ratios and background contributions. There are nine analysis regions defined in total in the $1\ell+\geq 1\tau_{\text{had}}$ channel, with one SR, one CR and one VR in each of the three categories. An overview of the region definitions in this channel is given in Table 10.2.

| | $1\ell+1\tau_{\text{had}}$OS | | | $1\ell+1\tau_{\text{had}}$SS | | | $1\ell+\geq 2\tau_{\text{had}}$ | | |
|---|---|---|---|---|---|---|---|---|---|
| | CR | VR | SR | CR | VR | SR | CR | VR | SR |
| $e/\mu$ definition | [M] | | | [M] | | | [M] | | |
| $N_{\text{jets}}$ | $\geq 4$ | | | $\geq 3$ | | | $\geq 2$ | | |
| $N_{b-\text{jets}}$ (77% DL1) | $\geq 2$ | $\geq 1$ | | $\geq 2$ | $\geq 1$ | | $\geq 2$ | $\geq 1$ | |
| $N_{\tau_{\text{had}}}$ | 1 | | | 1 | | | $\geq 2$ | | |
| $\tau_{\text{had}}$ ID | Medium | | | Medium | | | Loose | | |
| $\ell\tau_{\text{had}}$ charge | OS | | | SS | | | — | | |
| $p_{\text{T}}^{\ell}$ [GeV] | $\geq 25$ | | | $\geq 25$ | | | $\geq 25$ | | |
| $p_{\text{T},1}^{\tau}$ [GeV] | $\geq 50$ | 50–150 | $\geq 150$ | $\geq 50$ | 50–150 | $\geq 150$ | $\geq 50$ | 50–100 | $\geq 100$ |
| $p_{\text{T},2}^{\tau}$ [GeV] | — | | | — | | | $\geq 25$ | 25–50 | $\geq 50$ |
| $m_{\ell\tau}$ [GeV] | — | $\geq 200$ | | — | — | $\geq 200$ | — | | |
| $m_{\text{T}}(\ell, E_{\text{T}}^{\text{miss}})$ [GeV] | — | | | — | — | $\geq 100$ | — | | |
| $m_{\tau\tau}$ [GeV] | — | | | — | | | — | $\geq 100$ | |
| $E_{\text{T}}^{\text{miss}}$ [GeV] | — | $\geq 80$ | | — | — | $\geq 50$ | — | | |
| $m_{\text{eff}}$ [GeV] | $< 800$ | $\geq 800$ | | $< 800$ | $\geq 800$ | | $< 800$ | $\geq 800$ | |

TABLE 10.2: Overview of regions defined in the $1\ell+\geq 1\tau_{\text{had}}$ channel. Table adapted from Ref. [226].

| | $2\ell$OS+$1\tau_{\text{had}}$ | | | | $2\ell$OS+$\geq 2\tau_{\text{had}}$ | |
|---|---|---|---|---|---|---|
| | $\text{CR}^{Z}$ | $\text{CR}^{t\bar{t}}$ | VR | SR | VR | SR |
| $e/\mu$ definition | [M] | | | | [M] | |
| $e/\mu$ split by flavour | $ee/\mu\mu$ | $e\mu$ | $ee/\mu\mu$ | $ee/\mu\mu/e\mu$ | $ee/\mu\mu/e\mu$ | |
| $Z$-veto | Inverted | Yes | Yes | Yes | Yes | |
| $m_{\ell\ell}$ [GeV] | $> 12$ | | | | $> 12$ | |
| $N_{\text{jets}}$ | $\geq 2$ | | | | $\geq 2$ | |
| $N_{b-\text{jets}}$ (77% DL1) | $\geq 1$ | | | | $\geq 1$ | |
| $N_{\tau_{\text{had}}}$ | 1 | | | | $\geq 2$ | |
| $\tau_{\text{had}}$ ID | Loose/Medium | | Medium | | Loose | |
| $p_{\text{T}}^{\ell}$ [GeV] | $\geq 25$ | | | | $\geq 25$ | |
| $p_{\text{T},1}^{\tau}$ [GeV] | $\geq 25$ | $\geq 25$ | 25–150 | $\geq 150$ | $\geq 25$ | $\geq 75$ |
| $m_{\ell\tau}^{\text{min}}$ [GeV] | — | — | $< 100$ | $\geq 100$ | — | $\geq 50$ |
| $m_{\tau\tau}$ [GeV] | — | | | | $<100$ | $\geq 100$ |
| $m_{\text{eff}}$ [GeV] | — | $< 1000$ | — | — | — | — |

TABLE 10.3: Overview of regions defined in the $2\ell$OS+$\geq 1\tau_{\text{had}}$ channel. Table adapted from Ref. [226].

The events in the $2\ell$OS+$\geq 1\tau_{\text{had}}$ channel are required to have two OS light leptons satisfying the [M] definition, and at least one $\tau_{\text{had}}$ candidate with Loose or Medium

ID. In this channel lepton flavour is used in the definition of the regions. A selection of $m_{\ell\ell} > 12$ GeV in the dilepton invariant mass contributes to the suppression of backgrounds with resonant quarkonia or $Z$-boson decays, while a "$Z$-veto" of $|m_{\ell\ell} - m_Z| > 10$ GeV reduces the background contributions including an on-shell $Z$-boson candidate. In this channel, two dedicated CRs are defined used for the SF estimation related to the jet misidentification rate in the MC simulation for both Loose and Medium ID $\tau_{\text{had}}$ candidates. These CRs, $\text{CR}^{Z}$ and $\text{CR}^{t\bar{t}}$, are enriched in $Z$+jets and dileptonic $t\bar{t}$ events, respectively, and are not used in the final likelihood fit. The $\text{CR}^{Z}$ definition involves an inverted $Z$-veto, which allows the selection of events with $Z$-boson candidates. There are six analysis regions defined in total for this channel, and these regions are summarised in Table 10.3.

The events in the $2\ell\text{SS}/3\ell{+}{\geq}1\tau_{\text{had}}$ channel are required to have either two light leptons of the same charge ($2\ell$SS) or three light leptons ($3\ell$) of total charge equal to $\pm 1$, and at least one $\tau_{\text{had}}$ candidate with Loose ID. The sorting of lepton candidates in the $2\ell$SS case is done with respect to their $p_{\text{T}}$, while the lepton candidates in the $3\ell$ case are sorted based on their charge ($\ell_0$ is the OS lepton relative to the SS pair, and the other two $\ell_1$, $\ell_2$ are sorted with respect to the closest $\Delta R$ to $\ell_0$). There are three regions in total in the $2\ell\text{SS}/3\ell{+}{\geq}1\tau_{\text{had}}$ channel, which are summarised in Table 10.4.

| | $2\ell\text{SS}/3\ell{+}{\geq}1\tau_{\text{had}}$ | | |
|---|---|---|---|
| | VR | SR-L | SR-H |
| $e/\mu$ definition | [T] ($2\ell$SS) | | |
| | [M] OS, [T] SS ($3\ell$) | | |
| $Z$-veto | Yes | | |
| $m_{\ell\ell}$ [GeV] | $> 12$ | | |
| $p_{\text{T}}^{\ell}$ [GeV] | $\geq 25$ | | |
| $N_{\text{jets}}$ | $\geq 2$ | | |
| $N_{b-\text{jets}}$ (77% DL1) | $\geq 1$ | | |
| $N_{\tau_{\text{had}}}$ | $\geq 1$ | | |
| $\tau_{\text{had}}$ ID | Loose | | |
| $p_{\text{T},1}^{\tau}$ [GeV] | 25–125 | 125–225 | $\geq 225$ |

TABLE 10.4: Overview of the regions defined in the $2\ell\text{SS}/3\ell{+}{\geq}1\tau_{\text{had}}$ channel. Table adapted from Ref. [226].

The [T] selection criteria are applied to the SS pair of light-lepton candidates in this channel, in order to suppress contributions from events with non-prompt leptons, leptons from photon conversions, and leptons with misassigned charge. The light lepton with opposite charge to the SS lepton pair in the case of $3\ell$ events

is required to satisfy the [M] selection criteria. The selections $m_{\ell\ell} > 12$ GeV and $|m_{\ell\ell} - m_Z| > 10$ GeV are required similarly to the $2\ell$OS+$\geq 1\tau_{\text{had}}$ channel, while a $Z$-veto based on the trilepton mass is applied targeting the suppression of $Z \to \ell\ell\gamma^* \to 4\ell$ backgrounds. The regions in this channel are defined based on leading $\tau_{\text{had}}$ $p_{\text{T}}$, $p^{\tau}_{\text{T},1}$. Events with $25 < p^{\tau}_{\text{T},1} < 125$ GeV are populating a VR for background validation, while two SRs are defined for $125 \leq p^{\tau}_{\text{T},1} < 225$ GeV and $p^{\tau}_{\text{T},1} > 225$ GeV, respectively, called SR-L and SR-H.

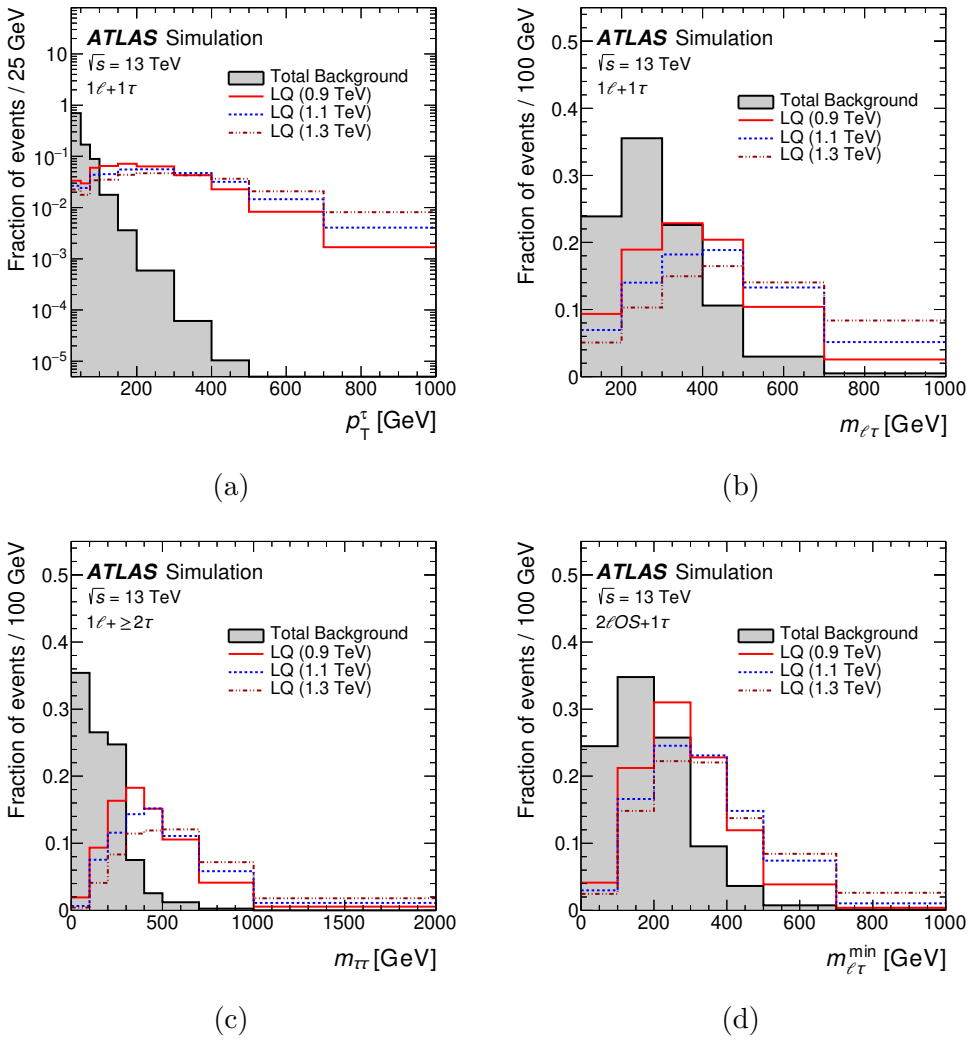



FIGURE 10.4: Shape comparison of distributions with high signal-to-background discrimination between different LQ signal mass points and the SM background (shaded histogram). The $p_{\text{T}}$ of the $\tau_{\text{had}}$ candidate (a), the invariant mass of the light lepton and the $\tau_{\text{had}}$ candidate (b), and the invariant mass of the two leading $\tau_{\text{had}}$ candidates (c) are shown for the $1\ell+\geq 1\tau_{\text{had}}$ channel. The minimum invariant mass of a light lepton and a $\tau_{\text{had}}$ candidate (d) is shown for the $2\ell$OS+$\geq 1\tau_{\text{had}}$ channel. Figures taken from Ref. [226].

The sensitivity in the $1\ell+\geq 1\tau_{\text{had}}$ channel is increased by requiring $\tau_{\text{had}}$ candidates with high $p_{\text{T}}$, and events with large invariant masses between the leading light-lepton and $\tau_{\text{had}}$ candidates or between the leading and subleading $\tau_{\text{had}}$ candidates (in case of more than one). The $\tau_{\text{had}}$ $p_{\text{T}}$ variable is also exploited in the $2\ell\text{OS}+\geq 1\tau_{\text{had}}$ and $2\ell\text{SS}/3\ell+\geq 1\tau_{\text{had}}$ channels, while in the former a useful variable is the minimum dilepton invariant mass between a light-lepton and a $\tau_{\text{had}}$ candidate in the event. The signal and background shapes of these variables in the $1\ell+\geq 1\tau_{\text{had}}$ and $2\ell\text{OS}+\geq 1\tau_{\text{had}}$ channels are shown in Figure 10.4.

The events in the $2\ell\text{OS}+0\tau_{\text{had}}$, $2\ell\text{SS}+0\tau_{\text{had}}$, and $3\ell+0\tau_{\text{had}}$ channels do not contain any $\tau_{\text{had}}$ candidates and are mainly used to improve the background estimation. The selection in the $2\ell\text{OS}+0\tau_{\text{had}}$ channel involves the presence of $2\ell\text{OS}$ $e\mu$ events with at least two jets and at least one $b$-jet, while the two lepton candidates should satisfy the [M] selection criteria. In this channel, a CR enriched in $t\bar{t}$ events is defined (called $t\bar{t}0\tau$ CR), which is used to derive corrections that improve the modelling of the $t\bar{t}$ background process. This region is not used in the final likelihood fit.

| | $2\ell\text{SS}+0\tau_{\text{had}}$ | | | | |
|---|---|---|---|---|---|
| | $2\ell\text{tt(e)}\pm$ | $2\ell\text{tt}(\mu)\pm$ | $2\ell\text{ttW}\pm$ | $2\ell\text{IntC}$ | $2\ell\text{MatC}$ |
| $e/\mu$ definition | | | [T] | | |
| $e/\mu$ combination | $ee/\mu e$ | $\mu\mu/e\mu$ | $ee/\mu\mu/e\mu/\mu e$ | $ee/e\mu/\mu e$ | $ee/e\mu/\mu e$ |
| Electron internal conversion veto | Yes | Yes | Yes | Inverted | Yes |
| Electron material conversion veto | Yes | Yes | Yes | Yes | Inverted |
| $N_{\text{jets}}$ | 2–3 | 2–3 | $\geq 4$ | $\geq 2$ | $\geq 2$ |
| $Z$-veto | | | Yes | | |
| $m_{ee}$ [GeV] | | | $\geq 12$ | | |
| $p_{\text{T}}^{\ell}$ [GeV] | | | $\geq 25$ | | |
| $N_{\text{jets}}$ | | | $\geq 2$ | | |
| $N_{b-\text{jets}}$ (77% DL1) | | | $\geq 1$ | | |

TABLE 10.5: Overview of regions defined in the $2\ell\text{SS}+0\tau_{\text{had}}$ channel. Table adapted from Ref. [226].

The $2\ell\text{SS}+0\tau_{\text{had}}$ and $3\ell+0\tau_{\text{had}}$ channels are used for the definition of CRs that participate in the final likelihood fit aiming to constrain some of the main background contributions in this analysis. The events in the $2\ell\text{SS}+0\tau_{\text{had}}$ channel contain two SS light-lepton candidates that satisfy the [T] selection criteria (except in the conversion CRs where the corresponding conversion vetoes are inverted), and are

sorted in lepton $p_{\mathrm{T}}$. There are eight CRs defined in total in this channel enriched in different backgrounds such as $t\bar{t}W$ ($2\ell$ttW CRs), non-prompt electrons or muons ($2\ell$tt(e) and $2\ell$tt($\mu$) CRs) and electrons from internal or material conversions ($2\ell$IntC and $2\ell$MatC CRs). The CR definitions in this channel are detailed in Table 10.5. In the definition of the non-prompt lepton CRs, the subleading lepton is always an electron in the $2\ell$tt(e) CRs (resulting in $ee/\mu e$ events) and always a muon in the $2\ell$tt($\mu$) CRs (resulting in $\mu\mu/e\mu$ events). This categorisation is based on the fact that the subleading lepton in $p_{\mathrm{T}}$ is more likely to be the non-prompt one. The events in the non-prompt lepton CRs are also required to have two or three jets. This requirement is to distinguish them from the $2\ell$ttW CRs, where at least four jets are required. The $2\ell$ttW, $2\ell$tt(e) and $2\ell$tt($\mu$) CRs are further split by their light-lepton total charge to $++$ and $--$ in order to exploit the discrimination between charge symmetric ($t\bar{t}$) and charge asymmetric ($t\bar{t}W$) backgrounds in the final fit.

The events in the $3\ell{+}0\tau_{\mathrm{had}}$ channel are required to have three light leptons with total charge equal to $\pm1$ and satisfying the [M] or [T] selection criteria. The lepton candidates are sorted based on their charge in this channel such that the OS lepton (relative to the SS pair) is denoted as $\ell_0$, and the remaining SS leptons are denoted as $\ell_1$ and $\ell_2$, where $\ell_1$ is the lepton with the smallest $\Delta R$ with $\ell_0$ and $\ell_2$ is the lepton with the largest $\Delta R$ with $\ell_0$. There are four CRs defined in total in this channel, and their definitions are summarised in Table 10.6. There are two CRs targeting events with leptons from internal or external conversions ($3\ell$IntC and $3\ell$MatC, respectively), which have one of the corresponding conversion vetoes inverted. The other two CRs have their $Z$-veto inverted, targeting in this way events with an on-shell $Z$-boson candidate. They are split according to number of jets to $3\ell$VV (for two to three jets) and $3\ell$ttZ (for at least four jets), since with these selection criteria they are enriched in these backgrounds.

### 10.1.5 Main background contributions

In the $1\ell{+}1\tau_{\mathrm{had}}$OS regions the dominant background is $t\bar{t}$ production, where both the light-lepton and $\tau_{\mathrm{had}}$ candidate are prompt since they originate from the $W$-boson decays ("true" $t\bar{t}$). The contribution from single-top processes is also quite significant in these regions. In the $1\ell{+}1\tau_{\mathrm{had}}$SS regions the dominant background is again the contribution from the $t\bar{t}$ process, but with one jet misidentified as a

| | | | $3\ell$+$0\tau_{\text{had}}$ | |
|---|---|---|---|---|
| | $3\ell$VV | $3\ell$ttZ | $3\ell$IntC | $3\ell$MatC |
| $e/\mu$ definition | [M] | [M] | [M]($\ell_0$), [T]($\ell_1$ and $\ell_2$) | [M]($\ell_0$), [T]($\ell_1$ and $\ell_2$) |
| Electron internal conversion veto | Yes | Yes | Inverted($\ell_1$ or $\ell_2$) | Yes($\ell_1$ and $\ell_2$) |
| Electron material conversion veto | Yes | Yes | Yes($\ell_1$ and $\ell_2$) | Inverted($\ell_1$ or $\ell_2$) |
| $N_{\text{jets}}$ | 2–3 | $\geq 4$ | $\geq 2$ | $\geq 2$ |
| $Z$-veto | Inverted | Inverted | Yes | Yes |
| $m_{\ell\ell}$ [GeV] | | | $\geq 12$ | |
| $p_{\text{T}}^{\ell}$ [GeV] | | | $\geq 25$ | |
| $N_{\text{jets}}$ | | | $\geq 2$ | |
| $N_{b-\text{jets}}$ (77% DL1) | | | $\geq 1$ | |

TABLE 10.6: Overview of the regions defined in the $3\ell$+$0\tau_{\text{had}}$ channel. Table adapted from Ref. [226].

$\tau_{\text{had}}$ candidate ("fake" $t\bar{t}$; result of the presence of a fake-$\tau_{\text{had}}$ candidate) regardless if the light lepton is prompt or not. Significant background contributions in these regions are also events from $t\bar{t}$ with real $\tau_{\text{had}}$ candidates, from $t\bar{t}W$ and from diboson processes. In the $1\ell$+$\geq$$2\tau_{\text{had}}$, $2\ell$OS+$1\tau_{\text{had}}$, and $2\ell$OS+$\geq$$2\tau_{\text{had}}$ regions, there is significant contribution of events from the $t\bar{t}$ process with one fake-$\tau_{\text{had}}$ candidate (about half of the total background), while the rest of the contributions belong to events from $t\bar{t}W$, $t\bar{t}Z/\gamma^*$, and $t\bar{t}H$ processes. In the $2\ell$SS/$3\ell$+$\geq$$1\tau_{\text{had}}$ regions the major background contributions include events with real leptons from $t\bar{t}W$, $t\bar{t}Z/\gamma^*$, $t\bar{t}H$, and $VV$ processes with real and fake-$\tau_{\text{had}}$ candidates.

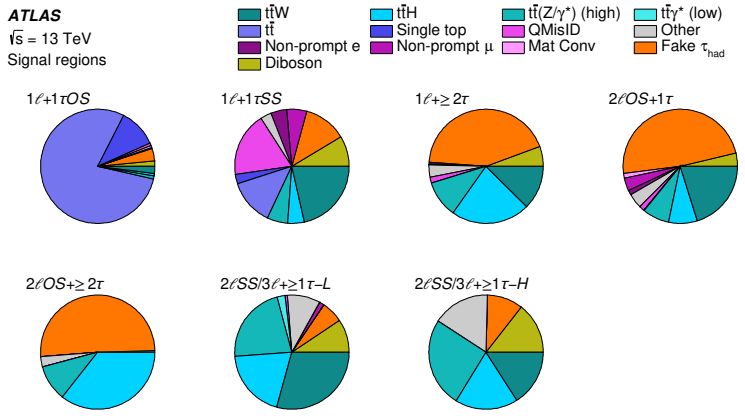



FIGURE 10.5: Background composition in the signal regions of the analysis after a likelihood fit to data under the background-only hypothesis. Figure taken from Ref. [226].

In all regions mentioned up to this point there are also smaller background contributions from events with real $\tau_{\text{had}}$ candidates, but with non-prompt leptons,

leptons from conversions, and leptons with misassigned charge. In the $2\ell$SS+$0\tau_{\text{had}}$ and $3\ell$+$0\tau_{\text{had}}$ regions the main background contributions vary depending on the targeted background contribution in each region. An overview of the background composition in the SRs, CRs and VRs of the analysis is shown in Figures 10.5, 10.6 and 10.7, respectively, after a likelihood fit under the background-only hypothesis.

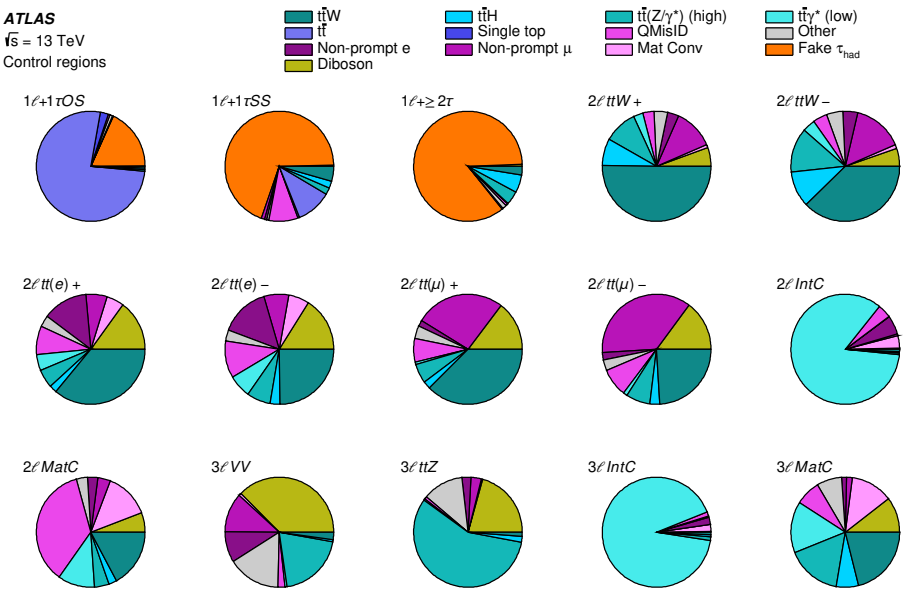



FIGURE 10.6: Background composition in the control regions of the analysis after a likelihood fit to data under the background-only hypothesis. Figure taken from Ref. [226].

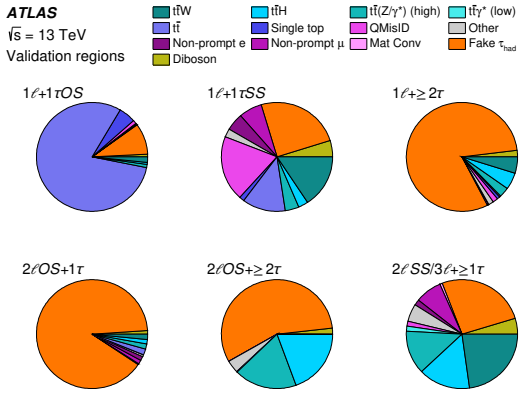



FIGURE 10.7: Background composition in the validation regions of the analysis after a likelihood fit to data under the background-only hypothesis. Figure taken from Ref. [226].

### 10.1.6 Signal and background modelling

#### 10.1.6.1 Signal modelling

The samples simulating the $LQ_3^d$ signal process are generated with the MadGraph5_aMC@NLO generator at NLO accuracy using the NNPDF 3.0 NLO PDF set, and interfaced with Pythia-8 for the PS and hadronisation processes (A14 tune). The decays of the scalar $LQ_3^d$ signal were modelled using MadSpin. The coupling parameter $\lambda$ (defined in Section 3.2) is set to $\lambda = 0.3$, for which the width of the $LQ_3^d$ resonance is equal to about 0.2% of its mass. Leptoquarks of $LQ_3^d$ type ($Q = -1/3$) decay into either a $t\tau$ or a $b\nu$ pair, respecting the charge conservation. In the simulated $LQ_3^d$ samples their decay mode is controlled by the branching fraction parameter $\beta$. Simulated samples are generated for $LQ_3^d$ mass points within the range of 0.5 TeV to 1.6 TeV with 100 GeV step for $\beta = 1$, corresponding to LQ pair production where each LQ is allowed to decay only into a $t\tau$ pair. Additional simulated samples are produced for $LQ_3^d$ mass points within the range of 0.5 TeV to 0.8 TeV with 100 GeV step and 0.8 TeV to 1.6 TeV with 50 GeV step for $\beta = 0.5$, corresponding to LQ pair production where the $LQ_3^d \to t\tau$ and $LQ_3^d \to b\nu$ decay modes have identical amplitudes.

#### Signal theory uncertainties

The signal predictions are normalised to the NNLOapprox+NNLL cross sections, which are computed for scalar pair production. The NLO values of the cross section obtained from the MC generators and the corresponding $K$-factors (NNLOapprox+NNLL to NLO predictions ratios) are summarised for each mass point in Table 3.3. The impact of QCD renormalisation ($\mu_R$) and factorisation ($\mu_F$) scale variations, shower parameter (var3c) variations, $\alpha_S$ and PDFs is evaluated on the signal acceptance for various SRs. The uncertainties are evaluated by comparing the $m_{\text{eff}}$ truth distributions in these SRs for each variation, and are summarised in Table 10.7 for various LQ mass points (0.9, 1.1, 1.3 and 1.5 TeV). The event selections for the truth events are chosen as close as possible to the reconstruction-level selections. The uncertainties due to QCD scale variations are taken from the envelope of independent variation pairs of $\mu_R$ and $\mu_R$ by factors of 0.5 or 2, and these are found to range from 2.7% to 6.9% depending on the SR.

$\mu_F/\mu_R$

| Signal region | Up | Down |
|---|---|---|
| $1\ell$+$1\tau_{\text{had}}$OS | 0.003 | -0.004 |
| $1\ell$+$1\tau_{\text{had}}$SS | 0.016 | -0.015 |
| $1\ell$+$\geq 2\tau_{\text{had}}$ | 0.022 | -0.011 |
| $2\ell$SS/$3\ell$+$\geq 1\tau_{\text{had}}$ | 0.002 | 0.003 |

Var3c

| Signal region | Up | Down |
|---|---|---|
| $1\ell$+$1\tau_{\text{had}}$OS | 0.04 | -0.052 |
| $1\ell$+$1\tau_{\text{had}}$SS | 0.034 | 0.008 |
| $1\ell$+$\geq 2\tau_{\text{had}}$ | -0.076 | -0.041 |
| $2\ell$SS/$3\ell$+$\geq 1\tau_{\text{had}}$ | -0.103 | -0.013 |

$\alpha_s$+PDF

| Signal region | Up/Down |
|---|---|
| $1\ell$+$1\tau_{\text{had}}$OS | ± 0.005 |
| $1\ell$+$1\tau_{\text{had}}$SS | ± 0.009 |
| $1\ell$+$\geq 2\tau_{\text{had}}$ | ± 0.009 |
| $2\ell$SS/$3\ell$+$\geq 1\tau_{\text{had}}$ | ± 0.012 |

(a) 0.9 TeV

$\mu_F/\mu_R$

| Signal region | Up | Down |
|---|---|---|
| $1\ell$+$1\tau_{\text{had}}$OS | 0.013 | -0.002 |
| $1\ell$+$1\tau_{\text{had}}$SS | -0.007 | -0.013 |
| $1\ell$+$\geq 2\tau_{\text{had}}$ | -0.003 | 0.005 |
| $2\ell$SS/$3\ell$+$\geq 1\tau_{\text{had}}$ | 0.069 | -0.018 |

Var3c

| Signal region | Up | Down |
|---|---|---|
| $1\ell$+$1\tau_{\text{had}}$OS | -0.011 | -0.009 |
| $1\ell$+$1\tau_{\text{had}}$SS | -0.004 | -0.009 |
| $1\ell$+$\geq 2\tau_{\text{had}}$ | -0.091 | -0.049 |
| $2\ell$SS/$3\ell$+$\geq 1\tau_{\text{had}}$ | -0.004 | -0.02 |

$\alpha_s$+PDF

| Signal region | Up/Down |
|---|---|
| $1\ell$+$1\tau_{\text{had}}$OS | ± 0.011 |
| $1\ell$+$1\tau_{\text{had}}$SS | ± 0.016 |
| $1\ell$+$\geq 2\tau_{\text{had}}$ | ± 0.022 |
| $2\ell$SS/$3\ell$+$\geq 1\tau_{\text{had}}$ | ± 0.032 |

(b) 1.1 TeV

$\mu_F/\mu_R$

| Signal region | Up | Down |
|---|---|---|
| $1\ell$+$1\tau_{\text{had}}$OS | 0.004 | 0.006 |
| $1\ell$+$1\tau_{\text{had}}$SS | 0.052 | -0.011 |
| $1\ell$+$\geq 2\tau_{\text{had}}$ | -0.005 | -0.057 |
| $2\ell$SS/$3\ell$+$\geq 1\tau_{\text{had}}$ | -0.029 | -0.044 |

Var3c

| Signal region | Up | Down |
|---|---|---|
| $1\ell$+$1\tau_{\text{had}}$OS | 0.001 | -0.033 |
| $1\ell$+$1\tau_{\text{had}}$SS | -0.003 | -0.011 |
| $1\ell$+$\geq 2\tau_{\text{had}}$ | 0.028 | -0.006 |
| $2\ell$SS/$3\ell$+$\geq 1\tau_{\text{had}}$ | -0.047 | 0.039 |

$\alpha_s$+PDF

| Signal region | Up/Down |
|---|---|
| $1\ell$+$1\tau_{\text{had}}$OS | ± 0.027 |
| $1\ell$+$1\tau_{\text{had}}$SS | ± 0.057 |
| $1\ell$+$\geq 2\tau_{\text{had}}$ | ± 0.053 |
| $2\ell$SS/$3\ell$+$\geq 1\tau_{\text{had}}$ | ± 0.077 |

(c) 1.3 TeV

$\mu_F/\mu_R$

| Signal region | Up | Down |
|---|---|---|
| $1\ell$+$1\tau_{\text{had}}$OS | 0.004 | 0.01 |
| $1\ell$+$1\tau_{\text{had}}$SS | -0.025 | -0.039 |
| $1\ell$+$\geq 2\tau_{\text{had}}$ | 0.052 | 0.009 |
| $2\ell$SS/$3\ell$+$\geq 1\tau_{\text{had}}$ | 0.06 | 0.0 |

Var3c

| Signal region | Up | Down |
|---|---|---|
| $1\ell$+$1\tau_{\text{had}}$OS | -0.012 | -0.009 |
| $1\ell$+$1\tau_{\text{had}}$SS | 0.002 | 0.009 |
| $1\ell$+$\geq 2\tau_{\text{had}}$ | -0.038 | -0.099 |
| $2\ell$SS/$3\ell$+$\geq 1\tau_{\text{had}}$ | -0.012 | -0.022 |

$\alpha_s$+PDF

| Signal region | Up/Down |
|---|---|
| $1\ell$+$1\tau_{\text{had}}$OS | ± 0.064 |
| $1\ell$+$1\tau_{\text{had}}$SS | ± 0.103 |
| $1\ell$+$\geq 2\tau_{\text{had}}$ | ± 0.097 |
| $2\ell$SS/$3\ell$+$\geq 1\tau_{\text{had}}$ | ± 0.111 |

(d) 1.5 TeV

TABLE 10.7: Theory uncertainties on the LQ signal acceptance due to QCD scale ($\mu_R$, $\mu_F$) variations, shower parameter variations, $\alpha_s$ and PDFs. The uncertainties are shown for (a) 0.9, (b) 1.1, (c) 1.3 and (d) 1.5 TeV. The $2\ell$SS/$3\ell$+$\geq 1\tau_{\text{had}}$ SR contains the sum of events of the SR-L and SR-H SRs.

The uncertainties due to PDFs are evaluated by taking the 68% C.I. of all acceptance variations from 100 NNPDF30 NLO PDF sets using the PDF4LHC recommendation [227]. The acceptance uncertainty due to the $\alpha_S$ variations in the nominal PDF is added in quadrature to the PDF uncertainty, and the total

$\alpha_S$+PDF uncertainties are estimated to 1-3.2% for LQ masses below 1 TeV, to 2.7-7.7% for LQ masses between 1.0 and 1.3 TeV, and to 6.4-11% for the LQ masses larger than 1.3 TeV. The shower uncertainties range from 4.7% to 10% depending on the SR.

#### 10.1.6.2 Background modelling

### $m_{\text{eff}}$ kinematic reweighting

The $t\bar{t}$+jets process contributes as a significant background in all signal regions, with either real reconstructed $\tau_{\text{had}}$ candidates or $\tau_{\text{had}}$s faked by jets with the presence of prompt or non-prompt leptons. The mismodelling of the top-quark $p_{\text{T}}$ spectrum in the $t\bar{t}$ simulation has been observed in detailed differential cross-section measurements [228, 229]. The mismodelling occurs at the high-$p_{\text{T}}$ tail, where the MC prediction is usually overestimated, while there is an additional effect at high jet multiplicity events, where the MC prediction is usually underestimated. This mismodelling affects several kinematic variables through the observed discrepancy between data and simulation. One of the affected variables is also the main discriminating variable of the analysis, $m_{\text{eff}}$, which is constructed based on the $p_{\text{T}}$ of all physics objects and it depends on the number of jets in the event.

| | $N_{\text{jets}}$ norm. | $a_0$ | $a_1$ | $m_{\text{eff}}$ fit range |
|---|---|---|---|---|
| $2j, \geq 1b$ | 1.049 ± 0.002 | 1.118 ± 0.005 | -3.44e-04 ± 1.42e-05 | $m_{\text{eff}} \geq 100$ GeV |
| $3j, \geq 1b$ | 1.044 ± 0.002 | 1.082 ± 0.006 | -1.93e-04 ± 1.27e-05 | $m_{\text{eff}} \geq 100$ GeV |
| $4j, \geq 1b$ | 1.051 ± 0.003 | 1.121 ± 0.008 | -2.33e-04 ± 1.36e-05 | $m_{\text{eff}} \geq 100$ GeV |
| $5j, \geq 1b$ | 1.067 ± 0.006 | 1.161 ± 0.012 | -2.52e-04 ± 1.67e-05 | $m_{\text{eff}} \geq 100$ GeV |
| $\geq 6j, \geq 1b$ | 1.088 ± 0.010 | 1.261 ± 0.018 | -2.99e-04 ± 1.94e-05 | $m_{\text{eff}} \geq 100$ GeV |

TABLE 10.8: The normalisation corrections for $N_{\text{jets}}$ distributions and the values of fit parameters of first-order polynomial ($a_0$+$a_1$·$m_{\text{eff}}$) in $m_{\text{eff}}$ variable determined from OS $e\mu$ events.

In order to correct this behaviour, dedicated corrections are derived in the $t\bar{t}0\tau$ CR as a function of $m_{\text{eff}}$ and jet multiplicity, which are referred to as "kinematic reweighting". Since $t\bar{t}$ and $tW$ processes interfere at NLO, their contributions are corrected simultaneously. The event yields of non-$t\bar{t}$ and non-$tW$ processes are subtracted from data, and the corrections are derived as the ratio of the reduced data to the sum of the $t\bar{t}$ and $tW$ prediction from the simulation. This procedure

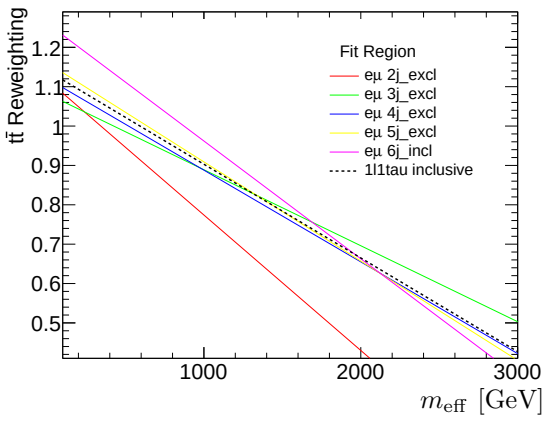
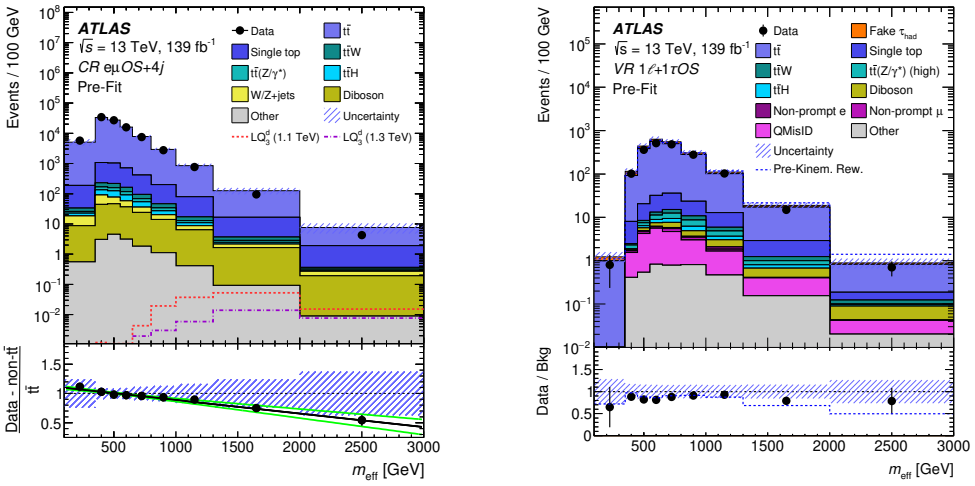



FIGURE 10.8: First-degree polynomials after fitted to the ratio of non-$t\bar{t}$ (and non-$tW$) subtracted data to the $t\bar{t}$ (and $tW$) prediction as a function of $m_{\text{eff}}$ per number of jet bins.

is performed per number of jets bin and the correction factors as a function of jet multiplicity vary from ∼1.05 for exactly two jets to ∼1.1 for at least six jets, as shown in Table 10.8. An additional correction is derived as a function of $m_{\text{eff}}$ in a similar way after the jet multiplicity spectrum is corrected. The corresponding ratio is parametrised as a first-degree polynomial and fitted per number of jets bin. The fitted first-degree polynomials are overlaid in Figure 10.8 showing the shapes differences for various jet multiplicity bins.

The mismodelling of $m_{\text{eff}}$ variable and the fit to the ratio are shown in the $t\bar{t}0\tau$ CR requiring exactly four jets in Figure 10.9a. The improvement in the modelling of $m_{\text{eff}}$ is demonstrated in the $1\ell{+}1\tau_{\text{had}}$OS VR, as shown in Figure 10.9b, where the prediction before the correction is also overlaid. The statistical uncertainty from the ratio fit to the first-degree polynomial is assigned as a systematic uncertainty related to this method. The $m_{\text{eff}}$-reweighting functions are also derived separately in the $1\ell{+}1\tau_{\text{had}}$OS channel and the difference between them is assigned as an additional systematic uncertainty accounting for potential differences between dileptonic and semileptonic $t\bar{t}$ kinematics.

The $Z$+jets contribution is either a negligible or a subdominant background in all signal regions. This background contribution exhibits the same behaviour as the $t\bar{t}$ contribution and it is corrected in a similar way. A CR enriched in $Z$+jets is defined, called $Z0\tau$ CR, where a similar $m_{\text{eff}}$ reweighting is derived for the $Z$+jets contribution.




(a) (b)

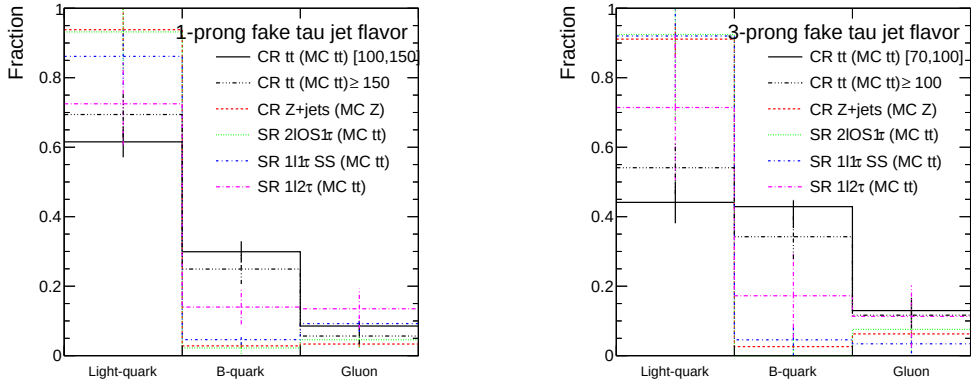
FIGURE 10.9: Data-to-simulation comparison in the $m_{\text{eff}}$ distribution before the likelihood fit to data in $t\bar{t}0\tau$ CR at exactly four jets (a), and in $1\ell{+}1\tau_{\text{had}}$OS VR (b). The derivation of the $m_{\text{eff}}$-reweighting correction is demonstrated in (a), where the green lines in the ratio pad denote the statistical uncertainty from the fit to the first-degree polynomial. The effect of the kinematic reweighting to the total background prediction prior to ("Pre-Kinem. Rew.") and after the reweighting is shown in (b). Figure taken from Ref. [226].

## Fake-$\tau_{\text{had}}$ estimation

In most channels where at least one $\tau_{\text{had}}$ is required, the major background contribution originates from $t\bar{t}$ events containing at least one fake-$\tau_{\text{had}}$ candidate. Therefore, the fake-$\tau_{\text{had}}$ background estimation depends on the accurate modelling of the $t\bar{t}$ process and the $\tau_{\text{had}}$ misidentification rate. After the $t\bar{t}$ and $Z$+jets contributions are corrected with the $m_{\text{eff}}$-reweighting procedure explained in the previous section, a strategy to correct the estimation of events with fake-$\tau_{\text{had}}$ candidates is followed. A CR enriched in these events is defined in the $1\ell{+}{\geq}2\tau_{\text{had}}$ channel by requiring OS $e\mu$ events with $m_{\text{eff}} < 1$ TeV, at least one Loose or Medium ID $\tau_{\text{had}}$, at least two jets and at least one $b$-jet. The upper threshold on $m_{\text{eff}}$ is used to remove the potential contamination from $\text{LQ}_3^{\text{d}}$ signal events.

This CR is referred to as $\text{CR}^{t\bar{t}}$ in Table 10.3 and it contains mostly dileptonic $t\bar{t}$ events. In these events the $\tau_{\text{had}}$ candidates originate from jets in principle, and they are used to derive correction scale factors (SFs) per $\tau_{\text{had}}$ candidate to account for the potential mismodelling of the fake-$\tau_{\text{had}}$ contribution. The SFs are measured as a function of $p_{\text{T}}^{\tau_{\text{had}}}$, and separately for one-prong and three-prong $\tau_{\text{had}}$ candidates. The SFs range from $1.07 \pm 0.06$ $(1.10 \pm 0.31)$ for $25 < p_{\text{T}}^{\tau_{\text{had}}} < 45$ (50) GeV, to

$0.57 \pm 0.19$ $(0.80 \pm 0.30)$ for $p_{\mathrm{T}}^{\tau_{\mathrm{had}}} \geq 100$ (75) GeV, for events with one-prong (three-prong) $\tau_{\mathrm{had}}$ candidates satisfying the Loose ID requirement. The same SFs for Medium ID $\tau_{\mathrm{had}}$ candidates do not differ from the ones derived for the Loose ID $\tau_{\mathrm{had}}$ definition, and they are the ones applied to all channels with at least one $\tau_{\mathrm{had}}$ candidate. The approach of deriving the SFs in a CR is valid if the flavour composition of the jets faking a $\tau_{\mathrm{had}}$ candidate in this CR is similar to that in the SRs, which is the case in this analysis as shown in Figure 10.10. The background events with at least one fake-$\tau_{\mathrm{had}}$ candidate are corrected on an event-by-event basis by the product of SFs, depending on their $\tau_{\mathrm{had}}$ candidate multiplicity prior to the final likelihood fit to data.




(a) (b)

FIGURE 10.10: Comparison of jet flavour of fake-$\tau_{\mathrm{had}}$ candidates in CRs and $1\ell$+$1\tau_{\mathrm{had}}$ SS, $1\ell$+$\geq$$2\tau_{\mathrm{had}}$ and $2\ell$OS+$1\tau_{\mathrm{had}}$ SRs for $t\bar{t}$ and $Z$+jets contributions with (a) one-prong, and (b) three-prong $\tau_{\mathrm{had}}$ candidates.

The total uncertainty on the SFs is used to define additional NPs in the fit (14 in total), per $p_{\mathrm{T}}^{\tau_{\mathrm{had}}}$ range and separately for one- and three-prong $\tau_{\mathrm{had}}$ candidates. This uncertainty is defined as the quadrature sum of the statistical uncertainty, the uncertainty in the estimation of events with real $\tau_{\mathrm{had}}$ candidates, and the difference between the nominal value of this SF to the one measured from a CR enriched in $Z$+jets events. This additional CR is referred to as $\mathrm{CR}^{Z}$ in Table 10.3 and it serves for the comparison of the SFs in a region with different jet-flavour composition of fake-$\tau_{\mathrm{had}}$ candidates (compared to $\mathrm{CR}^{t\bar{t}}$). Since the fake-$\tau_{\mathrm{had}}$ candidates in the events are treated as jets in the $m_{\mathrm{eff}}$ reweighting, the systematic uncertainties related to the PS, ME-to-PS matching and QCD radiation modelling in the $t\bar{t}$ events are treated as uncorrelated between events containing at least one fake-$\tau_{\mathrm{had}}$ candidate and the events without fake-$\tau_{\mathrm{had}}$ candidates.

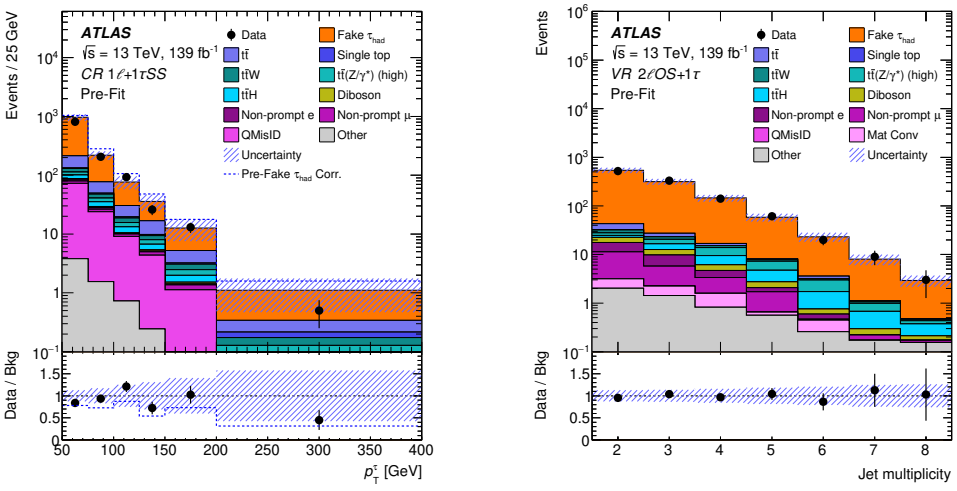
| Number of tracks / $p_{\mathrm{T}}^{\tau_{\mathrm{had}}}$ [GeV] | [25-45] ([25-50]) | [45-70] ([50-75]) | [70-100] (> 75) | > 100 |
|---|---|---|---|---|
| 1-prong | 1.07 ± 0.03 ± 0.05 | 0.88 ± 0.06 ± 0.02 | 0.66 ± 0.11 ± 0.28 | 0.57 ± 0.12 ± 0.15 |
| 3-prong | 1.10 ± 0.05 ± 0.31 | 1.09 ± 0.14 ± 0.37 | 0.80 ± 0.22 ± 0.20 | - |

TABLE 10.9: Fake-$\tau_{\mathrm{had}}$ scale factors for Loose RNN $\tau_{\mathrm{had}}$ ID estimated from the $t\bar{t}$-enriched region $\mathrm{CR}^{t\bar{t}}$. The total uncertainty is split to the statistical part and the systematics part.

| Number of tracks / $p_{\mathrm{T}}^{\tau_{\mathrm{had}}}$ [GeV] | [25-45]([25-50]) | [45-70] ([50-75]) | [70-100] | > 100 |
|---|---|---|---|---|
| 1-prong | 1.02 ± 0.05 | 0.90 ± 0.07 | 0.94 ± 0.13 | 0.72 ± 0.13 |
| 3-prong | 0.79 ± 0.05 | 0.72 ± 0.11 | 0.60 ± 0.12 | - |

TABLE 10.10: Fake-$\tau_{\mathrm{had}}$ scale factors for Loose RNN $\tau_{\mathrm{had}}$ ID estimated from the $Z$+jets-enriched region $\mathrm{CR}^{Z}$. The total uncertainty is statistical only.

The modelling of the fake-$\tau_{\mathrm{had}}$ background is greatly improved after the implementation of the kinematic reweighting and the $p_{\mathrm{T}}$-dependent fake-$\tau_{\mathrm{had}}$ SFs, as shown in Figure 10.11 for the $p_{\mathrm{T}}^{\tau_{\mathrm{had}}}$ and jet multiplicity distributions in the $1\ell$+$1\tau_{\mathrm{had}}$SS and $1\ell$+$\geq$$2\tau_{\mathrm{had}}$ channels before the final likelihood fit to data.




(a) (b)

FIGURE 10.11: Data-to-simulation comparison for (a) the $p_{\mathrm{T}}^{\tau}$ distribution in the $1\ell$+$1\tau_{\mathrm{had}}$SS CR, and (b) the jet multiplicity distribution in the $2\ell$OS+$1\tau_{\mathrm{had}}$ VR. The distributions are shown prior to the likelihood fit to data and after the $m_{\mathrm{eff}}$ reweighting and $p_{\mathrm{T}}$-dependent fake-$\tau_{\mathrm{had}}$ SF correction. The total background prediction is shown prior to the fake-$\tau_{\mathrm{had}}$ SF correction (dashed blue line). Figure taken from Ref. [226].

| | $1\ell+\geq1\tau_{\text{had}}$ | $2\ell\text{OS}+\geq1\tau_{\text{had}}$ | $2\ell\text{SS}/3\ell+\geq1\tau_{\text{had}}$ | $2\ell\text{SS}+0\tau_{\text{had}}$ | $3\ell+0\tau_{\text{had}}$ |
|---|---|---|---|---|---|
| Number of channels | 6 | 2 | 2 | 8 | 4 |
| $m_{\text{eff}}$ spectrum | 3 SRs | 2 SRs | 2 SRs | — | — |
| $H_{\text{T, lep}}$ spectrum | — | — | — | 6 CRs | 2 CRs |
| Event yield | 3 CRs | — | — | 2 CRs | 2 CRs |
| Total number of bins | 16 | 9 | 6 | 20 | 10 |

TABLE 10.11: Summary of the regions per channel, discriminating variable per region, and number of bins used in the statistical analysis. Table taken from Ref. [226].

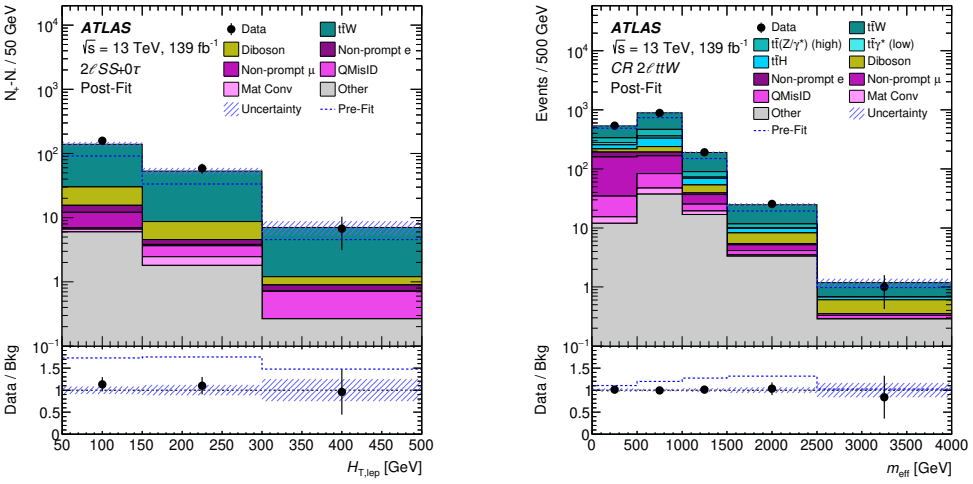
### 10.1.7 Analysis model and background validation

The CRs and SRs defined in Tables 10.2 – 10.6 are participating in a simultaneous maximum likelihood fit (except the CRs in $2\ell\text{OS}+\geq1\tau_{\text{had}}$ channel) to determine the background and $\text{LQ}_3^{\text{d}}$ signal yields that are most consistent with the data, as described in Section 9.4.4. There are 22 regions in total (15 CRs and 7 SRs) participating in this fit. The shape of the $m_{\text{eff}}$ variable is fitted in the SRs and CRs targeting irreducible backgrounds ($t\bar{t}W$, $VV$ and $t\bar{t}Z$ CRs), while the $H_{\text{T, lep}}$ variable or the number of events is fitted in the CRs. A summary of the variables fitted in each channel is shown in Table 10.11.

The background modelling is validated before this fit to real data in the CRs, VRs and SRs of this search. Real data are used for this check in all CR bins (due to low signal contamination), and the bins in the SRs that satisfy the 10% blinding criteria discussed in Section 8.4.3.

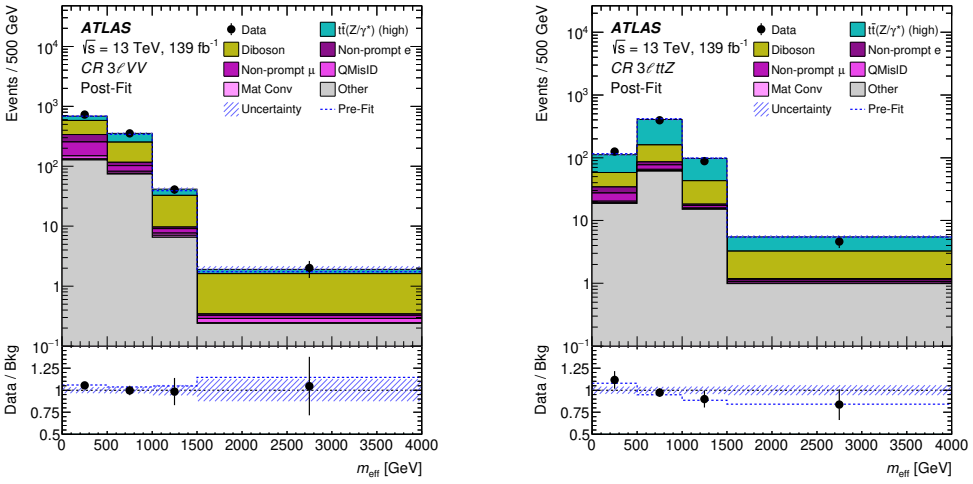
The modelling of the $m_{\text{eff}}$ variable (main discriminating variable fitted in the SRs) is also validated in some of the CRs ($2\ell$ttW, $3\ell$VV and $3\ell$ttZ), where the result of a likelihood fit to real data only in the CRs under the background-only hypothesis is extrapolated to these distributions that did not participate in the fit. These $m_{\text{eff}}$ distributions are shown in Figures 10.12 and 10.13, where the total background prediction is also shown before the fit (dashed blue line). Since the pre- and post-fit total background predictions differ in the $2\ell$ttW CR the modelling is also validated in an inclusive $2\ell\text{SS}+0\tau_{\text{had}}$ region in the $H_{\text{T, lep}}$ variable (fitted variable in CRs). This variable is shown in Figure 10.12a after subtracting negatively- from positively-charged events, where most of the charge-symmetric backgrounds are almost cancelled out, while the charge-asymmetric backgrounds remain. This is performed to demonstrate that the difference in the background predictions originates from $t\bar{t}W$ mismodelling, as shown in other analyses. The modelling is

greatly improved post-fit, where the free-floating normalisation factor (NF) for the $t\bar{t}W$ process is pulled upwards to cover the gap between data and simulation. A similar behaviour is observed in $2\ell\mathrm{tt(e)}+$ and $2\ell\mathrm{tt}(\mu)+$ CRs due to the $t\bar{t}W$ contamination in these regions.




(a) (b)

FIGURE 10.12: Data-to-simulation comparison in (a) the $H_{\mathrm{T,\,lep}}$ and (b) the $m_{\mathrm{eff}}$ distributions in the $2\ell\mathrm{SS}+0\tau_{\mathrm{had}}$ channel and $2\ell\mathrm{ttW}$ CR (without splitting it according to total charge), respectively. The distributions do not participate in the likelihood fit to data, but the "Post-Fit" result is extrapolated to them. $H_{\mathrm{T,\,lep}}$ distribution is shown after subtracting negatively- from positively-charged events. Figure taken from Ref. [226].




(a) (b)

FIGURE 10.13: Data-to-simulation comparison in the $m_{\mathrm{eff}}$ distribution in (a) $3\ell VV$ and (b) $3\ell t\bar{t}Z$ CRs. Figure taken from Ref. [226].

### 10.1.8 Distributions with partial signal-region selections

The distributions with high signal-to-background discrimination used in the SR definitions are shown in this section with all the SR selections applied, except for the selection on the variable displayed. These variables are shown in Figures 10.14 and 10.15. The total background prediction is shown after the likelihood fit to data, and prior to it (with an overlaid blue dashed line). The last bins in these distributions corresponding to the SR regime remained blinded at the initial stage of the analysis, and were only used to validate the background modelling.

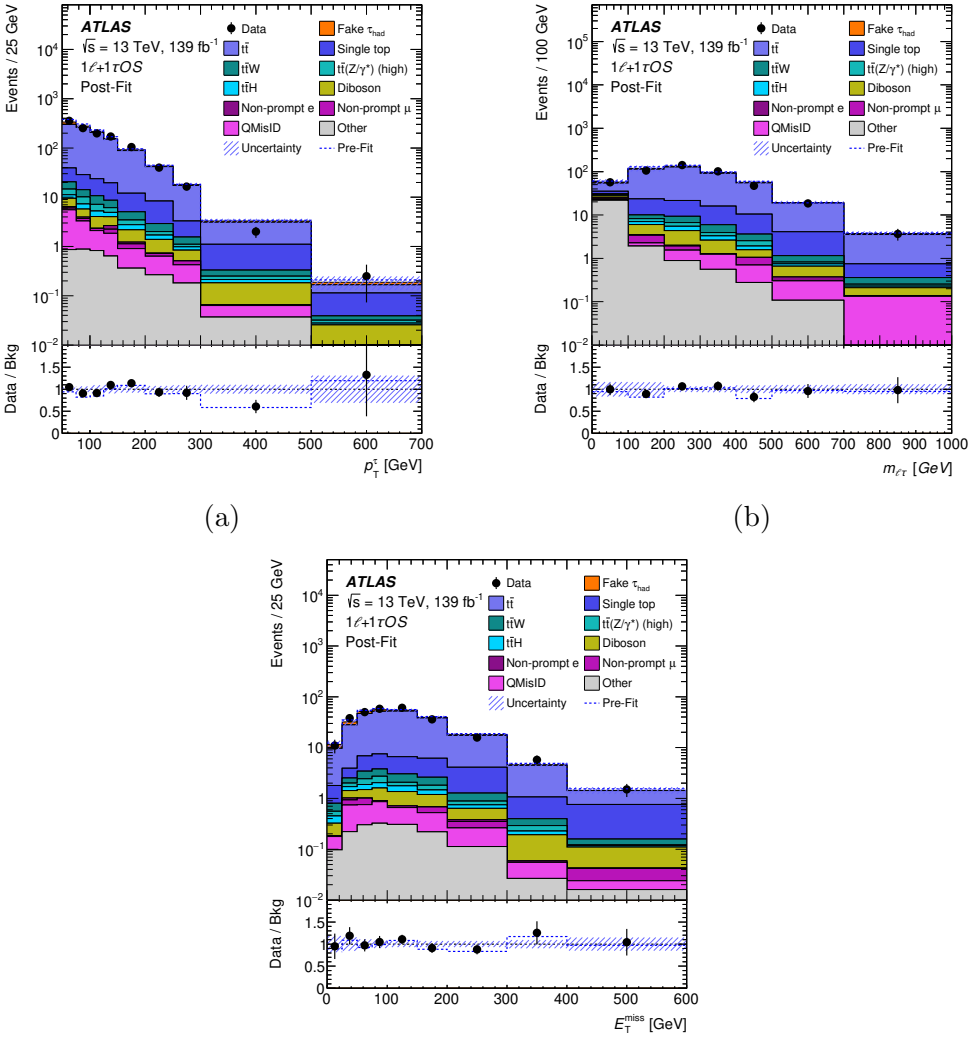



FIGURE 10.14: Data-to-simulation comparison in the distributions of (a) $p_{\mathrm{T}}^{\tau}$, (b) $m_{\ell\tau}$ and (c) $E_{\mathrm{T}}^{\mathrm{miss}}$ in $1\ell{+}1\tau_{\mathrm{had}}\mathrm{OS}$ channel, applying all the corresponding selections on these variables to define the SRs, except for the selection on the variable displayed. Figure taken from Ref. [226].

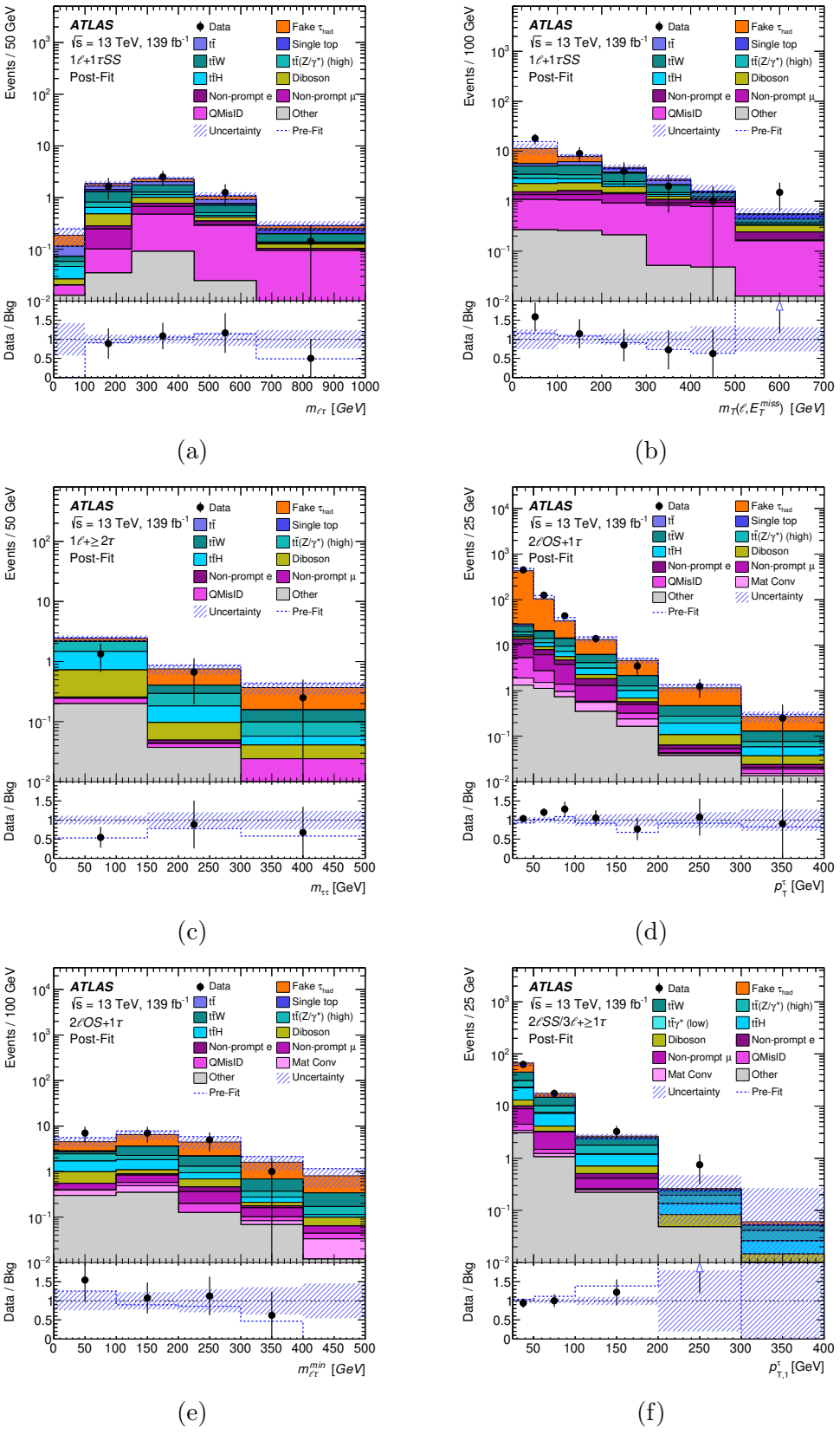



FIGURE 10.15: Data-to-simulation comparison in the distributions of (a) $m_{\ell\tau}$, (b) $m_{\mathrm{T}}(\ell, E_{\mathrm{T}}^{\mathrm{miss}})$, (c) $m_{\tau\tau}$, (d, f) $p_{\mathrm{T}}^{\tau}$, and (e) $m_{\ell\tau}^{\mathrm{min}}$ in $1\ell{+}1\tau_{\mathrm{had}}\mathrm{SS}$, $2\ell\mathrm{OS}{+}1\tau_{\mathrm{had}}$ and $2\ell\mathrm{SS}/3\ell{+}{\geq}1\tau_{\mathrm{had}}$ channels, prior to applying the corresponding selections on these variables to define the SRs. Figure taken from Ref. [226].

### 10.1.9 Systematic uncertainties

The systematic uncertainties of analyses including multiple leptons and $b$-jets in their final state are discussed in detail in Section 8.5. In this section the systematic uncertainties that are specific to this search are detailed. The leading sources of systematic uncertainty in this search originate from $\tau_{\text{had}}$ identification and energy scale calibration, followed by $t\bar{t}$ modelling. The systematic uncertainties concerning the $m_{\text{eff}}$ reweighting and fake-$\tau_{\text{had}}$ estimate are already discussed in Section 10.1.6.2. Apart from the aforementioned uncertainties, since reconstructed $\tau_{\text{had}}$ objects are used in this analysis, several systematic uncertainties are assigned to them related to their reconstruction and identification efficiencies. The background events containing true-$\tau_{\text{had}}$ candidates are additionally corrected with data to simulation SFs, and systematic uncertainties are also assigned to this calibration. The $\tau_{\text{had}}$-related uncertainties correspond to 21 additional NPs in total that are added to the likelihood function prior to the final fit to data and are summarised in Table 10.12.

| **Instrumental systematics on leptons** | | | |
|---|---|---|---|
| Type | Description | Systematics name | Application |
| | | **Hadronic Taus** | |
| Efficiencies | Reconstruction | TAU_SF_RECO_TOTAL | Event weight |
| | High-$p_{\text{T}}$ reco material transport | TRUETAU_RW_[STAT,SYST] | Event weight |
| | Identification RNN (1-prong or 3-prong) | TAU_SF_RNNID_1P[2530,GE40] | Event weight |
| | | TAU_SF_RNNID_3P[2530,GE40] | Event weight |
| | Identification RNN (high $p_{\text{T}}$) | TAU_SF_RNNID_HIGHPT | Event weight |
| | Electron Veto BDT | TAU_SF_ELEOLR_TOTAL | Event weight |
| | Electron Veto BDT (truth-matched $e$) | TAU_SF_TRUEELECTRON _ELEOLR_[STAT,SYST] | Event weight |
| Scale Factor | $p_{\text{T}}$ Scale | TAUS_TRUEHADTAU_SME_TES_MODEL | $p_{\text{T}}$ correction |
| | | TAUS_TRUEHADTAU_SME_TES_DETECTOR | $p_{\text{T}}$ correction |
| | | _[LowPT, HighPt1p, HighPt3p] | $p_{\text{T}}$ correction |
| | | TAUS_TRUEHADTAU_SME_TES_INSITU | $p_{\text{T}}$ correction |
| | | [FIT,EXP] | $p_{\text{T}}$ correction |
| | | TAUS_TRUEHADTAU_SME_TES_AFII | $p_{\text{T}}$ correction |

TABLE 10.12: Overview of additional experimental systematics concerning $\tau_{\text{had}}$ candidates.

Furthermore, in this search the extensive systematics model explained in Section 8.5 is not applied due to the lack of splitting in fake-lepton templates according to their PLV WP. The $\alpha_S$+PDF uncertainties are assigned to the $t\bar{t}$ events with real light leptons and $\tau_{\text{had}}$s, while there are also generator comparisons with

simulated $t\bar{t}$ samples from aMC@NLO + Pythia-8 and Powheg-Box + Herwig-7. Samples with variations in QCD radiation are also used for the derivation of the corresponding systematic uncertainties.

Since the modelling of the conversion CRs, $2\ell/3\ell$IntC and $2\ell/3\ell$MatC, depends on the $t\bar{t}$ contribution, associated extrapolation systematics are used based on a $Z \to \mu\mu e$ VR defined in Ref. [208]. Due to low statistics in this region, a flat prior of 25% is used as extrapolation uncertainty from the conversion CRs to all other regions of the fit.

Additionally, cross-section uncertainties are added in the fit to account for the part of the background contributions containing real-$\tau_{\text{had}}$ and prompt light-lepton candidates and it is not affected by the NFs left free-floating in the fit to correct the "fake"-background contributions. These background contributions together with their corresponding cross-section uncertainties are: $t\bar{t}$ (6%), $s$- and $t$-channel single-top (4%), $tW$ (5%) and $V$+jets (5%). Cross-section uncertainties are also assigned to $VV$ (6%) and $t\bar{t}Z$ (12%), since in this analysis their normalisation is not free-floating in the fit.

### 10.1.10 Results

#### 10.1.10.1 Template Fit to data

A maximum likelihood fit is performed in the templates defined in 22 analysis regions, as discussed in Section 10.1.7. Five normalisation factors $\hat{\lambda}^{t\bar{t}W}$, $\hat{\lambda}_e^{\text{HF}}$, $\hat{\lambda}_\mu^{\text{HF}}$, $\hat{\lambda}_e^{\text{MatC+QMisID}}$ and $\hat{\lambda}_e^{\text{IntC}}$ are left free-floating together with the signal strength $\mu$, as described in Section 9.4.4, with the difference that there are no free-floating NFs for $VV$ and $t\bar{t}Z$ backgrounds and these are replaced by the corresponding cross-section uncertainties. This is motivated by the fact that the NFs from the fit were very close to unity and consistent with the SM expectation. Moreover, since in this analysis the estimation of QMisID events is taken directly from simulation a common NF is used to additionally determine the normalisation of this background together with the normalisation of events from material conversions since the corresponding $2\ell/3\ell$MatC CRs are also enriched in QMisID events. The fitted values of the above NFs are shown in Figure 10.16, after a likelihood fit to data in all SRs and CRs considered. The likelihood fit is performed under the

background-only and signal-plus-background hypotheses for all available $LQ_3^d$ signal mass points (from which only the 900, 1100 and 1300 GeV mass points are shown for reference). The background normalisations are consistent with the SM expectation value.

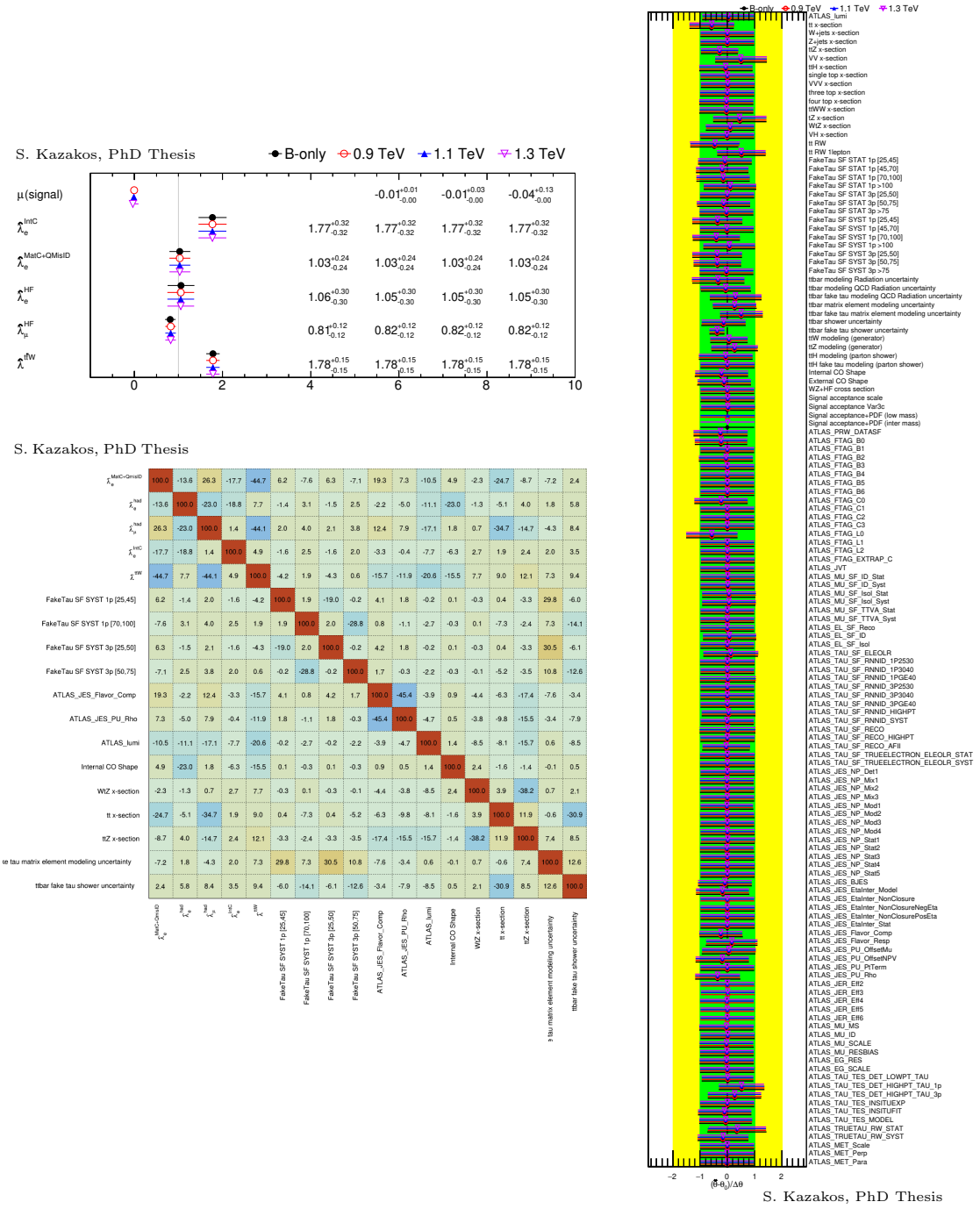
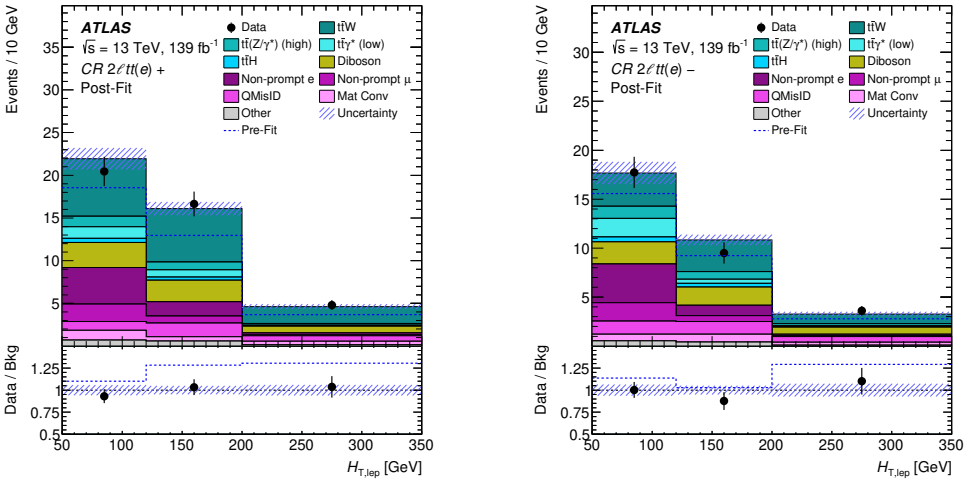



FIGURE 10.16: Fit results of a likelihood fit to data. The normalisation factors (upper left), correlation matrix (lower left) and pulls and constraints of the nuisance parameters (right) are shown. The correlation matrix corresponds to a fit under the background-only hypothesis, while the results of signal-plus-background fits with 900, 1100 and 1300 GeV $LQ_3^d$ signals are overlaid in the rest of the plots.

The pull in $\hat{\lambda}^{t\bar{t}W}$ is related to the known mismodelling of the $t\bar{t}W$ background, as reported by other analyses [208, 209]. Part of the reason of this pull can be explained by the $t\bar{t}W$ electroweak contribution, which was found out later that it was not included in the simulated sample list for this analysis. The pull in $\hat{\lambda}_e^{\mathrm{IntC}}$ is explained because of the large data-to-simulation discrepancy in $2\ell$IntC CR, which is attributed to low statistics. Since $t\bar{t}\gamma^*$(low) is not a significant background contribution in the SRs, the corresponding pull does not affect the results of the analysis significantly. The LQ signal strength is fitted to values close to zero for all the signal mass points used in the search, indicating that the fit does not favour the existence of LQs with these mass values. The systematic uncertainties are participating in the fit as nuisance parameters and the ones surviving the pruning selection are also shown in Figure 10.16 together with their pulls and constraints. The correlation matrix shown in the same figure corresponds to a fit under the background-only hypothesis.

In the results presented below the post-fit result shown corresponds to a likelihood fit under the background-only hypothesis, following the standard choice for BSM searches with fitted $\mu$ values close to zero. The distributions are shown after the fit, and the total background prediction prior to the fit is overlaid (dashed blue line). The CRs where the shape of a distribution ($H_{\mathrm{T,\,lep}}$) is fitted are shown after the likelihood fit in Figures 10.17 and 10.18.




(a) (b)

FIGURE 10.17: Data-to-simulation comparison in the $H_{\mathrm{T,\,lep}}$ distribution in the (a) $2\ell$tt(e)+ and (b) $2\ell$tt(e)- CRs of the $2\ell$SS+$0\tau_{\mathrm{had}}$ channel after the likelihood fit to data. Figure taken from Ref. [226].

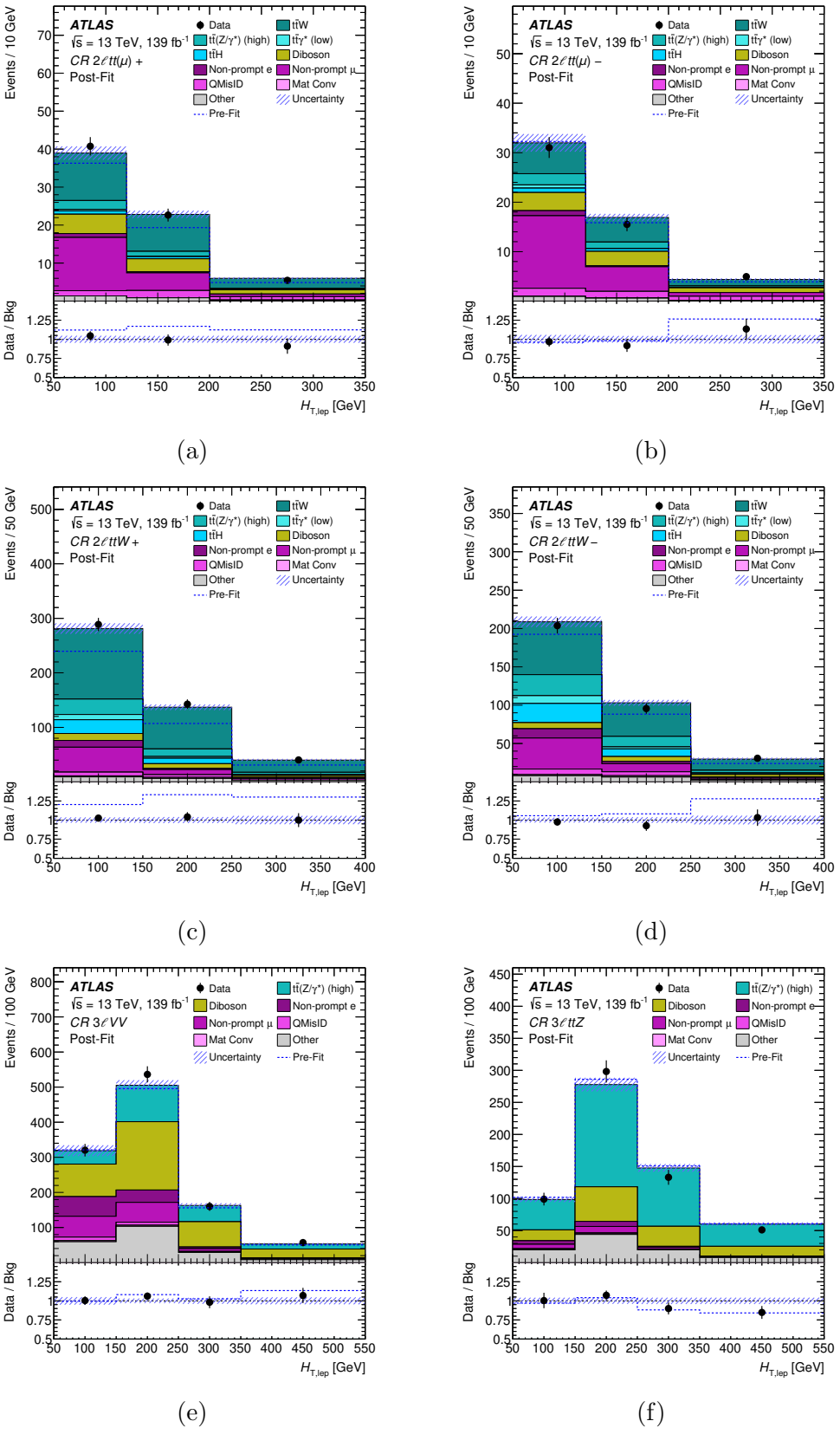



FIGURE 10.18: Data-to-simulation comparison in the $H_{\mathrm{T,\,lep}}$ distribution in the (a) $2\ell$tt(e)+, (b) $2\ell$tt(e)-, (c) $2\ell$ttW+, (d) $2\ell$ttW-, (e) $3\ell$VV and (f) $3\ell$ttZ CRs of the $2\ell$SS+$0\tau_{\mathrm{had}}$ and $3\ell$+$0\tau_{\mathrm{had}}$ channels after the likelihood fit to data. Figure taken from Ref. [226].

The $m_{\text{eff}}$ distribution in the SRs after the likelihood fit to data are shown in Figures 10.19 and 10.20, for $1\ell$ and $2\ell$ channels, respectively. The expected signal prediction for $\text{LQ}_3^{\text{d}}$s of $m_{\text{LQ}_3^{\text{d}}} = 1.1$ TeV is overlaid for illustrative purposes for $\mathcal{B} = 1$ and $\mu = 1$ as an unfilled red histogram added to the post-fit background. The binning of the $m_{\text{eff}}$ distribution in each SR is chosen as a result of optimisation studies trying to balance the adequate discrimination in the signal and background shapes, while maintaining a per-bin statistical uncertainty below 30%.

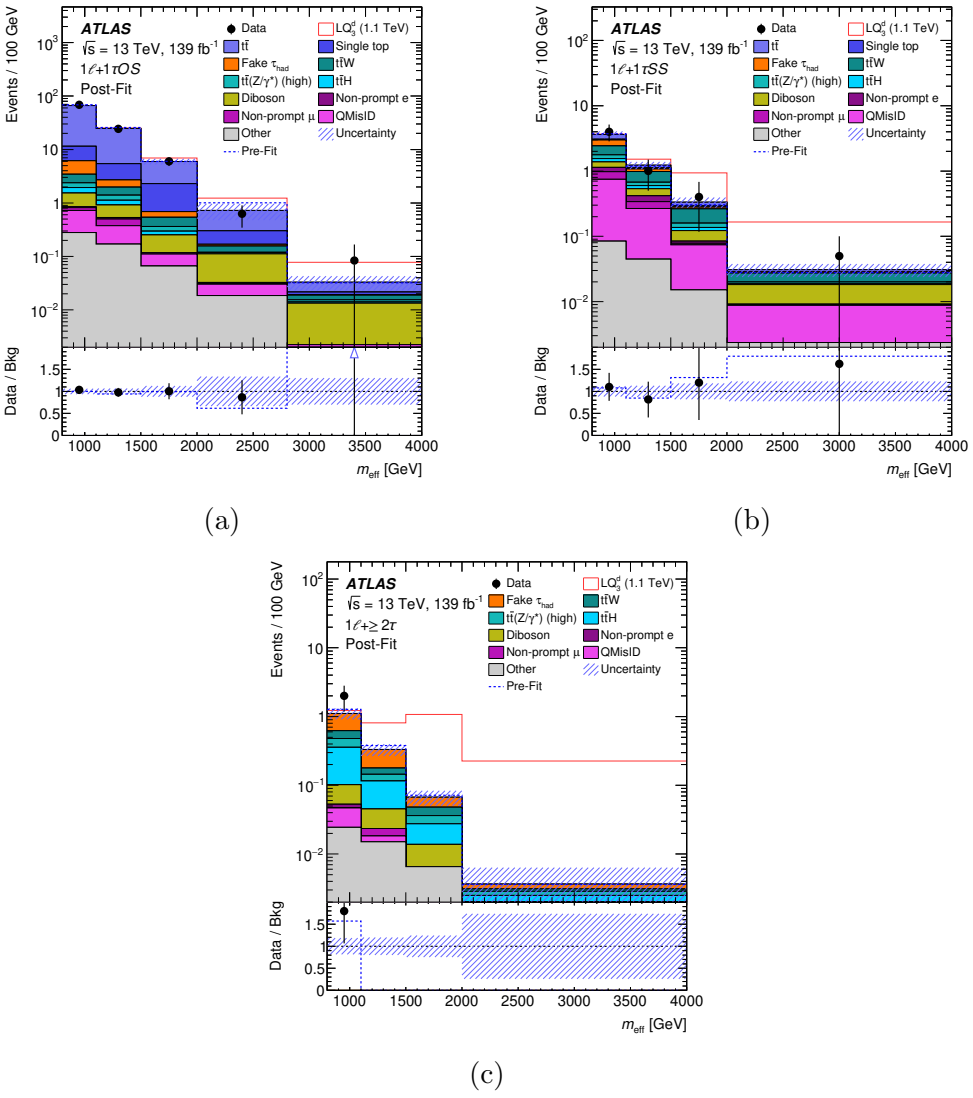



FIGURE 10.19: Data-to-simulation comparison of the $m_{\text{eff}}$ distribution in the (a) $1\ell{+}1\tau_{\text{had}}$OS, (b) $1\ell{+}1\tau_{\text{had}}$SS, and (c) $1\ell{+}{\geq}2\tau_{\text{had}}$ SRs of the $1\ell{+}{\geq}1\tau_{\text{had}}$ channel after the likelihood fit to data. The expected signal for $m_{\text{LQ}_3^{\text{d}}} = 1.1$ TeV, $\mathcal{B} = 1$ and $\mu = 1$ is shown as a unfilled red histogram added to the post-fit background for illustrative purposes. Figure taken from Ref. [226].

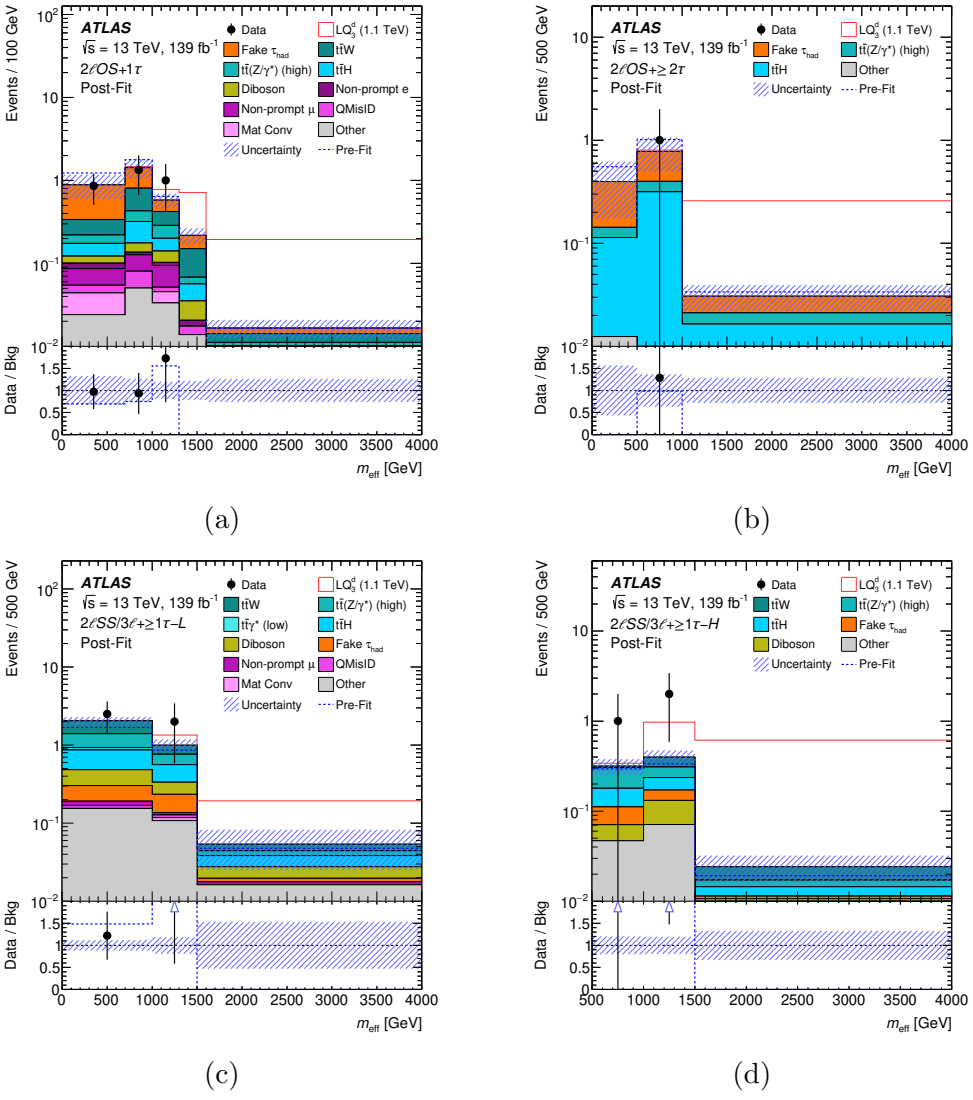
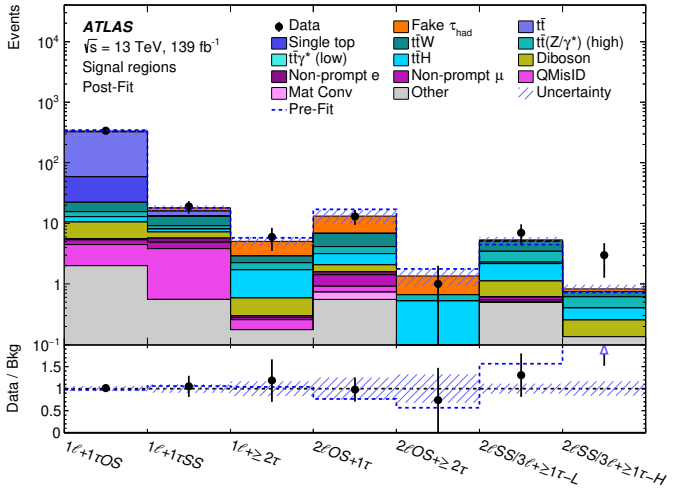
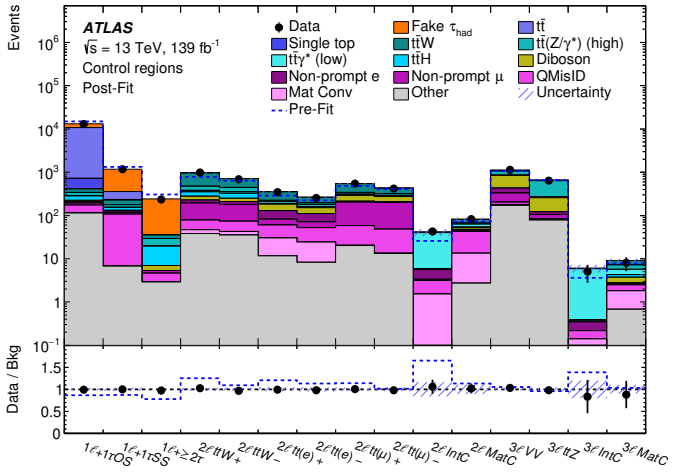


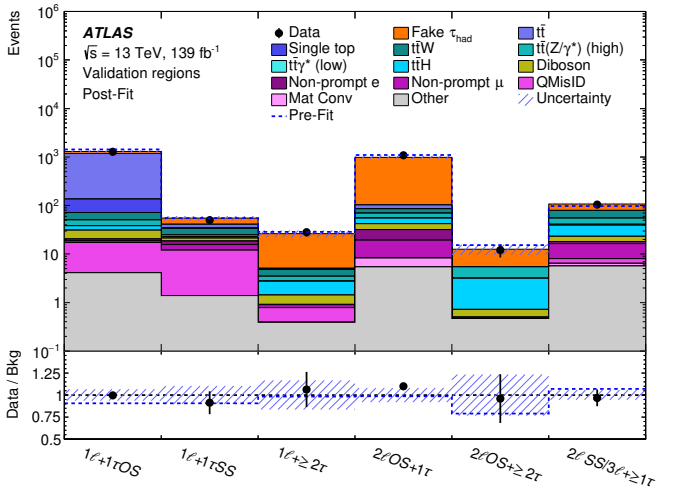

FIGURE 10.20: Data-to-simulation comparison in the $m_{\text{eff}}$ distribution in the (a) $2\ell\text{OS}{+}1\tau_{\text{had}}$, (b) $2\ell\text{OS}{+}{\geq}2\tau_{\text{had}}$, (c) $2\ell\text{SS}/3\ell{+}{\geq}1\tau_{\text{had}}$-L, and (d) $2\ell\text{SS}/3\ell{+}{\geq}1\tau_{\text{had}}$-H SRs of the $2\ell\text{OS}{+}{\geq}1\tau_{\text{had}}$ and $2\ell\text{SS}/3\ell{+}{\geq}1\tau_{\text{had}}$ channels after a likelihood fit to data. The expected signal for $m_{\text{LQ}_3^{\text{d}}} = 1.1$ TeV, $\mathcal{B} = 1$ and $\mu = 1$ is shown as an unfilled red histogram added to the post-fit background for illustrative purposes. Figure taken from Ref. [226].




(a)




(b)




(c)

FIGURE 10.21: Data-to-simulation post-fit comparison in the (a) 7 SRs and (b) 15 CRs participating in the likelihood fit. The post-fit result is propagated to the (c) 6 VRs, demonstrating the good background modelling. Figure taken from Ref. [226].

All the analysis regions in this search are shown after the fit in summary one-bin plots in Figure 10.21. A summary of the event yields in SRs is shown in Table 10.13.

| | $1\ell$+$1\tau_{\text{had}}$OS | $1\ell$+$1\tau_{\text{had}}$SS | $1\ell$+$\geq$$2\tau_{\text{had}}$ |
|---|---|---|---|
| Data | 339 | 19 | 6 |
| Total background | $340 \pm 20$ | $17.1 \pm 2.1$ | $5.2 \pm 1.2$ |
| Fake $\tau_{\text{had}}$ | $10.2 \pm 6.5$ | $1.8 \pm 1.7$ | $1.9 \pm 1.0$ |
| $t\bar{t}$ | $270 \pm 21$ | $2.4 \pm 1.0$ | — |
| Single top | $37.4 \pm 5.4$ | $0.79 \pm 0.56$ | — |
| $t\bar{t}W$ | $6.7 \pm 1.0$ | $3.93 \pm 0.59$ | $0.66 \pm 0.13$ |
| $t\bar{t}Z/\gamma^*$ (high mass) | $2.38 \pm 0.65$ | $1.11 \pm 0.30$ | $0.57 \pm 0.15$ |
| $t\bar{t}\gamma^*$ (low mass) | — | $0.03 \pm 0.01$ | — |
| $t\bar{t}H$ | $2.38 \pm 0.44$ | $0.87 \pm 0.21$ | $1.18 \pm 0.34$ |
| Diboson | $5.02 \pm 0.66$ | $1.70 \pm 0.27$ | $0.31 \pm 0.07$ |
| QMisID | $2.59 \pm 0.68$ | $3.38 \pm 0.90$ | $0.10 \pm 0.08$ |
| Other | $3.50 \pm 0.91$ | $1.14 \pm 0.38$ | $0.45 \pm 0.13$ |
| $\text{LQ}_3^{\text{d}}$ (0.9 TeV) | $80.3 \pm 9.2$ | $25.1 \pm 2.6$ | $51.9 \pm 9.3$ |
| $\text{LQ}_3^{\text{d}}$ (1.1 TeV) | $20.9 \pm 2.5$ | $6.92 \pm 0.74$ | $11.4 \pm 2.1$ |
| $\text{LQ}_3^{\text{d}}$ (1.3 TeV) | $6.02 \pm 0.75$ | $1.93 \pm 0.25$ | $2.89 \pm 0.57$ |

| | $2\ell$OS+$1\tau_{\text{had}}$ | $2\ell$OS+$\geq$$2\tau_{\text{had}}$ | $2\ell$SS/$3\ell$+$\geq$$1\tau_{\text{had}}$-L | $2\ell$SS/$3\ell$+$\geq$$1\tau_{\text{had}}$-H |
|---|---|---|---|---|
| Data | 13 | 1 | 7 | 3 |
| Total background | $14.6 \pm 3.3$ | $1.66 \pm 0.58$ | $5.38 \pm 0.68$ | $0.83 \pm 0.14$ |
| Fake $\tau_{\text{had}}$ | $8.0 \pm 3.4$ | $0.96 \pm 0.54$ | $0.33 \pm 0.07$ | $0.09 \pm 0.04$ |
| $t\bar{t}W$ | $2.68 \pm 0.51$ | — | $1.57 \pm 0.39$ | $0.13 \pm 0.05$ |
| $t\bar{t}Z/\gamma^*$ (high mass) | $0.86 \pm 0.26$ | $0.15 \pm 0.06$ | $1.10 \pm 0.20$ | $0.20 \pm 0.06$ |
| $t\bar{t}\gamma^*$ (low mass) | $0.02 \pm 0.01$ | — | $0.03 \pm 0.02$ | — |
| $t\bar{t}H$ | $1.07 \pm 0.19$ | $0.51 \pm 0.14$ | $1.09 \pm 0.27$ | $0.14 \pm 0.03$ |
| Diboson | $0.51 \pm 0.08$ | — | $0.53 \pm 0.10$ | $0.13 \pm 0.03$ |
| Non-prompt $e$ | $0.14 \pm 0.13$ | — | — | — |
| Non-prompt $\mu$ | $0.44 \pm 0.28$ | — | $0.06 \pm 0.06$ | — |
| QMisID | $0.19 \pm 0.13$ | — | $0.04 \pm 0.05$ | — |
| Mat Conv | $0.18 \pm 0.15$ | — | $0.01 \pm 0.02$ | — |
| Other | $0.55 \pm 0.22$ | $0.04 \pm 0.03$ | $0.61 \pm 0.28$ | $0.13 \pm 0.06$ |
| $\text{LQ}_3^{\text{d}}$ (0.9 TeV) | $26.0 \pm 3.9$ | $6.1 \pm 1.1$ | $6.02 \pm 0.90$ | $13.6 \pm 2.1$ |
| $\text{LQ}_3^{\text{d}}$ (1.1 TeV) | $6.4 \pm 1.0$ | $1.35 \pm 0.26$ | $1.09 \pm 0.17$ | $3.44 \pm 0.57$ |
| $\text{LQ}_3^{\text{d}}$ (1.3 TeV) | $1.69 \pm 0.31$ | $0.36 \pm 0.08$ | $0.20 \pm 0.05$ | $1.07 \pm 0.19$ |

TABLE 10.13: Overview of the predicted and observed yields in each signal region after a likelihood fit to data under the background-only hypothesis. The expected signal yields are also shown pre-fit for each region for $\mathcal{B} = 1$. Dashes are used to denote the contributions that are either negligible or not applicable. Table taken from Ref. [226].

#### 10.1.10.2 Expected and observed upper limits

No significant excess is observed over the SM expectation value after the likelihood fit to data in any of the SRs. This can be inferred already from Figures 10.16, 10.19 and 10.20, since the fitted signal strength $\mu$ for all $\mathrm{LQ}_3^{\mathrm{d}}$ signal mass points is close to zero and there are no or not enough data in the right tail of the $m_{\mathrm{eff}}$ distribution, where the LQ signal lives. The expected and observed $p_0$-values are shown as a function of $m_{\mathrm{LQ}_{\mathrm{mix}}^{\mathrm{d}}}$ in Figure 10.22 for both $\mathcal{B} = 0.5$ and $\mathcal{B} = 1$. The observed $p_0$-value is found to be consistent with the background-only hypothesis across the whole range of mass points and branching ratios considered. The expected $p_0$-value illustrates the significant expected sensitivity of the search, exceeding 5 standard deviations for $m_{\mathrm{LQ}_3^{\mathrm{d}}} < 1.21$ TeV and 3 standard deviations for $m_{\mathrm{LQ}_{\mathrm{mix}}^{\mathrm{d}}} < 1.36$ TeV in the $\mathcal{B} = 1$ case. This search is particularly optimised for $\mathcal{B} = 1$ signal samples, with remarkable sensitivity to $\mathrm{LQ}_3^{\mathrm{d}}$ signal samples of $\mathcal{B} = 0.5$.

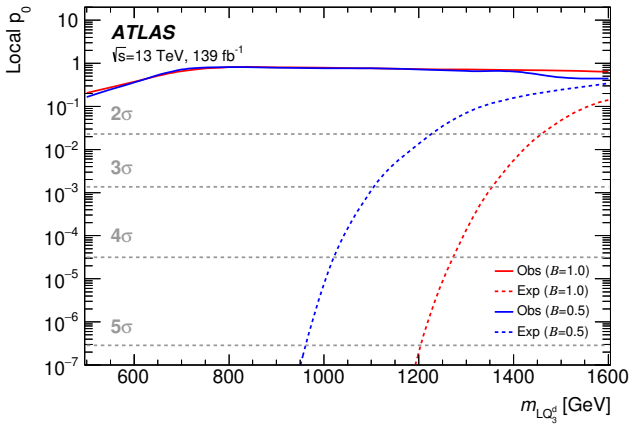
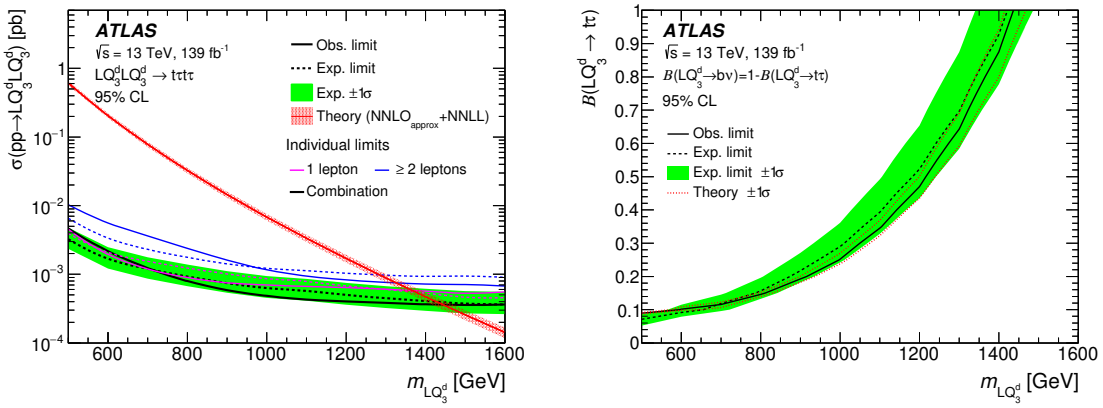



FIGURE 10.22: Observed local $p_0$ as a function of $\mathrm{LQ}_3^{\mathrm{d}}$ mass ($m_{\mathrm{LQ}_3^{\mathrm{d}}}$) for $\mathcal{B} = 1$ (solid red line) and $\mathcal{B} = 0.5$ (solid blue line). The expected local $p_0$ under the hypothesis of a $\mathrm{LQ}_3^{\mathrm{d}}$ signal at that mass is shown in dashed lines for the same $\mathcal{B}$ cases. Figure taken from Ref. [226].

Following the standard procedure in such cases of no discovery, expected and observed 95% CL upper limits are set on the $\mathrm{LQ}_3^{\mathrm{d}}$ production cross section as a function of $\mathrm{LQ}_3^{\mathrm{d}}$ mass, as shown in Figure 10.23a. These limits are shown for the combined case of including all SRs in the calculation and for the individual cases of considering only the $1\ell$ or $2\ell$ SRs. The theoretical prediction together with its $\pm 1\sigma$ uncertainty are also shown. The points where the line of the theoretical prediction crosses the expected and observed cross-section lines defines the corresponding limits of this search. The upper limit in cross section corresponds to the lower

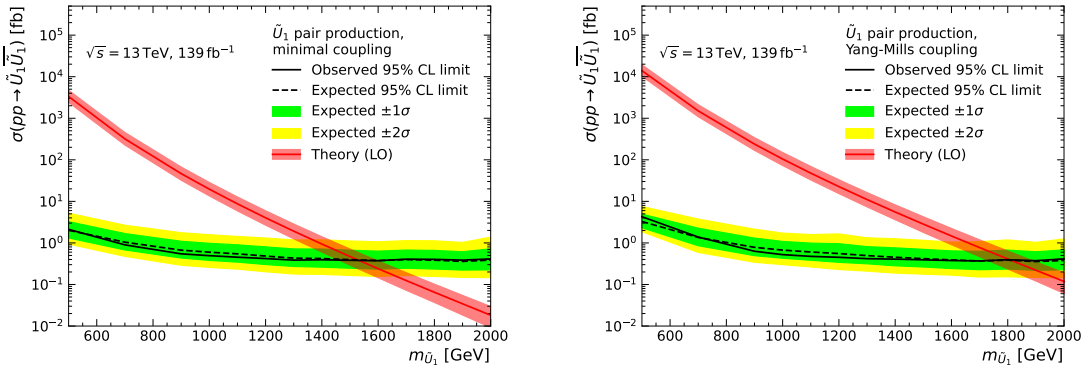
limit in $\mathrm{LQ}_3^\mathrm{d}$ mass that can be excluded. The expected and observed 95% CL lower limits on $m_{\mathrm{LQ}_3^\mathrm{d}}$ are found to be 1.41 and 1.43 TeV, respectively, for the $\mathcal{B} = 1$ case. For the $\mathcal{B} = 0.5$ case, the corresponding limits are 1.19 and 1.22 TeV, respectively. These limits were the most stringent ones in ATLAS and CMS for this final state at the time of the thesis writing, with this search being the first dedicated one in ATLAS in this channel that exploits the full Run-2 dataset and the sophisticated $\tau_\mathrm{had}$ reconstruction identification. The $1\ell{+}{\geq}1\tau_\mathrm{had}$ channel is leading the sensitivity of this search, with the $2\ell\mathrm{OS}{+}{\geq}1\tau_\mathrm{had}$ and $2\ell\mathrm{SS}/3\ell{+}{\geq}1\tau_\mathrm{had}$ channels to contribute to a significant improvement of the combined limit. The result of the limit changes by 4.5% (2.3%) between $m_{\mathrm{LQ}_3^\mathrm{d}} = 500$ GeV ($m_{\mathrm{LQ}_3^\mathrm{d}} = 1$ TeV) and $m_{\mathrm{LQ}_3^\mathrm{d}} = 1.6$ TeV after the inclusion of all systematic uncertainties (compared to the inclusion of the statistical uncertainty only), leading to the conclusion that this analysis is limited by the statistical uncertainty on data. In Figure 10.23b the expected and observed limits are shown in a 2D plane as a function of $\mathcal{B}$ and $\mathrm{LQ}_3^\mathrm{d}$ mass. The expected 95% confidence band is shown for $\pm1\sigma$ in both figures. The $\pm2\sigma$ band is not shown, since it was found to be different after a comparison of calculating it with the toy MC method instead of using the asymptotic approximation, as shown in Appendix C.




(a) (b)

FIGURE 10.23: (a) Expected and observed 95% CL upper limits on the $\mathrm{LQ}_3^\mathrm{d}$ pair production cross section as a function of $m_{\mathrm{LQ}_3^\mathrm{d}}$ and (b) 2D 95% CL exclusion contours on $\mathcal{B}$ as a function of $m_{\mathrm{LQ}_3^\mathrm{d}}$, in all analysis channels combined (assuming $\mathcal{B} = 1$). The green shaded band corresponds to the $\pm1$ standard deviation ($\pm1\sigma$) uncertainty around the combined expected limit. The theoretical prediction along with its $\pm1\sigma$ uncertainty are shown with a red line and band, respectively. The expected and observed limits are also shown independently for $1\ell$ and $2\ell$ channels. Figure taken from Ref. [226].

Since signal MC samples simulating the $\tilde{U}_1$ vector LQ model (introduced in Section 3.2.2) were not available by the time this search became public, the corresponding limits are calculated in the context of a reinterpretation approach as part of the LQ combination effort discussed in Section 10.3. The expected and observed 95% CL upper limits on the $\tilde{U}_1$ pair production cross section are set as a function of $m_{\tilde{U}_1}$ both for the minimal coupling (min) and Yang-Mills coupling (YM) scenarios, as shown in Figure 10.24. Both the expected and observed 95% CL lower limits on $m_{\tilde{U}_1^{\min}}$ are found to be around 1.53 TeV, and on $m_{\tilde{U}_1^{\mathrm{YM}}}$ around 1.81 TeV.




(a) (b)

FIGURE 10.24: Observed and expected 95% CL upper limits on the $\tilde{U}_1$ pair production cross section as a function of $m_{\tilde{U}_1}$ (assuming $\mathcal{B} = 1$) in all analysis channels combined for the (a) minimal coupling and (b) Yang-Mills coupling scenario. The green and yellow shaded bands correspond to the ±1 and ±2 standard deviation (±1$\sigma$, ±2$\sigma$) uncertainty around the combined expected limit. The theoretical prediction along with its ±1$\sigma$ uncertainty are shown with a red line and band, respectively.

## 10.2 Search for leptoquark pair production in $t\ell t\ell$ final states ($\ell = e, \mu$)

### 10.2.1 Introduction

The search discussed in this section targets $\mathrm{LQ}^{\mathrm{d}}_{\mathrm{mix}}$ pair production in the $t\ell t\ell$ final state, where $\ell$ corresponds to either electron or muon candidates ($tete$ and $t\mu t\mu$ final states). The subscript "mix" in the notation is used to denote exactly that these final states combine third generation quarks with leptons of the first two generations. Most of the LQ searches focus on channels where the quark and lepton are of the same generation, but the possibility of non-zero flavour-off-diagonal couplings in motivated as a potential explanation of the $B$-meson and $(g-2)_\mu$ anomalies (which require LQs with couplings to second or third generation quarks and leptons of any generation). In this decay mode, light-lepton candidates are produced directly from the LQ decay, as well as through the semileptonic decay of a top quark. These light leptons are used to trigger on the events of interest by passing the requirements of single-lepton or dilepton triggers. The top-quark pair is required to decay into final states containing one or two leptons, making this analysis orthogonal to that in Ref. [201], where both top quarks are required to decay hadronically into collimated decay products (boosted regime). The $t\ell t\ell$ final state contains two energetic $b$-jets originating from the top-quark decays and additional light-flavoured jets originating from ISR or FSR processes and from hadronic $W$-boson decays (originating from the top quarks). An illustrative Feynman diagram of this final state is shown in Figure 10.25, for the cases where one or both top quarks decay semileptonically.

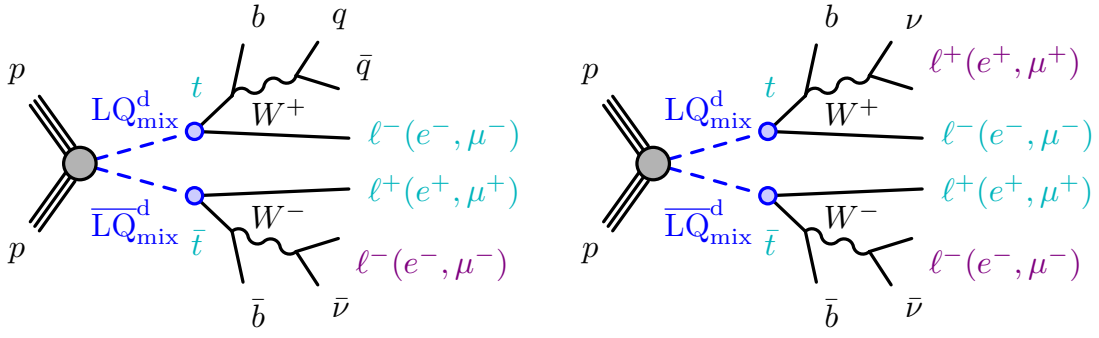
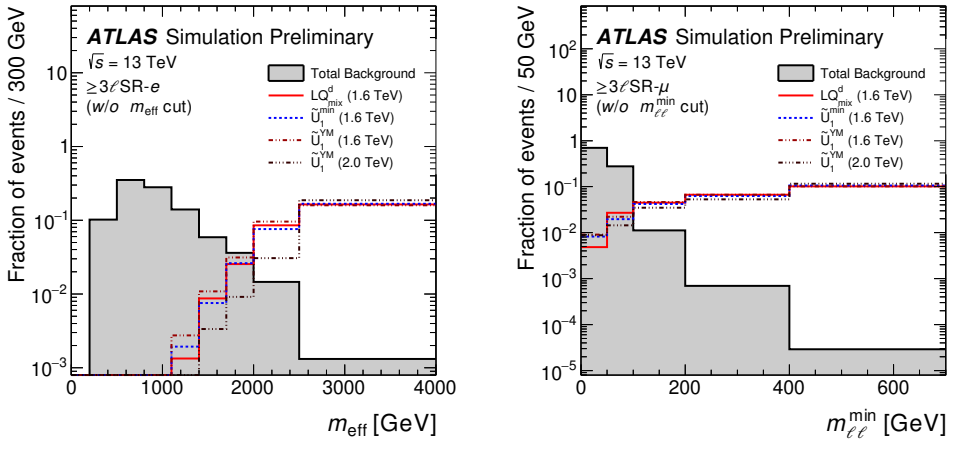



FIGURE 10.25: Illustrative Feynman diagram of $\mathrm{LQ}^{\mathrm{d}}_{\mathrm{mix}}$ pair production and decay modes in $3\ell$ (left) and $4\ell$ (right) channels. The same diagrams can be used to describe the corresponding modes of vector LQs ($\tilde{U}_1$). Figure taken from Ref. [230].

The selected events are categorised in channels, where the analysis regions are defined. There are regions defined in order to validate the background modelling of the dominant background contributions, while others are used in a maximum-likelihood template fit to real data to constrain these backgrounds simultaneously with the signal search. The signal search is performed in the high-$p_{\mathrm{T}}$ regime by applying selections on variables with strong discriminating power between signal and SM background. The signal samples used in the interpretation of the results correspond to the scalar $\mathrm{LQ}^{\mathrm{d}}_{\mathrm{mix}}$ case, while an additional interpretation is performed for the first time using an iso-singlet vector LQ ($\tilde{U}_1$) with electric charge $Q = +5/3$ [66] for two coupling assumptions to other gauge bosons (minimal coupling and Yang-Mills coupling options).

### 10.2.2 Event categorisation and discriminating variables

The events are selected if they contain at least two light leptons (electrons and muons), at least two jets and at least one $b$-jet and they are eventually categorised in channels. Three channels are defined based on light-lepton multiplicity in the event, $2\ell$ with same electric charge ($2\ell$SS), $3\ell$, and $4\ell$, where the corresponding analysis regions are defined. The $2\ell$SS channel is used for the CR definition, while $3\ell$ and $4\ell$ channels are used for the VR and SR definition by requiring at least three or four light leptons and exploiting the presence of energetic final-state objects.




(a) (b)

FIGURE 10.26: Comparison of (a) $m_{\mathrm{eff}}$ and (b) $m_{\ell\ell}^{\mathrm{min}}$ distributions in the $3\ell$ channel, between the $\mathrm{LQ}^{\mathrm{d}}_{\mathrm{mix}}$ signal for different mass values and the SM background (shaded histogram). Figure taken from Ref. [230].

The search is performed by following a cut-based approach fitting the shape of a discriminating variable in SRs. As in the LQLQ→ $t\tau t\tau$ analysis the effective mass, $m_{\text{eff}}$, is also used here (already defined in Equation 8.2). The discriminating power of this variable to distinguish the $\text{LQ}^{\text{d}}_{\text{mix}}$ signal from the SM background is demonstrated in Figure 10.26a for the $3\ell$ channel, where the two shapes are compared. Another variable with large discriminating power is the minimum dilepton mass between all possible dilepton pair combinations that can be formed within an event ($m_{\ell\ell}^{\text{min}}$). This variable is used for the region categorisation, and the signal and background shapes for this variable are shown in Figure 10.26b.

The RC jets already discussed in Section 7.4.1 were also studied in the context of this search in an attempt to define alternative discriminating variables other than $m_{\ell\ell}^{\text{min}}$, but it turned out that the signal-to-background separation power of $m_{\ell\ell}^{\text{min}}$ was larger, and therefore it was preferred.

### 10.2.3 Analysis region definitions

There are 7 CRs, 2 VRs, and 4 SRs defined in this search designed for signal search, background estimation, and background validation. The $2\ell$SS channel is used entirely for the definition of CRs. In this channel, events are required to have two light-lepton candidates of same charge with $p_{\text{T}} > 20$ GeV, at least two jets and at least one $b$-jet (at 85% DL1r OP). A CR is defined enriched in $t\bar{t}W$ background events by requiring [T] lepton definition (see Table 9.1) as the two leptons of this background contribution are most likely to be prompt. The purity in $t\bar{t}W$ events in this region is estimated to ∼50%, while the signal contamination is negligible. Two additional CRs enriched in events with non-prompt electrons and muons are defined, targeting the corresponding backgrounds. At least one of the leptons in these CRs is required to satisfy the [M] lepton definition, while the other should satisfy either the [M] or [T] definition, a requirement that makes these regions orthogonal to the $t\bar{t}W$ CR and the rest of the analysis regions. In the $2\ell$tt(e) CR, the subleading lepton is always required to be an electron, while in the $2\ell$tt($\mu$) CR it is required to be a muon. An additional selection of $m_T(\ell_0, E_{\text{T}}^{\text{miss}}) < 250$ GeV is applied in the non-prompt CR definitions aiming to reduce the $t\bar{t}W$ contamination in these CRs, where $m_T(\ell_0, E_{\text{T}}^{\text{miss}})$ is the transverse mass of the leading lepton and the missing transverse energy defined in Section 9.3. The selections applied for the definition of the $2\ell$SS CRs are shown in Table 10.14.

| | 2ℓSS (CR-only) | | |
|---|---|---|---|
| | 2ℓtt(e) | 2ℓtt($\mu$) | 2ℓttW |
| $e/\mu$ definition | [TM] + [MT] + [MM] | | [TT] |
| $e/\mu$ split by flavour | $ee/\mu e$ | $\mu\mu/e\mu$ | — |
| $\ell\ell$ charge | ++ or −− | | |
| $e$ internal conversion veto | Yes | | |
| $e$ material conversion veto | Yes | | |
| $N_{\text{jets}}$ | $\geq 2$ | | |
| $N_{b-\text{jets}}$ (85% DL1r) | 1 | | $\geq 2$ |
| $p_{\text{T}}^{\ell}$ [GeV] | $> 20$ | | |
| $m_{\text{T}}(\ell_0, E_{\text{T}}^{\text{miss}})$ [GeV] | $< 250$ | | — |

TABLE 10.14: Overview of analysis region definition in the 2ℓSS channel. Table taken from Ref. [230].

The 3$\ell$ channel is used to define eight analysis regions: four CRs, one VR and two SRs. In this channel events with three lepton candidates are selected and are required to have a total charge that is summed to $\pm 1$. The leptons in this channel are categorised based on their charge and $\Delta R$ variable. The leading lepton ($\ell_0$) is the one with opposite charge (OS) to the same-charge (SS) pair and it is required to have $p_{\text{T}} > 10$ GeV. The other two leptons of the SS pair ($\ell_1$, $\ell_2$) are sorted based on their $\Delta R$ to the OS lepton with $\ell_1$ being the closest and $\ell_2$ being the farthest, and are required to have $p_{\text{T}} > 20$ GeV. The leading lepton is required to satisfy the [L] definition criteria, while the rest leptons to satisfy the [M] definition criteria. The events containing opposite-charge (OS) lepton pairs of the same flavour (SF) are required to have a dilepton invariant mass of $m_{\ell^+\ell^-}^{\text{OSSF}} > 12$ GeV. There are regions enriched in diboson and $t\bar{t}Z$ background events by requiring at least one $Z$-boson candidate with an inverse $Z$-veto on dilepton mass. These regions are called 3ℓVV and $t\bar{t}Z$ CRs targeting the corresponding background contributions. The distinction between them is done by $b$-jet multiplicity, requiring one $b$-jet in the 3ℓVV and at least two $b$-jets in the $t\bar{t}Z$ CR. The purity of the targeted backgrounds is more than ∼60% in the associated regions. There are two additional CRs enriched in events containing leptons from photon conversions from $Z \to \mu\mu\gamma^*(\to ee)$ decays, which are labelled as 3ℓIntC and 3ℓMatC for internal and material conversions, respectively.

The SRs are defined based on light-lepton multiplicity and flavour. The $3\ell$SR-$e$ (SR-$\mu$) is required to contain at least two electron (muon) candidates, and a combined selection of $m_{\ell\ell}^{\text{min}} \geq 200$ GeV and $m_{\text{eff}} \geq 500$ GeV is applied. The events that are left by inverting the $m_{\ell\ell}^{\text{min}}$ selection (and removing the $m_{\text{eff}}$ requirement) are used to define a VR merged for the electron and muon channels. An overview of the selections used for the definition of the CRs, VR and SRs in $3\ell$ channel is shown in Table 10.15.

| | $3\ell$ | | | | | | |
|---|---|---|---|---|---|---|---|
| | CR | | | | VR | SR | |
| | $3\ell$VV | $3\ell$ttZ | $3\ell$IntC | $3\ell$MatC | $3\ell$VR | $3\ell$SR-$e$ | $3\ell$SR-$\mu$ |
| $e/\mu$ definition | [M] (SS pair), [L] (OS to SS pair) | | | | | | |
| $e/\mu$ split by flavour | — | | | | | $3e$ / $2e1\mu$ | $3\mu$ / $2\mu1e$ |
| Total charge | $\pm1$ | | — | | | $\pm1$ | |
| $e$ internal conversion veto | Yes | | Inverted ($\ell_1$ or $\ell_2$) | Yes ($\ell_1$ and $\ell_2$) | | Yes | |
| $e$ material conversion veto | Yes | | Yes ($\ell_1$ and $\ell_2$) | Inverted ($\ell_1$ or $\ell_2$) | | Yes | |
| $N_{\text{jets}}$ | $\geq 2$ | | $\geq 0$ | | | $\geq 2$ | |
| $N_{b-\text{jets}}$ (85% DL1r) | 1 | $\geq 2$ | 0 | | | $\geq 1$ | |
| $p_{\text{T}}^{\ell}$ [GeV] | $> 20$ (SS pair), $> 10$ (OS to SS pair) | | | | | $> 20$ | |
| $m_{\ell^+\ell^-}^{\text{OSSF}}$ [GeV] | $> 12$ | | | | | | |
| $\lvert m_{\ell^+\ell^-}^{\text{OSSF}} - m_Z \rvert$ [GeV] | $< 10$ | | $> 10$ | | | $> 10$ | |
| $\lvert m_{\ell\ell\ell} - m_Z \rvert$ [GeV] | — | | $< 10$ | | | — | |
| $m_{\ell\ell}^{\text{min}}$ [GeV] | — | | | | $< 200$ | $\geq 200$ | |
| $m_{\text{eff}}$ [GeV] | — | | | | — | $\geq 500$ | |

TABLE 10.15: Overview of analysis region definition in the $3\ell$ channel. Table taken from Ref. [230].

In the $4\ell$ channel the events contain four lepton candidates, which are required to satisfy the [L] lepton definition and have $p_{\text{T}} > 10$ GeV. The events are also required to have at least two jets and at least one $b$-jet (at 85% DL1r OP). A $Z$-veto is applied to all possible opposite-charge (OS) combinations in order to suppress $t\bar{t}Z$ and $VV$ background events. In this channel there is one VR and two SRs defined in a similar way as in the $3\ell$ channel. Events with at least three electron (muon) candidates are required in the $4\ell$SR-$e$ ($4\ell$SR-$\mu$), while in the case that there is equal number of electron and muon candidates the event is categorised based on the flavour of its leading lepton in $p_{\text{T}}$. Additional selections of $m_{\ell\ell}^{\text{min}} \geq 100$ GeV and $m_{\text{eff}} \geq 500$ GeV are applied. A VR labelled as $4\ell$VR is defined without

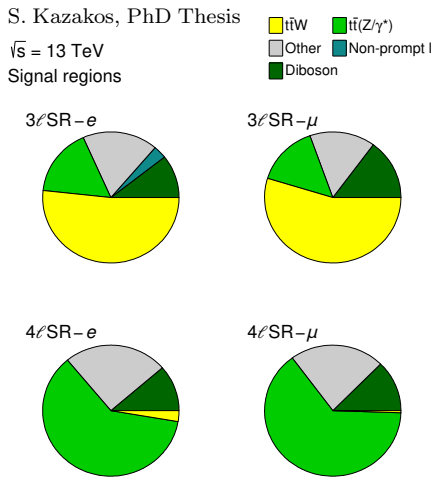
any splitting by lepton flavour by inverting the $m_{\ell\ell}^{\text{min}}$ selection and removing the selection on $m_{\text{eff}}$ to look at its whole spectrum. An overview of the selections used in the VR and SR definitions in this channel is shown in Table 10.16.

| | $4\ell$ | | |
|---|---|---|---|
| | VR | SR | |
| | $4\ell$VR | $4\ell$SR-$e$ | $4\ell$SR-$\mu$ |
| $e/\mu$ definition | [L] | | |
| $e/\mu$ split by flavour | — | $4e$ / $3e1\mu$ / $2e2\mu$ (lead $e$) | $4\mu$ / $3\mu1e$ / $2\mu2e$ (lead $\mu$) |
| Total charge | 0 | | |
| $N_{\text{jets}}$ | $\geq 2$ | | |
| $N_{b-\text{jets}}$ (85% DL1r) | $\geq 1$ | | |
| $p_{\text{T}}^{\ell}$ [GeV] | $> 10$ | | |
| $m_{\ell^+\ell^-}^{\text{OSSF}}$ [GeV] | $> 12$ | | |
| $\lvert m_{\ell^+\ell^-}^{\text{OSSF}} - m_Z \rvert$ [GeV] | $> 10$ | | |
| $m_{\ell\ell}^{\text{min}}$ [GeV] | $< 100$ | $\geq 100$ | |
| $m_{\text{eff}}$ [GeV] | — | $\geq 500$ | |

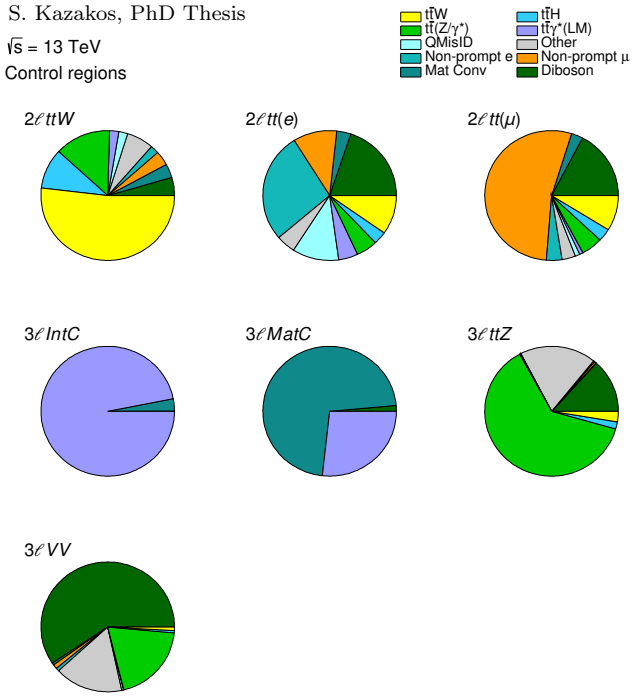
TABLE 10.16: Overview of analysis region definition in the $4\ell$ channel. Table taken from Ref. [230].

### 10.2.4 Main background contributions

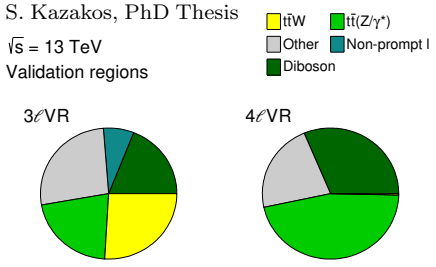
In the SRs and VR defined in $3\ell$ channel the dominant background is the $t\bar{t}W$ contribution followed by $t\bar{t}Z$ and $VV$ contributions. In the SRs and VR defined in $4\ell$ channel $t\bar{t}Z$ becomes the leading background followed by $VV$ and other background contributions. The proper estimation of subleading background contributions such as $t\bar{t}H$ and events containing "fake" leptons is required in order to get a reliable normalisation factor for the $t\bar{t}W$ background using the template fit method. Due to the low statistics in both channels some of the rare background contributions such as $t\bar{t}t\bar{t}$, $t\bar{t}WW$ and $tWZ$ become non-negligible in both $3\ell$ and $4\ell$ SRs. In the $2\ell$SS and $3\ell$ CRs the main background contributions vary depending on the targeted background contribution in each region. An overview of the background composition in the SRs, CRs and VRs of the analysis is shown in Figures 10.27a, 10.27b and 10.27c after a likelihood fit under the background-only hypothesis.




(a)




(b)




(c)

FIGURE 10.27: Background composition in the (a) signal, (b) control and (c) validation regions of the analysis after a likelihood fit to data under the background-only hypothesis.

### 10.2.5 Signal and background modelling

#### 10.2.5.1 Signal modelling

The samples simulating the scalar $LQ^{d}_{mix}$ signal process are generated by MadGraph5_aMC@NLO generator at NLO accuracy using the NNPDF 3.0 NLO PDF set and the LQ model from [74], and interfaced with Pythia-8 for the PS and hadronisation processes (A14 tune). The decays of the $LQ^{d}_{mix}$ signal were modelled using MadSpin. The coupling parameter $\lambda$ (defined in Section 3.2) is set to $\lambda = 0.3$, for which the width of the $LQ^{d}_{3}$ resonance is equal to about 0.2% of its mass. Leptoquarks of the $LQ^{d}_{mix}$ type ($Q = -1/3$) decay into either a $t\ell$ or a $b\nu$ pair, respecting the charge conservation. In the simulated $LQ^{d}_{mix}$ samples their decay mode is controlled by the branching fraction parameter $\beta$. Simulated samples are generated for $LQ^{d}_{mix}$ mass points within the range of 1.0 TeV to 1.9 TeV with 100 GeV step for $\beta = 1$, corresponding to LQ pair production, where each LQ is allowed to decay only into a $t\ell$ pair.

The samples simulating the vector $\tilde{U}_1$ signal samples are generated by MadGraph5_aMC@NLO generator at LO accuracy using the NNPDF 2.3 LO PDF set and the Boston model [73, 231], while they are interfaced with Pythia-8 for the PS and hadronisation processes (A14 tune). Vector LQs of $\tilde{U}_1$ type ($Q = +5/3$) decay into a $t\ell$ pair and their coupling parameter $\lambda$ is also set to $\lambda = 0.3$. Simulated samples are generated for $\tilde{U}_1$ pair production for both scenarios within the range of 1.0 TeV to 2.0 TeV with 100 GeV step.

#### Signal theory uncertainties

The predictions for scalar $LQ^{d}_{mix}$ signal are normalised to the NNLOapprox+NNLL cross sections computed for scalar pair production. The NLO values of the cross section obtained from the MC generators and the corresponding $K$-factors (NNLOapprox+NNLL to NLO predictions ratios) are summarised for each mass point in Table 3.3. The predictions for vector $\tilde{U}_1$ signal are normalised to the LO cross sections computed using MadGraph5_aMC@NLO + Pythia8, which are shown in Table 3.4.

| $LQ^{d}_{mix}$ mass [TeV] | 0.9 | | 1.1 | | 1.3 | | 1.5 | | 1.7 | | 1.9 | |
|---|---|---|---|---|---|---|---|---|---|---|---|---|
| Signal region | $\mu_F, \mu_R$ (Up \| Down) [%] | | | | | | | | | | | |
| SR3$\ell$-$e$ | +1.5 | -0.8 | +1.8 | -1.1 | +0.9 | -0.8 | +0.5 | -0.8 | +0.9 | -0.9 | +0.8 | -0.2 |
| SR4$\ell$-$e$ | +1.4 | -0.3 | +4.1 | -1.5 | +0.2 | -0.3 | +0.2 | -0.1 | +15.4 | -0.6 | +0.4 | -15.5 |
| | Var3c (Up \| Down) [%] | | | | | | | | | | | |
| SR3$\ell$-$e$ | -1.9 | -0.6 | -0.6 | 1.7 | 0.3 | 2.1 | -1.5 | 1.1 | 0.4 | 1.1 | 0.3 | 2.7 |
| SR4$\ell$-$e$ | -1.9 | 1.4 | -2.2 | -1.5 | 1.3 | -10.5 | 10.2 | 0.3 | 2.1 | -1.6 | 8.4 | 3.5 |
| | $\alpha_s$+PDF (Up / Down) [%] | | | | | | | | | | | |
| SR3$\ell$-$e$ | ± 0.7 | | ± 0.7 | | ± 0.7 | | ± 1.1 | | ± 1.8 | | ± 2.1 | |
| SR4$\ell$-$e$ | ± 0.6 | | ± 1.3 | | ± 2.0 | | ± 3.6 | | ± 6.8 | | ± 5.3 | |

TABLE 10.17: Theory uncertainties in percentages on the scalar $LQ^{d}_{mix}$ signal acceptances in the electron channel due to QCD scale ($\mu_R$, $\mu_F$) variations, shower parameter variations, the $\alpha_s$ and the PDFs.

| $LQ^{d}_{mix}$ mass [TeV] | 0.9 | | 1.1 | | 1.3 | | 1.5 | | 1.7 | | 1.9 | |
|---|---|---|---|---|---|---|---|---|---|---|---|---|
| Signal region | $\mu_F, \mu_R$ (Up \| Down) [%] | | | | | | | | | | | |
| SR3$\ell$-$\mu$ | +0.9 | -0.5 | +0.9 | -0.5 | +1.2 | -1.2 | +1.6 | -1.1 | +1.8 | -2.2 | +1.7 | -8.0 |
| SR4$\ell$-$\mu$ | +1.3 | -0.4 | +1.7 | -1.3 | +6.2 | -2.4 | +4.3 | -6.2 | +11.0 | -7.1 | +7.1 | -13.3 |
| | Var3c (Up \| Down) [%] | | | | | | | | | | | |
| SR3$\ell$-$\mu$ | -1.5 | -1.2 | 0.3 | 1.9 | -0.1 | 0.9 | -2.1 | 0.8 | 0.7 | 1.4 | 0.7 | 2.2 |
| SR4$\ell$-$\mu$ | 0.9 | 0.8 | 1.9 | -3.2 | 3.0 | -4.1 | 7.2 | 0.9 | -1.8 | -3.6 | 1.9 | 4.3 |
| | $\alpha_s$+PDF (Up / Down) [%] | | | | | | | | | | | |
| SR3$\ell$-$\mu$ | ± 0.4 | | ± 0.7 | | ± 0.7 | | ± 1.1 | | ± 1.4 | | ± 1.6 | |
| SR4$\ell$-$\mu$ | ± 0.4 | | ± 0.9 | | ± 2.2 | | ± 3.5 | | ± 5.7 | | ± 4.8 | |

TABLE 10.18: Theory uncertainties in percentages on the scalar $LQ^{d}_{mix}$ signal acceptances in the muon channel due to QCD scale ($\mu_R$, $\mu_F$) variations, shower parameter variations, the $\alpha_s$ and the PDFs.

The impact of QCD renormalisation ($\mu_R$) and factorisation ($\mu_F$) scale variations, shower parameter (var3c) variations, $\alpha_S$ and PDFs is evaluated on the signal acceptance for various SRs. The uncertainties are evaluated by comparing the $m_{\text{eff}}$ truth distributions in these SRs for each variation and for various LQ mass points (low: 0.9, 1.1, intermediate: 1.3, 1.5, and high: 1.7, 1.9 TeV). The event selections for the truth events are chosen as close as possible to the reconstruction-level selections. An envelope of independent pairs of $\mu_R$ and $\mu_R$ varied by factors of 0.5 or 2 are used for the estimation of the uncertainties due to QCD scale variations. These uncertainties vary from 1% to 6% for low and intermediate signal mass points according to the SR, and 5-15% for high mass points. The acceptance variations from 100 NNPDF30_NLO PDF sets are used in the computation of the PDF uncertainties. These uncertainties are added in quadrature to the acceptance uncertainty due to $\alpha_S$ variations. The total $\alpha_s$+PDF uncertainties are estimated to 1% for low $LQ^{d}_{mix}$ masses, 2-4% for the intermediate mass range, and 2-6% for the higher masses. The shower uncertainties vary from 1% to 10% depending on the SR. All these uncertainties are summarised in Tables 10.17 and 10.18 for *tete*

and $t\mu t\mu$ $\mathrm{LQ}^{\mathrm{d}}_{\mathrm{mix}}$ signals, respectively.

In the case of vector $\tilde{U}_1$ signals, the signal acceptance uncertainties due to QCD scale variations are estimated to 1% to 4% for low and intermediate signal mass points according to the SR, and they increase up to 8% for high mass points. The total $\alpha_S$+PDF uncertainties are estimated to 1-4% for low $\tilde{U}_1$ mass points, 1-6% for the intermediate masses, and up to 30% for the higher masses. The shower uncertainties vary from 1% to 20% depending on the SR. All these uncertainties are summarised in Tables 10.19 and 10.20 for the minimal coupling and Yang-Mills coupling scenarios, respectively, and they are found to be similar for the two cases. Since these uncertainties are also very close between the *tete* and $t\mu t\mu$ $\tilde{U}_1$ signals, only the numbers in the former are shown.

| $\tilde{U}_1^{\mathrm{min}}$ mass [TeV] | 0.9 | | 1.1 | | 1.3 | | 1.5 | | 1.7 | | 1.9 | |
|---|---|---|---|---|---|---|---|---|---|---|---|---|
| Signal region | $\mu_F, \mu_R$ (Up \| Down) [%] | | | | | | | | | | | |
| SR3$\ell$-$e$ | +0.6 | -0.9 | +0.8 | -0.7 | +0.7 | -1.4 | +1.4 | -1.7 | +0.7 | -0.9 | +0.6 | -1.2 |
| SR4$\ell$-$e$ | +2.3 | -2.9 | +2.3 | -2.3 | +2.0 | -2.4 | +1.9 | -3.6 | +4.6 | -6.6 | +6.9 | -7.6 |
| | Var3c (Up \| Down) [%] | | | | | | | | | | | |
| SR3$\ell$-$e$ | -1.6 | -1.2 | -1.5 | 0.3 | 1.1 | -1.4 | 0.6 | -0.7 | 0.5 | 0.9 | 2.9 | 1.5 |
| SR4$\ell$-$e$ | 2.0 | -11.0 | 7.7 | -7.6 | 4.0 | 3.4 | -0.6 | 13.0 | 4.3 | 5.5 | -4.9 | 6.8 |
| | $\alpha_s$+PDF (Up / Down) [%] | | | | | | | | | | | |
| SR3$\ell$-$e$ | ± 0.8 | | ± 0.6 | | ± 1.8 | | ± 2.4 | | ± 1.1 | | ± 5.0 | |
| SR4$\ell$-$e$ | ± 2.7 | | ± 4.8 | | ± 2.8 | | ± 5.4 | | ± 11.7 | | ± 29.0 | |

TABLE 10.19: Theory uncertainties in percentages on the vector $\tilde{U}_1^{\mathrm{min}}$ signal acceptances in the electron channel due to QCD scale ($\mu_R$, $\mu_F$) variations, shower parameter variations, the $\alpha_s$ and the PDFs.

| $\tilde{U}_1^{\mathrm{YM}}$ mass [TeV] | 0.9 | | 1.1 | | 1.3 | | 1.5 | | 1.7 | | 1.9 | |
|---|---|---|---|---|---|---|---|---|---|---|---|---|
| Signal region | $\mu_F, \mu_R$ (Up \| Down) [%] | | | | | | | | | | | |
| SR3$\ell$-$e$ | +1.0 | -1.2 | +1.0 | -1.4 | +1.0 | -1.3 | +0.7 | -0.6 | +1.0 | -2.0 | +1.3 | -2.2 |
| SR4$\ell$-$e$ | +0.6 | -0.4 | +0.7 | -1.0 | +2.8 | -4.1 | +2.2 | -4.1 | +1.0 | -0.5 | +1.6 | -1.8 |
| | Var3c (Up \| Down) [%] | | | | | | | | | | | |
| SR3$\ell$-$e$ | 1.0 | -3.3 | 1.2 | -0.1 | -0.1 | -0.4 | -0.3 | 1.4 | 1.7 | 0.4 | 1.1 | 0.2 |
| SR4$\ell$-$e$ | -13.5 | 8.2 | -2.7 | -13.4 | 19.9 | 12.2 | -0.6 | -1.1 | -9.4 | -5.2 | 3.3 | -1.7 |
| | $\alpha_s$+PDF (Up / Down) [%] | | | | | | | | | | | |
| SR3$\ell$-$e$ | ± 1.1 | | ± 1.5 | | ± 1.4 | | ± 0.5 | | ± 3.9 | | ± 7.9 | |
| SR4$\ell$-$e$ | ± 1.3 | | ± 0.7 | | ± 4.0 | | ± 6.1 | | ± 1.4 | | ± 7.0 | |

TABLE 10.20: Theory uncertainties in percentages on the vector $\tilde{U}_1^{\mathrm{YM}}$ signal acceptances in the electron channel due to QCD scale ($\mu_R$, $\mu_F$) variations, shower parameter variations, the $\alpha_s$ and the PDFs.

### 10.2.5.2 Background modelling

The techniques for background estimation and suppression used in these search are already described in detail in Section 9.4. No deviation from the material already covered is required for this analysis, thus no further description of the same methods is provided.

## 10.2.6 Analysis model and background validation

The CRs and SRs defined in Tables 10.14 – 10.16 are participating in simultaneous maximum likelihood fits to determine the background and LQ signal yields that are most consistent with the data, as described in Section 9.4.4. There are 11 regions in total (7 CRs and 4 SRs) participating in the fits. There are two similar fits performed including the same CRs, and in each one only the corresponding electron ($3\ell$SR-$e$, $4\ell$SR-$e$) or muon ($3\ell$SR-$\mu$, $4\ell$SR-$\mu$) SRs are included depending on which LQ signal is fitted ($tete$ signal in the electron SRs and $t\mu t\mu$ signal in the muon SRs). The shape of the $m_{\text{eff}}$ variable is fitted in the SRs and CRs targeting irreducible backgrounds ($2\ell$ttW, $3\ell$VV and $3\ell$ttZ CRs), while the number of events is fitted in the non-prompt lepton and conversion CRs ($2\ell$tt(e), $2\ell$tt($\mu$), $3\ell$IntC and $3\ell$MatC). A summary of the variables fitted in each channel is shown in Figure 10.28.

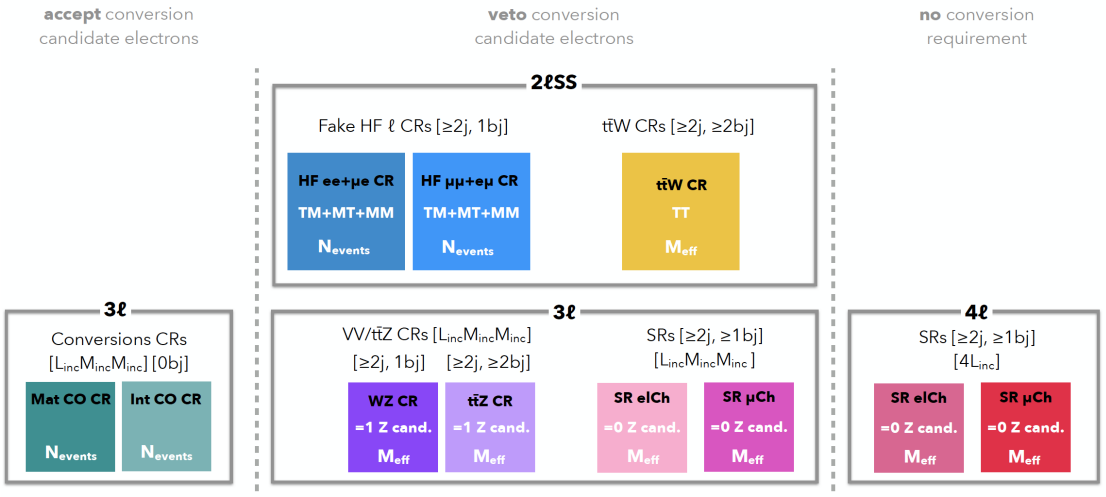
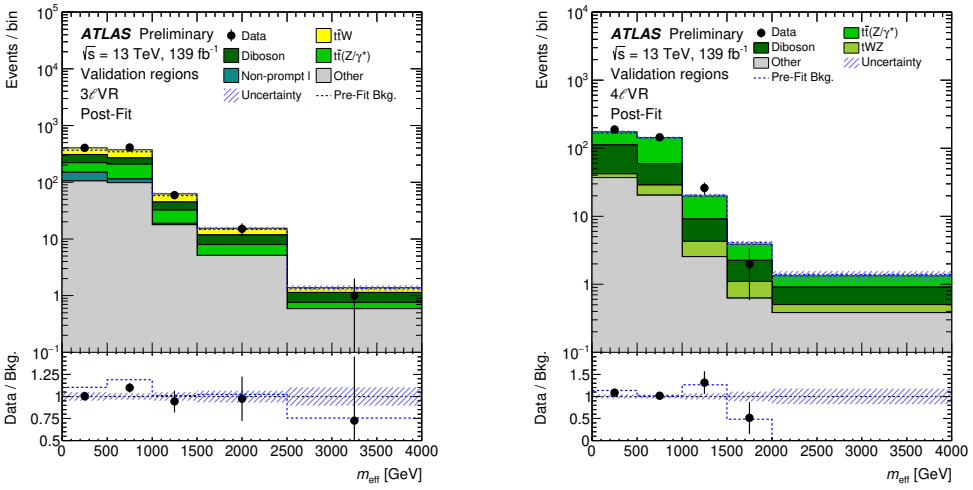



FIGURE 10.28: Illustrative sketch of the regions per channel and discriminating variable per region that are used in the likelihood fit to data. The number of jets and $b$-jets selections as well as the lepton definitions are also shown.

The background modelling is validated before this fit to real data in the CRs, VRs and SRs of this search. Real data are used for this check in all CR bins (due to low signal contamination), and the bins in the rest of the regions that satisfy the 5% blinding criteria discussed in Section 8.4.3.

The modelling of the $m_{\text{eff}}$ variable (main discriminating variable fitted in the SRs) is also validated in the VRs of this search in the $3\ell$ and $4\ell$ channels, respectively, which do not participate in the likelihood fit. The shapes of the $m_{\text{eff}}$ distribution are shown in Figure 10.29, where the post-fit result of a likelihood fit to CRs and SRs under the background-only hypothesis is propagated to these regions. There is good modelling across all bins in these distributions up to the point where there is no limitation by statistics. Since there was still some negligible signal events in these regions the last bin of the distributions remained blinded until the last stages of the analysis.




(a) (b)

FIGURE 10.29: Data-to-simulation comparison in the $m_{\text{eff}}$ distribution in (a) $3\ell$VR and (b) $4\ell$VR. Figure taken from Ref. [230].

### 10.2.7 Systematic uncertainties

The systematic uncertainties already described in Section 8.5 are also applied to this analysis since the same version of simulated MC samples is used in both analyses. The treatment of the systematic uncertainties is similar in this search, apart from the very sophisticated systematics model used for the $t\bar{t}W$ and $t\bar{t}Z$

background processes. In addition to these systematic uncertainties the ones concerning the signal modelling are also added, while the same applies to the ones concerning the hybrid High-$p_{\mathrm{T}}$ muon ID OP.

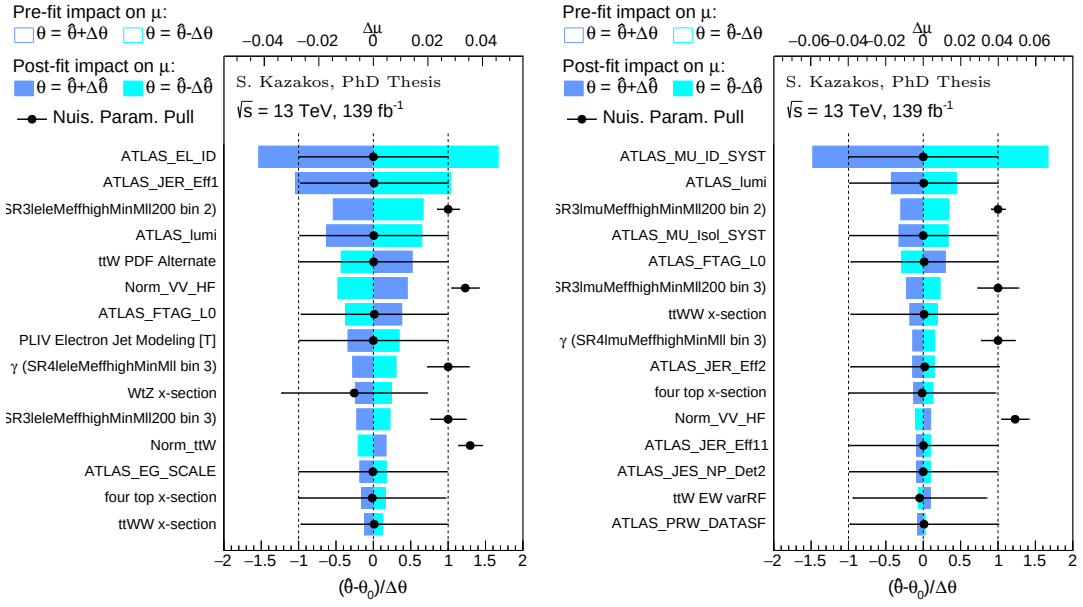



FIGURE 10.30: Ranking of the systematic uncertainties included in the fit according to their impact on the expected signal strength for (a) $m_{\mathrm{LQ}^{\mathrm{d}}_{\mathrm{mix}};e} = 1.6$ TeV and (b) $m_{\mathrm{LQ}^{\mathrm{d}}_{\mathrm{mix}};\mu} = 1.6$ TeV assuming $\mu = 1$. The filled blue rectangles correspond to the post-fit impact on $\mu$, both referring to the upper $x$-axis scale. The impact of each nuisance parameter (NP), $\Delta\mu$, is computed by comparing the nominal best-fit value of $\mu$ with the result of the fit when fixing the considered NP to its best-fit value, $\hat{\theta}$, shifted by its post-fit uncertainties $\pm\Delta\theta$ ($\pm\Delta\hat{\theta}$). The black points show the pulls of the NPs relative to their nominal values, $\theta_0$. These pulls and their relative post-fit errors, $\Delta\hat{\theta}/\Delta\theta$, refer to the lower $x$-axis scale. The nominal value for all NPs is $\theta_0 = 0$, with the exception of the normalisation factors and the MC statistical uncertainties ("gammas"), where the nominal value is 1.

The impact on the expected signal strength $\mu$ is shown in Figure 10.30 for the 15 most significant nuisance parameters and normalisation factors for the *tete* and $t\mu t\mu$ $\mathrm{LQ}^{\mathrm{d}}_{\mathrm{mix}}$ signals at $m_{\mathrm{LQ}^{\mathrm{d}}_{\mathrm{mix}}} = 1.6$ TeV assuming $\mu = 1$. As expected, electron- and muon-related instrumental uncertainties have the highest impact on the *tete* and $t\mu t\mu$ channels, respectively, followed by other instrumental uncertainties related to jets and $b$-jets, as well as some uncertainties on $t\bar{t}W$, $t\bar{t}WW$, $VV$, $tWZ$, and $t\bar{t}t\bar{t}$ background processes.

The same impact on the observed signal strength $\mu$ is shown in Figure 10.31 for the *tete* $\mathrm{LQ}^{\mathrm{d}}_{\mathrm{mix}}$ signal at $m_{\mathrm{LQ}^{\mathrm{d}}_{\mathrm{mix}}} = 1$ TeV, where $\mu$ is almost equal to zero. Since $\mu \sim 0$, it represents the impact of the systematic uncertainties on the background-only hypothesis, and therefore, similar results are expected for the $t\mu t\mu$ signal.

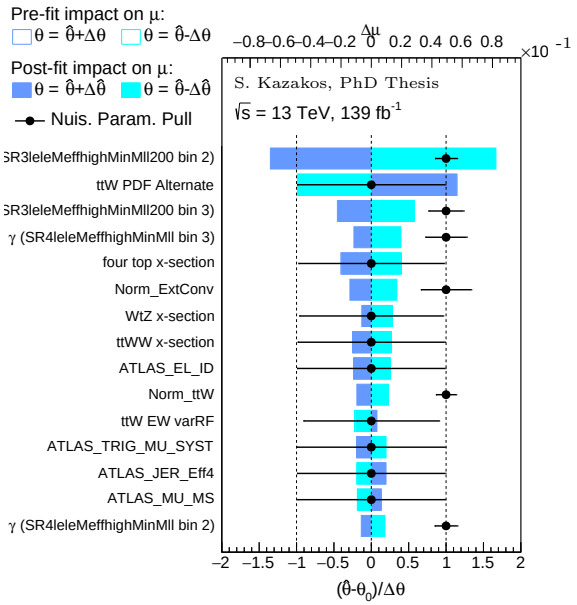



FIGURE 10.31: Ranking of the systematic uncertainties included in the fit according to their impact on the observed signal strength for $m_{\mathrm{LQ}^{\mathrm{d}}_{\mathrm{mix}};e} = 1$ TeV for $\mu$ almost equal to zero. The filled blue rectangles correspond to the post-fit impact on $\mu$, both referring to the upper $x$-axis scale. The impact of each NP, $\Delta\mu$, is computed by comparing the nominal best-fit value of $\mu$ with the result of the fit when fixing the considered NP to its best-fit value, $\hat{\theta}$, shifted by its post-fit uncertainties $\pm\Delta\theta$ ($\pm\Delta\hat{\theta}$). The black points show the pulls of the NPs relative to their nominal values, $\theta_0$. These pulls and their relative post-fit errors, $\Delta\hat{\theta}/\Delta\theta$, refer to the lower $x$-axis scale. The nominal value for all NPs is $\theta_0 = 0$, with the exception of the normalisation factors and the MC statistical uncertainties ("gammas"), where the nominal value is 1.

## 10.2.8 Results

### 10.2.8.1 Template Fit to data

Two maximum likelihood fits are performed in the templates defined in 7 CRs and 4 SRs (participating in pairs), as discussed in Section 10.2.6. Seven normalisation factors $\hat{\lambda}^{t\bar{t}W}$, $\hat{\lambda}^{\mathrm{HF}}_{e}$, $\hat{\lambda}^{\mathrm{HF}}_{\mu}$, $\hat{\lambda}^{\mathrm{MatC}}_{e}$, $\hat{\lambda}^{\mathrm{IntC}}_{e}$, $\hat{\lambda}^{VV\,\mathrm{HF}}$, and $\hat{\lambda}^{t\bar{t}Z}$ are left free-floating together with the LQ signal strength $\mu$, as described in Section 9.4.4. The fitted values of the above NFs are shown in Figures 10.32 and 10.33, after the likelihood fits to data in all SRs and CRs considered. The likelihood fits are performed under the background-only and signal-plus-background hypotheses for all available *tete* and $t\mu t\mu$ $\mathrm{LQ}^{\mathrm{d}}_{\mathrm{mix}}$ signal mass points (from which only 1200, 1400 and 1600 GeV mass points are shown for reference). In general the background normalisations obtained from the fit are consistent with their SM expectation value.

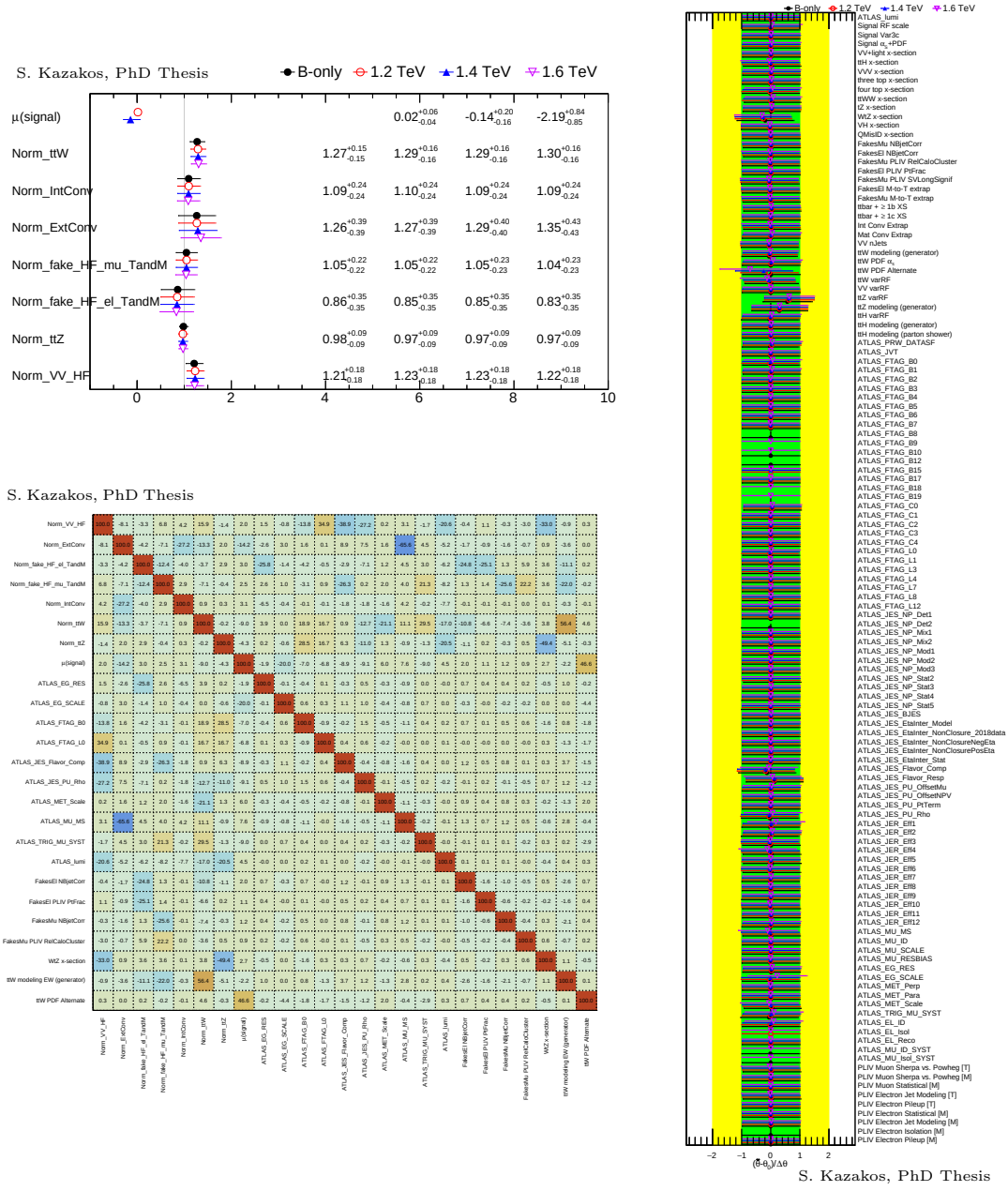



FIGURE 10.32: Fit results of a likelihood fit to data in CRs and electron SRs. The normalisation factors (upper left), correlation matrix (lower left) and pulls and constraints of the nuisance parameters (right) are shown. The correlation matrix corresponds to a fit under the background-only hypothesis, while the results of signal-plus-background fits with 1200, 1400 and 1600 GeV *tete* $\mathrm{LQ}^{\mathrm{d}}_{\mathrm{mix}}$ signals are overlaid in the rest of the plots.

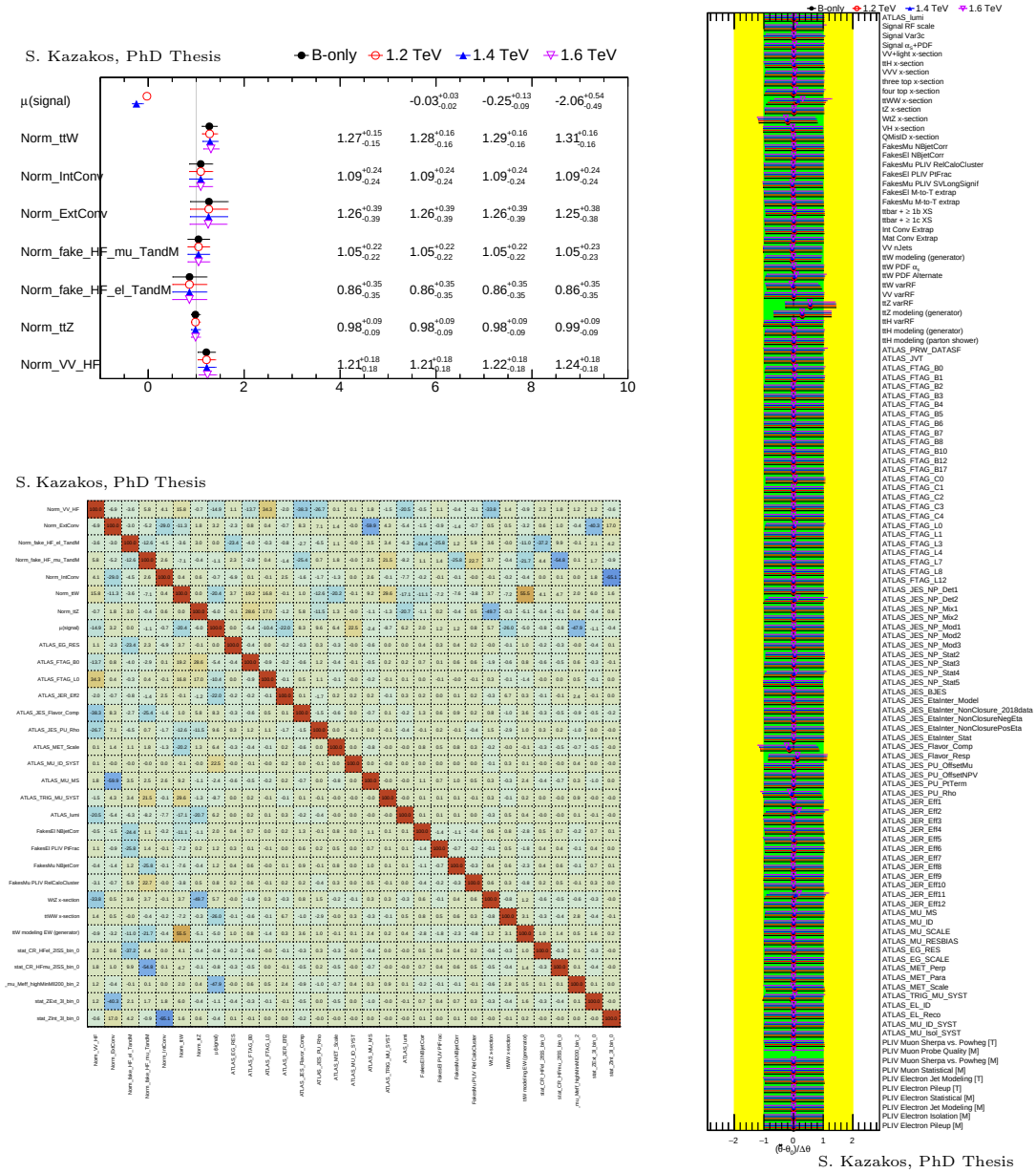



FIGURE 10.33: Fit results of a likelihood fit to data in CRs and muon SRs. The normalisation factors (upper left), correlation matrix (lower left) and pulls and constraints of the nuisance parameters (right) are shown. The correlation matrix corresponds to a fit under the background-only hypothesis, while the results of signal-plus-background fits with 1200, 1400 and 1600 GeV $t\mu t\mu$ $\mathrm{LQ}^{\mathrm{d}}_{\mathrm{mix}}$ signals are overlaid in the rest of the plots.

The slight pull in $\hat{\lambda}^{t\bar{t}W}$ is related to the known mismodelling of the $t\bar{t}W$ background, as explained in the LQLQ$\rightarrow t\tau t\tau$ analysis. The $t\bar{t}W$ NF fitted value is improved in this search due to the $t\bar{t}W$ electroweak contribution, which is properly taken into account. The slight pull in $\hat{\lambda}^{VV\,\mathrm{HF}}$ is further improved in the $t\bar{t}W$ analysis (Chapter 9) after the update of the $tZ$ sample by taking into account the proper NLO normalisation. The LQ signal strength is fitted to values close to zero for all the scalar and vector LQ signal mass points used in the search, indicating that the fit does not favour the existence of LQs with these mass values. The systematic uncertainties are participating in the fit as nuisance parameters and the ones surviving the pruning selection are also shown in Figures 10.32 and 10.33 together with their pulls and constraints. The correlation matrices shown in the same figures correspond to a fit under the background-only hypothesis considering all the CRs and only the electron or muon SRs.

In the results presented below the post-fit result shown corresponds to likelihood fits under the background-only hypothesis, following the standard choice for BSM searches with fitted $\mu$ values close to zero. The distributions are shown after the fits, and the total background prediction prior to the fits is overlaid (dashed blue line). The CRs where the shape of a distribution ($m_{\mathrm{eff}}$) is fitted are shown after a likelihood fit to all CRs and SRs in Figure 10.34.

All analysis regions in this search are shown after the fit as one-bin summary plots in Figure 10.36. A summary of the event yields in the SRs is shown in Table 10.21.

The $m_{\mathrm{eff}}$ distribution in the SRs after the likelihood fit to data is shown in Figure 10.35. The expected signal prediction for $\mathrm{LQ}^{\mathrm{d}}_{\mathrm{mix}}$s of $m_{\mathrm{LQ}^{\mathrm{d}}_{\mathrm{mix}}} = 1.6$ TeV is overlaid for illustrative purposes for $\mathcal{B} = 1$ and $\mu = 1$ as an unfilled violet histogram added to the post-fit background. The binning of the $m_{\mathrm{eff}}$ distribution in each SR is chosen as a result of optimisation studies trying to balance the adequate discrimination between the signal and the background shapes, while maintaining a per-bin statistical uncertainty below 30%.

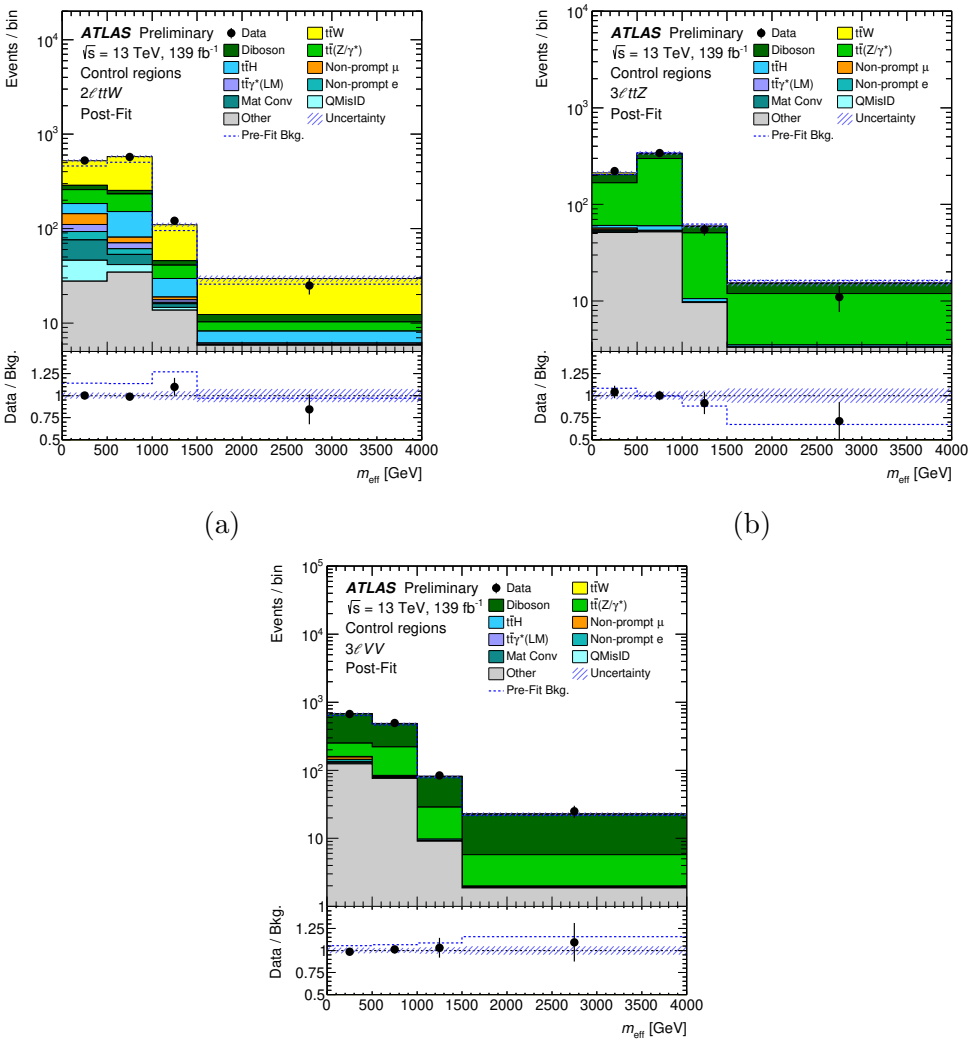



FIGURE 10.34: Data-to-simulation comparison of the $m_{\text{eff}}$ distribution in the (a) $2\ell$ttW, (b) $3\ell$ttZ, and (c) $3\ell$VV CRs of the $2\ell$SS and $3\ell$ channels after the likelihood fit to data under the background-only hypothesis. Figure taken from Ref. [230].

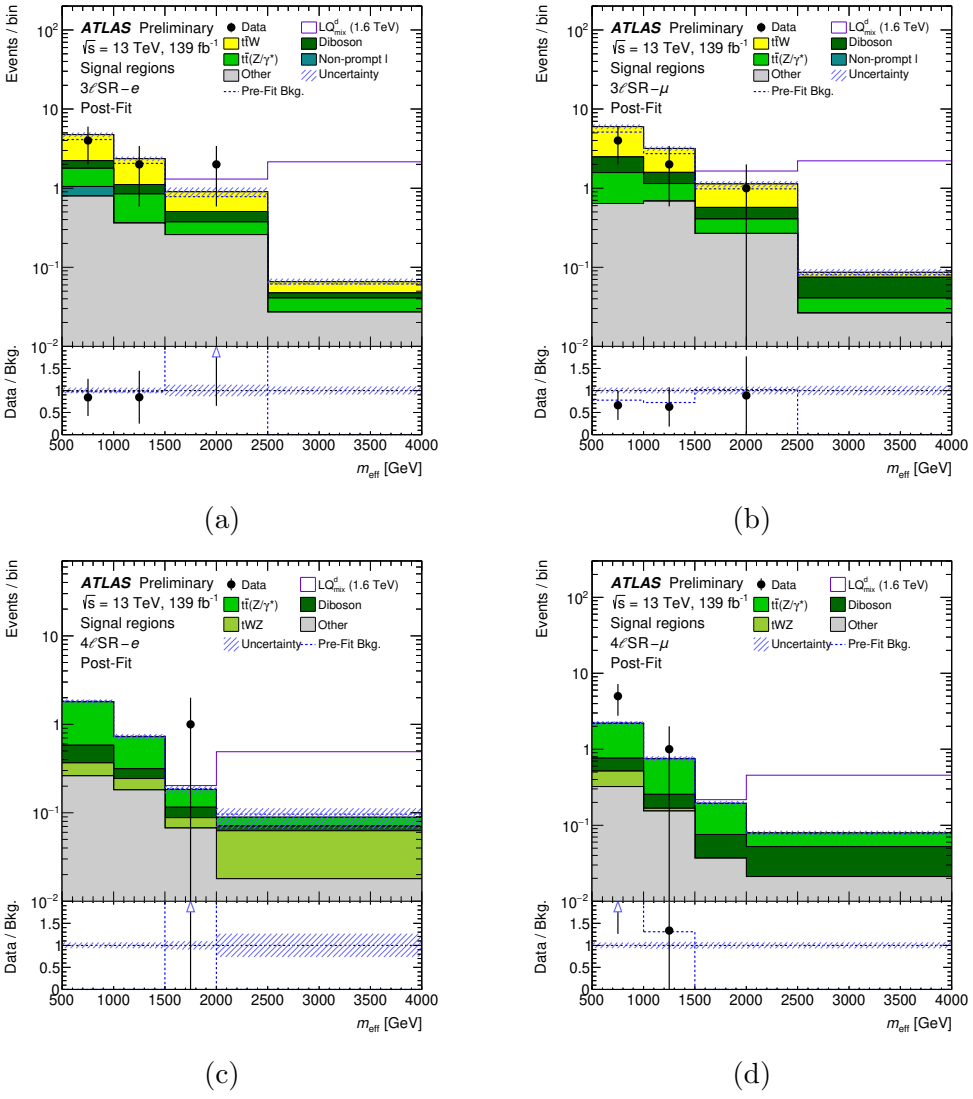
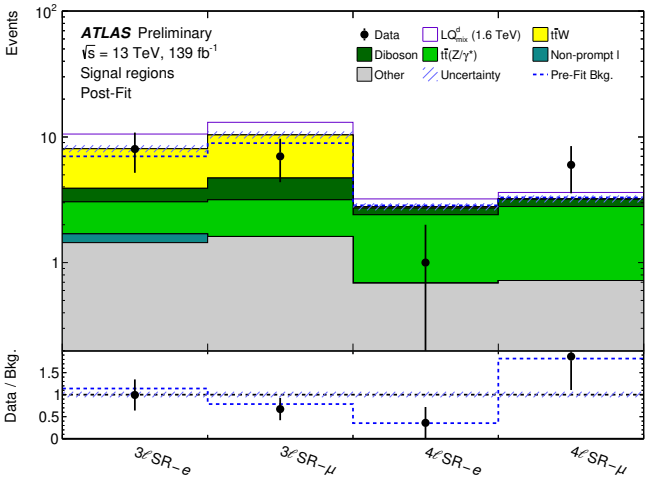
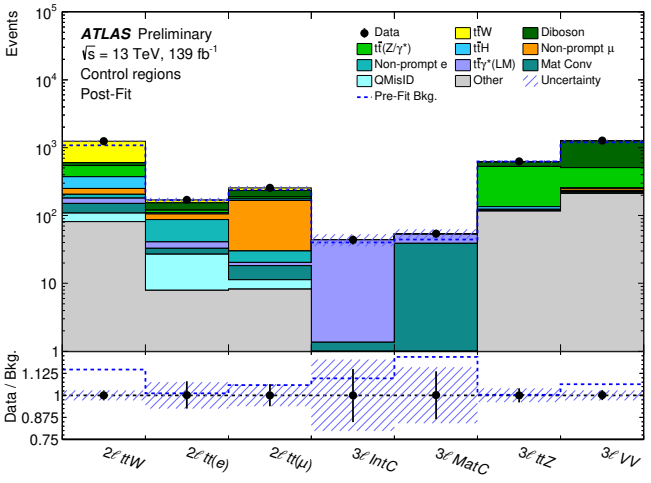


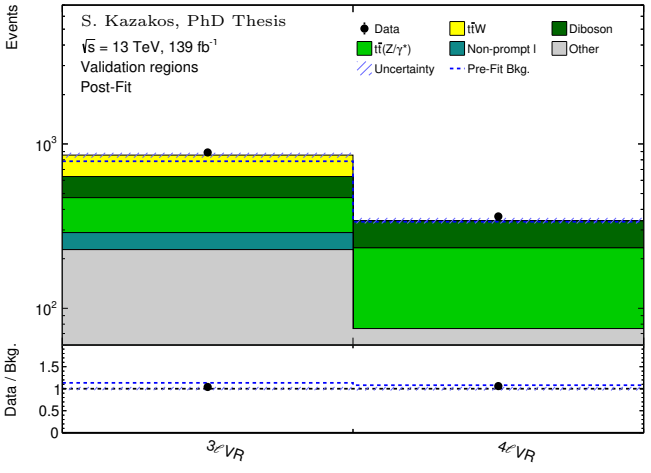

FIGURE 10.35: Data-to-simulation comparison of the $m_{\text{eff}}$ distribution in the (a) $3\ell$SR-e, (b) $3\ell$SR-$\mu$, (c) $4\ell$SR-e, and (d) $4\ell$SR-$\mu$SRs of the $3\ell$ and $4\ell$ channels after the likelihood fit to data under the background-only hypothesis using only the $3\ell$ and $4\ell$ SRs together with all the CRs. The expected $\text{LQ}^{\text{d}}_{\text{mix}}$ signal for $m_{\text{LQ}^{\text{d}}_{\text{mix}}} = 1.6$ TeV and $\mu = 1$ is shown as an unfilled violet histogram added to the post-fit background for illustrative purposes. Figure taken from Ref. [230].




(a)




(b)




(c)

FIGURE 10.36: Data-to-simulation post-fit comparison in the (a) 4 SRs and (b) 7 CRs participating in the likelihood fit. The post-fit result is propagated to the (c) 2 VRs, demonstrating the good background modelling. Figure taken from Ref. [230].

| | 3$\ell$SR-$e$ | 3$\ell$SR-$\mu$ | 4$\ell$SR-$e$ | 4$\ell$SR-$\mu$ |
|---|---|---|---|---|
| Data | 8 | 7 | 1 | 6 |
| Total background | 8.1 ± 0.6 | 10.2 ± 0.7 | 2.8 ± 0.2 | 3.3 ± 0.2 |
| $t\bar{t}W$ | 4.2 ± 0.6 | 5.6 ± 0.8 | — | — |
| Diboson | 0.9 ± 0.1 | 1.5 ± 0.2 | 0.32 ± 0.05 | 0.40 ± 0.04 |
| $t\bar{t}Z/\gamma^*$ | 1.33 ± 0.14 | 1.55 ± 0.15 | 1.69 ± 0.18 | 2.09 ± 0.21 |
| $tWZ$ | — | — | 0.23 ± 0.12 | 0.22 ± 0.12 |
| Non-prompt $\ell$ | 0.25 ± 0.16 | — | — | — |
| Other | 1.44 ± 0.22 | 1.61 ± 0.31 | 0.53 ± 0.10 | 0.54 ± 0.12 |
| $\mathrm{LQ}^{\mathrm{d}}_{\mathrm{mix}}$ 1.6 TeV | 2.5 ± 0.2 | 2.7 ± 0.2 | 0.42 ± 0.11 | 0.40 ± 0.05 |
| $\tilde{U}_1^{\mathrm{min}}$ 1.6 TeV | 4.5 ± 0.2 | 4.6 ± 0.3 | 0.7 ± 0.1 | 0.7 ± 0.1 |
| $\tilde{U}_1^{\mathrm{YM}}$ 1.6 TeV | 27 ± 1 | 29 ± 2 | 4.4 ± 0.2 | 4.2 ± 0.3 |
| $\tilde{U}_1^{\mathrm{YM}}$ 2.0 TeV | 2.0 ± 0.2 | 2.0 ± 0.2 | 0.31 ± 0.08 | 0.30 ± 0.03 |

TABLE 10.21: Overview of the predicted and observed yields in each signal region after a likelihood fit to data under the background-only hypothesis. The expected $\mathrm{LQ}^{\mathrm{d}}_{\mathrm{mix}}$ and $\tilde{U}_1$ signal yields are also shown pre-fit for each region for $\mu = 1$. Dashes are used to denote the contributions that either negligible or not applicable. Table taken from Ref. [230].

### 10.2.8.2 Expected and observed upper limits

No significant excess is observed over the SM expectation value after the likelihood fit to data in any of the SRs. This can be inferred already from Figures 10.32, 10.33 and 10.35, since the fitted signal strength $\mu$ for all $\mathrm{LQ}^{\mathrm{d}}_{\mathrm{mix}}$ signal mass points is close to zero and there are no or not enough data in the right tail of the $m_{\mathrm{eff}}$ distribution, where the LQ signal lives. The same conclusion is deducted for the $\tilde{U}_1$ vector LQ signal model for the minimal coupling and Yang-Mills coupling configurations. The expected and observed $p_0$-values are shown as a function of $m_{\mathrm{LQ}^{\mathrm{d}}_{\mathrm{mix}}}$ in Figure 10.37 for both $tete$ and $t\mu t\mu$ $\mathrm{LQ}^{\mathrm{d}}_{\mathrm{mix}}$ signals. The observed $p_0$-value is found to be consistent with the background-only hypothesis across the whole range of mass points considered. The expected $p_0$-value illustrates the significant expected sensitivity of the search, exceeding 5 standard deviations for $m_{\mathrm{LQ}^{\mathrm{d}}_{\mathrm{mix}}} < 1.5$ TeV and 3 standard deviations for $m_{\mathrm{LQ}^{\mathrm{d}}_{\mathrm{mix}}} < 1.6$ TeV in the $\mathcal{B} = 1$ scenario.

Following the standard procedure in such cases of no discovery, expected and observed 95% CL upper limits are set on the $\mathrm{LQ}^{\mathrm{d}}_{\mathrm{mix}}$ and $\tilde{U}_1$ production cross section as a function of LQ mass, as shown in Figures 10.38 and 10.39, respectively, separately for $tete$ and $t\mu t\mu$ signals. The theoretical prediction together with its $\pm 1\sigma$ uncertainty is also shown. The points where the line of the theoretical prediction crosses the expected and observed cross-section lines defines the corresponding

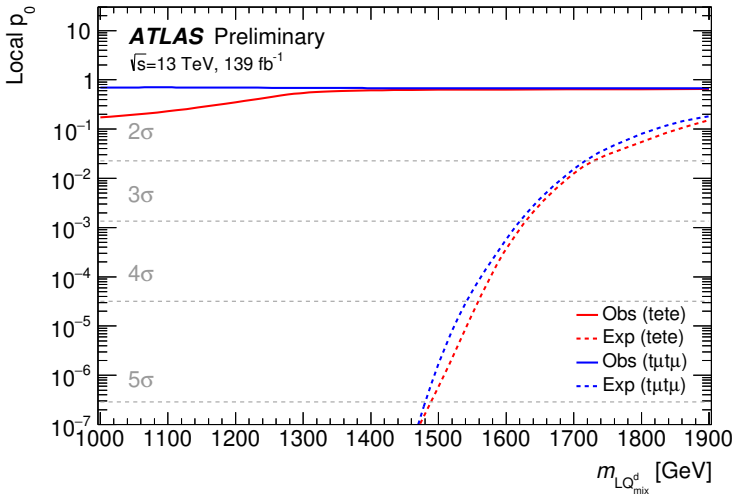



FIGURE 10.37: Observed local $p_0$ as a function of $\mathrm{LQ}^{\mathrm{d}}_{\mathrm{mix}}$ mass ($m_{\mathrm{LQ}^{\mathrm{d}}_{\mathrm{mix}}}$) for *tete* (red) and $t\mu t\mu$ (blue) signals assuming $\mathcal{B} = 1$. The expected local $p_0$ under the hypothesis of a $\mathrm{LQ}^{\mathrm{d}}_{\mathrm{mix}}$ signal at that mass is shown in dashed lines. Figure taken from Ref. [230].

limits of this search. The upper limit in cross section corresponds to the lower limit in $\mathrm{LQ}^{\mathrm{d}}_{\mathrm{mix}}$ mass that can be excluded. The expected and observed 95% CL lower limits on $m_{\mathrm{LQ}^{\mathrm{d}}_{\mathrm{mix}}}$ assuming $\mathcal{B} = 1$ are found to be 1.61 (1.62) TeV and 1.61 (1.64) TeV for the *tete* ($t\mu t\mu$) signal, respectively. In Figures 10.38c and 10.38d the same expected and observed limits are shown in a 2D plane as a function of $\mathcal{B}(\mathrm{LQ}^{\mathrm{d}}_{\mathrm{mix}} \to t\ell)$ and $\mathrm{LQ}^{\mathrm{d}}_{\mathrm{mix}}$ mass. The asymptotic formula is used to derive the upper limits on the $\mathrm{LQ}^{\mathrm{d}}_{\mathrm{mix}}$ pair production cross section. While the asymptotic approximation is used for the quoted limits, the same limits are also estimated using the toy MC method in the $m_{\mathrm{LQ}^{\mathrm{d}}_{\mathrm{mix}}}$ range of 1.0-1.8 TeV, as a cross-check due to the limited statistics in the SRs. This test resulted to a degradation in the limits by about 2.5% and a difference in the limits at the order of 5-30% depending on the LQ mass point.

The expected and observed 95% CL upper limits set on the vector $\tilde{U}_1$ pair production cross section for the *tete* ($t\mu t\mu$) $\tilde{U}_1$ signal are estimated to 1.71 (1.71) TeV and 1.71 (1.73) TeV, respectively, assuming the minimal coupling scenario. In the Yang-Mills coupling scenario the expected and observed 95% CL upper limits for the *tete* ($t\mu t\mu$) signal are estimated to 2.0 (1.98) TeV and 2.0 (2.0) TeV, respectively.

The result of the limits remains the same across all mass points after the inclusion of all systematic uncertainties (compared to the inclusion of the statistical

uncertainty only), leading to the conclusion that this analysis is limited by the statistical uncertainty on data. These limits were the most stringent ones in ATLAS and CMS for this final state at the time of the thesis writing, while the limits for $\mathcal{B}(\mathrm{LQ}^{\mathrm{d}}_{\mathrm{mix}} \to t\ell) = \mathcal{B}(\mathrm{LQ}^{\mathrm{d}}_{\mathrm{mix}} \to b\nu) = 0.5$ are very competitive to the previous ATLAS limits estimated in the corresponding search for $\mathrm{LQ}^{\mathrm{d}}_{\mathrm{mix}}$ in the mixed decay mode ($\mathrm{LQ} \to b\nu/t\ell$) [232].

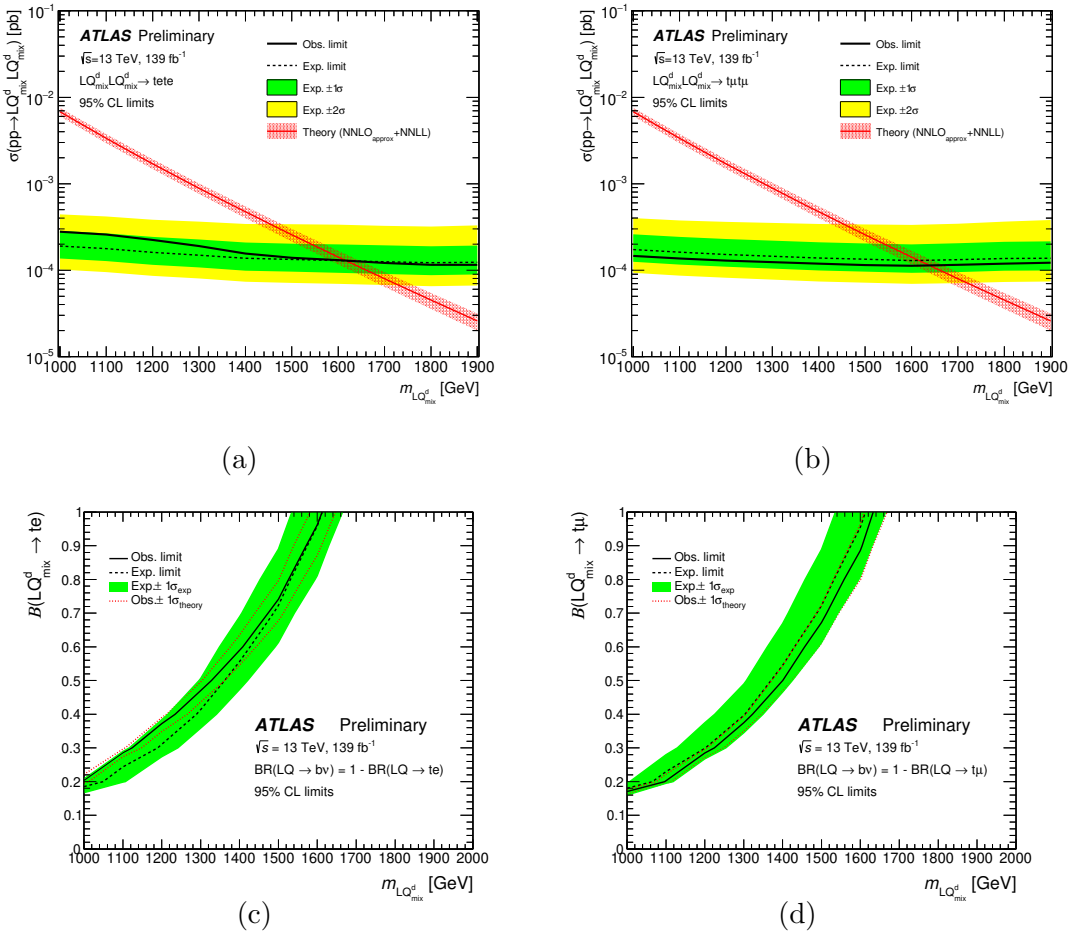



FIGURE 10.38: Observed and expected 95% CL upper limits on the $\mathrm{LQ}^{\mathrm{d}}_{\mathrm{mix}}$ pair production cross section as a function of $m_{\mathrm{LQ}^{\mathrm{d}}_{\mathrm{mix}}}$ for the (a) *tete* and (b) $t\mu t\mu$ $\mathrm{LQ}^{\mathrm{d}}_{\mathrm{mix}}$ signals. The green and yellow shaded bands correspond to the $\pm 1$ and $\pm 2$ standard deviation uncertainty ($\pm 1\sigma$, $\pm 2\sigma$) around the combined expected limit. The theoretical prediction along with its $\pm 1\sigma$ uncertainty are shown with a red line and band, respectively. The limits are scaled to different combinations of $\mathcal{B}(\mathrm{LQ}^{\mathrm{d}}_{\mathrm{mix}} \to t\ell)$ (since there is no acceptance to $\mathrm{LQ}^{\mathrm{d}}_{\mathrm{mix}} \to b\nu$) and are shown together with their $\pm 1\sigma$ uncertainties separately for the (c) *tete* and (d) $t\mu t\mu$ $\mathrm{LQ}^{\mathrm{d}}_{\mathrm{mix}}$ signals. Figure taken from Ref. [230].

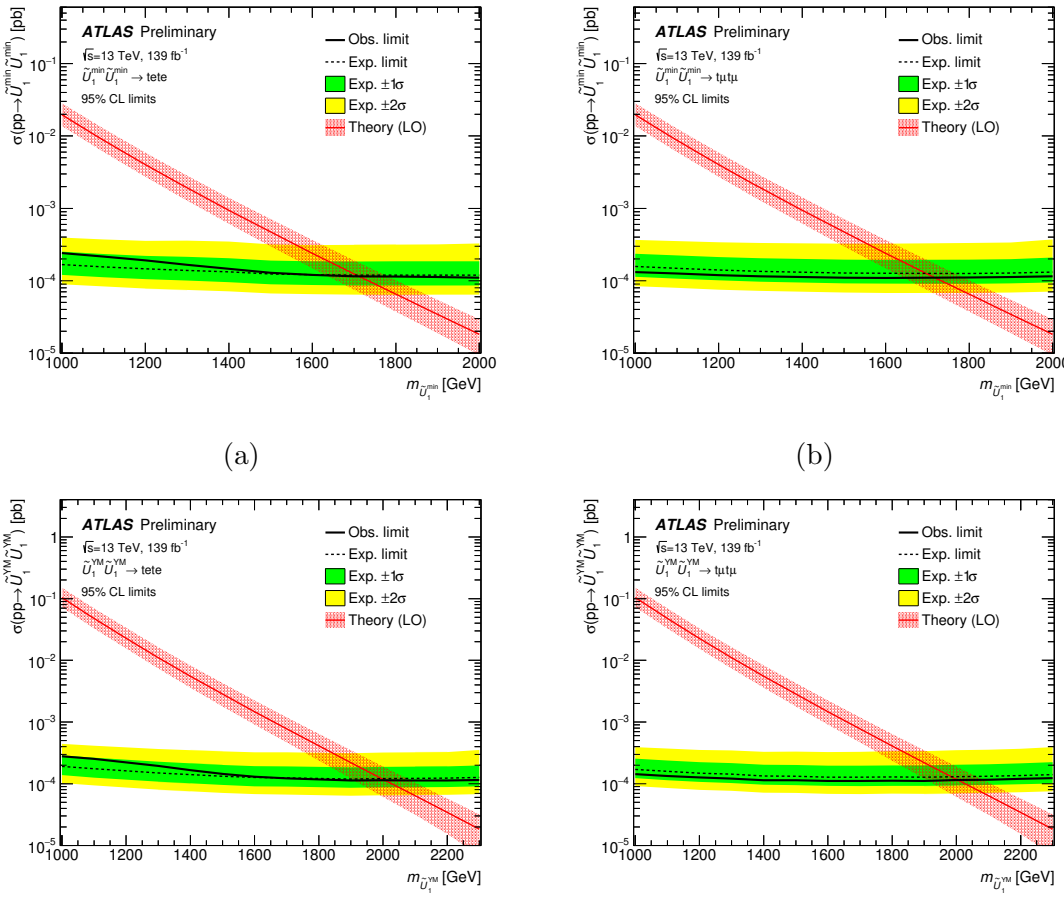



FIGURE 10.39: Observed and expected 95% CL upper limits on the $\tilde{U}_1$ pair production cross section as a function of $m_{\tilde{U}_1}$ shown for the minimal coupling scenario and decay of the $\tilde{U}_1^{\text{min}}$ into (a) $te$ or (b) $t\mu$, respectively, and for the Yang-Mills coupling scenario and decay of the $\tilde{U}_1^{\text{YM}}$ into (c) $te$ or (d) $t\mu$, respectively. The green and yellow shaded bands correspond to the $\pm 1$ and $\pm 2$ standard deviation uncertainty ($\pm 1\sigma$, $\pm 2\sigma$) around the combined expected limit. The theoretical prediction along with its $\pm 1\sigma$ uncertainty are shown with a red line and band, respectively. Figure taken from Ref. [230].

### 10.2.8.3 Event display of a leptoquark candidate event

The observed data in the third bin of SR3$\ell$-$e$ and the slight excess over the MC prediction in that bin suggest that these events can be studied as potential LQ candidates. For this reason, the event display (shown in Figure 10.40) is produced for one of the two events in that bin in order to visualise its properties and kinematics. The unique number of this event is 309940730 and it was recorded on

21/10/2017 by the ATLAS detector. The selected event contains two opposite-charge (OS) electron and one muon candidates along with five jets (one of which is $b$-tagged). The $p_{\mathrm{T}}$ of the electron candidates is 755 GeV and 683 GeV, the $p_{\mathrm{T}}$ of the muon candidate is 94 GeV and the $p_{\mathrm{T}}$ of the leading jet is 247 GeV. There is also non-negligible amount of $E_{\mathrm{T}}^{\mathrm{miss}}$ in the event, which is estimated to be 47 GeV, while the $m_{\mathrm{eff}}$ of the event is equal to 2.1 TeV.

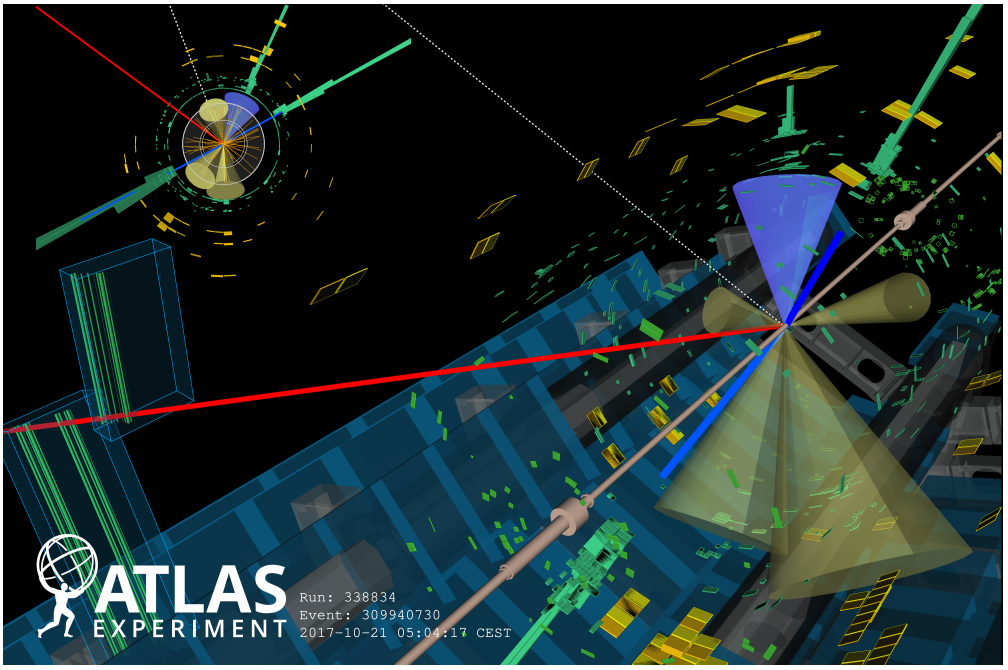



FIGURE 10.40: Event display of a potential LQ candidate decaying into a top quark and an electron. The electron (blue) and muon (red) candidate reconstructed tracks are shown. The jets and $b$-jets are shown with yellow and blue cones, respectively. The $E_{\mathrm{T}}^{\mathrm{miss}}$ of the event is denoted with a dashed white line. The energy deposits in the hadronic (electromagnetic) calorimeter are shown with yellow (green) boxes. Figure taken from Ref. [230].

## 10.3 Combination of leptoquark searches

The broad physics program concerning LQ searches in ATLAS involves currently single- and pair-produced LQs of different types according to their electric charge and the generation of quarks and leptons they decay into. Since there was no significant excess (above $3\sigma$) over the SM expectation value in any of the LQ searches performed in Run 2, 95% CL upper limits were set to the production cross section of the corresponding LQ types. Most of these searches, while being mostly orthogonal to each other, were dedicated analyses targeting specific LQ decay modes handled by the different branching ratios ($\mathcal{B}$). Therefore, a very promising effort is ongoing regarding the combination of these searches such that combined limits can be set on $\mathcal{B}$ as a function of LQ mass. An illustrative sketch of the targeted final states is shown in Figure 10.41, and an overview of the LQ analyses considered in the combination is given in Table 10.22.

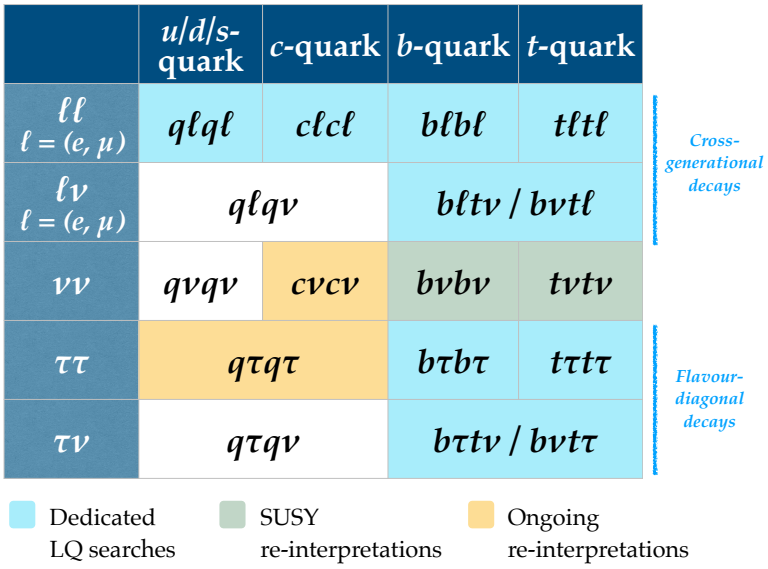



FIGURE 10.41: Overview of the LQ physics program concerning scalar LQ pair-production final states.

There are 9 different final states included in the combination effort all involving pair-production LQ searches. The difference in the event selection among these searches lies on the number of selected light-lepton and hadronic $\tau$-lepton candidates, as well as number of $b$-jets. Due to this difference, there is negligible overlap among the selected collision events that are used in the combinations.

Some of the targeted final states are studied in dedicated LQ searches, while others are covered from reinterpretations of other existing analyses (such as the SUSY searches for *stop* and *sbottom* squarks). The existing limits considered in the combinations from already public analyses are shown in the overlay summary plots in Figure 10.42. The results from the 36 $\text{fb}^{-1}$ searches are overlaid as a shaded grey area without any combination, while they mostly involve LQ reinterpretations of SUSY searches. The increase in the luminosity by a factor of ∼3.9 and the fact that the LQ searches with the full Run-2 dataset are dedicated searches, both contribute to an additional mass exclusion of 200-400 GeV depending on the different branching ratio values. The combinations are currently performed mainly for scalar LQs, while there is strong motivation to also add the vector LQ interpretations on the existing analyses within this effort in the cases that are not considered already. The scalar LQ models under consideration differ by their coupling strengths to electrons and muons, which might (in the $\text{LQ}_3$ case) or might not (in the $\text{LQ}_{\text{mix}}$ case) vanish, and by their electric charge ($\text{LQ}^{\text{u}}$ and $\text{LQ}^{\text{d}}$). The vector LQ models under consideration include the reinterpretations based either on the $U_1^{\text{min/YM}}$ vector LQ introduced in the Zurich model [233] or on the $\tilde{U}_1^{\text{min/YM}}$ vector LQ introduced in the Boston model [73, 231]. The $\tilde{U}_1$ is not participating in any of the combinations, since it is allowed to couple only to a right-handed up-type quark and a charged lepton, hence mixed decay modes as $\tilde{U}_1\tilde{U}_1 \to t\tau b\nu$ are not possible.

| **Search** | **Interpretation** | | | | | | | | |
|---|---|---|---|---|---|---|---|---|---|
| | **Scalar** | | | | **Vector** | | **Signal region** | | |
| Final State | $\text{LQ}_3^{\text{u}}$ | $\text{LQ}_3^{\text{d}}$ | $\text{LQ}_{\text{mix}}^{\text{u}}$ | $\text{LQ}_{\text{mix}}^{\text{d}}$ | $U_1^{\text{min/YM}}$ | $\tilde{U}_1^{\text{min/YM}}$ | $N_\ell$ | $N_{\tau_{\text{had}}}$ | $N_{b-\text{jets}}$ |
| $t\nu t\nu$ | ✓ | – | ✓ | – | ✓ | – | 0 | 0 | $\geq 2$ |
| $b\nu b\nu$ | – | ✓ | – | ✓ | – | – | 0 | 0 | $\geq 2$ |
| $t\tau b\nu$ / $t\nu b\tau$ | ✓ | ✓ | – | – | ✓ | – | 0 | 1 | $\geq 2$ |
| $b\tau b\tau$ | ✓ | – | – | – | ✓ | – | $\{0,1\}$ | $\{1,2\}$ | $\{1,2\}$ |
| $t\ell b\nu$ / $t\nu b\ell$ | – | – | ✓ | ✓ | – | – | 1 | $\geq 0$ | $\geq 1$ |
| $b\ell b\ell$ | – | – | ✓ | – | – | – | 2 | $\geq 0$ | $\{0,1,2\}$ |
| $t\tau t\tau$ | – | ✓ | – | – | – | ✓ | $\{1,2,3\}$ | $\geq 1$ | $\geq 1$ |
| $t\ell t\ell$ (lep) | – | – | – | ✓ | – | ✓ | $\{3,4\}$ | 0 | $\geq 2$ |
| $t\ell t\ell$ (had) | – | – | – | ✓ | – | – | 2 | – | – |

TABLE 10.22: Overview of individual analyses. The provided information on the signal region definitions is only a set of selected main characteristics. The $\tilde{U}_1^{\text{min/YM}}$ model is only used for reinterpretations of the $t\ell t\ell$ and $t\tau t\tau$ analyses (no combinations).

In general the sensitivity of the combination results is driven by the amount of

data statistics rather than systematic uncertainties. Different correlation schemes are used for instrumental uncertainties to demonstrate the independence of the obtained results on these choices, while any assumption on the correlation scheme across the different analyses does not affect the results significantly. Detector-related uncertainties are assumed to be correlated across analyses, when possible. The theoretical uncertainties are subdominant. A conservative approach is chosen, where the NPs corresponding to these uncertainties (related to background modelling and normalisation) are not correlated across the individual searches participating in the combinations.

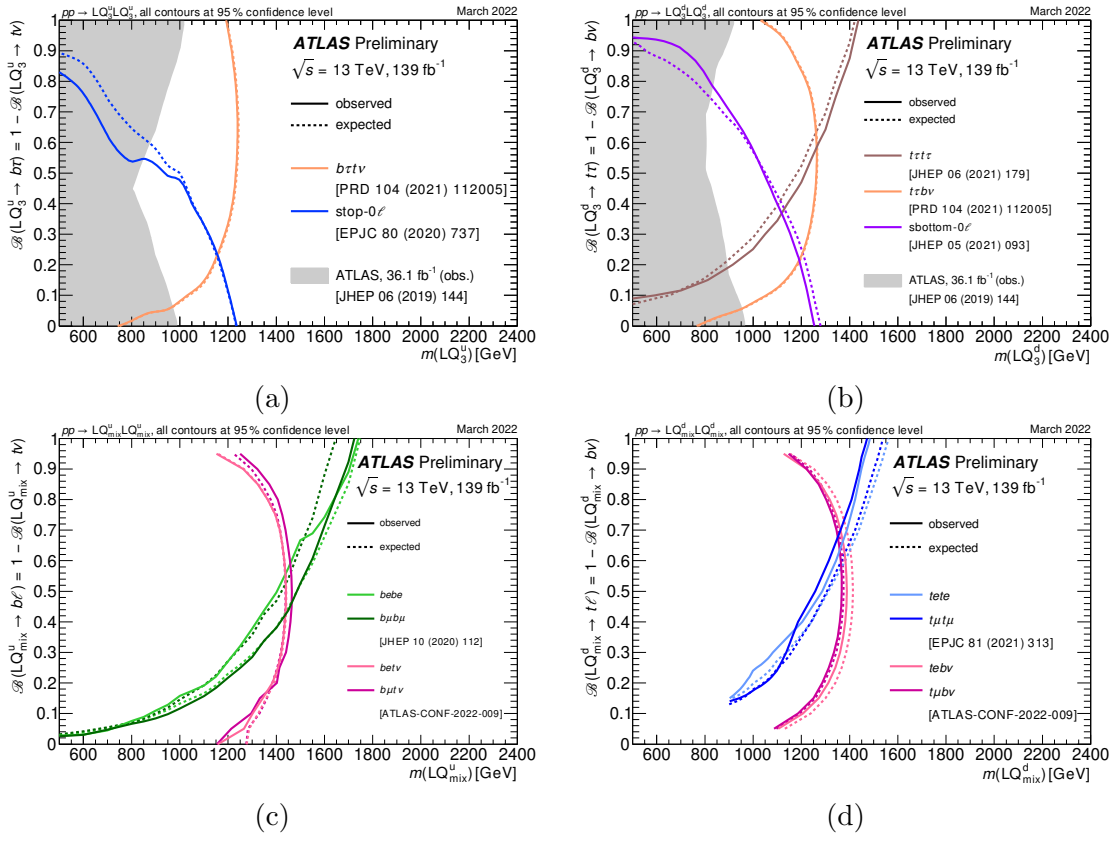



FIGURE 10.42: Summary plots of overlaid expected and observed 95% upper limits on branching ratio ($\mathcal{B}$) as a function of LQ mass for scalar LQ models. The results involve LQs of type: (a) $LQ_3^u$, (b) $LQ_3^d$, (c) $LQ_{mix}^u$ and (d) $LQ_{mix}^d$. Figure taken from Ref. [234].

On the technical side, the combinations are performed using the python-based libraries pyhf [235] and Cabinetry [236]. This choice is currently the recommended one used in combinations, facilitating a straightforward way of combining the workspaces of each search and allowing for a future publication of the corresponding likelihood functions that are often useful to theoretical physicists.

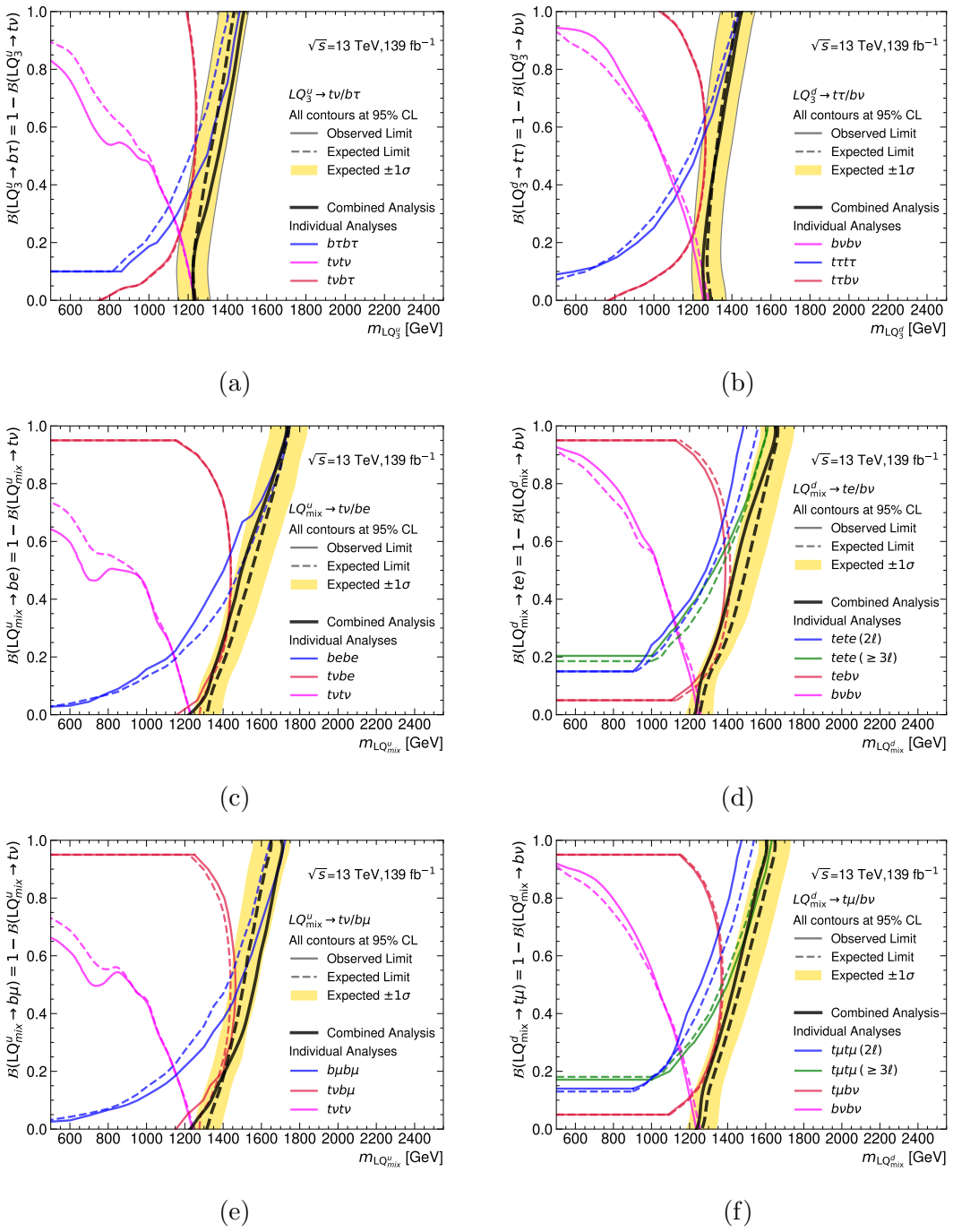



FIGURE 10.43: The 95% CL expected (dashed line) and observed (solid line) exclusion contours in the 2D $\mathcal{B}$ and LQ mass plane in the individual analyses after the corresponding combinations, taking into account all systematic uncertainties. The $\mathcal{B}$ values used in the limit setting are shown as light blue circles. The $\pm 1\sigma$ uncertainty on the expected contours is denoted with a shaded yellow band. The individual analyses of this thesis are contributing to the combinations in the subfigures (b), (d) and (f).

The expected and observed limits of the analyses shown in Table 10.22 are combined as a result of this effort and the combined limits on $\mathcal{B}$ as a function of LQ mass are shown in Figure 10.43.

The $t\tau t\tau$ analysis dominates in the corresponding combination at $\mathcal{B} = 1$ (Figure 10.43b), while it also extends the expected mass exclusion by more than 100 GeV at $\mathcal{B} = 0.5$. The combination of the current $t\ell t\ell$ analysis with the boosted $t\ell t\ell$ analysis improves the expected sensitivity by ∼50 (40) GeV in the $tete$ ($t\mu t\mu$) scenario at $\mathcal{B} = 1$, where these analyses dominate. At $\mathcal{B} = 0.5$, the combination of all the analyses extends the mass reach by ∼100-120 GeV for both $tete$ and $t\mu t\mu$ cases compared to the most sensitive searches. This is a non-negligible improvement given the steeply falling LQ pair-production cross section as a function of LQ mass. The combination effort itself is the first ever attempt for a LQ pair-production combination in ATLAS, aiming to a broader mass exclusion as a function of $\mathcal{B}$ than in each independent analysis separately.

# Chapter 11

# Conclusions

This dissertation presents a broad spectrum of physics analyses containing multiple leptons and $b$-tagged jets in their final state using data from proton-proton collisions at a center-of-mass energy of $\sqrt{s} = 13$ TeV recorded by the ATLAS detector at the LHC. The full Run-2 dataset is used, which corresponds to an integrated luminosity of 139 fb$^{-1}$. On the other hand, the LS2 period of the LHC at CERN offered the perfect opportunity for detector-related studies regarding the electron analysis on the ATLAS Tile calorimeter as a part of the upcoming Phase-II upgrade, which are also discussed in this thesis.

Following the discovery of the Higgs boson in 2012, there is an ongoing effort for the precise measurement of its properties. One of the most interesting aspects of the Higgs sector is the proper understanding of interactions of the Higgs boson with the quarks and leptons of the SM, and especially with the top quark, which is the heaviest quark in the SM. The interactions between the top quarks and the Higgs boson are controlled by the top-Higgs Yukawa coupling (with a value very close to unity), which can be estimated in processes where a top quark (or top-quark pair) is produced in association with a Higgs boson ($tH$ and $t\bar{t}H$). The $t\bar{t}H$ measurement in multilepton final states was performed in ATLAS with a partial Run-2 dataset (79 fb$^{-1}$) and reported a discrepancy between data and the state-of-art theoretical predictions for the associated production of a top-quark pair and a $W$ boson ($t\bar{t}W$), which was also reported by the CMS experiment. Therefore, the $t\bar{t}H$ measurement with the full Run-2 dataset was delayed in order to first perform a detailed measurement of the inclusive and differential cross sections for $t\bar{t}W$ production. The $t\bar{t}W$ contribution is one of the largest background processes

in the many physics analyses (such as the $t\bar{t}H$ and $t\bar{t}t\bar{t}$ measurements). The modelling of this process is quite challenging due to non-negligible higher-order corrections, something that moved many theorists and experimentalists to join this effort.

A large part of this dissertation is devoted to the $t\bar{t}W$ measurement in the multi-lepton final state. Due to the complexity of this final state, sophisticated methods were developed in order to control the different types of background contributions: $t\bar{t}$ events with non-prompt leptons from semileptonic $b$-quark decays or photon conversions ("fake leptons"), $t\bar{t}Z$, $t\bar{t}H$ and diboson events. The fake-background estimation is mostly based on MC simulation with small corrections derived via the extended Template Fit method, where control regions are defined enriched in the main background contributions and the normalisation of the contributions are left free-floating in a fit together with the signal strength. The "extended" label is used to denote the splitting of the fake-enriched regions according to operating points of the improved (non-)prompt lepton veto, a discriminant designed to suppress the non-prompt lepton contributions from HF decays. The background in the signal regions is corrected in this way, and in the case of the inclusive measurement the $t\bar{t}W$ signal strength is estimated simultaneously. The signal regions in the $2\ell$ and $3\ell$ channels are split according to jet and $b$-jet multiplicities, total lepton charge and lepton flavour in order to achieve a more precise measurement. The inclusive measurement confirmed that the $t\bar{t}W$ cross section is consistently higher than the SM expectation with an inclusive signal strength of $\mu_{t\bar{t}W} = 1.44^{+0.14}_{-0.13}$. The inclusive signal strength was measured separately for the $t\bar{t}W^+$ and $t\bar{t}W^-$ production with values $\mu_{t\bar{t}W^+} = 1.44 \pm 0.14$ and $\mu_{t\bar{t}W^-} = 1.43^{+0.21}_{-0.20}$, and also separately in the $2\ell$ and $3\ell$ channels with values $\mu^{2\ell}_{t\bar{t}W} = 1.44^{+0.14}_{-0.13}$ and $\mu^{3\ell}_{t\bar{t}W} = 1.59^{+0.31}_{-0.26}$.

The differential measurement of the $t\bar{t}W$ production cross section was an ambitious effort involving the unfolding of up to eight observables in a "stitched" signal region for both $2\ell$ and $3\ell$ channels at particle level. The Profile Likelihood Unfolding (PLU) method was selected for the unfolding as the most natural choice in the handling of systematic uncertainties, and mainly due to the fact that it could combine the extended Template Fit with the unfolding in a single framework, inheriting all the dedicated methods used for background estimation. In the PLU method the background in the signal region is corrected from the fit, followed by the simultaneous unfolding of the $t\bar{t}W$ sample. The unfolding is performed with individual per-bin normalisation factors for the $t\bar{t}W$ signal, which are afterwards

"translated" into cross-section units. The results from the differential measurement are consistent with those from the inclusive measurement, and they are also similar among the unfolded observables. The results are also in agreement with the behaviour reported by the $t\bar{t}H$ to multilepton measurement for the $N_{\text{jets}}$ and $N_{b-\text{jets}}$ observables, indicating that the measured $t\bar{t}W$ cross section is higher than the predicted one.

Another novel aspect of the $t\bar{t}W$ effort is related to the measurement of the relative charge asymmetry ($A_C^R$) both inclusively and differentially (for each unfolded observable). The motivation for this measurement was to understand if the $t\bar{t}W$ production is more asymmetric than expected, and to look into the systematic uncertainties impacting this measurement assuming that the majority of them is "cancelled" out due to the $A_C^R$ definition. In the majority of the unfolded bins, $A_C^R$ was found to be close to the value predicted by the SM ($A^R_{C,\,t\bar{t}W} = 0.322 \pm 0.003\,(\text{scale}) \pm 0.007\,(\text{PDF})$) with a few exceptions probably due to statistical fluctuation of the data, and a similar result is obtained from the inclusive measurement of this variable. The $A_C^R$ measurement is dominated by statistical uncertainty, while the systematic uncertainties with the largest impact are related to background normalisation factors, prompt and non-prompt background modelling and $t\bar{t}W$ modelling.

Apart from the above results, in the context of this measurement there were further developments in the already existing analysis and unfolding frameworks. These developments were centred around the sophisticated extended Template Fit method developed for an accurate background estimation, the unfolding part regarding the PLU method and the second-order Tikhonov regularisation, which was first implemented in this form as an outcome of this effort.

The rest of the analyses presented in this thesis are focused on searches for physics beyond the SM (BSM) and, particularly, in searches for leptoquarks. Leptoquarks are one of the most favoured BSM scenarios put forward by theorists as a promising explanation of the intriguing deviations reported in $B$-meson decays by the LHCb experiment and the $B$ factories. This thesis is targeting pair-produced leptoquarks with a mass in the TeV scale each coupling simultaneously into a top quark and a lepton ($e$, $\mu$, $\tau$-lepton). This effort is divided in two dedicated searches targeting $t\ell t\ell$ ($\ell = e, \mu$) and $t\tau t\tau$ signatures, respectively, which are both cut-based analyses performed in the high-$p_{\text{T}}$ regime. The main discriminating variable in both

searches is the effective mass, $m_{\text{eff}}$, which is defined as the scalar sum of $p_{\text{T}}$ of all physics objects considered and $E_{\text{T}}^{\text{miss}}$.

In the $t\ell t\ell$ search, the event categorisation is based on light-lepton multiplicity and selections on variables with high signal-to-background separation (such as the minimum dilepton mass between all possible lepton combinations, $m_{\ell\ell}^{\text{min}}$). The events are categorised in channels requiring two same-charge (or same-sign, SS), three or four light leptons. The $3\ell$ and $4\ell$ channels are used for the definition of signal and validation regions, where the former requires high $m_{\ell\ell}^{\text{min}}$ and the latter requires low $m_{\ell\ell}^{\text{min}}$. The $2\ell$SS and $3\ell$ channels are used for the definition of orthogonal control regions enriched in some of the main backgrounds of this analysis. The background estimation and suppression is performed with the same configuration and version of the Template Fit as in the $t\bar{t}W$ analysis, with the difference that the non-prompt lepton control regions are merged together for all lepton definitions related to PLIV. The main background contributions in this search are events originating from $VV$, $t\bar{t}Z$ and $t\bar{t}W$. No significant excess is found over the SM expectation value, and upper limits are set on the signal cross section and the branching ratio as a function of the leptoquark mass. The upper limits on the cross section correspond to lower limits in leptoquark mass. The expected and observed 95% CL lower limits on the mass of scalar leptoquarks $m_{\text{LQ}_{\text{mix}}^{\text{d}}}$ assuming a branching ratio of $\mathcal{B} = 1$ are found to be 1.61 (1.62) TeV and 1.61 (1.64) TeV for the $tete$ ($t\mu t\mu$) signal, respectively. The expected and observed 95% CL lower limits on the mass of vector leptoquarks $m_{\tilde{U}_1}$ in the minimal coupling scenario are found to be 1.71 (1.71) TeV and 1.71 (1.73) TeV, respectively, and in the Yang-Mills scenario they are found to be 2.0 (1.98) TeV and 2.0 (2.0) TeV, respectively.

In the $t\tau t\tau$ search, due to the increased complexity of this experimental signature, a sophisticated event categorisation is designed introducing signal and control regions based on the multiplicity of light leptons and hadronically decaying $\tau$-leptons ($\tau_{\text{had}}$). This type of categorisation is effectively probing the targeted signal signatures, while helping isolate low-background regions in which any significant excess would constitute a solid probe for new physics. Therefore, this search is performed in the $1\ell$, $2\ell$ and $3\ell$ channels, where the $\tau_{\text{had}}$ channels are used for the definition of signal and validation regions, and the zero $\tau_{\text{had}}$ channels for background estimation and validation. The background estimation and suppression is performed with an older configuration of the Template Fit in a similar way as in the $t\bar{t}W$ analysis. The

main background contributions resemble the ones of the $t\bar{t}W$ analysis, while there is also significant contribution of events containing fake-$\tau_{\text{had}}$ candidates, mostly in $1\ell$ and $2\ell$OS channels. No significant excess is found over the SM expectation value, and upper limits are set on the signal cross section and the branching ratio as a function of the leptoquark mass. The upper limits on the cross section correspond to lower limits in leptoquark mass. The expected and observed 95% CL lower limits on the mass of scalar leptoquarks $m_{\text{LQ}_3^{\text{d}}}$ assuming a branching ratio of ($\mathcal{B} = 0.5$) $\mathcal{B} = 1$ are found to be (1.19) 1.41 TeV and (1.22) 1.43 TeV, respectively. The expected and observed 95% CL lower limits on the mass of vector leptoquarks $m_{\tilde{U}_1}$ assuming a branching ratio of $\mathcal{B} = 1$ are both found to be 1.53 TeV in the minimal coupling scenario and 1.81 TeV in the Yang-Mills coupling scenario.

The results of $t\ell t\ell$ and $t\tau t\tau$ searches are part of a wider ATLAS program for leptoquark searches with numerous analyses using the ATLAS full Run-2 dataset, covering a wide range of leptoquark production and decay modes. These results discussed in this dissertation contributed to some of the main inputs used in a common leptoquark combination effort, where several leptoquark searches were combined according to their targeted leptoquark type. This effort resulted in a significant improvement of the current limits on leptoquark mass, increasing the excluded area of potential leptoquark production. Although there was no discovery in the $t\ell t\ell$ and $t\tau t\tau$ searches, the limits calculated in both analyses were the most stringent ones compared to other ATLAS and CMS searches at the time of the writing. At the same time the $t\tau t\tau$ search was the first dedicated ATLAS analysis in this final state paving the way for future searches with $\tau_{\text{had}}$ candidates. The inclusion of $\tau_{\text{had}}$ candidates was avoided in the past due to poor reconstruction and identification efficiencies, something that was greatly improved with the development of the tau RNN ID method.

The results of the $t\bar{t}W$ cross-section measurement together with the results of the leptoquark searches both cover different holes in the particle-physics puzzle that physicists try to understand throughout the years. The $t\bar{t}W$-like excess observed in data and the persistence of the $B$-meson anomalies along with the anomalous muon magnetic moment show that definitely this is not the end of the road for particle physics. More broadly, these findings combined with recent observations in physics concerning the neutrino masses, dark matter, and so on, are further questioning the validity of the SM at a more fundamental level opening a window to BSM physics scenarios. The LHC and the ATLAS experiment will continue to

collect data at 13.6 TeV and 14 TeV in the coming years. The LHC has recently resumed operations with the Run-3 $pp$ collision programme already underway and aiming to reach an unprecedented total integrated luminosity of about 300 $\text{fb}^{-1}$, initiating an era of potential fascinating discoveries and further understanding of how the universe works.

# Appendix A

# Test-beam results of electron analysis on Tile calorimeter

The results shown in this section correspond to electron and positron runs taken during the test-beam periods 2017-2021 at CERN. The runs can be browsed from the online Tile calorimeter database, which can be found at the following link: `https://pcata007.cern.ch/tileinfo/runinfo.php`.

The runs were taken with the beam incident to different cells of the long- and extended-barrel modules with an angle of $\theta_{\text{inc}} = \pm 20^{o}$ for various values of beam energy and high-voltage gain. The large offset in the 2018 data is attributed to a potential miscalibration issue, and the 2017 data were reanalysed to validate that the issue was present only in 2018. The ratio $E_{e}^{\text{raw}}/E_{\text{beam}}$ is calculated through the procedure described in Chapter 5, and it corresponds to the correction that should be applied on the EM scale in order the electron response to match the beam energy.

| Run | Cell | $E_{beam}$ [GeV] | HV gain | $E_e^{\text{raw}}/E_{\text{beam}}$ | Offset % |
|---|---|---|---|---|---|
| 614779 | A1 | 20 | 1 | 0.966 | 3.4 |
| 615380 | A1 | 20 | 5 | 0.961 | 3.9 |
| 615406 | A1 | 50 | 5 | 0.962 | 3.8 |
| 614778 | A2 | 20 | 1 | 0.971 | 2.9 |
| 615381 | A2 | 20 | 5 | 0.970 | 3.0 |
| 615405 | A2 | 50 | 5 | 0.980 | 2.0 |
| 615409 | A2 | 100 | 5 | 0.976 | 2.4 |
| 614521 | A3 | 20 | 2 | 1.014 | -1.4 |
| 614522 | A3 | 20 | 2 | 1.011 | -1.11 |
| 614527 | A3 | 20 | 2 | 1.013 | -1.3 |
| 614536 | A3 | 20 | 2 | 1.016 | -1.6 |
| 614777 | A3 | 20 | 1 | 0.979 | 2.1 |
| 615382 | A3 | 20 | 5 | 0.982 | 1.8 |
| 615404 | A3 | 50 | 5 | 1.014 | -1.4 |
| 615411 | A3 | 100 | 5 | 0.991 | 0.8 |
| 614776 | A4 | 20 | 1 | 0.992 | 0.8 |
| 615384 | A4 | 20 | 5 | 0.998 | 0.2 |
| 615403 | A4 | 50 | 5 | 1.005 | -0.5 |
| 615413 | A4 | 100 | 5 | 1.009 | -0.9 |
| 614775 | A5 | 20 | 2 | 0.962 | 3.8 |
| 615386 | A5 | 20 | 5 | 0.970 | 3.0 |
| 615402 | A5 | 50 | 5 | 0.983 | 1.7 |
| 615414 | A5 | 100 | 5 | 0.992 | 0.8 |
| 615388 | A6 | 20 | 5 | 0.998 | 0.2 |
| 615400 | A6 | 50 | 5 | 1.011 | -1.1 |
| 615416 | A6 | 100 | 5 | 1.023 | -2.3 |
| 615390 | A7 | 20 | 5 | 0.982 | 1.8 |
| 615399 | A7 | 50 | 5 | 0.988 | 1.2 |
| 615417 | A7 | 100 | 5 | 1.005 | -0.5 |
| 615391 | A8 | 20 | 5 | 0.952 | 4.8 |
| 615398 | A8 | 50 | 5 | 0.973 | 2.7 |
| 615418 | A8 | 100 | 5 | 0.983 | 1.7 |
| 615392 | A9 | 20 | 5 | 0.950 | 5.0 |
| 615396 | A9 | 50 | 5 | 0.968 | 3.2 |
| 615419 | A9 | 100 | 5 | 0.979 | 2.1 |
| 615394 | A10 | 20 | 5 | 0.929 | 7.1 |
| 615395 | A10 | 50 | 5 | 0.939 | 6.1 |

TABLE A.1: Results of the electron analysis with the beam incident to the long barrel (LBC module) taken during the 2017 test beam.

| Run | Cell | $E_{beam}$ [GeV] | HV gain | $E_e^{\text{raw}}/E_{\text{beam}}$ | Offset % |
|---|---|---|---|---|---|
| 812290 | A2 | 10 | 2 | 0.952 | 4.8 |
| 812306 | A2 | 10 | 5 | 0.928 | 7.2 |
| 812292 | A2 | 20 | 2 | 0.961 | 3.9 |
| 812308 | A2 | 20 | 5 | 0.940 | 6.0 |
| 812294 | A2 | 50 | 2 | 0.953 | 4.7 |
| 812307 | A2 | 50 | 5 | 0.942 | 5.8 |
| 812296 | A2 | 100 | 2 | 0.952 | 4.8 |
| 812305 | A2 | 100 | 5 | 0.944 | 5.6 |
| 811892 | A3 | 10 | 0.5 | 0.978 | 2.2 |
| 811882 | A3 | 10 | 1 | 0.972 | 2.8 |
| 811881 | A3 | 10 | 2 | 0.968 | 3.2 |
| 811868 | A3 | 10 | 5 | 0.944 | 5.6 |
| 811889 | A3 | 20 | 0.5 | 0.975 | 2.5 |
| 811883 | A3 | 20 | 1 | 0.985 | 1.5 |
| 811880 | A3 | 20 | 2 | 0.978 | 2.2 |
| 811871 | A3 | 20 | 5 | 0.964 | 3.6 |
| 811887 | A3 | 50 | 0.5 | 0.983 | 1.7 |
| 811884 | A3 | 50 | 1 | 0.974 | 2.6 |
| 811879 | A3 | 50 | 2 | 0.975 | 2.5 |
| 811873 | A3 | 50 | 5 | 0.970 | 3.0 |
| 811886 | A3 | 100 | 0.5 | 0.987 | 1.3 |
| 811885 | A3 | 100 | 1 | 0.986 | 1.4 |
| 811877 | A3 | 100 | 2 | 0.962 | 3.8 |
| 811874 | A3 | 100 | 5 | 0.982 | 1.8 |

TABLE A.2: Results of the electron analysis with the beam incident to the long barrel (LBC module) taken during the 2018 test beam.

| Run | Cell | $E_{beam}$ [GeV] | HV gain | $E_e^{\text{raw}}/E_{\text{beam}}$ | Offset % |
|---|---|---|---|---|---|
| 812127 | A13 | 10 | 0.5 | 0.924 | 7.6 |
| 812111 | A13 | 10 | 1 | 0.912 | 8.8 |
| 812106 | A13 | 10 | 2 | 0.912 | 8.8 |
| 812084 | A13 | 10 | 5 | 0.901 | 9.9 |
| 812125 | A13 | 20 | 0.5 | 0.930 | 7.0 |
| 812112 | A13 | 20 | 1 | 0.931 | 6.9 |
| 812104 | A13 | 20 | 2 | 0.931 | 6.9 |
| 812085 | A13 | 20 | 5 | 0.924 | 7.6 |
| 812123 | A13 | 50 | 0.5 | 0.936 | 6.4 |
| 812115 | A13 | 50 | 1 | 0.936 | 6.4 |
| 812103 | A13 | 50 | 2 | 0.929 | 7.1 |
| 812086 | A13 | 50 | 5 | 0.930 | 7.0 |
| 812120 | A13 | 100 | 0.5 | 0.925 | 7.5 |
| 812117 | A13 | 100 | 1 | 0.925 | 7.5 |
| 812100 | A13 | 100 | 2 | 0.917 | 8.3 |
| 812095 | A13 | 100 | 5 | 0.920 | 8.0 |
| 812073 | A14 | 10 | 0.5 | 0.907 | 9.3 |
| 812065 | A14 | 10 | 1 | 0.911 | 8.9 |
| 812055 | A14 | 10 | 2 | 0.911 | 8.9 |
| 812045 | A14 | 10 | 5 | 0.902 | 9.8 |
| 812078 | A14 | 20 | 0.5 | 0.919 | 8.1 |
| 812066 | A14 | 20 | 1 | 0.935 | 6.5 |
| 812056 | A14 | 20 | 2 | 0.931 | 6.9 |
| 812079 | A14 | 50 | 0.5 | 0.934 | 6.6 |
| 812067 | A14 | 50 | 1 | 0.941 | 5.9 |
| 812057 | A14 | 50 | 2 | 0.944 | 5.6 |
| 812049 | A14 | 50 | 5 | 0.944 | 5.6 |
| 812081 | A14 | 100 | 0.5 | 0.908 | 9.2 |
| 812069 | A14 | 100 | 1 | 0.911 | 8.9 |
| 812059 | A14 | 100 | 2 | 0.907 | 9.3 |
| 812051 | A14 | 100 | 5 | 0.906 | 9.4 |
| 812024 | A15 | 10 | 2 | 0.929 | 7.1 |
| 812012 | A15 | 10 | 5 | 0.903 | 9.7 |
| 812022 | A15 | 20 | 2 | 0.937 | 6.3 |
| 812013 | A15 | 20 | 5 | 0.916 | 8.4 |
| 812021 | A15 | 50 | 2 | 0.942 | 5.8 |
| 812014 | A15 | 50 | 5 | 0.936 | 6.4 |
| 812019 | A15 | 100 | 2 | 0.941 | 5.9 |
| 812016 | A15 | 100 | 5 | 0.939 | 6.1 |
| 811998 | A16 | 10 | 2 | 0.864 | 13.6 |
| 811987 | A16 | 10 | 5 | 0.867 | 13.3 |
| 811999 | A16 | 20 | 2 | 0.889 | 11.1 |
| 811990 | A16 | 20 | 5 | 0.897 | 10.3 |
| 812000 | A16 | 50 | 2 | 0.909 | 9.1 |
| 811991 | A16 | 50 | 5 | 0.904 | 9.6 |
| 812002 | A16 | 100 | 2 | 0.917 | 8.3 |
| 811994 | A16 | 100 | 5 | 0.912 | 8.8 |

TABLE A.3: Results of the electron analysis with the beam incident to the extended barrel (EBC module) taken during the 2018 test beam.

| Run | Cell | $E_{beam}$ [GeV] | HV gain | $E_e^{\text{raw}}/E_{\text{beam}}$ | Offset % |
|---|---|---|---|---|---|
| 2110258 | A4 | 10 | 1 | 0.994 | 0.6 |
| 2110251 | A4 | 20 | 1 | 1.002 | -0.2 |
| 2110289 | A4 | 50 | 1 | 1.001 | -0.1 |
| 2110325 | | | | | |
| 2110342 | | | | | |
| 2110344 | A4 | 100 | 1 | 1.006 | -0.6 |
| 2110362 | | | | | |
| 2110364 | | | | | |
| 2110382 | | | | | |
| 2110266 | A5 | 10 | 1 | 0.990 | 1.0 |
| 2110250 | A5 | 20 | 1 | 1.003 | -0.3 |
| 2110287 | A5 | 50 | 1 | 0.996 | 0.4 |
| 2110327 | | | | | |
| 2110340 | | | | | |
| 2110346 | A5 | 100 | 1 | 1.018 | -1.8 |
| 2110360 | | | | | |
| 2110366 | | | | | |
| 2110380 | | | | | |
| 2110264 | A6 | 10 | 1 | 0.971 | 2.9 |
| 2110249 | A6 | 20 | 1 | 0.976 | 2.4 |
| 2110286 | A6 | 50 | 1 | 0.987 | 1.3 |
| 2110329 | | | | | |
| 2110338 | | | | | |
| 2110348 | A6 | 100 | 1 | 0.994 | 0.6 |
| 2110358 | | | | | |
| 2110367 | | | | | |
| 2110379 | | | | | |
| 2110267 | A7 | 10 | 1 | 0.948 | 5.2 |
| 2110247 | A7 | 20 | 1 | 0.964 | 3.6 |
| 2110285 | A7 | 50 | 1 | 0.981 | 1.9 |
| 2110330 | | | | | |
| 2110336 | | | | | |
| 2110350 | A7 | 100 | 1 | 0.988 | 1.2 |
| 2110357 | | | | | |
| 2110368 | | | | | |
| 2110377 | | | | | |
| 2110269 | A8 | 10 | 1 | 0.950 | 5.0 |
| 2110246 | A8 | 20 | 1 | 0.976 | 2.4 |
| 2110283 | A8 | 50 | 1 | 0.988 | 1.2 |
| 2110331 | | | | | |
| 2110334 | | | | | |
| 2110352 | A8 | 100 | 1 | 0.995 | 0.5 |
| 2110370 | | | | | |
| 2110376 | | | | | |
| 2110271 | A9 | 10 | 1 | 0.967 | 3.3 |
| 2110245 | A9 | 20 | 1 | 0.988 | 1.2 |
| 2110281 | A9 | 50 | 1 | 0.982 | 1.8 |
| 2110332 | | | | | |
| 2110333 | | | | | |
| 2110353 | A9 | 100 | 1 | 0.997 | 0.3 |
| 2110355 | | | | | |
| 2110372 | | | | | |
| 2110374 | | | | | |

TABLE A.4: Results of the electron analysis with the beam incident to the long barrel (LBC module) taken during the September 2021 test beam. The 100 GeV runs are taken with the same settings and are analysed together in order to increase the statistics.

| Run | Cell | $E_{beam}$ [GeV] | HV gain | $E_e^{\text{raw}}/E_{\text{beam}}$ | Offset % |
|---|---|---|---|---|---|
| 2111025 | A2 | 10 | 2 | 0.964 | 3.593 |
| 2111045 | A2 | 20 | 2 | 0.980 | 1.998 |
| 2111073 | A2 | 50 | 2 | 0.990 | 0.980 |
| 2111295 | A2 | 100 | 2 | 0.982 | 1.744 |
| 2111330 | A2 | 150 | 2 | 0.970 | 2.984 |
| 2111026 | A3 | 10 | 2 | 0.976 | 2.4 |
| 2111049 | A3 | 20 | 2 | 0.999 | 0.1 |
| 2111071 | A3 | 50 | 2 | 0.990 | 1.0 |
| 2111296 | A3 | 100 | 2 | 0.994 | 0.6 |
| 2111321 | A3 | 150 | 2 | 0.992 | 0.8 |
| 2111028 | A4 | 10 | 2 | 0.964 | 3.6 |
| 2111051 | A4 | 20 | 2 | 0.984 | 1.6 |
| 2111069 | A4 | 50 | 2 | 0.975 | 2.5 |
| 2111298 | A4 | 100 | 2 | 0.981 | 1.9 |
| 2111323 | A4 | 150 | 2 | 0.980 | 2.0 |
| 2111029 | A5 | 10 | 2 | 0.979 | 2.1 |
| 2111053 | A5 | 20 | 2 | 0.995 | 0.5 |
| 2111068 | A5 | 50 | 2 | 0.998 | 0.2 |
| 2111299 | A5 | 100 | 2 | 0.997 | 0.3 |
| 2111324 | A5 | 150 | 2 | 0.987 | 1.3 |
| 2111031 | A6 | 10 | 2 | 0.943 | 5.7 |
| 2111054 | A6 | 20 | 2 | 0.961 | 3.9 |
| 2111066 | A6 | 50 | 2 | 0.957 | 4.3 |
| 2111301 | A6 | 100 | 2 | 0.969 | 3.1 |
| 2111325 | A6 | 150 | 2 | 0.964 | 3.6 |
| 2111033 | A7 | 10 | 2 | 0.944 | 5.6 |
| 2111055 | A7 | 20 | 2 | 0.969 | 3.1 |
| 2111064 | A7 | 50 | 2 | 0.966 | 3.4 |
| 2111302 | A7 | 100 | 2 | 0.971 | 2.9 |
| 2111327 | A7 | 150 | 2 | 0.972 | 2.8 |
| 2111034 | A8 | 10 | 2 | 0.945 | 5.5 |
| 2111057 | A8 | 20 | 2 | 0.976 | 2.4 |
| 2111062 | A8 | 50 | 2 | 0.983 | 1.7 |
| 2111304 | A8 | 100 | 2 | 0.982 | 1.8 |
| 2111328 | A8 | 150 | 2 | 0.979 | 2.1 |
| 2111036 | A9 | 10 | 2 | 0.947 | 5.3 |
| 2111059 | A9 | 20 | 2 | 0.966 | 3.4 |
| 2111060 | A9 | 50 | 2 | 0.976 | 2.4 |
| 2111305 | A9 | 100 | 2 | 0.980 | 2.0 |
| 2111329 | A9 | 150 | 2 | 0.972 | 2.8 |

TABLE A.5: Results of the electron analysis with the beam incident to the long barrel (LBC module) taken during the November 2021 test beam.

# Appendix B

# Unfolding optimisations and setup

## B.1 Parametrisation setups

Four parametrisation setups are used in the $t\bar{t}W$ differential cross-section measurement. There are two setups to measure the differential cross section per bin in the unfolded distribution and two analogous setups used for the unfolding of the $t\bar{t}W$ relative charge asymmetry, $A_C^R$. The parametrisations are implemented by redefining the $t\bar{t}W$ NFs in the likelihood function using the `Expressions` block of `TRExFitter`.

1. The first parametrisation (labelled as "differential") corresponds to the standard configuration with per-bin cross-section NFs in all fiducial regions $2\ell$SS $++/--$ and $3\ell$ $+/-$ described by the formula

$$\{\mu_j^{2\ell SS++}\}_{j=1}^m,\ \{\mu_j^{2\ell SS++}\}_{j=1}^m,\ \{\mu_j^{3\ell+}\}_{j=1}^m,\ \{\mu_j^{3\ell-}\}_{j=1}^m,$$

   where $m$ denotes the total number of bins of the particle-level distribution per region, without necessarily being the same between $2\ell$SS and $3\ell$ channels. This parametrisation setup is the standard one used for unfolding in the `TRExFitter` framework.

2. The second parametrisation (labelled as "inclusive") is defined by parametrising the NF of the first bin in each of the $2\ell$SS $++/--$ and $3\ell$ $+/-$ regions in

terms of the rest of cross-section NFs, such that the parameters of interest are

$$\{\mu_j^{2\ell SS++}\}_{j=2}^m,\ \{\mu_j^{2\ell SS++}\}_{j=2}^m,\ \{\mu_j^{3\ell+}\}_{j=2}^m,\ \{\mu_j^{3\ell-}\}_{j=2}^m$$

and

$$\mu^{2\ell SS++},\ \mu^{2\ell SS--},\ \mu^{3\ell+},\ \mu^{3\ell-}.$$

The parametrisation is described by the relation

$$\mu_1 = \frac{1}{N_1}\left(\mu N - \sum_{j=2}^{m} \mu_j N_j\right), \tag{B.1}$$

where $\mu_j$ is the NF of the $j^{\text{th}}$ bin in one of the four fiducial regions and $\mu$ is the inclusive NF for that region. The number of events in the $j^{\text{th}}$ bin of the particle-level signal distribution is denoted as $N_j$. Equation B.1 is obtained from the expression for the weighted average of $\mu$ defined as

$$\mu = \frac{1}{N}\left(\sum_{j=1}^{m} \mu_j N_j\right). \tag{B.2}$$

3. The relative charge asymmetry $A_C^R$ (introduced in Equation 9.9) can be parametrised as

$$A_C^R = \frac{\mu^+ N^+ - \mu^- N^-}{\mu^+ N^+ + \mu^- N^-}, \tag{B.3}$$

individually for $2\ell$SS and $3\ell$ channels, where $N^{+/-}$ corresponds to the number of events with positive or negative total lepton charge, respectively.

Using this formula the per-bin cross-section NFs can be redefined in the charge-split regions as

$$\begin{aligned} \mu_j^- &= \frac{1}{2}\frac{\mu_j N_j}{N_j^-}\left(1 - A_{C,j}^R\right), \\ \mu_j^+ &= \frac{1}{2}\frac{\mu_j N_j}{N_j^+}\left(1 + A_{C,j}^R\right). \end{aligned} \tag{B.4}$$

This configuration (labelled as "differential asymmetry") allows the charge-inclusive asymmetry rates to be extracted through the $\mu_j$, but it is required that the charge-split regions have the same binning. The parameters of interest for this setup are

$$\{\mu_j^{2\ell SS}\}_{j=1}^m,\ \{A_{C,j}^{R,2\ell SS}\}_{j=1}^m,\ \{\mu_j^{3\ell}\}_{j=1}^m,\ \{A_{C,j}^{R,3\ell}\}_{j=1}^m,$$

and the $t\bar{t}W$ NFs used to correlate the $t\bar{t}W$ component between the SR and CRs is defined as

$$\mu^{\pm} = \frac{1}{2N^{\pm}} \left[ \sum_{j=1}^{m} \mu_j N_j (1 \pm A_{C,j}^{R}) \right]. \tag{B.5}$$

4. In this parametrisation (labelled as "inclusive asymmetry") the cross-section NF of the first truth bin of a particle-level distribution can be expressed in terms of $A_C^R$ in a similar way as in parametrisation (2) as

$$\begin{aligned} \mu_1^{-} &= \frac{1}{2N_1^{-}} \left[ \mu N (1 - A_C^R) - \sum_{j=2}^{m} \mu_j N_j (1 - A_{C,j}^{R}) \right], \\ \mu_1^{+} &= \frac{1}{2N_1^{+}} \left[ \mu N (1 + A_C^R) - \sum_{j=2}^{m} \mu_j N_j (1 + A_{C,j}^{R}) \right]. \end{aligned} \tag{B.6}$$

Therefore, the parameters of interest in this configuration are

$$\{\mu_j^{2\ell SS}\}_{j=2}^{m},\ \{A_{C,j}^{R,2\ell SS}\}_{j=2}^{m},\ \{\mu_j^{3\ell}\}_{j=2}^{m},\ \{A_{C,j}^{R,3\ell}\}_{j=2}^{m},$$

and

$$\mu^{2\ell SS},\ A_C^{R,2\ell SS},\ \mu^{3\ell},\ A_C^{R,3\ell}.$$

The most interesting results are following the differential parametrisations (1) and (3). The inclusive parametrisations (2) and (4) are important since instead of providing the first truth bin of each fiducial region they provide additionally the inclusive $t\bar{t}W$ NFs based on which the $t\bar{t}W$ contribution in CRs is normalised. Moreover, the inclusive $t\bar{t}W$ NFs can be compared to the ones from the inclusive measurement as a validation check.

## B.2 Binning optimisation

Since PLU is a binned unfolding technique, the binning of the continuous variables is chosen based on certain criteria. The same binning is adopted between the particle-level and detector-level distributions to avoid potential underconstraints in the fit in the case of $N_{\text{bins}}^{\text{det.}} < N_{\text{bins}}^{\text{fid.}}$.

The binning-optimisation process starts with a distribution following a fine binning of 200 bins. The distributions are then rebinned based on the cumulative $t\bar{t}W$

distribution in order to have comparable fraction of $t\bar{t}W$ events and maintain a fraction of 60% of the total events in the diagonal elements of the migration matrix at each particle-level bin. The bins are merged sequentially from left to right until the maximum statistical uncertainty is reduced to 10%, 12%, 15%, and 16% in the $2\ell\text{SS}++$, $2\ell\text{SS}--$, $3\ell+$, and $3\ell-$ regions, respectively. The binning acquired from this procedure is manually rounded aiming for similar yields and uncertainty between the charge-split regions of the $2\ell$SS and $3\ell$ channels.

The steps of the binning-optimisation process are illustrated in Figure B.1 for the $p_{\text{T}}$ of the leading jet ($p_{\text{T},j_0}$), an observable that is not used in the unfolding in the end, but the process is equivalent for the rest of the observables. The optimised binning of the observables selected for unfolding is shown in Table 9.9 of Section 9.7.4. The binning is also optimised at the first stages of the analysis for the rest of the observables, with the optimal binning shown in Tables B.1 - B.3.

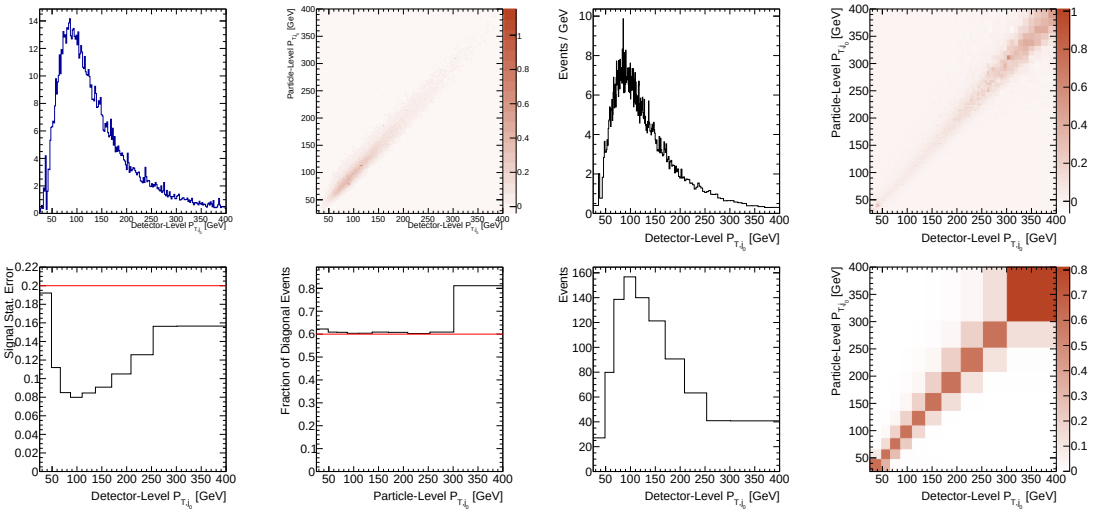



FIGURE B.1: Binning-optimisation process demonstrated using the $p_{\text{T},j_0}$ observable in the $2\ell\text{SS}++$ region. The $t\bar{t}W$ detector-level distribution together with the corresponding migration matrix is shown for the fine and optimal adaptive binning (top). The statistical uncertainty on the signal-plus-background prediction and the fraction of events in the diagonal elements of the migration matrix are also shown for the fine and optimal binning (bottom). The final merging of the bins in this observable is dominated by the limited detector resolution.

| Observable | Region | Binning |
|---|---|---|
| $p_{\mathrm{T},\ell_0^{\mathrm{SS}}}$ [GeV] | 2$\ell$SS | [20, 40, 50, 60, 70, 85, 100, 120, 150] |
| | 3$\ell$ | [15, 45, 60, 75, 95, 125, 150] |
| $p_{\mathrm{T},\ell_1^{\mathrm{SS}}}$ [GeV] | 2$\ell$SS | [20, 25, 30, 35, 40, 50, 60, 75, 100] |
| | 3$\ell$ | [15, 20, 27.5, 35, 45, 55, 80] |
| $p_{\mathrm{T},\ell^{\mathrm{OS}}}$ [GeV] | 2$\ell$SS | [0, 20] |
| | 3$\ell$ | [10, 20, 30, 45, 60, 80, 100] |
| $p_{\mathrm{T},j_0}$ [GeV] | 2$\ell$SS | [25, 65, 85, 110, 135, 170, 215, 300] |
| | 3$\ell$ | [25, 60, 80, 100, 130, 175, 250] |
| $p_{\mathrm{T},j_1}$ [GeV] | 2$\ell$SS | [25, 45, 60, 80, 100, 130, 175] |
| | 3$\ell$ | [25, 40, 55, 75, 100, 140] |
| $p_{\mathrm{T},b_0}$ [GeV] | 2$\ell$SS | [25, 40, 60, 90, 150, 300] |
| | 3$\ell$ | [25, 40, 60, 90, 150, 300] |
| $\lvert\eta_{\ell_0^{\mathrm{SS}}}\rvert$ | 2$\ell$SS | [0, 0.2, 0.4, 0.6, 0.85, 1.1, 1.35, 1.75, 2.5] |
| | 3$\ell$ | [0, 0.25, 0.5, 0.75, 1.05, 1.4, 2.5] |
| $\lvert\eta_{\ell_1^{\mathrm{SS}}}\rvert$ | 2$\ell$SS | [0, 0.2, 0.4, 0.6, 0.85, 1.1, 1.35, 1.75, 2.5] |
| | 3$\ell$ | [0, 0.25, 0.5, 0.75, 1.05, 1.4, 2.5] |
| $\lvert\eta_{\ell^{\mathrm{OS}}}\rvert$ | 2$\ell$SS | [0, 0.5] |
| | 3$\ell$ | [0, 0.25, 0.5, 0.75, 1.05, 1.4, 2.5] |
| $\lvert\eta_{j_0}\rvert$ | 2$\ell$SS | [0, 0.2, 0.4, 0.6, 0.8, 1.0, 1.25, 1.5, 2.5] |
| | 3$\ell$ | [0, 0.25, 0.5, 0.75, 1.1, 1.5, 2.5] |
| $\lvert\eta_{j_1}\rvert$ | 2$\ell$SS | [0, 0.2, 0.4, 0.6, 0.8, 1.0, 1.25, 1.5, 2.5] |
| | 3$\ell$ | [0, 0.25, 0.5, 0.75, 1.1, 1.5, 2.5] |
| $\lvert\eta_{b_0}\rvert$ | 2$\ell$SS | [0, 0.2, 0.4, 0.6, 0.8, 1.0, 1.3, 1.65, 2.5] |
| | 3$\ell$ | [0, 0.25, 0.5, 0.75, 1.1, 1.5, 2.5] |
| $\lvert\eta_{\ell}^{\mathrm{max}}\rvert$ | 2$\ell$SS | [0, 0.76, 0.95, 1.15, 1.29, 1.41, 1.59, 1.77, 1.9, 2.04, 2.19, 2.5] |
| | 3$\ell$ | [0, 0.76, 0.95, 1.15, 1.29, 1.41, 1.59, 1.77, 1.9, 2.04, 2.19, 2.5] |

TABLE B.1: Optimised binning for single-jet and lepton observables.

| Observable | Region | Binning |
|---|---|---|
| $E_{\mathrm{T}}^{\mathrm{miss}}$ [GeV] | 2$\ell$SS | [0, 45, 85, 135, 200] |
| | 3$\ell$ | [0, 45, 80, 120, 200] |
| $H_{\mathrm{T}}$ [GeV] | 2$\ell$SS | [90, 245, 300, 360, 425, 500, 580, 725, 1000] |
| | 3$\ell$ | [90, 250, 350, 500, 750, 1000] |
| $H_{\mathrm{T}}^{\mathrm{vis}}$ [GeV] | 2$\ell$SS | [60, 140, 200, 300, 600] |
| | 3$\ell$ | [90, 200, 250, 350, 600] |
| $H_{\mathrm{T}}^{\mathrm{vis,\,min}}$ [GeV] | 2$\ell$SS | [60, 140, 170, 200, 240, 280, 340, 600] |
| | 3$\ell$ | [90, 190, 235, 275, 325, 400, 600] |
| $\lvert\Delta\eta_{\ell_0^{\mathrm{SS}}\ell^{\mathrm{OS}}}\rvert$ | 2$\ell$SS | [0, 0.5] |
| | 3$\ell$ | [0, 0.2, 0.4, 0.7, 0.95, 1.35, 2.0] |
| $\lvert\Delta\eta_{\ell_1^{\mathrm{SS}}\ell^{\mathrm{OS}}}\rvert$ | 2$\ell$SS | [0, 0.5] |
| | 3$\ell$ | [0, 0.25, 0.5, 0.7, 1.0, 1.4, 2.0] |
| $\lvert\Delta\phi_{\ell_0^{\mathrm{SS}}\ell^{\mathrm{OS}}}\rvert/\pi$ | 2$\ell$SS | [0, 0.15, 0.3] |
| | 3$\ell$ | [0, 0.2, 0.4, 0.55, 0.7, 0.85, 1.0] |
| $\lvert\Delta\phi_{\ell_1^{\mathrm{SS}}\ell^{\mathrm{OS}}}\rvert/\pi$ | 2$\ell$SS | [0, 0.1] |
| | 3$\ell$ | [0, 0.2, 0.4, 0.55, 0.7, 0.85, 1.0] |
| $m_{\ell_0^{\mathrm{SS}}\ell^{\mathrm{OS}}}$ [GeV] | 2$\ell$SS | [0, 20] |
| | 3$\ell$ | [12, 50, 75, 110, 130, 170, 220] |
| $m_{\ell_1^{\mathrm{SS}}\ell^{\mathrm{OS}}}$ [GeV] | 2$\ell$SS | [0, 20] |
| | 3$\ell$ | [12, 30, 50, 70, 100, 130] |

TABLE B.2: Optimised binning for event-level and dilepton observables.

| Observable | Region | Binning |
|---|---|---|
| $\Delta R_{\ell j}^{\mathrm{min}}$ | 2$\ell$SS | [0.1, 0.5, 0.6, 0.75, 0.9, 1.05, 1.5] |
| | 3$\ell$ | [0.1, 0.5, 0.7, 0.8, 1.0, 1.5] |
| $\Delta R_{\ell^{\mathrm{OS}} j}^{\mathrm{min}}$ | 2$\ell$SS | [0.0, 0.5] |
| | 3$\ell$ | [0.1, 0.7, 1.0, 1.25, 1.5, 1.9, 2.5] |
| $\Delta R_{\ell_0^{\mathrm{SS}} j}^{\mathrm{min}}$ | 2$\ell$SS | [0.1, 0.65, 0.85, 1.05, 1.25, 1.45, 1.75, 2.5] |
| | 3$\ell$ | [0.1, 0.75, 1.0, 1.25, 1.6, 2.0, 2.5] |
| $\Delta R_{\ell_1^{\mathrm{SS}} j}^{\mathrm{min}}$ | 2$\ell$SS | [0.1, 0.65, 0.85, 1.05, 1.25, 1.45, 1.75, 2.5] |
| | 3$\ell$ | [0.1, 0.75, 1.0, 1.25, 1.6, 2.0, 2.5] |
| $\Delta R_{j_0 j_1}$ | 2$\ell$SS | [0.25, 1.1, 1.7, 2.15, 2.5, 2.8, 3.0, 3.3, 4.0] |
| | 3$\ell$ | [0.25, 1.0, 2.0, 2.5, 3.0, 3.5, 4.0] |
| $m_{jj^{\mathrm{fwd}}}^{\mathrm{max}}$ [GeV] | 2$\ell$SS | [15, 115, 160, 235, 325, 450, 550] |
| | 3$\ell$ | [15, 120, 175, 250, 350, 550] |

TABLE B.3: Optimised binning for lepton- and jet-related observables.

## B.3 Regularisation optimisation

Following the binning optimisation and the final choice on the fiducial space selection, an optimisation procedure is performed, where the $\tau$ regularisation parameters are optimised based on generation of pseudo-experiments with statistical bootstrapping. Due to the different signal over background ratios and statistical properties in each of the four fiducial regions ($2\ell$SS $++$ / $--$, $3\ell$ $+/-$), the optimisation is performed separately for each region. A set of 2000 pseudo-data samples is generated in the signal region following a signal-plus-background distribution smeared with Poisson statistics. This is repeated for each analysis channel and observable. The unfolding of each pseudo-experiment is performed including only statistical uncertainties and several metrics are calculated from this procedure. The $\tau$ parameters are scanned over a range of values. The median over the pseudo-experiments and the mean over the prediction in the unfolded bins are estimated and plotted for each scanned $\tau$ parameter and metric. The optimal $\tau$ value is identified as the largest possible value that keeps the $\chi^2/N_{\text{bins}}$ relatively stable with respect to the particle-level distribution (truth). This $\tau$ value is expected to maximally suppress the statistical fluctuation impact keeping bias at acceptable levels.

The metrics considered in this optimisation are summarised below:

- $\chi^2 = \Delta x_i V_{ij}^{-1} \Delta x_j$, where $\Delta x_i$ stands for the difference between the unfolded template and particle-level template in bin $i$ and $V_{ij}$ corresponds to the covariance matrix of the cross-section NFs. This metric is estimated by considering the particle-level template as the prior (Sherpa-2.2.10) or truth (aMC@NLO/MG) sample and acquiring the $V_{ij}$ matrix directly from TRExFitter or calculating it from pseudo-experiments (toys).

- Global correlation coefficient $\rho$, used to quantify the diagonality of the covariance matrix that is calculated with toys. It is defined as

$$\rho = \left\langle \sqrt{1 - (V_{ii} V_{ii}^{-1})^{-1}} \right\rangle_{\text{bins}} .$$

- Average relative uncertainty $\sigma$ from all bins calculated both from toys and using the TRExFitter covariance matrix. The standard deviation of the relative uncertainties is also calculated using toys.

- Average absolute bias of the unfolded distribution against its prior and the truth particle-level distribution estimated over all bins. The median over toys is taken either before or after the absolute value. In the case that the absolute value is taken before the median, it includes statistical effects, whereas statistical effects are marginalised when the median is taken before the absolute value and reproduces the results of an Asimov fit.
- Rate of unfolded results having at least one negative unfolded bin. Ideally this should be as low as possible.

The pseudo-data generation uses the aMC@NLO (NLO QCD)/MG (EW) + Pythia-8 $t\bar{t}W$ sample, either by using directly the distribution of this sample at detector-level (`altReco`) or by folding the particle-level distribution with the response matrix from Sherpa-2.2.10 (`altTruth`). The `altReco` configuration contains some bias due to the different response matrix for each generator, which is accounted for as an additional systematic uncertainty. The `altTruth` configuration includes only the bias originating from the choice to use a particle-level template from a specific generator versus another, which is not taken into account when the response matrix of an alternate MC sample is used. The estimate of the bias concerning the $\hat{\tau}$ choice becomes conservative under the hypothesis that the difference (at second order) of the true $t\bar{t}W$ particle-level distribution in data is comparable between the nominal and alternative MC sample predictions and the difference itself is not significant. If this assumption does not hold, it would mean that the bias is underestimated. The scans over the $\tau$ regularisation parameters are shown for the $N_{\text{jets}}$ and $N_{b-\text{jets}}$ distributions in Figures B.2 - B.5 for both `altTruth` and `altReco` configurations.

As shown in these figures, the increase of $\chi^2$ is observed at similar $\tau$ values between the `altTruth` and `altReco` configurations for all fiducial regions. The same scans are repeated for the rest of the unfolded observables, where the corresponding plots are omitted for brevity. The results of the optimal regularisation $\hat{\tau}$ parameters for each region are summarised in Table B.4.

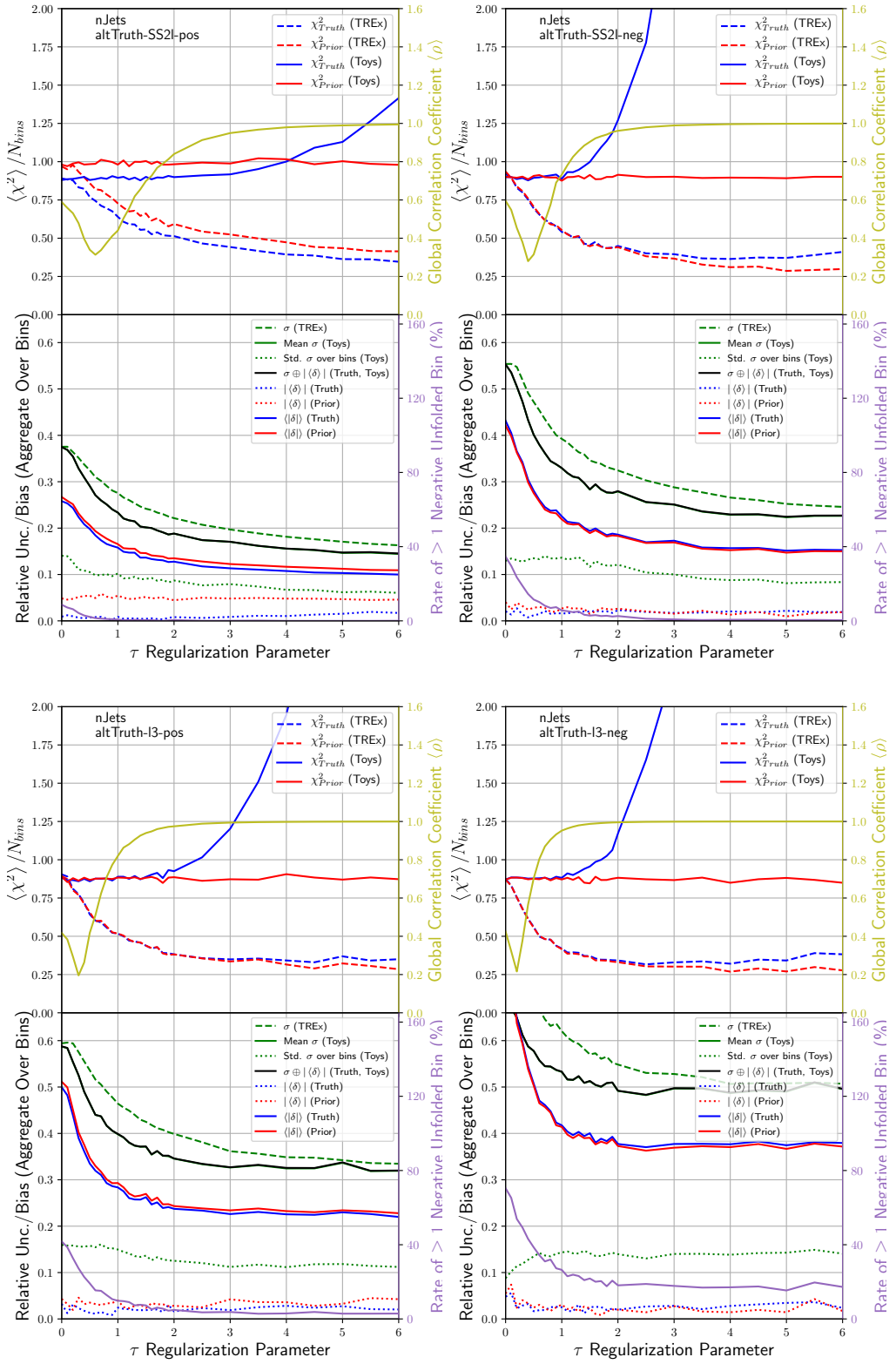



FIGURE B.2: Regularisation $\tau$ scans for $N_{\text{jets}}$ observable in the $2\ell\text{SS}++$ (top left), $2\ell\text{SS}--$ (top right), $3\ell+$ (bottom left), and $3\ell-$ (bottom right) regions using the `altTruth` configuration.

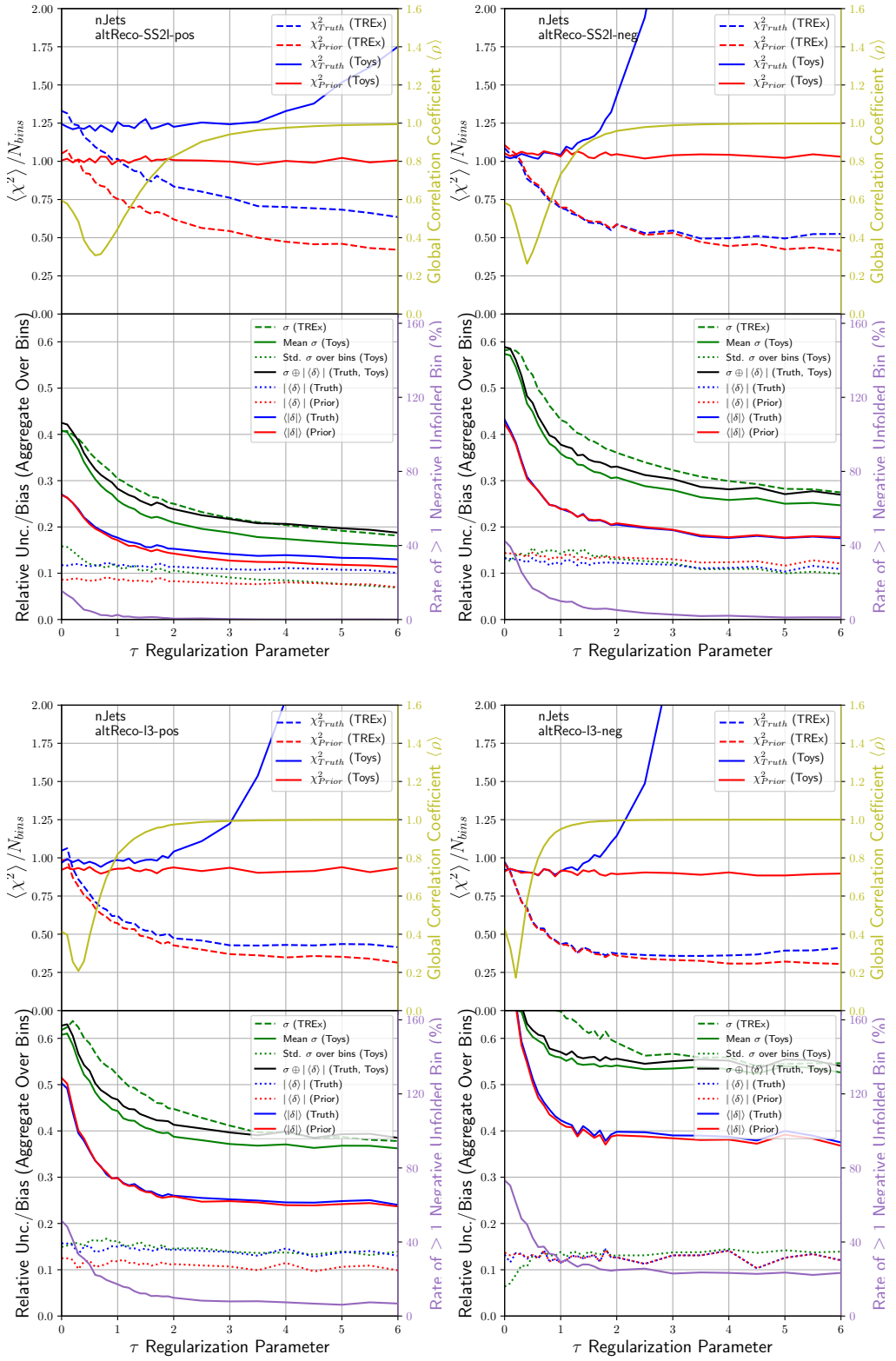



FIGURE B.3: Regularisation $\tau$ scans for $N_{\text{jets}}$ observable in the $2\ell\text{SS}++$ (top left), $2\ell\text{SS}--$ (top right), $3\ell+$ (bottom left), and $3\ell-$ (bottom right) regions using the `altReco` configuration.

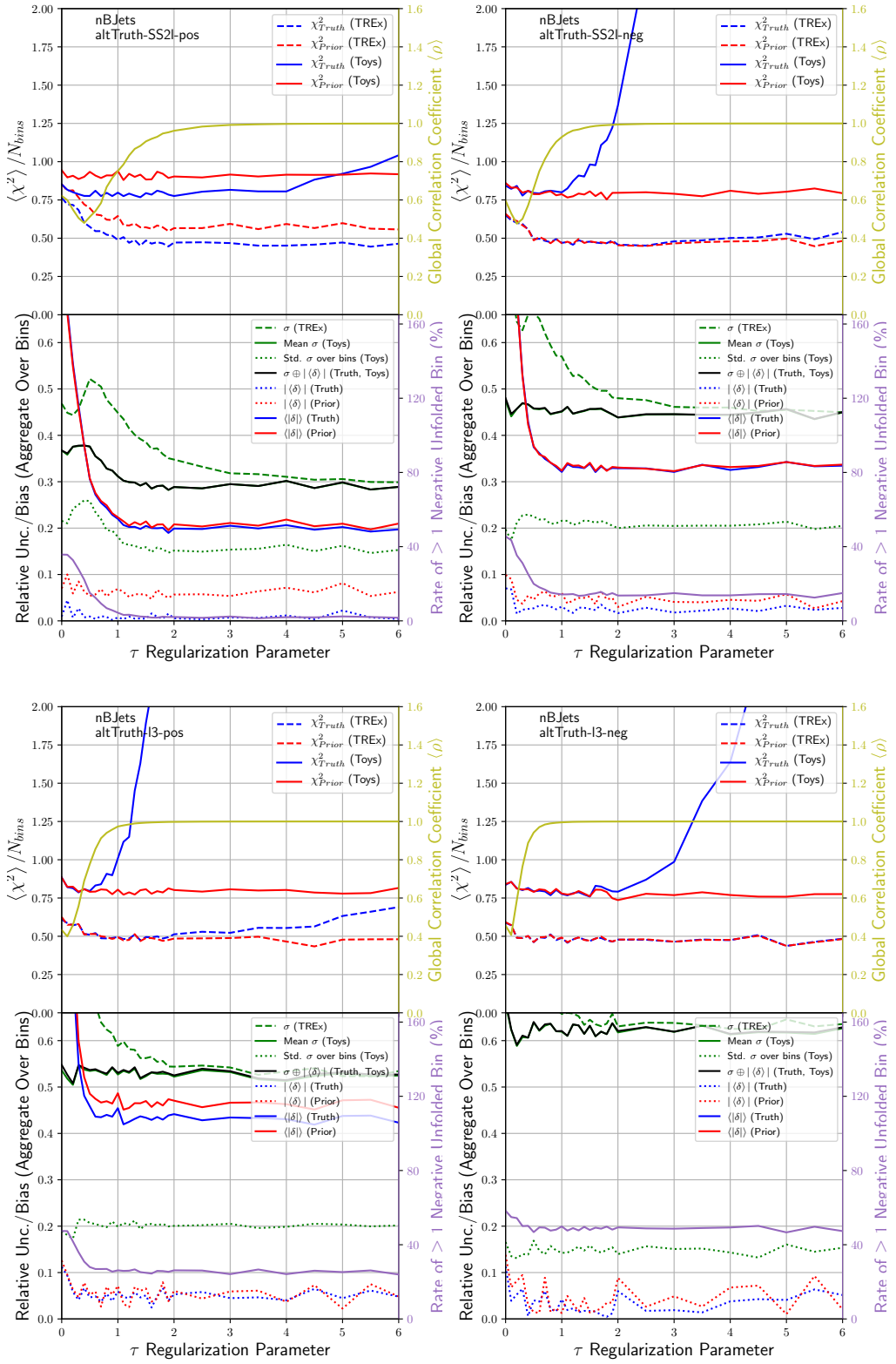



FIGURE B.4: Regularisation $\tau$ scans for $N_{b-\text{jets}}$ observable in the $2\ell\text{SS}++$ (top left), $2\ell\text{SS}--$ (top right), $3\ell+$ (bottom left), and $3\ell-$ (bottom right) regions using the `altTruth` configuration.

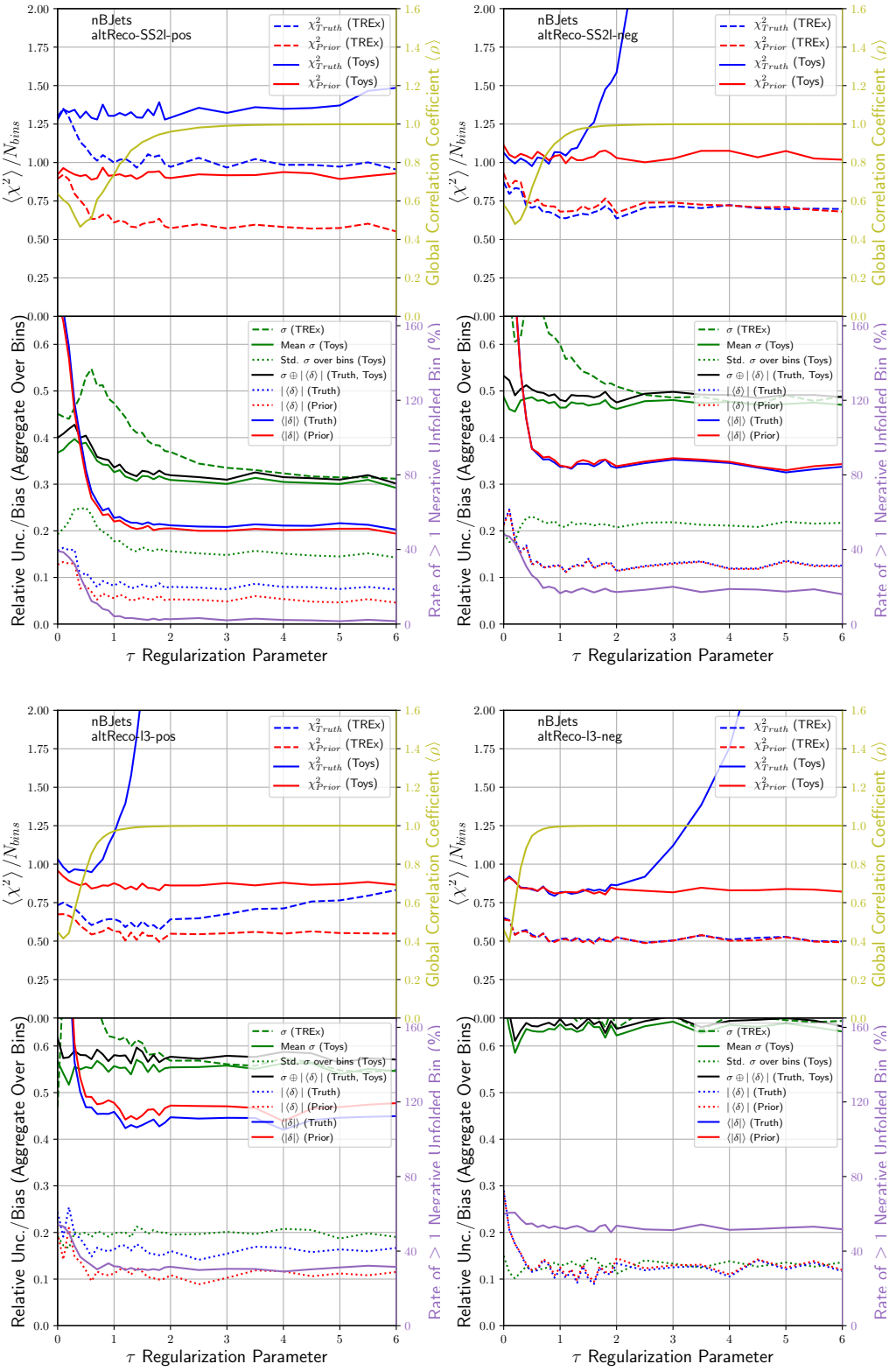



FIGURE B.5: Regularisation $\tau$ scans for $N_{b-\text{jets}}$ observable in the $2\ell\text{SS}++$ (top left), $2\ell\text{SS}--$ (top right), $3\ell+$ (bottom left), and $3\ell-$ (bottom right) regions using the `altReco` configuration.

| Observable | $2\ell\mathrm{SS}++$ | $3\ell+$ | $2\ell\mathrm{SS}--$ | $3\ell-$ |
|---|---|---|---|---|
| $\boldsymbol{N_{\mathbf{jets}}}$ | **3.0** | **1.0** | **1.5** | **1.0** |
| $\boldsymbol{N_{b-\mathbf{jets}}}$ | **4.0** | **1.0** | **0.5** | **1.5** |
| $H_{\mathrm{T}}$ | 2.0 | 3.0 | 2.0 | 1.5 |
| $\boldsymbol{H_{\mathrm{T,\,jets}}}$ | **2.0** | **1.5** | **1.5** | **1.0** |
| $\boldsymbol{H_{\mathrm{T,\,lep}}}$ | **2.0** | **2.0** | **1.6** | **2.0** |
| $H_{\mathrm{T}}^{\mathrm{vis}}$ | 2.0 | 0.7 | 1.0 | 0.5 |
| $H_{\mathrm{T}}^{\mathrm{vis,\,min}}$ | 0.0 | 0.0 | 0.0 | 0.0 |
| $E_{\mathrm{T}}^{\mathrm{miss}}$ | 3.0 | 1.0 | 2.0 | 1.0 |
| $p_{\mathrm{T},\,j_0}$ | 2.0 | 1.8 | 1.5 | 1.0 |
| $p_{\mathrm{T},\,j_1}$ | 1.0 | 1.0 | 2.0 | 0.0 |
| $p_{\mathrm{T},\,b_0}$ | 3.0 | 0.8 | 3.0 | 0.0 |
| $p_{\mathrm{T},\,\ell_0^{\mathrm{SS}}}$ | 2.5 | 2.5 | 2.0 | 0.8 |
| $p_{\mathrm{T},\,\ell_1^{\mathrm{SS}}}$ | 3.0 | 0.0 | 1.9 | 0.0 |
| $p_{\mathrm{T},\,\ell^{\mathrm{OS}}}$ | 0.0 | 1.3 | 0.0 | 2.0 |
| $\lvert\eta_{j_0}\rvert$ | 2.5 | 1.2 | 1.6 | 0.8 |
| $\lvert\eta_{j_1}\rvert$ | 2.0 | 2.5 | 2.0 | 1.2 |
| $\lvert\eta_{b_0}\rvert$ | 2.0 | 2.0 | 1.0 | 0.0 |
| $\lvert\eta_{\ell}^{\mathrm{max}}\rvert$ | 2.0 | 1.2 | 2.0 | 0.0 |
| $\lvert\eta_{\ell_0^{\mathrm{SS}}}\rvert$ | 3.0 | 1.8 | 3.0 | 1.5 |
| $\lvert\eta_{\ell_1^{\mathrm{SS}}}\rvert$ | 3.0 | 4.0 | 3.0 | 0.0 |
| $\lvert\eta_{\ell^{\mathrm{OS}}}\rvert$ | 0.0 | 1.5 | 0.0 | 0.0 |
| $\boldsymbol{m_{\ell_0^{\mathrm{SS}}\ell_1^{\mathrm{SS}}}}$ | **3.5** | **1.0** | **2.5** | **1.5** |
| $m_{\ell_0^{\mathrm{SS}}\ell^{\mathrm{OS}}}$ | 0.0 | 2.0 | 0.0 | 1.0 |
| $m_{\ell_1^{\mathrm{SS}}\ell^{\mathrm{OS}}}$ | 0.0 | 0.5 | 0.0 | 0.2 |
| $m_{\ell_0 b_0}$ | 2.0 | 0.6 | 2.0 | 0.9 |
| $\lvert\eta_{jj^{\mathrm{fwd}}}^{\mathrm{max}}\rvert$ | 4.0 | 2.0 | 2.0 | 1.0 |
| $\boldsymbol{m_{j_0 j_1}}$ | **3.0** | **2.0** | **2.0** | **1.0** |
| $\lvert\Delta\eta_{\ell_0^{\mathrm{SS}}\ell^{\mathrm{OS}}}\rvert$ | 0.0 | 1.5 | 0.0 | 0.0 |
| $\lvert\Delta\eta_{\ell_1^{\mathrm{SS}}\ell^{\mathrm{OS}}}\rvert$ | 0.0 | 2.0 | 0.0 | 1.2 |
| $\boldsymbol{\lvert\Delta\eta_{\ell_0^{\mathrm{SS}}\ell_1^{\mathrm{SS}}}\rvert}$ | **2.0** | **3.0** | **2.5** | **2.2** |
| $\lvert\Delta\phi_{\ell_0^{\mathrm{SS}}\ell^{\mathrm{OS}}}\rvert/\pi$ | 0.0 | 1.0 | 0.0 | 0.0 |
| $\lvert\Delta\phi_{\ell_1^{\mathrm{SS}}\ell^{\mathrm{OS}}}\rvert/\pi$ | 0.0 | 1.0 | 0.0 | 0.0 |
| $\boldsymbol{\lvert\Delta\phi_{\ell_0^{\mathrm{SS}}\ell_0^{\mathrm{SS}}}\rvert/\pi}$ | **2.0** | **0.7** | **1.3** | **0.6** |
| $\Delta R_{\ell j}^{\mathrm{min}}$ | 2.0 | 3.5 | 1.4 | 1.8 |
| $\Delta R_{\ell^{\mathrm{OS}} j}^{\mathrm{min}}$ | 0.0 | 1.6 | 0.0 | 1.0 |
| $\Delta R_{\ell_0\, b_0}$ | 3.0 | 3.0 | 1.5 | 1.5 |
| $\Delta R_{\ell_0^{\mathrm{SS}} j}^{\mathrm{min}}$ | 3.0 | 2.0 | 3.0 | 0.8 |
| $\Delta R_{\ell_1^{\mathrm{SS}} j}^{\mathrm{min}}$ | 3.0 | 2.0 | 3.0 | 0.8 |
| $\Delta R_{j_0 j_1}$ | 3.0 | 1.5 | 2.0 | 0.0 |

TABLE B.4: List of proposed observables to be unfolded and the optimal regularisation parameter $\hat{\tau}$ for these observables in each region. The entries in bold correspond to the selected variables that are unfolded.

The $\chi^2$ parameter is underestimated in the `altTruth` configuration with the TRExFitter option due to the overestimation in total uncertainty for $\tau > 0$. The $\chi^2$ obtained by TRExFitter related to the distribution at particle level is locally minimised at large $\tau$ values in some of the regions because of the competing effects between uncertainty underestimation and bias. However, the $\chi^2$ values in the large $\tau$ region are kept low due to the unbiased nature of the second-derivative Tikhonov regularisation at zeroth and first order. The minimisation of the global correlation coefficient takes place consistently in the low-$\tau$ region. The optimal choice, $\hat{\tau}$, succeeds in maintaining the rate of having at least one negative unfolded bin and the average bin uncertainties to their minimal values, proving that PLU is able to suppress the impact of statistical fluctuations with minimal induced bias.

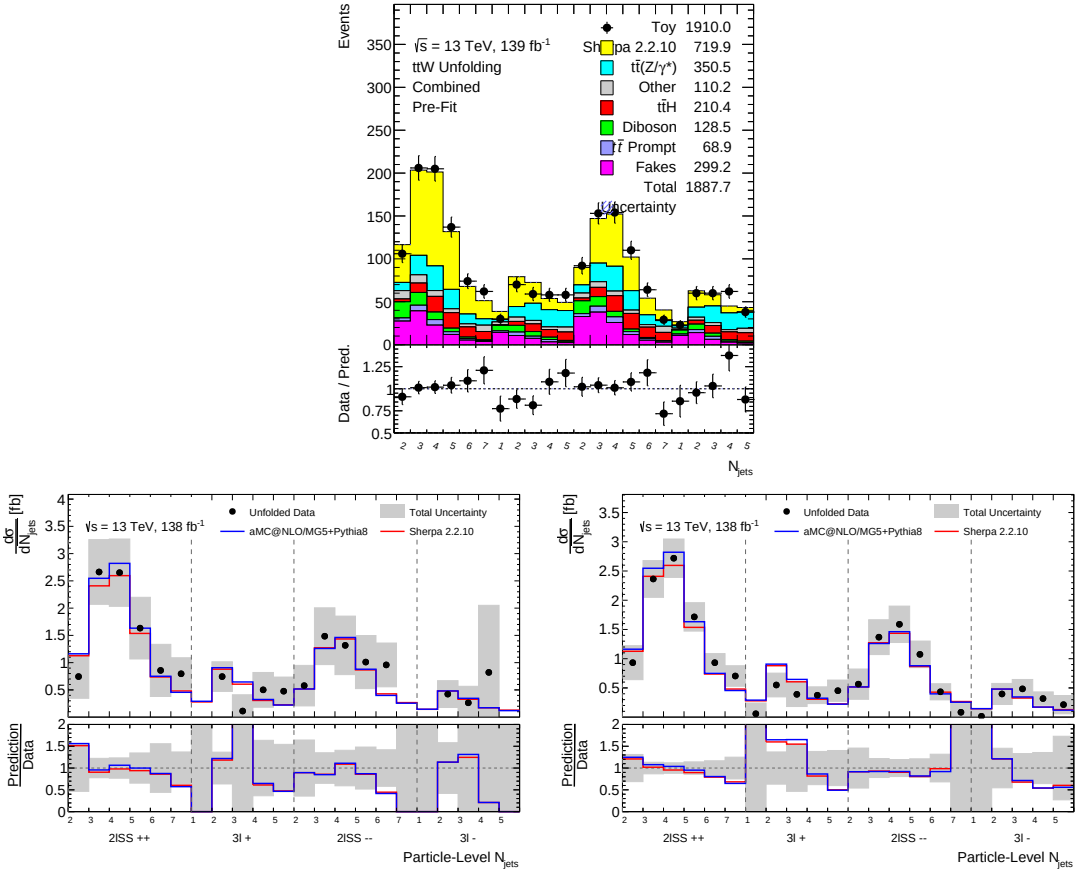



FIGURE B.6: A single toy unfolding fit to $N_{\text{jets}}$, from top to bottom-right: pre-fit plot, unregularised result, and regularised result.

The effect of regularisation (after the above optimisation) is demonstrated in a single pseudo-experiment, where the $N_{\text{jets}}$ distribution is unfolded using a set of Poisson-smeared pseudo-data generated with the `altTruth` configuration, including only statistical uncertainties. This test is summarised in Figure B.6, where the

$t\bar{t}W$ distribution is unfolded with and without regularisation. In the case of the regularised unfolding, the regularisation provides a better result in the bins where the simulated prediction overshoots the pseudo-data and smoothens the unfolded distribution, while reducing the total uncertainty (here statistical only).

## B.4 Sensitivity, closure and stress tests

Following the regularisation-optimisation process, various stress tests are performed to prove the robustness of the method and estimate the expected sensitivity. A simplified version of the extended template fit is used for this purpose, where only the dominant systematic uncertainties are considered and cross-section uncertainties are assigned to the background contributions. The background contributions and their considered uncertainties are: fake leptons (25%), $t\bar{t}H/t\bar{t}Z$ (11%), $VV$ (6%), $t\bar{t}t/tZ/tWZ/VH$ (50%) and $t\bar{t}t\bar{t}/VVV$ (30%). In the production of the templates the "fake"-lepton backgrounds (non-prompt HF, conversions, QMisID) are all taken from the $t\bar{t}$ simulated MC sample as a single template.

These sensitivity tests are based on fits to pseudo-data (Asimov) and the unfolded distributions in the SR of the $N_{\text{jets}}$ and $N_{b-\text{jets}}$ observables are shown in Figure B.7. The uncertainties on the inclusive normalisation factors (NFs) for the $t\bar{t}W$ signal acquired from this fit are 14%, 27%, 21%, and 39% for the $2\ell\text{SS}++$, $2\ell\text{SS}--$, $3\ell+$, and $3\ell-$ regions, respectively, for the $N_{\text{jets}}$ observable, while a bit higher values are acquired for the $N_{b-\text{jets}}$ observable. A perfect closure is achieved in this fit due to the remarkable agreement of the unfolded result and SHERPA-2.2.10 nominal sample at particle level.

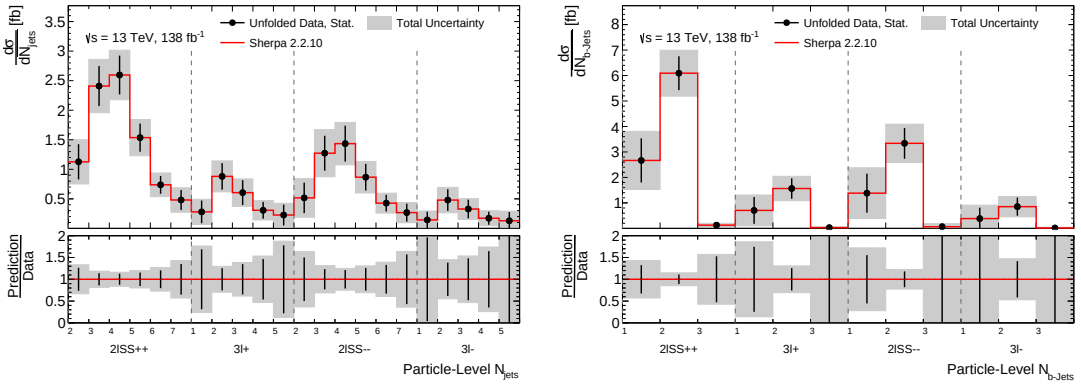



FIGURE B.7: Unfolded distributions in simplified template fit unfolding setup Asimov fits.

| 2ℓSS++ | |
|---|---|
| Category | $\sigma(\mu)/\mu$ |
| FullSyst | 0.098157 |
| ME | 0.097147 |
| Scale | 0.007070 |
| Muon | 0.006981 |
| FTAG | 0.006620 |
| JES | 0.005920 |
| Pileup | 0.005871 |
| Trigger | 0.003421 |
| EGamma | 0.003128 |
| JER | 0.002718 |

| 3ℓ + | |
|---|---|
| Category | $\sigma(\mu)/\mu$ |
| FullSyst | 0.126692 |
| ME | 0.124424 |
| Scale | 0.015927 |
| FTAG | 0.011254 |
| Trigger | 0.008246 |
| Muon | 0.007889 |
| Pileup | 0.007232 |
| JES | 0.006349 |
| JER | 0.004133 |
| EGamma | 0.002228 |

| 2ℓSS-- | |
|---|---|
| Category | $\sigma(\mu)/\mu$ |
| FullSyst | 0.101064 |
| ME | 0.100068 |
| Muon | 0.007428 |
| Pileup | 0.006460 |
| FTAG | 0.006430 |
| JES | 0.006173 |
| Scale | 0.004516 |
| Trigger | 0.004047 |
| EGamma | 0.003324 |
| JER | 0.003199 |

| 3ℓ- | |
|---|---|
| Category | $\sigma(\mu)/\mu$ |
| FullSyst | 0.104134 |
| ME | 0.101628 |
| FTAG | 0.010051 |
| Scale | 0.009841 |
| Muon | 0.008083 |
| Trigger | 0.006713 |
| JES | 0.006231 |
| Pileup | 0.005822 |

TABLE B.5: Grouped impact tables for the per-channel inclusive cross section normalisation factors when unfolding the $N_{\text{jets}}$ distribution. Systematics groups that do not appear have a very small impact, and this causes the impact-estimation procedure to fail.

The grouped impact configuration of TRExFitter is used to evaluate the ranking of the modelling systematic uncertainties on the $t\bar{t}W$ signal. In this configuration the systematic impact is calculated by the quadrature difference between the result of a fit with all the uncertainties considered and the result of a fit when one group of uncertainties is removed. The process is repeated for all systematic groups and parameters of interest. Apart from the inclusion of systematic uncertainties, there are also theoretical uncertainties on the generator modelling labelled as "ME" (defined by comparison to MADGRAPH5_AMC@NLO), on the renormalisation and factorisation scales labelled as "Scale" and uncertainties on the PDF modelling. The results of the grouped systematic impacts for each fiducial region are summarised in Table B.5. The ME uncertainty is the dominant one, while the PDF uncertainties have a minor impact.

Stress tests are also performed in order to ensure that the second-derivate Tikhonov regularisation is unbiased for shape differences between real and simulated data up to first order. This is validated by unfolding the $t\bar{t}W$ sample in the $N_{\text{jets}}$ distribution using Asimov data and injecting either a +40% normalisation effect separately into the 2ℓSS and 3ℓ regions or a ±20% slope into the SHERPA-2.2.10 templates at particle level. The unfolded results obtained from these stress tests are shown in Figure B.8. Perfect closure is achieved in all the unfolded bins validating the unbiased nature of the regularisation against linear shape effects. Similar behaviour is observed in the rest of the observables that are not shown for brevity.

Apart from the above tests, closure checks are performed by using the alternate

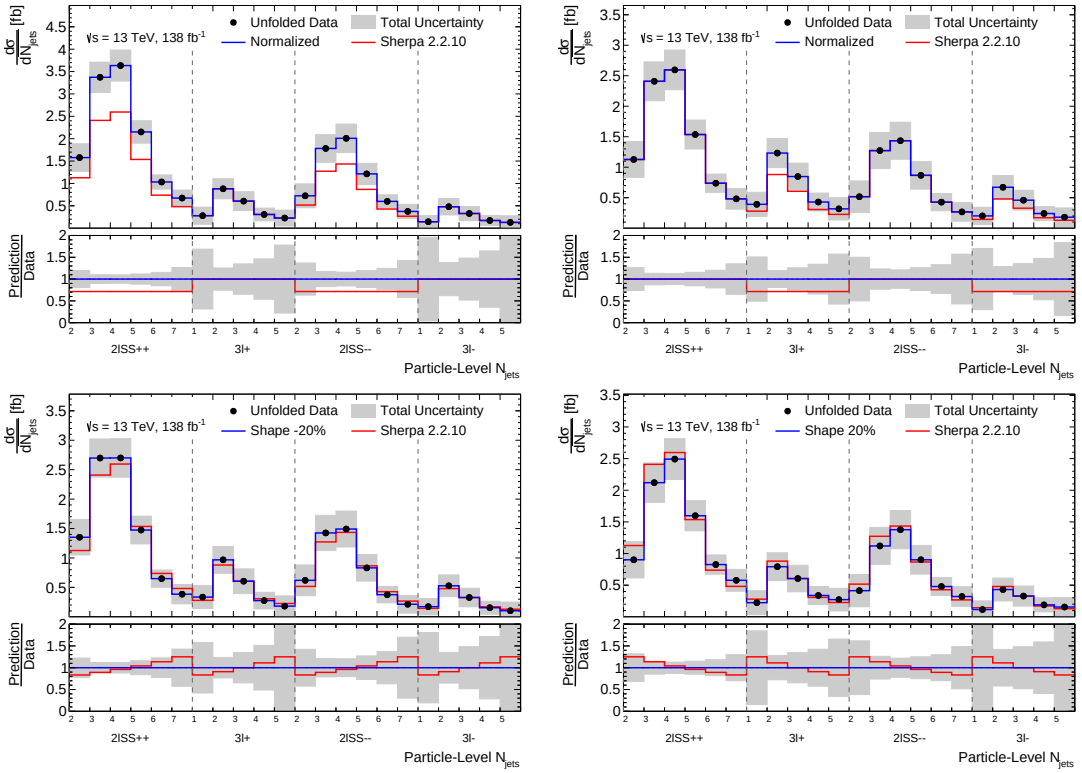



FIGURE B.8: Unfolded distributions for $N_{\text{jets}}$ in simplified template fit unfolding stress tests with +40% normalisation to $2\ell$SS and $3\ell$ channels (top) and $\pm 20\%$ linear shape (bottom).

MC sample (MG5_aMCNLO + PYTHIA-8) sample in the `altTruth` unfolding configuration described in Section B.3. The results are summarised in Tables B.6 and B.7 for the $N_{\text{jets}}$ and $N_{b-\text{jets}}$ observables, as representative cases for the rest of the unfolded observables. The unfolded distributions from this check are shown in Figure B.9. The slight non-closure observed is explained as an artifact due to regularisation. Non-closure uncertainties can be derived for each observable from fits with statistical uncertainties only, where the background contributions are fixed in the SR. The last columns in Tables B.6 and B.7 could be used as non-closure uncertainties at any time, but at this stage of the analysis they are not included in the fit allowing for the unfolded result to be quoted before and after these uncertainties are applied. Another reason for not including the non-closure uncertainties is that a Gaussian treatment for them is problematic, and the fit itself produces a conservative version of these uncertainties due to pulls in the nuisance parameters (NPs) and background NFs, which could absorb the difference between the nominal and alternate signal samples.

| $N_{\text{jets}}$ | | | | |
|---|---|---|---|---|
| Channel | Bin | $d\sigma/dX$ [fb] | | |
| | | Pseudo-data | \|SHERPA-2.2.10 − Pseudo-data\| | \|(MG5_aMC@NLO + PYTHIA-8) − Pseudo-data\| |
| $2\ell\text{SS}++$ | [2,3) | $1.29 \pm 0.31$ | 0.11 | 0.01 |
| | [3,4) | $2.82 \pm 0.34$ | 0.28 | 0.02 |
| | [4,5) | $3.07 \pm 0.35$ | 0.32 | 0.03 |
| | [5,6) | $1.79 \pm 0.25$ | 0.15 | 0.00 |
| | [6,7) | $0.83 \pm 0.16$ | 0.04 | 0.01 |
| | [7,8) | $0.51 \pm 0.18$ | 0.00 | 0.01 |
| $3\ell+$ | [1,2) | $0.28 \pm 0.16$ | 0.02 | 0.00 |
| | [2,3) | $0.87 \pm 0.20$ | 0.06 | 0.01 |
| | [3,4) | $0.62 \pm 0.19$ | 0.05 | 0.01 |
| | [4,5) | $0.31 \pm 0.13$ | 0.02 | 0.01 |
| | [5,6) | $0.22 \pm 0.15$ | 0.01 | 0.01 |
| $2\ell\text{SS}--$ | [2,3) | $0.57 \pm 0.26$ | 0.02 | 0.00 |
| | [3,4) | $1.40 \pm 0.31$ | 0.07 | 0.02 |
| | [4,5) | $1.59 \pm 0.32$ | 0.09 | 0.01 |
| | [5,6) | $0.96 \pm 0.24$ | 0.03 | 0.01 |
| | [6,7) | $0.46 \pm 0.15$ | 0.00 | 0.02 |
| | [7,8) | $0.27 \pm 0.16$ | 0.01 | 0.01 |
| $3\ell-$ | [1,2) | $0.14 \pm 0.12$ | 0.01 | 0.00 |
| | [2,3) | $0.47 \pm 0.16$ | 0.03 | 0.00 |
| | [3,4) | $0.32 \pm 0.14$ | 0.02 | 0.01 |
| | [4,5) | $0.17 \pm 0.10$ | 0.01 | 0.00 |
| | [5,6) | $0.12 \pm 0.13$ | 0.00 | 0.00 |

TABLE B.6: Non-closure results in differential cross section for the $N_{\text{jets}}$ observable using the MG5_aMC@NLO sample for the pseudo-data generation.

| $N_{b-\text{jets}}$ | | | | |
|---|---|---|---|---|
| Channel | Bin | $d\sigma/dX$ [fb] | | |
| | | Pseudo-data | \|SHERPA-2.2.10 − Pseudo-data\| | \|(MG5_aMC@NLO + PYTHIA-8) − Pseudo-data\| |
| $2\ell\text{SS}++$ | [1,2) | $3.24 \pm 0.90$ | 0.44 | 0.00 |
| | [2,3) | $6.93 \pm 0.70$ | 0.45 | 0.01 |
| | [3,4) | $0.14 \pm 0.07$ | 0.00 | 0.00 |
| $3\ell+$ | [1,2) | $0.74 \pm 0.44$ | 0.09 | 0.00 |
| | [2,3) | $1.53 \pm 0.35$ | 0.08 | 0.00 |
| | [3,4) | $0.03 \pm 0.04$ | 0.00 | 0.00 |
| $2\ell\text{SS}–$ | [1,2) | $1.59 \pm 0.77$ | 0.14 | 0.00 |
| | [2,3) | $3.59 \pm 0.62$ | 0.07 | 0.00 |
| | [3,4) | $0.07 \pm 0.13$ | 0.00 | 0.00 |
| $3\ell$- | [1,2) | $0.39 \pm 0.38$ | 0.04 | 0.00 |
| | [2,3) | $0.82 \pm 0.30$ | 0.03 | 0.00 |
| | [3,4) | $0.01 \pm 0.03$ | 0.00 | 0.00 |

TABLE B.7: Non-closure results in differential cross section for the $N_{b-\text{jets}}$ observable using the MG5_aMC@NLO sample for the pseudo-data generation.

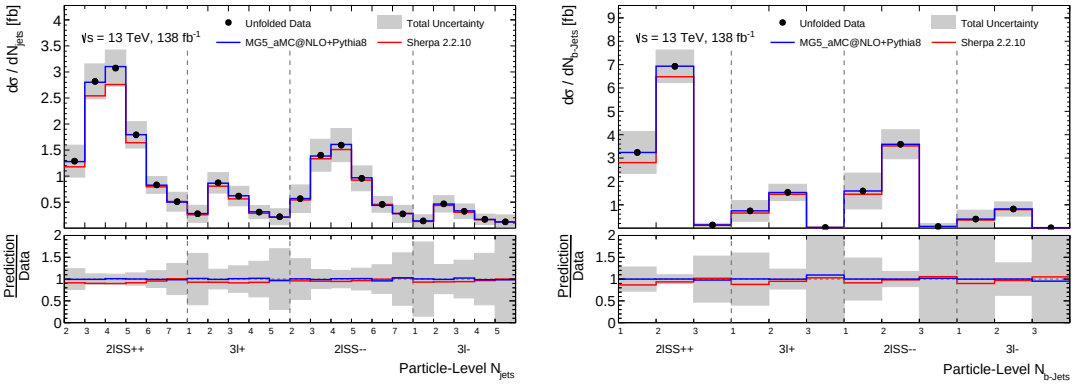



FIGURE B.9: Unfolded distributions from closure tests performed with a simplified template fit setup using the `altTruth` configuration.

A final stress test is performed to further validate the robustness of the unfolding method. The signal sample is split in half, where the first half (sample A) is used for unfolding (as a particle-level template with a corresponding response matrix) and the second half (sample B) is used to generate the pseudo-data for the unfolding. Since the samples have equal number of MC statistics their statistical fluctuations are expected to also be the same. There are two variations in which this test can be performed.

- **Variation (1):** The $t\bar{t}W$ component of the pseudo-data is generated by forward-folding of the particle-level template of sample B using the nominal response matrix of sample A.
- **Variation (2):** The $t\bar{t}W$ component is built directly from sample B at detector level, which is the same as forward-folding the particle-level distribution of sample B with the response matrix of sample B.

The unfolding procedure is proved to be robust against MC statistical uncertainties, something that can be inferred by the very small observed non-closure against the sample at particle level.

The samples in this check are divided according to their parity of the event number (to odd and even), resulting to samples of equal statistics. Each subsample is weighted with an additional factor of 2.0, since each subsample is normalised to the total MC weight of the unsplit sample. All background contributions are considered in the SR and are kept fixed without systematic uncertainties included. The test is performed by unfolding the $N_{\text{jets}}$ distribution in the SR with and without the use of regularisation for both variations.

The agreement between the even-numbered signal events stacked to the background prediction and the pseudo-data generated from the odd-numbered signal with the same background prediction is demonstrated before and after the unfolding in Figures B.10 and B.12 for Variation (1) and (2), respectively. There are two cases after the fit with and without regularisation to which the unfolded distribution is compared, as shown in Figures B.11 and B.13.

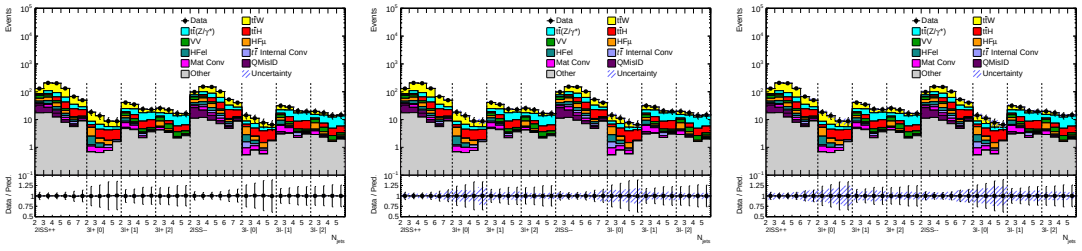



FIGURE B.10: Comparisons of signal-plus-background prediction to pseudo-data generated with independent statistics of the $t\bar{t}W$ sample in Variation (1), shown before (left) and after the fit for the unregularised (middle) and regularised (right) case.

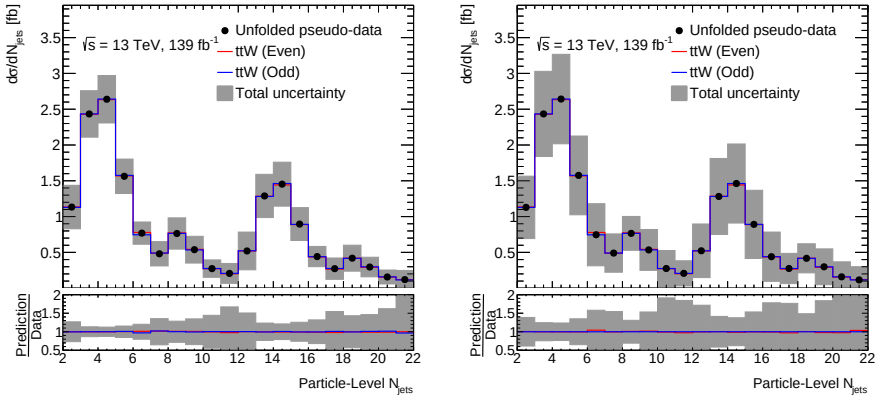



FIGURE B.11: Comparison of unfolded distributions to the two $t\bar{t}W$ samples obtained using half the nominal statistics in the regularised (left) and unregularised (right) case in Variation (1).

In Variation (1), perfect closure is achieved in the case without regularisation and almost perfect closure otherwise. In Variation (2), MC statistical fluctuations between the $t\bar{t}W$ subsamples are visible in the unfolded distribution relative to both particle-level distributions. These fluctuations are reduced in the regularised case, and they are lower than the statistical uncertainty of the pseudo-data. Larger fluctuations are observed in the $3\ell$ channel due to the additional splitting by the number of OSSF lepton pairs at detector level. This is also reflected in the slight pre-fit disagreement that appears to be larger in these regions. In this variation,

there is not perfect closure even in the unregularised case due to the fit being overconstrained in the $3\ell$ channel, while almost perfect closure is shown in the $2\ell$SS channel since the detector-level bins are able to constrain almost fully the truth bins.

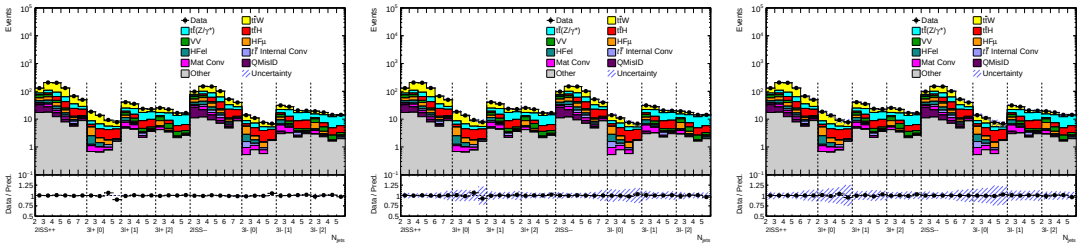



FIGURE B.12: Comparisons of signal-plus-background prediction to pseudo-data generated with independent statistics of the $t\bar{t}W$ sample in Variation (2), shown before (left) and after the fit for the unregularised (middle) and regularised (right) case.

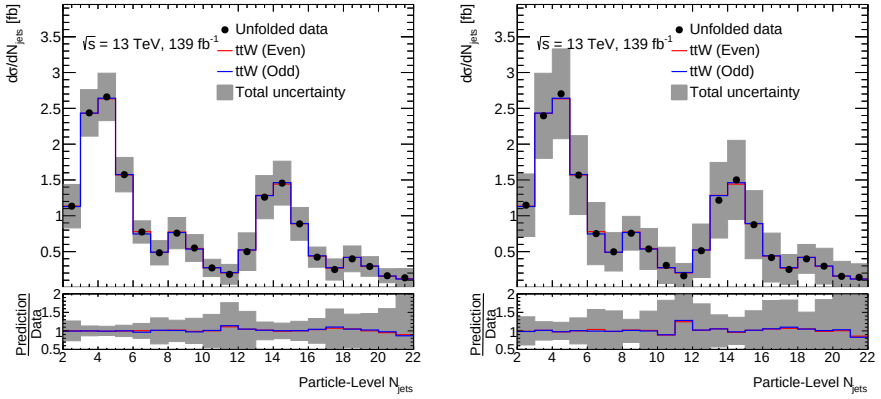
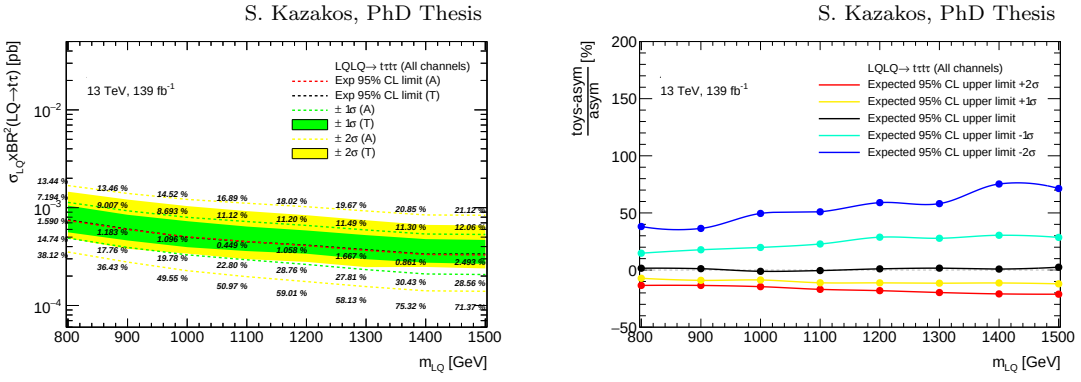



FIGURE B.13: Comparison of unfolded distributions to the two $t\bar{t}W$ samples obtained using half the nominal statistics in the regularised (left) and unregularised (right) case in Variation (2).

# Appendix C

# Limit comparison between the asymptotic approximation and the toy MC method

A comparison of the expected upper limits in the LQLQ→ $t\tau t\tau$ analysis is performed between the ones calculated using the asymptotic approximation and the ones calculated using the toy MC method. This check is motivated due to the low background prediction in the rightmost bins of the $m_{\text{eff}}$ distribution in the SRs considered.




(a) (b)

FIGURE C.1: Comparison of expected upper limits between the calculation using the asymptotic approximation (A) compared to the one using the toy MC method (T). The limits are shown in (a) with dashed black (red) lines for the T (A) case. The $\pm 1\sigma$ and $\pm 2\sigma$ bands are shown as shaded bands (dashed lines) for the T (A) case. The percentage difference between T and A is given in (a) and it is also shown separately in (b). Only the statistical uncertainty is considered for the simulated samples.

For this purpose, sets of 15 thousand toy pseudo-experiments were generated per $\mu$ scanning point and per $LQ_3^d$ signal mass point under the assumption of $B=1$. The pseudo-experiments were generated by considering only the statistical uncertainty on the simulated MC samples due to the statistically dominated results. The results of the comparison are shown in Figure C.1. The difference in the expected limit ranges from $\sim$0.45% to $\sim$2.5%. The $+1\sigma$ and $+2\sigma$ bands seem to agree within $\sim$20%, the $-1\sigma$ bands within $\sim$30%, while there is a larger discrepancy in the $-2\sigma$ bands at the order of $\sim$75%. Due to this discrepancy in the $-2\sigma$ bands only the central limit and $\pm1\sigma$ bands can be considered as valid under the asymptotic approximation.

# Bibliography


[1] S. L. Glashow, *Partial-symmetries of weak interactions*, Nuclear Physics **22** (1961) 579, ISSN: 0029-5582 (cit. on p. 5).

[2] S. Weinberg, *A Model of Leptons*, Phys. Rev. Lett. **19** (1967) 1264, ISSN: 1079-7114 (cit. on p. 5).

[3] A. Salam, *Gauge unification of fundamental forces*, Rev. Mod. Phys. **52** (1980) 525, ISSN: 1539-0756 (cit. on p. 5).

[4] A. Purcell, *Go on a particle quest at the first CERN webfest. Le premier webfest du CERN se lance à la conquête des particules*, BUL-NA-2012-269. 35/2012, 2012, URL: `https://cds.cern.ch/record/1473657` (cit. on p. 6).

[5] ATLAS Collaboration, *Observation of a new particle in the search for the Standard Model Higgs boson with the ATLAS detector at the LHC*, Phys. Lett. B **716** (2012) 1, ISSN: 0370-2693 (cit. on p. 8).

[6] CMS Collaboration, *Observation of a new boson at a mass of 125 GeV with the CMS experiment at the LHC*, Phys. Lett. B **716** (2012) 30, ISSN: 0370-2693 (cit. on p. 8).

[7] F. Englert and R. Brout, *Broken Symmetry and the Mass of Gauge Vector Mesons*, Phys. Rev. Lett. **13** (1964) 321, ISSN: 1079-7114 (cit. on pp. 8, 17).

[8] P. W. Higgs, *Broken Symmetries and the Masses of Gauge Bosons*, Phys. Rev. Lett. **13** (1964) 508, ISSN: 1079-7114 (cit. on pp. 8, 17).

[9] P. W. Higgs, *Broken symmetries, massless particles and gauge fields*, Physics Letters **12** (1964) 132, ISSN: 0031-9163 (cit. on pp. 8, 17).

[10] M. Thomson, *Modern Particle Physics*, Cambridge University Press, 2013 (cit. on pp. 10, 27, 34, 70).

[11] ATLAS Collaboration, *Determination of the strong coupling constant and test of asymptotic freedom from Transverse Energy-Energy Correlations in multijet events at $\sqrt{s} = 13$ TeV with the ATLAS detector*, ATLAS-CONF-2020-025, 2020, URL: https://cds.cern.ch/record/2725553 (cit. on p. 16).

[12] R. L. Workman et al., *Review of Particle Physics*, PTEP **2022** (2022) 083C01 (cit. on pp. 24, 26, 49).

[13] LHC Higgs Cross Section Working Group, *Handbook of LHC Higgs Cross Sections: 1. Inclusive Observables*, 2011, arXiv: 1101.0593v3 [hep-ph] (cit. on p. 25).

[14] ATLAS Collaboration, *Combined measurements of Higgs boson production and decay using up to 80 $fb^{-1}$ of proton-proton collision data at $\sqrt{s} = 13$ TeV collected with the ATLAS experiment*, Phys. Rev. D **101** (2020) 012002, ISSN: 2470-0029 (cit. on p. 26).

[15] D0 Collaboration, *Search for High Mass Top Quark Production in $p\overline{p}$ Collisions at $\sqrt{s} =$ 1.8 TeV*, Phys. Rev. Lett. **74** (1995) 2422, ISSN: 1079-7114 (cit. on p. 26).

[16] CDF Collaboration, *Observation of Top Quark Production in $\overline{p}p$ Collisions with the Collider Detector at Fermilab*, Phys. Rev. Lett. **74** (1995) 2626, ISSN: 1079-7114 (cit. on p. 26).

[17] P. Minkowski, *$\mu \to e\gamma$ at a rate of one out of $10^9$ muon decays?*, Phys. Lett. B **67** (1977) 421, ISSN: 0370-2693 (cit. on p. 27).

[18] R. N. Mohapatra and G. Senjanović, *Neutrino Mass and Spontaneous Parity Nonconservation*, Phys. Rev. Lett. **44** (1980) 912, ISSN: 1079-7114 (cit. on p. 27).

[19] R. Frederix, D. Pagani, and M. Zaro, *Large NLO corrections in and hadroproduction from supposedly subleading EW contributions*, JHEP **02** (2018) 31, ISSN: 1029-8479 (cit. on pp. 28, 29).

[20] F. F. Cordero, M. Kraus, and L. Reina, *Top-quark pair production in association with a $W^{\pm}$ gauge boson in the POWHEG-BOX*, Phys. Rev. D **103** (2021) 094014, ISSN: 2470-0029 (cit. on p. 29).

[21] LHC Higgs Cross Section Working Group, *Handbook of LHC Higgs Cross Sections: 4. Deciphering the nature of the Higgs sector*, 2017, arXiv: 1610.07922 [hep-ph] (cit. on pp. 29, 159, 160).

[22] ATLAS Collaboration, *Top Quarks + X Summary Plots November 2022*, ATL-PHYS-PUB-2022-049, 2022, URL: https://cds.cern.ch/record/2840589 (cit. on p. 30).

[23] R. Frederix and I. Tsinikos, *On improving NLO merging for $t\bar{t}W$ production*, JHEP **11** (2021) 29, ISSN: 1029-8479 (cit. on p. 31).

[24] A. Kulesza, L. Motyka, D. Schwartländer, T. Stebel, and V. Theeuwes, *Associated top quark pair production with a heavy boson: differential cross sections at NLO + NNLL accuracy*, Eur. Phys. J. C **80** (2020) 428, ISSN: 1434-6052 (cit. on p. 31).

[25] L. Buonocore et al., *Associated production of a W boson with a top-antitop quark pair: next-to-next-to-leading order QCD predictions for the LHC*, (2023), arXiv: 2306.16311 (cit. on pp. 31, 213).

[26] H. Georgi and S. L. Glashow, *Unity of All Elementary-Particle Forces*, Phys. Rev. Lett. **32** (1974) 438, ISSN: 1079-7114 (cit. on pp. 34, 39).

[27] J. Wess and B. Zumino, *Supergauge transformations in four dimensions*, Nucl. Phys. B **70** (1974) 39, ISSN: 0550-3213 (cit. on pp. 34, 39).

[28] A. Salam and J. Strathdee, *Super-symmetry and non-Abelian gauges*, Phys. Lett. B **51** (1974) 353, ISSN: 0370-2693 (cit. on pp. 34, 39).

[29] A. G. Riess et al., *Observational Evidence from Supernovae for an Accelerating Universe and a Cosmological Constant*, Astron. J. **116** (1998) 1009, ISSN: 1538-3881 (cit. on p. 35).

[30] F. Zwicky, *On the Masses of Nebulae and of Clusters of Nebulae*, Astrophys. J. **86** (1937) 217, ISSN: 0004-637X (cit. on p. 35).

[31] P. Young, J. E. Gunn, J. Kristian, J. B. Oke, and J. A. Westphall, *Q0957+561 : detrailed models of the gravitational lens effect.*, Astrophys. J. **244** (1981) 736, ISSN: 0004-637X (cit. on p. 35).

[32] D. Clowe, A. Gonzalez, and M. Markevitch, *Weak-Lensing Mass Reconstruction of the Interacting Cluster 1E 0657–558: Direct Evidence for the Existence of Dark Matter**, Astrophys. J. **604** (2004) 596, ISSN: 0004-637X (cit. on p. 35).

[33] N. Aghanim et al.,
*Planck 2018 results - V. CMB power spectra and likelihoods*,
Astron. Astrophys. **641** (2020) A5, ISSN: 0004-6361 (cit. on p. 36).

[34] Wikimedia Commons, *File:Galactic Rotation-fr.svg — Wikimedia Commons, the free media repository*, 2022,
URL: `https://commons.wikimedia.org/w/index.php?title=File:Galactic_Rotation-fr.svg&oldid=634750903` (cit. on p. 36).

[35] Wikimedia Commons,
*File:1e0657 scale.jpg — Wikimedia Commons, the free media repository*, 2020,
URL: `https://commons.wikimedia.org/w/index.php?title=File:1e0657_scale.jpg&oldid=418941390` (cit. on p. 36).

[36] Super-Kamiokande Collaboration,
*Evidence for Oscillation of Atmospheric Neutrinos*,
Phys. Rev. Lett. **81** (1998) 1562, ISSN: 1079-7114 (cit. on p. 36).

[37] G. Kane, *Modern Elementary Particle Physics: Explaining and Extending the Standard Model*, 2nd ed., Cambridge University Press, 2017 (cit. on p. 37).

[38] Muon g-2 Collaboration, *Final report of the E821 muon anomalous magnetic moment measurement at BNL*, Phys. Rev. D **73** (2006) 072003 (cit. on pp. 39, 47).

[39] Muon g-2 Collaboration, *Measurement of the Positive Muon Anomalous Magnetic Moment to 0.46 ppm*, Phys. Rev. Lett. **126** (2021) 141801 (cit. on pp. 39, 46, 47).

[40] J. C. Pati and A. Salam, *Lepton number as the fourth "color"*,
Phys. Rev. D **11** (1975) 703, ISSN: 2470-0029 (cit. on p. 39).

[41] P. H. Frampton and B.-H. Lee, *SU(15) grand unification*,
Phys. Rev. Lett. **64** (1990) 619, ISSN: 1079-7114 (cit. on p. 39).

[42] E. Witten, *Symmetry breaking patterns in superstring models*,
Nucl. Phys. B **258** (1985) 75, ISSN: 0550-3213 (cit. on p. 39).

[43] M. Dine, V. Kaplunovsky, M. Mangano, C. Nappi, and N. Seiberg,
*Superstring model building*, Nucl. Phys. B **259** (1985) 549,
ISSN: 0550-3213 (cit. on p. 39).

[44] R. Barbier et al., *R-Parity-violating supersymmetry*, Phys. Rep. **420** (2005) 1, ISSN: 0370-1573 (cit. on p. 40).

[45] N. Zwane, *Long-lived particle searches in R-parity violating MSSM*, J. Phys. G **44** (2017) 105003, ISSN: 0954-3899 (cit. on p. 40).

[46] B. Gripaios, *Composite leptoquarks at the LHC*, JHEP **02** (2010) 45, ISSN: 1029-8479 (cit. on p. 40).

[47] H. Harari, *A schematic model of quarks and leptons*, Phys. Lett. B **86** (1979) 83, ISSN: 0370-2693 (cit. on p. 40).

[48] B. Schrempp and F. Schrempp, *Light leptoquarks*, Phys. Lett. B **153** (1985) 101, ISSN: 0370-2693 (cit. on p. 40).

[49] E. Farhi and L. Susskind, *Technicolour*, Phys. Rep. **74** (1981) 277, ISSN: 0370-1573 (cit. on p. 41).

[50] J. Fuentes-Martín and P. Stangl, *Third-family quark-lepton unification with a fundamental composite Higgs*, Phys. Lett. B **811** (2020) 135953, ISSN: 0370-2693 (cit. on p. 41).

[51] Belle Collaboration, *Measurement of the branching ratio of $\overline{B} \to D^{(*)}\tau^-\overline{\nu}_\tau$ relative to $\overline{B} \to D^{(*)}\ell^-\overline{\nu}_\ell$ decays with hadronic tagging at Belle*, Phys. Rev. D **92** (2015) 072014, ISSN: 2470-0029 (cit. on p. 42).

[52] BABAR Collaboration, *Evidence for an Excess of $\overline{B} \to D^{(*)}\tau^-\overline{\nu}_\tau$ Decays*, Phys. Rev. Lett. **109** (2012) 101802, ISSN: 1079-7114 (cit. on p. 42).

[53] BABAR Collaboration, *Measurement of an excess of $\overline{B} \to D^{(*)}\tau^-\overline{\nu}_\tau$ decays and implications for charged Higgs bosons*, Phys. Rev. D **88** (2013) 072012, ISSN: 2470-0029 (cit. on p. 42).

[54] Belle Collaboration, *Measurement of the branching ratio of $\bar{B}^0 \to D^{*+}\tau^-\bar{\nu}_\tau$ relative to $\bar{B}^0 \to D^{*+}\ell^-\bar{\nu}_\ell$ decays with a semileptonic tagging method*, (2016), arXiv: 1603.06711 [hep-ex] (cit. on p. 42).

[55] LHCb Collaboration, *Publisher's Note: Measurement of the Ratio of Branching Fractions $\mathcal{B}(\overline{B}^0 \to D^{*+}\tau^-\overline{\nu}_\tau)/\mathcal{B}(\overline{B}^0 \to D^{*+}\mu^-\overline{\nu}_\mu)$*, Phys. Rev. Lett. **115** (2015) 159901, ISSN: 1079-7114 (cit. on p. 42).

[56] Belle Collaboration, *Measurement of the $\tau$ lepton polarization in the decay $\bar{B} \to D^*\tau^-\bar{\nu}_\tau$*, (2016), arXiv: 1608.06391 [hep-ex] (cit. on p. 42).

[57] D. Choudhury, A. Kundu, R. Mandal, and R. Sinha,
*$R_{K^*}$ and $R(D^{(*)}$ anomalies resolved with lepton mixing*,
Nucl. Phys. B **933** (2018) 433, ISSN: 0550-3213 (cit. on p. 42).

[58] LHCb Collaboration,
*Test of Lepton Universality Using $B^+ \to K^+\ell^+\ell^-$ Decays*,
Phys. Rev. Lett. **113** (2014) 151601, ISSN: 1079-7114 (cit. on p. 42).

[59] LHCb Collaboration, *Tests of Lepton Universality Using $B^0 \to K^0_S\ell^+\ell^-$ and $B^+ \to K^{*+}\ell^+\ell^-$ Decays*, Phys. Rev. Lett. **128** (2022) 191802,
ISSN: 1079-7114 (cit. on p. 42).

[60] LHCb Collaboration,
*Averages of b-hadron, c-hadron, and $\tau$-lepton properties as of 2018*,
Eur. Phys. J. C **81** (2021) 1, ISSN: 1434-6052 (cit. on p. 43).

[61] LHCb Collaboration,
*Test of lepton universality with $B^0 \to K^{*0}l^+l^-$ decays*,
JHEP **08** (2017) 55, ISSN: 1029-8479 (cit. on p. 43).

[62] LHCb Collaboration, *Test of lepton universality in beauty-quark decays*,
Nat. Phys. **18** (2022) 277, ISSN: 1745-2481 (cit. on pp. 43, 44).

[63] LHCb Collaboration,
*Measurements of $R(K)$ and $R(K^*)$ with the full LHCb Run 1 and 2 data*,
2022, URL: `https://indico.cern.ch/event/1187945` (cit. on p. 44).

[64] LHCb Collaboration, *Branching Fraction Measurements of the Rare $B^0_s \to \phi\mu^+\mu^-$ and $B^0_s \to f'_2(1525)\mu^+\mu^-$ Decays*,
Phys. Rev. Lett. **127** (2021) 11, ISSN: 1079-7114 (cit. on p. 45).

[65] LHCb Collaboration,
*Measurement of CP-Averaged Observables in the $B^0 \to K^{*0}\mu^+\mu^-$ Decay*,
Phys. Rev. Lett. **125** (2020) 011802, ISSN: 1079-7114 (cit. on p. 45).

[66] W. Buchmüller and D. Wyler, *Constraints on SU(5)-type leptoquarks*,
Phys. Lett. B **177** (1986) 377, ISSN: 0370-2693 (cit. on pp. 47, 280).

[67] W. Buchmüller, R. Rückl, and D. Wyler,
*Leptoquarks in lepton-quark collisions*, Phys. Lett. B **191** (1987) 442,
ISSN: 0370-2693 (cit. on pp. 47, 49).

[68] V. Gherardi, D. Marzocca, and E. Venturini,
*Low-energy phenomenology of scalar leptoquarks at one-loop accuracy*,
JHEP **01** (2021) 138, ISSN: 1029-8479 (cit. on p. 49).

[69] A. Angelescu, D. Bečirević, D. A. Faroughy, and O. Sumensari, *Closing the window on single leptoquark solutions to the B-physics anomalies*, JHEP **10** (2018) 183, ISSN: 1029-8479 (cit. on p. 50).

[70] I. Bigaran and R. R. Volkas, *Getting chirality right: Single scalar leptoquark solutions to the $(g-2)_{e,\mu}$ puzzle*, Phys. Rev. D **102** (2020) 075037, ISSN: 2470-0029 (cit. on p. 50).

[71] J. Blümlein and R. Rückl, *Production of scalar and vector leptoquarks in $e^+e^-$ annihilation*, Phys. Lett. B **304** (1993) 337, ISSN: 0370-2693 (cit. on p. 49).

[72] J. Blümlein, E. Boos, and A. Kryukov, *Leptoquark pair production in hadronic interactions*, Z. Phys. C - Particles and Fields **76** (1997) 137, ISSN: 1431-5858 (cit. on p. 50).

[73] B. Diaz, M. Schmaltz, and Y.-M. Zhong, *The Leptoquark Hunter's Guide: Pair Production*, JHEP **10** (2017) 097 (cit. on pp. 51, 286, 305).

[74] T. Mandal, S. Mitra, and S. Seth, *Pair production of scalar leptoquarks at the LHC to NLO parton shower accuracy*, Phys. Rev. D **93** (2016) 035018 (cit. on pp. 51, 286).

[75] J. Blümlein, E. Boos, and A. Kryukov, *Leptoquark Pair Production Cross Sections at Hadron Colliders*, (1998), arXiv: `9811271 [hep-ph]` (cit. on p. 54).

[76] V. Ahrens, A. Ferroglia, M. Neubert, B. D. Pecjak, and L. L. Yang, *Renormalization-group improved predictions for top-quark pair production at hadron colliders*, JHEP **09** (2010) 97, ISSN: 1029-8479 (cit. on p. 55).

[77] W. Beenakker et al., *NNLL resummation for stop pair-production at the LHC*, JHEP **05** (2016) 153, ISSN: 1029-8479 (cit. on p. 55).

[78] W. Beenakker, C. Borschensky, M. Krämer, A. Kulesza, and E. Laenen, *NNLL-fast: predictions for coloured supersymmetric particle production at the LHC with threshold and Coulomb resummation*, JHEP **12** (2016) 133, ISSN: 1029-8479 (cit. on p. 55).

[79] LHC Physics working group,
*Stop-antistop (sbottom-antisbottom) production cross sections computed at NLO+NLL and NNLOapprox+NNLL*, 2021,
URL: https://twiki.cern.ch/twiki/bin/view/LHCPhysics/SUSYCrossSections13TeVstopsbottom (cit. on p. 55).

[80] E. Lopienska, *The CERN accelerator complex, layout in 2022. Complexe des accélérateurs du CERN en janvier 2022*, General Photo, 2022,
URL: https://cds.cern.ch/record/2800984 (cit. on p. 62).

[81] W. Herr and B. Muratori, *Concept of luminosity*, 2006,
URL: https://cds.cern.ch/record/941318 (cit. on p. 63).

[82] R. Bruce et al., *LHC Run 2: Results and challenges*, 2016,
URL: https://doi.org/10.18429/JACoW-HB2016-MOAM5P50 (cit. on p. 64).

[83] R. Alemany-Fernandez et al.,
*Operation and Configuration of the LHC in Run 1*,
CERN-ACC-NOTE-2013-0041, 2013,
URL: https://cds.cern.ch/record/1631030 (cit. on p. 64).

[84] S. Fartoukh et al.,
*LHC Configuration and Operational Scenario for Run 3*,
CERN-ACC-2021-0007, 2021,
URL: https://cds.cern.ch/record/2790409 (cit. on p. 64).

[85] ATLAS Collaboration, *ATLAS Public Luminosity plots*, 2022,
URL: https://twiki.cern.ch/twiki/bin/view/AtlasPublic/LuminosityPublicResultsRun2 (cit. on p. 64).

[86] ATLAS Collaboration,
*The ATLAS Experiment at the CERN Large Hadron Collider*,
JINST **3** (2008) S08003, ISSN: 1748-0221 (cit. on pp. 65, 72, 74, 76, 77).

[87] ATLAS Collaboration,
*The ATLAS Inner Detector commissioning and calibration*,
Eur. Phys. J. C **70** (2010) 787, ISSN: 1434-6052 (cit. on pp. 67, 68).

[88] ATLAS Collaboration, *Track Reconstruction Performance of the ATLAS Inner Detector at $\sqrt{s} = 13$ TeV*, ATL-PHYS-PUB-2015-018, 2015,
URL: https://cds.cern.ch/record/2037683 (cit. on p. 69).

[89] G. Hallewel and N. Wermes,
*ATLAS pixel detector : Technical Design Report*, ATLAS-TDR-11, 1998,
URL: https://cds.cern.ch/record/381263 (cit. on p. 69).

[90] M. Capeans et al., *ATLAS Insertable B-Layer Technical Design Report*,
ATLAS-TDR-19, 2010, URL: https://cds.cern.ch/record/1291633
(cit. on p. 69).

[91] ATLAS Collaboration,
*Performance of the ATLAS trigger system in 2015*,
Eur. Phys. J. C **77** (2017) 317, ISSN: 1434-6052 (cit. on pp. 78, 79).

[92] ATLAS Collaboration, *Luminosity determination in pp collisions at $\sqrt{s} = 13$ TeV using the ATLAS detector at the LHC*,
ATLAS-CONF-2019-021, 2019,
URL: https://cds.cern.ch/record/2677054 (cit. on p. 80).

[93] V. Cindro et al., *The ATLAS Beam Conditions Monitor*,
JINST **3** (2008) P02004, ISSN: 1748-0221 (cit. on p. 80).

[94] P. Jenni, M. Nordberg, M. Nessi, and K. Jon-And, *ATLAS Forward Detectors for Measurement of Elastic Scattering and Luminosity*,
CERN-LHCC-2008-004; ATLAS-TDR-18, 2008,
URL: https://cds.cern.ch/record/1095847 (cit. on pp. 81, 100).

[95] A. Sopczak, *MPX Detectors as LHC Luminosity Monitor*,
IEEE Trans. Nucl. Sci. **62** (2015) 3225, ISSN: 1558-1578 (cit. on p. 81).

[96] S. van der Meer, *Calibration of the effective beam height in the ISR*, 1968,
URL: https://cds.cern.ch/record/296752 (cit. on p. 81).

[97] A. Sivolella et al., *Tile-in-ONE: A web platform which integrates Tile Calorimeter data quality and calibration assessment*,
J. Phys. Conf. Ser. **664** (2015) 052034, ISSN: 1742-6588 (cit. on p. 83).

[98] ATLAS Collaboration, *Technical Design Report for the Phase-II Upgrade of the ATLAS Tile Calorimeter*,
CERN-LHCC-2017-019; ATLAS-TDR-028, 2017,
URL: https://cds.cern.ch/record/2285583
(cit. on pp. 83–85, 87, 89, 90, 100).

[99] P. Adragna et al.,
*Testbeam studies of production modules of the ATLAS Tile Calorimeter*,
Nucl. Instrum. Methods A **606** (2009) 362, ISSN: 0168-9002
(cit. on pp. 84, 92, 95, 97).

[100] ATLAS Collaboration, *The HL-LHC project*, 2022,
URL: `https://hilumilhc.web.cern.ch/content/hl-lhc-project`
(cit. on p. 86).

[101] ATLAS and CMS Collaborations, *Snowmass White Paper Contribution: Physics with the Phase-2 ATLAS and CMS Detectors*,
ATL-PHYS-PUB-2022-018, 2022,
URL: `https://cds.cern.ch/record/2805993` (cit. on p. 86).

[102] F. C. Argos, B. A. Valero, and A. C. Duato,
*Development of the PreProcessor Modules for the Upgrade of the ATLAS Tile Calorimeter Towards the High-Luminosity LHC*,
ATL-TILECAL-PROC-2022-011, 2022,
URL: `https://cds.cern.ch/record/2824907` (cit. on p. 90).

[103] T. Zenis, *Upgrade of ATLAS Hadronic Tile Calorimeter for the High Luminosity LHC*, ATL-TILECAL-PROC-2022-008, 2022,
URL: `https://cds.cern.ch/record/2824224` (cit. on p. 90).

[104] ATLAS Collaboration, *TileCalPhase2 Prevessin Setup (Fall 2018) TWiki*, 2022, URL: `https://twiki.cern.ch/twiki/bin/view/Atlas/TileCalPhase2PrevessinSetupFall2018` (cit. on p. 91).

[105] ATLAS Collaboration,
*Readiness of the ATLAS Tile Calorimeter for LHC collisions*,
Eur. Phys. J. C **70** (2010) 1193, ISSN: 1434-6052 (cit. on p. 95).

[106] I. Georgescu, *Simulating parton showers*, Nat. Rev. Phys. **3** (2021) 73, ISSN: 2522-5820 (cit. on p. 107).

[107] J. C. Collins and D. E. Soper, *The Theorems of Perturbative QCD*,
Annu. Rev. Nucl. Part. Sci. **37** (1987) 383, ISSN: 0163-8998
(cit. on p. 108).

[108] R. D. Ball et al., *Parton distributions from high-precision collider data*,
Eur. Phys. J. C **77** (2017) 663, ISSN: 1434-6052 (cit. on p. 109).

[109] G. Altarelli and G. Parisi, *Asymptotic freedom in parton language*,
Nucl. Phys. B **126** (1977) 298, ISSN: 0550-3213 (cit. on p. 109).

[110] X. Artru and G. Mennessier, *String model and multiproduction*, Nucl. Phys. B **70** (1974) 93, ISSN: 0550-3213 (cit. on p. 112).

[111] B. R. Webber, *A QCD model for jet fragmentation including soft gluon interference*, Nucl. Phys. B **238** (1984) 492, ISSN: 0550-3213 (cit. on p. 112).

[112] G. Marchesini and B. R. Webber, *Monte Carlo simulation of general hard processes with coherent QCD radiation*, Nucl. Phys. B **310** (1988) 461, ISSN: 0550-3213 (cit. on p. 112).

[113] B. R. Webber, *Fragmentation and hadronization*, Int. J. Mod. Phys. A **15** (2000) 577, ISSN: 0217-751X (cit. on p. 112).

[114] D. Amati and G. Veneziano, *Preconfinement as a property of perturbative QCD*, Phys. Lett. B **83** (1979) 87, ISSN: 0370-2693 (cit. on p. 113).

[115] T. Sjostrand, S. Mrenna, and P. Skands, *PYTHIA 6.4 physics and manual*, JHEP **05** (2006) 026, ISSN: 1126-6708 (cit. on p. 114).

[116] T. Sjöstrand et al., *An introduction to PYTHIA 8.2*, Comput. Phys. Commun. **191** (2015) 159, ISSN: 0010-4655 (cit. on p. 114).

[117] J. Bellm et al., *Herwig 7.0/Herwig++ 3.0 release note*, Eur. Phys. J. C **76** (2016) 196, ISSN: 1434-6052 (cit. on pp. 114, 156).

[118] T. Gleisberg et al., *Event generation with SHERPA 1.1*, JHEP **02** (2009) 007, ISSN: 1029-8479 (cit. on p. 115).

[119] S. Schumann and F. Krauss, *A parton shower algorithm based on Catani-Seymour dipole factorisation*, JHEP **03** (2008) 038, ISSN: 1029-8479 (cit. on p. 115).

[120] S. Höche, F. Krauss, S. Schumann, and F. Siegert, *QCD matrix elements and truncated showers*, JHEP **05** (2009) 053, ISSN: 1029-8479 (cit. on p. 115).

[121] S. Alioli, P. Nason, C. Oleari, and E. Re, *A general framework for implementing NLO calculations in shower Monte Carlo programs: the POWHEG BOX*, JHEP **06** (2010) 43, ISSN: 1029-8479 (cit. on p. 115).

[122] E. Re, *Single-top Wt-channel production matched with parton showers using the POWHEG method*, Eur. Phys. J. C **71** (2011) 1547, ISSN: 1434-6052 (cit. on p. 115).

[123] J. Alwall, M. Herquet, F. Maltoni, O. Mattelaer, and T. Stelzer, *MadGraph 5: going beyond*, JHEP **06** (2011) 128, ISSN: 1029-8479 (cit. on p. 115).

[124] J. Alwall et al., *The automated computation of tree-level and next-to-leading order differential cross sections, and their matching to parton shower simulations*, JHEP **07** (2014) 79, ISSN: 1029-8479 (cit. on pp. 115, 160).

[125] S. Frixione and B. R. Webber, *Matching NLO QCD computations and parton shower simulations*, JHEP **06** (2002) 029, ISSN: 1029-8479 (cit. on p. 115).

[126] D. J. Lange, *The EvtGen particle decay simulation package*, Nucl. Instrum. Methods A **462** (2001) 152, ISSN: 0168-9002 (cit. on pp. 115, 159).

[127] P. Artoisenet, R. Frederix, O. Mattelaer, and R. Rietkerk, *Automatic spin-entangled decays of heavy resonances in Monte Carlo simulations*, JHEP **03** (2013) 15, ISSN: 1029-8479 (cit. on pp. 116, 159).

[128] S. Agostinelli et al., *Geant4—a simulation toolkit*, Nucl. Instrum. Methods A **506** (2003) 250, ISSN: 0168-9002 (cit. on p. 116).

[129] W. Lukas, *Fast Simulation for ATLAS: Atlfast-II and ISF*, J. Phys. Conf. Ser. **396** (2012) 022031, ISSN: 1742-6588 (cit. on p. 117).

[130] ATLAS Collaboration, *The ATLAS Simulation Infrastructure*, Eur. Phys. J. C **70** (2010) 823, ISSN: 1434-6052 (cit. on p. 117).

[131] J. Pequenao and P. Schaffner, *How ATLAS detects particles: diagram of particle paths in the detector*, 2013, URL: https://cds.cern.ch/record/1505342 (cit. on p. 119).

[132] J. Pequenao and P. Schaffner, *Tracking tutorial*, 2018, URL: https://indico.cern.ch/event/34087/contributions/802944/attachments/669263/919934/IDTracking_A_Salzburger.pdf (cit. on p. 121).

[133] R. Frühwirth, *Application of Kalman filtering to track and vertex fitting*, Nucl. Instrum. Methods A **262** (1987) 444, ISSN: 0168-9002 (cit. on p. 121).

[134] ATLAS Collaboration, *Early Inner Detector Tracking Performance in the 2015 Data at $\sqrt{s} = 13$ TeV*, ATL-PHYS-PUB-2015-051, 2015, URL: https://cds.cern.ch/record/2110140 (cit. on pp. 121, 122).

[135] ATLAS Collaboration, *Reconstruction of primary vertices at the ATLAS experiment in Run 1 proton–proton collisions at the LHC*, Eur. Phys. J. C **77** (2017) 332, ISSN: 1434-6052 (cit. on p. 122).

[136] ATLAS Collaboration, *Primary vertex reconstruction at the ATLAS experiment*, J. Phys. Conf. Ser. **898** (2017) 042056, ISSN: 1742-6588 (cit. on p. 122).

[137] W. Lampl et al., *Calorimeter Clustering Algorithms : Description and Performance*, ATL-LARG-PUB-2008-002; ATL-COM-LARG-2008-003, 2008, URL: https://cds.cern.ch/record/1099735 (cit. on pp. 123, 132).

[138] ATLAS Collaboration, *Improved electron reconstruction in ATLAS using the Gaussian Sum Filter-based model for bremsstrahlung*, ATLAS-CONF-2012-047, 2012, URL: https://cds.cern.ch/record/1449796 (cit. on p. 123).

[139] ATLAS Collaboration, *Electron reconstruction and identification in the ATLAS experiment using the 2015 and 2016 LHC proton–proton collision data at $\sqrt{s} = 13$ TeV*, Eur. Phys. J. C **79** (2019) 639, ISSN: 1434-6052 (cit. on pp. 123, 124, 127).

[140] ATLAS Collaboration, *Electron and photon performance measurements with the ATLAS detector using the 2015–2017 LHC proton-proton collision data*, JINST **14** (2019) P12006, ISSN: 1748-0221 (cit. on p. 125).

[141] ATLAS Collaboration, *Electron and photon energy calibration with the ATLAS detector using LHC Run 1 data*, Eur. Phys. J. C **74** (2014) 3071, ISSN: 1434-6052 (cit. on p. 126).

[142] ATLAS Collaboration, *Electron and photon energy calibration with the ATLAS detector using 2015-2016 LHC proton-proton collision data*, JINST **14** (2019) P03017, ISSN: 1748-0221 (cit. on p. 126).

[143] ATLAS Collaboration, *Electron and photon energy calibration with the ATLAS detector using data collected in 2015 at $\sqrt{s} = 13$ TeV*, ATL-PHYS-PUB-2016-015, 2016, URL: https://cds.cern.ch/record/2203514 (cit. on p. 127).

[144] ATLAS Collaboration, *Muon reconstruction and identification efficiency in ATLAS using the full Run 2 pp collision data set at $\sqrt{s} = 13$ TeV*, Eur. Phys. J. C **81** (2021) 578, ISSN: 1434-6052 (cit. on pp. 130, 131).

[145] ATLAS Collaboration, *Topological cell clustering in the ATLAS calorimeters and its performance in LHC Run 1*, Eur. Phys. J. C **77** (2017) 490, ISSN: 1434-6052 (cit. on p. 132).

[146] Y. L. Dokshitzer, G. D. Leder, S. Moretti, and B. R. Webber, *Better jet clustering algorithms*, JHEP **08** (1997) 001, ISSN: 1029-8479 (cit. on p. 132).

[147] S. D. Ellis and D. E. Soper, *Successive combination jet algorithm for hadron collisions*, Phys. Rev. D **48** (7 1993) 3160 (cit. on p. 132).

[148] M. Cacciari, G. P. Salam, and G. Soyez, *The anti-kt jet clustering algorithm*, JHEP **04** (2008) 063, ISSN: 1029-8479 (cit. on pp. 132, 133).

[149] ATLAS Collaboration, *Jet reconstruction and performance using particle flow with the ATLAS Detector*, Eur. Phys. J. C **77** (2017) 466, ISSN: 1434-6052 (cit. on p. 134).

[150] B. Nachman, P. Nef, A. Schwartzman, M. Swiatlowski, and C. Wanotayaroj, *Jets from jets: re-clustering as a tool for large radius jet reconstruction and grooming at the LHC*, JHEP **02** (2015) 75, ISSN: 1029-8479 (cit. on pp. 134, 135).

[151] ATLAS Collaboration, *Jet reclustering and close-by effects in ATLAS Run 2*, ATLAS-CONF-2017-062, 2017, URL: https://cds.cern.ch/record/2275649 (cit. on p. 134).

[152] ATLAS Collaboration, *Jet energy scale and resolution measured in proton–proton collisions at $\sqrt{s} = 13$ TeV with the ATLAS detector*, Eur. Phys. J. C **81** (2021) 689, ISSN: 1434-6052 (cit. on pp. 136–139).

[153] ATLAS Collaboration, *Jet global sequential corrections with the ATLAS detector in proton–proton collisions at $\sqrt{s} = 8$ TeV*, ATLAS-CONF-2015-002, 2015, URL: https://cds.cern.ch/record/2001682 (cit. on p. 137).

[154] ATLAS Collaboration, *Identification and rejection of pile-up jets at high pseudorapidity with the ATLAS detector*, Eur. Phys. J. C **77** (2017) 580, ISSN: 1434-6052 (cit. on p. 140).

[155] ATLAS Collaboration, *Tagging and suppression of pileup jets*, ATL-PHYS-PUB-2014-001, 2014, URL: https://cds.cern.ch/record/1643929 (cit. on p. 140).

[156] ATLAS Collaboration, *Optimisation and performance studies of the ATLAS b-tagging algorithms for the 2017-18 LHC run*, ATL-PHYS-PUB-2017-013, 2017, URL: https://cds.cern.ch/record/2273281 (cit. on p. 142).

[157] ATLAS Collaboration, *Identification of Jets Containing b-Hadrons with Recurrent Neural Networks at the ATLAS Experiment*, ATL-PHYS-PUB-2017-003, 2017, URL: https://cds.cern.ch/record/2255226 (cit. on pp. 142, 143).

[158] G. Piacquadio and C. Weiser, *A new inclusive secondary vertex algorithm for b-jet tagging in ATLAS*, J. Phys. Conf. Ser. **119** (2008) 032032, ISSN: 1742-6596 (cit. on p. 142).

[159] ATLAS Collaboration, *Expected performance of the ATLAS b-tagging algorithms in Run-2*, ATL-PHYS-PUB-2015-022, 2015, URL: https://cds.cern.ch/record/2037697 (cit. on p. 143).

[160] ATLAS Collaboration, *Flavour-tagging efficiency corrections for the 2019 ATLAS PFlow jet b-taggers with the full LHC Run II dataset*, FTAG-2020-001, 2020, URL: http://atlas.web.cern.ch/Atlas/GROUPS/PHYSICS/PLOTS/FTAG-2020-001 (cit. on p. 144).

[161] ATLAS Collaboration, *ATLAS flavour-tagging algorithms for the LHC Run 2 pp collision dataset*, CERN-EP-2022-226; FTAG-2019-07, 2019, arXiv: 2211.16345v1 [physics.data-an], URL: https://cds.cern.ch/record/2842028 (cit. on pp. 143, 144).

[162] ATLAS Collaboration, *ATLAS b-jet identification performance and efficiency measurement with $t\bar{t}$ events in pp collisions at $\sqrt{s} = 13$ TeV*, Eur. Phys. J. C **79** (2019) 970, ISSN: 1434-6052 (cit. on pp. 145, 146).

[163] ATLAS Collaboration, *Measurement of b-tagging efficiency of c-jets in $t\bar{t}$ events using a likelihood approach with the ATLAS detector*, ATLAS-CONF-2018-001, 2018, URL: https://cds.cern.ch/record/2306649 (cit. on p. 146).

[164] ATLAS Collaboration, *Calibration of light-flavour b-jet mistagging rates using ATLAS proton–proton collision data at $\sqrt{s} = 13$ TeV*, ATLAS-CONF-2018-006, 2018, URL: https://cds.cern.ch/record/2314418 (cit. on p. 146).

[165] ATLAS Collaboration, *Identification of hadronic tau lepton decays using neural networks in the ATLAS experiment*, ATL-PHYS-PUB-2019-033, 2019, URL: https://cds.cern.ch/record/2688062 (cit. on pp. 147–150).

[166] ATLAS Collaboration, *Identification and energy calibration of hadronically decaying tau leptons with the ATLAS experiment in pp collisions at $\sqrt{s} = 8$ TeV*, Eur. Phys. J. C **75** (2015) 303, ISSN: 1434-6052 (cit. on p. 147).

[167] ATLAS Collaboration, *Reconstruction, Energy Calibration, and Identification of Hadronically Decaying Tau Leptons in the ATLAS Experiment for Run-2 of the LHC*, ATL-PHYS-PUB-2015-045, 2015, URL: https://cds.cern.ch/record/2064383 (cit. on pp. 148, 150, 152).

[168] G. Pospelov and (for the Atlas Hadronic Calibration Group), *The overview of the ATLAS local hadronic calibration*, J. Phys. Conf. Ser. **160** (2009) 012079, ISSN: 1742-6596 (cit. on p. 150).

[169] ATLAS Collaboration, *Reconstruction of hadronic decay products of tau leptons with the ATLAS experiment*, Eur. Phys. J. C **76** (2016) 295, ISSN: 1434-6052 (cit. on p. 151).

[170] ATLAS Collaboration, *Measurement of the tau lepton reconstruction and identification performance in the ATLAS experiment using pp collisions at $\sqrt{s} = 13$ TeV*, ATLAS-CONF-2017-029, 2017, URL: https://cds.cern.ch/record/2261772 (cit. on p. 152).

[171] T. Sjöstrand, S. Mrenna, and P. Skands,
*A brief introduction to PYTHIA 8.1*,
Comput. Phys. Commun. **178** (2008) 852, ISSN: 0010-4655
(cit. on p. 155).

[172] ATLAS Collaboration, *Further ATLAS tunes of Pythia6 and Pythia8*,
ATL-PHYS-PUB-2011-014, 2011,
URL: `https://cds.cern.ch/record/1400677` (cit. on p. 155).

[173] ATLAS Collaboration, *Measurements of the inclusive and differential production cross-sections of a top-quark-antiquark pair in association with a Z boson at* $\sqrt{s} = 13$ *TeV with the ATLAS detector*,
ATLAS-CONF-2020-028, 2020,
URL: `https://cds.cern.ch/record/2725734` (cit. on p. 156).

[174] M. L. Mangano, M. Moretti, F. Piccinini, and M. Treccani,
*Matching matrix elements and shower evolution for top-pair*,
JHEP **01** (2007) 013, ISSN: 1126-6708 (cit. on p. 158).

[175] S. Catani, F. Krauss, B. R. Webber, and R. Kuhn,
*QCD Matrix Elements + Parton Showers*, JHEP **11** (2002) 063,
ISSN: 1126-6708 (cit. on p. 158).

[176] F. Cascioli, P. Maierhöfer, and S. Pozzorini,
*Scattering Amplitudes with Open Loops*,
Phys. Rev. Lett. **108** (2012) 111601, ISSN: 1079-7114 (cit. on p. 158).

[177] T. Gleisberg and S. Höche, *Comix, a new matrix element generator*,
JHEP **12** (2008) 039, ISSN: 1126-6708 (cit. on p. 158).

[178] M. Cacciari, M. Czakon, M. Mangano, A. Mitov, and P. Nason,
*Top-pair production at hadron colliders with next-to-next-to-leading logarithmic soft-gluon resummation*, Phys. Lett. B **710** (2012) 612,
ISSN: 0370-2693 (cit. on p. 159).

[179] P. Bärnreuther, M. Czakon, and A. Mitov,
*Percent-Level-Precision Physics at the Tevatron: Next-to-Next-to-Leading Order QCD Corrections to* $q\overline{q} \to t\bar{t} + X$,
Phys. Rev. Lett. **109** (2012) 132001, ISSN: 1079-7114 (cit. on p. 159).

[180] M. Czakon and A. Mitov, *NNLO corrections to top pair production at hadron colliders: the quark-gluon reaction*, JHEP **01** (2013) 80,
ISSN: 1029-8479 (cit. on p. 159).

[181] M. Czakon and A. Mitov, *NNLO corrections to top-pair production at hadron colliders: the all-fermionic scattering channels*, JHEP **12** (2012) 54, ISSN: 1029-8479 (cit. on p. 159).

[182] M. Czakon, P. Fiedler, and A. Mitov, *Total Top-Quark Pair-Production Cross Section at Hadron Colliders Through $\mathcal{O}(\alpha_S^4)$*, Phys. Rev. Lett. **110** (2013) 252004, ISSN: 1079-7114 (cit. on p. 159).

[183] A. Djouadi, J. Kalinowski, and M. Spira, *HDECAY: a program for Higgs boson decays in the Standard Model and its supersymmetric extension*, Comput. Phys. Commun. **108** (1998) 56, ISSN: 0010-4655 (cit. on p. 160).

[184] W. Beenakker et al., *Higgs Radiation Off Top Quarks at the Tevatron and the LHC*, Phys. Rev. Lett. **87** (2001) 201805, ISSN: 1079-7114 (cit. on p. 160).

[185] W. Beenakker et al., *NLO QCD corrections to $t\bar{t}H$ production in hadron collisions*, Nucl. Phys. B **653** (2003) 151, ISSN: 0550-3213 (cit. on p. 160).

[186] S. Dawson, L. H. Orr, L. Reina, and D. Wackeroth, *Next-to-leading order QCD corrections to $p\,\vec{p}\,t\bar{t}h$ at the CERN Large Hadron Collider*, Phys. Rev. D **67** (2003) 071503, ISSN: 2470-0029 (cit. on p. 160).

[187] S. Dawson, C. Jackson, L. H. Orr, L. Reina, and D. Wackeroth, *Associated Higgs boson production with top quarks at the CERN Large Hadron Collider: NLO QCD corrections*, Phys. Rev. D **68** (2003) 034022, ISSN: 2470-0029 (cit. on p. 160).

[188] S. Frixione, V. Hirschi, D. Pagani, H.-S. Shao, and M. Zaro, *Weak corrections to Higgs hadroproduction in association with a top-quark pair*, JHEP **09** (2014) 65, ISSN: 1029-8479 (cit. on p. 160).

[189] S. Frixione, V. Hirschi, D. Pagani, H.-S. Shao, and M. Zaro, *Electroweak and QCD corrections to top-pair hadroproduction in association with heavy bosons*, JHEP **06** (2015) 184, ISSN: 1029-8479 (cit. on p. 160).

[190] Y. Zhang, W.-G. Ma, R.-Y. Zhang, C. Chen, and L. Guo, *QCD NLO and EW NLO corrections to $tt\bar{H}$ production with top quark decays at hadron collider*, Phys. Lett. B **738** (2014) 1, ISSN: 0370-2693 (cit. on p. 160).

[191] S. Frixione, E. Laenen, P. Motylinski, and B. R. Webber, *Single-top production in MC@NLO*, JHEP **03** (2006) 092, ISSN: 1126-6708 (cit. on p. 161).

[192] $t\bar{t}W/t\bar{t}H$ ML analysis team, *Git repository of GroupFrameWork 1*, 2018, URL: `https://gitlab.cern.ch/atlasHTop/ttHMultiAna` (cit. on p. 162).

[193] $t\bar{t}W/t\bar{t}H$ ML analysis team, *Git repository of GroupFrameWork 2*, 2018, URL: `https://gitlab.cern.ch/atlasHTop/ttHMultiGFW2` (cit. on p. 162).

[194] *TRexFitter framework twiki page*, URL: `https://twiki.cern.ch/twiki/bin/view/AtlasProtected/TtHFitter` (cit. on p. 162).

[195] *TRexFitter framework gitlab project*, URL: `https://gitlab.cern.ch/TRExStats/TRExFitter/` (cit. on p. 162).

[196] ATLAS Collaboration, *Performance of the ATLAS muon triggers in Run 2*, JINST **15** (2020) P09015 (cit. on p. 163).

[197] ATLAS Collaboration, *Performance of electron and photon triggers in ATLAS during LHC Run 2*, Eur. Phys. J. C **80** (2020) 47 (cit. on p. 163).

[198] ATLAS Collaboration, *Operation of the ATLAS trigger system in Run 2*, JINST **15** (2020) P10004 (cit. on p. 163).

[199] ATLAS Collaboration, *Search for new phenomena with top quark pairs in final states with one lepton, jets, and missing transverse momentum in pp collisions at* $\sqrt{s} = 13$ *TeV with the ATLAS detector*, JHEP **04** (2021) 174, ISSN: 1029-8479 (cit. on p. 166).

[200] CMS Collaboration, *Search for third-generation scalar leptoquarks decaying to a top quark and a lepton at* $\sqrt{s} = 13$ *TeV*, Eur. Phys. J. C **78** (2018) 707, ISSN: 1434-6052 (cit. on p. 170).

[201] ATLAS Collaboration, *Search for pair production of scalar leptoquarks decaying into first- or second-generation leptons and top quarks in proton–proton collisions at* $\sqrt{s} = 13$ *TeV with the ATLAS detector*, Eur. Phys. J. C **81** (2021) 313 (cit. on pp. 170, 279).

[202] T. Junk, *Confidence Level Computation for Combining Searches with Small Statistics*, (1999), arXiv: 9902006 [hep-ex] (cit. on p. 180).

[203] G. Cowan, K. Cranmer, E. Gross, and O. Vitells, *Asymptotic formulae for likelihood-based tests of new physics*, Eur. Phys. J. C **71** (2011) 1554, ISSN: 1434-6052 (cit. on p. 180).

[204] ATLAS Collaboration, *Search for supersymmetry at $\sqrt{s} = 13$ TeV in final states with jets and two same-sign leptons or three leptons with the ATLAS detector*, Eur. Phys. J. C **76** (2016) 259 (cit. on p. 182).

[205] ATLAS Collaboration, *Search for supersymmetry in final states with two same-sign or three leptons and jets using 36 $fb^{-1}$ of $\sqrt{s} = 13$ TeV pp collision data with the ATLAS detector*, JHEP **09** (2017) 084 (cit. on p. 182).

[206] ATLAS Collaboration, *Search for squarks and gluinos in final states with same-sign leptons and jets using 139 $fb^{-1}$ of data collected with the ATLAS detector*, JHEP **06** (2020) 046 (cit. on p. 182).

[207] CMS Collaboration, *Search for physics beyond the standard model in events with jets and two same-sign or at least three charged leptons in proton–proton collisions at $\sqrt{s} = 13$ TeV*, Eur. Phys. J. C **80** (2020) 752 (cit. on p. 182).

[208] ATLAS Collaboration, *Analysis of $t\bar{t}H$ and $t\bar{t}W$ production in multilepton final states with the ATLAS detector*, ATLAS-CONF-2019-045, 2019, URL: https://cds.cern.ch/record/2693930 (cit. on pp. 182, 193, 195, 196, 243, 268, 270).

[209] ATLAS Collaboration, *Evidence for $t\bar{t}t\bar{t}$ production in the multilepton final state in proton–proton collisions at $\sqrt{s} = 13$ TeV with the ATLAS detector*, Eur. Phys. J. C **80** (2020) 1085, ISSN: 1434-6052 (cit. on pp. 182, 193, 195, 270).

[210] CMS Collaboration, *Measurement of the cross section for top quark pair production in association with a W or Z boson in proton–proton collisions at $\sqrt{s} = 13$ TeV*, JHEP **08** (2018) 011 (cit. on p. 183).

[211] ATLAS Collaboration, *Measurement of the $t\bar{t}Z$ and $t\bar{t}W$ production cross sections in multilepton final states using 3.2 $fb^{-1}$ of pp collisions at $\sqrt{s} = 13$ TeV with the ATLAS detector*, Eur. Phys. J. C **77** (2017) 40 (cit. on p. 183).

[212] ATLAS Collaboration, *Measurement of the $t\bar{t}Z$ and $t\bar{t}W$ cross sections in proton-proton collisions at $\sqrt{s} = 13$ TeV with the ATLAS detector*, Phys. Rev. D **99** (2019) 072009 (cit. on p. 183).

[213] CMS Collaboration,
*Measurement of the cross section of top quark-antiquark pair production in association with a W boson in proton-proton collisions at $\sqrt{s} = 13$ TeV*, (2022), arXiv: 2208.06485 [hep-ex],
URL: https://cds.cern.ch/record/2824578 (cit. on p. 183).

[214] ATLAS Collaboration, *Measurement of the Higgs boson production cross section in association with a vector boson and decaying into $WW^*$ with the ATLAS detector at $\sqrt{s} = 13$ TeV*, ATL-COM-PHYS-2021-206, 2021,
URL: https://cds.cern.ch/record/2765898 (cit. on pp. 194, 195).

[215] ATLAS Collaboration,
*Measurement of the total and differential cross-sections of $t\bar{t}W$ production in pp collisions at 13 TeV with the ATLAS detector*,
ATLAS-CONF-2023-019, 2023,
URL: http://cds.cern.ch/record/2855337 (cit. on pp. 212–214).

[216] G. Bevilacqua et al., *NLO QCD corrections to off-shell production at the LHC: correlations and asymmetries*, Eur. Phys. J. C **81** (2021) 675,
ISSN: 1434-6052 (cit. on pp. 213, 214).

[217] G. Choudalakis, *Unfolding in ATLAS*, (2011),
arXiv: 1104.2962 [hep-ex] (cit. on p. 216).

[218] A. Höcker and V. Kartvelishvili, *SVD approach to data unfolding*,
Nucl. Instrum. Methods A **372** (1996) 469, ISSN: 0168-9002
(cit. on p. 216).

[219] L. B. Lucy,
*An iterative technique for the rectification of observed distributions*,
Astron. J. **79** (1974) 745, ISSN: 0004-6256 (cit. on p. 216).

[220] W. H. Richardson,
*Bayesian-Based Iterative Method of Image Restoration**,
JOSA **62** (1972) 55 (cit. on p. 216).

[221] G. D'Agostini,
*A multidimensional unfolding method based on Bayes' theorem*,
Nucl. Instrum. Methods A **362** (1995) 487, ISSN: 0168-9002
(cit. on p. 216).

[222] G. Choudalakis, *Fully Bayesian Unfolding*, (2012),
arXiv: `1201.4612 [hep-ex]` (cit. on p. 216).

[223] A. Andreassen, P. T. Komiske, E. M. Metodiev, B. Nachman, and
J. Thaler, *OmniFold: A Method to Simultaneously Unfold All Observables*,
Phys. Rev. Lett. **124** (2020) 182001, ISSN: 1079-7114 (cit. on p. 216).

[224] B. Bullard, *UnfoldingDemo*, 2020, URL:
`https://gitlab.cern.ch/bbullard/UnfoldingDemo/-/tree/master`
(cit. on p. 221).

[225] ATLAS Collaboration, *Searches for third-generation scalar leptoquarks in* $\sqrt{s} = 13$ *TeV pp collisions with the ATLAS detector*,
JHEP **06** (2019) 144, ISSN: 1029-8479 (cit. on p. 245).

[226] ATLAS Collaboration, *Search for pair production of third-generation scalar leptoquarks decaying into a top quark and a* $\tau$*-lepton in pp collisions at* $\sqrt{s} = 13$ *TeV with the ATLAS detector*, JHEP **06** (2021) 179,
ISSN: 1029-8479 (cit. on pp. 246–252, 254, 255, 260, 262–266, 270–277).

[227] J. Butterworth et al., *PDF4LHC recommendations for LHC Run II*,
J. Phys. G **43** (2016) 023001 (cit. on p. 257).

[228] ATLAS Collaboration, *Measurement of the* $t\bar{t}$ *production cross-section and lepton differential distributions in* $e\mu$ *dilepton events from pp collisions at* $\sqrt{s} = 13$ *TeV with the ATLAS detector*,
Eur. Phys. J. C **80** (2020) 528 (cit. on p. 258).

[229] ATLAS Collaboration, *Measurements of top-quark pair differential and double-differential cross-sections in the* $\ell$*+jets channel with pp collisions at* $\sqrt{s} = 13$ *TeV using the ATLAS detector*,
Eur. Phys. J. C **79** (2019) 1028 (cit. on p. 258).

[230] ATLAS Collaboration,
*Search for leptoquark pair production decaying into $t\ell^-\bar{t}\ell^+$ in multilepton final states in pp collisions at 13 TeV with the ATLAS detector*,
ATLAS-CONF-2022-052, 2022,
URL: https://cds.cern.ch/record/2816335
(cit. on pp. 279, 280, 282–284, 290, 296–303).

[231] M. Schmaltz and Y.-M. Zhong,
*The Leptoquark Hunter's Guide: Large coupling*, JHEP **01** (2019) 132
(cit. on pp. 286, 305).

[232] ATLAS Collaboration, *Search for pair-produced scalar and vector leptoquarks decaying into third-generation quarks and first- or second-generation leptons in pp collisions with the ATLAS detector*,
ATLAS-CONF-2022-009, 2022,
URL: https://cds.cern.ch/record/2805213 (cit. on p. 301).

[233] M. J. Baker, J. Fuentes-Martín, G. Isidori, and M. König,
*High-$p_T$ signatures in vector–leptoquark models*,
Eur. Phys. J. C **79** (2019) 334 (cit. on p. 305).

[234] ATLAS Collaboration,
*Summary Plots from ATLAS Searches for Pair-Produced Leptoquarks*,
ATL-PHYS-PUB-2022-012, 2022,
URL: https://cds.cern.ch/record/2805984 (cit. on p. 306).

[235] L. Heinrich, M. Feickert, and G. Stark, *pyhf: v0.6.3*,
https://github.com/scikit-hep/pyhf/releases/tag/v0.6.3, 2020,
URL: https://doi.org/10.5281/zenodo.1169739 (cit. on p. 306).

[236] ATLAS Collaboration, *Building and steering template fits with cabinetry*,
2021, URL: https://doi.org/10.5281/zenodo.4627038 (cit. on p. 306).

[237] ATLAS Collaboration, *Performance of 2019 recommendations of ATLAS Flavor Tagging algorithms with Variable Radius track jets*,
FTAG-2019-006, 2019, URL: http://atlas.web.cern.ch/Atlas/GROUPS/PHYSICS/PLOTS/FTAG-2019-006.